



Photoluminescence spectroscopy of crystalline semiconductors

G.D. Gilliland

Emory University, Physics Department, Atlanta, GA 30322, USA

Received 4 January 1995, accepted 1 July 1996

Abstract

The objective of this review article is to give an overview of the current state-of-the-art of photoluminescence (PL) spectroscopy as a characterization tool in the study of semiconductors. A detailed description of all of the PL spectroscopic techniques will be given together with examples from the literature of their use. These examples will be the primary tool used to convey the essential aspects and usefulness of the variety of PL techniques discussed throughout this review. The primary examples of semiconductor materials examined with these techniques will be of the prototypical direct-gap and indirect-gap semiconductors, gallium arsenide and silicon, respectively. Additionally, PL characterization of structures with lower dimensionality (quantum wells, superlattices, quantum wires, and quantum dots) will be shown. This article will not cover the history of this type of spectroscopy, inelastic light scattering, infrared spectroscopy, or reflectance, etc. The focus is intended to be experimental in nature, and will be supplemented by theory where appropriate and necessary. There are several fine review articles and books dealing with the subject of photoluminescence, and radiative recombination in general, and this article is only intended to supplement these sources © 1997 Elsevier Science S.A. All rights reserved.

Keywords: Photoluminescence; Crystallinity; Semiconductors

1. Introduction

The advent of the laser in 1960 increased the popularity of optical spectroscopy as a useful tool for the characterization of materials. This powerful source of monochromatic, coherent, pulsed or continuous wave (cw), and possibly tunable radiation has allowed spectroscopic studies of materials previously unattainable with conventional incoherent light sources. In fact, the laser is responsible for the development of the field of non-linear optics. The evolution of spectroscopic detection techniques has also been hastened by the laser since non-linear frequency mixing techniques have become useful in detecting photoexcited luminescence from materials, and ultrafast laser sources have prompted the development of fast detection electronics. Thus, as a result of the invention of the laser, spectroscopy has flourished and grown as a powerful tool for the characterization of materials and semiconductor devices. Another motivating factor in the rapid evolution of optical spectroscopy is the possible application of light emitting devices and the ever present need for new devices based upon new materials.

Photoluminescence (PL) spectroscopy is a useful technique for the study and characterization of materials and dynamical processes occurring in materials. However, PL spectroscopy, like all other experimental techniques, does not give a universal, all-encompassing view of every aspect of the properties of a particular material, or, even more specifically of the optical properties of the material. Thus, in order to obtain a complete picture of the properties and/or dynamics of a system, it may be necessary to rely upon complementary information gathered from other types of experiments. An example of this might be the use of secondary ion mass spectroscopy (SIMS) or Hall measurements together with PL measurements to characterize and quantify electrically and optically active defects or dopants in semiconductors. In this review article, the primary objective is to outline the current

state-of-the-art of PL spectroscopy relating to the characterization of properties of and processes in semiconductors, specifically the prototypical direct- and indirect-gap semiconductors, GaAs and Si, respectively, together with GaAs quantum-confined structures. Additionally, where possible, the relation and complementary nature of other experimental techniques will be shown.

1.1. What is photoluminescence spectroscopy?

The radiative emission of photons is in some ways the inverse of the absorption of photons. In an emission process an electron (or possibly a quasi-particle) occupying a higher energy state makes a quantized (i.e. discrete) transition to an empty lower-energy state. For a radiative transition the energy difference between these two states is emitted as electromagnetic radiation, i.e. photons, whereas for non-radiative transitions, this energy difference is emitted in the form of heat, i.e. phonons. This recombination is a non-equilibrium process since energy must be conserved. Considering, for simplicity, only radiative transitions, Fermi's Golden Rule states that the radiation rate is determined by the product of empty lower states (density of final states) and the density of carriers in the higher-energy state. This is similar to the rate of absorption. However, there are some important differences between absorption and emission in this simplistic picture. First, absorption is commonly described by the mean free path for photon decay (i.e. Beer's law), whereas emission is expressed as a rate of photon generation per unit volume. Second, absorption may involve all states in the semiconductor, typically yielding a broad spectrum. Emission processes only occur between a narrow band of states occupied by the thermalized electrons with a narrow band of empty states (containing the holes) at the top of the valence band. This commonly yields a spectrum (energy distribution of emitted photons) much narrower than that of the absorption spectrum. Lastly, Einstein's *A* and *B* coefficients governing spontaneous emission and absorption and stimulated emission, respectively, show the equivalence of absorption and stimulated emission, and, at the same time, the distinction between spontaneous emission of radiation and these other stimulated processes. The Einstein expressions also show the relationship between these processes. Since energy must be conserved, a semiconductor which emits photons must not be in equilibrium and therefore must have energy injected from an excitation source. The source of excitation allows distinctions to be made in the emission process. Excitation by an electric current (injection through a Schottky barrier or breakdown) results in electroluminescence. Electron beam excitation (with, for example, a scanning electron microscope (SEM)) results in cathodoluminescence. Mechanical excitation yields triboluminescence. Incandescence is a result of thermal excitation. Thermoluminescence is a thermal excitation process which may be a bit more complicated than incandescence. Chemiluminescence is caused by light emission during a chemical reaction. In general, light-emission processes are termed luminescence. Lastly, photoluminescence is a result of optical excitation (i.e. absorption). There are two further classifications of luminescence processes which may be made. Phosphorescence is a luminescence process which may continue for a considerable time after the cessation of the excitation source (this occurs in the phosphors of a television screen or CRT). Fluorescence, on the other hand, only occurs during the excitation. In this article, we will deal primarily with PL processes (a fluorescence process), but may briefly mention other relevant luminescence processes.

Photoluminescence from semiconductors is most commonly characterized via spectroscopic techniques. These techniques involve measuring the energy distribution of emitted photons after optical excitation. This energy distribution is then analyzed in order to determine properties of the material, including defect species, defect concentrations, possible stimulated emission, etc. This technique for material characterization has achieved significant success and popularity in this regard at least partly due to the simplicity of the technique and the absence of sample processing requirements. Despite the

power and utility of this characterization technique, PL spectroscopy, in the "garden variety" form described above, has several fundamental limitations. First, this cw spectroscopy only determines the energy eigenvalues of the system ($E = \langle \Psi_f | H | \Psi_i \rangle$), and does not yield any direct information regarding the eigenstates or wavefunctions. Second, it does not provide any information regarding the temporal kinetics, transport dynamics, or spatial distribution of the light emission. These limitations are especially important since most semiconductor science and technology deals with either high-speed devices, nanostructured devices, or transport devices. For these reasons considerable effort has been expended with the goal of expanding the capabilities of this conventional PL spectroscopy. Time-resolved PL spectroscopy, spatially-resolved PL spectroscopy, time- and spatially-resolved PL spectroscopy, and near-field scanning optical microscopy are examples of techniques developed in response to these deficiencies. Time-resolved PL spectroscopy may provide information regarding recombination kinetics, surface recombination, and transport dynamics, etc. Moreover, this technique is sensitive to the wavefunction, ($\tau^{-1} \propto |\langle \Psi_f | \Psi_i \rangle|^2$). Spatially-resolved PL spectroscopy is sensitive to sample inhomogeneities and transport. Time- and spatially-resolved PL spectroscopy is especially sensitive to carrier transport. Lastly, the recently developed technique of near-field scanning optical microscopy has been utilized to measure surface topology of semiconductor nanostructures. In this article each of these extensions to the basic PL spectroscopic technique will be discussed.

1.2. How is photoluminescence spectroscopy used to characterize semiconductors?

Photoluminescence spectroscopy has been widely recognized for many years as a useful tool for characterizing the quality of semiconductor materials as well as for elucidating the physics which may accompany radiative recombination. Characterization studies of semiconductors commonly quote results of X-ray diffraction, reflection high-energy electron diffraction (RHEED) oscillation, transmission electron microscopy (TEM), SEM, Hall, absorption, and PL measurements. Each of these characterization techniques is useful in determining specific aspects concerning the material, and no one of them alone is capable of fully characterizing all relevant properties of a semiconductor. In this regard, PL is useful in quantifying: (1) optical emission efficiencies, (2) composition of the material (i.e. alloy composition), (3) impurity content, and (4) layer thicknesses (i.e. quantum well thicknesses), etc.

In order to demonstrate the utility of PL for assessing these properties and for studying the physics of semiconductors, we will initially review the basic semiconductor physics relevant to recombination processes. We will first review semiconductor band structure, free-carrier properties, quasi- and many-particle states, impurities, recombination processes, and the properties of nanostructures as these properties relate to the emission process.

1.2.1. Band structure

The valence electrons of atomic species are responsible for the well-known energy levels and transitions of gaseous elements. These free-ion energy levels become significantly altered when a large number of atoms are assembled to form a solid. The Pauli exclusion principle alters the distribution of the free-ion energy levels into a series of bands. This new distribution of energy levels depends strongly upon the interatomic distance, and is thus anisotropic. Every semiconductor is fully and uniquely characterized by this band structure. In examining recombination processes in semiconductors it is more convenient and useful to envision this band structure in reciprocal or momentum space rather than real space. At zero temperature, electrons occupy only the lower energy bands, and the highest such occupied band is called the valence band. The next highest energy band is termed the conduction

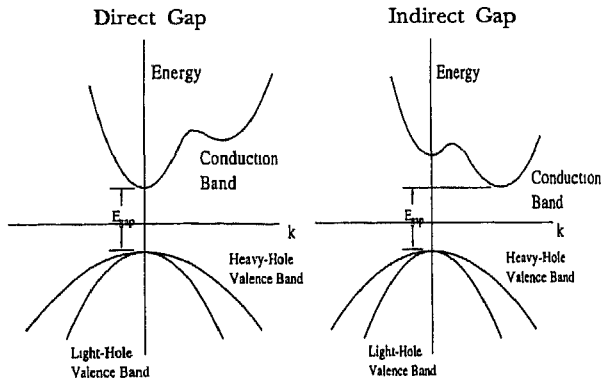


Fig. 1. Typical band structures of direct- and indirect-gap semiconductors.

band (there are actually many valence and conduction bands). The two most important and useful quantities for characterizing semiconductor materials are the minimum energy difference between the conduction and valence bands (the bandgap) and the relative momentum difference between the conduction band minimum and the valence band maximum. If this momentum difference is zero then the semiconductor is termed a direct-gap semiconductor, and if this momentum difference is non-zero, then it is termed an indirect-gap semiconductor. Direct-gap semiconductors differ from indirect-gap semiconductors in the electronic structure of the conduction band in momentum space. Fig. 1 shows typical dispersion relations (energy vs. k) for both direct-gap and indirect-gap semiconductors. These two quantities are important in characterizing the light-emission properties (i.e. photoluminescence) of semiconductors because the characteristic energy range of the emission is related to the bandgap, and the relative intensity and temporal response of the emission is governed by the bandstructure.

1.2.2. Free-carrier properties

Hall measurements have clearly shown that there are two types of free-carriers in semiconductors, electrons and holes. Electrons usually move (are scattered) within the conduction bands and make transitions between conduction and valence bands (both intra- and inter-band scattering). Holes, on the other hand, are confined to move (be scattered) within the valence bands of the semiconductor. These free carriers are most commonly characterized by their origin (free or defect related), density, mass, and scattering time. In an intrinsic semiconductor (undoped with impurities), the product of the electron (n) and hole (p) densities is related to the fundamental energy gap of the semiconductor as

$$np = N_c N_v \exp\left[\frac{-E_g}{kT}\right] \quad (1)$$

where N_c and N_v are the conduction band and valence band density of states, and are given by

$$N_{c(v)} = \frac{1}{\sqrt{2}} \left[\frac{m_{e(h)}^* kT}{\pi \hbar^2} \right]^{3/2} \quad (2)$$

As a result, the intrinsic concentration of free carriers in semiconductors is directly related to the energy gap, and at 300 K for GaAs this density is $\sim 10^6 \text{ cm}^{-3}$, and for Si it is $\sim 10^{10} \text{ cm}^{-3}$. This intrinsic concentration is the fundamental limit for the minimum free-carrier concentration of these semiconductors. Another useful quantity for characterizing the properties of semiconductors is the Fermi energy. The fermion nature of free carriers requires obedience to the Pauli exclusion principle,

and, concomitantly, the use of Fermi statistics. The Fermi energy represents the energy at which the occupation probability of electrons is exactly 50%. In an intrinsic semiconductor this Fermi energy lies at midgap. In order to achieve higher doping levels, semiconductors are commonly doped with an impurity which either has an excess of electrons or a deficiency of electrons, and, therefore, acts as a donor or an acceptor, respectively. Selective doping with donors (acceptors) can raise (lower) the Fermi energy with respect to this midgap position, and as a result the concentration of electrons (holes) will also increase. The exact details of this doping to form an extrinsic semiconductor depends upon the chemical nature of the impurity. Doping can easily achieve free-carrier concentrations above 10^{20} cm $^{-3}$.

The mass of these free electrons or holes is not that of an electron. The periodic potential of the atomic cores of the semiconductor, which alters the energy levels of the valence electrons of the constituent atoms of the semiconductor, also restricts the motion of the free carriers. These free electrons or holes are confined to move within the energy bands described above, and, this motion can equivalently be described as that of a free electron ($(\hbar^2 k^2) / (2m^*)$) with an effective mass, m^* . This is known as the effective mass approximation. This mass is, therefore, indicative of the bandstructure of the semiconductor. Further, this description (the effective mass description) is only adequate near the bottom (top) of the conduction (valence) bands where they are approximately parabolic. Lastly, the scattering of free carriers may be a result of any number of mechanisms, including phonon scattering, impurity scattering, and free-carrier scattering. These scattering mechanisms all affect the mobility of the free carriers which is related to the scattering time as $\mu = e\tau/m^*$.

1.2.3. Quasi- and many-particle states

In addition to the single-particle states for free electrons and free holes, it has been conclusively demonstrated that many-particle states may be formed, especially at very low temperatures. There are many different species of many-particle states, including excitons, biexcitons, excitonic molecules, electron–hole plasmas, and electron–hole liquids. An exciton is a quasi-particle consisting of a Coulomb-correlated electron–hole pair. The exciton was first postulated in 1931 by Frenkel, and followed by Wannier's development in 1937 [1]. These Frenkel and Wannier excitons are tightly and loosely coupled electron–hole quasi-particles, respectively. In semiconductors, the large dielectric constant reduces the strength of the Coulomb interaction, and, therefore, the appropriate description for excitons in semiconductors is that of Wannier. This quasi-particle is a composite boson formed from spin 1/2 fermions, and is analogous to the hydrogen atom since it results from the Coulomb attraction of negatively (electron) and positively (hole) charged particles. The increased mass of the electron and hole forming the exciton, together with the dielectric screening of the Coulomb interaction, drastically reduces the Rydberg of this quasi-particle compared with that of the hydrogen atom. Excitons are intrinsic quasi-particles which may be ionized into the constituent free carriers. Thus, the quasi-particle binding energy lowers its energy with respect to the fundamental energy gap, while retaining essentially the same dispersion. Biexcitons and excitonic molecules are quasi-particles formed through van der Waals binding of two or more excitons. An electron–hole plasma (EHP) is a high-density phase whereby the excitonic Coulomb correlation between a single electron and hole is lost due to the screening of the Coulomb interaction. At low temperatures, if the density of free excitons is increased, there will exist a phase transition from an ensemble of neutral particles (excitons) at low densities to an ensemble of charged particles (electrons and holes) at high densities. This is the well-known Mott or metal–insulator transition. Simplistically, this occurs at densities comparable to the close-packing density of excitons, and is given by $n \approx 25/(a_0)^3$. The electron–hole liquid is a condensed state which only occurs at very low temperatures and moderate densities. This phase is characterized by a incom-

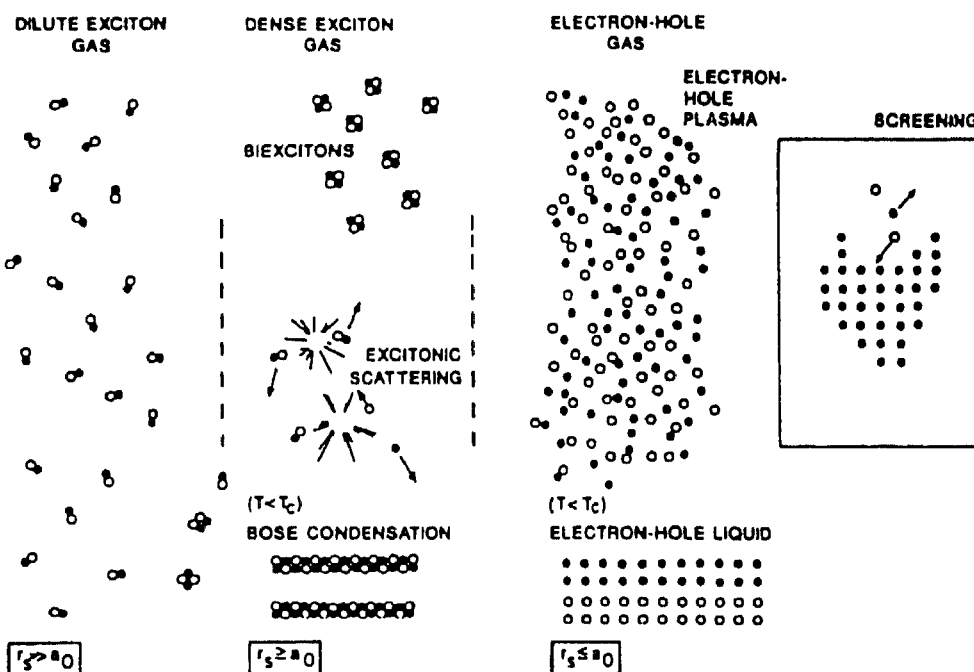


Fig. 2. Illustration of various electronic and excitonic processes which may yield the emission of radiation in semiconductors. Here, r_s is the mean interparticle distance. As the density increases excitons may condense into biexcitons, scatter off one another, or even condense into a Bose condensate. At still higher densities an electron-hole liquid or plasma may form. (After Cingolani and Ploog [2].)

pressible, constant density, just as in a liquid. It is a many-particle state whose energetics only allow formation below a critical temperature and density, and is characterized by a binding energy (related to the critical temperature) which depends upon the bandstructure of the semiconductor. Fig. 2 shows a schematic representation of some of the quasi-particles which may exist in a crystal and give rise to radiative emission. Each of these quasi-particles is characterized by a density regime in which it may be the dominant species [2]. Fig. 3 shows the density regime and energy scale at which these quasi-particles exist for both bulk and two-dimensional structures. All of these many-particle states give rise to distinct spectral signatures and properties which will be discussed below.

1.2.4. Impurities

As mentioned above, the controlled chemically and spatially selective introduction of impurities into semiconductors is vital to the realization of semiconductor devices, such as light-emitting diodes, etc. Impurities may be classified in many ways, including whether they are chemical or physical defects, whether they act as donors or acceptors or neutral impurities, or whether they yield shallow or deep levels. Chemical defects are atomic elements distinct from those of the pure lattice which are incorporated substitutionally or interstitially or in pairs. Physical defects include vacancies, interstitials, and defect pairs. Donors are elements which contribute an extra electron to the conduction band, whereas acceptors are elements which contribute an extra hole to the valence band. In GaAs some of the most common donors and acceptors are Si and Be, respectively. Some elements, namely the group IV elements, when doped into a III-V semiconductor may theoretically act as either a donor or acceptor, and are termed amphoteric. However, other physical realities, such as preferential site occupation (Si on a Ga site) cause one type of electrical behavior to be predominant. Shallow impurities are characterized by a dispersion which mimics that of a nearby energy band (i.e. the Γ point of the conduction

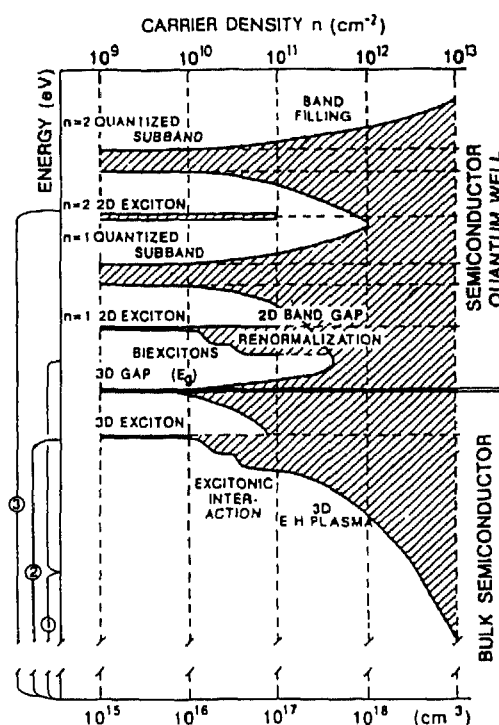


Fig. 3. Illustration of the energy spectrum of the various radiative recombination processes which may occur in semiconductors as a function of carrier density. (After Cingolani and Ploog [2].)

band in GaAs). The effective mass approximation works remarkably well for these shallow impurity states. In contrast deep impurities have wavefunctions which are highly localized in real space and concurrently delocalized in momentum space. Thus, the energy level structure is not derived solely from a single conduction band, and is, therefore, not like effective mass. It is evident that the energetic proximity of an impurity level with a band edge (either conduction or valence band) is not truly indicative of the shallow or deep nature of the impurity.

Many-particle states involving impurities may also be formed in semiconductors. Most important among these are donor-bound and acceptor-bound excitons, and donor-acceptor pairs. A donor-bound exciton consists of a free hole which has combined with a neutral donor to form a positively charged excitonic ion, and similarly for an acceptor-bound exciton. The Coulomb interaction between a donor and an acceptor may also cause the formation of a donor-acceptor pair. These pairs act as stationary molecules where the extra electron of the donor is partially-shared with the acceptor.

1.2.5. Recombination processes

Excitation of a non-equilibrium density of electrons and holes, excitons, or any other number of quasi-particles ultimately will lead to the recombination and simultaneous emission of photons. This is called radiative recombination. If the recombination proceeds through the emission of phonons instead of photons, then the recombination is termed non-radiative recombination. There are many possible radiative recombination mechanisms, and Fig. 4 illustrates a few. Band-to-band recombination is the across-bandgap transition of a free electron in the conduction band to a free hole in the valence band. As a result this emission occurs only at energies equal to or greater than the bandgap. Recombination at energies greater than the bandgap is due to the recombination of "hot carriers" which have

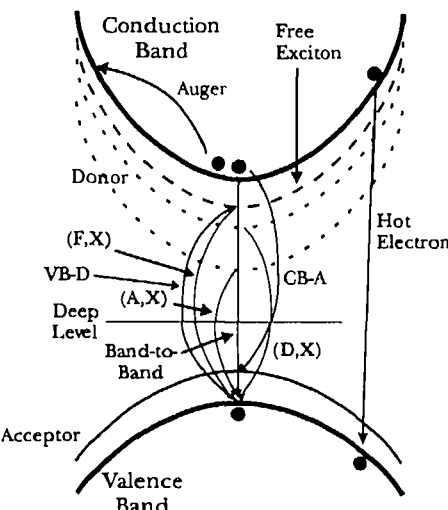


Fig. 4. Illustration of several possible radiative recombination mechanisms. See text for explanation

not fully relaxed to the bottom (top) of the conduction (valence) band prior to recombination. Free electrons and holes may become bound via the Coulomb interaction to form free excitons, which are the simplest lowest energy intrinsic quasiparticle states in a semiconductor. Free-to-bound transitions involve the radiative recombination of a free carrier with a carrier bound to an impurity, and they come in two varieties: donor-to-valence band and conduction band-to-acceptor. This emission primarily occurs at energies less than the bandgap. Excitons may also become bound at impurities (either donors or acceptors) and give rise to subbandgap radiation. Donor–acceptor pair emission involves the radiative recombination of an electron bound to a donor and a hole bound to an acceptor. This emission occurs below the bandgap and is sensitive to the relative distance between the donor and acceptor impurity pair. Recombination via an intermediary state (i.e. deep level) has been termed Shockley–Read–Hall recombination, and is primarily non-radiative in nature. Auger recombination is a three-body process whereby the recombination energy is given non-radiatively to another particle such as an electron in the form of kinetic energy. (There are many forms of Auger recombination.) Most of the recombination mechanisms mentioned thus far give rise to broad emission lines. In contrast, excitonic recombination usually gives rise to narrow emission lines. Thus, the spectral signatures of this excitonic recombination (free excitons, impurity-bound excitons, biexcitons, etc.) is useful in identifying the recombining species. In addition to these direct recombination processes, indirect recombination involving the simultaneous emission of phonon(s) and a photon is also possible. Again, this type of emission yields spectral signatures which are easily identifiable, and will be discussed below.

1.2.6. Properties of nanostructures

Nanostructured semiconductors offer the possibility of engineering the energy bandstructure of a material to enhance specific mechanisms advantageous for specific devices. This altered electronic structure is achieved through reduction of the dimensionality of a portion of a device. Very small structures are grown which effectively confine carriers to a small region of space, thereby reducing their phase space by one, two, or even three dimensions. As a result it is possible to fabricate structures wherein the carriers are free to move in only two, one, or zero dimensions. These structures are referred to as quantum wells, quantum wires, and quantum dots, respectively.

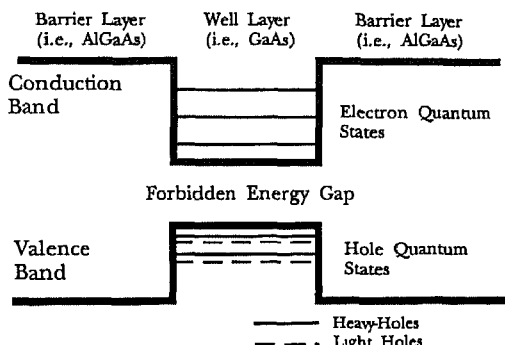


Fig. 5. Schematic band structure of a typical quantum well. Solid (dashed) lines in valence band represent heavy-hole (light-hole) states.

The first demonstrations of the fabrication of nanostructures and of their novel properties occurred in 1974. In that year Esaki and Chang [3] reported the oscillatory behavior of the perpendicular differential conductance due to resonant electron tunneling across the potential barriers which confine electrons. In the same year, Dingle, et al. [4] demonstrated the quantization of energy levels in quantum wells through absorption measurements. This result has proven to be a classic textbook example of the manifestations of quantum mechanics, and is quoted often. The primary factor in allowing the development of such nanostructures was the technological breakthrough in crystal growth achieved by the non-equilibrium growth techniques, molecular beam epitaxy (MBE) and organometallic vapor-phase epitaxy (OMVPE). These techniques allow for epitaxial deposition of single atomic layers and the growth of atomically-abrupt heterostructures which was not possible prior to their development.

Nanostructures were of interest to the scientific and applied science community due to the possibilities afforded by their unique properties. Among the first new types of devices predicted was a Bloch oscillator [1]. Since their introduction, nanostructures have found application as diodes, light-emitting diodes, lasers, transistors, resonant-tunneling diodes, and gyromagnetic devices. The unique and novel properties of nanostructures are: the different dispersion in the density of states, the geometrical and size dependence of the electronic bandstructure, the effective carrier confinement, and the possibility for precise control of electronic and hole wavefunctions.

The simplest example of a semiconductor nanostructure is the quantum well, shown in Fig. 5. This structure is identical to the one-dimensional particle-in-a-box found in quantum mechanics texts. The quantum well is formed through precise growth of three different epitaxial layers, such that the middle layer has a smaller energy bandgap than the first and last barrier materials. Thus, both electrons and holes are confined within the middle, smaller bandgap layer. The energy levels and wavefunctions are then determined through the solution of Schrödinger's equation. These are shown for the example given in Fig. 5. For an infinitely deep well, the energy eigenvalues are given by

$$E_n = \frac{\hbar^2}{2m^*} \left[\frac{n\pi}{L_z} \right]^2 \quad (3)$$

where L_z is the width of the middle or well layer of the structure. Thus, by fabricating structures of various dimensions, the electronic structure may be altered, and this is true for both electrons and holes.

The confinement of carriers induced by the fabrication of nanostructures causes large changes in the dispersion relation of the density of states for free carriers. This dispersion is also strongly dependent upon the dimensionality of the carriers. Fig. 6 shows a comparison between the density of states of

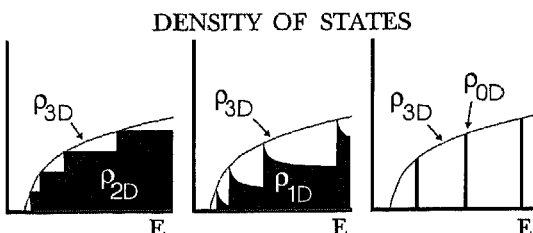


Fig. 6. Density of states of low-dimensional structures.

three- and two-dimensional (3D and 2D) structures. Wavefunctions of electrons and holes in reduced-dimensionality structures may be obtained by solving Schrödinger's equation taking into account the appropriate boundary conditions of continuity of probability current across the interfaces. Also, the confinement potential of the nanostructure lifts the degeneracy between the $J_z = \pm 3/2$ and $J_z = \pm 1/2$ valence bands since they correspond to different masses [2]. Thus, the heavy-hole and light-hole bands are no longer degenerate in semiconductor nanostructures. The Coulomb interaction between electrons and holes is also enhanced in lower dimensional structures. For the ideal 2D case, the excitonic energy eigenvalues (due to this Coulombic interaction) are given by

$$E_n^{2D} = E_g - \frac{E_b}{\left(n - \frac{1}{2}\right)^2} \quad (4)$$

where E_b is the three-dimensional excitonic binding energy or Rydberg energy. As a result, the binding energy in a perfect 2D system is four times that of the 3D excitonic binding energy. In real quantum wells, the exciton binding energy depends strongly on the well width due to wavefunction leakage into the confining barriers. The 2D exciton has the following properties: (1) the excitonic absorption depends on the well width since the exciton envelope function depends on L_z ; (2) narrow excitonic peaks in absorption and emission reflect momentum conservation (k conservation), and broadening of these lines may occur due to relaxation of this k conservation by processes which destroy translational symmetry such as disorder, alloy fluctuations, interface roughness, and carrier localization; (3) the LO-phonon interaction is reduced in III-V nanostructures, leading to excitons which are still bound at room temperature; and (4) the exciton oscillator strength in quantum wells increases as the excitonic wavefunction shrinks with the well width of the quantum well.

In even lower dimension structures, i.e. quantum wires and quantum dots, the density of states varies as $E^{-1/2}$ and as a delta function, respectively. Thus, the spectral features are even narrower than in bulk or quantum well structures. The oscillator strengths of excitonic transitions also increases dramatically over those in bulk structures. Applications of such structures yield specific advantages. For instance, quantum dot lasers are predicted to have a lasing threshold 100 times smaller than those of a quantum well laser [5].

1.3. Scope of the review

The motivation for this review is to exhibit the variety and wealth of information about semiconductors that may be obtained through PL spectroscopies, in their many forms. PL spectroscopy has a wide range of capabilities. PL may be utilized for characterization of such technologically relevant quantities as wafer uniformity and quality and for quantification of such scientifically important processes as hot-carrier cooling. This review will demonstrate the application of PL spectroscopy to technological and scientific issues. It is not intended to be a historical review or a completely exhaustive

review of any aspect of PL spectroscopy. There are many excellent reviews of optical spectroscopy and its application to semiconductors, including articles and books by Bebb and Williams [6], Pankove [7], Perkowitz [8], and Smith [9], to name just a few.

This review will focus on examples of the application of this technique to the study of semiconductors. Since PL involves the emission of photons and photon emission is a first-order process in a direct-gap material, versus a second-order process in an indirect-gap material, the primary example which will be given throughout the review will be of the prototypical direct-gap semiconductor, GaAs. Nevertheless, some examples of PL emission in the prototypical indirect-gap semiconductor, Si, will also be given insofar as the emission is fundamentally different than in GaAs. Further, PL emission in semiconductor nanostructures based upon the GaAs/AlGaAs heterostructure system will be given to elucidate quantum confinement, reduced-dimensionality, and atomic-scale structural effects.

The article is organized as follows. Section 2 will introduce the most common form of PL spectroscopy, cw PL. This technique only provides spectral information, and is useful for identifying intrinsic recombination (i.e. excitonic, electron–hole liquid, etc.), defect recombination, hot-carrier recombination, and phonon-assisted recombination. In section 3, time-resolved PL spectroscopic techniques will be reviewed. Attention will be given to the technique, analysis of the data, and information deduced from these measurements. Time-resolved measurements are useful for characterizing non-radiative decay, surface recombination, carrier localization, and recombination mechanisms (i.e. bimolecular, Auger, etc.). Section 4 will review a relatively more recent variety of PL spectroscopy, namely spatially-resolved PL. There are many varieties of this technique, and each will be outlined briefly. These measurements are useful for characterizing wafer uniformity and the atomic-scale structure of nanostructures. When combined with the time-resolved technique, this technique becomes even more powerful, yielding quantitative information about free-carrier transport, excitonic transport, potential gradients, and spectral migration.

1.4. Properties of example semiconductors

1.4.1. Gallium arsenide

Gallium arsenide (GaAs) is a direct bandgap semiconductor with an energy gap of 1.424 eV at room temperature. The valence band is degenerate at $k=0$ with the light- and heavy-hole valence bands. The split-off valence band is higher in energy (hole energy) by 0.34 eV due to spin-orbit splitting. The electron effective mass is $0.067m_0$, whereas the heavy (light) hole effective mass is $0.45m_0$ ($0.082m_0$). Here m_0 is the free-electron mass. The conduction band is characterized by a total angular momentum quantum number $J=1/2$. Including spin-orbit interaction, the valence band top splits into two bands, which are characterized by total angular momentum quantum numbers $J=1/2$ and $J=3/2$. The upper $J=3/2$ valence band is fourfold degenerate at $k=0$, and splits into two Kramers doublets, the heavy-hole and light-hole bands for $k \neq 0$. The dielectric constant is 12.6.

1.4.2. Silicon

Silicon (Si) is an indirect semiconductor with an energy gap of 1.125 eV at room temperature. The indirect gap has a conduction band minimum in the [001] direction which occurs at $k_m \sim 0.85 \pm 0.01$ of the zone boundary lattice vector in the X direction. This gives rise to a camel's back band structure. At the minimum energy point, the conduction band has elliptical constant energy surfaces with electron effective masses of $m_l = 0.9163m_0$ and $m_t = 0.1905m_0$, where m_l is the longitudinal mass and m_t is the transverse mass. The heavy- and light-hole effective masses are $m_{hh} = 0.537m_0$

and $m_{lh} = 0.153m_0$. The valence-band split-off band, which is higher in energy by 44 meV, has a hole effective mass of $m_{so} = 0.29m_0$. The dielectric constant is 11.7.

1.4.3. GaAs nanostructures

Nanostructures are most commonly fabricated from layers of GaAs and AlGaAs. The primary reason for this is simply due to the close lattice match between these materials, with lattice constants that differ by only 0.3%. Bulk GaAs crystals have T_d point group symmetry. In GaAs/AlGaAs quantum wells, the point group of the zincblende GaAs layer is lowered to D_{2d} . The reduction in symmetry lifts the original fourfold degenerate Γ_8 valence band states into twofold degenerate Γ_6 and Γ_7 heavy-hole and light-hole states, respectively. This is important since the selection rules for optical transitions are impacted by this reduction in symmetry. For the electric-dipole transition operator, transitions are allowed for confined states with the same envelope wavefunction symmetry under spatial reflection. Dingle et al. [4] also noted that in the infinite-well approximation, only transitions between confined valence and conduction band states with the same principal quantum number, n , were allowed. Observation shows that these transitions are indeed the strongest.

Our general discussion of nanostructures given above noted the theoretical enhancement in binding energy of an exciton in a quantum well. The binding energy of a bulk 3D exciton in GaAs is 4.2 meV, and, therefore, the theoretical limit in a perfect 2D quantum well would be ~ 16 meV. However, since the confining potentials of quantum wells are not infinite, the actual binding energies are dependent upon the well width of the quantum well. Fig. 7 shows the experimentally determined exciton binding energies for both heavy- and light-holes [10]. The observed binding energy decreases

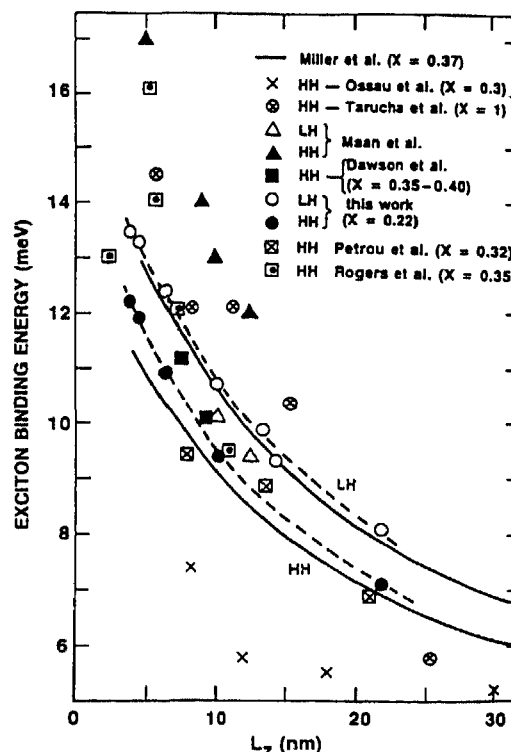


Fig. 7. Excitonic binding energies versus well width in GaAs/AlGaAs quantum wells. Data are from references cited in Ref. [10]. (After Koteles and Chi [10].)

with decreasing well width and then at zero well width (i.e. bulk layer) it decreases to the bulk value of 4.2 meV. Lower dimension structures also exhibit similar effects in the excitonic binding energies.

2. Cw photoluminescence

2.1. Experimental techniques

Fig. 8 shows a typical generic arrangement of equipment for cw PL measurements. Excitation of a non-equilibrium population of electrons and holes is most commonly achieved by using a laser. Lasers are used for excitation to allow localized spatial resolution, well-defined penetration depth, and a monoenergetic initial distribution of electrons and holes. The penetration depth is defined as the point at which 90% of the non-reflected radiation is absorbed by the sample, and for semiconductors the penetration depths are typically sub-micron for above-gap light. These sub-micron penetration depths (for visible lasers) are the primary reason for performing PL measurements in a back-scattering geometry, as shown in Fig. 8, instead of in a transmission geometry. The large dielectric constant of most semiconductors results in relatively large Fresnel reflection losses. At normal incidence the reflection of laser light is $\sim 35\%$ for Si and $\sim 30\%$ for GaAs. The resulting PL is then collected from the same sample surface as the surface excited by the incident excitation radiation. This generic experimental set-up allows for separate focusing of the laser excitation and imaging of the PL. Spectral resolutions of 0.1 Å are easily attainable with commercially available instruments. It is also possible to measure PL spectra with a Fourier transform instrument (FTIR). However, these instruments have more commonly been utilized in infrared spectroscopy.

PL is detected by a photomultiplier tube (PMT) after being spectrally dispersed by a spectrometer. There are many varieties of PMT detectors, and the appropriate detector depends upon the spectral range of interest. For GaAs in the visible range of the spectrum out to 900 nm, the S-20 response PMTs with a GaAs photocathode are most suitable because of their relatively high quantum efficiency and flat spectral response. In order to detect PL from Si, a different detector is required since PMTs are barely able to cover the spectral range near the Si bandgap. S-1 type PMTs are suitable for detecting PL out to 1200 nm, but their quantum efficiency and spectral response are lower and decreases rapidly

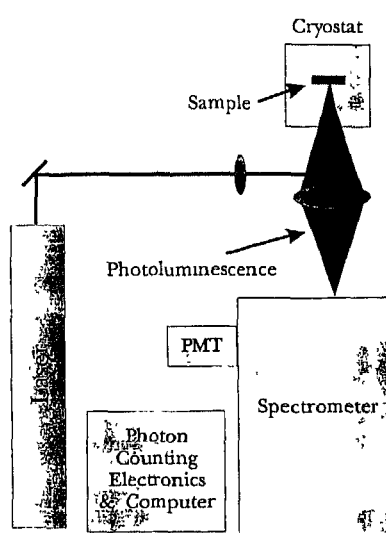


Fig. 8. Generic experimental arrangement of instrumentation for cw PL measurements.

with increasing wavelength, respectively. PMTs with InGaAs photocathodes are efficient out to 1100 nm. Measurement of photon intensity at any wavelength may then be accomplished in two ways. In the analog-detection mode the current from the PMT is measured directly. In the photon-counting mode the electron pulses derived from the detected photons are counted as a means of measuring the PL intensity. PL spectra are then displayed as histograms, i.e. numbers of counts versus wavelength. Photon counting is more sensitive to weak signals than analog detection, but requires more sophisticated instrumentation.

The optics used in cw PL measurements are designed to maximize the collection of PL from the sample. This requires a collection lens with a small *f*-number (i.e. short focal length and large diameter), and an imaging lens with an *f*-number matched to that of the spectrometer. Further, for the best response it is advantageous to focus the dispersed light transmitted through the exit slits of the spectrometer onto a small spot on the photocathode of the PMT. Also, optics may be utilized to focus the laser beam to a small spot on the sample surface.

2.2. Intrinsic and extrinsic recombination

2.2.1. Free-carrier recombination (band-to-band recombination)

Free-carrier radiative recombination occurs at energies greater than or equal to the fundamental bandgap of the semiconductor. This type of recombination process requires the presence, in close proximity, of both an electron and a hole. Therefore, the recombination rate is proportional to the product of the non-equilibrium populations of electrons and holes. Expressing the carrier concentrations as a deviation from their equilibrium values, n_0 for electrons and p_0 for holes, the total carrier concentrations are $n = n_0 + \Delta n$ and $p = p_0 + \Delta p$. The total recombination rate is

$$R \propto \frac{np}{(n_i)^2} \quad (5)$$

where n_i is the intrinsic carrier concentration of the semiconductor. Being more explicit, this may be expressed as

$$R \propto \frac{(n_0 + \Delta n)(p_0 + \Delta p)}{n_0 p_0} = \frac{n_0 p_0 + \Delta n p_0 + \Delta p n_0 + \Delta n \Delta p}{n_0 p_0} \quad (6)$$

Assuming that the non-equilibrium carrier densities are small, the last term, $\Delta n \Delta p$, which is quadratic in small quantities, may be neglected, yielding

$$R \propto \frac{n_0 p_0 + \Delta n p_0 + \Delta p n_0}{n_0 p_0} \quad (7)$$

Examining now just the non-equilibrium contribution to the recombination rate

$$\frac{\Delta R}{R} = \frac{\Delta n}{n_0} + \frac{\Delta p}{p_0} \quad (8)$$

it is clear that the recombination is dominated by the minority carrier species. For example, in a n-type semiconductor $n_0 \gg p_0$ and the non-equilibrium recombination rate becomes

$$\frac{\Delta R}{R} = \frac{\Delta p}{p_0} \quad (9)$$

and the recombination is controlled by the non-equilibrium population of holes. This is a very important

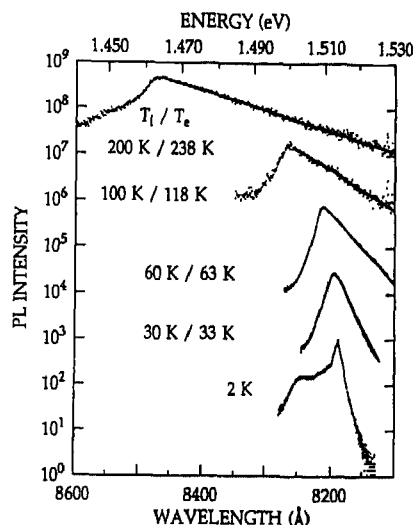


Fig. 9 Temperature dependence of the PL spectra of a 9.82 μm thick GaAs/AlGaAs double heterostructure. Solid lines are fits using a Maxwell-Boltzmann distribution, with the derived electronic temperatures shown versus lattice temperature. (After Wolford et al. [11])

aspect of radiative recombination in semiconductors; namely, the recombination rate is governed by the minority-carrier species. The probability for radiative recombination is given by

$$B = \frac{R}{(n_i)^2} \quad (10)$$

The temperature dependence of the radiative recombination may be obtained by noting that the free-carrier densities depend on temperature through the conduction-band and valence-band densities-of-states and the exponential factor (Eq. (1)). This yields a recombination rate approximately proportional to $T^{-3/2}$.

The spectrum of the band-to-band recombination is governed by the equilibrium energetics of the free electrons and free holes. The energy distribution describing these energetics is the Fermi-Dirac distribution, which, at high temperatures, is approximately a Boltzmann distribution. Thus, the electrons and holes are distributed above the bottom of the conduction and valence bands, respectively, with a Boltzmann tail and temperature characteristic of the temperature of each carrier population. Fig. 9 shows the cw PL spectra of a nominally undoped GaAs epilayer versus lattice temperature [11]. The high-energy side clearly exhibits this Boltzmann tail, with a single characteristic carrier temperature equal to the lattice temperature. The low-energy side of the band-to-band emission is governed by residual impurity states within the forbidden gap of the semiconductor, and is therefore, considerably more complicated.

The peak energy of the band-to-band recombination peak is indicative of the bandgap of the semiconductor. The fundamental bandgap of semiconductors is well known to be temperature dependent. This temperature dependence is most commonly fit with the empirical Varshni relation [12]

$$E_{\text{gap}} = A + BT^2/(C + T) \quad (11)$$

where A , B , and C are empirical constants characteristic of a material. However, the error in fitting the PL spectra with this relation is large enough to make distinguishing among semiconductors through analysis of such data not practical. Another more physical model for the temperature dependence of the semiconductor bandgap was given by Lautenschlager et al. [12] and Manoogian and Leclerc [13]:

$$E(T) = E_B - a_B \left[1 + \frac{2}{e^{\Theta/T} - 1} \right] \quad (12)$$

where Θ is the average phonon frequency.

2.2.2. Free-exciton recombination

The theory of excitons has been reviewed by several authors, including Dexter and Knox [14], Elliot [15], Dimmock [16], and Reynolds and Collins [17]. These texts provide an excellent introduction to the concept and properties of excitons, and this section will only deal with their cw PL emission properties in GaAs, Si, and GaAs-based nanostructures. One of the most important properties of free excitons is their ability to move throughout the crystal. The energy of an exciton consists of two parts, the Coulomb interaction energy between the electron and hole which binds them together into this quasiparticle, and their translational kinetic energy. This kinetic energy establishes thermal equilibrium of the excitonic ensemble which is manifested in the PL emission spectrum. The radiative recombination of excitons is essentially the annihilation of the exciton, and can only occur for excitons with momentum equal to the photon momentum.

2.2.2.1. GaAs

The existence of free excitons in GaAs was first confirmed through the absorption measurements of Sturge in 1962 [18]. This showed the free-exciton energy to be 1.5152 eV. Absorption measurements also showed evidence for the $n = 2$ excited state at 1.5183 eV [19]. Poor sample quality prevented the observation of free-exciton emission in GaAs until 1967 [20]. (Extrinsic transitions compete much more effectively with excitons in emission than in absorption.) Figs. 10–12 shows more recent examples of free-exciton photoluminescence in an undoped MBE-prepared GaAs epilayer [21–24]. The intensity of excited states decreases rapidly ($\text{as } n^{-3}$), and thus far only the $n = 2$ excited state has been observed in luminescence. There are several important factors which may influence free-exciton recombination in GaAs, and there are several theoretical considerations which affect the interpretation of spectra.

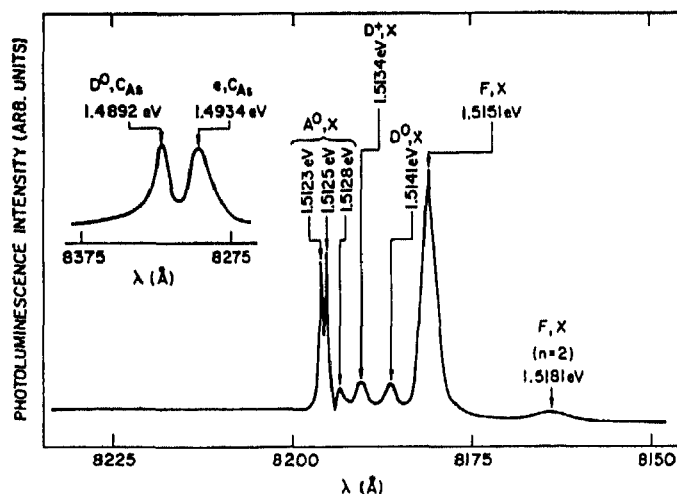


Fig. 10. 5 K PL spectrum of an undoped MBE-grown GaAs epilayer grown at 670 °C. (After Heiblum et al. [21].)

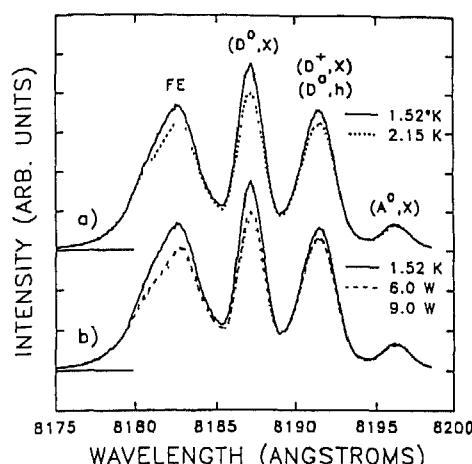


Fig. 11. (a) PL spectra in the near-edge vicinity at 1.52 and 2.15 K. (b) Comparison of PL spectra with no pump laser (—), 6.0 W peak power pump laser (---) and 9.0 W pump laser (···) (After Ramsbey et al. [22].)

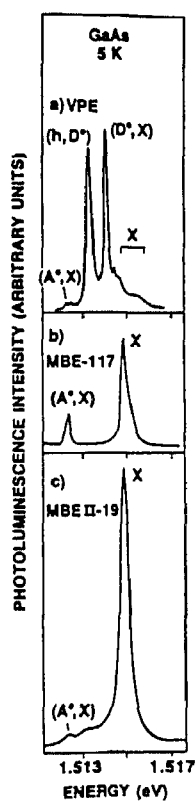


Fig. 12. Low-temperature, high-resolution PL spectra of two MBE-prepared samples and one VPE-prepared GaAs sample. (Reprinted from Koteles et al., *Solid State Commun.*, 62 (1987) 703 with permission from Elsevier Science Ltd., Pergamon Imprint, The Boulevard, Langford Lane, Kidlington OX5 1GB, UK.)

Free-exciton recombination in GaAs is not commonly observed in GaAs epilayers, and almost never observed in GaAs substrates. The effects of impurities, defects, strain, and poor interfaces and/or surfaces tend to dominate the emission spectra, thereby, completely masking the true intrinsic properties of free excitons. Figs. 13 and 14 show some early measurements of PL from "high-purity" GaAs

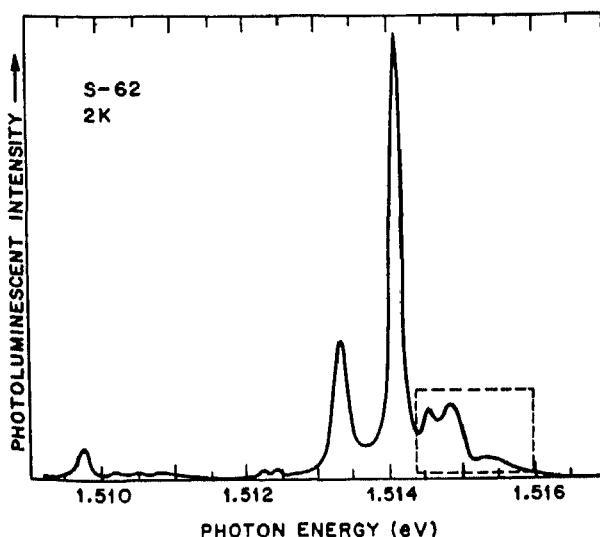


Fig. 13. 2 K PL spectrum of high-purity GaAs after excitation at 632 nm. (After Sell et al. [25].)

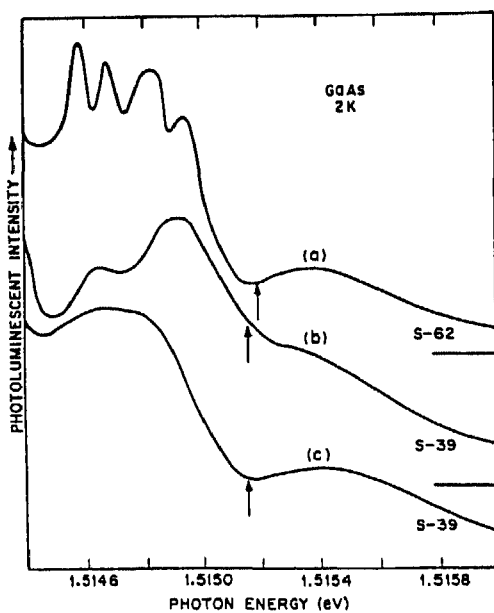


Fig. 14. 2 K PL spectrum in the vicinity of the free-exciton emission after excitation with 1.0 mW mm^{-2} for (a) and (c) and 0.1 mW mm^{-2} for (b). (After Sell et al. [25].)

epilayers [25]. The energy region which is now accepted as the free-exciton resonance energy, 1.51515 eV, exhibits a dip with a peak on either side which may vary from sample to sample. The peak on the high-energy side was termed the upper polariton branch (UPB) and the peak on the low-energy side was termed the lower polariton branch (LPB). This nomenclature has persisted, even though it has been recently shown to be due to an incorrect interpretation of the data, as will be discussed below [26,27]. Fig. 15 shows the PL spectra of undoped heterostructure samples grown by metal-organic chemical vapor deposition (MOCVD) and MBE, as well as a MOCVD-prepared homostructure [28]. All exhibit a peak at the free-exciton energy, but the relative strength and lineshape of the peak is clearly sample dependent. Free-exciton emission is also rapidly quenched with increasing temperature,

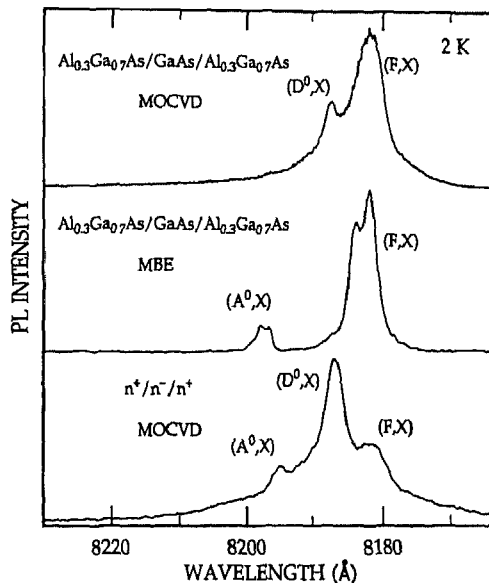


Fig. 15. Low-temperature PL spectra from MOCVD- and MBE-prepared GaAs/AlGaAs double heterostructures, and an MOCVD-prepared GaAs homostructure. (After Wolford et al. [28].)

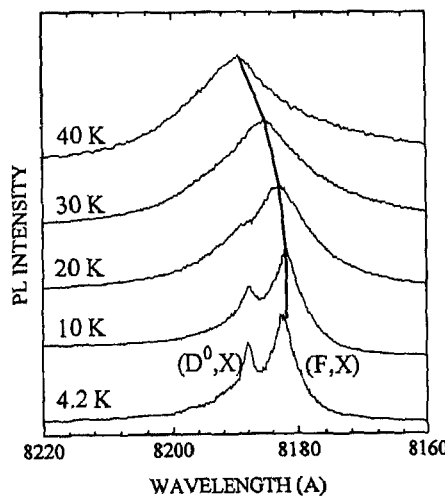


Fig. 16. PL spectra versus temperature for a GaAs/AlGaAs double heterostructure. Free-exciton emission is evident at low temperatures, but becomes "washed out" with increasing temperature.

as shown in Fig. 16 [29]. Bloss et al. [30] have also shown that the free-exciton lineshape may depend critically upon the layer thickness, as shown in Fig. 17. Most low-temperature studies of the emission properties of GaAs have resulted in near-edge impurity-bound exciton recombination as the dominant emission process. However, high purity is not the only requirement for prominent free-exciton emission. Fig. 18 demonstrates this important point. Here the excitonic dip and so-called UPB and LPB emissions are evident, but the prominent excitonic emission, as shown in Fig. 10, is absent [31]. Hall measurements on these samples show the net carrier concentration to be 10^{13} – 10^{14} cm $^{-3}$ at 300 K.

Thus, it is clear that high sample purity is a necessary but not sufficient condition for prominent free-exciton emission. Another important factor is the quality of the surfaces or interfaces of the GaAs layer [11,28,32]. The problem of surface or interface states in GaAs is well known, especially among

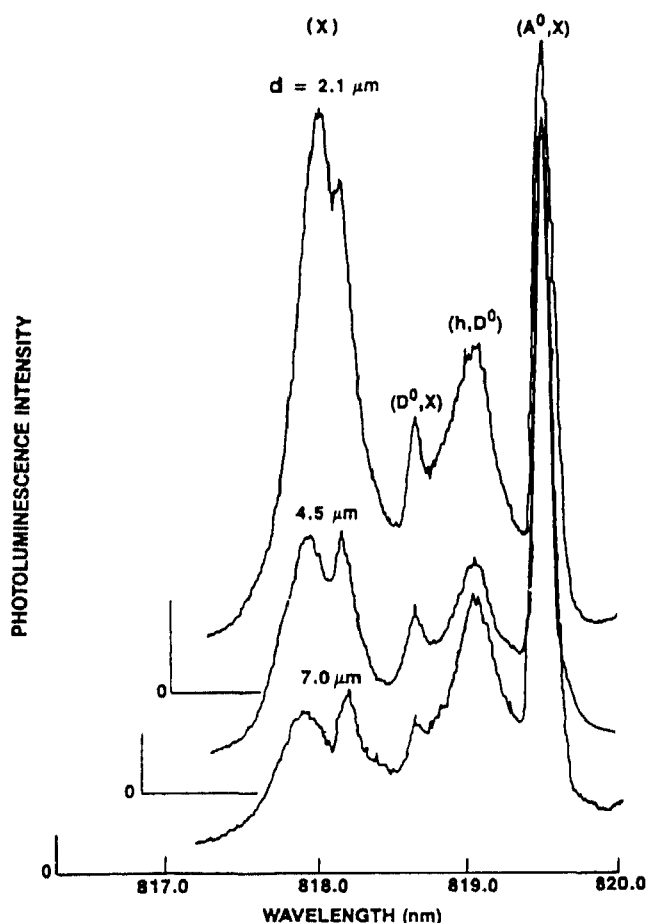


Fig. 17 Thickness dependence of the PL spectra in the near-edge region of GaAs. (Reprinted from Bloss et al., *Solid State Commun.*, 54 (1985) 103 with permission from Elsevier Science Ltd., Pergamon Imprint, The Boulevard, Langford Lane, Kidlington OX5 1GB, UK.)

the photovoltaic community where this deleterious effect may reduce the efficiency of solar cells. This same problem also affects free-exciton recombination. Fig. 19 shows the PL spectrum of a high-quality, undoped (10^{15} cm^{-3}) GaAs/AlGaAs double heterostructure with a measured surface recombination velocity of $< 40 \text{ cm s}^{-1}$ [33–36] together with the PL spectrum of the same sample after chemical-etch removal of the top AlGaAs passivation layer. Removal of this top layer causes the prominent free-exciton emission to transform into the UPB/LPB branch emission commonly observed in GaAs substrates and other lower quality material. Fig. 20 shows a similar effect [37]. Here the upper spectrum which exhibits the UPB/LPB structure is of a VPE-prepared GaAs epilayer with a bare surface. The lower spectrum is of the same sample but after chemically treating the sample with Na_2S , a chemical surface treatment well known to passify surface states in GaAs epilayers. Although the emission in this case is not of a prominent free-exciton peak, it does not exhibit the UPB/LPB structure. The broadened emission probably results from strain induced by the different coefficients of thermal expansion of the GaAs and Na_2S layers. Further evidence for the importance of surfaces on the free-excitonic emission has been demonstrated by Fisher and Stoltz [38]. They measured the low-temperature PL spectra of samples cleaved in air and cleaved in ultra-high vacuum and found that the UPB/LPB structure was absent in the UHV-cleaved samples. Non-radiative surface recombination and bandbending are considerably reduced in samples with UHV-cleaved surfaces. Thus, the absence of

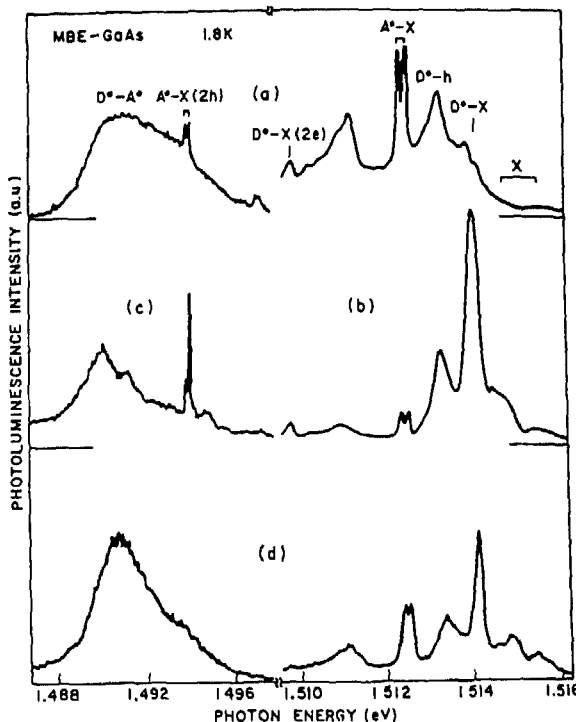


Fig. 18. 1.8 K PL spectra of various MBE-grown, n-type GaAs epilayers (a), (b), (c) two-hole replica spectrum, and (d) p-type sample. (After Dingle et al. [31].)

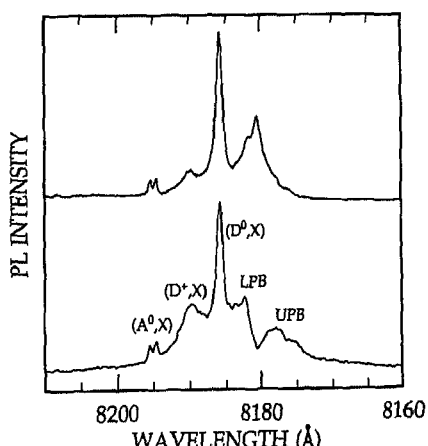


Fig. 19. Low-temperature PL spectra of a GaAs/AlGaAs double heterostructure before and after chemical etch removal of the top AlGaAs barrier layer.

the UPB/LPB structure in the UHV-cleaved structures may be attributed to an improved surface. It may therefore be concluded that surfaces may significantly affect free-exciton emission.

Phonon replicas of the free-exciton as well as the edge-bound excitons may also be observed in high-purity GaAs [39]. Reynolds et al. [39] examined the resonantly excited (at the free-exciton energy) PL spectra of high-purity GaAs layers grown by CVD. Fig. 21 shows the phonon sidebands associated with the emission. The solid curve corresponds to resonant excitation at the free-exciton energy, while the dashed line represents resonant excitation at the neutral donor-bound exciton. This

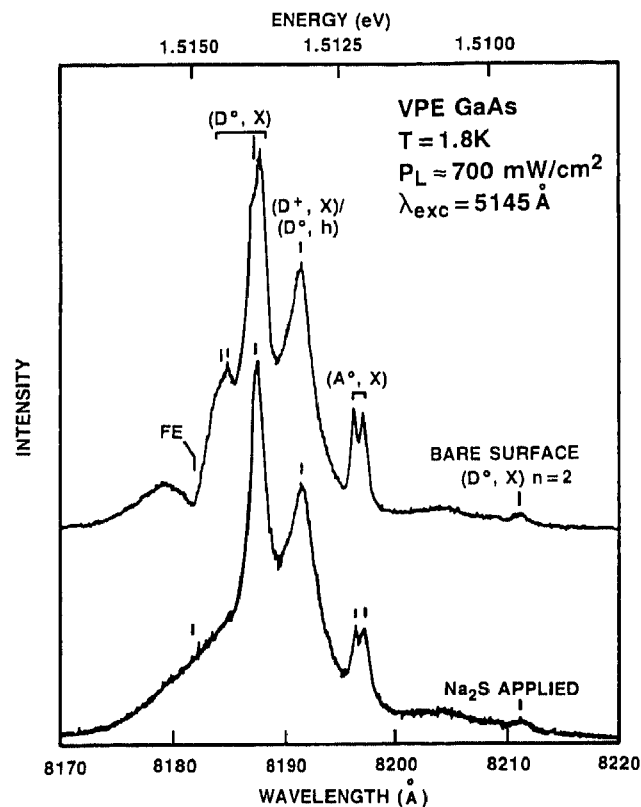


Fig. 20. 1.8 K PL spectra of VPE-grown GaAs layers before and after application of Na_2S . (After Skromme et al. [37].)

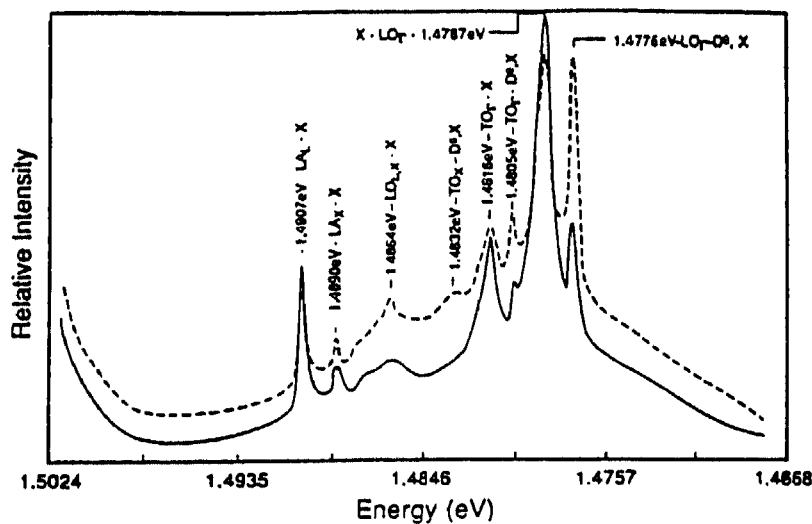


Fig. 21. Phonon sidebands related to the near-edge emission of a high-purity chemical vapor deposition GaAs sample. (After Reynolds et al. [39].)

data shows that most phonons are more strongly coupled to the free exciton than to the bound exciton. The active phonon modes are the LO and the TO modes of the free exciton and the donor-bound exciton at the Γ point; the TO mode of the donor-bound exciton at the X point, the LO phonon of the

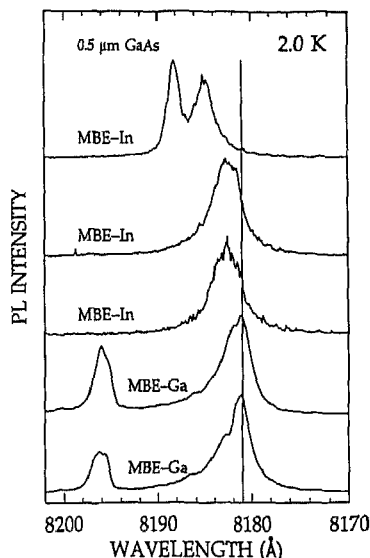


Fig. 22. PL spectra of several MBE-prepared, In-backed GaAs samples at 2 K, showing the strain-induced shift of the free-exciton resonance energy.

free exciton at the L and/or X point, and the LA phonon of the free exciton at the X and L points of the Brillouin zone. They also found that the phonon sidebands were not observed in lower quality material.

Another important factor in the free-exciton emission of GaAs layers is strain. Free-exciton energies are extremely sensitive to even minute amounts of strain in a sample. This strain may even be a result of improper mounting of the sample for PL measurements. Another source of strain may arise during growth of the sample. Fig. 22 shows PL spectra for several MBE-prepared samples grown at 600 °C. The free-exciton energies are shifted slightly from the known resonance energy. This is a result of the growth procedure. It has been common to grow GaAs epilayers by mounting the GaAs substrate with indium backing. At the growth temperature this indium diffuses into virtually the entire substrate, thus forming an InGaAs alloy. After growth the sample is cooled down to room temperature and the resulting sample in reality consists of a InGaAs substrate with a strained GaAs epilayer grown on top. This interpretation has been confirmed by taking a sample which was mounted with Ga metal during growth, measuring the PL spectrum, and then evaporating In to the back, heating it to 600 °C for 1 h, and then measuring the low-temperature PL spectrum. The result, shown in Fig. 22, clearly shows a shift in the FE emission after In annealing.

Just as important to the fabrication of high-quality GaAs layers is the interpretation of the spectra. As noted above, the original interpretation of the spectra in the vicinity of the free-exciton resonance has often involved the concept of the exciton-polariton and the upper- and lower-polariton branches [25]. Other interpretations included reabsorption [40] and exciton-electron scattering [41]. All of these interpretations were put forth in an effort to explain the commonly observed doublet at the free-exciton resonance energy in the PL spectra. The most popular of these theories was the exciton-polariton. The polariton nature of the exciton was first postulated in 1958 by Pekar [42] and Hopfield [43]. The exciton-polariton is a quasi-particle formed through the coupling of photons and excitons. Most recently, the work of Lee et al. [27], Koteles et al. [26], and Steiner et al. [44] have demonstrated, through comparison of spectra on high-purity MBE-grown samples with a theory based on the elastic scattering of exciton polaritons from residual neutral impurities, the true origin of this doublet. Fig. 23 shows the PL spectra of samples with varying concentrations of donor impurities (with the highest

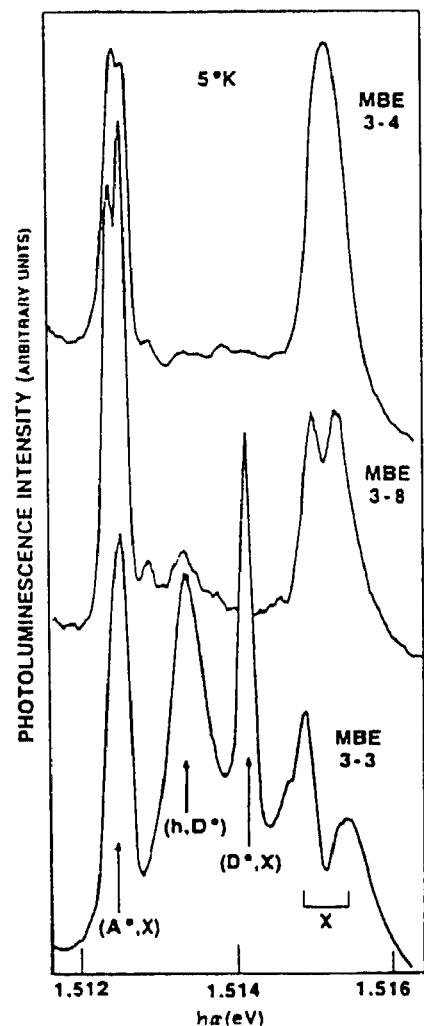


Fig. 23. 5 K PL spectra of three MBE-prepared GaAs samples. (After Koteles et al. [26].)

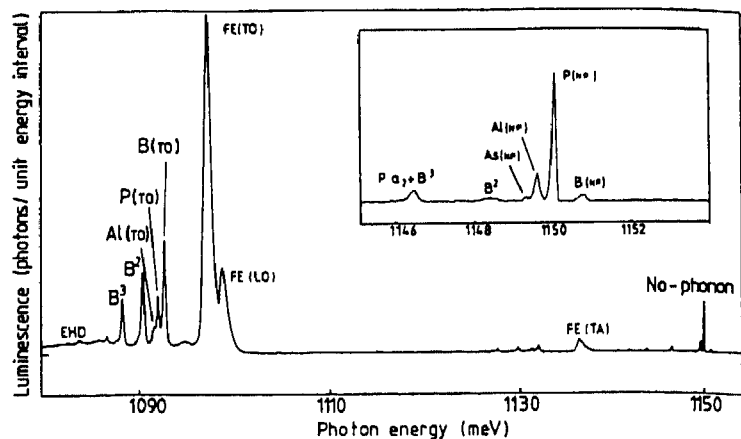


Fig. 24. Low-temperature PL spectrum from near-intrinsic Si with resistivity $> 20 \text{ k}\Omega \text{ cm}$. Low concentrations of B, P, Al, and As are evident. (After McLColley and Lightowers, *Semiconductor Sci. Technol.*, 2 (1987) 157.)

concentration in sample 3-3 and the lowest in sample 3-4) [26,27]. Clearly the increase in donor concentration yields the doublet structure. Their calculations further demonstrate that neutral donors are an order-of-magnitude more effective in scattering excitons, yielding the doublet structure. Importantly, this model also relies upon the effects of a “dead layer” at the surface in order to yield the same doublet structure [44]. Thus, the current prevailing view regarding free-exciton emission involves both exciton–polariton scattering by neutral donors and the effects of a “dead layer” at the surface. This model also explains the wide variability in spectra from sample to sample. Another important point refuting the early assignment of the UPB and LPB peaks in the PL spectra is the known longitudinal/transverse free-exciton splitting in GaAs of 0.08 meV [45]. The longitudinal/transverse exciton splitting corresponds to the energy separation between the UPB and LPB. Experimentally the observed splittings between the commonly observed doublet structure is approximately 0.8 meV, an order-of-magnitude larger than the theoretically predicted value.

2.2.2.2. Silicon

Since Si is an indirect-gap semiconductor, the emission of photons must be accompanied by the simultaneous emission of phonons in order to conserve momentum. The phonons which are allowed within the conduction band are the LO, TO, and TA phonons [17]. Additionally, a weak no-phonon component has been reported [46], which arises as a result of small deviations from cubic symmetry. Fig. 24 shows the luminescence spectrum of a near-intrinsic Si sample which exhibits the no-phonon free-exciton emission as well as the TA, LO, and TO phonon replicas [47]. Thewalt and McMullan [48] find a no-phonon free-exciton energy of 1154.54 ± 0.07 meV. The relative intensities of the various phonon replica peaks are temperature dependent, and above ~ 15 K occur in the following proportions [49]

$$\text{TA:LO:TO} = 0.03:0.1:1$$

The shape of the emission bands associated with free-exciton recombination and the phonon replicas is given by

$$I(E) \approx (E - E_0)^{1/2} \exp\left[-\frac{(E - E_0)}{kT}\right] \quad (13)$$

where E_0 is the threshold for luminescence [50]. This is often called the Maxwell–Boltzmann distribution. Fig. 25 shows the free-exciton phonon replicas versus excitation power [51]. The small energy difference between the LO and TO phonons gives rise to the “doublet” structure evident in the spectra. With increasing temperature the linewidth of the emission increases linearly. This is a result of the growth of the mean kinetic energy of the free-exciton gas with increasing temperature. This can then be taken advantage of to determine the temperature of the sample. By properly fitting the overlapping spectrum of the LO and TO phonon replicas, including phonon broadening and spectrometer slit broadening, the temperature of the free-exciton gas may be determined. Fig. 26 shows an example of such fits with the derived temperatures shown.

Thus, there are two primary differences in the free exciton emission of Si and GaAs. Free-exciton emission is forbidden in Si, and allowed in GaAs. Consequently, the observed free-exciton emission in Si is actually a phonon replica. Lastly, the lineshape of free-exciton emission in Si is well known and allows precise determination of excitonic temperatures. In contrast, the theoretical form of the free-exciton lineshape in GaAs is unknown.

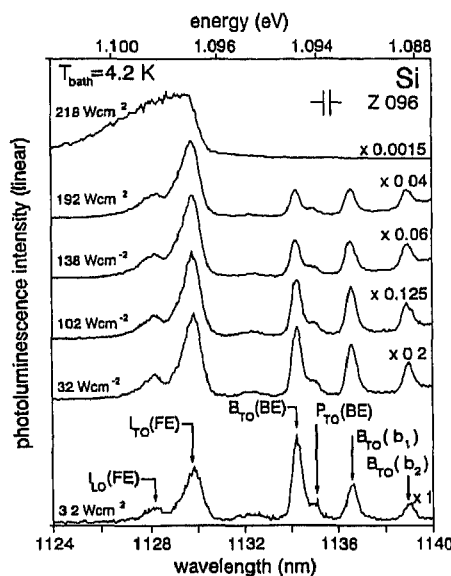


Fig. 25. PL spectra of a Si sample versus excitation intensity. (After Pelant et al. [51].)

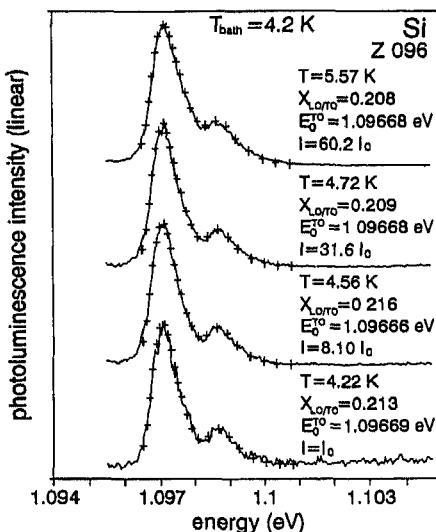


Fig. 26. Si PL spectra versus excitation intensity in the spectral vicinity of the TO- and LO-phonon replicas of the free exciton. (After Pelant et al. [51].)

2.2.2.3. GaAs nanostructures

In 1974 Dingle, et al. [4] fabricated the first nanostructure, a GaAs/AlGaAs quantum well, and demonstrated the quantum confinement effects of the structure through absorption measurements. The excitonic nature of the low-temperature emission from such structures was not demonstrated until 1981 by Weisbuch et al. [52]. The features observed by Weisbuch et al., shown in Fig. 27, required an intrinsic mechanism that can explain the exciton broadening with well thickness. Further, they required an excitonic model. In 1984 Bastard et al. [53] examined the Stokes shift between the peak in the PL emission spectrum and the peak in the PL excitation (PLE) spectrum. Fig. 28 shows their results for a 70 Å thick GaAs/Al_{0.52}Ga_{0.48}As quantum well. They observe a 5.8 meV linewidth in the

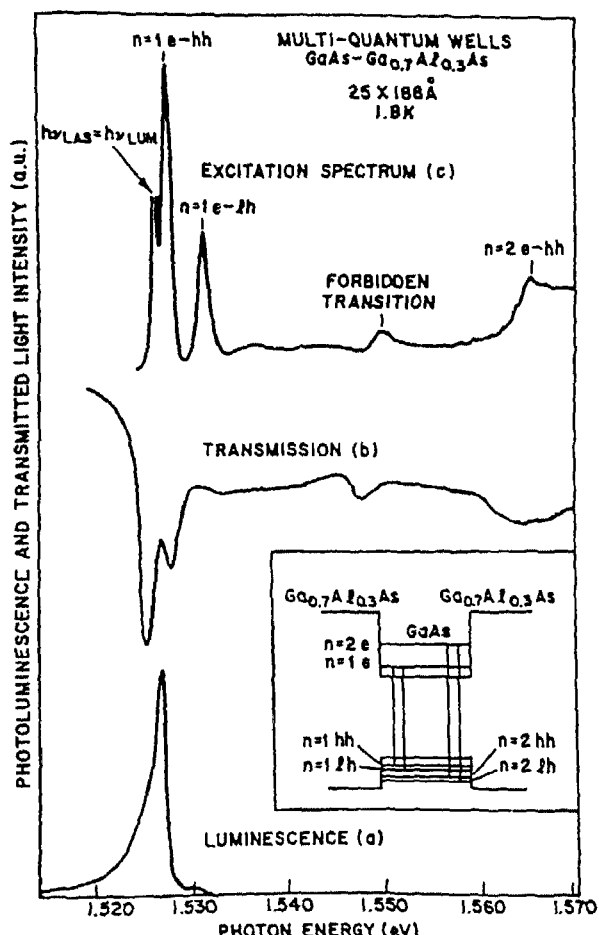


Fig. 27. (a) PL, (b) absorption, and (c) PLE spectra of a multiple quantum well sample at 1.8 K. PLE was detected at 1.525 eV. (Reprinted from Weisbuch et al., *Solid State Commun.*, 37 (1981) 219 with permission from Elsevier Science Ltd , Pergamon Imprint, The Boulevard, Langford Lane, Kidlington OX5 1GB, UK)

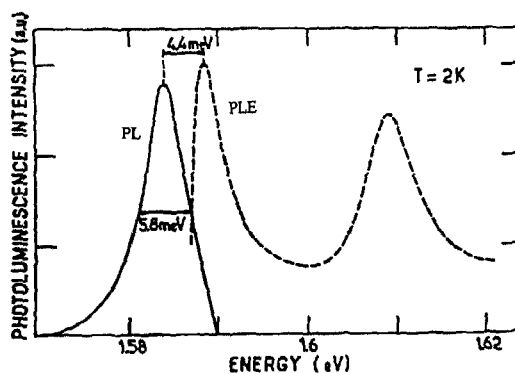


Fig. 28. PL (—) and PLE (---) spectra of a 70 Å GaAs/AlGaAs quantum well at 2 K. (After Bastard et al. [53])

PL spectrum and a 4.4 meV Stokes shift between absorption and emission spectra. The PLE spectrum clearly shows the absorption peaks due to heavy-hole and light-hole excitons. The PL emission is attributed to the heavy-hole exciton with the light-hole exciton absent in the spectrum. Their lineshape

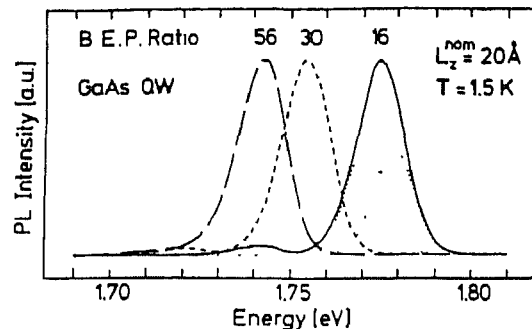


Fig. 29. BEP ratio dependence of the PL spectra of a 2 nm quantum well at 1.5 K. (After Munnix et al. [60].)

analysis of the PL emission did not exhibit a Boltzmann tail ($\exp(-E/kT)$) on the high-energy side. They concluded that the Stoke's shift and the lack of thermalization among the excitons is due to the localization of the excitons on intrinsic interface defects. Bimberg and coworkers [54–57] later showed that the luminescence from quantum wells always consists of a doublet, which is sometimes unresolved. Their measurements showed that the emission lineshape of this doublet depends upon the growth parameters such as the growth rate and As_4/Ga beam equivalent pressure ratio [58–60]. Fig. 29 shows the PL spectra of three 20 Å quantum wells grown with three different beam equivalent pressure ratios. Their lineshape analysis shows that each spectrum consists of three lines. They attribute the low-energy line to the free electron to carbon–acceptor transition. Further, they find the main peak is actually a doublet. The temperature and excitation density dependence of the PL spectra shows that this peak is extrinsic in nature, and is most probably an exciton bound to a C acceptor. The remaining high-energy peak is due to the recombination of the $n = 1$ heavy-hole free exciton. Miller and coworkers [61,62] and Meynadier et al. [63] also found evidence for extrinsic emission in GaAs quantum wells. There have also been clear reports of free excitons contributing to the room-temperature PL of GaAs/AlGaAs quantum wells [64–70]. Fig. 30 shows the temperature dependence of the PL emission of a single quantum well structure [2]. The exciton luminescence exhibits a rather sharp line even at room temperature, and shows the red-shift expected with increasing temperature. Confirmation of the excitonic nature of these peaks is given by the coincidence of the luminescence peaks with the excitonic resonances in the reflectance spectra.

Further technological developments in the growth of GaAs quantum wells have significantly improved the PL emission properties of free excitons in quantum wells. Fig. 31 shows the cw PL

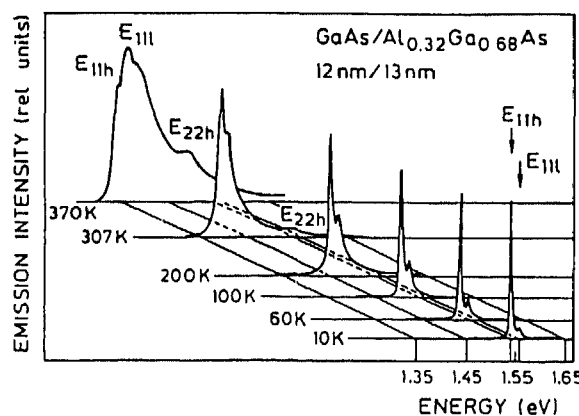


Fig. 30. Temperature dependence of the PL from a 12 nm GaAs quantum well (After Cingolani and Ploog [2].)

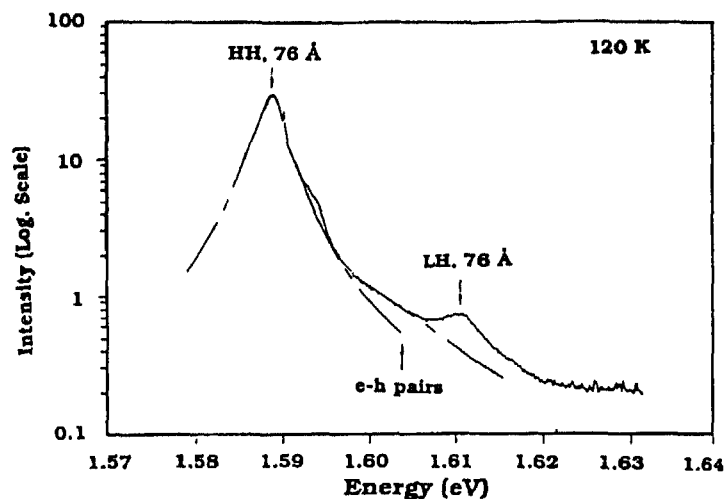


Fig. 31. Cw PL spectrum at 120 K of a 76 Å quantum well. ---, Lorentzian lineshape. Heavy-hole excitons, light-hole excitons, and free electrons and holes contribute to the observed spectrum.

spectrum of a 76 Å GaAs quantum well [71]. Note that both the heavy-hole and light-hole free-exciton emissions are evident. The appearance of the light-hole free exciton is a result of the 120 K lattice temperature. Low-temperature PL measurements versus excitation power demonstrate the improvement in linewidth of quantum well free-exciton emission, as shown in Fig. 32. At a density of $2 \times 10^9 \text{ cm}^{-2}$ the linewidth is 1.7 meV. At low temperature and low excitation density, the linewidth is predominantly Gaussian with a small Lorentzian component with a width of 0.34 meV, the homogeneous linewidth. With increasing excitation intensity the Lorentzian increases in width. The current record for minimum, low-temperature free-exciton PL linewidth in a quantum well is 0.65 meV, as shown in Fig. 33 [72]. The two narrow lines associated with the heavy-hole free-exciton emission correspond to an approximately one-monolayer fluctuation in the well thickness. Kusano et al. [73] examined the 3D to 2D transition region for quantum wells and found that even for well widths as

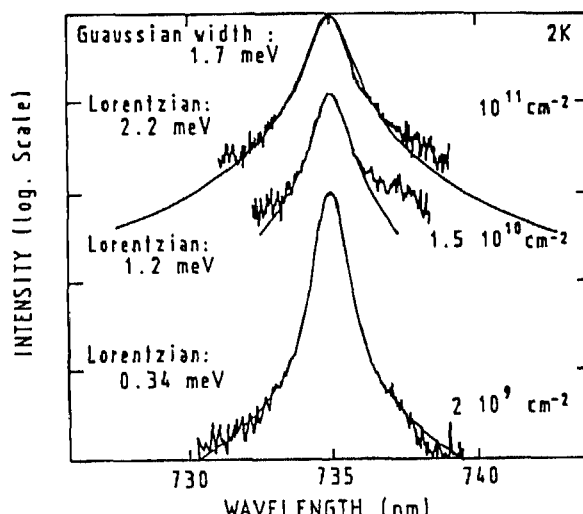


Fig. 32. PL lineshapes after resonant excitation at different excitation densities. The fit is a convolution of a Gaussian lineshape (1.7 meV linewidth) with a density-dependent Lorentzian lineshape.

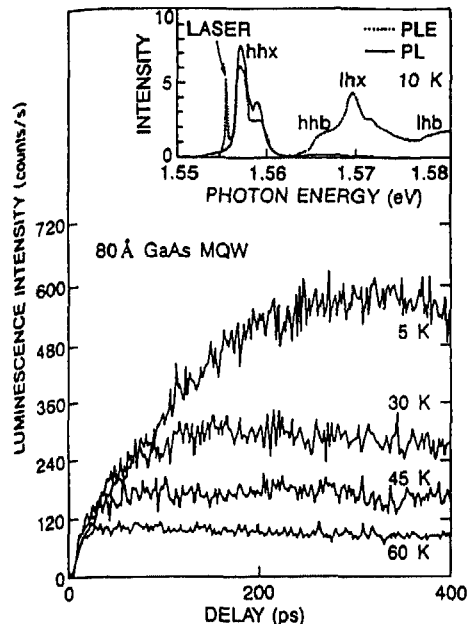


Fig. 33. PL intensity of the exciton luminescence versus time and temperature. Inset shows cw PL and PLE spectra at 10 K. hhx and lhx are heavy-hole and light-hole exciton transitions and hbx and lhb are corresponding band-to-band transitions. (After Damen et al. [72].)

large as 2010 \AA , which is 20 times larger than the exciton Bohr radius, quantum size effects are still present. They also find that the exciton coherence length is greater than 4000 \AA .

Just as with bulk GaAs layers, the issue of exciton-polaritons is important in quantum wells [45,74–78]. Andreani and Bassani [77] have made extensive calculations of the properties of exciton-polaritons in GaAs quantum wells, including the effects of the exchange interaction, dispersion, and lifetimes. Kusano et al. [74] observed discrete fine structures in the luminescence of the free-exciton band in a GaAs quantum well, as shown in Fig. 34. This fine structure was explained as due to the quantization of the exciton polariton along its dispersion curve (Fig. 35).

The excitonic nature of the luminescence of quantum well wires and quantum dots fabricated from GaAs/AlGaAs is less understood than for quantum wells. Although, free excitons in such reduced dimensionality structures certainly exist, most studies have concentrated upon examination of the quantum confinement and fabrication issues. This will be addressed in sections 2.3.4 and 2.3.5.

2.2.3. Defect photoluminescence

PL has proven to be an extremely useful tool for the characterization of defects in semiconductors. Impurity concentrations as low as $\sim 10^{12} \text{ cm}^{-3}$ are detectable without sample destruction. It is also possible to identify impurities through their unique spectral signatures. It is also sometimes possible to distinguish between simple centers and more complex centers. A simple center is an impurity which is incorporated substitutionally for the cation or anion of the crystalline lattice and contributes only one carrier (electron or hole) to the binding [6]. Complex centers may involve impurities in interstitial lattice positions or combinations of multiple impurities. With the exception of several simple pair recombination mechanisms, this review will deal only with simple centers, focusing upon the emissions associated with donors, acceptors, and deep levels. As an example, Fig. 36 shows an approximate energy level diagram of shallow impurity related emissions which are commonly observed in GaAs.

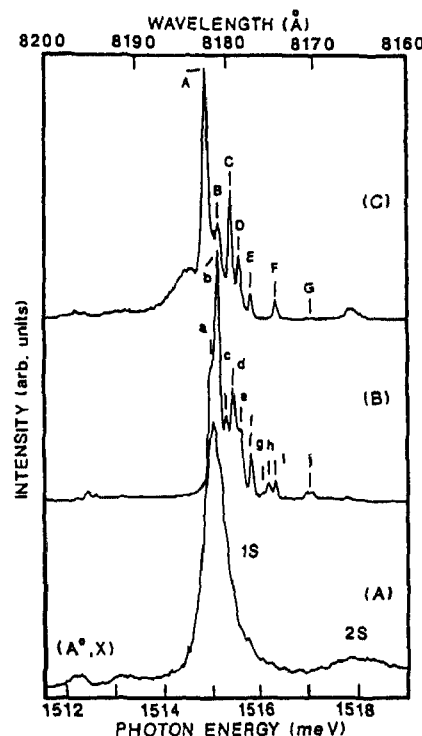


Fig. 34. PL spectra of undoped GaAs epitaxial films taken at a lattice temperature of 1.8 K. The film thicknesses are (a) 5200 Å, (b) 2010 Å, and (c) 990 Å. (Reprinted from Kusano et al., *Solid State Commun.*, 72 (1989) 215, with permission from Elsevier Science Ltd., Pergamon Imprint, The Boulevard, Langford Lane, Kidlington OX5 1GB, UK.)

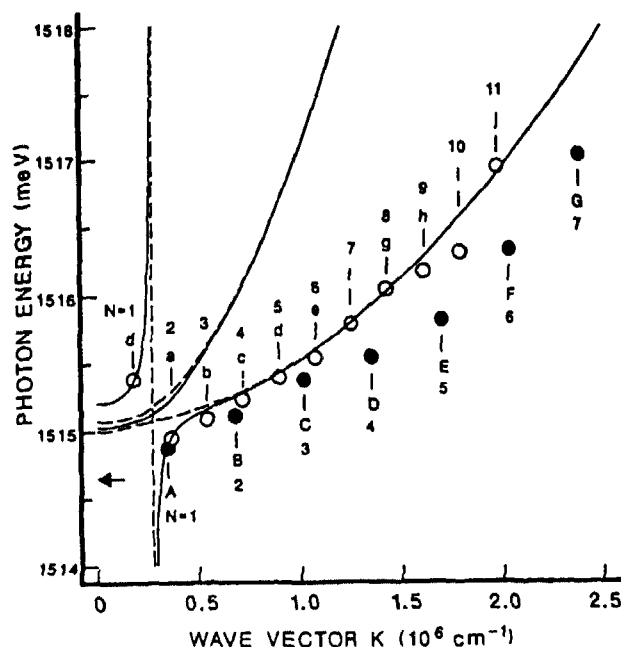


Fig. 35. Dispersion curve of the exciton-polariton. PL peak emission energies for the (○) 2010 and (●) 990 Å quantum wells (Reprinted from Kusano et al., *Solid State Commun.*, 72 (1989) 215, with permission from Elsevier Science Ltd., Pergamon Imprint, The Boulevard, Langford Lane, Kidlington OX5 1GB, UK.)

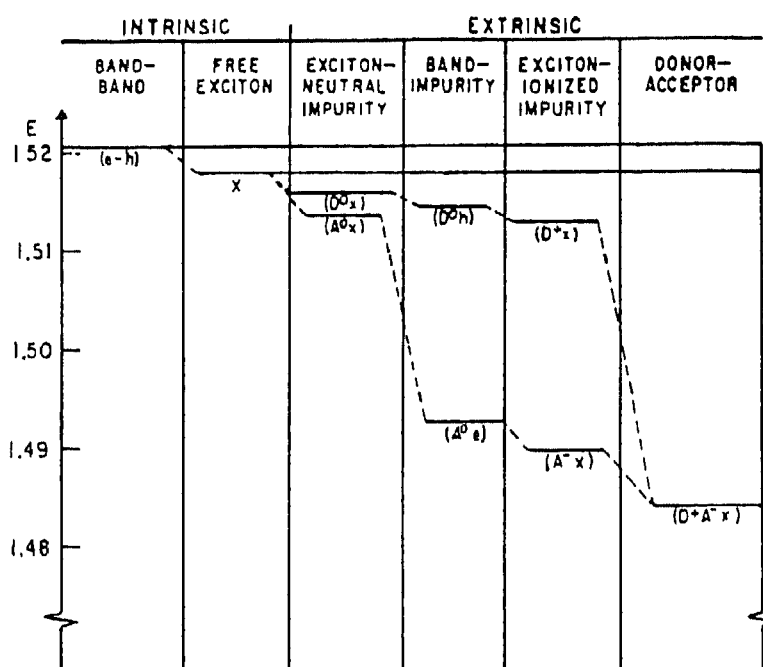
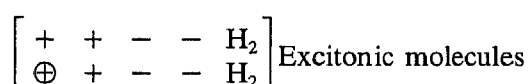
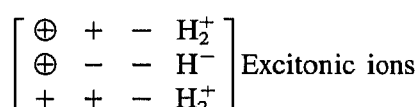


Fig. 36. Relative energies of several possible intrinsic and extrinsic emission and absorption processes in GaAs [6].

2.2.3.1. Bound excitons

A point defect may increase the binding energy of a free exciton. An exciton may become bound at an impurity if the total energy of the system is reduced. Lampert [79] first considered the formation of bound excitons by drawing an analogy with the hydrogen molecule H_2 and hydrogen molecule ion H_2^+ . He calculated the binding energy of a number of possible excitonic complexes in terms of the effective mass ratio of the constituent carriers. The simplest set of such excitonic complexes are:



An exciton bound to an ionized donor, D^+ , consists of a donor ion, \oplus , and electron, $-$, and a hole, $+$. This will be denoted by (D^+, X) . Likewise, an exciton may be bound to an ionized acceptor, yielding (A^-, X) . Excitons may also become bound to neutral donors or acceptors, (D^0, X) and (A^0, X) , respectively. The spectral signatures associated with each of these types of impurity complexes is sensitive to the chemical species of the impurity due to the differences in central-cell potential of the impurities with respect to that of the lattice ion for which it substitutes. Thus, the PL spectra of these bound excitons, which exhibit very sharp no-phonon lines in undoped to moderately doped samples, can be used to fingerprint the donors and, particularly, the acceptors to which the excitons bind. Often, both free excitons and bound excitons may be observed simultaneously in the emission spectrum of a sample.

2.2.3.1.1. GaAs

The binding energies of donors and acceptors in GaAs are of the order of 5 meV and 30 meV, respectively, varying slightly from one impurity to another. Fig. 37 shows a schematic energy level diagram of several common bound exciton complexes in GaAs (note that the binding energy of the free exciton shown is not correct, it is now generally accepted to be 4.2 meV) [6]. The most common donors in GaAs are Si and Ge, whereas the most common acceptors in GaAs are C and Be. Table 1 lists the optical activation energy of several common donors and acceptors in GaAs. The activation energies observed in optical measurements are prevalently larger than those obtained through analyses of electrical transport data. There is some ambiguity in the electrical activity of some impurities, namely the group IV impurities are amphoteric, possibly acting as either donors or acceptors. However, in practice there is often a site-occupancy preference which favors the formation of donors over acceptors, or vice versa. For Si impurities, under normal growth conditions, Si donors outnumber Si acceptors by as much as 1000:1 [80]. In contrast, C tends to preferentially occupy As sites, and, therefore, act predominantly as acceptors in GaAs.

Some of the earliest and most comprehensive work on identification of impurity-related emissions in GaAs crystals was performed in the 1970s [81–83]. GaAs films at that time were not of the quality and purity of films which may be grown today using modern growth techniques such as MBE.

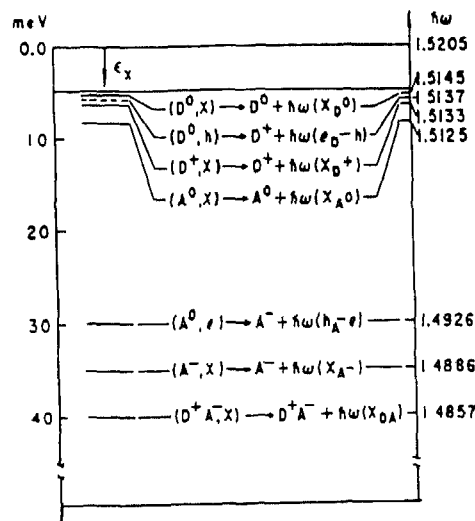


Fig. 37. Near-edge exciton complexes in GaAs [6].

Table 1
Optical activation energies of donors and acceptors in GaAs [80,99,108,593]

Donors		Acceptors	
Impurity	Activation energy (meV)	Impurity	Activation energy (meV)
Si	5.801	Cd	34.7
Ge	5.937	Zn	30.7
S	5.854	Mg	28.4
Se	5.9	Be	28.0
Te	5.786	C	26.0
Sn	5.816	Si	34.5
		Ge	40.4
		B	71

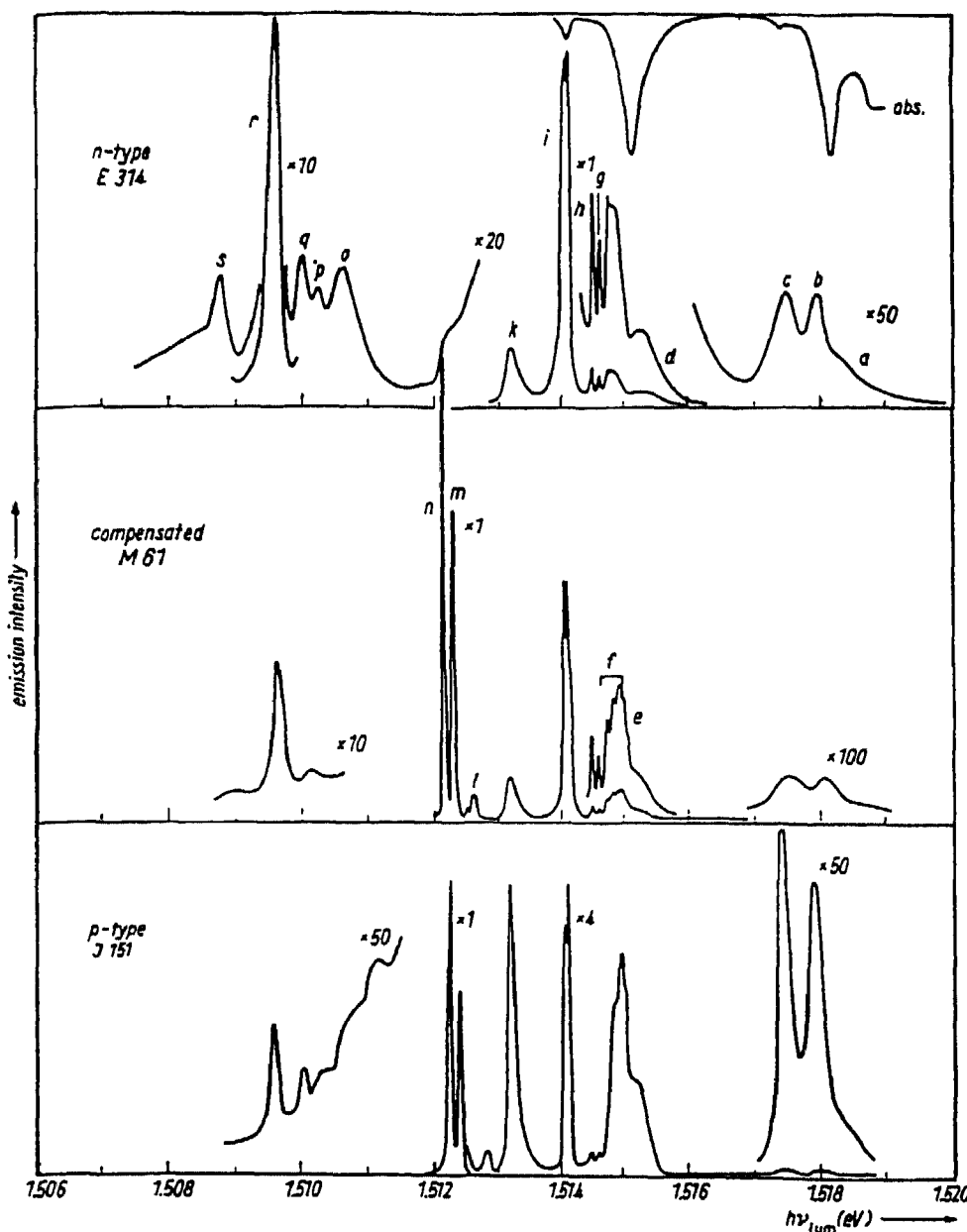


Fig. 38. PL spectra of three LPE-prepared GaAs samples at 18 K. (After Heim and Hiesinger [81].)

Nevertheless, it was possible to identify many impurity complexes in those lower quality films, and Fig. 38 shows a high-resolution PL spectra with the various emission lines labeled from a to s. Table 2 lists each of these emission lines. Fig. 39 shows a typical low-temperature (1.6 K) PL spectrum of high-quality epitaxial GaAs with some of the most ubiquitous PL emission peaks clearly evident [22]. The near-edge bound-exciton emissions are energetically just below the free-exciton peak. Figs. 11, 20, 23 and 40 show PL spectra of these bound exciton emission lines in the vicinity of the near-edge region. These spectra are just some of the many data from which the excitonic transition energies may be obtained [26,37,45,84-90]. The published wavelengths corresponding to the recombination of specific species often vary by a few angströms, and this may be attributed to variances in spectral

Table 2
List of PL emission lines in GaAs [81]

Line	Energy (eV) (± 0.1 meV)	Assignment
a	1.5186	$n = 3$ state of neutral donor or high-energy tail of the $n = 2$ exciton emission
b	1.5181	$n = 2$ state of the free exciton
c	1.5175	$n = 2$ state of the neutral donor
d	1.5153	$n = 1$ state of the free exciton, upper polariton branch
e	1.515	Free exciton, lower polariton branch
f	1.5148-1.515	Excited states of (D^0, X) or excitons bound to complexes involving neutral donors
g	1.5147	Excited states of (D^0, X) or excitons bound to complexes involving neutral donors
h	1.5146	Excited states of (D^0, X) or excitons bound to complexes involving neutral donors
i	1.5141	Exciton bound to neutral donor (D^0, X)
k	1.5133	Exciton bound to ionized donor (D^+, X) or valence band to neutral donor transition (D^0, h)
l	1.5128	$J = 1/2$ exciton bound to neutral acceptor (A^0, X)
m	1.5124	$J = 3/2$ exciton bound to neutral acceptor (A^0, X)
n	1.5122	$J = 5/2$ exciton bound to neutral acceptor (A^0, X)
o	1.5108	Two-electron transition of a free exciton recombining in the vicinity of a neutral donor
p	1.5104	Two-electron transitions of lines f, g, and h
q	1.5101	Two-electron transitions of lines f, g, and h
r	1.5097	Two-electron transitions of (D^0, X) with the donor left in the $n = 2$ state
s	1.5089	Two-electron transitions of (D^0, X) with the donor left in the $n = 3$ state

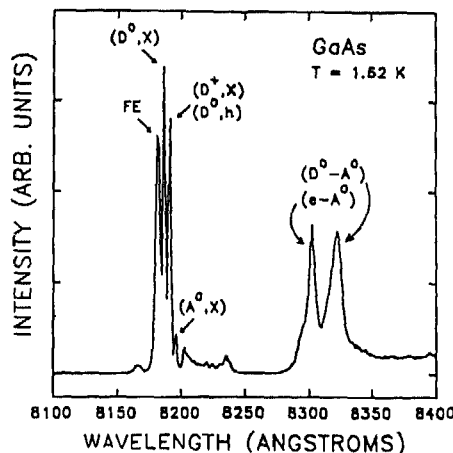


Fig. 39 Low-temperature PL spectrum of epitaxial GaAs. (After Ramsbey et al. [22].)

calibrations or shifts due to crystal stress induced by a variety of factors, including sample mountings. In Fig. 11, (a relatively low-resolution spectrum), the peak labeled (D^0, X) at 8187 Å (1.5145 eV) is due to the radiative recombination of excitons bound to neutral shallow donors. The energy levels induced by $j-j$ coupling of two electrons and a single hole gives rise to a single $J = 3/2$ level, yielding a single PL no-phonon emission line [82,83]. The peak at 8192 Å (1.5133 eV) corresponds to two spectrally overlapping processes: the recombination of excitons bound to ionized shallow donors (labeled D^+, X), and free holes recombining with neutral donors (labeled D^0, h). The peak at 8196 Å (1.5125 eV) is due to the recombination of excitons bound to shallow neutral acceptors (labeled A^0, X). As seen in Figs. 20, 40 and 41 this peak is in reality several peaks [37,45,90]. Early spectroscopy of the acceptor-bound exciton emission near 1.5121 eV revealed doublets, triplets, and even spectra with four lines in this region [82,91]. The splitting observed here has been attributed to the effects of $j-j$ coupling between the two holes and one electron at the acceptor site which compose

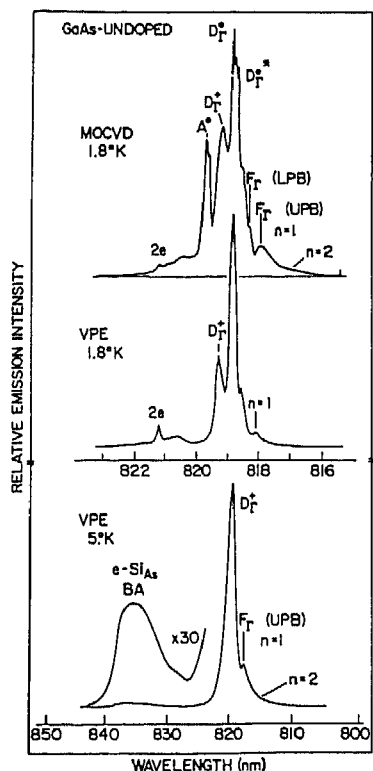


Fig. 40. Low-temperature PL spectra of n-type VPE-grown GaAs, and MOCVD-grown GaAs samples. (Reprinted from Wolford et al., *Solid State Commun.*, 53 (1985) 1069, with permission from Elsevier Science Ltd., Pergamon Imprint, The Boulevard, Langford Lane, Kidlington OX5 1GB, UK.)

the acceptor-bound exciton. Fig. 42 shows two possible models for the energy level structures for the (A^0, X) bound exciton. The differences in the models is the mechanism which yields the doublet splitting, hole-hole interaction or crystal-field interaction [83]. In total this model predicts four exciton levels and two strong emission lines for the (A^0, X) bound exciton from the $J = 5/2$ and $J = 3/2$ levels (and weakly from the $J = 1/2$ level also), and possibly more in the event of any symmetry-lowering strain. Importantly, Haynes' rule does not hold for the common chemical substituent acceptors in GaAs (i.e. C, Zn, and Cd) since the exciton localization energy is not sensitive to changes in the acceptor binding energy due to changes in the acceptor [80].

It is also possible to observe excited states and replicas of the bound exciton emission peaks [92]. Fig. 43 shows a low-temperature PL spectrum with the second, third, and fourth excited non-rigid rotator states of the (D^0, X) line present between the donor-bound exciton and the free exciton, at 8183 Å [93]. Here the hole can be excited to a rotation around the fixed donor, in analogy to the rotation of diatomic molecules. Reynolds et al. [94] observed up to the fifth excited non-rigid rotator state of the (D^0, X) line. These donor-bound exciton excited states have been modeled by Benoit a la Guillaume and Lavallard [95], Rühle and Klingenstein [96], Sharma and Rodriguez [97], and Herbert [98]. However, an exact interpretation of these excited states is difficult. This figure also shows the "two-electron" replicas of the (D^0, X) emission, denoted by $(D^0, X)_{n=2}$. Fig. 44 shows the lowest five excited states of the (D^0, X) emission together with the two-electron replicas ~4.4 meV lower in energy [99]. Figs. 45 and 46 show the corresponding "two-hole" replicas of the (A^0, X) emission, labeled by $2h^+$ for both C and Be acceptors [80,100]. Ashen et al. [80] tabulated the energies of these acceptor-bound exciton and two-hole-related emissions for a variety of acceptors. The two-hole

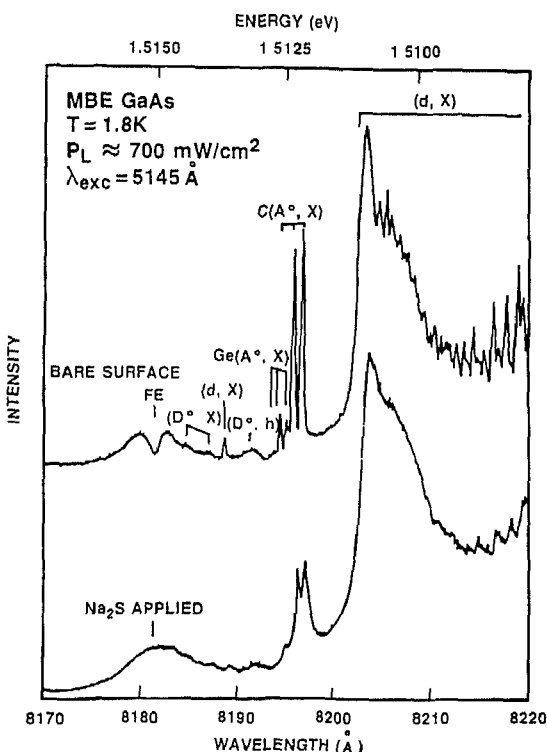


Fig. 41 PL spectra of a p-type MBE sample before and after application of a Na₂S surface passivant. (After Skromme et al [37])

transition associated with an acceptor-bound exciton involves the following process. There is a small probability when the bound exciton recombines that part of the recombination is transferred to the acceptor at the site at which the acceptor is bound. The hole at this acceptor is then left in an excited state which may then recombine. The energy difference between the observed two-hole peak and the principal bound exciton peak is the energy needed to excite the acceptor from the ground to the excited state.

More than one impurity species may also be present simultaneously in a single sample, and possibly evident in the PL spectra. Figs. 41 and 47 show examples of this [37,80,101]. Here, the recombination of excitons bound at both C and Ge acceptors is evident at ~8196 Å and ~8195 Å, respectively (Fig. 41), and of Si, C, and Ge (Fig. 47). The binding energies of typical shallow acceptors are five times larger than those of typical donors, and the observed chemical shifts between different acceptors are also larger than for different donors [80]. The smaller binding energies of donor-bound excitons compared to acceptor-bound excitons is a direct consequence of the difference in effective mass of electrons and holes. For the case of the donor-bound exciton its transition energy depends on the chemical shift due to the differences between the actual binding energy of the donor and the value predicted by the effective mass approximation, Ry(D⁰) = 5.175 meV [102]. This chemical shift results from the interaction with the non-Coulombic potential in the vicinity of the impurity [99]. The large Bohr radius of impurities in GaAs makes this interaction small. This explains why the binding energies of all known shallow donor species in GaAs differ by less than 0.24 meV [103]. Nevertheless, Karasyuk et al. [99] recently used a Fourier transform instrument to obtain high-resolution (0.03 meV) spectra of various donor-bound excitons. Fig. 48 shows the (D⁰,X) transitions as well as the n = 2 two-electron satellite transition (D⁰,X)_{n=2} for three different GaAs samples. Ge,

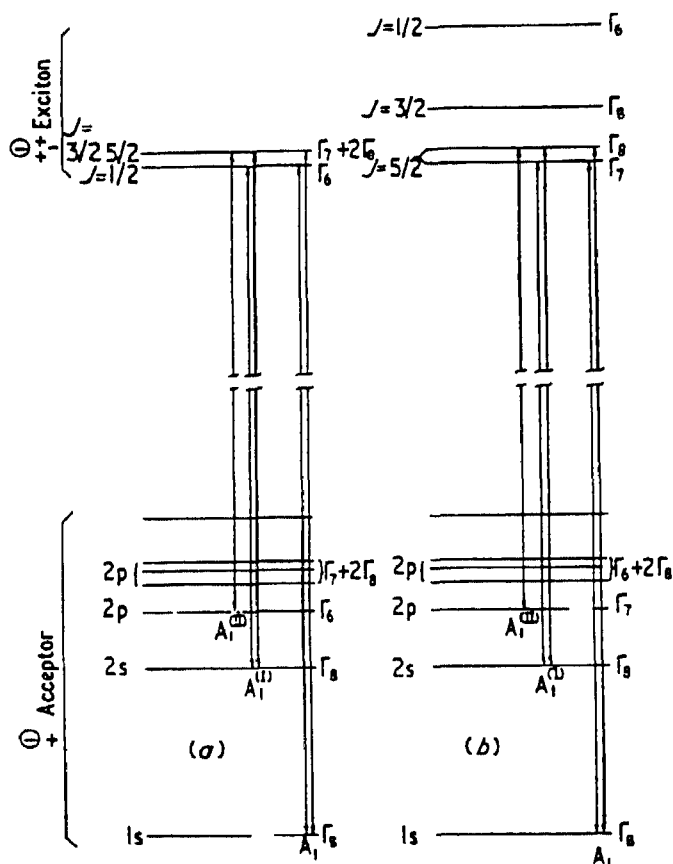


Fig. 42. Energy level diagram of an exciton bound to a neutral acceptor (a) The hole–hole interaction causes the doublet splitting, with the electron–hole and crystal-field interactions unresolved. (b) The doublet splitting is caused by the crystal-field interaction. Forbidden electric dipole transitions are $\Gamma_6 \rightarrow \Gamma_6$ and $\Gamma_7 \rightarrow \Gamma_7$ in both cases. (From White et al., *J. Phys. C: Solid State Phys.*, 5 (1972) 1772.)

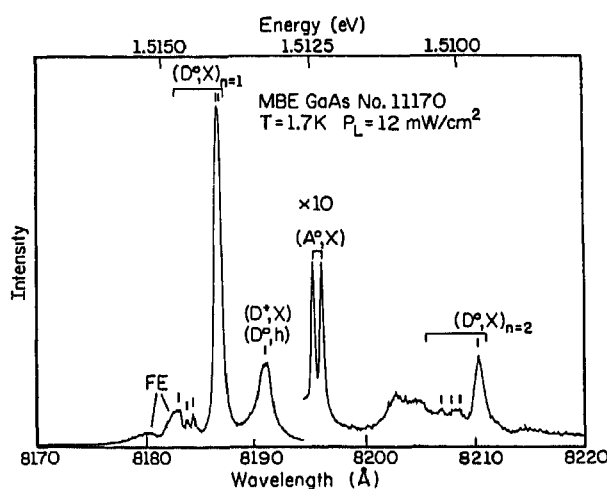


Fig. 43. Low-temperature PL spectrum of a high-purity GaAs layer grown by MBE. (After Skromme et al [92].)

S, Sn, and Si donors are clearly evident in the spectra, in unequal amounts for each of the three samples. Note that the relative energy positions correspond to the binding energies shown in Table 2. In GaAs the very small differences in energy levels for many different donor impurities makes it difficult to

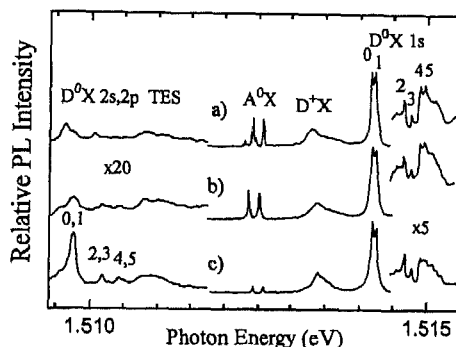


Fig. 44. PL spectra of three different GaAs samples. D^0X labels the principal transitions from the ground (0) or excited states (1–5) of the neutral donor-bound excitons to the ground (1s) state of the neutral donors. $D^0X\ 2s,\ 2p\ TES$ labels the two-electron satellite transitions. (After Karasyuk et al. [99].)

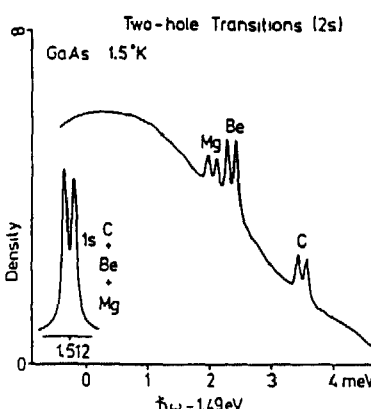


Fig. 45. Two-hole replicas of C, Be, and Mg acceptors in LPE GaAs. Inset shows that the 1s transition is the same for all three impurities, and is therefore useless for chemical fingerprinting. (Reprinted from Ashen et al., *J. Phys. Chem. Solids*, 36 (1975) 1041, with permission from Elsevier Science Ltd., Pergamon Imprint, The Boulevard, Langford Lane, Kidlington OX5 1GB, UK.)

use free (hole) to bound (electron) emission or bound exciton emission for differentiating between such impurities. The situation for acceptors is considerably better since the chemical shifts range from a few millielectronvolts to several hundred millielectronvolts. Lipari and Baldereschi [104] calculated the energy levels of shallow acceptors using a scheme in which the total angular momentum of the hole (3/2) is coupled to the orbital momentum associated with the hydrogenic envelope function. They found that the ground state, which is relatively highly localized, experiences greater perturbations among the chemical impurity species and exhibits a larger increase in binding energy than the excited states. Thus, the ground state energies of the acceptor-bound excitons provides the clearest means for spectrally distinguishing among acceptor impurities. Fig. 49 shows a compendium of the shallow acceptor-related emissions in GaAs. As discussed above, the two-hole transitions allow determination of the electronic structure of acceptor impurities. In this regard Fig. 50 shows the PL spectrum of a Ge-doped GaAs sample which also evidently contains Zn and C acceptors [105]. From this data and data for samples doped with other acceptors, the energy level scheme for C, Zn, Si, and Ge acceptors in GaAs may be determined, and is shown in Fig. 51. Note that the p-symmetric excited states vary significantly in energy from one acceptor to another.

The intensities of the PL emission lines depend on the number of excitons in that state, their energy distribution, and the transition probability for radiative recombination. For example, in Fig. 11 the sample is p-type but the (D^0,X) line is more intense than the (A^0,X) peak. This is because the

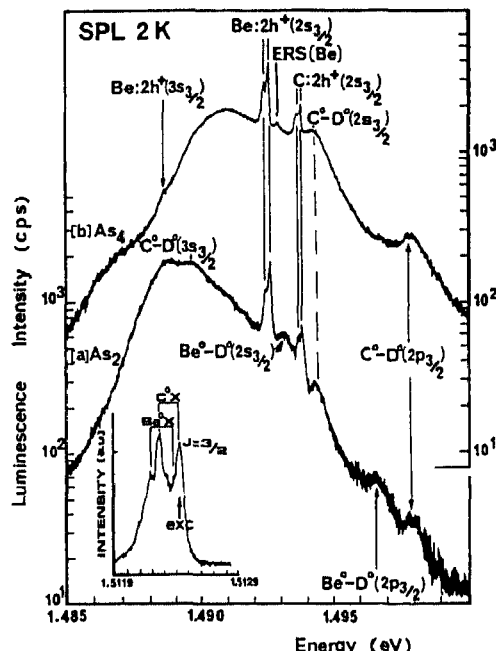


Fig. 46. Selectively excited (on the carbon (A^0, X) transition) PL spectrum for As_4^- - and As_2 -grown samples. Inset shows the (A^0, X) doublet emission. (After Garcia et al. [100].)

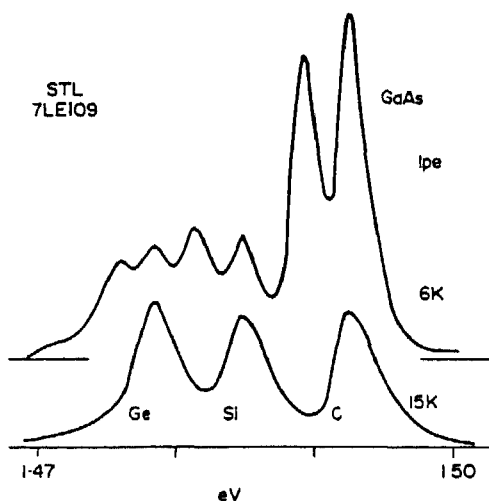


Fig. 47. PL spectra of high-purity, LPE-grown GaAs at 6 K and 15 K. At the higher temperature the P-related transitions are no longer evident and the free-to-bound transitions also become weaker (Reprinted from Ashen et al., *J. Phys. Chem. Solids*, 36 (1975) 1041, with permission from Elsevier Science Ltd., Pergamon Imprint, The Boulevard, Langford Lane, Kidlington OX5 1GB, UK.)

oscillator strength (transition probability) for (D^0, X) is much higher than it is for (A^0, X). Further, more complicated effects, such as the interaction between defects and concentration quenching, may muddle the interpretation of spectra. It is also clear that very slight changes in sample temperature and/or excitation power can alter the relative intensities of the emission lines. In particular, the temperature dependence of the (D^0, X) and (D^+, X) emission lines are significantly different at low temperatures [6]. The (D^0, X) emission decreases rapidly with increasing temperature, while the (D^+, X) line remains relatively constant. Fig. 52 shows the integrated intensity of the (D^+, X) emission line versus inverse temperature. Fits to the data yield an activation energy of approximately 7 meV.

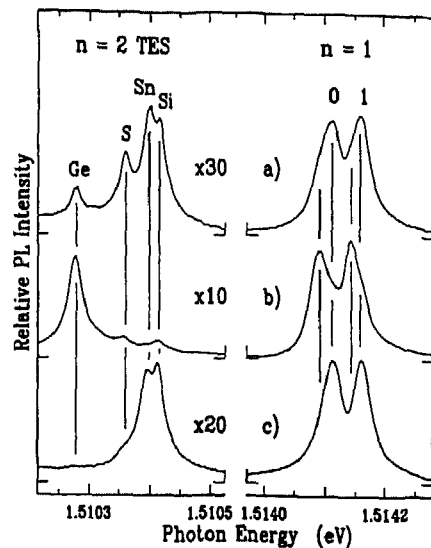


Fig. 48. Comparison of high-resolution ($3 \mu\text{eV}$) PL spectra for three samples. Spectra clearly show presence of different shallow donor species. The chemical shifts between the various donors are clearly evident in the TES transitions, but not in the principal transitions (After Karasyuk et al. [99].)

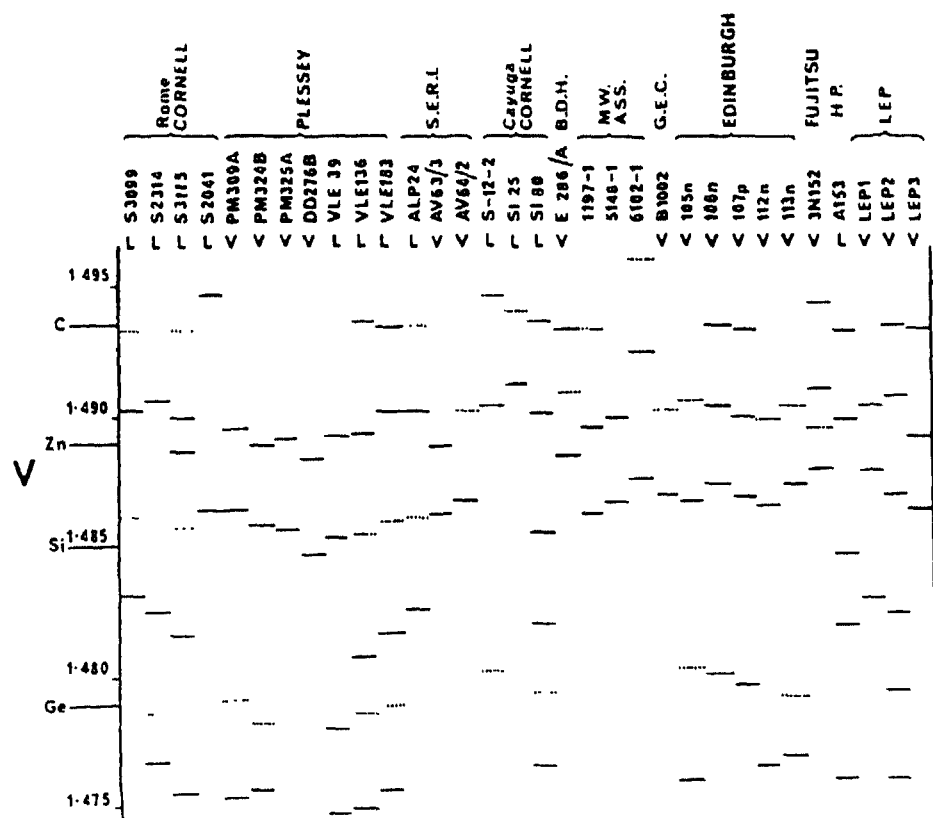


Fig. 49. Observed energies of a variety of PL emission bands in GaAs below 15 K. (Reprinted from Ashen et al., *J. Phys. Chem. Solids*, 36 (1975) 1041, with permission from Elsevier Science Ltd., Pergamon Imprint, The Boulevard, Langford Lane, Kidlington OX5 1GB, UK.)

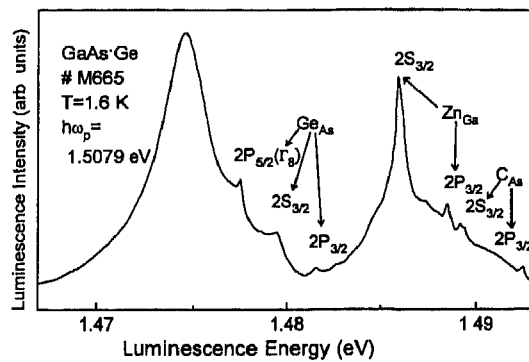


Fig. 50. Selective pair luminescence of a Ge-doped GaAs sample at 1.6 K. Evident in the spectrum are the $2P_{3/2}$, $2S_{3/2}$ and $2P_{5/2}(\Gamma_8)$ states of the Ge acceptor together with some excited states associated with residual Zn and C acceptors. (After Kisker et al. [105].)

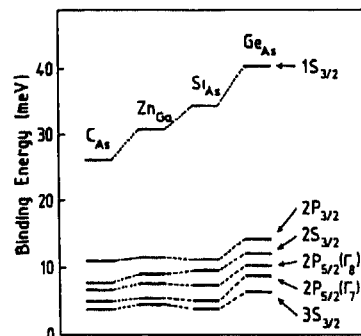


Fig. 51. Energy level diagram of C, Zn, Si, and Ge acceptors in GaAs. The zero of energy in this diagram is the top of the valence band. (After Kisker et al. [105].)

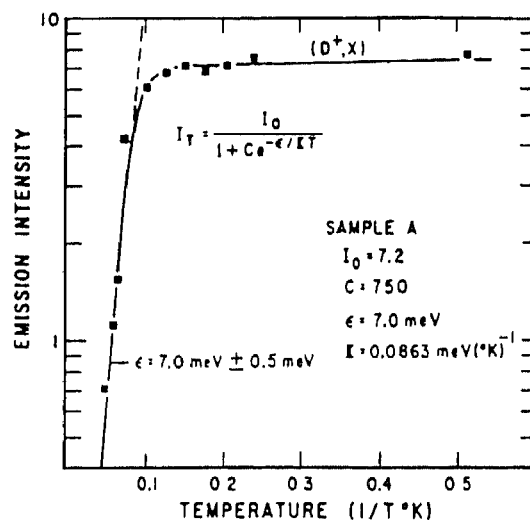


Fig. 52. Emission intensity (integrated) of the (D^+, X) near-edge exciton complex versus inverse temperature [6].

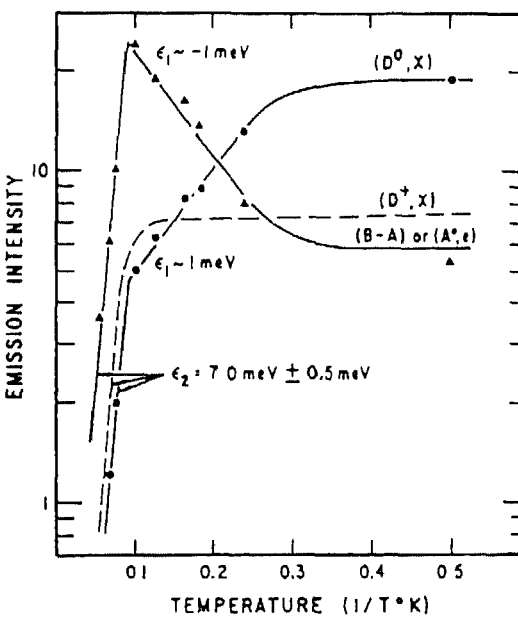
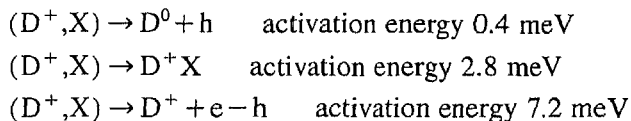


Fig. 53. Inverse temperature dependence of the (D^0, X) bound exciton and the band-to-acceptor emission [6]

There are three possibilities for the thermal dissociation of this bound exciton complex



This data is consistent with the thermal dissociation into an ionized donor (D^+) and a free electron-hole pair ($e^- h$). Fig. 53 shows the temperature dependence of the (D^0, X) bound exciton and the band-to-acceptor (e, A^0) emission lines. The quenching of the (D^0, X) emission is accompanied by an increase in the (e, A^0) emission. This indicates that the (D^0, X) complex thermally dissociates by emitting a free electron to the conduction band which may then recombine with a neutral acceptor radiatively. These are two examples of the possible connection between the spectrally distinct emission lines observed in low-temperature PL spectra.

(i) Dependence upon growth parameters

The details of the near-edge emissions are also strongly dependent upon the growth technique and growth parameters. This is evident in the spectra of Fig. 38 where the background impurity has changed from n-type to compensated to p-type [81]. Differences in growth technique also may lead to changes in the PL spectra, as shown in Fig. 40, where samples were grown by VPE and MOCVD [90]. In MBE growth the PL spectra are also sensitive to the source materials. Garcia et al. [100] and Kunzel and Ploog [106] have grown GaAs layers using both As_2 and As_4 and found significant differences, particularly in the carbon acceptor incorporation. Fig. 54 shows the near-edge PL spectra for samples grown with As_2 and As_4 . Dimeric arsenic clearly gives reduced (A^0, X) emissions associated with reduced carbon-acceptor incorporation.

(ii) Other less-common shallow impurities

Fig. 55 shows the PL spectrum of Se-doped GaAs and the bound exciton associated with this impurity [107]. Fig. 56 shows the PL spectrum of Zn-doped p-type GaAs [107]. These data yield ionization energies of 6 meV and 26 meV, respectively. The ionized Se-exciton emission and the neutral Zn-exciton emission are clearly resolved as a doublet and triplet with separations of 0.2 meV,

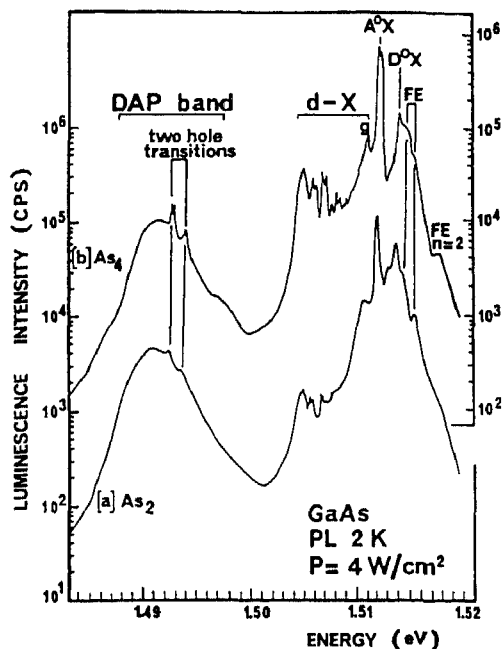


Fig. 54. 2 K PL spectra of Be-doped GaAs grown from (a) As₂ and (b) As₄. (After Garcia et al. [100].)

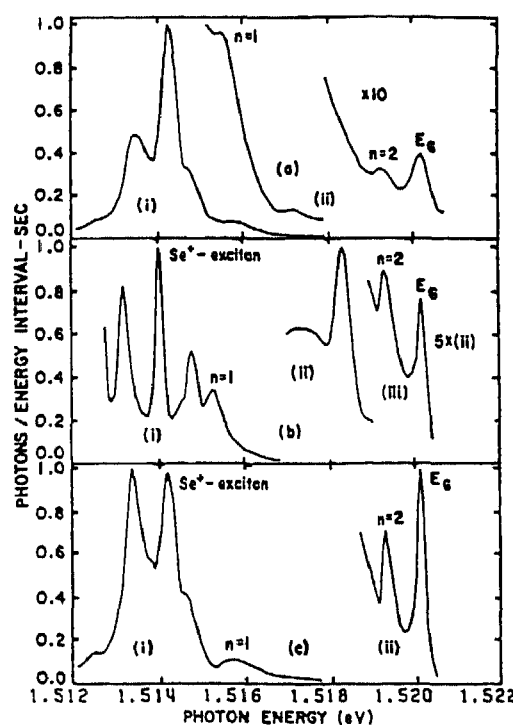


Fig. 55. PL spectra of (a) n-type GaAs; (i) 2.08 K, (ii) 1.38 K; (b) p-type GaAs; (i) 4.2 K, (ii) 1.46 K, (iii) 1.36 K; and (c) high-resistivity GaAs; (i) 2.12 K, and (ii) 1.38 K. (After Gilleo et al. [107].)

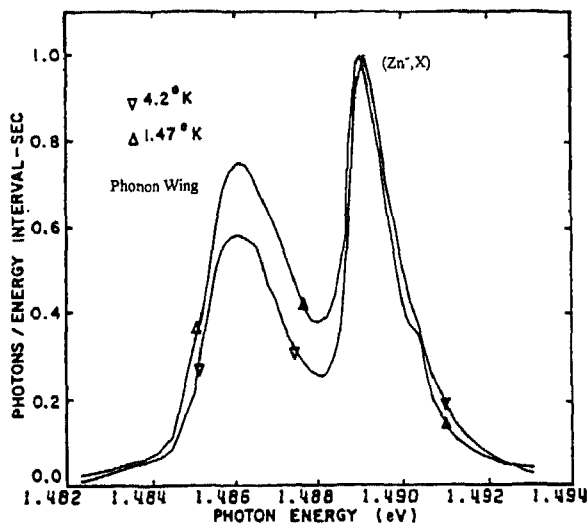


Fig. 56. Temperature dependence of phonon replica compared to no-phonon line of Zn-bound exciton line. (After Gilleo et al [107].)

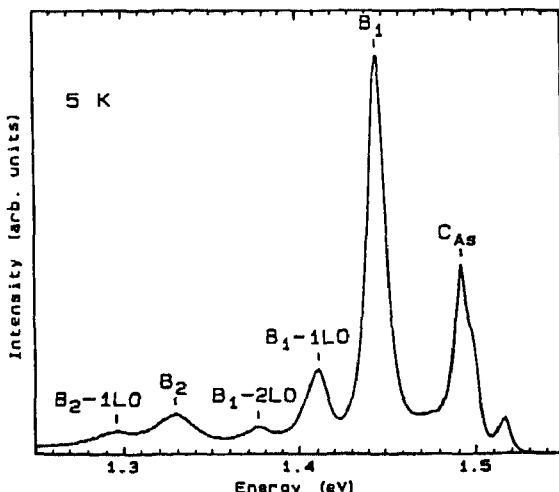


Fig. 57. Low-temperature PL spectrum of B-doped GaAs. (After Brierley et al [108].)

and linewidths of 0.1 meV. This structure is due to the exchange splitting of the states formed from the electrons and holes via j-j coupling, as noted above for other acceptor-bound excitons. Boron also acts as an acceptor when incorporated in GaAs. The B_{As} impurity is a double acceptor with an activation energy of 72 meV, as shown in Fig. 57 [108]. Boron is clearly a deeper level than the C acceptor. As discussed above, Fig. 48 shows Ge, S, Sn, and Si donor-bound exciton transitions clearly in the spectra [99]. From these spectra, the binding energies of the donors are determined as shown in Table 2.

(iii) Passivation of impurities

Hydrogen has been widely used to passivate the effects of impurities in semiconductor layers; that is to improve the electrical and optical properties which were degraded by the presence of the impurities [109–115]. The neutralization of shallow impurities in GaAs through the incorporation of atomic hydrogen is responsible for the observed decrease in free-carrier concentration and the observed increase in mobility. Fig. 58 shows a PL spectrum of a sample before and after hydrogenation. Using the full width at half-maximum (FWHM) of the dominant impurity emission peak (D⁰,X) as a relative measure of the sample purity [116], it is clear that the hydrogenation-induced reduction of the linewidth

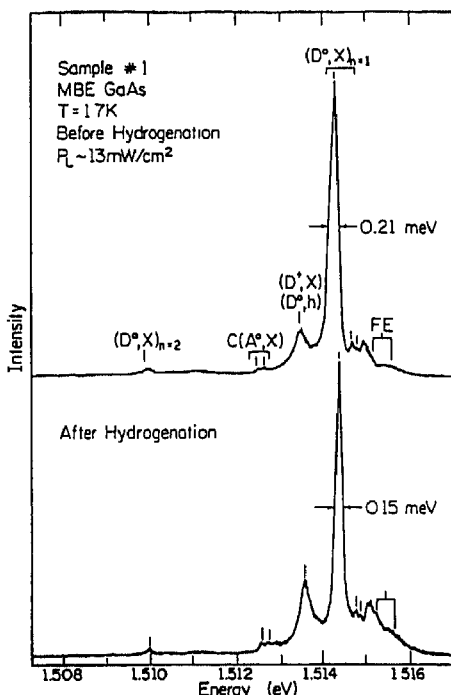


Fig. 58. PL spectra of MBE-grown GaAs before and after hydrogenation. (After Pan et al. [109].)

of this peak from 0.21 meV to 0.15 meV signifies a reduction in the total impurity concentration in the sample.

(iv) Defect-induced bound excitons

In 1980 Künzel and Ploog first reported the observation of a series of PL emission lines in the 1.504 to 1.511 eV spectral region of GaAs epilayers grown by MBE [106]. Subsequent to this report there have been many studies of these emission lines [92,117–129], with the highest-resolution study by Reynolds et al. [128] and Skolnick et al. [129] yielding about 50 peaks within this 7 meV energy range. There has also been an observation of these lines in GaAs layers grown by MOVPE [130]. Bhattacharya et al. [117] observed these emission lines in Be-doped GaAs. These studies showed that there are two specific types of emission, the Contour-Skromme type [131,132] and the Skolnick–Reynolds type [133,134]. Eaves and Halliday [135] modeled these lines as due to the recombination of excitons bound to acceptor pairs of varying separation. Litton et al. [136] attributed the spectrum to distant donor–acceptor pairs. Akimoto et al. [137] gave some evidence suggesting polynuclear carbonyls might be responsible for these PL emission lines. In recent years the bound exciton model has gained support from polarization studies and PL time-decay studies [121]. Fig. 59 shows a high-resolution PL spectra polarized in orthogonal directions for an MBE epilayer of GaAs [121]. All of these bound exciton emission lines are transitions from the lowest state of the bound exciton to the ground state of the defect. In this figure and within the context of this model, line 47 is assigned to an isolated point defect, whereas the other lines, with increasing energy, are assigned to pairs of defects of decreasing separation. The polarization of the emission of these lines indicates that these defects (impurities and native defects) are preferentially incorporated at specific lattice sites during growth. The fact that the energies of these lines are precisely reproducible suggests that the complexes are pairs whose separations are determined by the crystal lattice. Ohnishi et al. [123] have examined the growth conditions necessary to observe these defect-induced bound exciton emissions. They find that

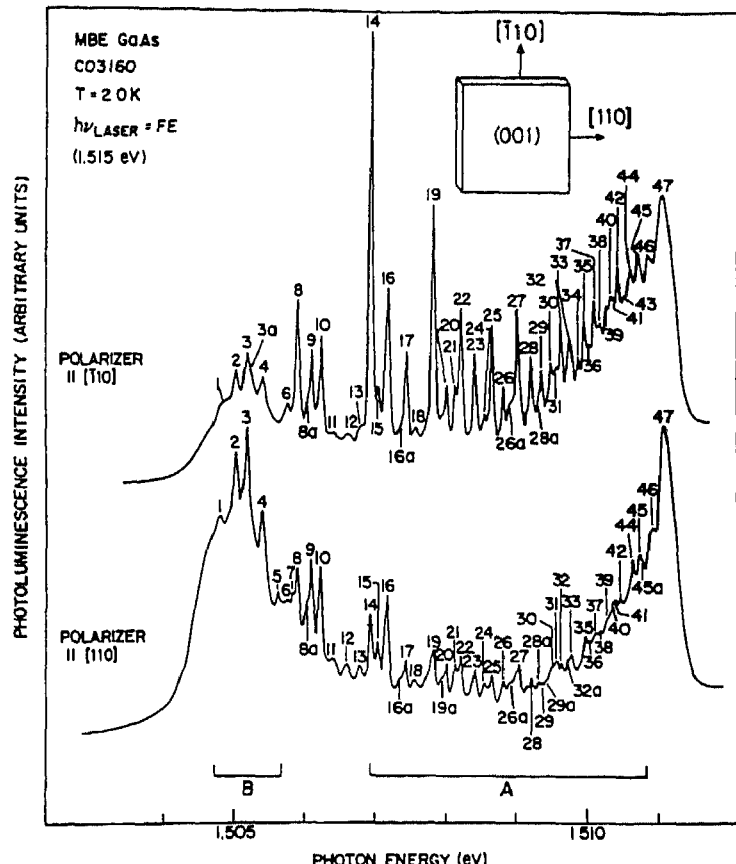


Fig. 59 2 K PL spectra of a 6 μm thick GaAs layer after excitation at 1.5153 eV for two different detection polarizations. (After Skolnick et al. [121].)

these emissions can only be formed in specifically crystallographically oriented substrates and the type of PL features are especially dependent upon the growth temperature and any annealing temperature. Fig. 60 shows the PL spectra of MBE GaAs grown on various substrates. The shape of the defect-induced bound exciton lines clearly changes with substrate orientation. Makita [138] examined the PL spectra of dual ion-implanted C- and O-doped GaAs and results indicate that these bound exciton emissions may be attributed to a complex between C_{As} and interstitial O atoms. Finally, the g-line shown in Fig. 61 has been directly established by Contour et al. [131] to be due a carbon acceptor-bound exciton, with a binding energy of 22.9 meV. They also observed the two-hole satellite corresponding to this bound exciton. These results were further confirmed by Makita et al. for C-implanted GaAs [139]. Takeuchi et al. [140] implanted C, Mg, Zn, and Cd acceptors and observed the g-line as well as the [g-g] line, as shown in Fig. 62. They find that g is related to C, and that for high C concentrations, $> 10^{16} \text{ cm}^{-3}$, [g-g] was simultaneously observed. They also found that implantation of donor impurities does not produce g or [g-g] line emissions. [g-g] appears to only be present in uncompensated material (with an extremely small background concentration of donor impurities), and was attributed to an acceptor-acceptor pair emission [138].

2.2.3.1.2. Silicon

Davies recently reviewed the optical properties of luminescence centers in silicon [141]. This seminal review provides a thorough examination of the donors, acceptors, deep levels, and impurity complexes in Si. Table 3 lists some of the most common donors and acceptors in Si, together with

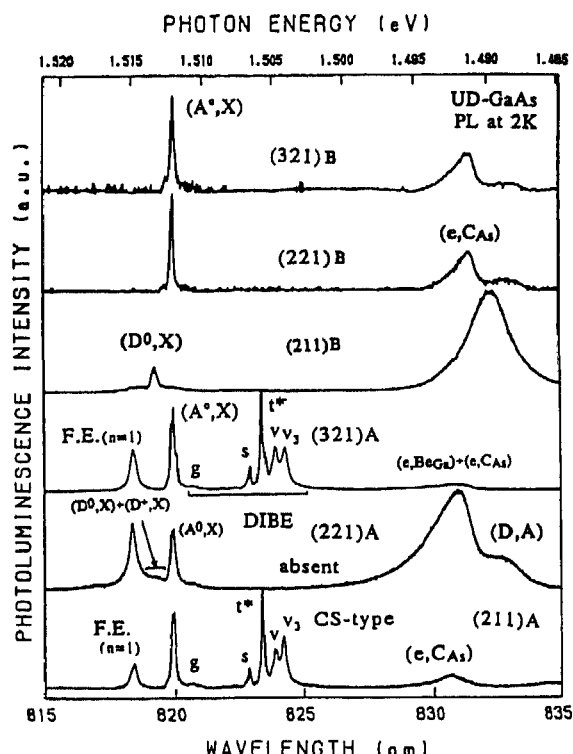


Fig. 60 PL spectra of MBE-grown, undoped GaAs, on (211)A, (221)A, (321)A, (211)B, (221)B, and (321)B substrates. (After Ohnishi et al. [123].)

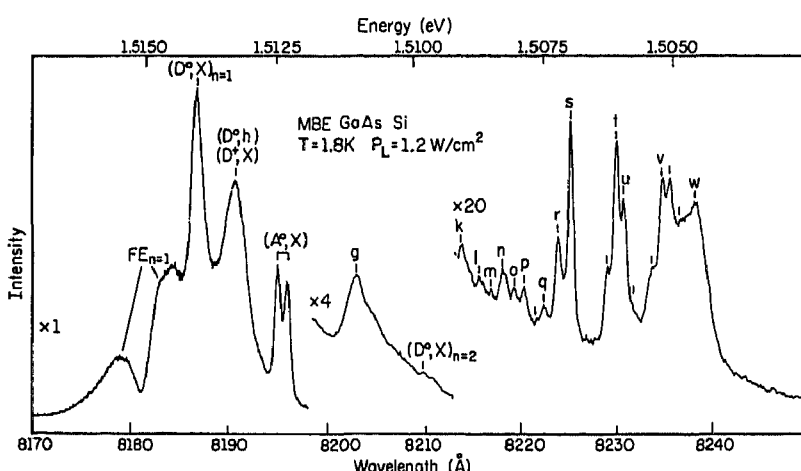


Fig. 61. 1.8 K PL spectrum of Si-doped MBE-grown GaAs epilayer. Evident in the spectrum are the free and bound excitons together with the sharp-line "defect"-related peaks. (After Skromme et al. [92].)

their binding energies. The substitutional group V impurities (P, As, Sb, Bi) and the interstitial group I impurity Li are effective mass donors in Si. The substitutional group III impurities (B, Al, Ga, In, and Tl) are effective mass acceptors in Si. In 1960 Haynes [142] showed that the sharp line emissions near the bandgap of Si are due to donor or acceptor-bound exciton recombination. Fig. 63 shows the PL spectra of a nominally undoped sample (dashed curve) and an As-doped ($8 \times 10^{16} \text{ cm}^{-3}$) sample. The two sharp lines at 1.091 and 1.149 eV are due to As impurities. Haynes examined similar

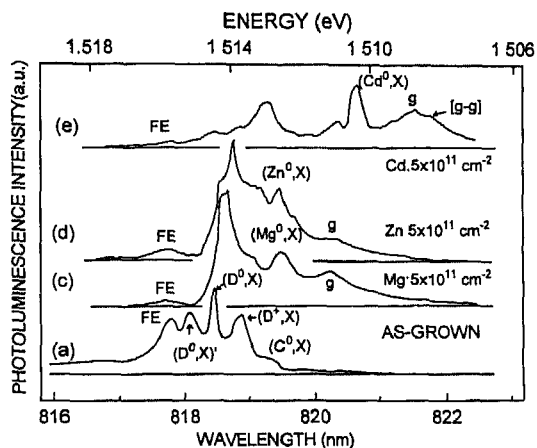


Fig. 62. PL spectra of nominally-undoped GaAs (a) and acceptor-implanted (c) Mg, (d) Zn, and (e) Cd GaAs. (After Takeuchi et al [140].)

Table 3
Optical activation energies of donors and acceptors in Si [141]

Donors		Acceptors	
Impurity	Activation energy (meV)	Impurity	Activation energy (meV)
P	4.7	B	3.8
As	5.4	Al	5.1
Sb	5.0	Ga	5.7
Bi	7.7	In	14.0
Li	3.6	Tl	43.8

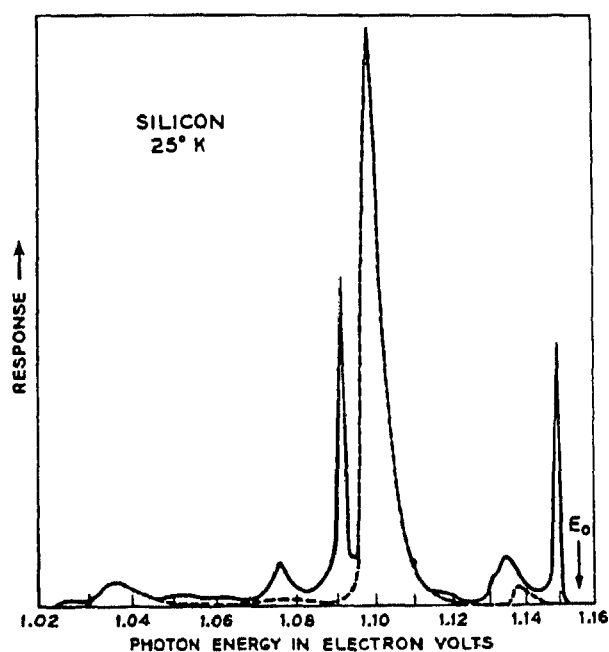


Fig. 63 PL spectra at 25 K of (1) high-purity Si sample, and (2) a sample containing $8 \times 10^{16} \text{ cm}^{-3}$ As atoms (solid line). (After Haynes [142].)

spectra for various other donors and acceptors in Si and arrived at the empirical rule, named after him, that the bound exciton dissociation energy is proportional to the impurity ionization energy ($E_D = 0.1E_i$). Fig. 64 shows this Haynes rule plot for various group-V donors and group-III acceptors. The PL spectrum from donors in Si, at low excitation powers and low temperatures, is qualitatively identical for all donors [143]. Fig. 65 shows the PL from Si doped with P to a level of $3.2 \times 10^{14} \text{ cm}^{-3}$. A zero-phonon line together with phonon replicas (phonon energies of 18, 56, and 58 meV), is evident in the spectra and is labeled a_1 . Acceptor-bound exciton spectra are similar with an additional splitting in the zero-phonon lines of Al, Ga, and In dopants. The binding energies of different donors and acceptors in Si are different enough that the PL spectrum provides a good "signature" for each particular impurity [141,144,145]. Fig. 66 shows the PL spectra for a Si sample with a B concentration of $1.3 \times 10^{13} \text{ cm}^{-3}$. The inset reveals that P and As are also present with concentrations of $1.8 \times 10^{12} \text{ cm}^{-3}$ and $3 \times 10^{11} \text{ cm}^{-3}$, respectively. Note the clear evidence in the PL spectra of impurity concentrations down to 10^{11} cm^{-3} . The presence of the phonon replicas in the bound exciton emission of Si is unlike GaAs where no phonon replicas of the near-edge bound exciton emissions were typically present, except for the report of Reynolds et al. [39]. Fig. 67 shows PL spectra of Si samples doped with P, Sb, As, and Bi in the TO-phonon assisted region [146,147]. The peaks in the spectra are consistent with the Kirczenow shell model for donor-bound exciton luminescence shown in Figs. 68–71. show the PL spectra of Si samples doped with Ga, In, and Al [147]. Differences in the spectra allow for unambiguous identification of impurities.

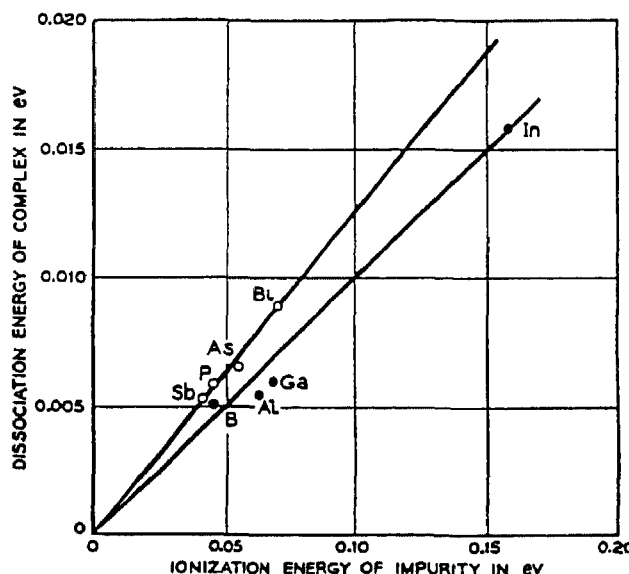


Fig. 64. Dissociation energy of a bound exciton versus ionization energy of the impurity. (After Haynes [142].)

With increasing excitation power, the bound exciton emissions become considerably more complicated. At high powers the bound exciton line of, for example, B, a_1 , is supplemented by lines a_2 , a_3 , and a_4 , shown in Fig. 65. As the excitation power is increased these higher index lines become stronger in the spectra [148,149]. These additional lines are due to the formation of bound multi-exciton complexes, where a_2 , a_3 , and a_4 , correspond to the recombination of a second, third, and fourth exciton bound to the donor, respectively. Another good example of such bound multi-exciton complexes is given by the interstitial Li donor. Fig. 72 shows the PL emission with six excitons bound to the Li donor [150].

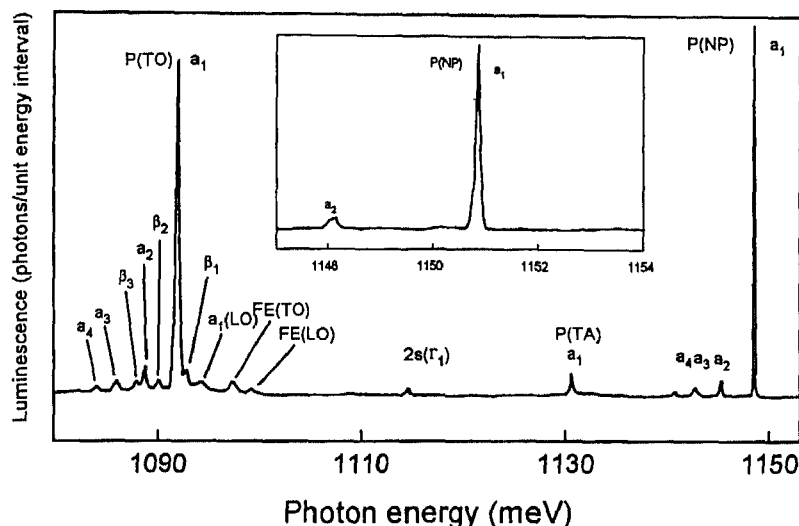


Fig. 65. Low-temperature PL spectrum of P-doped Si. (From Lightowlers et al., *J. Phys. C: Solid State Phys.*, 10 (1977) L713.)

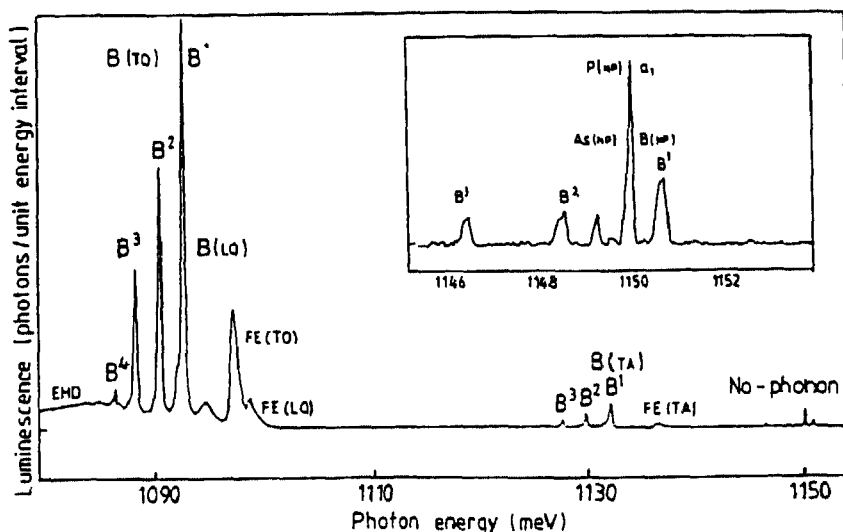


Fig. 66. Low-temperature PL spectrum of B-doped Si. (From McL. Colley and Lightowlers, *Semicond. Sci. Technol.*, 2 (1987) 157)

As the concentration of impurities is increased the narrow emissions evident in the low-impurity concentration samples broaden considerably. Fig. 73 shows the PL spectra for P-doped Si with donor concentrations ranging from 4×10^{18} to $1.5 \times 10^{20} \text{ cm}^{-3}$ [151]. This broadening represents the many-body interaction of electrons, which will be discussed below. Clearly, the fine structure of the bound exciton emission is washed out at high impurity concentrations, and, therefore, the ability to distinguish chemically between impurities at high concentrations is not likely.

Davies [141] has given a good synopsis of other defect or impurity-related recombination centers in Si. Here, a few of them are summarized. Carbon may form complexes with many other impurities, yielding many different recombination centers. The following is a list of PL emissions which have been identified with C complexed with: (1) another C atom, 969 meV; (2) one O atom, 789 meV; (3) one N atom, 745.6 meV; (4) one Ga atom, 875 meV; (5) four lithium atoms, 1082 and 1045

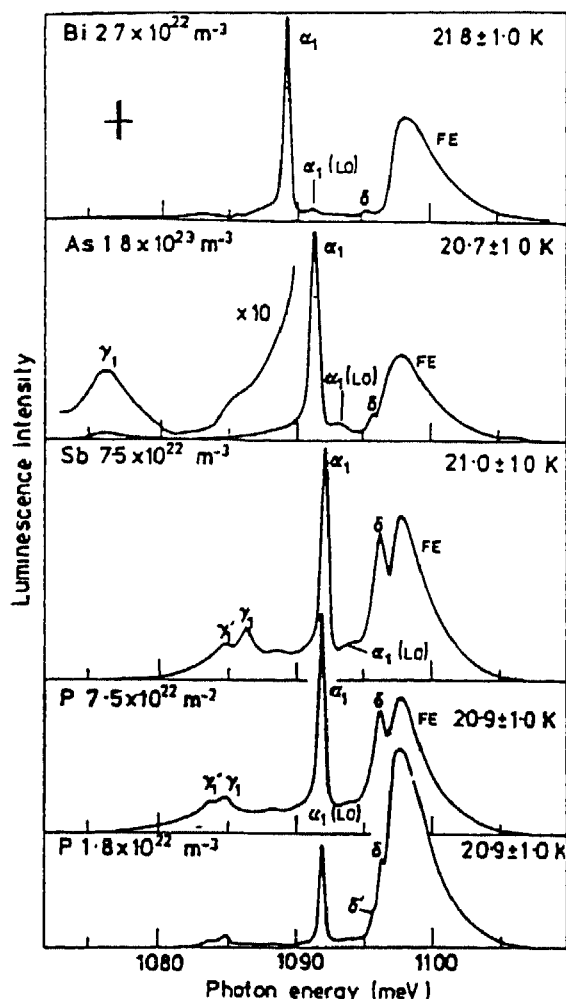


Fig. 67. PL spectra of the TO-phonon assisted recombination of the bound exciton associated with Bi-, As-, Sb-, and P-doped Si. (From Lightowlers et al., *J. Phys. C: Solid State Phys.*, 10 (1977) L713.)

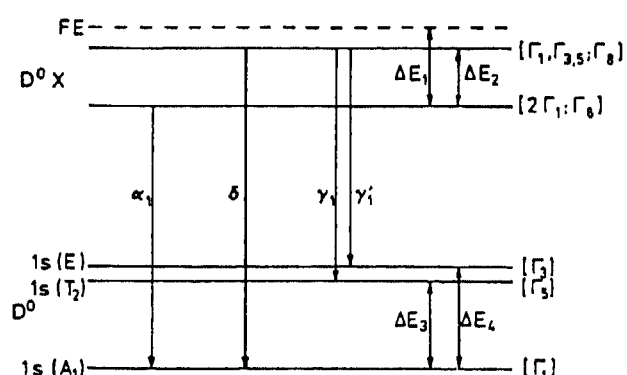


Fig. 68. Energy level diagram for the neutral donor and the single bound exciton (D^0, X). (From Lightowlers et al., *J. Phys. C: Solid State Phys.*, 10 (1977) L713.)

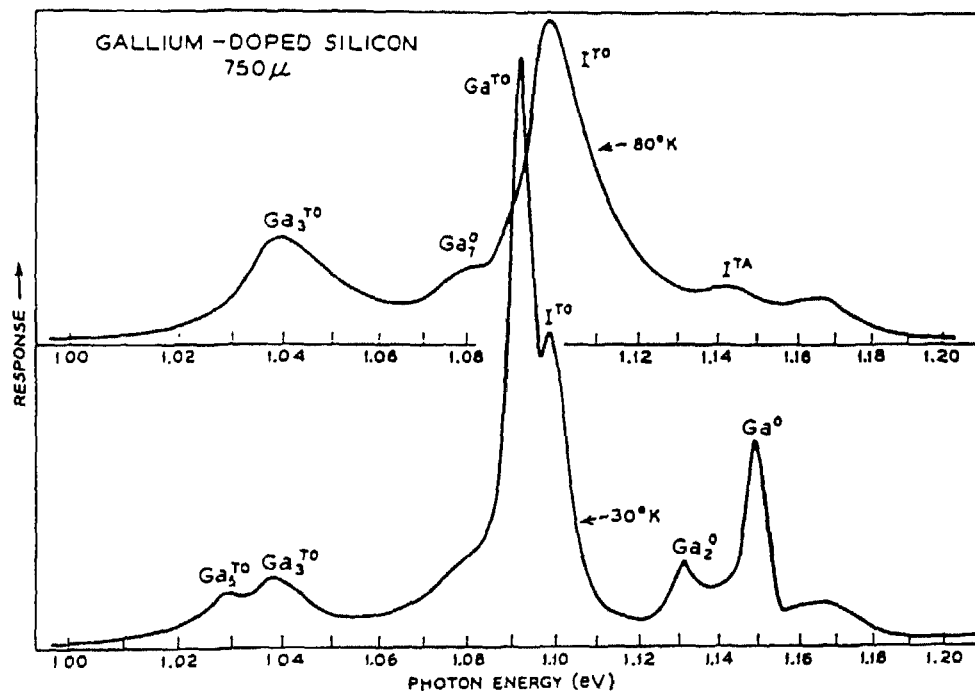


Fig. 69. PL spectra of a Ga-doped ($1.5 \times 10^{17} \text{ cm}^{-3}$) Si sample at 30 and 80 K (After Dean et al. [147].)

meV; (6) Be, 1117 meV; and (7) various radiation damage centers. Fig. 74 shows both of the four Li atom complexes at 1082 and 1045 meV, denoted by S and Q, respectively [152]. The Q lines arise from the radiative recombination of an exciton bound at a four lithium atom center, whereas the S lines arise from the radiative recombination of an exciton bound at a four-lithium atom center but with a near-neighbor C atom. Oxygen also produces luminescent centers, although not for isolated interstitial O atoms [141]. C–O complexes give rise to the 789 meV line, as shown in Fig. 75 [153]. The 969 meV C–C band is shown in Fig. 76 where the concentration of C is $9.7 \times 10^{16} \text{ cm}^{-3}$. This complex involves a substitutional C and interstitial C atom complexed together. The II line at 1018 meV is a radiation damage induced recombination center. Fig. 77 shows the PL spectrum of this center.(i) Passivation of impurities

Hydrogen has also been utilized to passivate shallow impurities in Si. Quantification of the passivating properties of hydrogen incorporation into semiconductors may be readily probed by examination of the bound exciton PL. Fig. 78 shows the PL spectra of several samples implanted with B, In, and Tl before and after treatment in atomic H [154]. The unshaded lines are due to emission from the high-purity Si substrate. The shaded lines clearly show the passivating effects of atomic H on the shallow impurity emission by a factor of more than 10 in the near-surface region ($\sim 1 \mu\text{m}$). This effect was also demonstrated to not be due to a non-luminescing dead layer at the surface.

2.2.3.1.3. *GaAs nanostructures*

Bandstructure engineering and spatially selective doping offers the possibility for the fabrication of unique semiconductor structures. In particular, impurity doping of GaAs nanostructures allows for the fabrication of useful devices. In such structures the optical properties of the impurities may be altered by the quantum-confinement effects of nanostructures. Most of the studies of such structures deal with quantum wells. Shanabrook and Comas [155] were the first to report donor-related complexes

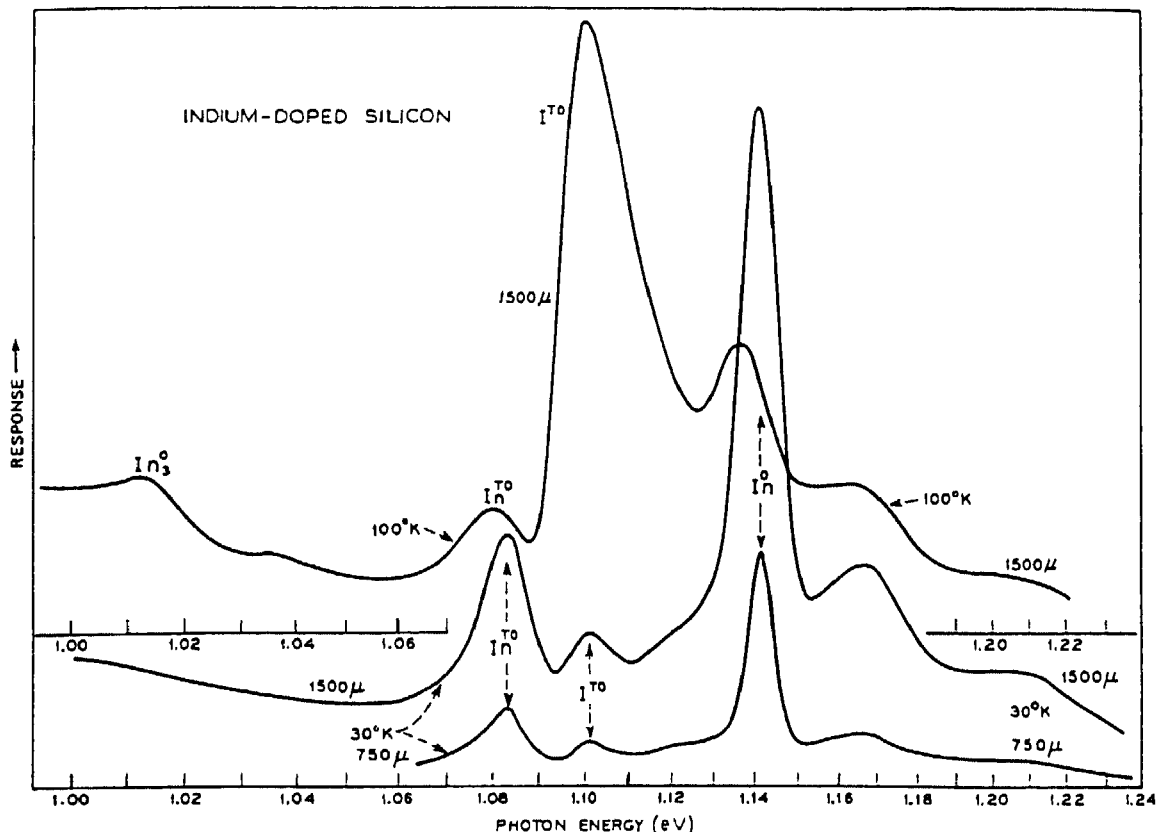


Fig. 70. PL spectra of an In-doped ($1.5 \times 10^{16} \text{ cm}^{-3}$) Si sample at 30 and 100 K for two different sample thicknesses. (After Dean et al [147].)

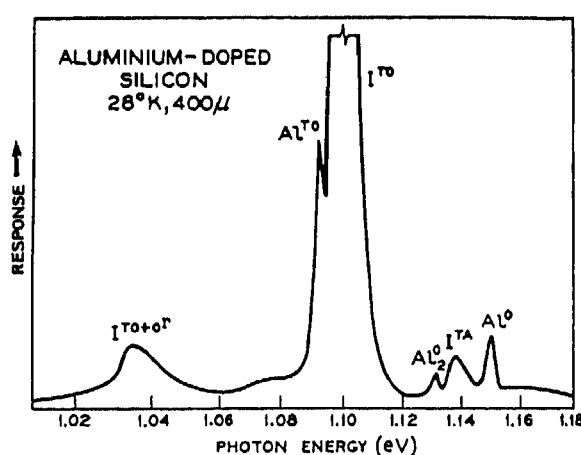


Fig. 71 PL spectrum of Al-doped ($2 \times 10^{16} \text{ cm}^{-3}$) Si sample at 28 K. I denotes intrinsic emission lines. (After Dean et al [147].)

in GaAs quantum wells. That same year, Reynolds et al. [156] reported sharp emission lines associated with (D^0, X) transitions in unintentionally doped quantum wells. This same type of transition was observed by Nomura et al. [157] and Liu et al. [158], as shown in Fig. 79. Here peak (i) is the heavy-hole free exciton, peak (ii) is the confined neutral Si-donor-bound exciton (D^0, X) , peak (iii) is the

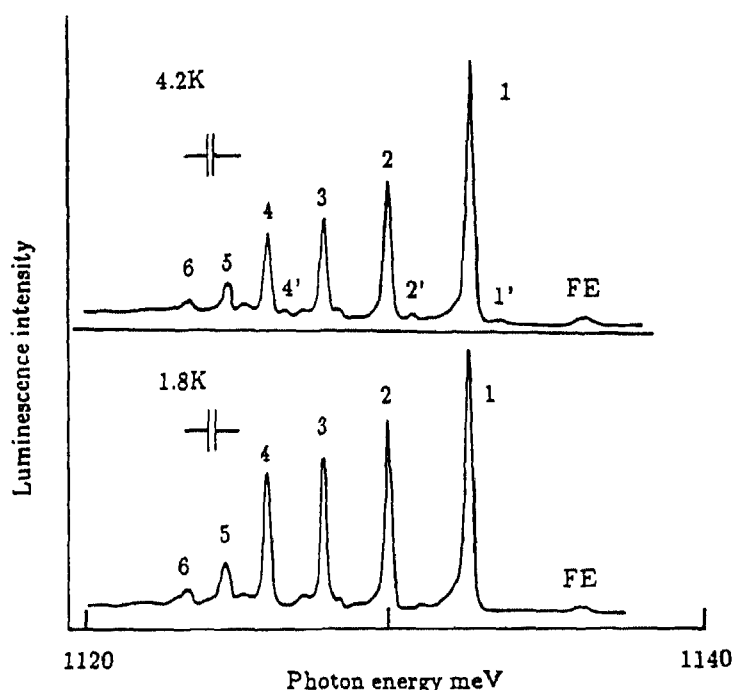


Fig. 72. Low-temperature PL spectra of Li-donor bound multi-excitons in Si [150].

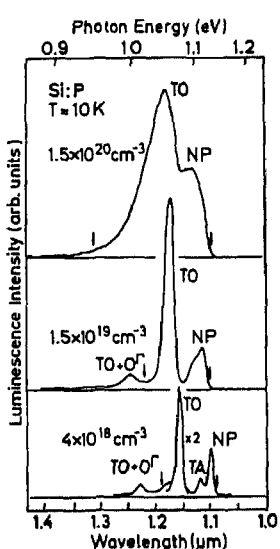


Fig. 73. Donor concentration dependence of the PL spectra in heavily P-doped Si. Arrows indicate the high-energy cutoff energy of the no-phonon line and the low-energy side of the TO replica. (After Wagner [151].)

confined ionized Si-donor-bound exciton (D^+, X), and peak (iv) is the Si donor to valence band transition (D^0, h). Reynolds et al. [159] have further investigated impurity recombinations in quantum wells and have observed a unique feature of impurity-related emissions in quantum wells. They found that the binding energy of excitons changes with the location of the donors (i.e. at the center of the quantum well versus the edge). This variation was also found to depend upon the well thickness, or equivalently the degree of quantum confinement. They investigated GaAs/AlGaAs quantum wells

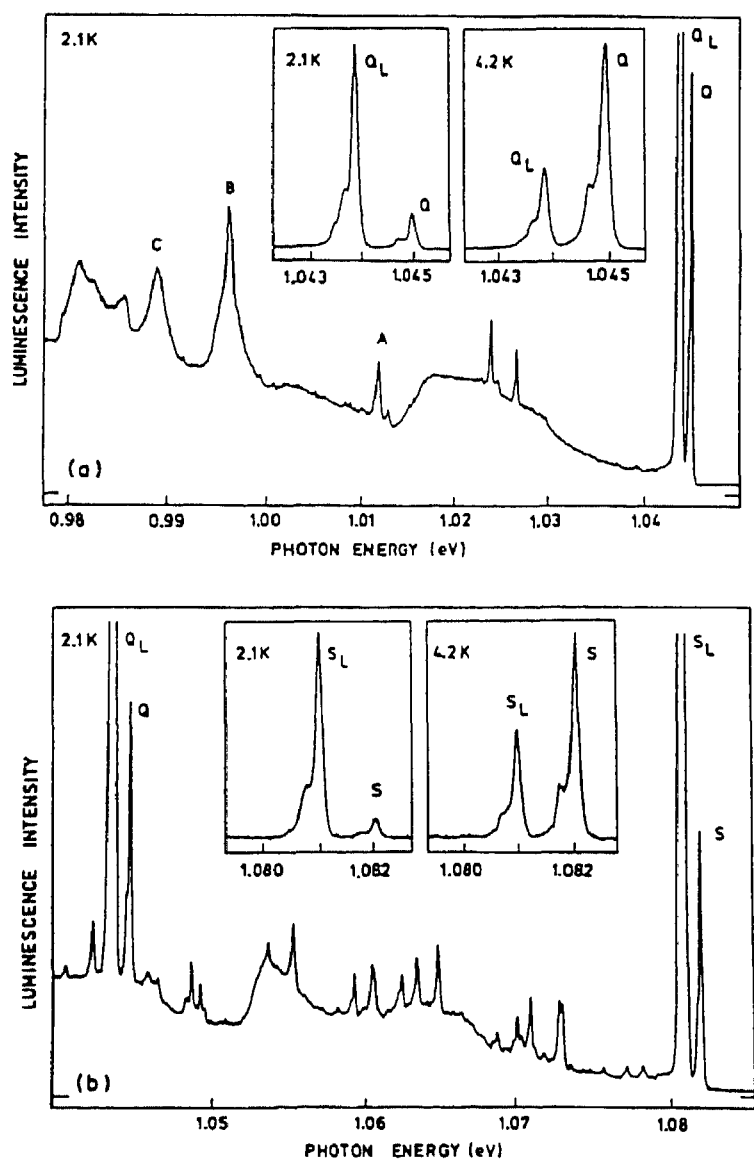


Fig. 74 PL spectra of Li-diffused Si ($\sim 1.5 \times 10^{17} \text{ cm}^{-3}$). Starting material was (a) high-purity float-zone Si with C and O concentrations $< 10^{15} \text{ cm}^{-3}$, (b) high-purity float-zone Si with C concentration of $1.7 \times 10^{17} \text{ cm}^{-3}$ and O concentration $< 10^{16} \text{ cm}^{-3}$. (After Lightowlers et al. [152].)

grown by MBE with well thicknesses varying from 75 to 350 Å, with Si-donor doping at the center or the edge of the well or the center of the AlGaAs barriers. Fig. 80 shows the low-temperature PL spectra of center-doped, edge-doped, and barrier-doped 350 Å quantum wells. Their results show that the center-doped well and center-doped barrier samples exhibit narrower (D^0, X) transitions than edge-doped quantum well samples. Minimum PL linewidths are on the order of 0.15 meV. Fig. 81 shows the variation of the binding energies of excitons to neutral donors (taken from the energy difference between the D^0, X and X transitions) doped selectively at the center and edges of the GaAs wells and at the centers of the AlGaAs barriers as a function of the heavy-hole free-exciton emission energy (quantum confinement). These results clearly show that the binding energies of these donor-bound exciton complexes increases with decreasing well width down to about 50–100 Å, and then they

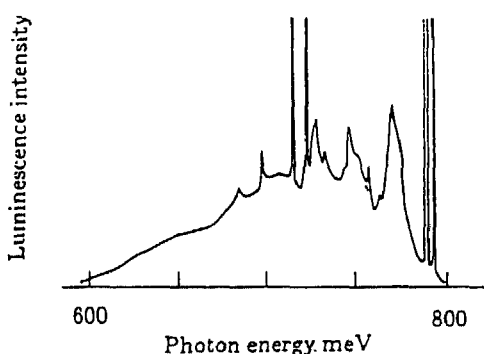


Fig. 75 Low-temperature (26 K) PL spectrum of the 789 meV vibronic emission band in Si [153].

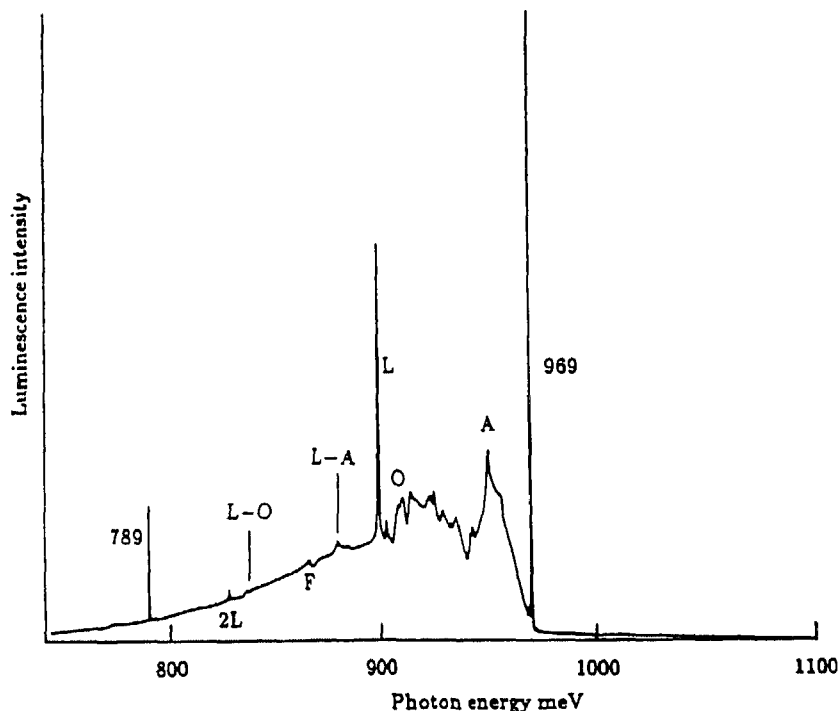


Fig. 76 PL spectrum of float-zone Si with $9.7 \times 10^{16} \text{ cm}^{-3}$ C atoms after irradiation with $2 \times 10^{17} \text{ cm}^{-3}$ 2 MeV electrons at 200 K and subsequent annealing for 3 h at 325 K [141].

decrease. This increase in binding energy is due to the increase in donor as well as exciton binding energy, and consequently that of (D^0, X) . Fig. 82 shows the well width dependence of the binding energy of the C acceptor-bound exciton doped in the center of the well [160]. Fig. 83 shows the PL spectrum of a 400 Å quantum well, with all of the heavy-hole and light-hole bound excitons evident in the spectra [161]. Just as with bulk GaAs epilayers, it is possible to observe two-electron satellite transitions in nanostructures. Fig. 84 shows resonant excitation PL of the Si-donor-bound exciton in a 100 Å GaAs/ $\text{Al}_{0.3}\text{Ga}_{0.7}\text{As}$ quantum well. The two-electron satellite transitions are evident in the second and third spectra when the excitation is resonant with the bound exciton [162].

D^- centers consist of two-electron ions which are formed by adding a second electron to a shallow hydrogenic donor (D^0). This complex is the semiconductor analog of the H^- ion. In the D^- ion, the two indistinguishable electrons mutually screen each other from the positive donor center. The binding

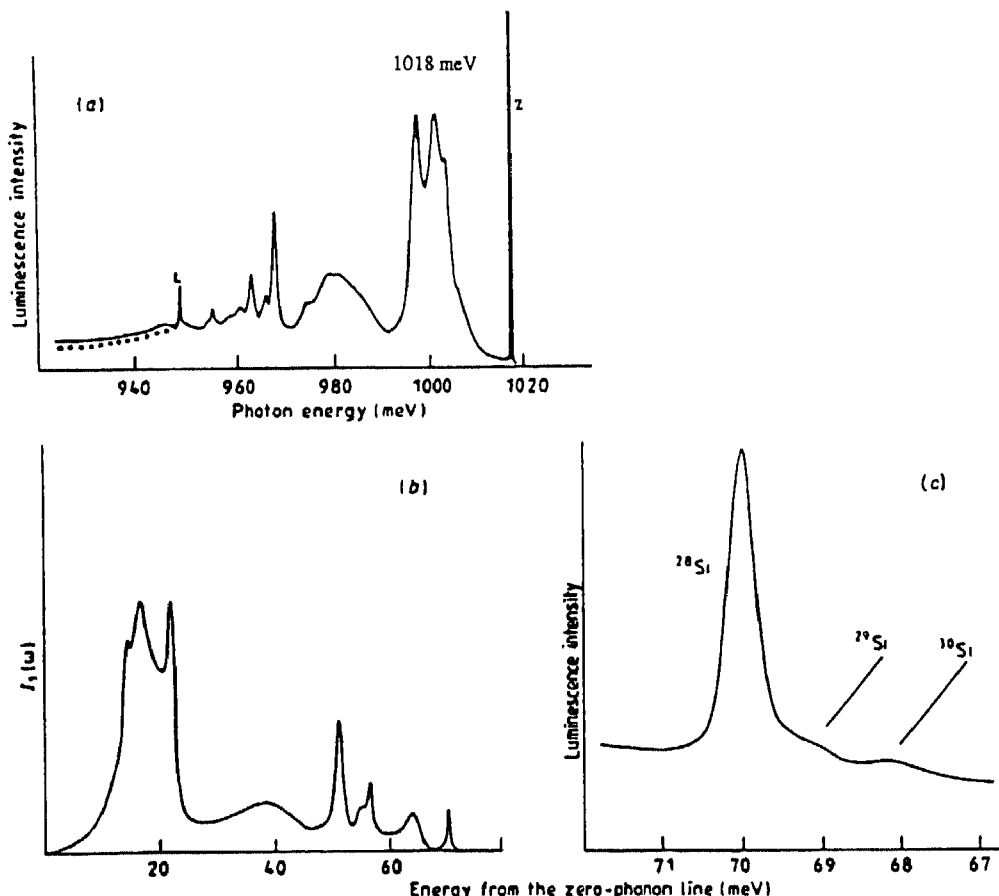


Fig. 77. PL spectrum of the (a) 1018 meV band in Si, (b) the one-phonon contribution, and (c) the 70 meV local mode labelled L in (a) at 2 K [141]

energy of this center is predicted to be 0.055 Ry [163]. Observation of this center has proven difficult due to this small binding energy; however, quantum confinement may substantially increase this binding energy. Recently, Holmes et al. [164] performed far-infrared magneto-spectroscopy on Si-donor planar-doped quantum wells, and proven the existence of the D⁻ center. Subsequently, Fu et al. [165] measured the PL spectra of this same set of samples (shown in Fig. 85). The (D⁻,X) is clearly evident between the (D⁰,X) and free exciton transitions, and becomes more prominent for higher planar dopings (samples 2–4).

Acceptor-bound excitons have also been studied in quantum wells [166–169]. Fig. 86 shows the PL spectra of a quantum well which clearly exhibits the heavy-hole and light-hole acceptor-bound excitons, A⁰HHX and A⁰LHX, respectively [167]. These bound excitons also exhibit the satellite peaks associated with the two-hole transitions. Fig. 87 shows the selectively excited PL spectrum which clearly shows the (A⁰,X)_{n=2} emissions. This data shows that the two-hole emission is enhanced when the excitation is resonant with the bound exciton peak [168]. Haynes' rule is also valid in quantum wells. Fig. 88 shows the dependence of the acceptor-bound exciton binding energy on the transition energy for the 1s to 2s transition of the Be acceptor which binds the exciton [169].

The relative intensity of free exciton PL emission to bound exciton emission is also sensitive to the growth conditions [60]. Fig. 89 shows the ratio of these emission lines and the integrated PL intensity for two different quantum wells as a function of the group V to group III flux, or beam

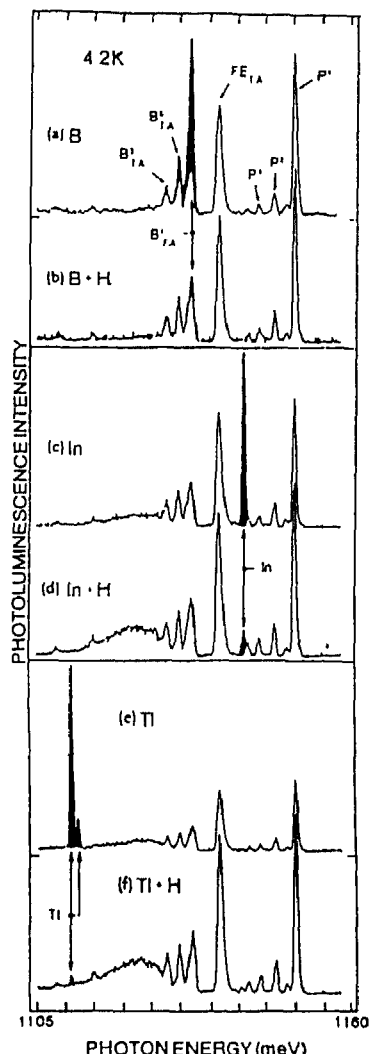


Fig. 78 4.2 K PL spectra of Si in the spectra vicinity of the TA-phonon replica. The spectra show the bound exciton emission for samples implanted with B, In, and Ti before (a), (c), and (e) and after (b), (d), and (f) exposure to atomic H (After Thewalt et al. [154].)

equivalent pressure (BEP) ratio. Clearly, the free exciton emission becomes relatively stronger with higher BEP ratios. This is a result of a higher As coverage at the growth front which reduces the acceptor incorporation in the lattice. However, at the same time the overall PL emission intensity decreases with higher BEP ratios. This is due to the enhanced formation of deep centers with increasing As flux, probably the formation of an As-antisite defect. In this regard near-infrared PL emission exhibits a line near 0.8 eV, which has been attributed to the As-antisite defect, possibly EL2. The growth rate is also an important factor. Fig. 90 shows the bound exciton/free exciton ratio versus the growth rate. The trend for increased impurity incorporation with increased growth rate indicates a preferential desorption of impurities at low growth rates. Lastly, the incorporation of impurities at heterointerfaces is dependent both upon which interface is being grown and upon the length of the growth interrupt time [170]. Fig. 91 shows the PL spectra for samples with various growth interrupt times at the normal and inverted interfaces. Longer growth interrupts increase the incorporation of impurities, and this impurity incorporation is more prevalent at the inverted interfaces. Further, this

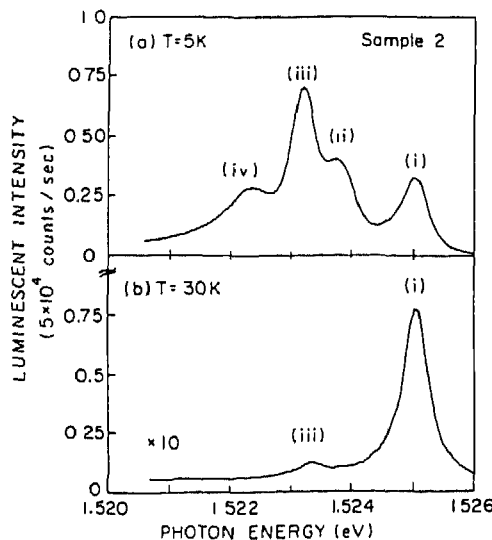


Fig. 79. PL spectra at (a) 5 K and (b) 30 K for a center doped 210 Å quantum well (After Liu et al [158].)

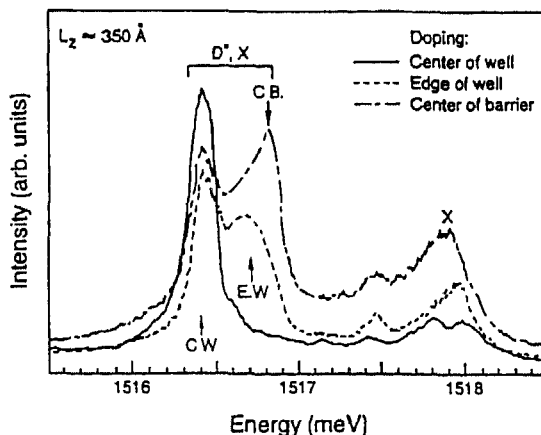


Fig. 80. PL spectra from center-doped (—), edge-doped (---), and center-barrier-doped (-·-) 350 Å quantum wells (After Reynolds et al. [159].)

data indicates that non-radiative recombination centers, which cause a reduction in the overall PL emission, have a higher density with increasing growth interrupt and for interrupts at the inverted interfaces. The nature of this non-radiative defect can only be speculated upon, but deep-level transient measurements show that oxygen is incorporated at the AlGaAs surface [171].

2.2.3.2. Shallow impurity concentrations

The determination of the density of shallow donor and acceptor impurities, N_D and N_A , respectively, in semiconductors is critical to the understanding of impurity incorporation in material growth and in the design and fabrication of semiconductor devices. The most commonly used experimental technique for the determination of these important quantities is the temperature-dependent Hall technique, and free-carrier mobility and density analyses as developed by, for example, Wolfe et al. [172]. Reliable Hall measurements require uniform layers with good ohmic contacts. Further, good ohmic contacts are technologically problematical in some semiconductor materials and for some impurity

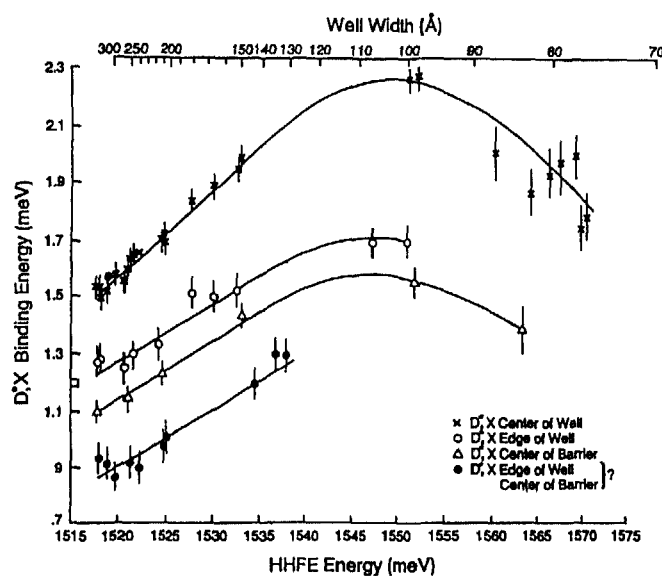


Fig. 81. Neutral donor bound exciton binding energies versus heavy-hole free-exciton energy for samples doped at the center and edge of the well and the center of the barrier. (After Reynolds et al [159].)

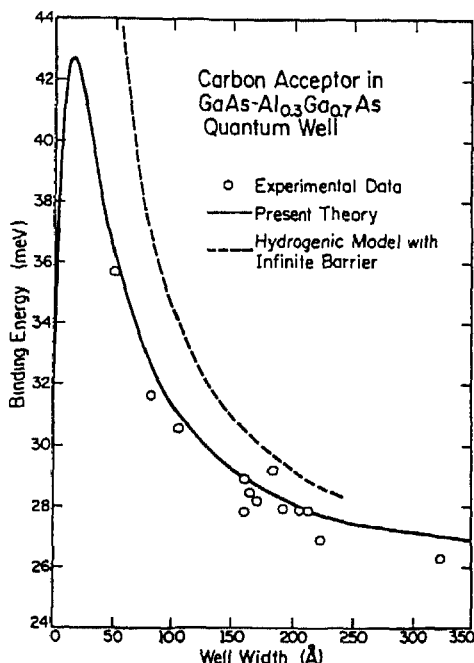


Fig. 82. Well-width dependence of the energy of the Γ_7 center-doped C-acceptor ground state. ●, experimental results; —, theoretical calculation; ---, infinite-barrier hydrogenic binding energy (After Masselink et al. [160].)

concentrations. Further, for thin, high-purity layers the correction for surface and interface carrier depletion becomes unreliable since most of the layer may be depleted. Also, impurity concentrations obtained from these types of analyses are sensitive to the types of scattering mechanisms included in the analysis. In contrast, PL measurements do not require sample destruction or fabrication of contacts. Further, less detailed analyses and modeling of the data is required. The importance of PL in measuring

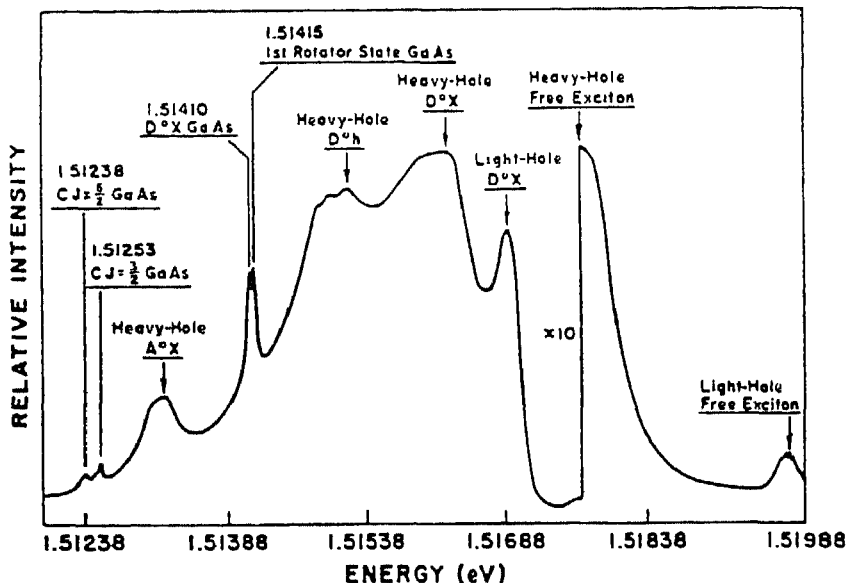


Fig. 83 PL spectrum of a 400 Å GaAs/Al_{0.25}Ga_{0.75}As quantum well structure. (After Reynolds et al [161].)

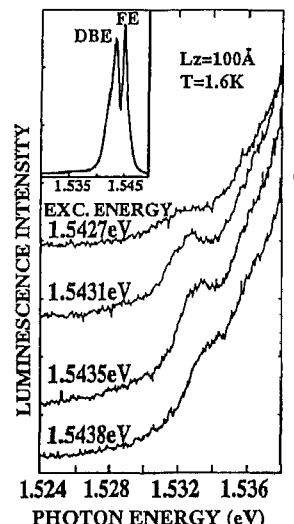


Fig 84. Selectively-excited PL spectra of a center-doped 100 Å wide GaAs quantum well doped with Si to $5 \times 10^{16} \text{ cm}^{-3}$. Resonance with the donor bound exciton occurs at 1.5435 eV excitation energy, spectrum c. (After Holtz et al., *J. Electron. Mater.*, 23 (1994) 513, a publication of The Minerals, Metals, and Materials Society, Warrendale, PA 15086, USA.)

donor and acceptor concentrations is that all donors and acceptors are made neutral by the above-bandgap excitation light. The PL signal simultaneously measures the concentrations of all donors and acceptors, which is in sharp contrast to electrical measurements which are only sensitive to the uncompensated fraction of the majority species.

In Si it has been shown that the densities of different impurity species may be obtained with high precision, over a limited range of concentrations, through measurements of the PL spectra [47,173]. This involves precise measurements of the intensities of the recombination lines of excitons bound to neutral impurities and free excitons. In order to correct for experimental variables, the ratio of the intensities of the bound and free excitons is used. Kaminskii et al. [174] have shown that the ratio of

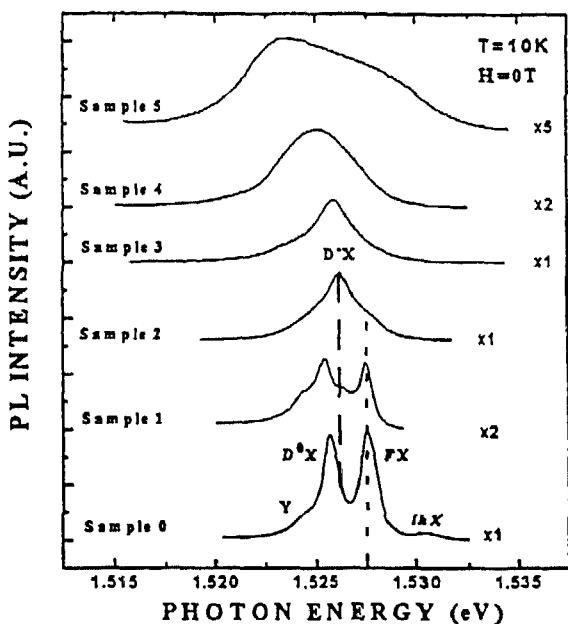


Fig. 85. PL spectra of six quantum well samples which were doped to $2 \times 10^{10} \text{ cm}^{-2}$ in the well and with a barrier doping from 0 to $3.2 \times 10^{11} \text{ cm}^{-2}$ from bottom to top. (After Fu et al. [165].)

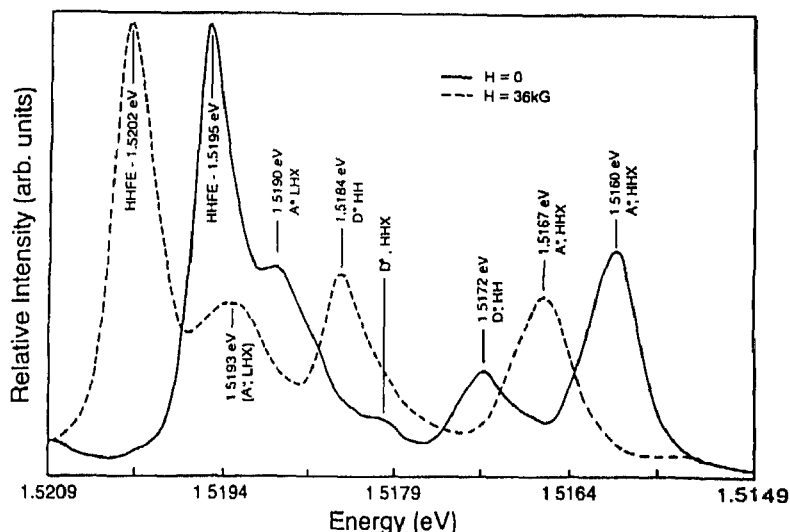


Fig. 86. 2 K PL spectra from a 350 Å GaAs quantum well at 0 and 36 kG magnetic fields. (After Reynolds et al. [167].)

the PL emitted by the bound excitons and the free excitons is remarkably linear in impurity concentration, allowing concentration measurements in the range of 10^{12} – 10^{16} cm^{-3} . Fig. 92 shows the measured integrated intensity ratio of the bound exciton zero-phonon line to the free-exciton peak height for the shallow impurities boron, aluminum, and phosphorous. The boron acceptor has approximately 10 times less zero-phonon emission in comparison with aluminum. This results from the fact that only 1% of the boron PL is emitted in the zero-phonon line compared with 20% for aluminum.

PL transitions related to impurity states may also be used as an approximate indication of the concentration of impurities in GaAs [175–178]. Kamiya and Wagner [179] analyzed PL lineshapes

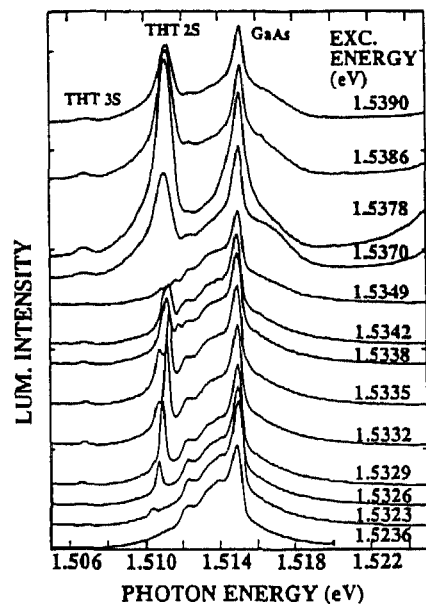


Fig. 87. Selectively-excited PL spectra at 1.6 K of a 150 Å GaAs quantum well [168].

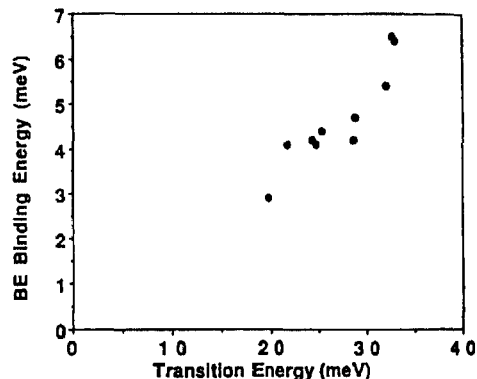


Fig. 88. Bound exciton binding energy versus the energy for the $2s(\Gamma_6)-2s(\Gamma_6)$ transition for the Be acceptor. The transition energies are derived from the two-hole transition spectra. The almost linear dependence observed here suggests that Hayne's rule may be valid for quantum wells (After Holtz et al. [169].)

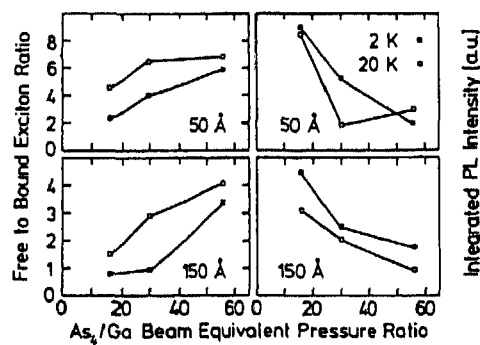


Fig. 89. 2 and 20 K integrated PL intensity and free exciton-to-bound exciton ratio versus BEP ratio. (After Munnix et al. [60].)

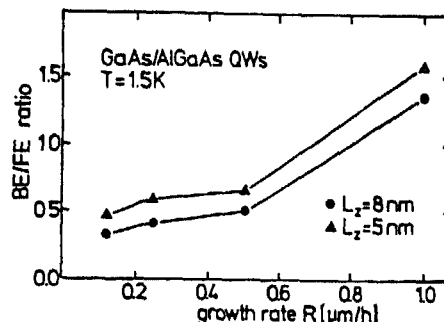


Fig. 90. Bound exciton/free exciton intensity ratios versus growth rate for an 8 and 5 nm quantum well. Spectra were taken at 1.5 K. (After Munnix et al [60].)

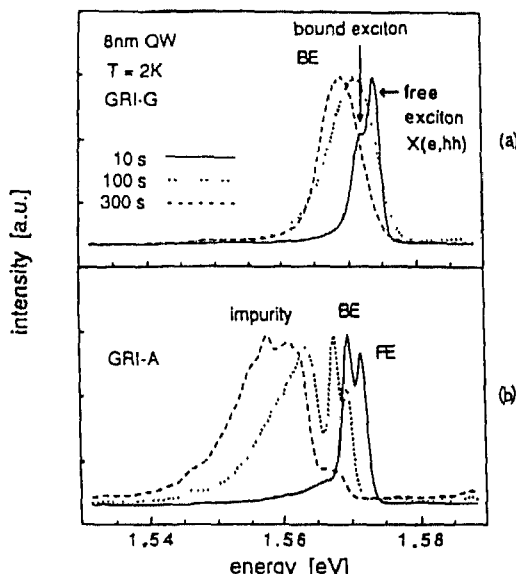


Fig. 91. Low-temperature PL spectra of an 80 Å quantum well for growth interrupts (a) at the GaAs surface, and (b) at the AlGaAs surface. Growth interrupts were 10, 100, and 300 s in duration (After Köhrbrück et al [170].)

and found that analysis of the electron to acceptor (e, A^0) and donor-to-acceptor pair (DAP) recombination lines allowed determination of the compensation ratio of donors and acceptors in n-type GaAs. More recently, Lu et al. [180] determined the compensation ratio N_A/N_D , from the excitonic spectrum, and N_A from the DAP recombination radiation in both high-purity n-type and p-type GaAs epilayers. Fig. 93 shows a typical low-temperature PL spectrum for high-purity GaAs grown by MOCVD and obtained using an excitation of 10 mW cm^{-2} . In this material the dominant acceptor is carbon, and for low concentrations of impurities ($< 3 \times 10^{15} \text{ cm}^{-3}$), excitonic peaks are clearly observed. The spectra in this figure correspond to different $N_A/N_D = \theta$ ratios. This data clearly shows that as the compensation ratio increases, in n-type material, the acceptor-bound exciton peak (A^0, X) increases relative to the donor peaks. For p-type material, the (A^0, X) peak is stronger than either of the donor-bound exciton peaks. The excitonic intensity ratio was obtained by lineshape fitting each of the bound exciton peaks, (A^0, X), (D^0, X), and (D^+, X), with Lorentzians. Fig. 94 shows the compensation ratio as a function of the ratios of these bound-exciton peak emission intensities. In a similar fashion, the acceptor density may be obtained through intensity ratio measurements [180]. Another means for determining the compensation ratio has been given by Kamiya and Wagner [181]. This method relies

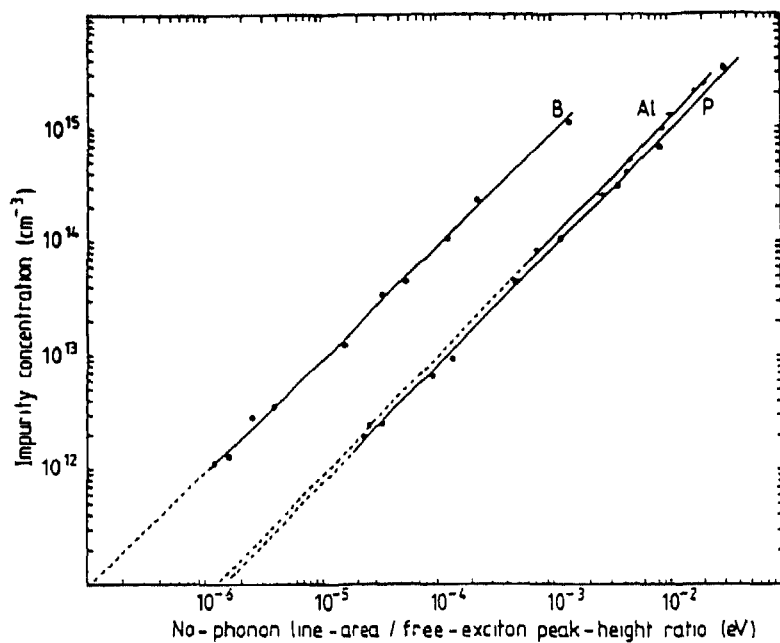


Fig. 92. Calibration of impurity concentration for B, Al, and P dopants obtained from the ratio of bound-exciton no-phonon integrated intensity to the free-exciton peak height. (From P. McL. Colley and E.C. Lightowlers, *Semicond. Sci. Technol.*, 2 (1987) 157.)

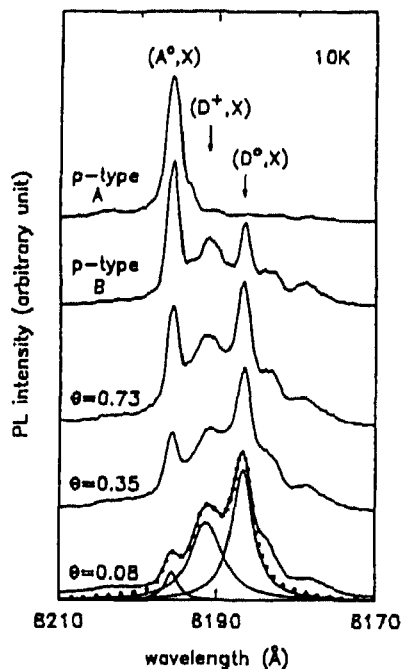


Fig. 93. Near-edge PL spectra at 10 K for various samples with different density ratios N_A/N_D for both n-type and p-type layers. Bottom spectrum shows theoretical fits with three Lorentzian line shapes. (After Lu et al. [180].)

upon a lineshape analysis of the donor–acceptor pair and band-to-acceptor PL emission lines. Fig. 95 shows a comparison between this lineshape analysis theory and the emission spectra for a sample. The result yields the compensation ratio for the sample.

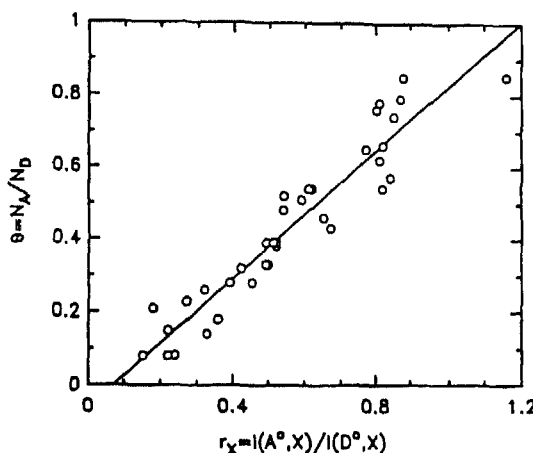


Fig. 94. Compensation ratio $\theta = N_A/N_D$ for various n-type GaAs layers plotted versus the intensity ratio of the acceptor to donor bound exciton peaks. The linear fit to the data yields $\theta = 0.89r_X - 0.06$, where r_X is the bound exciton intensity ratio. (After Lu et al. [180].)

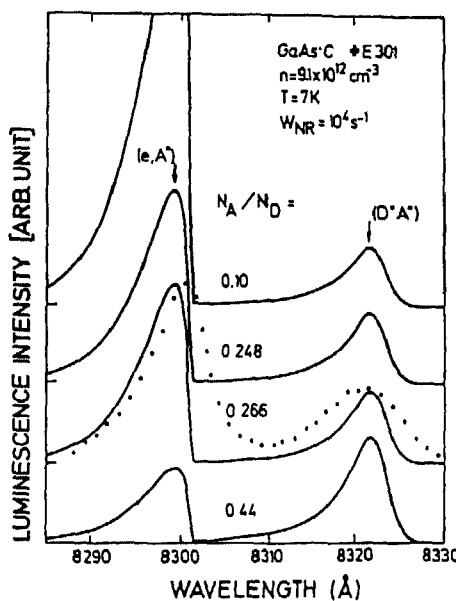


Fig. 95 PL spectra at 7 K (●) together with several calculated lineshapes. (After Kamiya and Wagner [181])

2.2.3.3. Free-to-bound transitions

At low temperatures and in high-purity material, excitonic states tend to be the lowest energy states in a semiconductor. However, even at low temperatures a fraction of the excited electron-hole pairs exist as free carriers. This may give rise to band-to-band recombination. It may also give rise to recombination with an electron (hole) and an acceptor (donor) level. These emissions are denoted by (e,A^0) and (D^0,h) , respectively. The donor-to-valence band transition has already been encountered in our discussion of bound excitons (section 2.2.3.1). Fig. 43 shows the (D^0,h) emission peak which overlaps with the (D^+,X) bound exciton peak. The opposite case of band-to-acceptor emission, (e,A^0) , is shown in Fig. 96 [92]. The lineshape for (e,A^0) emission is given by [6]

$$I(E) \propto \sqrt{\hbar\omega - E_g + E_A} [\exp(-(\hbar\omega - E_g + E_A)/kT)] \quad (14)$$

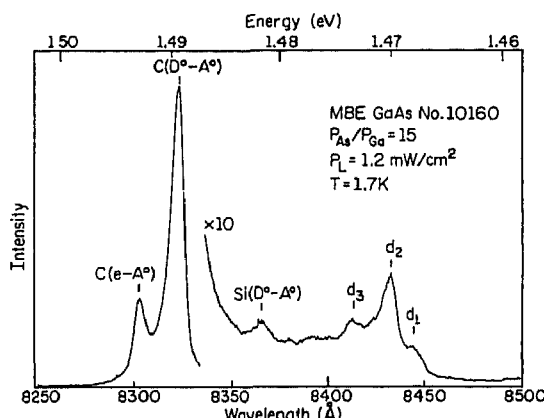


Fig. 96. PL spectrum of GaAs sample grown at low As/Ga ratio and a substrate temperature of 630 °C. (After Skromme et al [92])

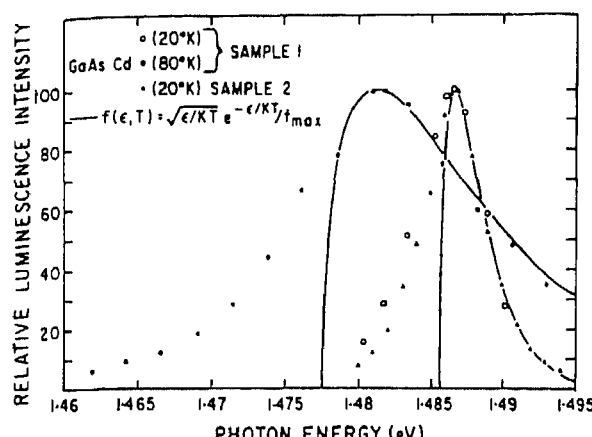


Fig. 97. PL spectra of GaAs:Cd at 20 and 80 K for two different samples. Solid symbols represent data at 80 K and open symbols represent data at 20 K. (Reprinted from E.W. Williams and H.B. Bebb, *J. Phys. Chem. Solids*, 30 (1968) 289, with permission from Elsevier Science Ltd., Pergamon Imprint, The Boulevard, Langford Lane, Kidlington OX5 1GB, UK.)

Fig. 97 shows a comparison of the (e, A^0) emission observed from GaAs doped with Cd with this theoretical expression. This lineshape fitting allows a determination of the binding energy of the acceptor, E_A . Fig. 98 shows the (e, A^0) transitions of GaAs samples doped with C, Zn, and Si, clearly demonstrating the differences in the (e, A^0) spectral position with different impurities due to differences in binding energy [182]. The energies for the C, Zn, and Si (e, A^0) transition are 1.49382 eV, 1.489 eV, and 1.485 eV, respectively. Fig. 99 shows the (e, A^0) transition at 1.4782 eV for Ge-doped GaAs, which is the deepest simple acceptor in GaAs [105].

Free-to-bound emission lines have also been observed in Si [183] and GaAs nanostructures [63,158,167]. Shannabrook and Comas [184] reported the first observation of (D^0, HH) emission in a GaAs quantum well structure. Fig. 86 shows the PL spectrum of a GaAs quantum well structure with the (D^0, HH) free-to-bound transition evident between the heavy-hole donor-bound exciton and the heavy-hole acceptor-bound exciton. Meynadier et al. [63] modeled their observed spectra and concluded that the acceptors are primarily incorporated at the well interface within approximately 10 Å on either side. Holtz et al. [169] also observed band-to-acceptor transitions in selectively excited (at the bound exciton line) PL of a 94 Å quantum well.

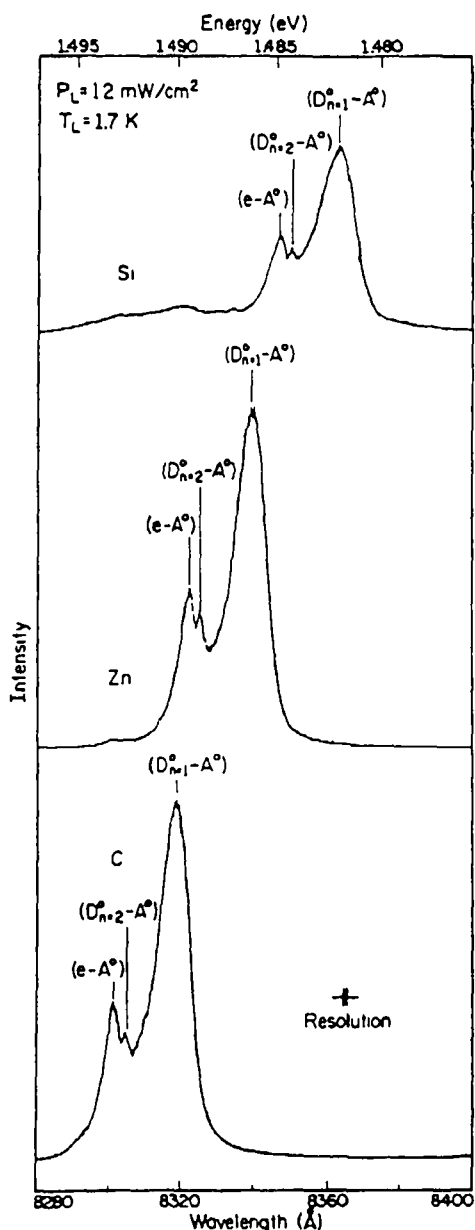


Fig. 98. PL spectra of three different GaAs epilayer samples at 1.7 K. From bottom to top the samples were MBE-grown with C acceptors, AsCl₃ VPE grown with Zn acceptors, and LPE grown with Si acceptors (After Skromme and Stillman [182])

2.2.3.4. Donor-acceptor pair transitions

Donors and acceptors may interact with one another to form pairs which behave as stationary molecules imbedded in the semiconductor. The interaction is through the Coulomb interaction which lowers their binding energies. Donor-acceptor pair (DAP) complexes consist of four point charges



The recombination energy of a distant donor-acceptor pair is given by

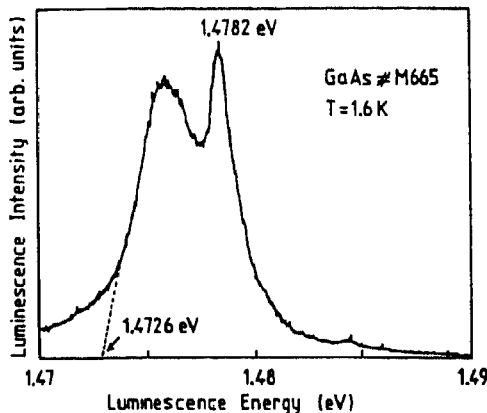


Fig. 99 Free-to-bound luminescence spectrum from a Ge-doped GaAs sample. The dashed line shows an extrapolation of the DAP to infinite pair separations. (After Kisker et al. [105].)

$$\hbar\omega = E_g - (E_A + E_D) + \frac{e^2}{\epsilon R} \quad (15)$$

where ϵ is the dielectric constant, E_A and E_D are the acceptor and donor binding energies, respectively, and R is the distance between the donor and acceptor forming the pair (neglecting an additional term due to wavefunction overlap). Importantly, the donors and acceptors are substitutional, and therefore exist at fixed lattice sites. As such, the donor–acceptor pairs formed have discrete radii, or distances between the donor and acceptor. As a result the energy spectrum produced by this pair interaction may span a large range. For distant donors and acceptors R is very large and the Coulomb interaction is small. The recombination energy is then at $E_g - (E_A + E_D)$. As the donors and acceptors pair at closer range all the way to nearest neighbors, the Coulomb interaction may yield states inside the conduction or valence bands, $e^2/\epsilon R > (E_A + E_D)$. There is also a distinction that may be made in compound semiconductors between the types of impurities which pair. Impurities which substitute on the same sublattice, i.e. both for anions or cations, are called type I, whereas if they are on different sublattices then they are called type II [185].

Since the unambiguous identification of donor–acceptor pairs by Hopfield et al. [185] in 1963 there has been much work examining the properties of these pairs. Foremost among these is the work of Dean which gives an extensive review of the subject [186]. In this review, Dean provides tables (Tables 2 and 3 in Ref. [186]) for type-I and type-II pair distributions for zincblende crystals which are useful for analysis of pair spectra. These tables illustrate the explanation for the many sharp lines observed in the DAP spectrum of, for example, GaP [186]. The appearance of a large number of sharp no-phonon lines whose energies may be accounted for by very simple relationships is a hallmark of DAP emission. However, it is not always a trait of DAP emission. In GaAs the sum of acceptor and donor binding energies are typically small. Thus, the DAP emission energies predicted by Eq. (15) are above the bandgap energy (since $e^2/\epsilon R > (E_A + E_D)$). The first suggestion of DAP emission in GaAs was by Lucovsky et al. [187] for the 1.49 eV transition in Zn-doped GaAs layers. They observed five characteristics of this line which they considered to be evidence proving the DAP origin of this emission.

1. The line shifts to higher energies with increasing excitation intensity.
2. The emission band narrows significantly with increasing excitation intensity.
3. As the donor concentration in the sample is increased the band shifts toward higher energies.
4. The intensity of the band decreases rapidly as the temperature increases to 35 K.

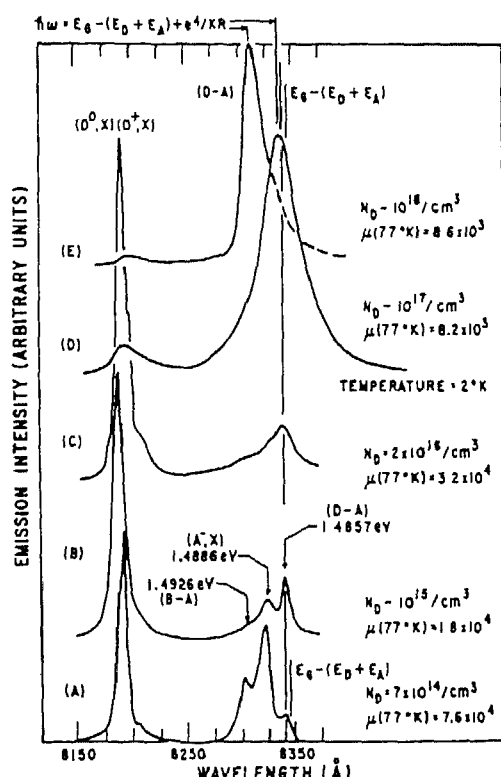


Fig. 100. Low-temperature PL spectra in n-type GaAs showing the concentration dependence of the DAP recombination [188].

5. The band shifts to higher energies as the temperature is increased.

Fig. 100 demonstrates the third point, namely the increase in peak energy of the DAP band with increasing donor concentration [188].

DAP emission has also been examined in relatively high-purity GaAs. Fig. 96 exhibits DAP spectra associated with both C and Si acceptors. Kisker et al. [105] used selective pair luminescence to determine the energy level structure of C, Zn, Si, and Ge acceptors in GaAs. This method is based upon the fact that the DAP emission energy is a function of the distance between acceptors and donors. By exciting the DAP with tunable light, a site-selective distribution of DAPs are excited. This then yields a series of peaks which correspond to the energy difference between the ground and excited states of the acceptor. Fig. 50 demonstrates this technique with a Ge-doped GaAs sample. The peaks shown correspond to the $1S_{3/2} \rightarrow 2P_{3/2}$, $1S_{3/2} \rightarrow 2S_{3/2}$, and $1S_{3/2} \rightarrow 2P_{5/2}$ energy splittings of the Ge acceptor. Peaks due to C and Zn acceptors are also observed. Fig. 46 shows similar results of Garcia et al. [100] with C and Be as the dominant acceptors. Two-hole transitions are also clearly evident in the spectra. (Note that the detailed structure depends upon the precursors used in growth.) In addition to the structure observed in DAP spectra due to excited states of the acceptors, it is also possible to observe structure in the DAP spectra associated with excited states of donors. Skromme and Stillman [182] examined VPE-, LPE-, MOCVD-, and MBE-prepared samples and observed the $(D_{n=2}^0 - A^0)$ peak in approximately a quarter of the samples examined. Fig. 98 clearly shows this excited-state DAP transition associated with C, Zn, and Si acceptors in the energy region between (e, A^0) and $(D_{n=1}^0 - A^0)$ emissions. This new peak was also found to decrease in intensity rapidly with increasing temperature, and is absent above 20 K. Lastly, Skromme et al. [189] have observed two new shallow acceptors in VPE- and MOCVD-grown GaAs through examination of the DAP and (e, A^0) portion of the

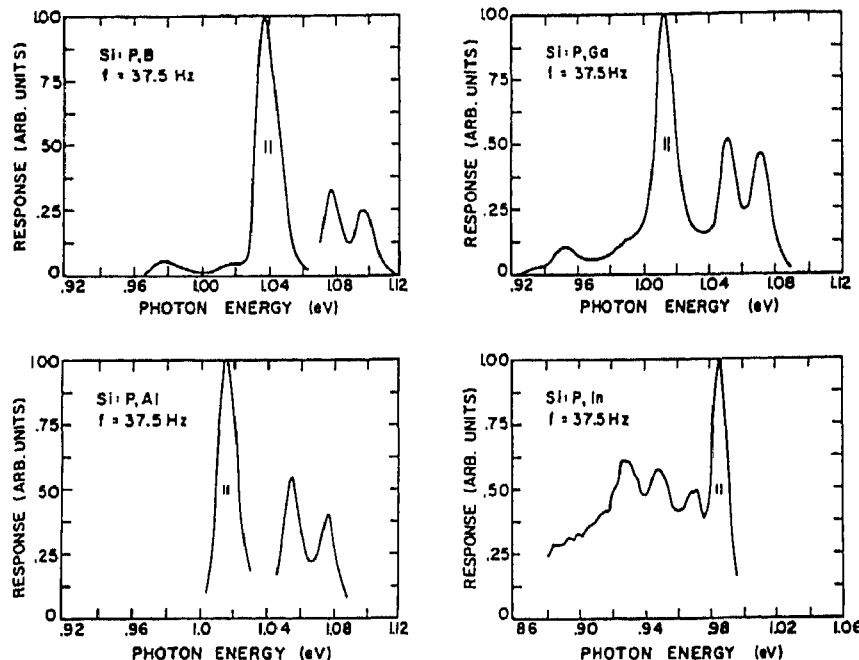


Fig. 101. PL spectra of co-doped Si samples (P,B), (P,Al), (P,Ga), and (P,In). Spectra were obtained by chopping at 37.5 Hz. (After Enck and Honig [190].)

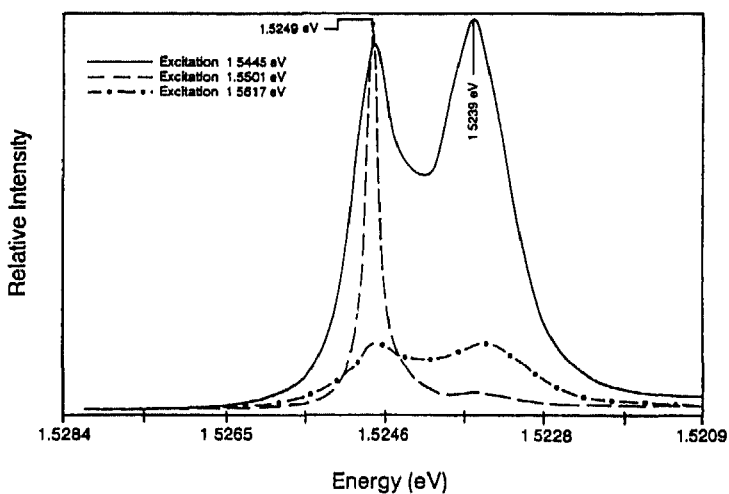


Fig. 102. PL spectra of a GaAs quantum well structure after excitation at three different energies. (After Reynolds et al. [191].)

spectrum. The origin of these levels is not known, but may be due to unidentified chemical contaminants such as Hg, Ca, Sr, or Ba.

DAP emission has also been observed in Si [190]. Enck and Honig [190] examined Si samples co-doped with donors (P, Sb, As, Bi) and acceptors (B, Al, Ga, In, B) of various concentrations. Fig. 101 shows the PL spectra of samples doped with (P,B), (P,Al), (P,Ga), and (P,In), respectively. (Note this data was taken using phase-sensitive detection and the chopping speed is shown in the figures. This allows for some rough time resolution to be obtained.) The spectra generally consist of three lines of comparable magnitude and one weaker line at lower energy. These lines correspond to,

from highest to lowest energy, a no-phonon transition, a TA phonon assisted transition, a TO phonon assisted transition, and a transition involving two TO phonons, respectively.

Reynolds and coworkers [191,192] have recently observed donor–acceptor pair emission in GaAs/AlGaAs quantum wells. Fig. 102 shows the PL spectra of a MBE-prepared quantum well (well thickness, 200 Å) with three different excitation energies. The peak at 1.5249 eV is the heavy-hole free-exciton transition, whereas the peak at 1.5239 eV is attributed to donor–acceptor pair emission. Their time-resolved PL and magnetic-field measurements are consistent with a bound-to-bound transition for this 1.5239 eV line. As mentioned above DAP emission is well known to depend on the separation of donors and acceptors constituting the pair. Reynolds et al. [191] showed that this 1.5239 eV emission was consistent with this interpretation. Using the binding energy of a donor in the center of a 200 Å well (10 meV) and the acceptor binding energy of 46 meV, the spatial separation between donors and acceptors may be calculated using Eq. (15). This yields a separation of 40–50 Å, which is considerably smaller than the Bohr radius of the exciton in this size quantum well. This explains the observed decay rate and energy position of this peak.

2.2.3.5. Additional defect lines

In addition to the forest of defect-induced bound exciton lines observed at energies just below the (A^0, X) emissions and above the (e, A^0) emissions, it is commonly observed that a series of four lines appear on the low-energy side of the (e, A^0) and DAP emissions, in the energy range 1.466–1.482 eV [92,119,120]. At the low temperatures at least four distinct peaks, labeled d_1 – d_4 are evident, as shown in Fig. 103. At these temperatures Skromme et al. [92] attributed these peaks to $(D^0 - A^0)$ recombination involving four moderately deep acceptor levels with ionization energies of 47.9, 45.8, 43.7, and 40.1 meV for d_1 to d_4 , respectively. Further, they find that this defect-related luminescence is a $(D^0 - A^0)$ recombination at low temperatures and low excitation powers which transforms to (e, A^0) at high temperatures and high excitation powers, as shown in Fig. 104. Importantly, they conclude that there exists a correlation between the 1.504–1.511 eV and 1.466–1.482 eV peaks. Skolnick et al. [119] find that these emission lines are strongly polarized, just as the 1.504–1.511 eV emission lines were, implying preferential incorporation of the acceptors along the $\langle 110 \rangle$ directions.

2.2.3.6. Deep levels

Deep impurities are defects which are dominated by short-range forces and exhibit distinctly different properties from those of shallow donors and acceptors. Deep levels are not adequately described within the context of effective mass theory. They are characterized not by their energy separation from either the conduction or valence bands, but by their dispersion in momentum space. Deep levels are strongly localized in real space, and delocalized in momentum space [193].

2.2.3.6.1. Isoelectronic impurities

Perhaps one of the most studied of the isoelectronic impurities in semiconductors is nitrogen [194–196]. Thomas and Hopfield [194] and Wolford et al. [195,196] demonstrated their existence in GaP. In GaP isolated N impurities form strongly radiative bound states. These neutral lattice defects cause trapping by their strongly electronegative core which may attract and bind an electron. Subsequently, the charged center captures a hole and forms the bound excitonic states A ($J=1$) and B ($J=2$) characteristic of isoelectronic traps. In GaP these A and B levels are 33 meV below the indirect X conduction band. Selection rules predict that radiative recombination is dipole allowed from the A level and forbidden from the B level.

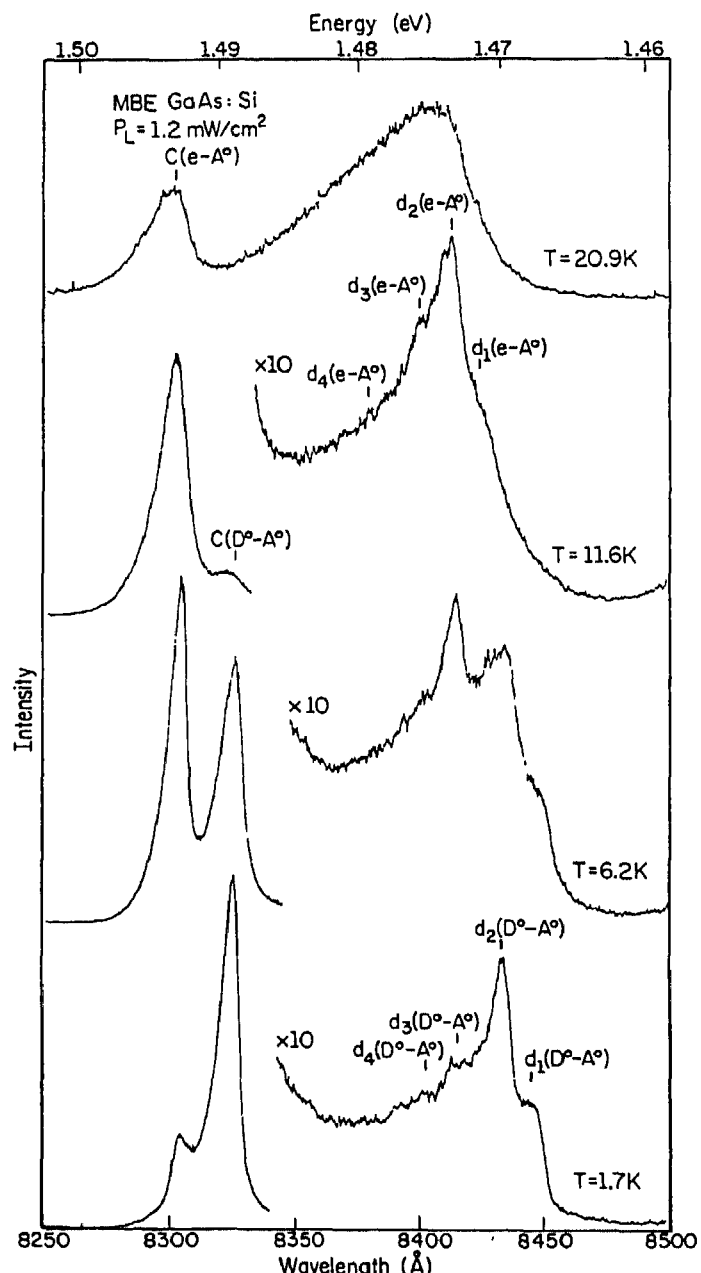


Fig. 103. DAP and free-to-bound emissions at four different lattice temperatures. (After Skromme et al. [92].)

Wolford et al. [195] reported the first observation of N isoelectronic traps in GaAs [197]. This deep level enters the forbidden bandgap of the material through the application of hydrostatic pressure. Fig. 105 shows the PL spectra of an undoped GaAs sample at various pressures (this technique will be examined in more detail in section 2.4.1) [195,196]. At ambient pressure and pressures less than 20 kbar, the spectra (top spectrum) are indicative of high-purity GaAs, with no indication of emission related to N impurities. However, near 24 kbar the donor-bound exciton line weakens and two sharp no-phonon lines with associated phonon replicas appear. At these pressures GaAs is direct gap. Fig. 106 shows the PL spectra of N-doped GaAs at 63 kbar where GaAs is indirect in comparison to N-

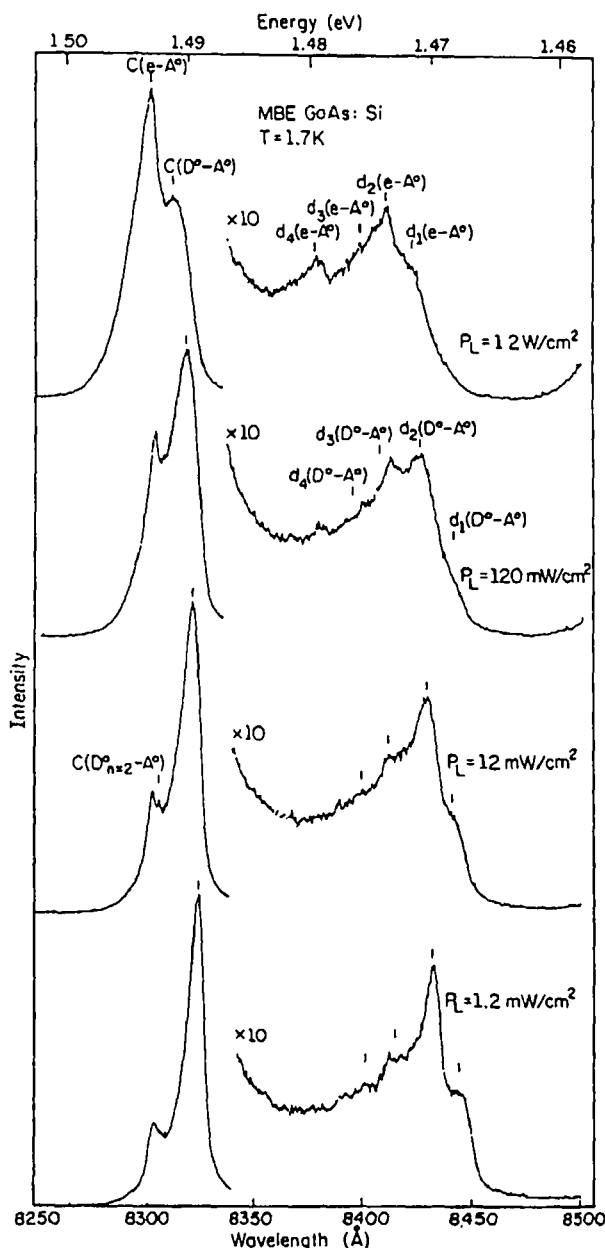


Fig. 104 DAP and free-to-bound emissions versus excitation intensity (After Skromme et al. [92])

doped GaP which is also indirect. The similarities are clearly evident. The A and B no-phonon lines are plainly evident together with the LA, TO^X, LO^X, LO^G, and TO^G phonon replicas. Optical overtones (i.e. multiple phonon assisted emission peaks) are also present through 5LO, and their intensities are well described by

$$I_n = I_0 S_{\text{LO}}^n / n! \quad (16)$$

where S_{LO} is the phonon coupling strength [198]. The pressure dependence of the peaks evident in the spectra of Figs. 105 and 106 are summarized in Fig. 107. This data shows that the N_x level forms a resonant state above the conduction band edge for pressures less than ~ 22 kbar.

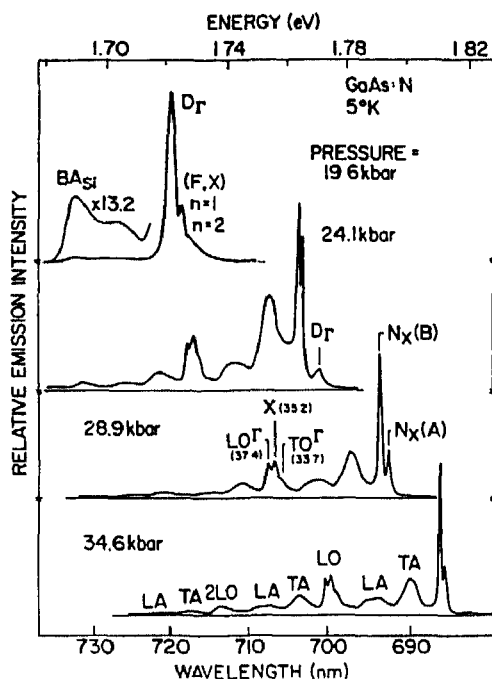


Fig. 105. PL spectra at 5 K of GaAs under pressure. (After Wolford et al. [196].)

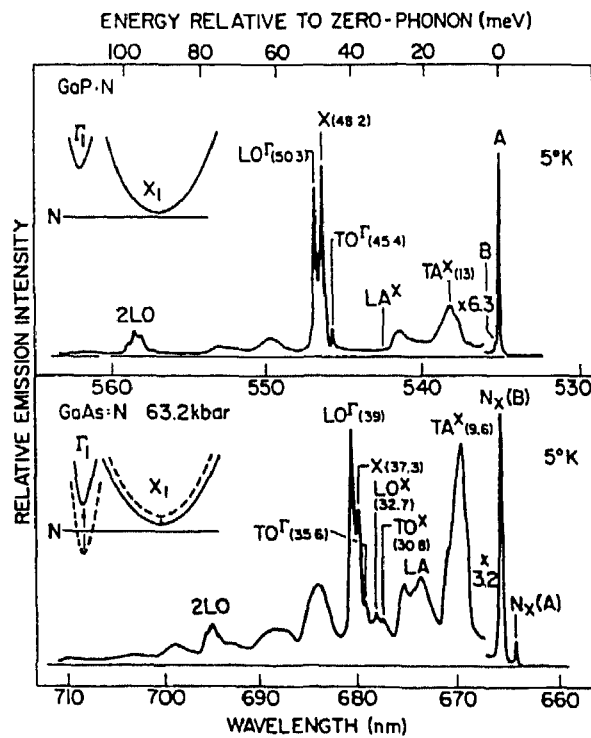


Fig. 106 PL spectra at 5 K of indirect-gap GaP:N and GaAs N at 63.2 kbar. (After Wolford et al. [196])

Liu et al. [199,200] observed the luminescence of nitrogen pairs, NN_2 , in GaAs where the N concentration was doped to 10^{17} cm^{-3} , well above the solubility limit in GaAs (10^{14} cm^{-3}). Fig. 108 shows the PL spectra of a N-doped sample at various pressures. The zero-pressure data in Fig. 108(a)

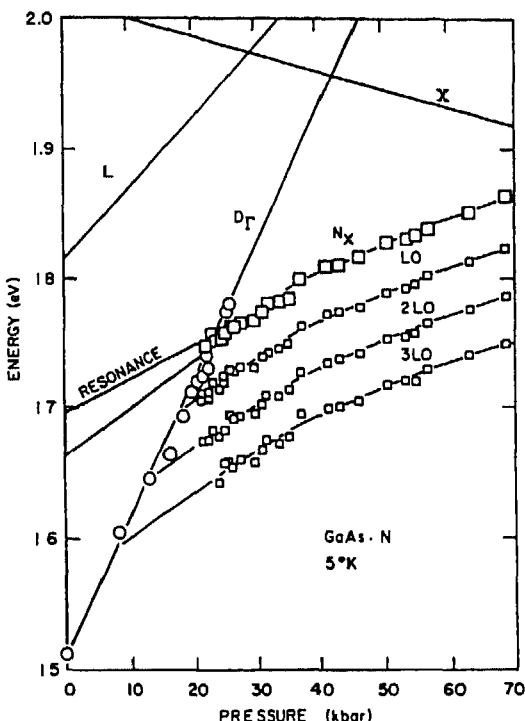


Fig. 107. Pressure dependence of the N_x and D_T transitions (After Wolford et al [196].)

exhibit a narrow line 12 meV below the donor-bound exciton line. This is the NN_1 pair emission line. Liu et al. found that this line is similar to the NN_1 line in GaP:N and represents a defect oriented in the $\langle 110 \rangle$ direction. Importantly at these low pressures the N deep level is still above the conduction band edge, and is not evident in the spectra. As the pressure is increased, up to 25 kbar, additional pair lines appear, for pairs NN_i with $i \leq 10$. Fig. 109 shows a summary of the peaks observed in the pressure data for pressures up to 35 kbar. Note that the pair emissions are not evident above ~ 25 kbar. This is attributed to the higher concentration of N levels than N pair levels.

Isoelectronic centers in Si generally appear to form from a neutral ground state of the defect core which tightly binds a hole with a typical binding energy of a few hundred meV [201]. This positive center then binds an electron in a shallow effective-mass orbit with a binding energy typically of 0.1 eV or less. This is the so-called pseudodonor model. The luminescence of several isoelectronic centers in Si was discussed in section 2.2.3.1.2.

2.2.3.6.2. Transition metal ions

The 3d transition metal ions (i.e. the iron group) have an electronic structure consisting of multiple 3d electrons outside of the closed $2p^6$ shell. As a result the intracenter 3d–3d transitions are sensitive to the crystalline environment, the so-called crystal field. Additionally, the 2s electrons may participate in bonding to the semiconductor so that the metal ion behaves as a deep acceptor. The activation energies of some of the 3d transition metal ions in GaAs are: Cr, 0.85 eV; Mn, 0.114 and 0.112 eV; Fe, ~ 0.5 and 0.2 eV; Co, 0.58 eV; and Cu, 0.17, 0.155, and 0.165 eV [6]. The characteristic of the low-temperature PL spectrum of Cr-doped GaAs is a sharp zero-phonon line at 0.839 eV, as shown in Fig. 110 [202]. Uihlein and Eaves [203] have shown that the Cr luminescent center has a

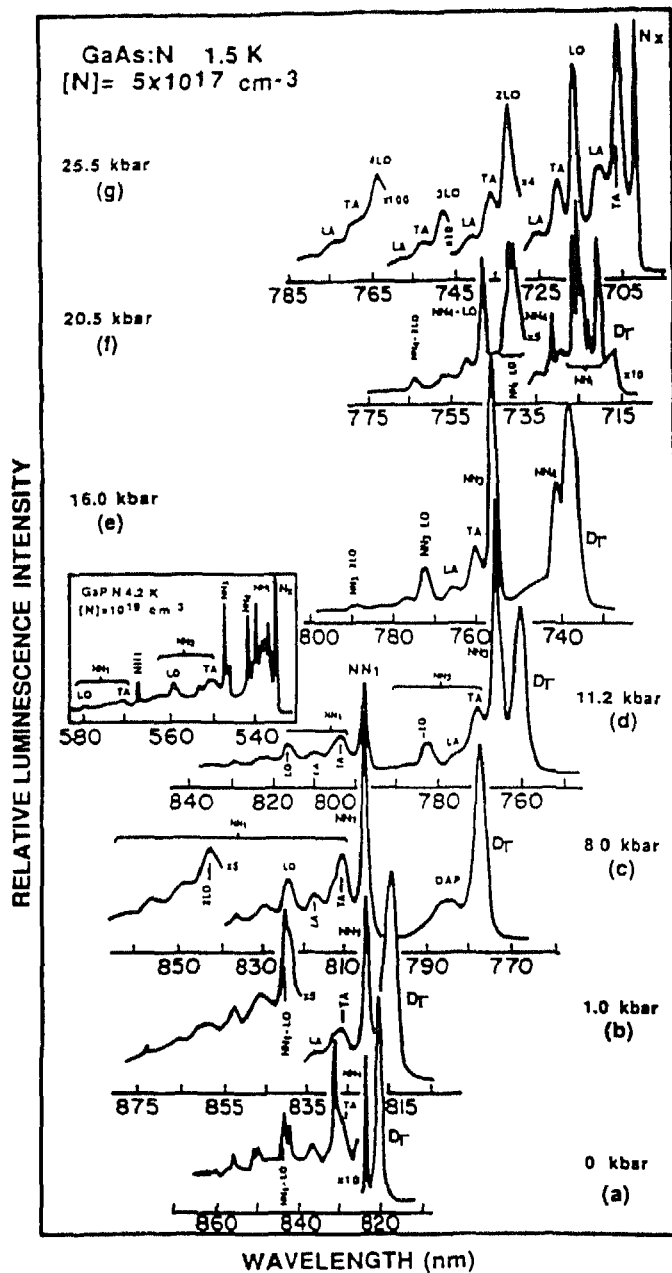


Fig. 108 1.5 K PL spectra of N-doped GaAs at different pressures. The NN_i peaks are aligned in consecutive spectra for clarity purposes. Phonon replicas involve TA, LA, and TO phonons. (After Liu et al. [200].)

(111) C_{3v} axial symmetry. PL measurements combined with annealing studies have shown that the most probable candidate for this complex is Cr_{Ga}-V_{As} [202,204]. Manganese is incorporated substitutionally into GaAs at a Ga site, forming an acceptor 110 meV above the valence band [141,205–207]. Shen et al. [205] have examined Mn⁺-implanted MBE-prepared GaAs layers. They observe the well-known Mn-related deep acceptor emission at ~1.41 eV, as well as a donor-bound exciton emission (Mn⁰,X), band-to-Mn acceptor emission (e,Mn⁰), DAP emission (D⁰,Mn⁰), a new emission line ‘‘G’’ at 1.5043 eV, and another new emission line ‘‘H’’ at 1.495 eV (not shown in the figure).

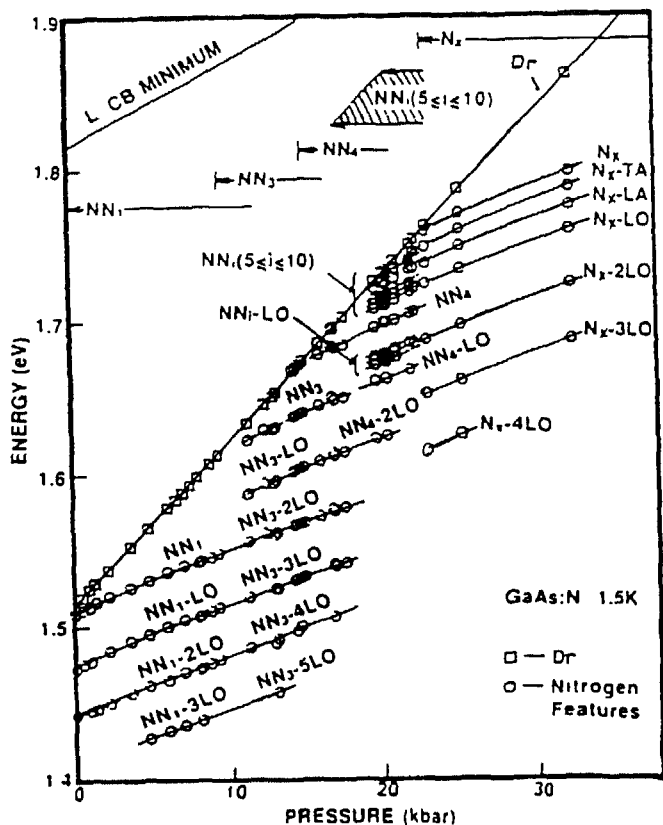


Fig. 109 PL peak energies of the various nitrogen levels in GaAs versus pressure. (After Liu et al. [199].)

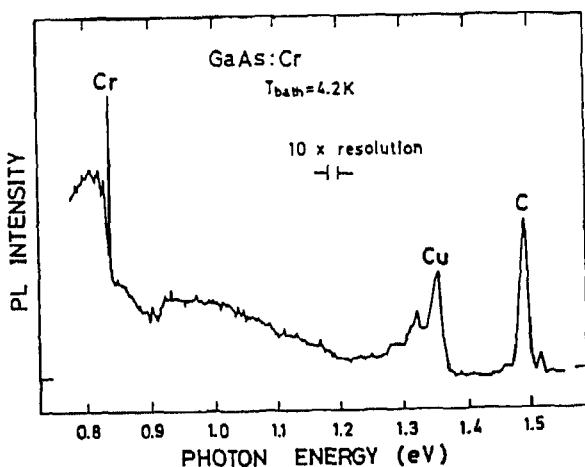


Fig. 110. 4.2 K PL spectrum of Cr-doped GaAs. (After Hsu et al. [202])

Note that the free-to-bound and bound-to-bound transitions associated with Mn acceptors are much deeper than the similar transitions associated with C acceptors. The exact origin of the "G" and "H" Mn-related luminescent centers is presently unknown. Fig. 111 shows the PL spectra of Cu-diffused LEC grown GaAs [208]. The 1.36 eV peak is associated with Cu luminescent centers [209–211]. The Cu luminescent center is thought to be related to Cu_{Ga}^- , a singly charged acceptor on a Ga site.

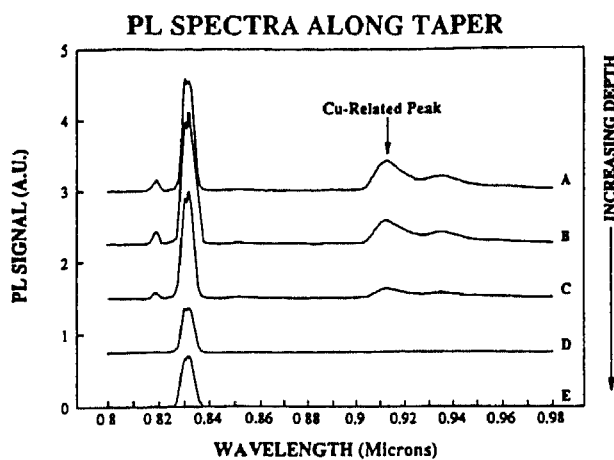


Fig. 111. PL spectra of a Cu-diffused GaAs sample versus depth into the sample. (After Third et al. [208].)

Transition metal ions doped into Si produced deep, bound excitons [201]. Singh et al. [201] used Fourier transform PL and Fourier transform PL-excitation spectroscopy to study Si doped with Ag, Au, and Fe. They found that the electronic structure of the deep-bound exciton systems of these defect centers is well described by a pseudodonor model of isoelectronic centers. Fig. 112 shows the PL spectrum of the 735 meV band in Fe-doped Si. The PL emission consists of three zero-phonon lines at 734.7, 735.1, and 737.7 meV. Also evident in the spectra are bands associated with the strong coupling of these zero-phonon lines to the phonon modes. Fe1 and Fe2 are transitions from the spin-triplet state which are forbidden, but lower in energy, and therefore more heavily populated at low temperatures. Fe3 is due to a transition from the spin-singlet state which is allowed. As temperature is increased the Fe3 line increases in intensity, consistent with the higher thermal occupation of this allowed level. Singh et al. have proposed that the 735 meV PL band is due to the radiative recombination of a defect containing an interstitial iron atom, and perhaps other unknown constituents, resulting in an overall trigonal symmetry (consistent with uniaxial stress measurements). Ag-doped Si has a dominant PL emission at low temperatures at 780 meV. Au-doped Si also has a dominant PL emission at 780 meV. There is only a 4 meV difference in the energy of the Ag- and Au-related emissions. The structure of the emission bands is similar to that of iron-doped Si, namely, consisting of three no-phonon emission bands and several phonon replicas.

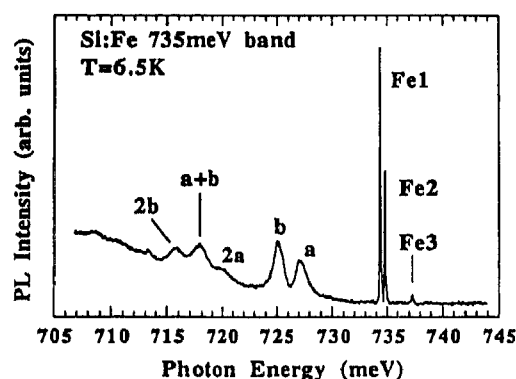


Fig. 112. Low-temperature PL spectrum of the 735 meV emission band in Fe-doped Si. Spectrum shows the quasilocalized phonon modes a and b. (Reprinted from Singh et al., *Solid State Commun.*, 93 (1995) 415, with kind permission from Elsevier Science Ltd., The Boulevard, Langford Lane, Kidlington OX5 1GB, UK.)

2.2.3.6.3. Rare-earth ions

The concept of doping rare-earth ions into semiconductors was first proposed by Bell in 1963 [212]. Research in this area has been driven by possible applications involving the emissions originating from the intracenter 4f–4f transitions of the trivalent rare-earth ion. (The primary interest has been to utilize the 4f–4f 1.54 μm transition of Er^{3+} for fiber-optic communications.) The most serious difficulty has been in doping large concentrations of rare-earth ions into semiconductors, and doing so while retaining high crystal quality. By far the most studied of the rare-earth-doped elements are erbium and ytterbium doped into GaAs, InP, and Si [213–218]. Pomrenke et al. [213] have done perhaps the earliest and most extensive study of the optical properties of rare-earth-doped (implanted) GaAs. Fig. 113 shows the near-infrared PL spectra of Er ion-implanted (with a near-surface concentration of 10^{18} cm^{-3}) GaAs samples after annealing at the temperature shown. The forest of emission lines centered at 1.54 μm is due to the transitions between the weakly crystal-field-split spin-orbit levels of Er^{3+} , $^4\text{I}_{13/2} \rightarrow 4\text{I}_{15/2}$. The multiple lines apparent in the spectra result from the crystal-field splitting of each J -manifold of the spin-orbit energy levels. Thus, the number and position of these lines is indicative of the local environment of the rare-earth ion in the semiconductor. The multiplicity of these lines is an indication that the site symmetry of the Er^{3+} ion is lower than cubic [216]. At low temperatures only the lowest levels of the J -manifold of the upper state of the Er^{3+} ion is populated (i.e. the $^4\text{I}_{13/2}$ level). However, as temperature is increased more of the levels within the crystal-field-split J -manifold are occupied and may then be involved in radiative emission. Fig. 114 illustrates this effect [216]. At 6 K only eight lines are evident in the PL spectrum. However, as the temperature is increased to 77 K many more lines are evident. This provides a means for calculating the energy level structure of each

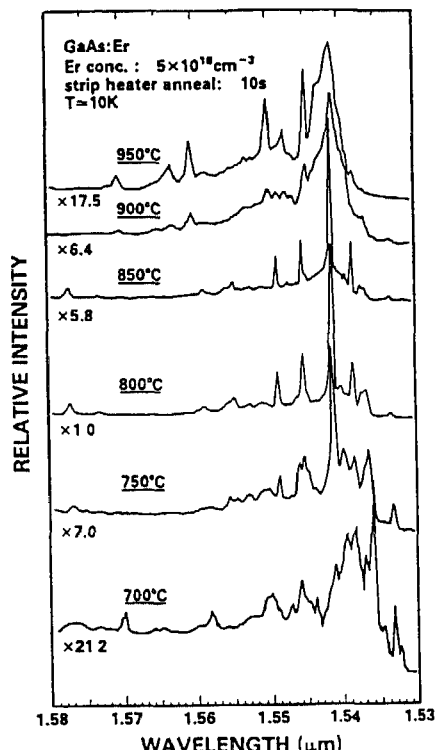


Fig. 113 10 K PL spectra of GaAs implanted with Er at 350, 130, and 50 keV Er after annealing at the indicated temperature for 10 s. (After Pomrenke et al. [213].)

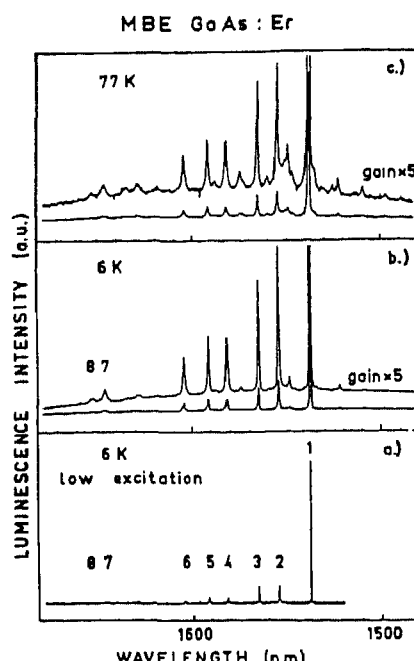


Fig. 114. PL spectra versus temperature of Er:GaAs sample grown by MBE. (a) $T=6\text{ K}$, excitation power < 1 mW; (b) $T=6\text{ K}$, excitation power 100 mW; and (c) $T=77\text{ K}$, excitation power 100 mW. (After Ennen et al. [216].)

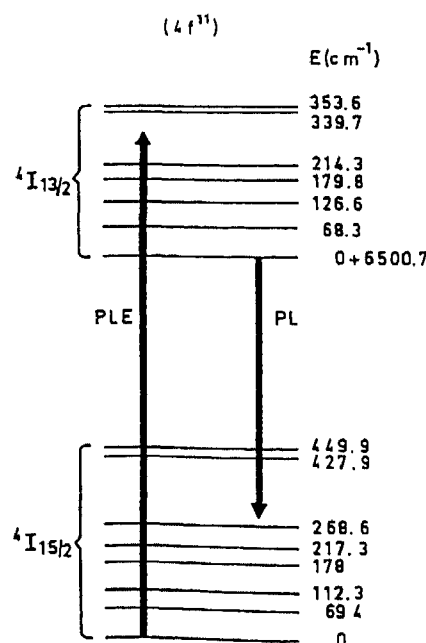


Fig. 115. Energy level diagram of the noncubic Er^{3+} complex in GaAs as derived from PL and PLE measurements. (After Ennen et al. [216].)

J -manifold, as shown in Fig. 115. Another important fact evident in Fig. 114 is that the PL intensity decreases with increasing temperature. This is a significant problem in the technological application of these materials. The properties of Er^{3+} -doped Si are much the same. Fig. 116 shows the PL spectrum

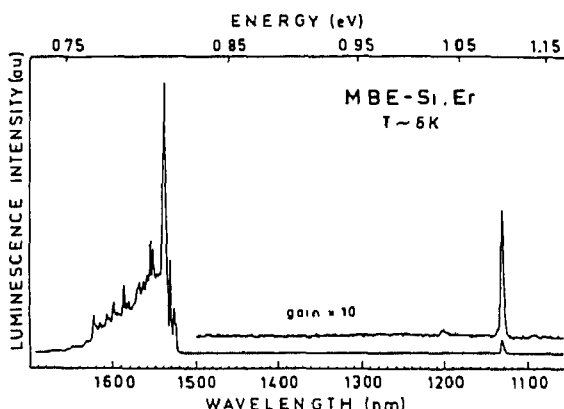


Fig. 116. PL spectrum of Er-doped Si epilayer at 6 K. (After Ennen et al. [214].)

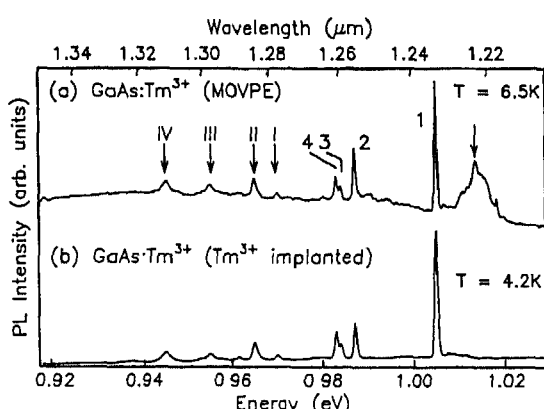


Fig. 117. PL spectra of the $^3\text{H}_5 \rightarrow ^3\text{H}_6$ intracenter transition of Tm³⁺. (a) Doping during MOVPE growth; (b) implanted after growth.

of a Si layer grown by MBE and implanted with Er³⁺ [214]. The TO replica of the intrinsic free-exciton emission is evident in the spectrum at ~ 1130 nm. The multiple sharp lines at $1.54 \mu\text{m}$ are due to the near-infrared intracenter Er³⁺ transition described above. For both GaAs and Si, the largest problem in achieving efficient room-temperature intracenter rare-earth emission from Er³⁺ is that only a small fraction of Er³⁺ ions are optically active, and other impurities, such as oxygen, play a crucial role in the process of Er³⁺ luminescence [217,218]. As another example of rare-earth doping in semiconductors, Dornen et al. [219] have examined thulium-doped (implanted) GaAs. Fig. 117 shows the fine structure of the PL emission at 1.0 eV which is due to the $^3\text{H}_5 \rightarrow ^3\text{H}_6$ transition of Tm³⁺.

2.2.3.7. Other deep levels

There are a number of other deep luminescent centers in both GaAs and Si. Among the most well known is the EL2 center in GaAs [220,221]. Nissen et al. [220] examined the fine structure of the 0.61 eV photoluminescence band which arises from the deep defect EL2 in semi-insulating GaAs. Fig. 118 shows the 0.61 eV photoluminescence spectra of a bulk GaAs sample, obtained with a Fourier transform instrument. Curve (a) is the spectrum of an unperturbed sample at 2 K. Curve (b) is the spectrum of a sample at 8 K in a magnetic field of 12 T, and curve (c) is the spectrum of a sample under a uniaxial stress of 260 MPa. The transition which gives rise to this 0.61 eV emission is from a shallow, hydrogenic bound state, associated with the lowest (Γ) conduction-band edge, to the EL2

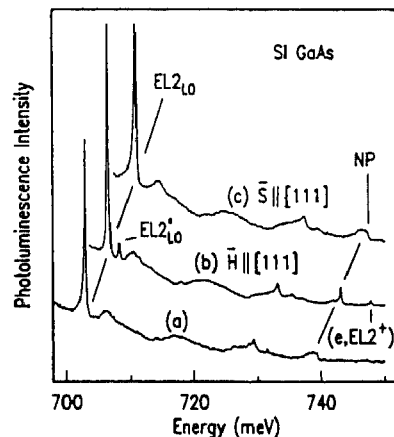


Fig. 118. Near-infrared PL spectra of the no-phonon and LO-phonon replica of the 0.61 eV EL2 emission band under a variety of experimental conditions: (a) unperturbed sample at 2 K, (b) magnetic field of 12 T at 8 K, and (c) uniaxial stress of 260 MPa and temperature of 2 K. (After Nissen et al. [220].)

ground state ($\text{EL2}_{n=2}^0 \rightarrow \text{EL2}_{n=1}^0$). The no-phonon transition (NP) and the LO-phonon-assisted transition are the sharpest spectroscopic signatures of EL2. The results presented by Nissen et al. are strong evidence that EL2 is due to the point defect As_{Ga} (the Arsenic antisite). The $\text{EL2}_{n=2}^0 \rightarrow \text{EL2}_{n=1}^0$ transition does not split with the application of uniaxial stress, and the *g*-factor is isotropic. They, therefore, conclude that the EL2 defect retains the full T_d symmetry, and is not due to an $\text{As}_{\text{Ga}}-\text{As}_i$ arsenic–antisite interstitial pair with C_{3v} symmetry.

Another deep center in GaAs is the EL0 center, which is associated with the presence of oxygen [222–225]. Fig. 119 shows the PL spectra versus temperature of GaAs:O [226]. This emission at 0.635 eV is due to the EL0 center. The linewidth of the EL0 transition increases with temperature due to electron–phonon coupling as [198]

$$W = (8 \ln 2) S (\hbar \omega)^2 (2\bar{n} + 1)^{1/2} \quad (17)$$

where *S* is the Huang–Rhys electron–phonon coupling constant. Fig. 120 shows the 0.635 eV emission width versus temperature together with the theoretical fit using Eq. (17). Yu [226] attributes this

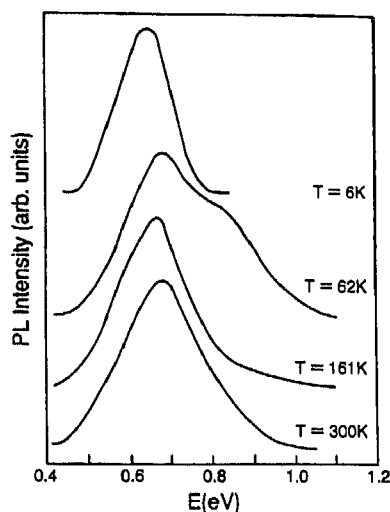


Fig. 119. Near-infrared PL spectra versus temperature of the 0.635 eV EL0 emission. (After Yu [226].)

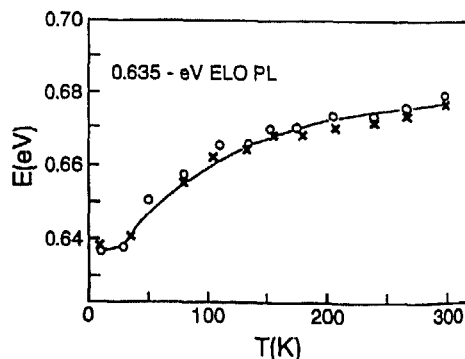


Fig. 120. Energy of the 0.635 eV emission peak versus temperature from 4 to 300 K. (After Yu [226].)

emission to a complex nearest-neighbor center, $V_{\text{Ga}}-\text{O}_{\text{As}}$, in agreement with the model proposed by Wager and Van Vechten [227].

2.2.4. Biexcitons

It has been demonstrated that excitons may interact to produce excitonic molecules under appropriate circumstances of low temperatures and high-purity samples. An example of this type of multiple exciton complex has been given in section 2.2.3.1.2 for bound multi-exciton complexes in Si. The binding of more than one exciton together to form an excitonic molecule may also occur for free-excitons. In bulk GaAs the calculated binding energy of a biexciton is only ~ 0.13 meV [228], and therefore they are expected to be difficult to observe. Nevertheless, 'tHooft et al. [229] have claimed

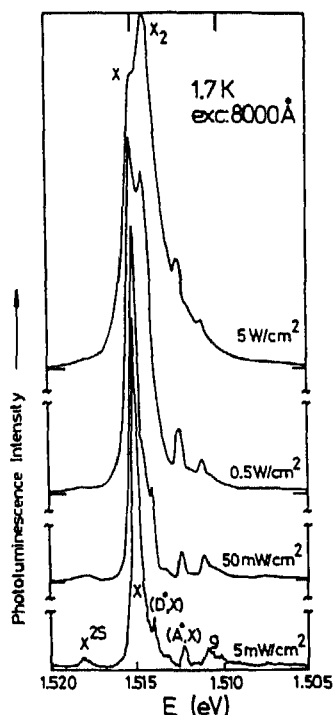


Fig. 121. PL spectra of a 1.5 μm MBE-prepared GaAs epilayer at 1.7 K versus excitation power. Spectra are scaled to the same height and shifted for clarity sake [229].

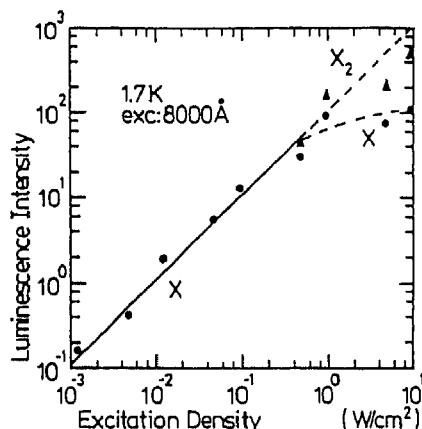


Fig. 122 PL intensity of the free-exciton emission line versus excitation density. At high excitation densities the biexciton line becomes dominant [229].

to observe biexciton emission in bulk GaAs. Fig. 121 shows the PL spectra of a high-purity, MBE-grown GaAs layer 1 μm thick versus excitation power. At low powers all of the emissions commonly seen in high-purity GaAs, as discussed above, are observed. With increasing power a new line appears at 1.5146 eV, and this line becomes dominant at excitation powers above 1 W cm^{-2} . This line has a binding energy of 0.5 meV, slightly larger than the predicted biexciton binding energy [228]. Fig. 122 shows the excitation power dependence of the free-exciton and biexciton emission lines. The free-exciton line increases linearly with power up to 1 W cm^{-2} whereupon it begins to saturate. At this point the biexciton emission continues to increase linearly.

Even more convincing observations of biexcitons have been made in GaAs quantum wells [230–234]. Quantum confinement in two dimensions increases the binding energy to about 1 meV. Miller et al. [235] were the first to report evidence of biexciton luminescence in a GaAs quantum well. Fig. 123 shows the evolution of the free-exciton and biexciton emissions versus excitation power in a GaAs quantum well. This biexciton line has a binding energy of 1.1 meV. The separation between the biexciton emission and the $n=1$ exciton emission was found to vary from 1.5 to 0.6 meV, depending upon the GaAs well width. Pantke et al. [233] calculated a binding energy of 1.8 meV from four-wave mixing measurements. Kleinman [236] has calculated the biexciton binding energy versus well width, and found that the binding energy decreases monotonically from 1.7 meV for a 10 Å well to 0.45 for a 500 Å well. The variation of the exciton and biexciton luminescence intensity on excitation

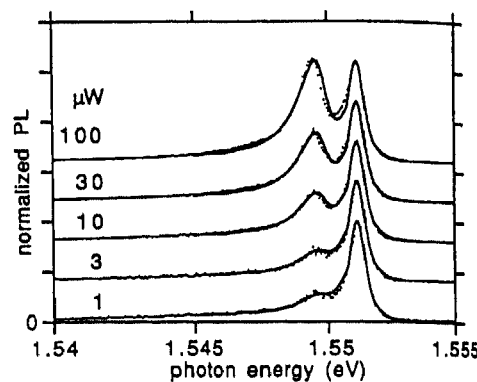


Fig. 123. PL spectra versus excitation level showing the emergence of the biexciton emission [232].

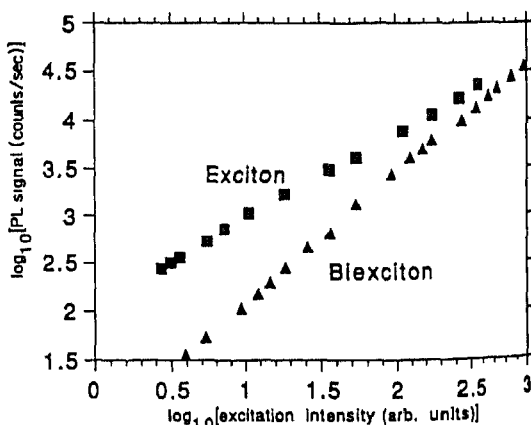
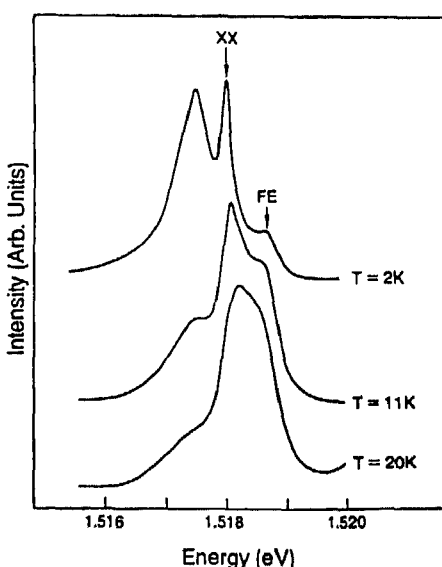


Fig. 124. Power dependence of the exciton and biexciton emission intensity [232].

Fig. 125. PL spectra of a 300 Å quantum well versus temperature for excitation with 1250 mW cm^{-2} [231].

power is shown in Fig. 124. The biexciton intensity increases as $I_{\text{biex}} \propto I_{\text{ex}}^{1.6}$. The reduction in power exponent from the intuitively expected value of 2 is a result of the short radiative lifetime of the biexciton. The biexciton emission also rapidly quenches with increasing temperature as shown in Fig. 125 (denoted by XX).

The biexciton has also been observed in Si [48,237–239]. The biexciton in Si has been observed to decay in two modes [48]. In the first, one of the constituent excitons of the biexcitons recombines radiatively leaving behind a free exciton and emitting a near-infrared photon. This emission is shown in Fig. 126. Here the emission is actually the TA phonon replica of the biexciton, and it is flanked by the free exciton and boron bound exciton lines. The second mode of decay involves the complete annihilation of the biexciton via a no-phonon process, yielding a green photon having an energy of roughly twice the Si band gap [48,240]. This green luminescence is shown in Fig. 127. This data yields a biexciton binding energy of 1.2 meV. Fig. 128 shows the dependence of the biexciton emission intensity versus the free-exciton emission intensity [238]. The slope of 2 clearly shows the biexciton origin of the emission.

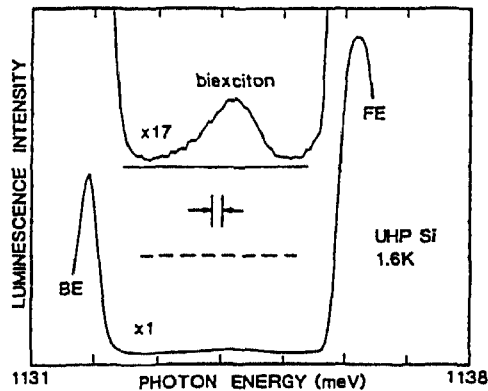


Fig. 126. TA-phonon replica of the biexciton at 1.6 K. Bottom edge of the box represents zero signal [48].

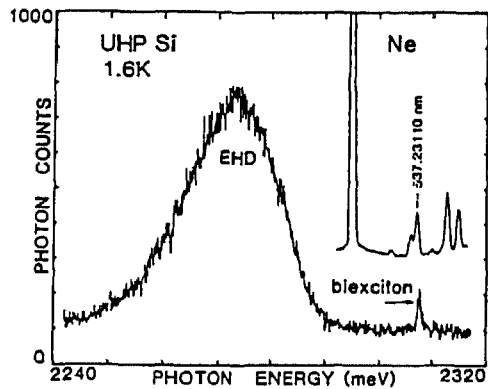


Fig. 127. Green PL of the biexciton and EHL at 1.6 K [48].

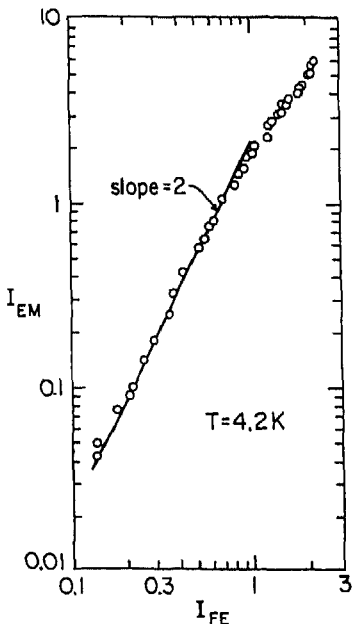


Fig. 128. Excitonic molecule peak emission intensity versus exciton peak emission intensity versus excitation level [238].

It has already been noted (section 2.2.3.1.2) that even more than two excitons may be bound together to form a stable quasi-particle. In this case these multi-excitons were bound to a defect. In 1972 Wang and Kittel [241] pointed out that the conduction band degeneracy in indirect-gap semi-

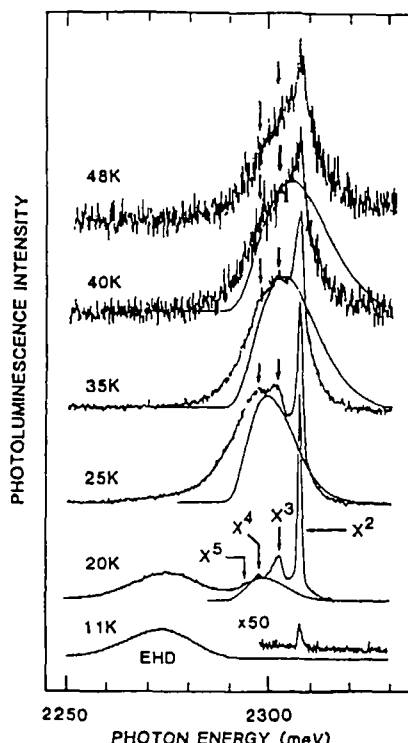


Fig. 129. Temperature dependence of the green PL in high-purity Si. The EHL emission vanishes near 25 K. The biexciton line (X^2) is apparent at all temperatures, while the X^3 - X^5 polyexcitons appear at only elevated temperatures (> 20 K)

conductors allows the possible formation of more complex excitonic systems. In Si twelve electrons (six equivalent X valleys) could be placed into the same ground state without violating the Pauli exclusion principle. Morgan [242] later showed that such polyexcitons with up to six electron-hole pairs (excitons) would be stable in Si. In 1987, 15 years after their prediction, Steele et al. [237] reported the discovery of polyexcitons in Si. They observed these polyexcitons in the green photoluminescence region of the spectrum, just as with the biexcitons. Fig. 129 shows the PL spectra of high-purity Si in the green portion of the spectrum versus temperature. At low temperatures (11 K) the spectrum is dominated by the electron-hole liquid emission, and evidence for a very weak biexciton (X^2) is present. As the temperature is increased to 20 K, the EHL emission becomes much weaker, and the X^2 line is dominant. The structure on the low-energy side of the biexciton shows additional peaks which they attribute to polyexcitons, X^3 , X^4 , and X^5 . The X^3 (X^4) emission line is due to a transition from a ground-state triexciton (tetra-exciton) to a ground-state free exciton (biexciton). They also observe that the polyexciton emission intensity dependence on the free-exciton density is even more pronounced than for biexcitons, as expected. The narrow emission lines are due to the unique recombination process of polyexcitons which give rise to green luminescence. For example, a biexciton must involve the recombination of electrons in opposite conduction band valleys, and therefore the emission is not directly broadened by the thermal kinetic energy of the biexcitons.

2.2.5 Electron-hole liquid

The electron-hole liquid (EHL) is the condensation of non-equilibrium charge carriers into the metallic degenerate Fermi liquid of electrons and holes [243,244]. The EHL is a degenerate, two-component Fermi liquid. The EHL has the lowest mass density of all known liquids, causing it to be

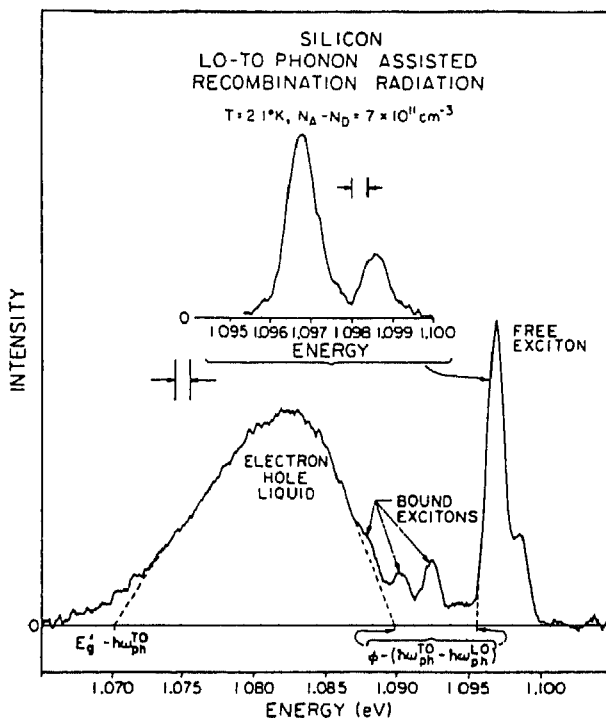


Fig. 130. PL spectrum at 2.1 K from high-purity Si. Here, the peaks correspond to the LO- and TO-phonon replicas. (After Hammond et al. [243].)

extremely sensitive to external influences. The formation and binding energy of the EHL requires inclusion of many-body effects incorporating the kinetic, exchange, and correlation energies of electrons and holes [244]. EHL has not been conclusively observed in GaAs, but it has been definitively observed in Si and Ge. The favorable factors for EHL formation in Si over GaAs are: (1) the multi-valley nature of the conduction band which lowers the average kinetic energy; (2) the relatively heavy electron mass which also reduces the average kinetic energy; and (3) the indirect bandgap which makes radiative recombination forbidden, yielding long lifetimes which allow the carriers to thermalize with the lattice prior to recombination. The EHL is characterized by a constant density, and a binding energy characteristic of the semiconductor. This also means that EHL may only form at temperatures less than some critical temperature corresponding to the binding energy. In Si the binding energy is 28 K [244]. Fig. 130 shows the LO- and TO-phonon assisted recombination in high-purity Si at 2.1 K. The spectrum may be clearly resolved showing both the LO and TO components of the free exciton as well as the LO- and TO-phonon assisted EHL recombination, centered at 1.082 eV. The lineshape of the EHL luminescence may be calculated for each phonon-assisted recombination line from

$$I_{\text{EHL}}(\hbar\omega) = A \int dE_e dE_h \rho_e(E_e) \rho_h(E_h) (e^{(E_e - E_F^h)/kT} + 1)^{-1} (e^{(E_h - E_F^h)/kT} + 1)^{-1} \delta(E_g + E_e + E_h - \hbar\omega_{ph} - \hbar\omega) \quad (18)$$

where ρ_e and ρ_h are the electron and hole density-of-states functions [243]. Lineshape fits to data similar to that shown in Fig. 130 yields a condensate density of 3.3×10^{18} cm⁻³ at 2.2 K. Further analysis of this type leads to a phase diagram for the quasi-particles which may exist in Si. Fig. 131 shows the phase diagram of non-equilibrium charge carriers in Si. Despite the fact that EHL has not been observed in the direct-gap semiconductor GaAs, it has been observed in indirect-gap Al_xGa_{1-x}As

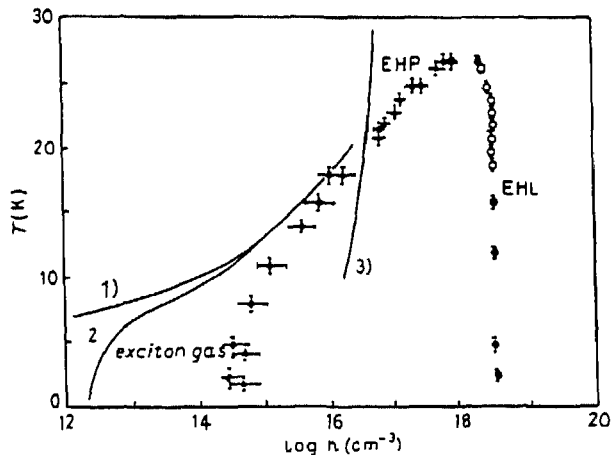


Fig. 131. Temperature–density phase diagram of the exciton gas, electron–hole plasma, and electron–hole liquid in Si. (After Keldysh [244].)

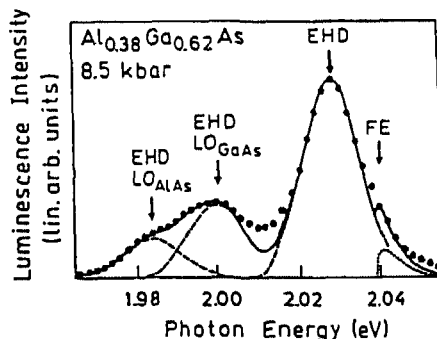


Fig. 132. PL spectrum and lineshape analysis of AlGaAs epilayer at 8.5 kbar. —, overall lineshape; ---, no-phonon and phonon replicas of the EHL; ···, indirect-exciton emission line. (After Kalt et al. [245].)

[245]. Fig. 132 shows the PL spectrum of a 38% AlGaAs sample at 8.5 kbar pressure. The electron–hole droplet (EHD) phonon-assisted emission is clearly evident.

2.2.6. Electron–hole plasma

The Mott transition or metal–insulator transition is a phenomenon involving a phase transformation in which the dominant species of carrier changes from an electrically charged species to an electrically-neutral species [246]. In semiconductors this transition may occur for the exciton–electron–hole plasma system. Dissociation of free excitons into free electrons and free holes is a metal–insulator transition. This dissociation may occur thermally or through increasing the density of free excitons. If the free-exciton density is such that the inter-exciton separation is less than the Bohr radius of the free exciton, then the Coulomb correlation between the electron and hole forming the exciton is lost, and the system is in a plasma state, an electron–hole plasma (EHP). The exciton is effectively screened. This is illustrated schematically in Fig. 133. In GaAs it has been thoroughly demonstrated that an EHP is readily realized when the generated carrier density becomes greater than the Mott density [247–251]. Fig. 134 shows the PL spectra of a bulk GaAs sample versus excitation power [247]. The “P” band is excitonic related. The “HDP” band is due to the recombination of a high-density electron–hole plasma, and the “PLS” band results from radiative recombination of an electron–hole pair in the

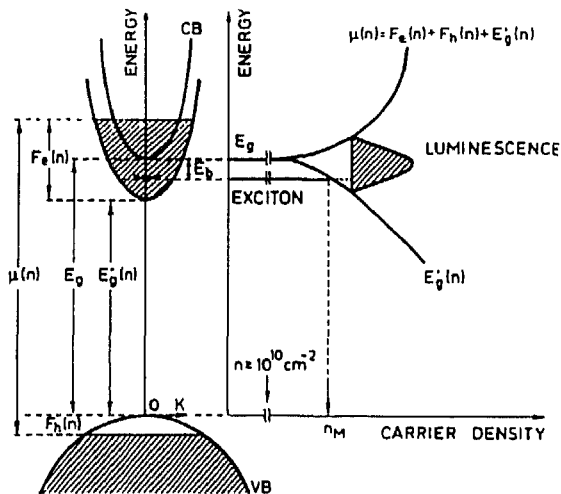


Fig. 133. Sketch of the carrier-density-induced changes in the band structure of a direct-gap semiconductor. Here, $F_{e,h}$ are the quasi-Fermi levels (After Cingolani and Ploog [2])

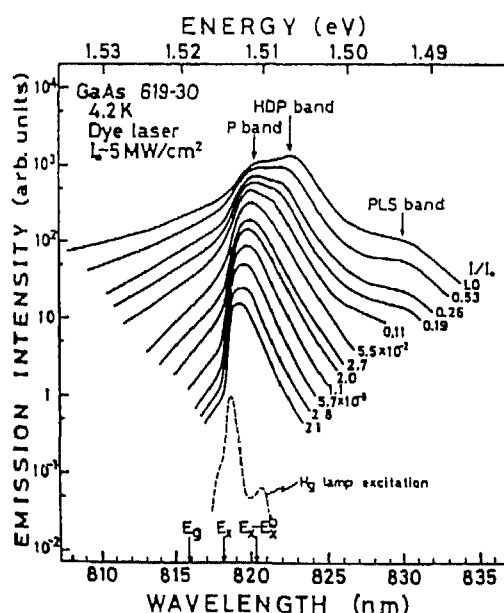


Fig. 134 Excitation dependence of the PL spectra from GaAs at 4.2 K on a semi-logarithmic scale (After Moriya and Kushida [247].)

HDP state with the simultaneous excitation of a plasmon. Göbel et al. [248] determined the Mott density of bulk GaAs to be $5 \times 10^{16} \text{ cm}^{-3}$. Nather and Quagliano [250] have determined the plasma density and temperature through lineshape fits, as shown in Fig. 135. Capizzi et al. [252] found that lineshape fits required k conservation to achieve good fits. Further, the plasma temperature is a strong function of the plasma density, as shown in Fig. 136 [251]. Here the dashed line is calculated from the Mott criteria. Fig. 137 shows the PL spectra of a high-purity Si sample under various conditions of lattice temperature and laser excitation power [253,254]. At 30 K and at high excitation powers, the lineshape, a broad almost symmetrical line, is indicative of an electron-hole plasma. Fig. 138 shows the half-maximum of the PL on the low-energy side for each peak at various temperatures versus excitation power. There is a clear shift in emission energy at high powers, characteristic of an

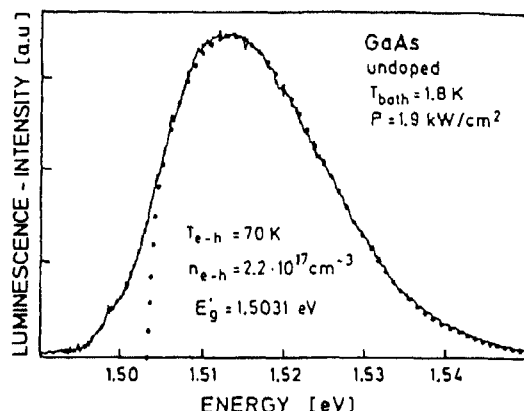


Fig. 135 PL spectrum of the 3D-confined dense EHP in GaAs. Dots represent a calculated lineshape including momentum conservation. (Reprinted from Nather and Quagliano., *Solid State Commun.*, 50 (1984) 75, with permission from Elsevier Science Ltd., Pergamon Imprint, The Boulevard, Langford Lane, Kidlington OX5 1GB, UK.)

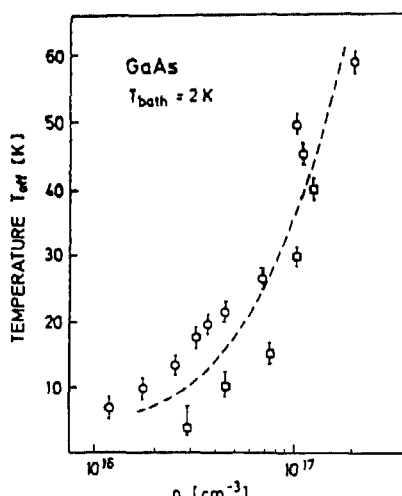


Fig. 136 Temperature versus density of the EHP in GaAs. The carrier concentration was determined from the experimentally determined Fermi energy. The line is calculated from the Mott criterion. (After Hildebrand et al [251].)

EHP. Here, I_D represents the Mott density. The phase diagram for the EHP in Si is shown in Fig. 131. The EHP has also been observed in quantum wells. Fig. 139 shows the PL of a MOCVD-grown quantum well under low and high excitation [255]. The high-excitation spectra is due to recombination of an EHP.

2.2.6.1. Bandgap renormalization—*intrinsic semiconductors*

Bandgap renormalization is a phenomenon which results from many-body effects of highly degenerate systems. This can occur in a dense electron-hole plasma in an intrinsic semiconductor. It has been demonstrated that the plasma-density dependence of the bandgap renormalization is a universal law if densities and energies are expressed in units appropriate to the material. [256] This phenomenon is well understood in bulk semiconductors.

The bandgap renormalization in direct-gap semiconductors with low polar coupling is a result of the exchange and correlation effects. It is difficult to obtain accurate values for the chemical potential

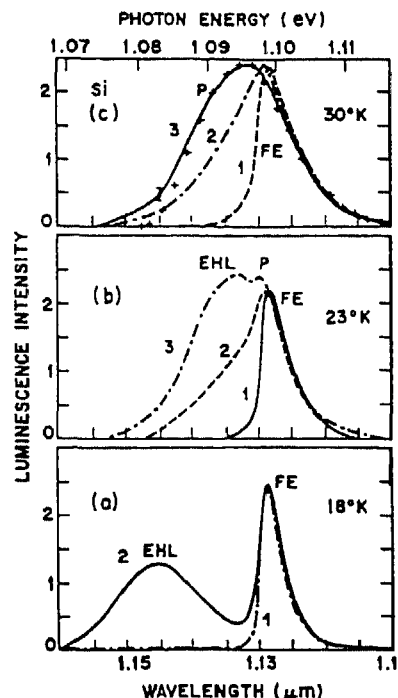


Fig. 137. PL spectra of Si at various temperatures and excitation powers. (a) 18 K spectra at 0.05 and 1 mW for curves 1 and 2, respectively; (b) 23 K spectra at 0.05, 0.4, and 2 mW, and (c) 30 K spectra at 0.05, 1, and 4 mW for curves 1, 2, and 3, respectively. +, calculated EHP lineshape with $n = 3 \times 10^{18} \text{ cm}^{-3}$ and $T = 30 \text{ K}$. (After Shah et al [253].)

and quasi-fermi energy through PL measurements. Nevertheless, the PL lineshape is influenced by these important quantities. The chemical potential at any temperature is given by [251]

$$\mu(n, T) = E_g' + E_F^e + E_F^h \quad (19)$$

where the quasi-Fermi energies are determined from the relations

$$n = p = \left(\frac{m_d^{e,h} k T}{2\pi\hbar^2} \right)^{3/2} f_{1/2}^{e,h}(E_F^{e,h}/kT) \quad (20)$$

where

$$f_{1/2}^{e,h}\left(\frac{E_F^{e,h}}{kT}\right) = \frac{2}{\sqrt{\pi}} \int_0^\infty \frac{\sqrt{x} dx}{\exp[x - E_F^{e,h}/(kT)] + 1} \quad (21)$$

Using these expressions, the reduced bandgap energy is given by

$$E_g(r_s) = \left(\frac{B_g}{r_s^2} \right) - \left(\frac{C_g}{r_s} \right) - D_g \quad (22)$$

where $r_s = [3/4\pi r_0^3 n]^{1/3}$ and r_0 is the exciton Bohr radius. For bulk GaAs $B_g = 0.352$, $C_g = 3.187$, and $D_g = 0.261$. Fig. 140 shows the PL spectra of bulk GaAs for various excitation intensities. The EHP emission is clearly evident with increasing excitation density at lower energies than the bulk excitonic feature. The effective carrier temperature may be easily determined from the slope of the high-energy tail of the emission. Lineshape analysis reveals that the recombination of the EHP occurs without k

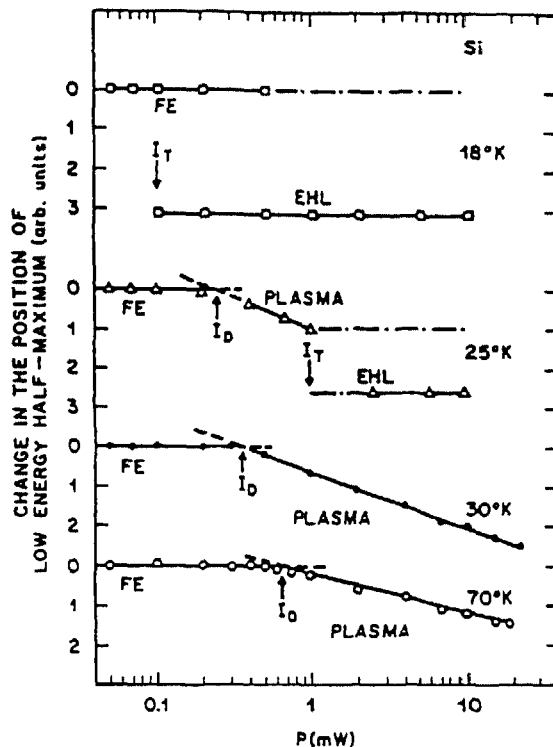


Fig. 138. Temperature and power dependence of the spectral position of the low-energy half-maximum of photoexcited Si. I_D and I_T represent the thresholds for the onset of EHP and EHL emissions. (After Shah et al. [253].)

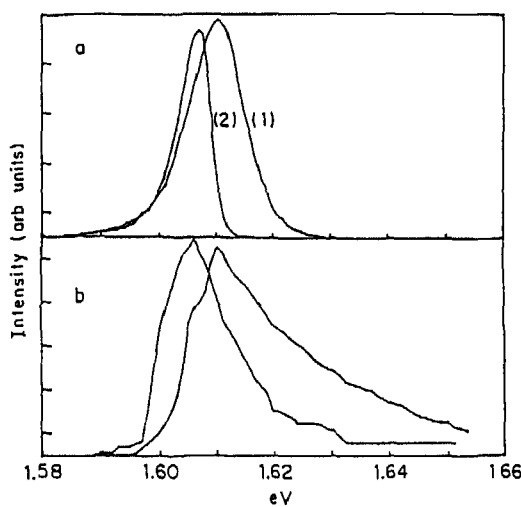


Fig. 139. cw PL spectra of an 80 Å GaAs quantum well grown by MOCVD. Spectra (1) and (2) correspond to the backscattering and perpendicular geometries, respectively. The two lower traces correspond to low and high excitation with 10^{15} and 10^{16} photons cm^{-2} per pulse. (After Fekete et al. [255].)

conservation in the plasma [251,257]. Further, as expected from Eq. (22), the density dependence of the reduced bandgap varies as $n^{1/3}$ [258].

Bohnert et al. [259] investigated the bandgap renormalization of $\text{Al}_x\text{Ga}_{1-x}\text{As}$ at both the G and X points of the Brillouin zone. Fig. 141 shows the spectra of an $\text{Al}_x\text{Ga}_{1-x}\text{As}$ layer with Al compositions

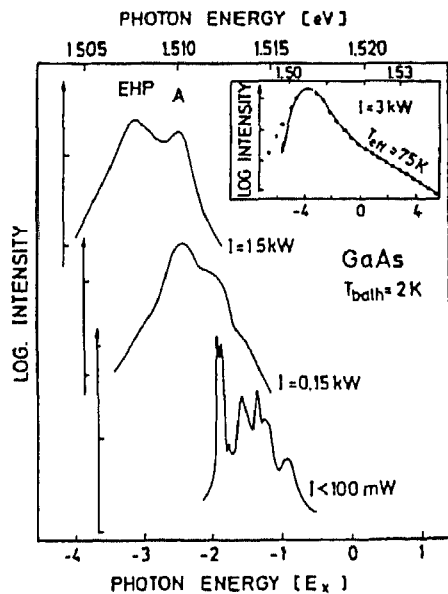


Fig. 140 2 K PL spectra of GaAs at three different excitation pump intensities [251].

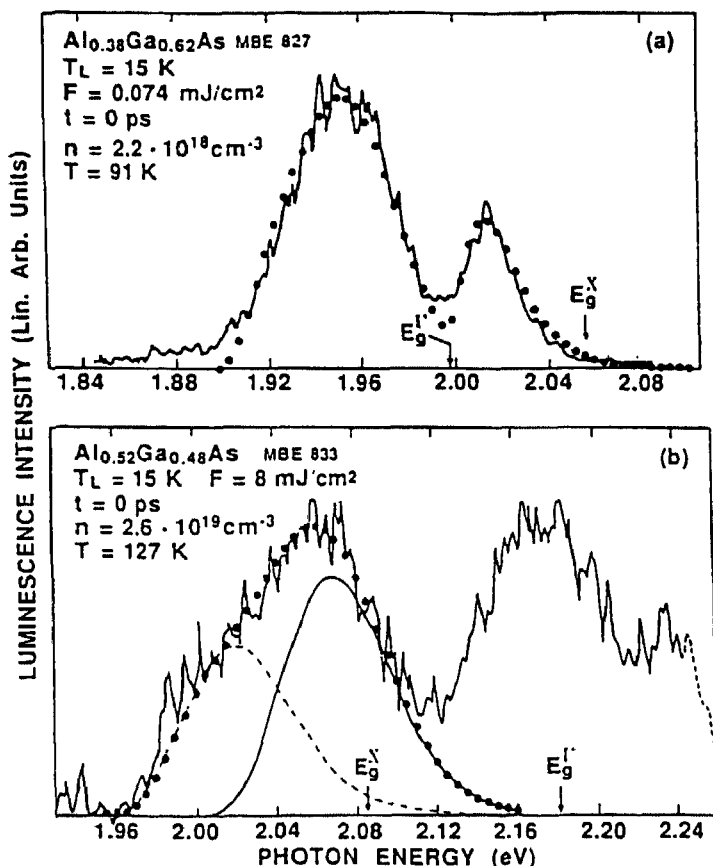


Fig. 141. Line-shape fits and time-resolved PL spectra for two AlGaAs epilayers (a) below and (b) above the direct-indirect crossover composition. --- and —, contributions from phonon-assisted and quasi-direct transitions, respectively. (After Bohnert et al [259].)

near the direct–indirect crossover. In the direct-gap material ($x=0.38$) the low-energy emission band is due to the bimolecular recombination from the direct-gap Γ conduction band EHP, whereas the high-energy band arises from the bimolecular recombination from the indirect X conduction band. In contrast for alloy compositions yielding an indirect bandgap ($x=0.52$), the bands are reversed in energy. They performed lineshape fits of the spectra assuming relaxed k conservation, and obtained carrier densities and plasma temperatures. The arrows in the figures mark both the direct and indirect conduction band edges at both compositions of the alloy. The red-shift of the emission peaks is indicative of bandgap renormalization.

Tränkle et al. [258,260] examined the dimensionality dependence of the bandgap renormalization in GaAs quantum wells of various well widths. They find that the absolute bandgap shift is much larger in 2D than in 3D. However, if energies are scaled to the Rydberg of the system, then they find that the 2D bandgap shift is effectively smaller than in 3D due to the reduced efficiency of screening in a 2D EHP. Further, if scaled properly, it is independent of the material properties. Fig. 142 shows the PL spectra and lineshape fits of the EHP in a 21 Å GaAs/AlGaAs quantum well. Lineshape fits were obtained using the expression

$$I(\hbar\omega) \propto \sum_{i,j}^{\infty} \int_{E_i^0}^{\infty} \int_{E_j^0}^{\infty} m_i m_j f_e(E_i) f_h(E_j) \delta(E_i - E_j - \hbar\omega) dE_i dE_j, \quad (23)$$

where the sum is over electron and hole subbands, and $f_{e,h}$ are the Fermi distributions of electrons and holes [252]. Adding an additional broadening, as suggested by Lansberg [261] yields the fits shown in the figure with the densities and plasma temperatures shown. Fig. 143 shows the bandgap shift versus interparticle separation (related to the inverse density) for both quantum well and bulk GaAs layers. Here the energy shift has been scaled according the Rydberg of the system ($E_{02D}=10.0$ meV and $E_{03D}=3.9$ meV). Again, the density dependence of the bandgap renormalization has been found to vary as $n^{1/3}$ [262].

2.2.6.2. Bandgap shrinkage—extrinsic semiconductors

Heavily-doped semiconductors exhibit a temperature-dependent bandgap shrinkage which results from bandgap narrowing due to merging of the impurity band with either the conduction or valence band and the variation in the bandgap with temperature, which has been discussed in section 2.2.1 [263–265]. Fig. 144 shows the PL emission spectra of C-doped bulk GaAs epilayers versus hole concentration, with concentrations up to $9 \times 10^{19} \text{ cm}^{-3}$. From this data the effective bandgap shrinkage due to C doping is obtained, shown in Fig. 145. The hole concentration dependence of the bandgap shrinkage is well represented by

$$\Delta E_g = -Ap^{1/3} \quad (24)$$

2.2.7. Two-dimensional electron gas and two-dimensional hole gas

One of the most successful applications of the technology of bandgap engineering has been the development of the high-electron mobility transistor (HEMT) or modulation-doped field-effect transistor (MODFET). These devices consist of intentionally doped and undoped layers of AlGaAs and GaAs. The free-electrons resulting from the intentional doping of an AlGaAs layer transfer to the lower-energy GaAs layer adjacent to it. The non-uniform doping and conduction-band offset yield a narrow triangularly-shaped quantum well for these electrons at the interface between the AlGaAs and

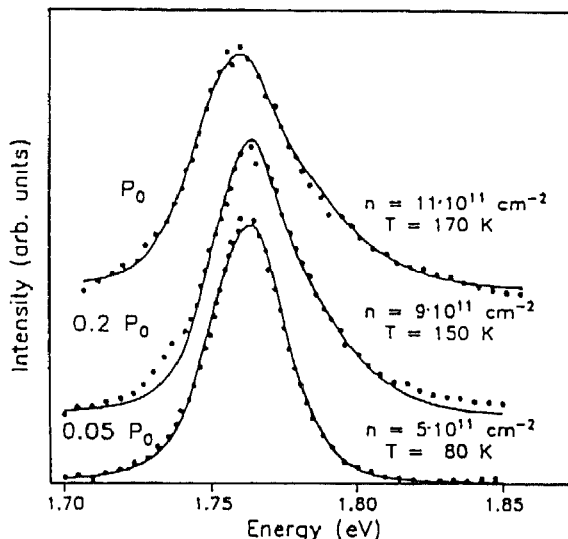


Fig. 142. PL spectra versus excitation intensity ($P_0 = 500 \text{ kW cm}^{-2}$) for a 21 \AA quantum well (After Tränkle et al. [260].)

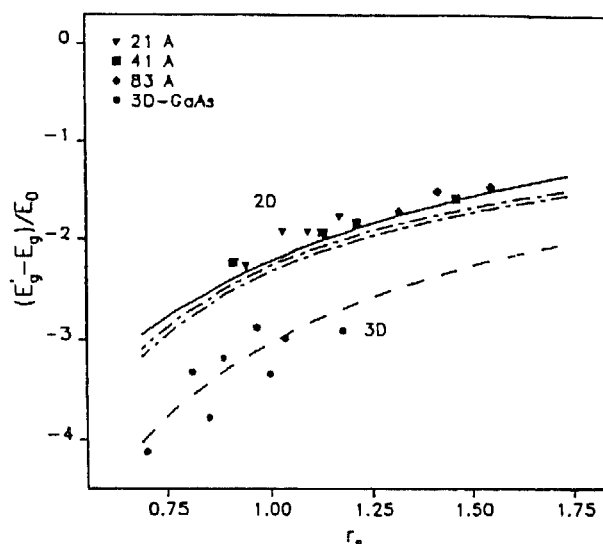


Fig. 143. Bandgap shift versus interparticle distance, r_s , for both 2D and 3D GaAs structures. The bandgap is scaled by the 2D and 3D Rydberg energies. — and ---, correspond to theoretical calculations. (After Tränkle et al. [260].)

GaAs layers. The advantage of such structures is that the impurities (donors) giving rise to the free carriers (electrons) are spatially separated from them, thereby reducing the Coulomb scattering and increasing the free-carrier mobility. The same principle also holds for holes. The result of fabricating such a structure is a one-component plasma. Fig. 146 shows the PL spectra of both halves of a modulation-doped AlGaAs/GaAs heterostructure with a two-dimensional electron gas (2DEG) in which one-half has the top AlGaAs layer chemically-etched removed [35]. The unetched portion shows a prominent peak between the free-exciton peak, X, and the acceptor-bound exciton peak. This peak is absent in the PL spectrum of the etched half of the sample. Thus, it is associated with the heterointerface and has been identified as due to the recombination of the 2DEG with photoexcited holes. The 2DEG peak is 0.9 meV lower in energy than the bulk free-exciton peak, and two or three times wider

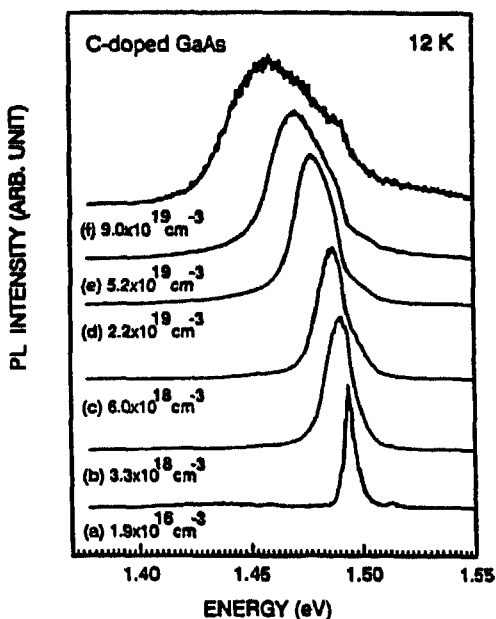


Fig. 144. 12 K PL spectra of C-doped GaAs epilayers for various hole concentrations. (After Kim et al. [263].)

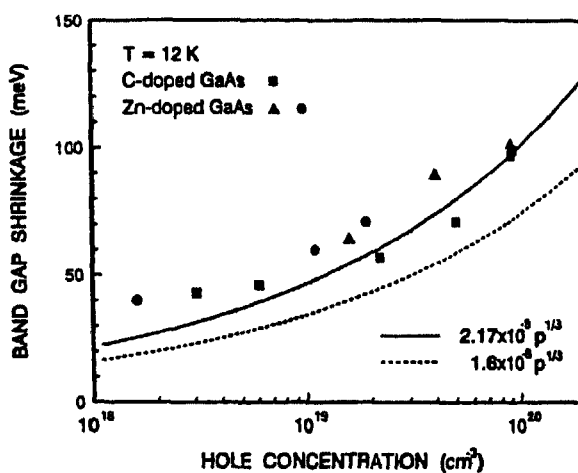


Fig. 145 Energy shift of the bandgap versus hole concentration in C-doped GaAs. (After Kim et al. [263].)

than the bound exciton emission. Detailed analysis of the 2DEG lineshape also provides some insight into the nature of this emission process. Peric et al. [266] have examined the PL lineshape of several 2DEG samples. The low-temperature PL spectra exhibit a broad PL line extending from the first conduction-subband edge up to the Fermi energy. This broad line has been attributed to radiative recombination between the high-density electrons and localized holes. Also the relaxation of momentum conservation has allowed the observation of an enhanced PL intensity near the Fermi energy. Also, samples with near-degeneracy between the Fermi energy and the conduction subbands exhibit a sharp Fermi-edge singularity [2,267]. The Fermi-edge singularity manifests itself as an enhancement of the luminescence intensity at the Fermi edge. It is a consequence of many-body interactions between electrons and holes. The enhancement of the emission intensity at the Fermi edge is due to a transfer of excitonic oscillator strength from unoccupied subbands to occupied states at the Fermi edge. Fig.

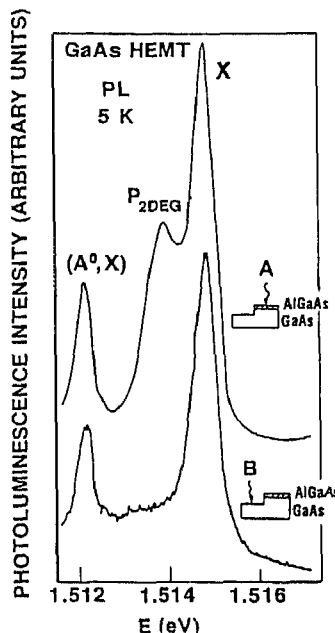


Fig. 146. Low-temperature PL spectra of modulation-doped GaAs/AlGaAs heterostructures, for excitation on both the etched and unetched part of the structure. The 2DEG is only evident for excitation of the heterointerface. (After Koteles and Chi [35].)

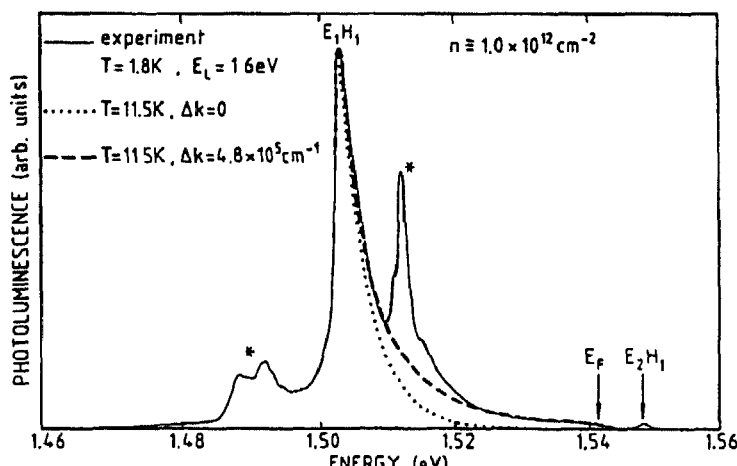


Fig. 147. PL spectrum of the E₁H₁ emission in a n-type GaAs quantum well. The dotted line corresponds to a calculation considering only vertical transitions, whereas the dashed line includes the relaxation of momentum conservation. (After Peric et al. [266].)

Fig. 147 shows the PL spectrum of a modulation-doped sample with $1.3 \times 10^{12} \text{ cm}^{-2}$ electrons. The E₁H₁ line is the 2DEG recombination. The emission has a high-energy tail extending up to the Fermi energy. At this energy, which happens to coincide closely with the second conduction subband, a bump attributed to the Fermi-edge singularity appears [266]. From their lineshape analysis of the 2DEG peak they conclude that there is evidence for partial breakdown of the momentum selection rule.

Emission from a two-dimensional hole gas (2DHG) has also been observed [268,269]. Fig. 148 shows the PL spectra of a Be δ-doped double heterostructure sample at two excitation powers. The dominant sharp line is the recombination associated with bound excitons. The broad emission at lower energies, which is more prominent at higher excitation powers, is associated with the 2DHG. Fig. 149

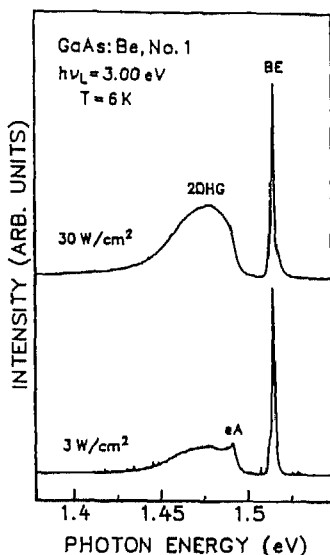


Fig. 148. PL spectra of a Be d-doped GaAs sample at two different excitation intensities. The 2DHG becomes prominent at high excitation intensities (After Richards et al. [268])

shows several examples of the Fermi-edge singularity for a 2DHG. Sample Nos. 2, 3, and 4 have Be concentrations of 3×10^{12} , 8×10^{12} , and $3 \times 10^{13} \text{ cm}^{-2}$, respectively. The vertical line marks the Fermi-edge singularity. With increasing density the 2DHG peak broadens and shifts to lower energies, until, in the most heavily doped sample it splits into two peaks. The sharp edge on the high-energy side of the 1.496 eV emission in sample No. 4 disappears for temperatures $> 20 \text{ K}$, thus confirming its identification as the Fermi-edge singularity.

2.2.8. Hot carriers and intervalley scattering

Optical excitation allows the injection of both electrons and holes at energies well above the bottom of the conduction band and/or valence band. These electrons and holes may not be in thermal equilibrium with the lattice, and will eventually ‘cool’, through a variety of mechanisms, to the lattice temperature. If the lifetime of the hot carriers is too short, they may recombine prior to reaching the lattice temperature. The mechanisms which may facilitate cooling are phonon emission, intervalley scattering, and carrier–carrier scattering [270]. There are many studies which have attempted to separate the effects of these mechanisms, with varying success. For example, in GaAs intervalley scattering is possible for excess energies greater than 300 meV, and is possible with the assistance of large wavevector optical or acoustic phonons. Carrier–carrier scattering becomes important at high excitation densities.

Mirlin et al. [271] and Fasol et al. [272,273] used the PL of hot electrons recombining with neutral acceptors to examine the cascade LO-phonon emission induced cooling of hot electrons as well as the intervalley scattering of electrons. Mirlin et al. examined the depolarization in an external magnetic field of the hot-electron emission which is isotropized through energy relaxation. In the Faraday configuration, the field-dependent depolarization varies as

$$\frac{\rho(H)}{\rho(O)} = \frac{1}{1+4\omega_c^2\tau^2} \quad (25)$$

where ω_c is the cyclotron frequency and τ is the lifetime of electrons in the initial state determined by

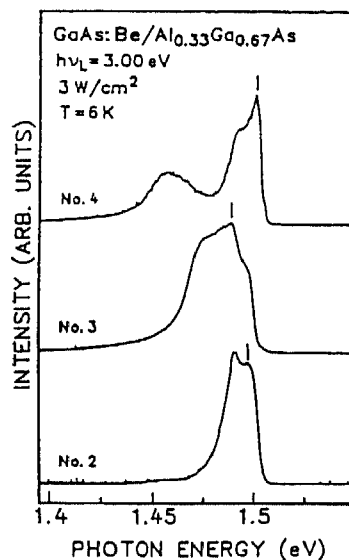


Fig. 149. PL spectra at 6 K of three Be-doped GaAs double heterostructures with dopant concentrations ranging from 7.4×10^{11} to $3.1 \times 10^{13} \text{ cm}^{-2}$ from bottom to top. (After Richards et al. [268].)

all possible inelastic scattering processes, including phonon emission and intervalley scattering. Through excitation at excess electron energies which do and do not allow intervalley scattering they are able to separate the scattering rates of these processes, yielding a Γ -L intervalley scattering time of 0.25 ps and a LO-phonon emission time of 0.1 ps. Fig. 150 shows a schematic diagram of the cascade phonon emission process together with the PL spectrum of a Ge-doped GaAs sample, obtained by Fasol et al. The weak (10^5 weaker than the bandgap-related emissions) oscillatory peaks are due to cascade LO-phonon emission. They also examined this hot-electron cooling in samples doped with

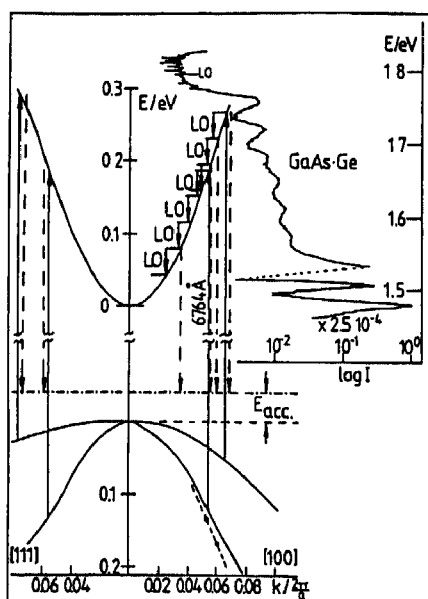


Fig. 150. Schematic of thermalization of hot electrons by LO-phonon emission. Inset shows spectrum of PL due to (e, A^0) recombination. (After Fasol et al. [272].)

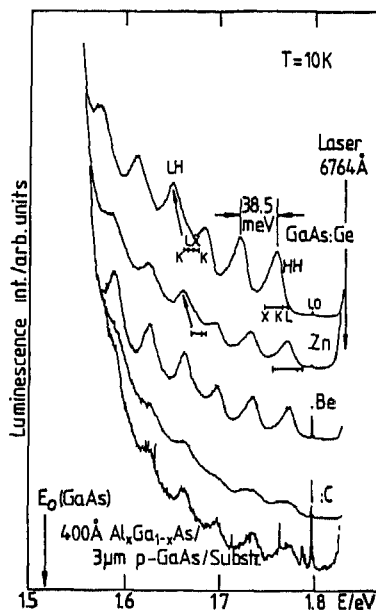


Fig. 151. Hot (e, A^0) PL spectra for GaAs doped with Ge, Zn, Be, and C acceptors. (After Fasol et al. [272].)

various acceptors, including C, Be, Zn, and Ge. Fig. 151 shows their results, where they find that the separation between the peaks is 6% larger than the LO-phonon energy, thus indicating emission of renormalized phonons. Lastly, they find that the luminescence peaks shift according to the acceptor binding energy, thereby proving that the recombination is between hot electrons and neutral acceptors.

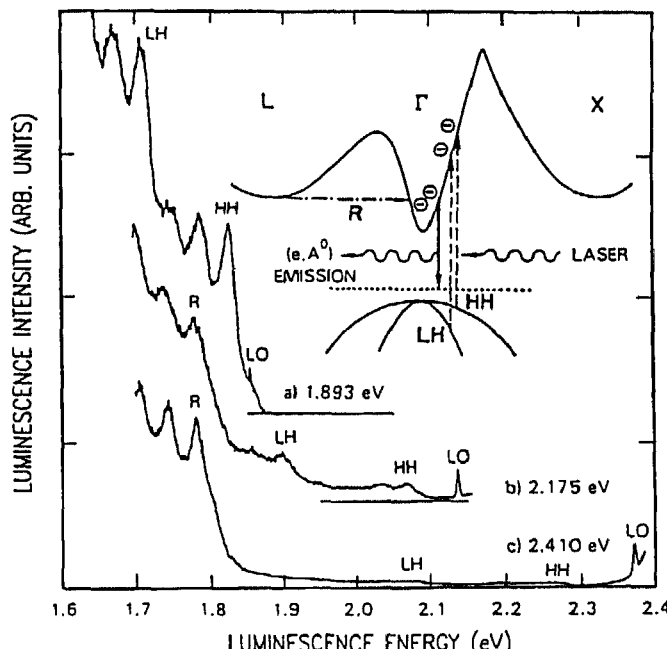


Fig. 152. Hot (e, A^0) PL spectra of GaAs·Mg ($1.2 \times 10^{17} \text{ cm}^{-3}$) at 25 K. Laser excitation was at (a) 1.893 eV, (b) 2.175 eV, and (c) 2.410 eV. (After Ulbrich et al. [275].)

Recently, Kash and coworkers [274–277] have also used the cw luminescence of hot electrons at neutral acceptors to quantify the same aspects of these hot carriers. The known polar optical phonon emission time by hot electrons, $\tau_{po} \approx 180$ fs (reported values for this emission time range from 100 to 180 fs) [273], is used as a “built-in clock” for determining scattering times. In Fig. 152 the hot (e, A^0) luminescence is shown for three different excitation energies. All measurements were done with low excitation densities in order to minimize the effects of carrier–carrier interaction. The spectra show three distinct oscillations with periods of ~ 37 meV, the zone-center LO-phonon energy. Again, the oscillatory peaks represent cascade LO-phonon emission. The peak marked ‘‘R’’ (for re-entrant), which only appears for excitation at energies greater than the threshold to create electrons that can scatter to the X and L valleys, represents intervalley scattering of electrons excited in the L valley which scatter to the Γ valley. By fitting the integrated area of the first heavy-hole peak versus excitation energy, they derive intervalley scattering times for scattering from $\Gamma \rightarrow X$ and $\Gamma \rightarrow L$, as $\tau_{\Gamma X}^0 / \tau_{po} = 179$ and $\tau_{\Gamma L}^0 / \tau_{po} = 7.14$, respectively. The energy dependence of the intervalley scattering times are given by

$$\tau_{\Gamma L} = \tau_{\Gamma L}^0 \left[\frac{(E_e - E_L - E_{ze})}{E_{ze}} \right]^{-1/2} \quad (26)$$

and similarly for $\tau_{\Gamma X}$. Here E_{ze} is the energy of the zone-edge phonons primarily responsible for the intervalley scattering. This then corresponds to $\tau_{\Gamma L} = 3\tau_{po}$ for electrons 0.48 eV above the conduction band minimum.

Shah et al. [278] have found that LO-phonon emission is the dominant energy loss mechanism in GaAs quantum well structures. They find that the energy loss rate for electrons is 25 times smaller than for holes, and attribute this difference to a large non-equilibrium optical phonon population. They determined the carrier temperature from the Fermi–Dirac distribution function fits the high-energy side of the PL emission spectrum and also measure the total power input per carrier through I – V measurements. Yang et al. [270] have also examined the PL of hot electrons in GaAs quantum wells. Fig. 153 shows the high-energy side of the PL spectrum of a modulation-doped 137 Å quantum well with an areal electron density of $2.4 \times 10^{11} \text{ cm}^{-2}$. The spectrum decreases exponentially for more than three decades even at energies one LO-phonon energy above the bandgap energy. This implies several things about the electron energy distribution. First, it can be characterized by a single electronic temperature. This is as expected for energies above the LO-phonon energy of 36.6 meV. Moreover, this might be expected to lead to different electronic temperatures for electrons above and below this energy. At lower energies electron–electron scattering attempts to maintain an equilibrium distribution

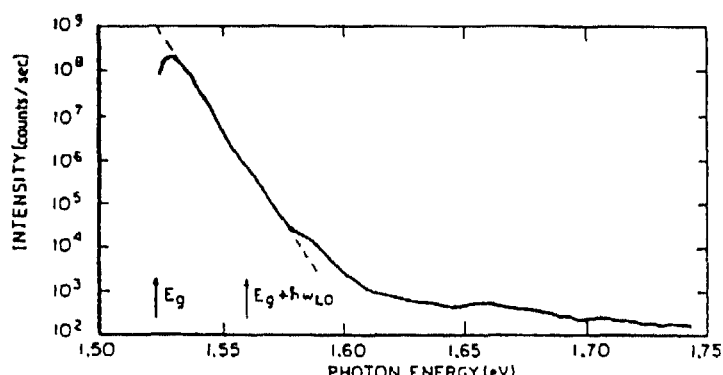


Fig. 153. PL spectrum of a GaAs quantum well at a lattice temperature of 5 K. Dashed line shows exponential slope over three decades from which an electronic temperature of 58 K is derived (After Yang et al. [270].)

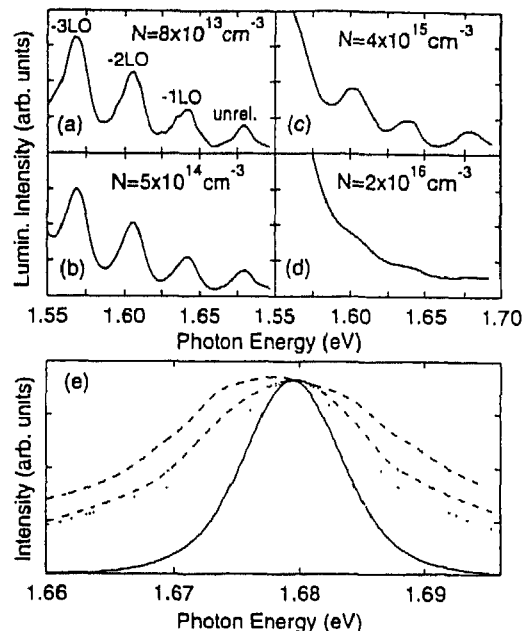


Fig. 154 (a)–(d) Hot electron PL spectra of GaAs versus excitation density at a lattice temperature of 10 K (e) Spectrum of the first PL peak for carrier densities ranging from 8×10^{13} to $4 \times 10^{15} \text{ cm}^{-3}$ (from narrowest to widest). —, spectrum of the laser. (After Leitenstorfer et al [279])

described by an electronic temperature. Thus, LO-phonon emission tends to cut-off the high energy part of the Boltzmann tail, while electron-electron scattering tends to repopulate it. The observation of a single electronic temperature means that electron-electron scattering is more rapid than LO-phonon emission. By examining the plasma temperature versus absorbed power density, they find that the dominate energy-loss mechanism is LO-phonon emission.

Kash et al. [274,275] as well as Leitenstorfer et al. [279] performed investigations versus excitation power (injected carrier density) for excitation below the threshold for intervalley scattering which showed that these oscillatory peaks disappear at high injected carrier densities (as shown in Fig. 154). This further demonstrates the importance of carrier-carrier scattering at high carrier densities. In part (e) the spectral profile of the first PL peak is shown as a function of density increasing from 8×10^{13} to $4 \times 10^{15} \text{ cm}^{-3}$ for the dotted, dotted-dashed, and dashed lines together with the spectral profile of the laser. The spectra become wider with increasing excitation density, and are all considerably broader than that of the laser spectrum. Time resolution from these cw measurements may be obtained through analysis of the spectral width of successive peaks in the cascade emission shown in Fig. 152. Each successive peak occurs at time intervals of $\sim 160 \text{ fs}$, the LO-phonon emission time. Fig. 155 shows the spectral width of this first peak versus excitation density together with the spectral widths of the first two lower energy peaks which occur at 160 and 320 fs later in time due to LO-phonon emission. The large width of the peaks, compared to that of the laser spectrum, is attributed to the coherent interaction of the laser pulse with the polarization of the sample, together with dephasing events giving rise to a non-equilibrium electron distribution. Fig. 156 shows the excitation energy dependence of the integrated intensity of the peaks corresponding to the (a) first heavy-hole peak and (b) the re-entrant peak (corresponding to carriers which have scattered back to the Γ valley). This data shows that at an excitation energy of 2.1 eV $\sim 50\%$ of the carriers have scattered from the Γ valley into either the X or L valleys. Kash et al.'s polarization measurements have also shown the heavy-hole valence band is strongly warped, which leads to a broadening of the PL distribution [277].

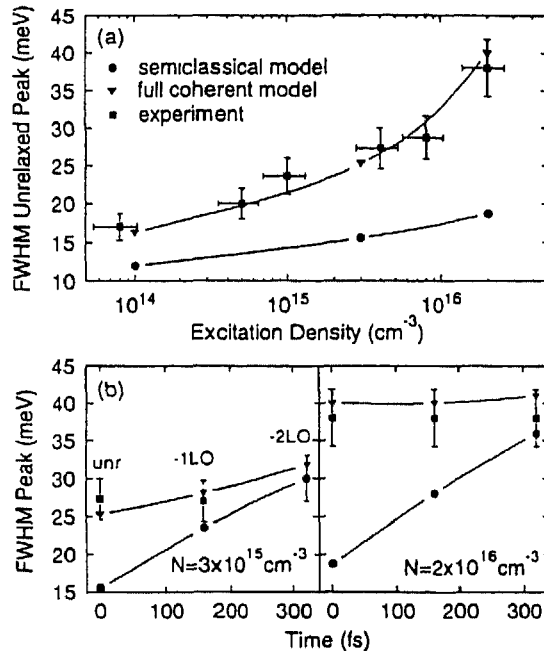


Fig. 155. (a) Spectral width (FWHM) of the first PL peak versus excitation density (■), together with models with coherent (▼) and incoherent (●) carrier dynamics. (b) Spectral width of the first, second, and third PL peaks for two different excitation densities versus time. Time scale was calculated with an LO-phonon emission time of 160 fs (After Leitenstorfer et al. [279].)

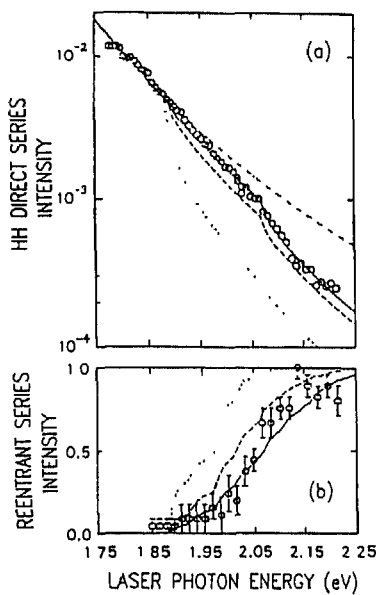


Fig. 156. Excitation energy dependence of the hot (e, A^0) PL in GaAs. (a) ○, integrated emission intensity of the highest-energy hh peak. (b) ○, intensity of the reentrant spectra. Curves are theoretical models. (After Ulbrich et al. [275].)

In total, these cw measurements have shown the immense amount of information that may be gleaned from detailed analysis very subtle features in the spectra, even concerning processes that occur on a femtosecond timescale.

2.3. Characterization of structures

Photoluminescence measurements are also useful for characterizing and quantifying some of the basic optical, electronic, and structural properties of semiconductors. Most obvious among these abilities is that of quantifying the emission efficiency. However, it is also useful for quantifying alloy composition, intervalley coupling, new emission mechanisms associated with structure, layer thicknesses, fluctuations in layer thicknesses, optical properties versus growth conditions, and incorporation of impurities in precise locations of layers.

2.3.1. Bulk layers

An example of the usefulness of PL spectroscopy for characterizing many aspects of bulk semiconductors has been given by Kuech et al. [280]. They studied the growth, electrical, and optical properties of the premier lattice-matched ternary alloy system, $\text{Al}_x\text{Ga}_{1-x}\text{As}$ grown by MOVPE. Their study examined the incorporation of defects, PL emission intensity versus growth parameters, and the PL emission versus alloy composition. A cross-section of the spectra for a variety of undoped $\text{Al}_x\text{Ga}_{1-x}\text{As}$ samples is shown in Fig. 157. Spectra of the direct bandgap samples, $x \leq 0.45$, exhibit two prominent features which correspond to transitions of excitons bound to neutral impurities, (B^0,X) , and the broad lower-energy peak consisting of the band-to-acceptor, (e,A^0) , and donor-to-acceptor transitions, DAP. The (B^0,X) line had a linewidth ranging from 3.6 to 6.8 meV for $x = 0.05$ to 0.30. They also observed PL emission from samples with an indirect bandgap with $x \leq 0.8$. No emission was observed for higher Al content samples. The emission intensity in the indirect-gap materials is lower than in the direct-gap alloys, as shown in the figure. The PL of these samples also exhibited phonon replicas. Both of these observations are consistent with the indirect nature of the bandgap. They also observed a significant variation in the integrated emission intensity versus growth temperature and alloy composition, as shown in Fig. 158. At low growth temperatures the PL intensity is very sensitive

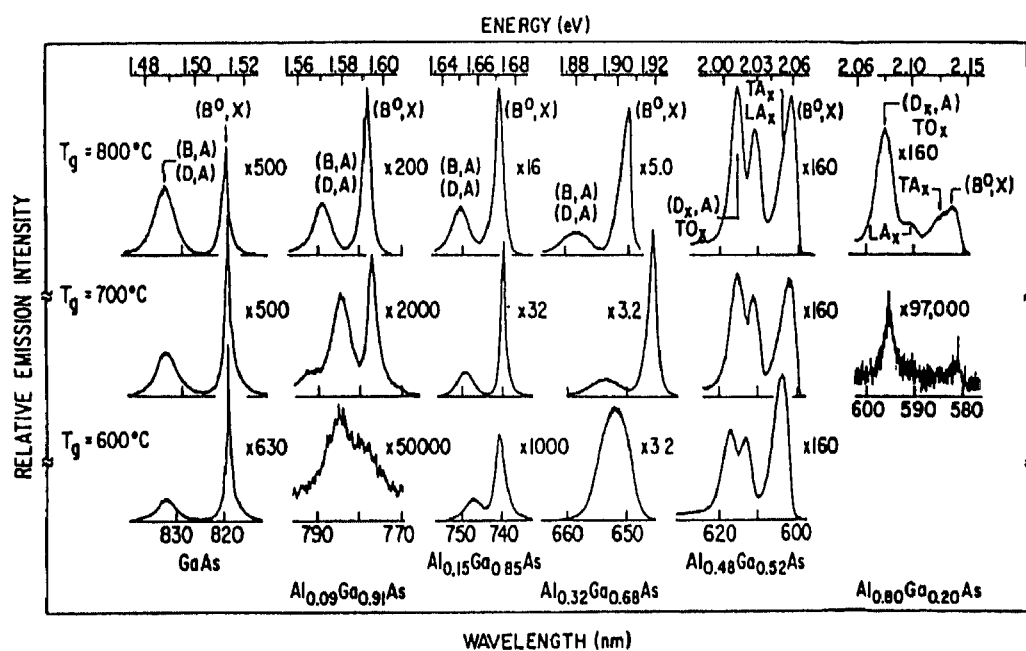


Fig. 157. PL spectra of nominally undoped $\text{Al}_x\text{Ga}_{1-x}\text{As}$ versus growth temperature and alloy composition. (After Kuech et al. [280].)

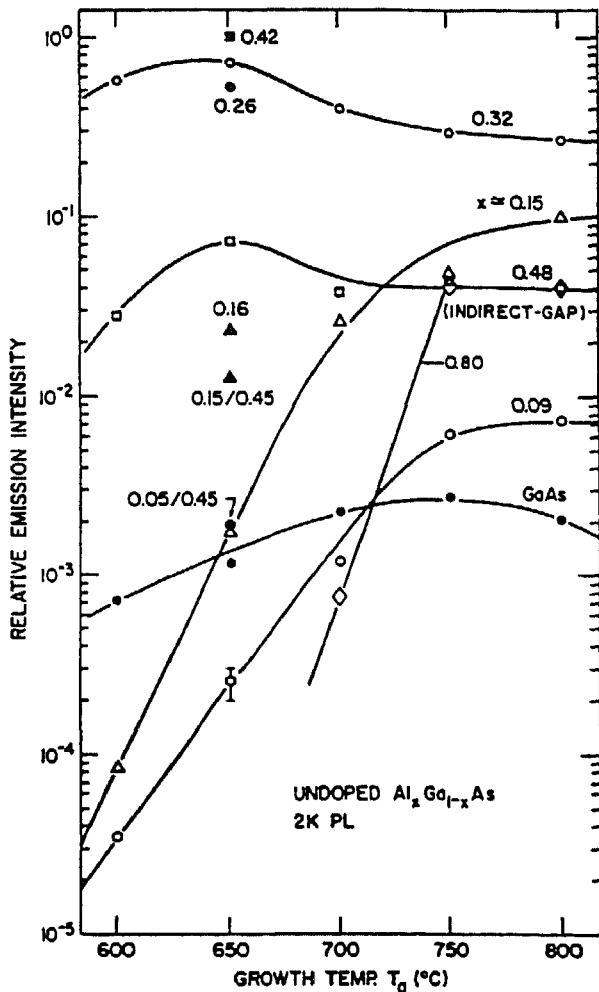


Fig. 158. Growth-temperature dependence of the relative emission intensity of the near band-edge PL for various $\text{Al}_x\text{Ga}_{1-x}\text{As}$ epilayers. (After Kuech et al. [280].)

to the Al content of the alloy. The integrated intensity of samples in the composition range $0.25 \leq x \leq 0.80$ is relatively independent of the growth temperature. The differences in PL intensity versus Al composition reflect differences in background impurity concentrations, carrier lifetime, and penetration depth of the pump laser. They conclude (from the results of the entire study) that the PL intensity is primarily influenced by the incorporation of oxygen.

2.3.2. Heterostructures

In 1984 Yuan et al. [281] observed a new luminescence feature in the low-temperature PL spectrum of GaAs/AlGaAs epilayers. Fig. 159 shows the 1.4 K PL spectra of a GaAs/AlGaAs heterostructure versus excitation power. Bound-exciton, band-to-acceptor, and DAP emissions are clearly evident. However, a new peak, labeled H, is also present energetically between the near-edge bound excitons and the free-to-bound transitions. This strong, broad, and asymmetric line's peak energy increases roughly logarithmically with the excitation power. Most importantly this emission is associated with the heterointerface. Fig. 160 shows the PL spectra of heterostructure samples in which

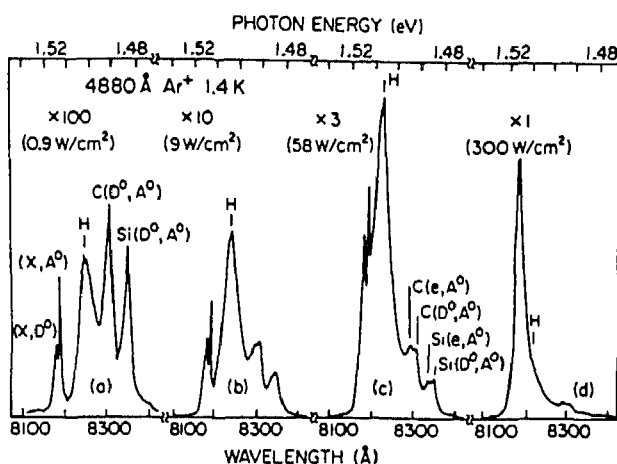


Fig. 159. Excitation intensity dependence of the PL emission spectra in LPE-prepared graded AlGaAs/GaAs heterostructures. (After Yuan et al. [281])

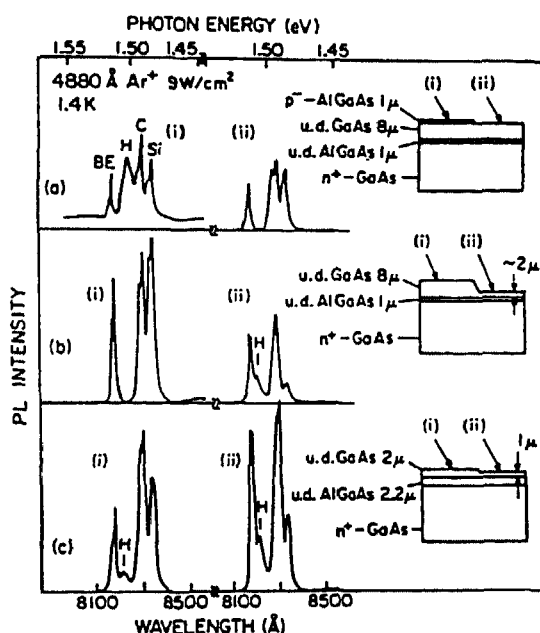


Fig. 160 PL spectra of several step-etched GaAs/AlGaAs heterostructure samples (After Yuan et al. [281])

part of the structure has been chemically-etched removed. H-band PL disappears upon removal of the top AlGaAs layer. Yuan et al. attribute this new emission band in their n-n GaAs/AlGaAs structures as due to the recombination of electrons trapped in the potential notch next to the heterointerface caused by the bandbending there with free holes in the valence band at some distance away from the heterointerface. They attribute the power dependence of the emission energy as a result of photoexcited carrier screening of the built-in heterointerface field. This screening drives the bandstructure "flat band" and causes a blue-shift of the emission energy.

2.3.3. Quantum wells and superlattices

PL spectroscopy may be utilized to characterize quantum wells and superlattices in many ways. Determination of quantum well widths is easily accomplished in emission measurements. Interfacial roughness may also be quantified through PL measurements. Determination of band offsets and band

alignments may be achieved through detailed PL spectroscopy. Systematic PL measurements coupled with an empirical growth parameter study may also show optimal conditions for nanostructure fabrication.

2.3.3.1. Multiple quantum wells, well width, and novel structures

Fig. 161 is a good example of a study utilizing PL spectroscopy to characterize the widths of various wells in a multiple quantum well sample [282]. The sample was grown by MOCVD with 54% Al barriers and four quantum wells with widths shown in the figure. The arrows correspond to the calculated emission wavelength obtained with a simple finite-barrier, square-well potential. The emission from quantum well structures has also been shown to reflect fluctuations in the well width of the structures down to the monolayer level. Gammon et al. [283] measured the PL emission of a quantum well sample at various points across the wafer (separated by 300 μm), as shown in Fig. 162. At each spatial point a doublet is observed in the spectrum which corresponds to a change in the

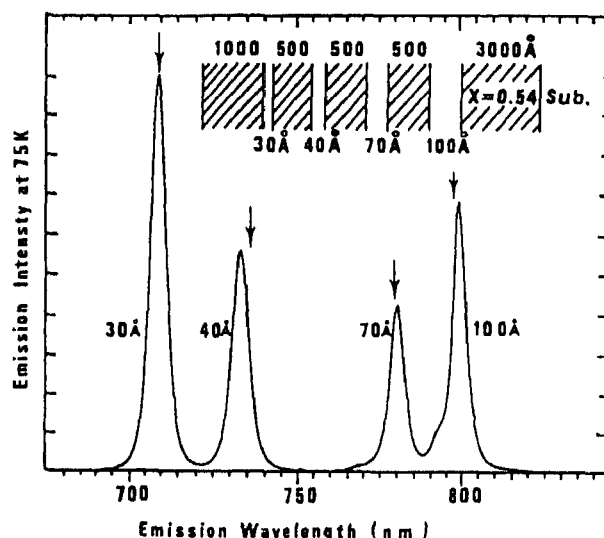


Fig. 161. 75 K PL spectrum of a GaAs/Al_{0.54}Ga_{0.46}As multiple quantum sample, with well widths of 100, 70, 40, and 30 \AA . (After Kawai et al. [282].)

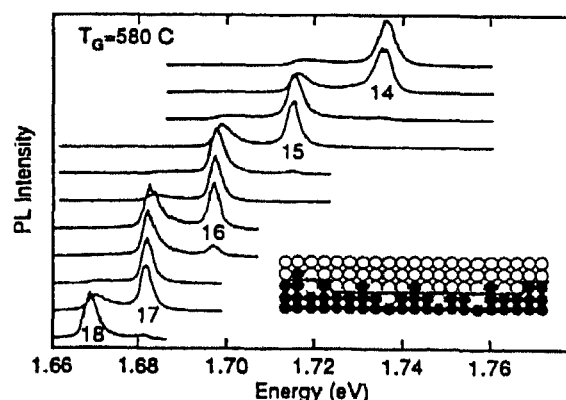


Fig. 162. PL spectra of a GaAs quantum well obtained at various positions across a wafer. The numbers represent the quantum well width in monolayers. Inset is a schematic diagram of the quantum well interface. (After Gammon et al. [283].)

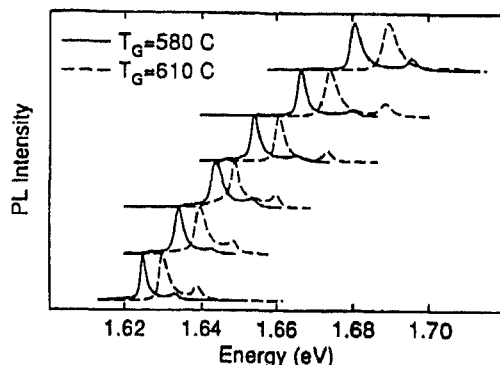


Fig. 163. PL spectra from two different quantum well samples grown at different temperatures at various positions across the wafer (After Gammon et al. [283].)

confinement energy due to a single monolayer difference in GaAs well width. In this study the samples were not rotated during growth in order to maximize the variation in well width across the wafer, and this is reflected in the variation in well width evident in the spectra. They also find that variation in the growth temperature leads to significant differences in the PL spectra. Fig. 163 shows the PL spectra at various points across the wafer for samples grown at $580\text{ }^\circ\text{C}$ and $610\text{ }^\circ\text{C}$. There is a shift in the emission energy by 40% of the doublet splitting, and this shift may only be explained as due to changes in microscopic heterointerfacial roughness. This will be examined below. Lastly, PL may be used to examine the properties of novel structures, such as the fractal quantum wells, as shown by Gourley et al. [284]. These structures are grown such that the AlGaAs composition is varied in a fractal sequence between layers in order to create a highly branched, self-similar distribution of quantum wells. Fig. 164 shows a semilog plot of the room-temperature PL spectra of four fractal quantum well samples where the smallest length scale is indicated. The higher energy peaks, between 1.5 and 1.8 eV, are due to recombination in higher branches of the fractal quantum well. Changes in the structure are clearly evident in this region of the spectrum.

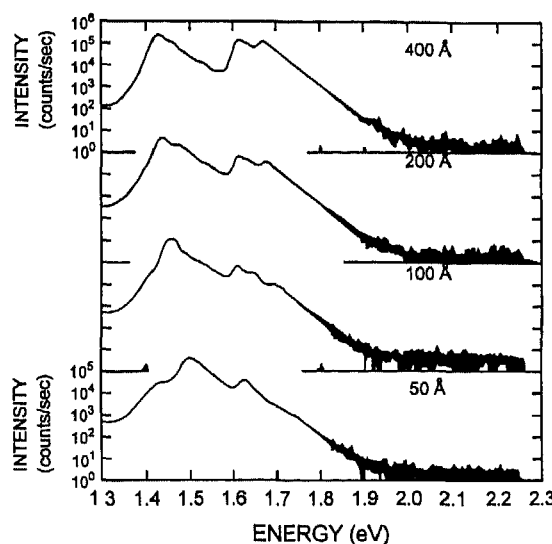


Fig. 164. PL spectra of several fractal quantum wells at 300 K (After Gourley et al. [284].)

2.3.3.2. Growth optimization

The luminescence from AlGaAs/GaAs quantum wells may also be maximized through optimization of the heterointerfaces. It is well known that the heterointerfaces in a AlGaAs/GaAs/AlGaAs quantum well are not equivalent [285]. The normal interface (AlGaAs grown on GaAs) is widely considered to be of better quality than the inverted interface (GaAs grown on AlGaAs). Increasing the growth temperature improves the inverted interface, while growing thicker AlGaAs layers makes the inverted interface worse [286]. Incorporation of carbon and/or oxygen have been blamed for the inferior properties of the inverted interfaces. Masselink et al. [286] have examined the luminescence properties of single quantum wells grown with abrupt heterointerfaces, graded heterointerfaces, or graded superlattice heterointerfaces. Fig. 165 shows the PL spectra of the graded interface and superlattice interface samples versus excitation power. The superlattice interface sample is dominated at all powers by the free-exciton emission, whereas the graded interface sample is dominated at low powers by the emission of bound excitons. They find that the graded superlattice interface sample has superior optical properties, as quantified by the emission intensity (160 times enhancement) and free-exciton linewidth (near-intrinsic 2 meV linewidth), and weak impurity-related emissions. This method of improving the quality of quantum structures is now widely used. Fujiwara and Ploog [287] have further investigated the improvement of quantum well luminescent properties through utilization of all-binary AlAs/GaAs heterostructures using AlAs/GaAs short-period superlattices instead of the ternary alloy cladding layers. Fig. 166 shows a comparison in the emission properties of quantum wells clad by a ternary alloy and an all-binary short-period superlattice. The quantum well emission

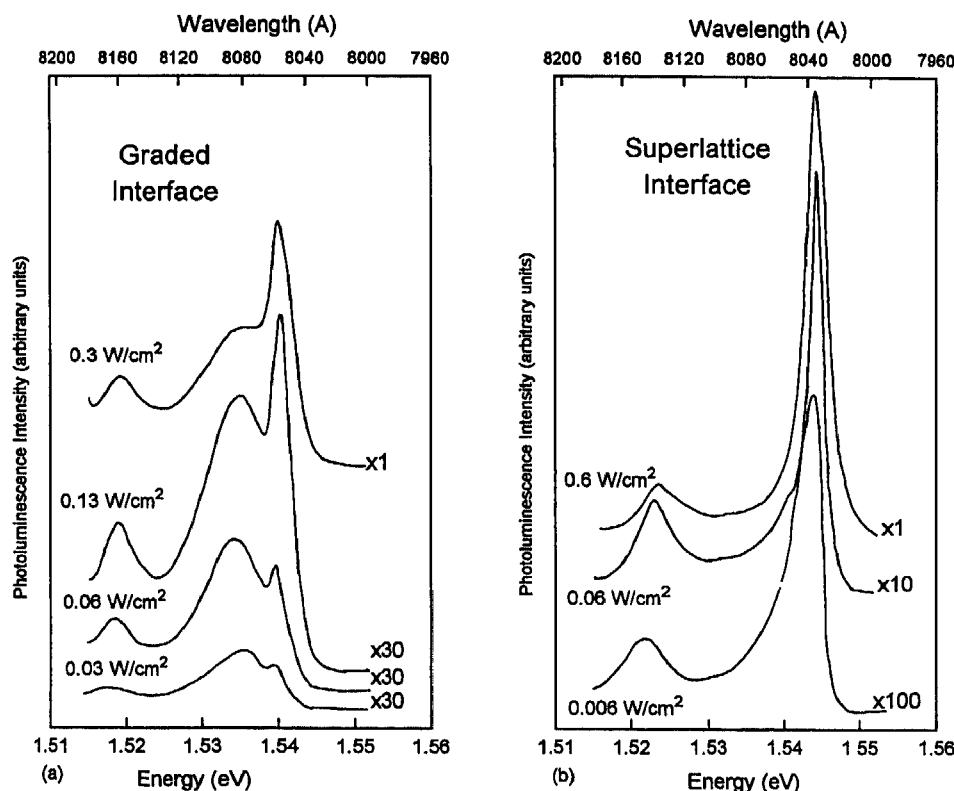


Fig. 165. Low-temperature PL spectra versus laser excitation power of samples with graded alloy (a) and graded superlattice (b) interfaces. (After Masselink et al. [286].)

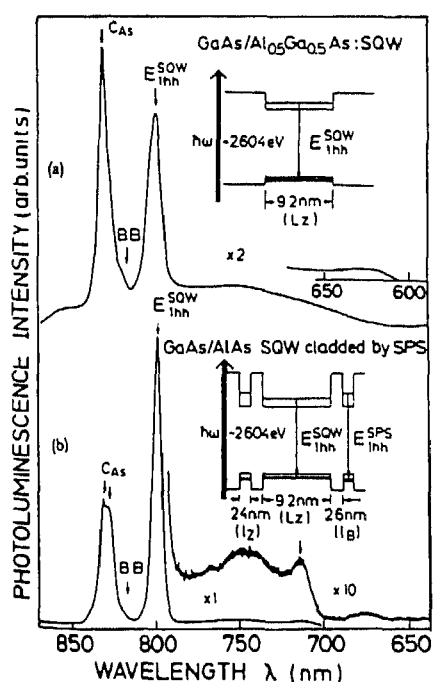


Fig. 166. Low-temperature PL spectra of two quantum well samples: (a) AlGaAs cladding layers and (b) GaAs/AlAs short-period superlattice cladding layers. (After Fujiwara and Ploog [287].)

linewidth is much narrower for the short-period superlattice cladding than the ternary alloy cladding. Also, the intensity ratio is 2.6.

As mentioned above some features of quantum well luminescence must incorporate the effects of heterointerfacial roughness on some length scale in order to qualitatively explain the observations. A model has emerged which relates the PL linewidth of the quantum well excitonic recombination with the heterointerfacial roughness, or disorder, experienced by the excitons. This model assumes well-width fluctuations of one monolayer [76] and quantifies the PL linewidth as a function of the relative "island" size of the interfacial roughness and the lateral extent of the exciton [288]. This model predicts that the luminescence features will be sharp when the island size is larger than the lateral extent of the exciton, whereas in the opposite limit, the linewidth will be large when the island size is comparable to the lateral extent of the exciton. This type of model is schematically illustrated in Fig. 167 [289].

2.3.3.3. Heterointerfacial roughness

PL spectroscopy has proven extremely useful in characterizing interfacial disorder in nanostructured systems. This topological disorder may produce measurable changes in the spectra, including peak energy shifts, linewidth changes, and changes in lineshape. The structure-dependent inhomogeneous linewidth of exciton emission in quantum well structures may arise from two different mechanisms: (1) a layer-to-layer thickness variation in the sample, leading to changes in confinement energies for the different layers; and (2) thickness fluctuations with each layer. Weisbuch et al. [290] were among the first to examine these issues in quantum wells. They find that the interlayer thickness fluctuations are less than one-tenth of the intralayer thickness fluctuations, which are one monolayer.

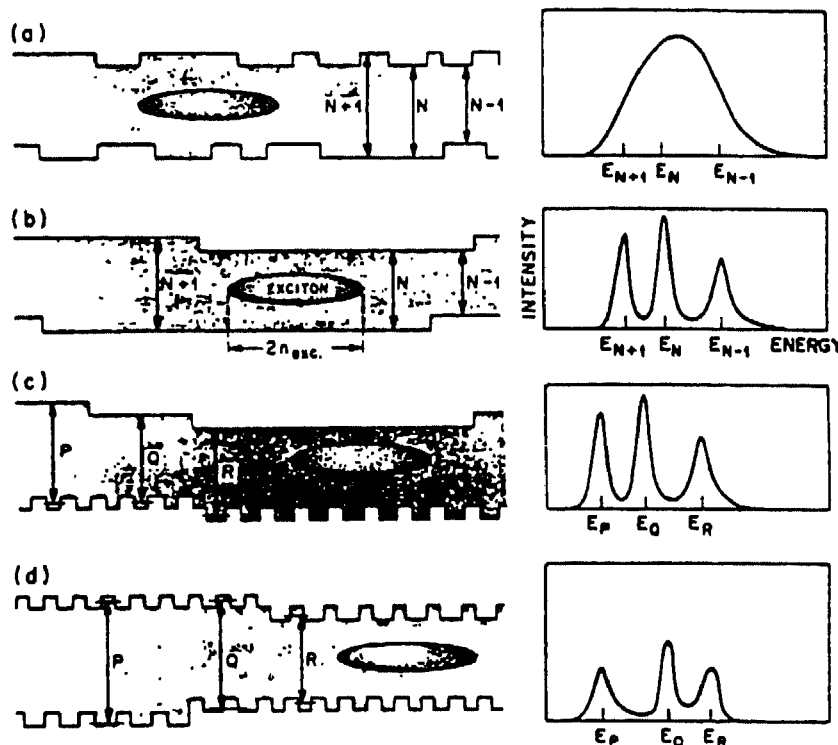


Fig. 167. Illustration of three possible interfacial roughness configurations in a heterostructure quantum well. (a) Broad PL lines result from the rough interfacial configuration. (b) Spectrally-resolved emission lines, with energy separations corresponding to integer multiples of a GaAs monolayer results from large monolayer-flat interfacial regions. (c) and (d) Sharp luminescence lines may also result from an interfacial configuration consisting of microroughness at either or both interfaces. (After Kopf et al. [289].)

Thus, the reproducibility of the layer thickness during growth is better than 0.1 monolayer. Fig. 168 shows their measured excitonic linewidths versus confinement energy (well width). The solid lines represent model calculations based upon one- or two-monolayer intralayer fluctuations. These fluctu-

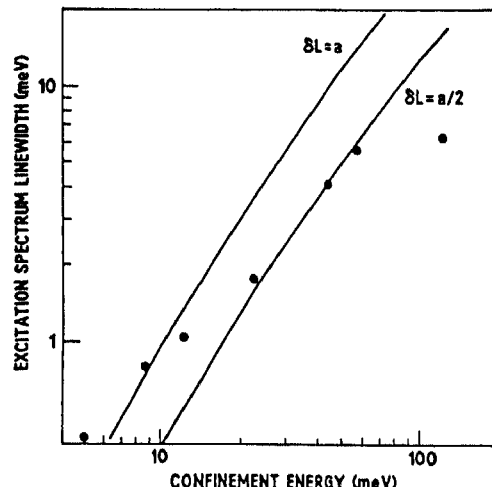


Fig. 168. Confinement energy dependence of the excitation spectrum line width for a series of GaAs quantum well samples grown under approximately similar conditions. Solid lines represent well-width fluctuations of half and one monolayer. (Reprinted from C. Weisbuch et al., *Solid State Commun.*, 38 (1981) 709, with permission from Elsevier Science Ltd., Pergamon Imprint, The Boulevard, Langford Lane, Kidlington OX5 1GB, UK.)

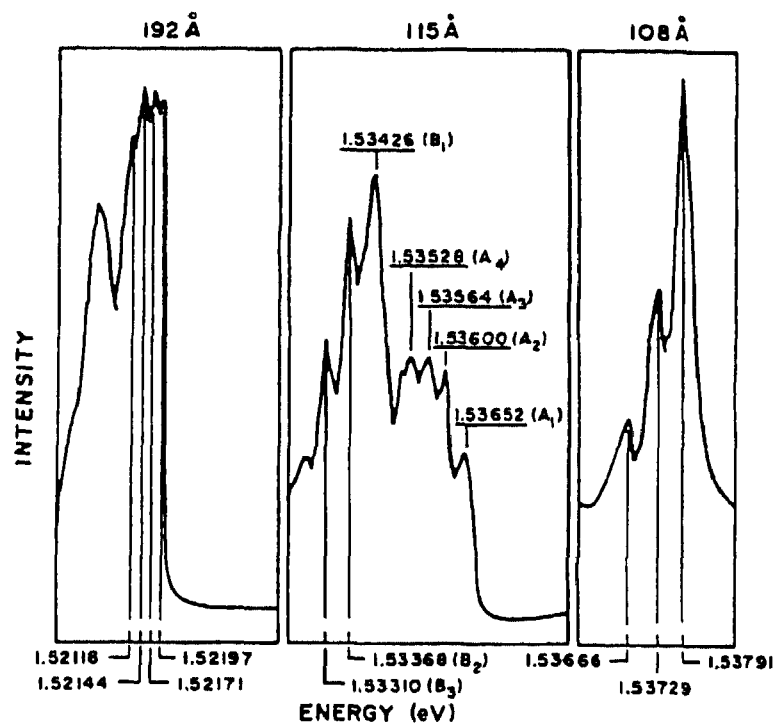


Fig. 169. Fine structure evident in the free exciton transitions of quantum wells with various well sizes. For the 115 Å well, the A series of lines correspond to fine structure of the free exciton, whereas the B series of lines correspond to the donor-bound exciton. (After Singh et al. [291].)

ations in well thickness within a layer may lead to exciton localization or trapping at these intrinsic interface defects. Fig. 28 shows the PL and PL excitation (PLE) spectra of a 70 Å quantum well. There is a 4.4 meV Stokes shift between the peaks of the absorption and emission lines of the heavy-hole exciton. This is an indication that the excitons are localized at the interface defects (well-width fluctuations), and that the emission comes from these localized excitons.

Kawai et al. [282] investigated the "island" structure of AlGaAs/GaAs quantum wells grown by MOCVD. Their examination of multiple quantum well luminescence peak energy, linewidth, and power dependence leads to the conclusion that the average fluctuation in well thickness over the interface caused by island formation is also less than a monolayer. Singh et al. have examined the microscopic structural quality of MBE-grown GaAs/AlGaAs multiple quantum well samples using very high-resolution PL spectroscopy [291]. Their spectra, shown in Fig. 169, reveal extremely sharp excitonic transitions with energy separations corresponding approximately to half-monolayer fluctuations in GaAs well widths. They only observe these half-monolayer well-width fluctuations in structures grown under optimal conditions. Kohl et al. [292] observed a strong dependence of the exciton population of three observed different island regions, representing fluctuations by a single monolayer for each island, on the excitation wavelength and excitation intensity. They find that the intensity ratios of the corresponding exciton transitions for each island vary with excitation intensity strongly, and do not reflect the area ratios of these islands.

The effects of growth interrupts were examined by Köhrbrück et al. [170]. They find that the PL emission energy shifts to lower energies with increasing growth interruption time. They examined samples with growth interrupts at only the normal interfaces and only the inverted interfaces, and conclude that the AlGaAs surface is largely unaffected by growth interrupts, whereas the GaAs surface

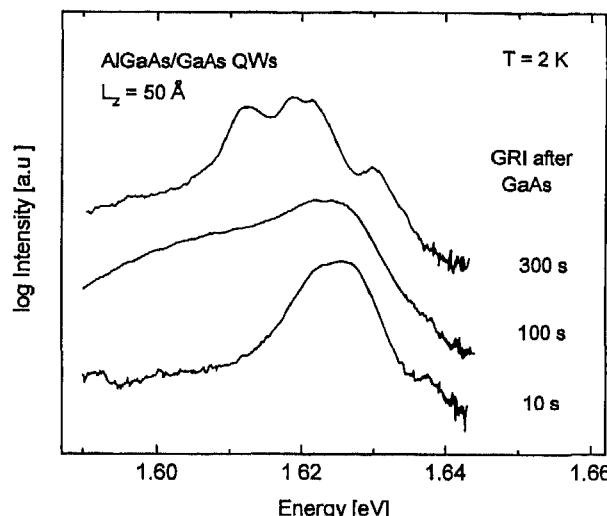


Fig. 170. PL spectra of GaAs samples grown by MBE with various growth interrupt times. (After Munnix et al [60])

becomes smoother with increasing growth interruption time. Fig. 170 demonstrates this effect [60]. In these spectra samples with growth interrupts at the normal interface were examined versus growth interrupt time. The longest growth interrupt leads to three distinct peaks, revealing the existence of two monolayer steps at the GaAs interface. Continuing in this vein, they find that decreasing growth rates lead to smoother interfaces. Their results also indicate that non-radiative traps, of unknown origin, are incorporated more readily at the inverted interface than at the normal interface [56,57,170]. Miller et al. [62,293] found that an extrinsic layer at the interfaces was correlated with increased interfacial roughness. They suggest that the impurity is probably carbon which "floats" on the $\text{Al}_x\text{Ga}_{1-x}\text{As}$ interface during growth (as alluded to earlier), and is incorporated at the start of GaAs growth on this $\text{Al}_x\text{Ga}_{1-x}\text{As}$ layer. Petroff et al. [294] have demonstrated that interface roughness in quantum well superlattices is related to trapped impurities at interfaces. They find that more superlattice layers below the active quantum well improves the luminescence efficiency. They suggest that impurities or complexes originating from the substrate as well as from the AlGaAs layer are trapped or removed by the superlattice. They speculate that C and O may become trapped in the GaAs layer near the GaAlAs-GaAs interfaces. Another possibility might be due to misfit strain between AlGaAs and GaAs layers. Fujiwara et al. [295] compared the PL spectra of MBE-grown GaAs quantum wells grown with and without growth interrupts. They found (Fig. 171) that samples grown with 2 min growth interrupts exhibit distinct spectral lines corresponding to monolayer fluctuations of well widths and island formation with minimum linewidths of 2.8 meV, whereas samples grown without interrupts have minimum linewidths of ~5.0 meV, and increase, predominantly on the high-energy side, with increasing excitation power. High excitation leads to saturation of the islands with the widest well thickness. Kopf et al. [289] have also demonstrated the effects of growth interruption on the photoluminescence of quantum wells. They find that uninterrupted growth yields an emission which has only one peak, whereas the sample with growth interrupts (120 s at each heterointerface) yields a spectrum with three distinct lines. Each peak may be assigned to a monolayer fluctuation either way from the nominal nine-monolayer quantum well. The linewidths of each of these peaks are considerably narrower than that for the uninterrupted sample. Based on this evidence they conclude that growth interrupts yield extended monolayer flat regions of the interfaces, i.e. abrupt, atomically smooth interfaces and discrete thicknesses of the quantum well. Kopf et al. [296] further examined the change in the growth-interrupted interfaces of a GaAs/AlGaAs quantum well through both low-temperature PL spectroscopy

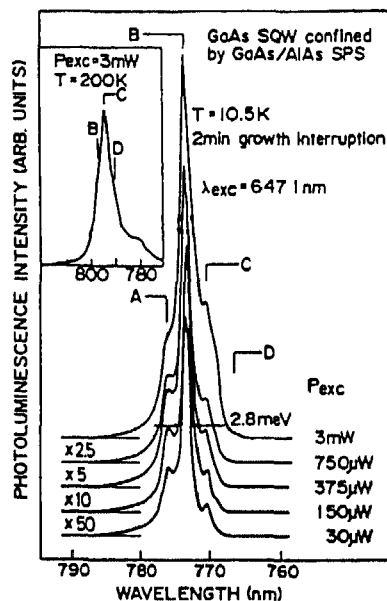


Fig 171. Power dependence of the 10.5 K PL spectra of a GaAs quantum well grown with growth interrupts and short-period superlattices confining the quantum well. Inset shows PL spectra at 200 K (After Fujiwara et al. [295].)

and scanning tunneling microscopy (STM) measurements. Samples were grown in two environments, one with 10^{-10} Torr of O₂ present, and one with a base pressure of 5×10^{-11} Torr and no intentional contaminants. Consecutive growth-interrupted quantum well samples under the first growth conditions exhibited a PL spectra with splittings into several peaks which shifted as the laser spot was scanned across each sample, as shown in Fig. 172. Growth under the ultra-high vacuum ambient yielded no variation in emission energy as the laser was scanned across the wafer or from sample to sample, as shown in Fig. 173. These results are consistent with a bimodal distribution of interfacial roughness for growth in the O₂ environment, whereas large islands are formed for UHV growth conditions. Thus, they conclude that interfacial roughness is very sensitive to background O₂. Massies et al. [297] examined the effect of substrate misorientation of the heterointerfacial roughness of MBE-prepared quantum wells. They examined the interfacial roughness of quantum well structures grown by MBE on GaAs (001) substrates exactly oriented or 4° misoriented towards (111) Ga and (111) As planes. Fig. 174 shows the PL spectra of samples grown with misorientation in different crystallographic directions. Sharp luminescence features are observed for substrates tilted toward the (111) Ga plane. This implies pseudosmooth heterointerfaces. In contrast, considerable broadening is observed for substrates misoriented towards the (111) As plane, implying rough interfaces.

Finally, Seidel et al. [298] examined the effects of intermixing induced by annealing GaAs quantum wells at 850 °C in an As-rich atmosphere for several hours. They find that the PL emission broadens and shifts toward slightly higher energies. The broadening appears to be due to the development of an impurity line 10 meV below the exciton peak, and they attribute it to neutral acceptors located close to the interfaces. They find that the energy shifts are linear with annealing time, and derive an intermixing diffusion constant of $D_{\text{Ga-Al}} = 0.2 \times 10^{-18} \text{ cm}^2 \text{ s}^{-1}$.

2.3.3.4. Band alignment

The most important property characterizing a semiconductor heterojunction is the energy alignment of the two band structures. The difference in fundamental energy gap between the two layers composing the heterojunction must be distributed in some fashion between the conduction and valence

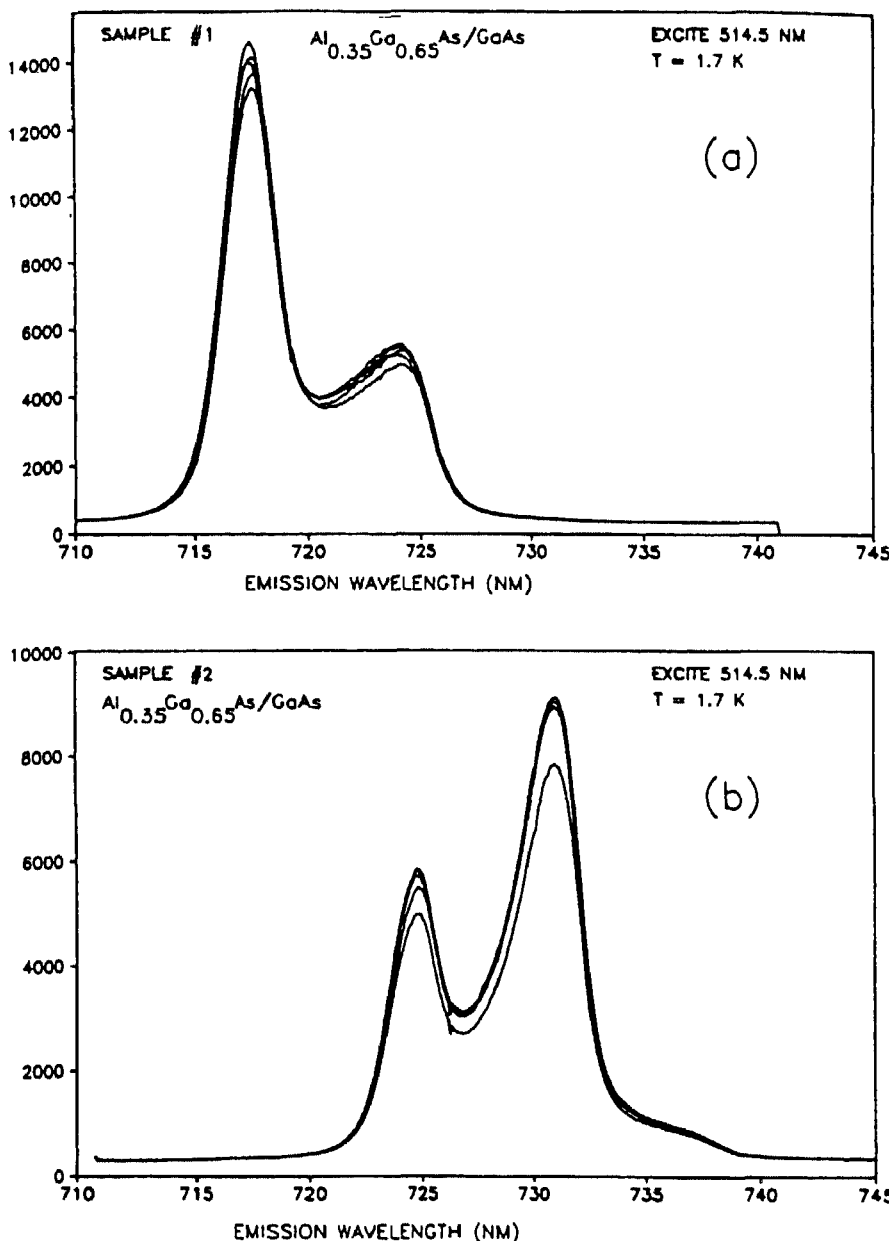


Fig. 172. PL spectra of GaAs quantum well samples grown with interrupts under UHV conditions. Sample 1 (2) is a 25 Å (28 Å) well. PL peak emission energies do not change as the laser is scanned across the sample and for different samples (for a given well width). (After Kopf et al. [296].)

bands. This energy difference between conduction (valence) bands is termed the conduction (valence) band offset. The first measurements of the band offsets in a semiconductor heterojunction were based on optical measurements [299]. This work relied on a comparison of the measured exciton energies in simple square GaAs quantum wells to calculated values for the energies of the quantum-confined excitonic states. The difficulty with this result is that both the electron and hole energies are increased by quantum confinement, and, therefore, it is only the difference in the effective electron and hole masses which permits the calculation of the valence- and conduction-band offsets. The result was that

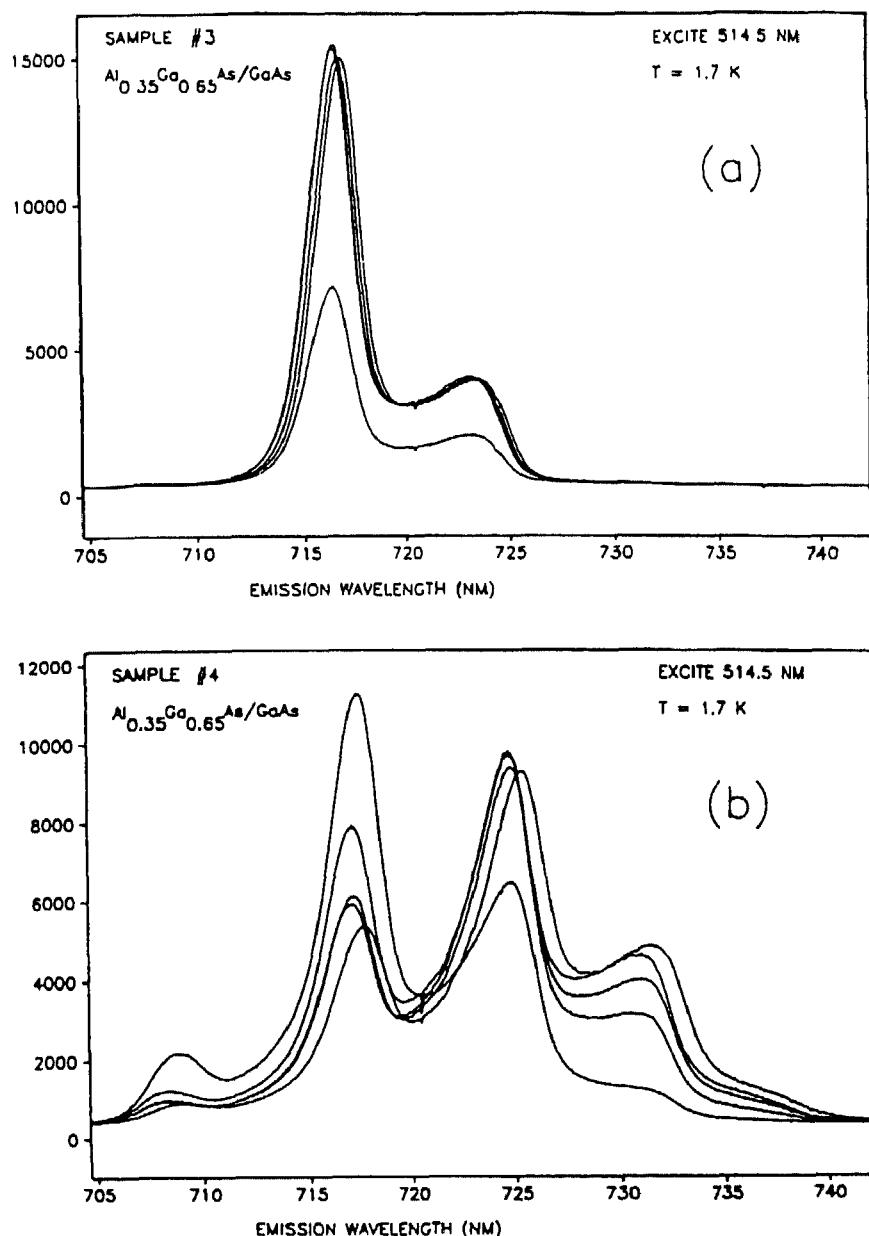


Fig. 173. Low-temperature PL spectra of growth-interrupted quantum wells grown in an O_2 (1×10^{-10} torr) atmosphere. Sample 3 (4) is a 25 Å (28 Å) quantum well. Here, the PL peak emission energy changes as the laser is scanned across the sample, and from sample-to-sample. (After Kopf et al. [296].)

85% of the band offset appears in the conduction band. This band offset is not generally accepted as the correct value today. Wolford et al. [90,300] have utilized hydrostatic pressure as a perturbing tool to deduce the band offsets for $\text{GaAs}/\text{Al}_x\text{Ga}_{1-x}\text{As}$ heterostructures. The application of hydrostatic pressure was used to drive the lowest confined states associated with the Γ conduction band minimum of the GaAs well up in energy to the point where it crosses with the indirect conduction band edge of the $\text{Al}_x\text{Ga}_{1-x}\text{As}$ barrier layers. When the X-edge of the $\text{Al}_x\text{Ga}_{1-x}\text{As}$ layers is lower in energy than the Γ quantum-confined conduction band edge of the GaAs well layer, the structure becomes type II. In

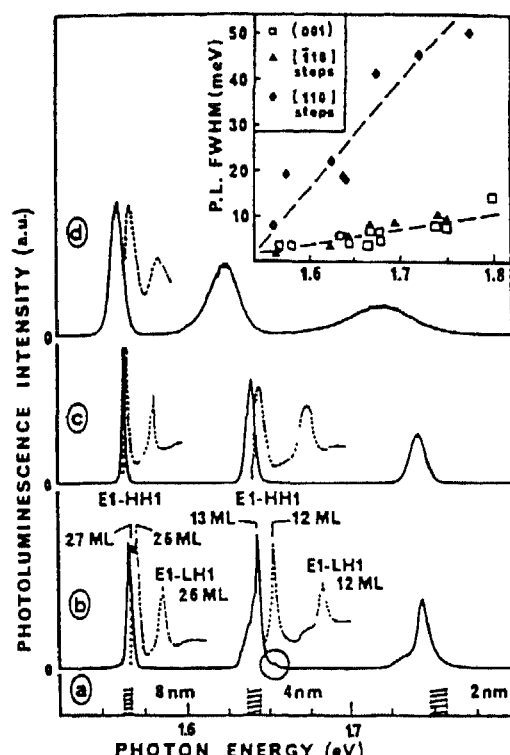


Fig. 174. 2 K PL spectra versus substrate orientation. Dotted lines are PLE spectra. (a) Cross-hatched areas show expected energy of E1–HH1 transitions including uncertainties in layer thicknesses. Substrate orientations include (b) GaAs (001) substrate, (c) substrate with [10] steps, and (d) substrate with [110] steps. Inset shows the spectral widths of emission lines versus emission energy. (After Massies et al. [297].)

their experiments Wolford et al. examined the pressure dependence of the emission from multiple quantum well and superlattice samples grown by MOCVD. (The technique of high-pressure spectroscopy will be described in section 2.4.1.) Fig. 175 shows the 8 K PL spectra of a GaAs/Al_{0.28}Ga_{0.72}As superlattice with $\sim 70 \text{ \AA}$ GaAs wells. The Γ -confined transitions increase in energy with pressure at a rate of $10.7 \text{ meV kbar}^{-1}$, which follows the shift of the Γ conduction band edge of bulk GaAs. At 31 kbar and above, the intensity of the emission decreases significantly, and the energy of the main emission peak shifts down in energy with increasing pressure. At 31 kbar a new emission line appears as a shoulder on the $\Gamma_{\text{1e}}-\Gamma_{\text{1hh}}$ direct transition. This new emission line is the indirect, type-II X_e– Γ_{1hh} transition. Fig. 176 shows a summary of the pressure results for two superlattice samples with Al_xGa_{1-x}As compositions of $x=0.28$ and $x=0.70$. Clearly, the $\Gamma_{\text{1e}}-\Gamma_{\text{1hh}}$ tracks the direct edge of bulk GaAs. In contrast the X_e– Γ_{1hh} transition tracks the X-conduction band edge of AlAs. Most important is the fact that the direct–indirect crossing occurs at different pressures for the two different superlattices. For the $x=0.28$ composition superlattice this crossing occurs at ~ 29.5 kbar, whereas for the $x=0.70$ superlattice it occurs near 18 kbar. The band offsets may be derived from this data using the relations

$$\text{PL}_{\text{1e}-\text{1hh}}^{\Gamma-\Gamma}(P) = \sum_{\text{1e}-\text{1hh}}^{\Gamma-\Gamma}(P) - E_x^{\Gamma-\Gamma} - \Delta_{\text{ss}}^{\Gamma-\Gamma} \quad (27)$$

$$\Delta E_V = E_{\text{gB}}^X - \sum_{\text{1e}-\text{1hh}}^{\Gamma-\Gamma}(P) + \Delta_{\text{1hh}}^{\Gamma} + \Delta_{\text{1e}}^X \quad (28)$$

where $E_x^{\Gamma-\Gamma}$ is the internal exciton binding energy of 9 meV, $\Delta_{xx}^{\Gamma-\Gamma}$ is the Stokes shift of the direct

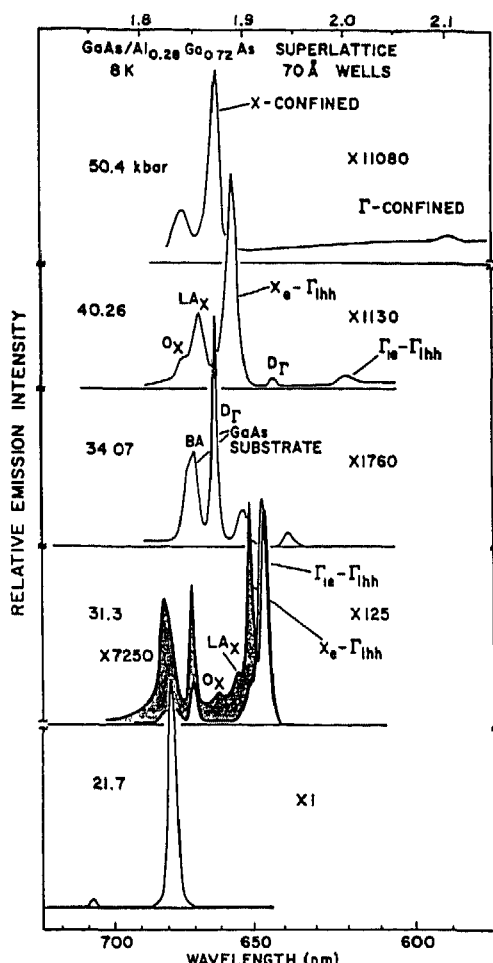


Fig. 175. 8 K PL spectra of a 40-period GaAs/Al_{0.28}Ga_{0.72}As superlattice with $\sim 70 \text{ \AA}$ wells versus pressure. Stippled spectrum represents a 10 \times reduction in incident power density. (After Wolford et al [300].)

transition (which they found from comparison of PL and PLE measurements to be ~ 4 meV), $E_{gB}^X(P)$ is the pressure-dependent indirect gap, Δ_{1e}^X is the electron localization energy, and Δ_{1hh}^Γ is the hole localization energy. Wolford et al. assumed that the electron and hole localization energies may be neglected since they are small and are effectively canceled by the exciton terms of opposite signs. They find that their data supports a 0.68:0.32 distribution of the bandgap difference in the conduction and valence bands, respectively. This is true for both of the composition superlattices examined. Several years later Wilson [301] also used type-II structures to determine the band offsets, only without utilizing high-pressure measurements. He found that the valence band offset is 5.25 meV/(percent Al), which corresponds to a 535 meV valence band offset for the GaAs/AlAs heterostructure system.

2.3.3.5. Type-II structures

Staggered alignment type-II structures have electron and hole ground states in different layers of the nanostructure without any overlap between conduction bands in one layer and valence bands of another [302,303]. In broken-gap type-II structures neither the valence nor conduction band lies within

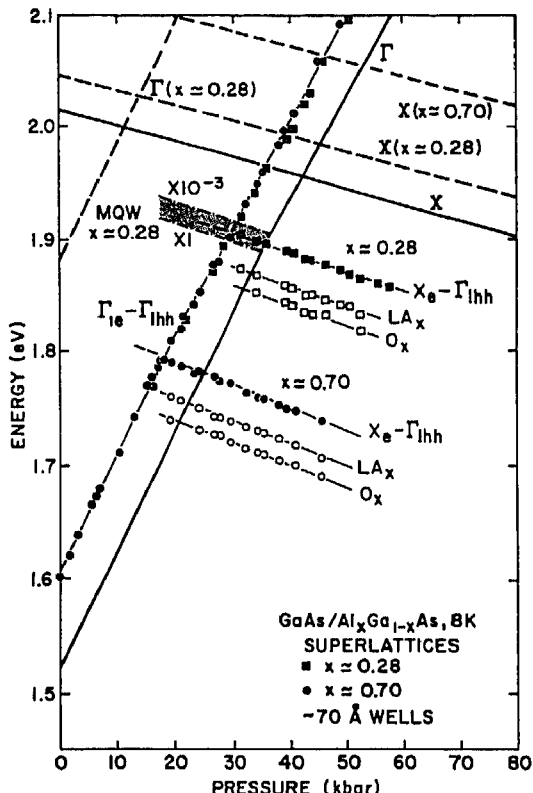


Fig. 176 Summary of the PL transition energies obtained versus pressure at 8 K. (After Wolford et al. [300].)

the gap of the other layers. For the $(\text{GaAs})_m/(\text{AlAs})_n$ system, a staggered type-II band alignment results for GaAs layer thicknesses $< 35 \text{ \AA}$ ($m < 13$) and AlAs layer thicknesses $> 15 \text{ \AA}$ ($n > 6$) [302] or possibly through the application of hydrostatic pressure [304,305]. In these structures, the hole ground state is in the GaAs layer (at the Γ point), whereas the electron ground state is in the AlAs layer (at the X-point). This type-II alignment results from the quantum confinement in the GaAs layer which raises the $n = 1$ electron ground state above the X conduction band edge in the AlAs [303,306]. This is shown schematically in Fig. 177 [307]. This spatial separation of electrons and holes is responsible for the dramatically different optical and electronic properties in these structures compared to type-I systems. Further, at low temperatures excitons may form which are indirect both in real space and in momentum space [307].

The first published study of the PL emission from GaAs/AlAs type-II structures was by Drummond and Fritz [308]. This work, and all subsequent work, has firmly established the spectral signatures of type-II emission [309,310]. The spectra consistently show a no-phonon emission and several phonon replicas at lower energies (as shown in Fig. 178). Some of these phonon replicas have been identified as involving zone-boundary AlAs X-point phonons [311].

Type-II structures have many interesting features which allow a unique opportunity for investigation of mechanisms not readily observable in other structures. First, the three-fold degeneracy of the X-electron states in the AlAs layers is lifted by several mechanisms, including strain-induced splitting of X_Z and $X_{X,Y}$ levels [309,312,313], electronic mass anisotropy ($m_e(X_Z) = 1.1m_0$ and $m_e(X_{X,Y}) = 0.19m_0$) [311], Γ -X mixing due to the superlattice potential [307,312], and Γ -X mixing due to interface roughness or disorder [307,312]. This lifting of the degeneracy leads to distinctly different optical properties depending upon whether X_Z or $X_{X,Y}$ is the ground state. It is now well

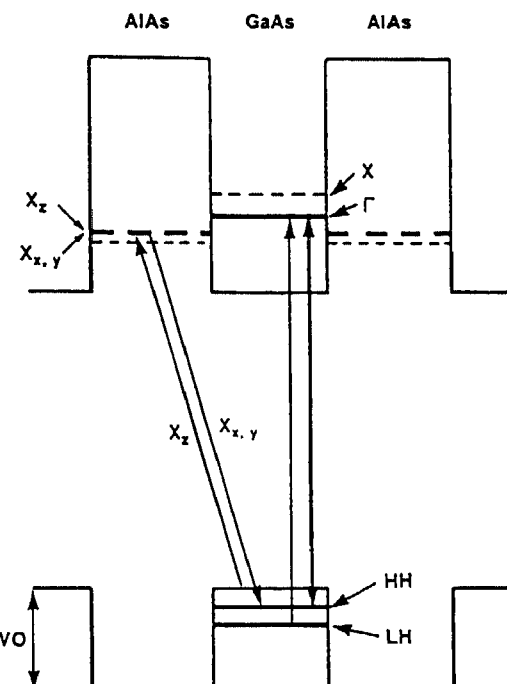


Fig. 177. Conduction and valence bands of a GaAs/AlAs short-period superlattice together with the quantum-confined energy levels. (After Finkman et al [307])

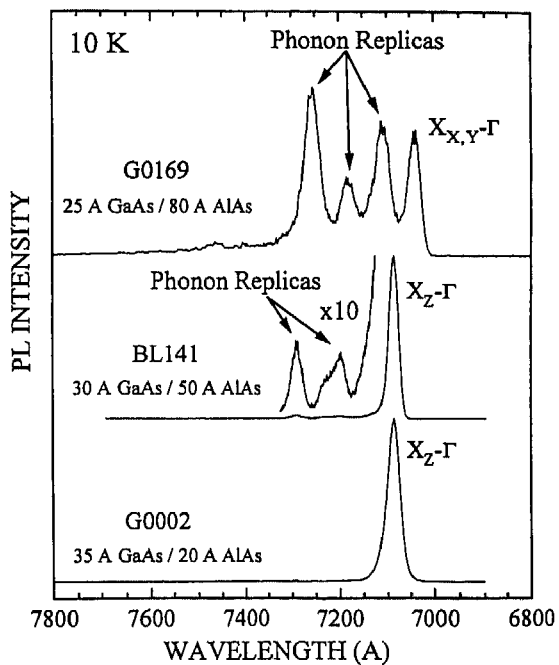


Fig. 178. Low-temperature PL spectra of three typical type-II GaAs/AlAs short-period superlattices.

established that these X levels cross in energy for certain thicknesses of the layers (for 30 Å GaAs layers X_Z is lowest for AlAs layers less than 55 Å thick, whereas $X_{X,Y}$ is the electronic ground state for thicker AlAs layers) [311,313]. Second, the excitonic recombination is doubly forbidden. Nev-

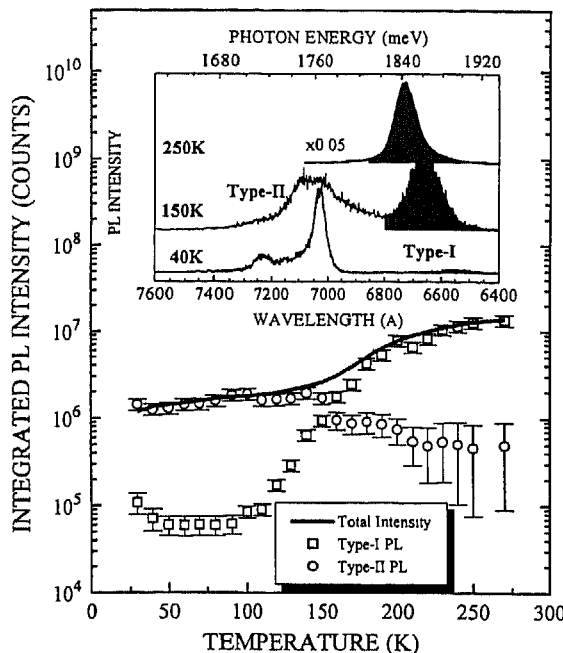


Fig. 179. Integrated PL intensity for type I (\circ), type II (\square) and the total (—) emissions versus temperature for a type-II GaAs/AlAs superlattice. The inset displays three PL spectra taken at $T = 40, 150$ and 250 K. The shaded area indicates the type-I emission.

ertheless, a prominent no-phonon line is present, as shown in Fig. 178. This emission must, therefore, involve some hybridization of the X and Γ electron levels. Thus, the electronic ground state (i.e. X_Z versus $X_{X,Y}$) may be determined by examining the PL spectrum. In Fig. 178 the sample with the $X_{X,Y}$ ground state exhibits much weaker emission and more prominent (relatively) phonon replicas, whereas for the samples with X_Z electronic ground states the no-phonon line is much stronger and the phonon replicas weaker. Γ - X mixing due to the superlattice potential and also to interfacial roughness or disorder is commonly cited as the mechanism responsible for this no-phonon emission [307,312]. Third, photoexcitation of carriers occurs entirely within the GaAs layers (type-I transition) [302,311]. Subsequent to photoexcitation the electrons undergo a real-space scattering from the Γ -point in the GaAs layer to the X -point in the AlAs layer [314]. This is a very fast real-space charge transfer process. Lastly, type-II excitons actually straddle the heterointerfaces, and are thus especially sensitive to the microscopic structure of the heterointerfaces.

Van Kesteren et al. [315] measured the optically-detected magnetic resonance of various type-II structures and determined that quantum wells with AlAs layers thinner than 55 \AA the X_Z conduction-band valley is lowest in energy, while for quantum wells with thicker AlAs layers the $X_{X,Y}$ valleys are lowest in energy [313]. Ge et al. [316] studied the energy levels of very short-period $(\text{GaAs})_n/(\text{AlAs})_n$ superlattices ($n \leq 4$). Their results show that the lowest conduction bands are $X_{X,Y}$ for $n \leq 3$ and X_Z for $n = 4$, respectively. Laks and Zunger [317] have predicted that for a monolayer superlattice, i.e. $(\text{GaAs})_1/(\text{AlAs})_1$, the lowest conduction band is at the L -point, although this has not been experimentally verified.

It is also sometimes possible to observe type-I and type-II emissions simultaneously in the same structure. Fig. 179 illustrates the thermally activated integrated intensity crossover of the type-II ($X_{X,Y}-\Gamma$) to type-I ($\Gamma-\Gamma$) emission in the short-period superlattice structure. PL spectra at temperatures of 40, 150 and 250 K are shown in the inset. At $T = 40$ K, the spectrum is dominated by the $X_{X,Y}-\Gamma$ no-phonon line at 7030.6 \AA (1763.5 meV) and its phonon sidebands. The type-I $\Gamma-\Gamma$ transition at 6554.2

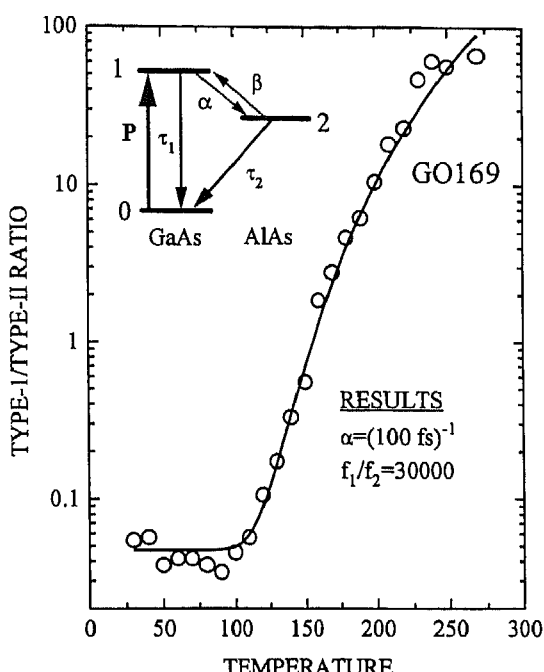


Fig. 180 The PL intensity ratio of type-I to type-II integrated emission versus temperature. The solid line is a best fit to the data using a rate equation model as shown in the inset

Å (1891.6 meV) is extremely weak (indicated by the shaded area). As the temperature increases, the type-I emission intensity is significantly enhanced and its peak position shifts to lower energy while the type-II no-phonon peak shows little change. When the temperature reaches 150 K, the type-I and type-II emissions have approximately the same strength, whereas at $T = 250$ K, the direct $\Gamma-\Gamma$ transition totally dominates the PL spectrum. Remarkably, the integrated intensity of the type-I peak increases by three orders of magnitude as the temperature increases from 40 to 250 K. In this figure, the integrated PL intensities of both the type-I (open squares) and the type-II (open circles) transitions versus temperature are shown. The solid line represents the total integrated luminescence intensity of the sample. The integrated type-I intensity rises in an Arrhenius fashion with temperature for $T > 50$ K while the type-II emission diminishes gradually. This is indicative of a thermal population of the GaAs Γ electron states as a result of the transfer of electrons from the lower X states in the AlAs barriers ($X \rightarrow \Gamma$ transfer). The intensity cross-over occurs at ~ 150 K. The total luminescence intensity shows a striking increase above 150 K, due to the more efficient type-I emission. That is because the type-I recombination has a shorter lifetime and it is less affected by non-radiative decay when compared to the type-II recombination. A three-level model may be used to quantitatively fit the ratio of the type-I to type-II emissions. Fig. 180 shows the results of such a model, and the derived Γ -X interlayer electron scattering time of 100 fs for this structure.

2.3.4. Quantum well wires

Due to the relative immaturity of the technology for fabrication of GaAs quantum wires, PL spectroscopy is primarily useful for demonstrating the one-dimensional confinement of carriers [318]. Studies of kinetics and dynamics in quantum well wires are more difficult since these nanostructures are often dominated by extrinsic processes most commonly associated with fabrication defects at the interfaces [319]. Many techniques have arisen in the last few years for the fabrication of quantum

well wires, including MOCVD growth in photolithographically-defined V-grooves etched in a GaAs substrate [320–325], holographic and e-beam lithography and etching of quantum well structures [326–333], selective epitaxy using a masking material [334], MBE growth on (311)-oriented substrates producing corrugated GaAs/AlAs superlattice wires [335], deposition of carbon stressors on a GaAs quantum well to produce a strain-confined quantum well wire [336], MBE growth on a tilted substrate to produce quantum well wire arrays (with the periodicity determined by the vicinal surface misorientation angle) [337–339], ion implantation defined quantum wires [33,340], cleaved-edge overgrowth [341], and MBE growth of serpentine-superlattice quantum well wires [342–344]. Fig. 181 shows the PL spectra at 20 K of quantum wires with lateral widths from 35 nm to 7 nm, which were grown on V-grooved substrates. The quantum well wire emission lies prominently between the bulk GaAs emission and the quantum well emission, and is blue-shifted for increased confinement. The width of these emission lines is approximately 20 meV. Fig. 182 shows the measured energy shift of the PL emission associated with the quantum well wires versus lateral width of the wires. The solid

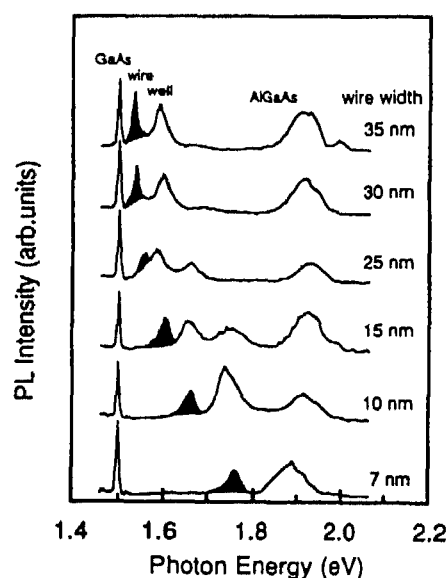


Fig. 181. 9 K PL spectra of quantum wire structures with lateral widths shown (After Kono et al. [324].)

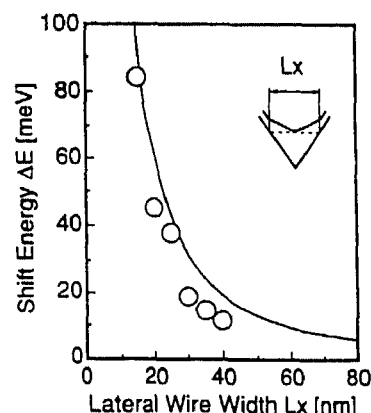


Fig. 182. Energy shift of the PL peaks versus the lateral quantum wire width. Solid line is the theory assuming a triangular wire cross-section (From Arakawa et al., *Semicond. Sci. Technol.*, 8 (1993) 1082.)

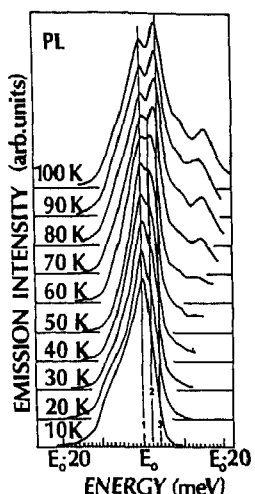


Fig. 183. PL spectra versus temperature. Vertical lines show position of first three transitions involving excitonic center-of-mass quantized states. (After Rinaldi et al. [326])

line represents a calculation of the energy shift of a triangular-shaped wire, which corresponds to the energy shift of a rectangular-shaped quantum well wire of lateral dimensions 60% of the triangular-shaped wire. Excited states in quantum well wires may also be observed, especially at higher temperatures, as shown in Fig. 183 [326]. Here, states up to $n=3$ are observed, especially near 100 K, and higher subbands may also be observed through increased photoexcitation. Under high excitation conditions, exceeding the Mott density, the excitons are screened and form a dense electron-hole plasma, as discussed in section 2.2.6. Fig. 184 shows that the spectra exhibit a step-like background reflecting the occupation of 2D subbands of the quantum well from which the quantum well wires have been fabricated ($n_z=1$ and $n_z=2$). Clearly evident in these spectra are also transitions (up to $n_y=5$) from the quantized states perpendicular to the quantum well confinement direction, the y direction. Rinaldi et al. [325] found that the lineshape of the PL emission from their MBE-prepared quantum wires grown on V-grooved substrates was adequately described by the relation

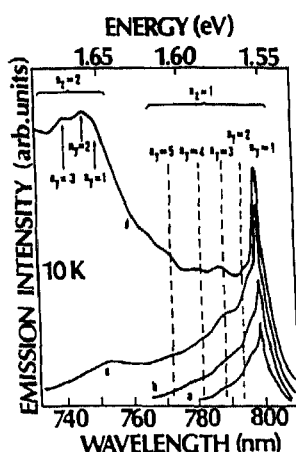


Fig. 184. PL spectra at excitation power densities of (a) $0.125I$, (b) $0.25I$, (c) $0.5I$, and (d) I , where $I = 1 \text{ MW cm}^{-2}$. (After Rinaldi et al. [326].)

$$I(\hbar\omega) \approx \int D(E) G(\hbar\omega - E) f(\hbar\omega) dE \quad (29)$$

where

$$D(E) = \sum_i \frac{1}{\sqrt{E - E_{gi}}}$$

is the one-dimensional density of states convoluted with a Gaussian function to account for inhomogeneous broadening, E_{gi} is the excitonic transition energy of the i th subband, and $f(\hbar\omega)$ is the Boltzmann distribution function. Their fits included both the $n=1$ and $n=2$ subbands with a spectral broadening of 8 meV which results from the fluctuation in width of the quantum well wires.

Quantum well wires also exhibit a large anisotropy in the emission and absorption properties. Fig. 185 shows the PL spectra and PLE spectra of a single quantum well reference sample and a quantum well wire array sample [337]. The angle θ is the polarization angle of the excitation laser light with respect to the horizontal, and the sample was mounted with the wire direction at 45° to the horizontal. The emission at 764 nm, blue-shifted from the reference sample, has a width of 7.7 meV and is associated with the quantum well wires. The tail on the high-energy side is an indication of the broadening of the ground state due to inhomogeneities in the lateral widths of the quantum well wires. The PLE spectra show that the ratio of the electron-light-hole transition to the electron-heavy-hole transition depends strongly on the polarization of the incident light. This sensitivity was not observed in the reference quantum well sample. This optical anisotropy is evidence for two-dimensional quantum confinement. The anisotropy is also evident in the emission spectra, as shown in Fig. 186 for excitation with s- and p-polarized light [329]. The two distinct emission lines here represent transitions to the hh_{11} and hh_{12} excitonic states.

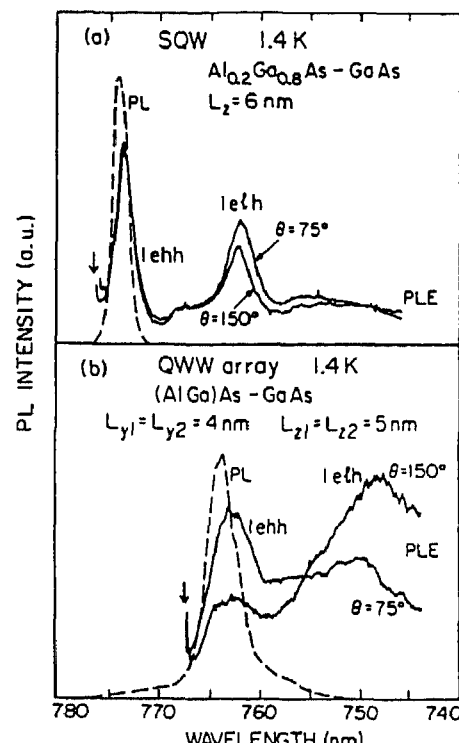


Fig. 185. PL (---) and PLE (—) spectra of a (a) quantum well and (b) quantum well wire array. θ is the polarization angle of the excitation light. (After Tsuchiya et al. [337].)

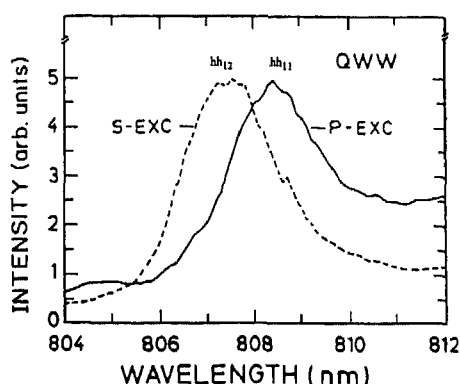


Fig. 186. CW PL spectra of a 70 nm quantum well wire sample after polarized excitation. (After Kohl et al. [329].)

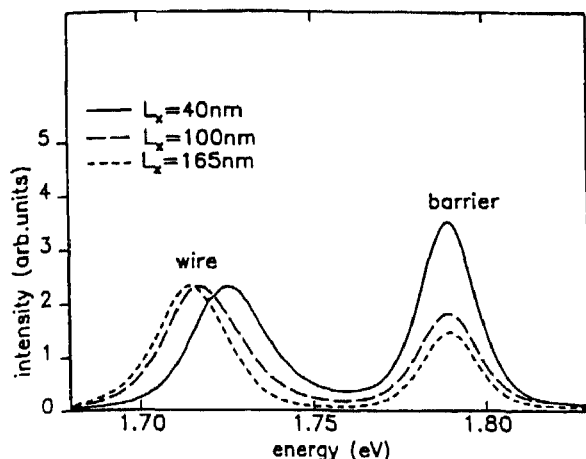


Fig. 187 PL spectra of quantum wire samples with different mask widths at 2 K. (After Leier et al. [340].)

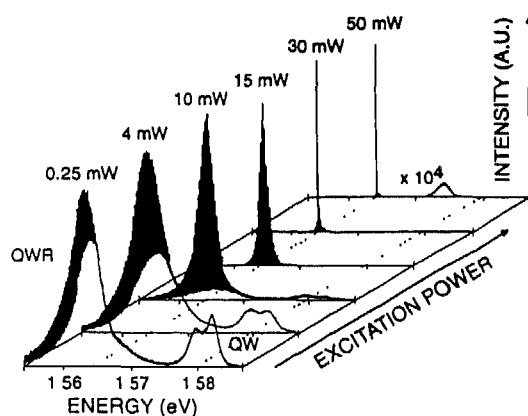


Fig. 188. TE-polarized PL spectra versus excitation power. Threshold for stimulated emission occurs at 10 mW of power. (From Wegscheider et al., *Semicond. Sci. Technol.*, 9 (1994) 1933.)

Quantum wires may also be defined through ion implantation. Fig. 187 shows the PL spectra of three implantation-defined quantum wires of various widths [340]. The blue-shift with decreasing wire size is clearly evident. Cleaved-edge overgrowth yields T-shaped intersections of several nm quantum wells grown along [001] and, after an in-situ cleave, along the [110] crystal axis. Wegscheider et al. [340] have reported the first PL spectra of quantum wires defined by ion implantation.

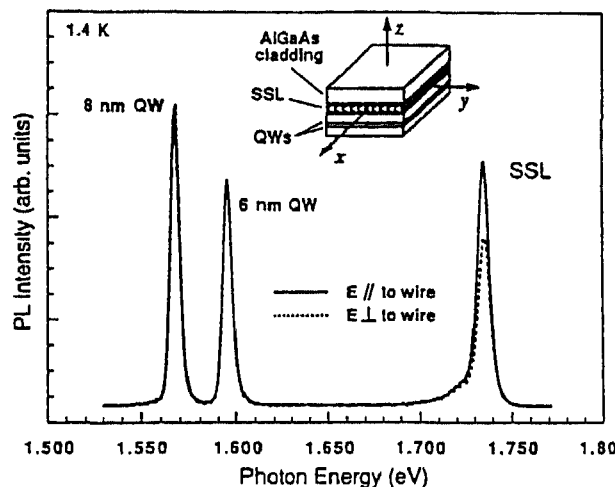


Fig. 189. Polarization dependence of the PL spectra obtained for a quantum well wire sample. Inset defines geometry. (After Miller et al. [343].)

eider et al. [341] fabricated such quantum well wire structures and observed stimulated emission from them. Fig. 188 shows the PL spectra of the quantum well wire at various excitation powers. The distinct line narrowing at higher excitation powers is a clear indication of stimulated emission. Remarkably, they do not observe any bandgap renormalization at high excitation densities. This is an indication of the excitonic nature of the gain, rather than the free-carrier gain commonly observed in III–V nanostructures. Serpentine superlattices quantum-wire arrays are fabricated through epitaxial growth on vicinal (100) substrates with a linear sweep of the deposition. This yields parabolic arcs for the lateral barriers which define the wire [342,343]. Fig. 189 shows the polarization-dependent PL spectra of a serpentine superlattice quantum wire. The peak at 1.735 eV is associated with the serpentine superlattice and has a spectral width of 7.0 meV, and a 23% polarization. This linear polarization along the wires is in agreement with 1D electron-to-heavy hole transitions. Miller et al. [343] conclude on the basis of their measurements that their structures exhibit 1D valence band states and 2D conduction band states. In summary, PL spectroscopy clearly demonstrates the one-dimensional confinement of quantum-wire structures, but significant technological improvements in fabrication are required prior to more detailed studies of dynamical and kinetic effects in such 1D structures.

2.3.5. Quantum dots

Fabrication of quantum dots has been accomplished with a variety of techniques, as with quantum wires, including etch definition [345], selective and non-selective epitaxy on patterned substrates [320,334,346–348], strain-induced lateral confinement [349], laser-beam induced intermixing [350], and nanolithography [333,351–355]. In general quantum dots suffer the same difficulties of fabrication as do quantum wires. Luminescence studies have almost universally found weak luminescence, much more so than the predicted 0D enhancement to the luminescent efficiency [356]. This weak emission efficiency has been widely attributed to extrinsic effects such as etch damage, surface recombination, and surface or interfacial disorder [329,340,357–359]. PL studies of etched quantum dots suggest that non-radiative recombination limits the quantum dots to sizes of ≥ 50 nm [360]. It has also been suggested that inhibited energy relaxation of electrons prevents emission due to the orthogonality of states in the quantum dot [319]. Wang et al. [358] have also found that some recovery of the luminescence intensity may be achieved by overgrowth of etched dots. Fig. 190 shows the 5 K PL

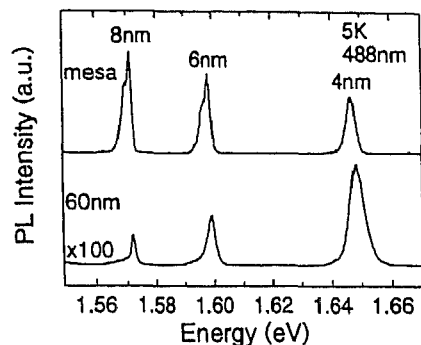


Fig. 190. PL spectra at 5 K of a quantum dot sample with 60 nm dots and a controlled mesa structure (After Wang et al [358])

spectra of 60 nm etch-defined quantum dots and mesa structures. The quantum dot intensity is only 1% of that of the mesa. They further found that the PL emission versus dot size is controlled by a combination of an “intrinsic” process and an “extrinsic” process. Inclusion of the effects of surface recombination (this “extrinsic” process) due to carrier diffusion to the surface yields agreement with their data, with a surface recombination velocity of $S = 1 \times 10^5 \text{ cm s}^{-1}$. This is a reasonable number for bare GaAs surfaces, as will be shown in section 3.2.8. Clausen Jr. et al. [359] have also examined the non-radiative decay in GaAs/AlGaAs etch-defined quantum dots. They find that the emission intensity decreases as the dot size decreases. They model this observation in terms of exciton diffusion and surface recombination, and extract surface recombination velocities of $10^6\text{--}10^{10} \text{ cm s}^{-1}$. Tan et al. [349] have demonstrated the fabrication of strain-induced quantum well dots. Fig. 191 shows the PL spectra of a three quantum well sample before and after etch-defining the strain-induced dots. The lower energy peaks in the etched samples are due to the quantum dots, and the larger red-shift of 14 meV for the 12 nm strain-induced quantum well dot is a result of its proximity to the stressor layer. They find that the PL intensity of the dots is degraded by only 20% compared to the reference sample, thus demonstrating the low-damage nature of their fabrication approach. Nagamune et al. [348] have grown GaAs quantum dots with lateral dimensions of 25 nm through in-situ MOCVD selective growth

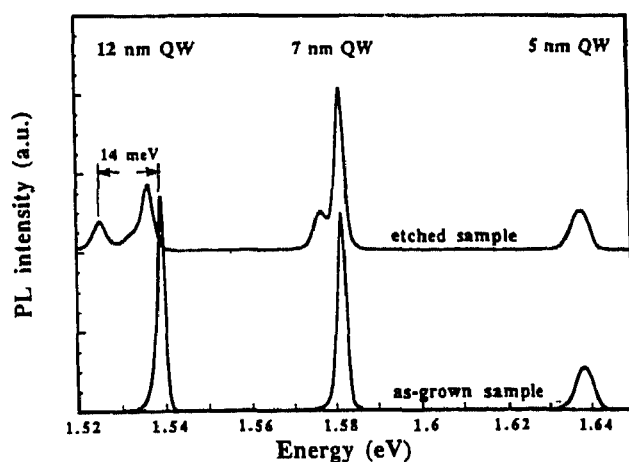


Fig. 191. PL spectra of as-grown and etched strain-induced quantum dot samples (After Tan et al. [349].)

on masked substrates. Fig. 192 shows the PL spectrum of their sample where the emission at 1.530 eV corresponds to the GaAs dot, while that at 1.511 eV and 1.493 eV originate from impurities in the bulk. The broad peak at 1.59 eV is associated with thin GaAs quantum wells with a thickness of 60 Å which were grown on (110) sidewalls of the AlGaAs plinths. The intensity of the PL spectra due to the GaAs quantum dots is very large when the filling factor is taken into account. The blue-shift (due to 3D quantum confinement) of the emission is 19 meV, which is slightly larger than that of 150 Å thick quantum wells (16 meV), but considerably smaller than the theoretical value of 35 meV. Brunner et al. [350] examined the PL emission from single GaAs/AlGaAs quantum dots created by focused laser-beam induced intermixing of a 30 Å quantum well. Fig. 193 shows the PL spectra of single dot structures of lateral sizes ranging from 1000 nm down to 300 nm. As the dot size decreases the spectra exhibit a blue-shift and a splitting of the emission. The 450 nm dot exhibits three main peaks corresponding to the $n = 1, 2$, and 3 lateral quantum numbers. At still smaller dot sizes the splitting decreases to intermixing within the dot itself. Importantly, these spectra are considered to not be inhomogeneously broadened since the measurements were conducted on a single quantum dot.

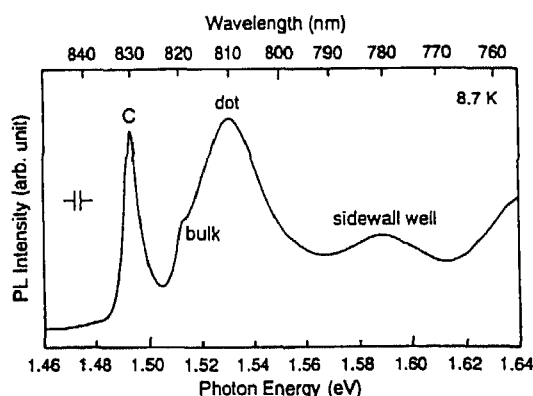


Fig. 192. PL spectrum at 8.7 K of a GaAs quantum dot. (After Nagamune et al. [348].)

2.4. Additional perturbations

Most PL studies combine some perturbation to the system with the spectroscopic measurement in order to elucidate a specific aspect of the dynamics of the semiconductor. These perturbations may alter, in a controllable fashion, for example, the electronic structure, the crystal symmetry, the Fermi level, and the Bohr radii of carriers. Among the most common perturbations are high pressure, electric fields, magnetic fields, and uniaxial stress. In this section the effects of these four perturbations on the PL spectra of semiconductors will be examined.

2.4.1. High pressure

Pressure has been recognized as a powerful tool in the study of semiconductors. Early studies showed that the band structure and energy levels of impurities are very sensitive to pressure-induced changes in the interatomic distance. Hydrostatic pressure is a fundamental thermodynamic perturbation

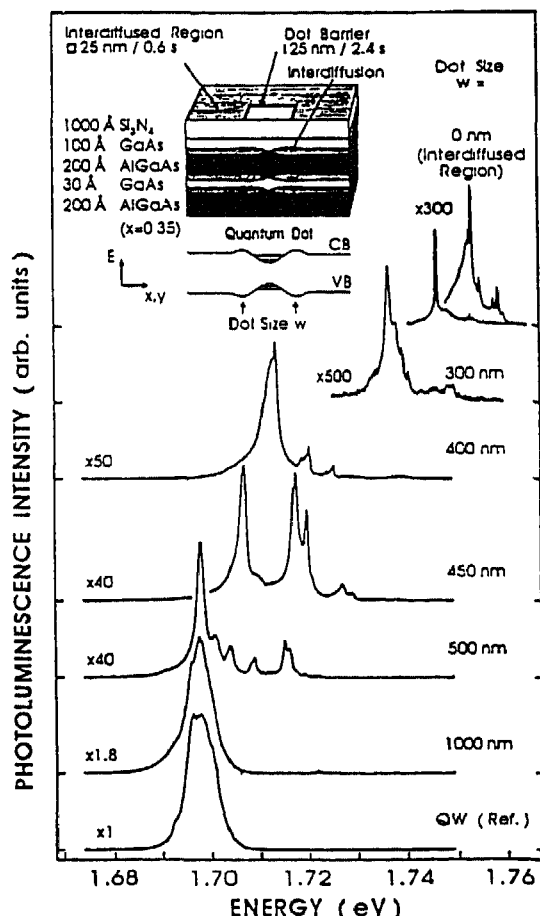


Fig. 193. PPL spectra of single quantum dots of various size. Inset shows a diagram of the dot structure which was fabricated by focused laser beam-induced interdiffusion of a 30 Å GaAs quantum well. (After Brunner et al. [350].)

which may be used to continuously vary interatomic distances, thereby also continuously changing the electronic structure of the semiconductor. High pressure is useful in determining fundamental material parameters, examining localizing potentials and band structure in the formation of defect levels, observing "mixing" between different electronic states, and inducing new electronic structure. Unlike other perturbations such as electric or magnetic fields, uniaxial stress, temperature, and alloying, hydrostatic pressure maintains both the symmetry of the crystal and the atomic order. Another particular advantage of pressure studies is that changes in the electronic structure (with pressure) may be examined in a single sample where the composition, densities and types of impurities, defects, etc. is unchanged. This is crucial in examining the changes in PL emission intensities as the electronic structure is changed.

High-pressure measurements are performed by placing the sample in a diamond anvil cell (DAC). There are many types of DACs, and Fig. 194 shows a typical cell [361]. This particular type of cell consists of matched pairs of brilliant-cut, gem-quality diamonds which are mounted in hardened metal platens. The metal gasket is a thin stainless-steel sheet with a ~300 µm hole drilled in it. The sample, suitably thinned to fit in the DAC, is placed in this hole, between the faces of the diamonds. In addition, a transparent pressure-transmitting medium (typically argon, methanol–ethanol–water solution, liquid helium, or n-pentane/isopentane) and a small piece of ruby are placed in this pressure volume with

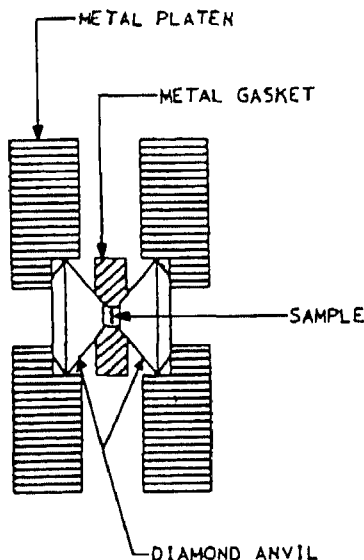


Fig. 194. Cross-sectional view of a diamond anvil cell. Metal platens hold diamonds in place. The pressure medium and sample is contained between the diamonds and inside the metal gasket. (After Wolford [361].)

the sample. The high pressures thus generated may be hydrostatic to better than one part in 600 [90]. At low and moderate pressures (≤ 300 kbar) the luminescence from the R-lines of ruby are used to calibrate the pressure. The R1-line emission of the ruby shifts to lower energy with pressure from its ambient emission energy of 14406.74 cm^{-1} at a rate of 0.76 cm^{-1} per kbar of pressure [362]. Ruby fluorescence may also give some indication to the hydrostaticity of the pressure. Although the R1 emission line from ruby is several cm^{-1} broad, any pressure-induced broadening of this emission line may be an indication of slight non-hydrostatic pressure. (A possibly better and more sensitive indicator of non-hydrostatic pressure may be any broadening of the bound exciton luminescence in GaAs [90].) Laser excitation and PL collection is then done through one of the diamonds in the DAC.

The PL spectrum of bulk GaAs changes drastically with hydrostatic pressure. Fig. 195 shows the PL spectra of an undoped, n-type bulk sample of GaAs at pressures from 4 to 60 kbar [361]. Below ~ 41 kbar the dominant emissions are due to direct free excitons (F_Γ , $n=1,2$), donor-bound excitons (D_Γ), and band-to-Si-acceptor recombinations. At higher pressures (≥ 42 kbar) the bulk GaAs bandstructure is indirect. The emissions at these pressures are dominated by the indirect free excitons (F_X), indirect donor-bound excitons ($D^0 X$), and their phonon replicas. Near the direct-indirect crossover, donor recombination from both the direct and indirect edges is observed simultaneously. Fig. 196 shows a summary of the pressure dependence of all emission peaks versus pressure. This demonstrates clearly that these near-edge states shift linearly with pressure, as expected for shallow "effective-mass" impurities. Assuming indirect-gap free exciton and donor-exciton binding energies of 22 meV and 18 meV, respectively, and a direct donor-bound exciton energy of 8 meV, yields the pressure coefficients of the direct (Γ) and indirect (X) gaps of $10.7 \text{ meV kbar}^{-1}$ and $-1.34 \text{ meV kbar}^{-1}$, respectively. The direct-indirect Γ -X crossover occurs at 41.3 kbar. Extrapolating the results back to atmospheric pressure gives the GaAs X-gap at 2.010 eV.

High pressure also affects the band structure of alloys. In $\text{Al}_x\text{Ga}_{1-x}\text{As}$ the band ordering changes from Γ -L-X to X-L- Γ for $x \leq 0.45$ (initially direct bandgap) with the application of pressure [363]. Fig. 197 shows the peak energies of the PL emission in an $\text{Al}_{0.3}\text{Ga}_{0.7}\text{As}$ sample versus pressure. In this figure peaks B and D are associated with indirect-donor-acceptor pair emissions, and peak C is a TA phonon replica. For this composition of alloy, the direct-indirect crossover occurs at 14 kbar (assuming

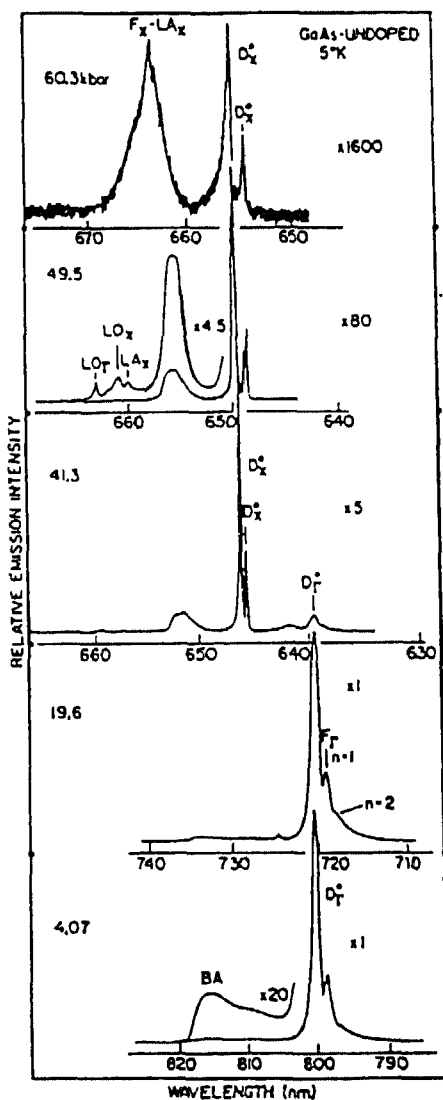


Fig. 195. 5 K PL spectra of undoped n-type GaAs epilayers versus hydrostatic pressure. (After Wolford [361].)

the indirect free-exciton is 30 meV below the X conduction band and the direct-donor-bound exciton is 10 meV below the direct conduction band).

In silicon the indirect X-edge decreases in energy with pressure at a rate of -1.8 ± 0.2 meV kbar^{-1} [141]. Northrop and Wolford [364] have examined the pressure dependence of luminescing impurity centers in Si at 1018 meV, 970 meV, and 790 meV, known as the I_1 , G, and C centers, respectively. All three of these centers are complexes and exhibit low symmetry. The G center consists of a C pair. The C center is known to contain C and O, and the origin of the I_1 center is unknown. Fig. 198 shows the pressure-dependent PL spectra for a low-doped (10^{15} cm^{-3}) Si sample at 15 K. The I_1 spectra consist of an intense no-phonon line at 1018 meV at atmospheric pressure, and phonon replicas at lower energies. The no-phonon line increases in energy with increasing pressure, thereby not following the bandgap change with pressure. This is an indication of the "deep-level" nature of the complex associated with I_1 emission. Fig. 199 shows the PL spectra versus pressure for H^+ -implanted Si samples. In this data several luminescing centers are evident, most notably among them is the G

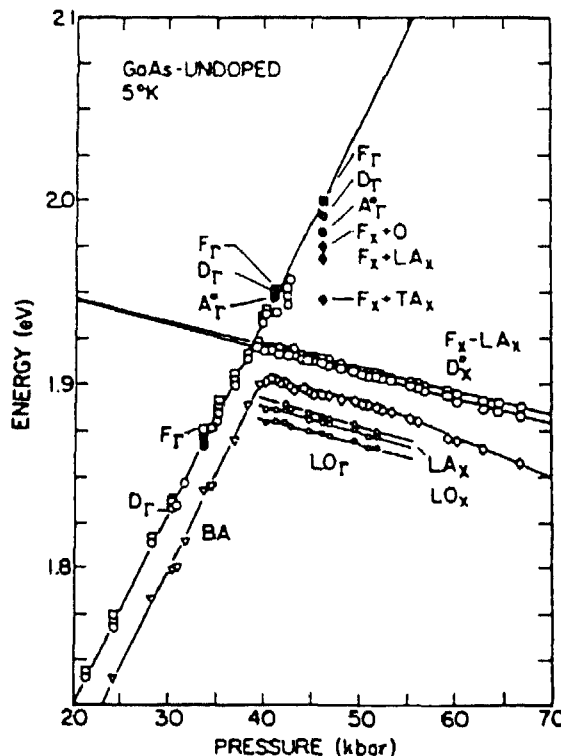


Fig. 196. 5 K PL and PLE peak energies of undoped n-type GaAs epilayers versus hydrostatic pressure. The direct-indirect crossover occurs at 41.3 kbar. (After Wolford [361].)

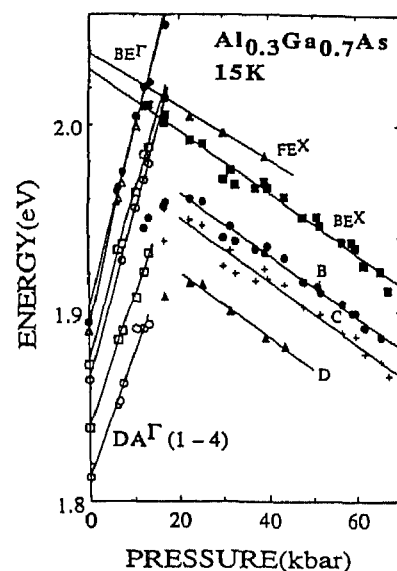


Fig. 197. PL peak energies of $\text{Al}_{0.3}\text{Ga}_{0.7}\text{As}$ epilayer at 15 K versus hydrostatic pressure. (After Roach et al. [363].)

center. (E represents a local vibrational mode.) Fig. 200 summarizes the pressure dependence of all the spectral features evident in Figs. 198 and 199. This data yields the pressure dependence of the X-edge as $-1.68 \pm 0.05 \text{ meV kbar}^{-1}$. The pressure coefficient of the I_1 line varies from $0.45 \text{ meV kbar}^{-1}$

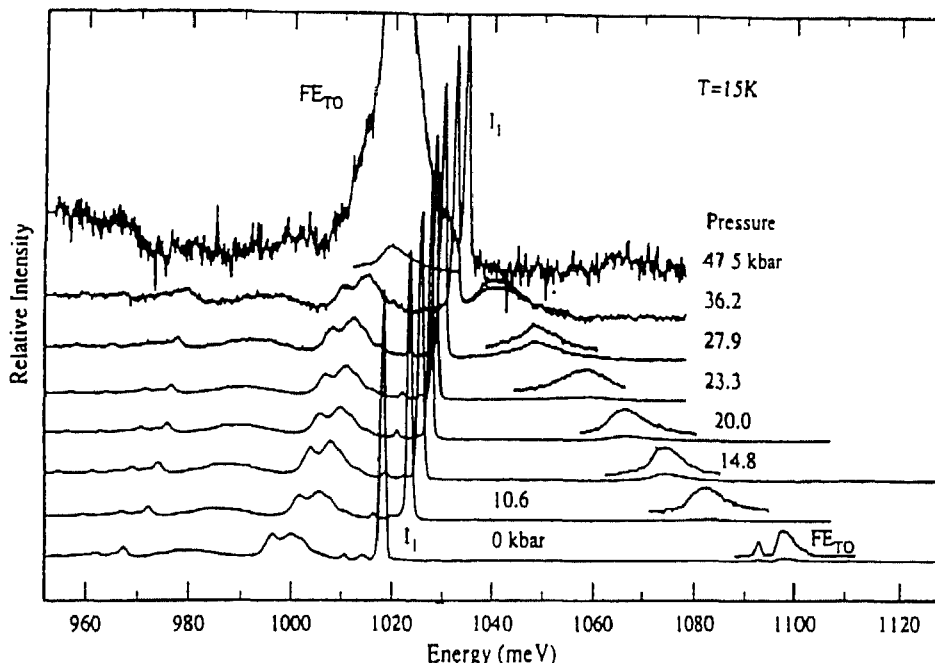


Fig. 198. Hydrostatic pressure dependence of PL spectra from a Si^+ -implanted sample. Here the I_1 intensity is normalized (After Northrop and Wolford [364].)

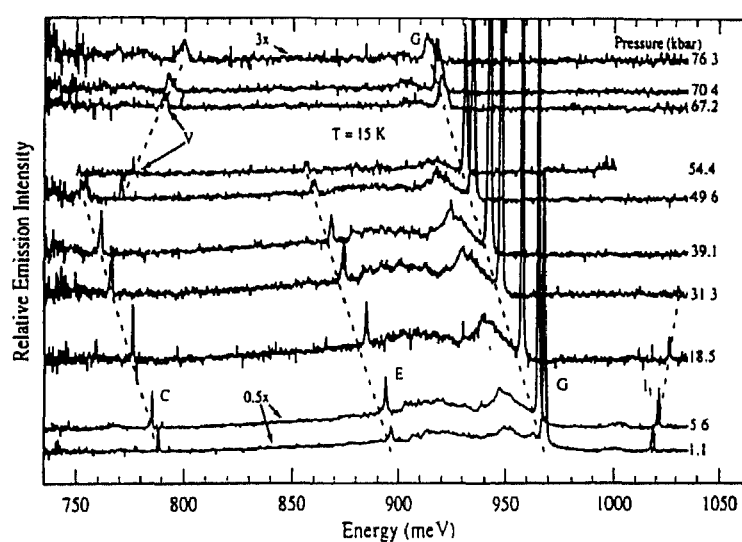


Fig. 199. Hydrostatic pressure dependence of the PL spectra from an H^+ -implanted sample. (After Northrop and Wolford [364].)

at low pressures to $0.25 \text{ meV kbar}^{-1}$ above 25 kbar . This suggests a pressure-dependent change in electronic-state mixing. The I -line decreases in energy with pressure at a rate of $-0.74 \text{ meV kbar}^{-1}$. The C-line also decreases in energy with pressure at a rate of $-0.71 \text{ meV kbar}^{-1}$. At pressures above 49 kbar a new emission line appears, the V-line. Its energy increases with pressure at a rate of $1.02 \text{ meV kbar}^{-1}$. The origin of this V-line is currently unknown.

It has already been shown (in section 2.3.3.4) that pressure studies of quantum wells are useful for determining band offsets. Pressure is also useful in testing the validity of the "effective-mass"

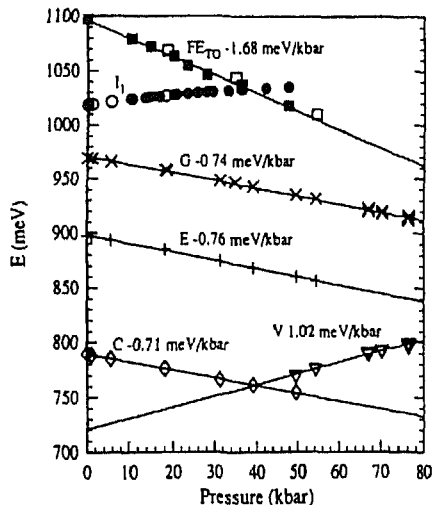


Fig. 200. Hydrostatic pressure dependence of the no-phonon line peak energies together with the TO-phonon replica of the free exciton. The solid circles and filled squares are data from the Si^+ sample, whereas all other data are from the H^+ samples. (After Northrop and Wolford [364].)

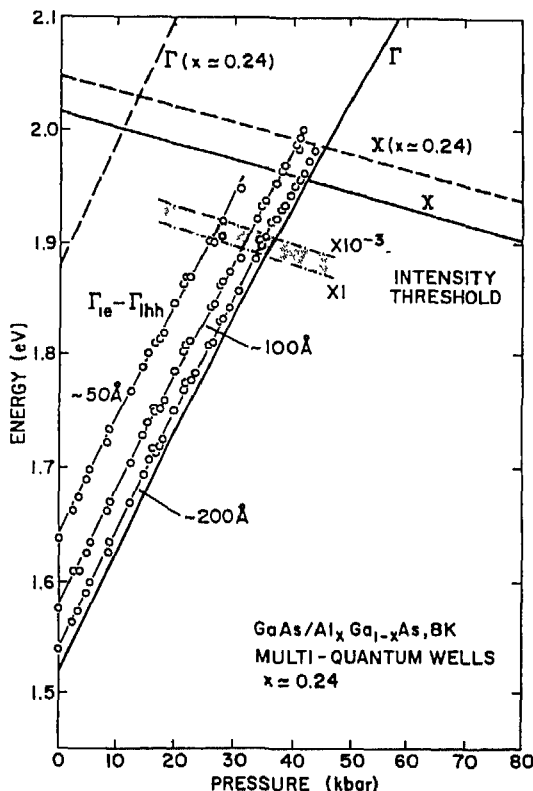


Fig. 201. Pressure dependence of the PL peak energies of a three-well $\text{GaAs}/\text{Al}_{0.24}\text{Ga}_{0.76}\text{As}$ multiple quantum well together with the pressure dependence of the G and X gaps of GaAs and $\text{Al}_{0.24}\text{Ga}_{0.76}\text{As}$. Well widths are 200, 100, and 50 Å. PL intensities decrease by more than a factor of 1000 in the vicinity of the shaded region. (After Wolford et al. [305].)

approximation which is commonly used to describe the energy levels of quantum wells. Fig. 201 shows the pressure dependence of the ground state PL transitions in a three-well multiple quantum well $\text{GaAs}/\text{Al}_{0.24}\text{Ga}_{0.76}\text{As}$ sample [305,361]. Clearly, the $\Gamma_{1e} - \Gamma_{1hh}$ transition energies follow the GaAs

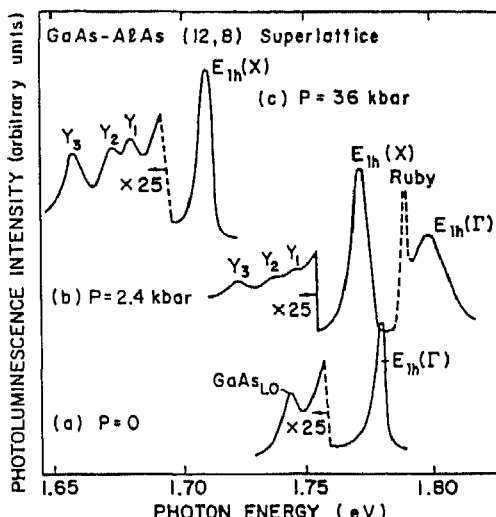


Fig. 202. PL spectra at 15 K of GaAs/AlAs superlattice at three pressures. At atmospheric pressure the structure is type I, with a strong no-phonon emission line, and weaker localization-induced LO-phonon replicas. At higher pressures the type I to type II crossover occurs, as evidenced by the phonon replicas. (After Spain et al [365].)

bandgap with increasing pressure. The observed displacement to higher energies is a result of quantum-confinement effects. Detailed least-squares fittings of the slopes of this data reveals that the 200 Å, 100 Å, and 50 Å transition energies increase at a rate of 10.4 meV kbar⁻¹, 10.2 meV kbar⁻¹, and 9.9 meV kbar⁻¹, respectively. This trend is an indication that the pressure dependence is due to the increasing spread of the wavefunctions in momentum space as well width is decreased, and is not due to changes in the mass of electrons or holes. This is an example of “shallow” states with a small amount of “deep” character. Also evident in Fig. 201 is that the PL intensity of the 50 Å well decreases dramatically with pressure above 25 kbar, and this decrease in emission moves successively to the next wider well with increasing pressure. This “threshold” occurs at pressures below the direct-indirect crossover. This threshold is a result of the crossover of the GaAs well direct edge (Γ) with the Al_{0.24}Ga_{0.76}As indirect X-edge in the adjacent layer. This is consistent with the band-offset measurements reported in section 2.3.3.4. Thus the excitons are no longer bound in the quantum well and may escape to the Al_{0.24}Ga_{0.76}As barriers.

Pressure may also be used to induce a transition from a type-I band alignment to a type-II band alignment. Fig. 202 shows the PL spectra of a GaAs/AlAs superlattice sample versus pressure [365]. At atmospheric pressure the emission is consistent with a type-I band alignment and a $\Gamma_{1e}-\Gamma_{1hh}$ transition. At 2.4 kbar, however, the type-I to type-II transition is evident. The $X_{1e}-\Gamma_{1hh}$ transition occurs at lower energy than the $\Gamma_{1e}-\Gamma_{1hh}$ transition. At still higher pressures (36 kbar) the $\Gamma_{1e}-\Gamma_{1hh}$ transition is no longer evident. At the onset of the type-I to type-II transition three additional peaks become evident in the spectra, Y₁, Y₂, and Y₃. These are the well-known phonon replicas which commonly occur in type-II spectra. Fig. 203 shows the variation of the PL peak energies versus pressure for several GaAs/AlAs superlattices. The $\Gamma_{1e}-\Gamma_{1hh}$ transition energy increases with pressure at a rate consistent with the pressure dependence of the GaAs conduction band edge. In contrast, the $X_{1e}-\Gamma_{1hh}$ transition energy decreases with pressure at a rate (-2.25 meV kbar⁻¹) greater than that of the X-indirect edge of GaAs. This is a result of the pressure dependence of the GaAs/AlAs valence-band offset. The energy differences between the Y_i lines ($i=1-3$) and the $X_{1e}-\Gamma_{1hh}$ no-phonon line

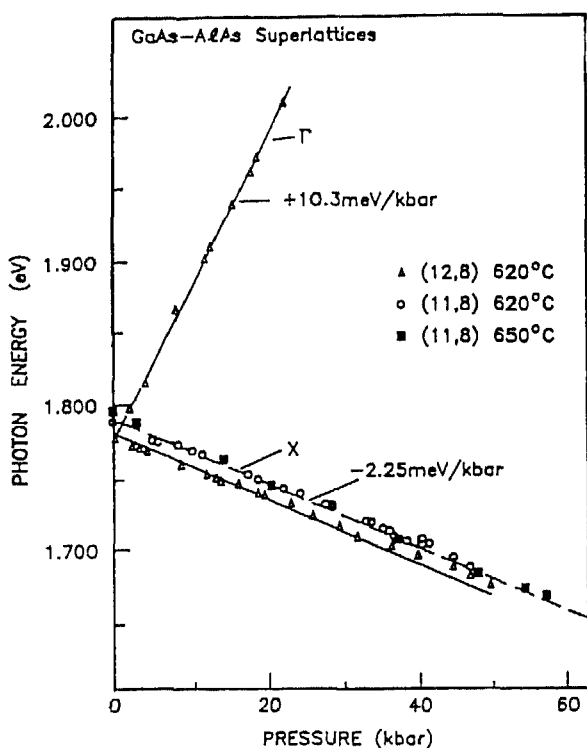


Fig. 203. Pressure dependence of the PL peak energies at 1.5 K. (After Spain et al. [365])

are the phonon energies. The spectra show that these phonon energies increase by $\sim 5\%$ with pressure from 0 to 60 kbar. This is consistent with Raman scattering measurements versus pressure.

Pressure may also be utilized to study the change of effective mass of carriers with pressure. Pressure-induced changes in the band structure of a semiconductor affect the curvature of the $E-k$ dispersion curves, thereby modifying the electron and hole effective masses. Zhou et al. [366] recently examined the high-pressure, magnetophotoluminescence of modulation-doped quantum well samples. Fig. 204 shows the magnetophotoluminescence spectra at 5 T for pressures from atmospheric pressure to 13 kbar. Below 9 kbar the spectra exhibit Landau-like peaks, labeled (0-0), (1-1) for band-to-band recombination, and (0-A), (1-A) for band-to-acceptor emissions. At higher pressures the spectra are indicative of magnetoexcitonic behavior. There is a transition from a linear shift to a diamagnetic shift. At 1 atm of pressure the slopes of the Landau fans, shown in Fig. 205, yield electron and hole effective masses of $0.067m_0$ and $0.62m_0$, respectively. The hole effective mass does not change significantly with pressure [367], and therefore the observed change in the fan diagram must be the result of a change in the electron effective mass. This yields a change of the electron effective mass of $0.9 \pm 0.3\% \text{ kbar}^{-1}$.

2.4.2. Magnetic field

Photoluminescence measurements in a magnetic field are a valuable probe of the electronic structure of free carriers, free excitons, and impurities in semiconductors. Fig. 206 shows a typical schematic equipment arrangement for magnetoluminescence measurements. Here the magnetic field is generated by a superconducting solenoid immersed in liquid helium. Helmholtz coils are also used for experiments allowing both Faraday (field parallel to laser excitation k vector) and Voigt (field perpendicular to laser excitation k vector) geometries.

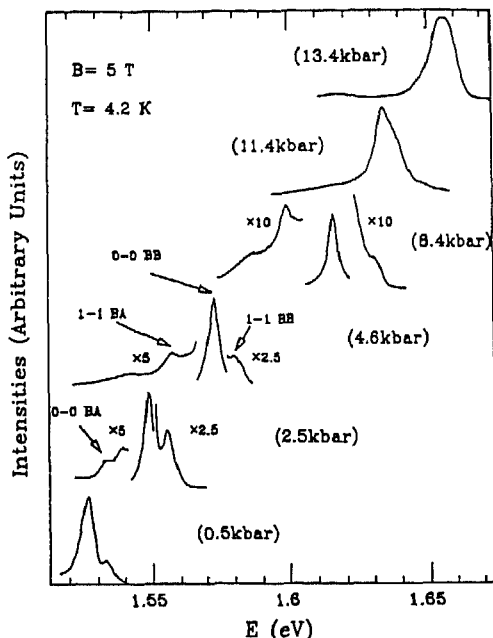


Fig. 204. Magneto-PL spectra of a modulation-doped quantum well sample at 4.2 K versus pressure in a magnetic field of 5 T. The peaks labeled (0-0), (1-1), etc. are Landau-like, the peaks labeled (BB) band-to-band, and those labeled (0-A), (1-A), etc. band-to-acceptor, respectively (After Zhou et al. [366].)

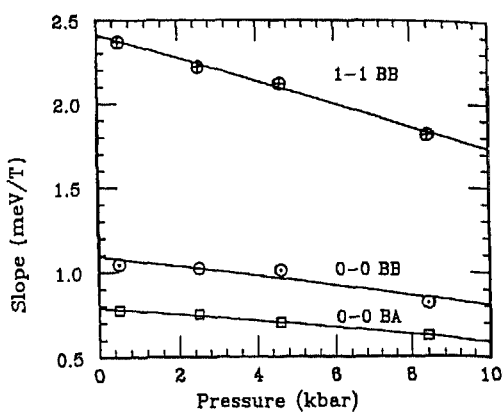


Fig. 205. Slopes of the Landau fans as a function of pressure. (After Zhou et al. [366].)

Magnetic fields may be used to alter the energy spectrum of free carriers in the conduction and valence bands (i.e. electrons and holes). The resulting energy levels are a set of Landau subbands with a quasi-1D dispersion in the direction along the magnetic field, with a separation given by the cyclotron energies, $\hbar\omega_{c,e,h}$. Allowed optical transitions occur between electron and hole Landau levels with identical Landau quantum numbers, and these transitions allow a determination of the reduced effective mass of the electron-hole system [368]. Lyo et al. [369] and Reynolds et al. [368] have also found that it is possible to observe transitions which are non-allowed ($\Delta n \neq 0$) and off-diagonal. These off-diagonal transitions allow the independent determination of electron and hole masses without having to rely on conduction band to acceptor transitions. The energy of the transition is given by

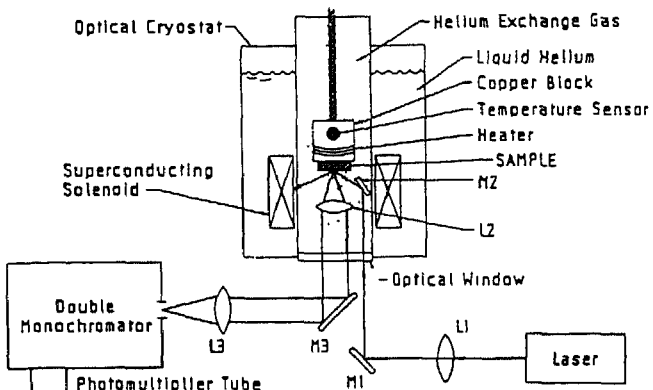


Fig. 206. Typical experimental arrangement of instrumentation for magnetoluminescence measurements

$$E(n_e, n_h) = \left(n_e + \frac{1}{2} \right) \frac{\hbar e B}{m_e^* c} + \left(n_h + \frac{1}{2} \right) \frac{\hbar e B}{m_h^* c} \quad (30)$$

For allowed transitions ($n_e = n_h$) the transition energies clearly yield the reduced mass of the electron-hole system. The parity-forbidden off-diagonal elements allow determination of the electron and hole effective masses independently. Fig. 207 shows the transition energies of a modulation-doped single-heterojunction GaAs/AlGaAs structure versus field as obtained from PL and PL-excitation measurements. The Landau-level assignments reveal evidence for both allowed and forbidden transitions. These data yield a reduced electron-hole pair mass of $0.07m_e$. From the forbidden transitions, the electron effective mass is found to be $0.085m_e$, which yields a heavy-hole effective mass consistent with the electron-hole pair reduced mass.

Recently, Gubarev et al. [370] observed very sharp PL lines in the magnetoluminescence spectra of bulk GaAs. Their experiments were performed in the Faraday geometry and included polarization differentiation. Excitation was 10–70 meV above the bandgap. Fig. 208 shows the PL spectra taken at magnetic fields from 6 to 6.8 T with near resonant excitation. The emission line is strongly dependent upon the magnetic field, shifting to higher energies and becoming more intense with increasing field. The spectral position of the line is governed by the strength of the magnetic field, whereas the intensity is governed by the “detuning” of the excitation from the emission line. Fig. 209 shows the magnetoluminescence spectra of the sample taken with both polarizations of light. Here the excitation and detection energies were fixed and the magnetic field was scanned. There are more than 14 resonances which do not occur at the same field for the two different polarizations. These peaks correspond to successive interband optical transitions between Landau levels and are evident in the spectrum when the Landau transition energy matches the detection wavelength. The energy difference between the peaks for the two circular polarized excitation/detection configurations is an indication that light-hole levels are involved in the observed transitions. Fig. 210 shows the Landau fan diagrams for the data shown in Figs. 208 and 209. At zero field the Landau levels converge to the same energy $E_0 = 1518$ meV, approximately the direct-gap of GaAs. Gubarev et al. analyzed their spectra by taking into account band non-parabolicity and including transitions with both heavy and light holes. For the conduction band there are two sets of Landau levels corresponding to different spins $\sigma = \alpha, \beta$ with energies

$$E_\sigma^c = E_g + \hbar \omega_c \left(n + \frac{1}{2} \right) + \frac{\hbar^2 k_z^2}{2m_e^*} + \mu_B g_e^* \sigma H \quad (31)$$

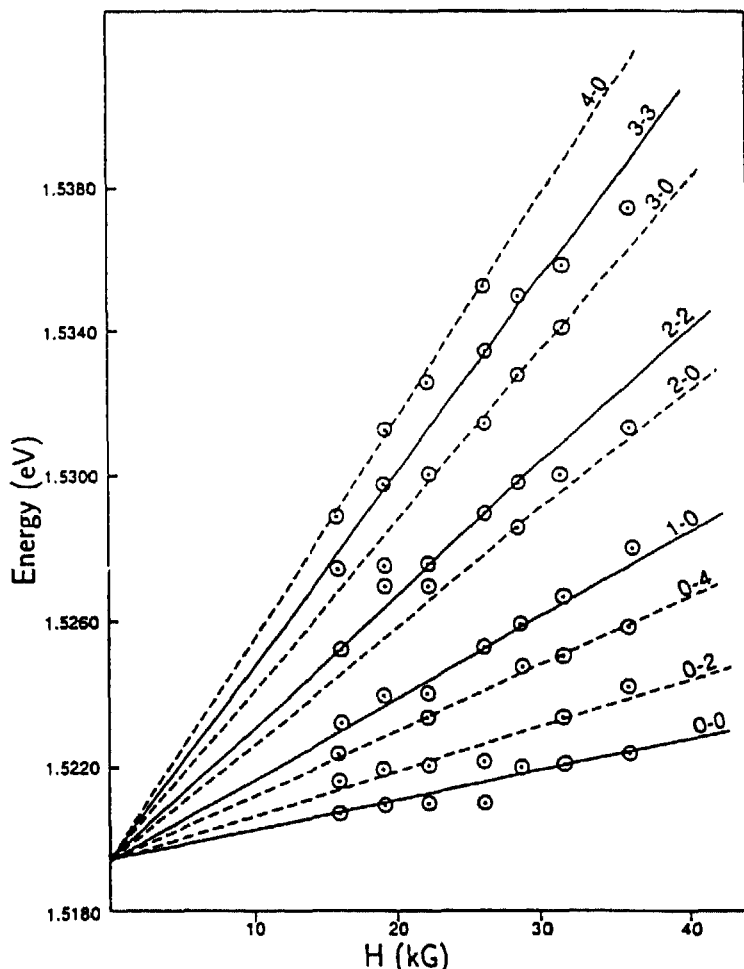


Fig. 207 Landau fan diagram derived from PLE measurements on a GaAs/AlGaAs single-heterojunction sample. Solid (dashed) lines are allowed (forbidden) transitions. (After Reynolds et al. [368].)

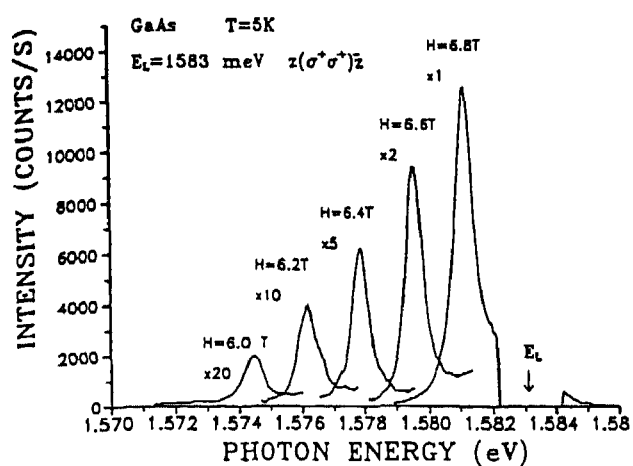


Fig. 208. GaAs PL spectra versus magnetic field in the $z(\sigma^+ \sigma^+)z$ configuration. (After Gubarev et al. [370].)

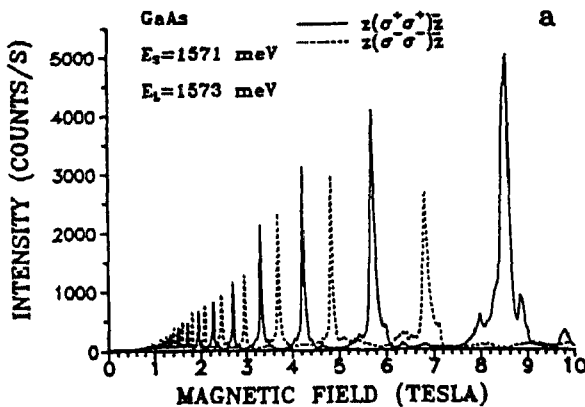


Fig. 209. PL intensity at 1571 meV as a function of magnetic field in the $z(\sigma^+\sigma^+)z$ (—) and $z(\sigma^-\sigma^-)z$ (---) configurations (After Gubarev et al [370].)

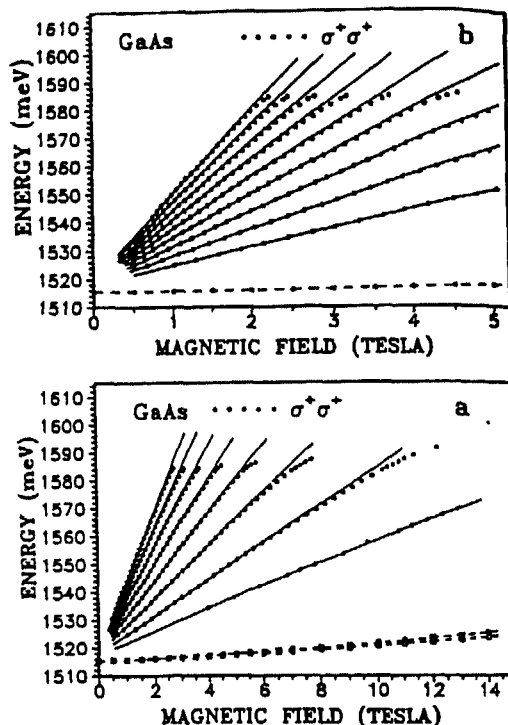


Fig. 210. Fan diagrams of the magneto-PL peak energies in the $z(\sigma^+\sigma^+)z$ configuration. Lines are quadratic (in H) fits. Upper panel is a blow-up of the low-field region (After Gubarev et al. [370])

where n is the Landau level index, $\omega_c^e = eH/m_e c$ is the cyclotron frequency, and E_g is the energy gap. For the valence band the situation is considerably more complex, and the energies of the light- and heavy-hole bands are given in terms of the Luttinger parameters. The cyclotron frequencies for both light and heavy holes in the classical limit are given by

$$\omega \pm = \frac{eH}{m_0 c} [\gamma_1 \pm (\gamma'^2 + 3\gamma''^2)^{1/2}] \quad (32)$$

where γ_1 , γ' , and γ'' are related to the Luttinger parameters. The selection rules allow transitions with

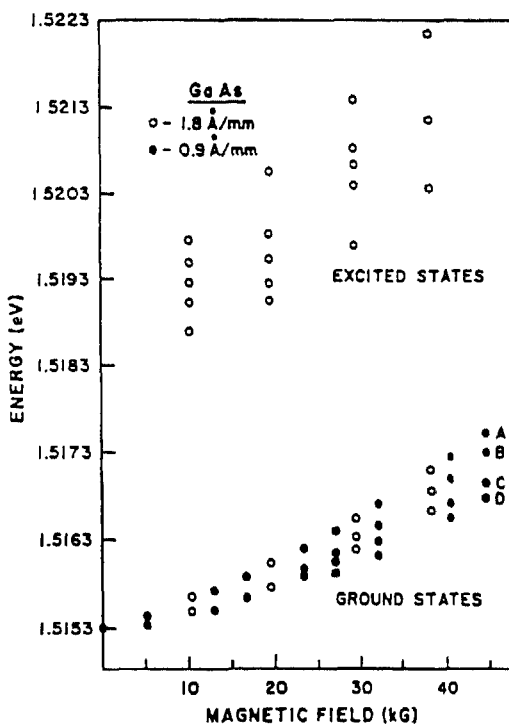


Fig. 211. Magnetic-field dependence of the excitonic ground and excited states of the free exciton in GaAs. (After Nam et al [371].)

$n=m$ for σ^+ transitions and $n=m-2$ for σ^- transitions. The energy difference between different Landau levels yields the reduced mass of the electrons and holes. Assuming an electronic effective mass of $0.067m_0$, Gubarev, et al. find a light-hole effective mass of $m_{lh} = (0.078 \pm 0.002)m_0$.

Nam et al. [371] examined the magnetoluminescence of free excitons in GaAs. Fig. 211 shows the magnetic field dependence of the ground and excited states of the free exciton. The $n=1$, $n=2$, and $n=3$ states are evident in the data. The $n=2$ zero-field energy is 1.5185 eV. From these data the exciton binding energy of 4.2 ± 0.3 meV and the bandgap energy of 1.5195 ± 0.0005 eV are deduced. At low fields the quadratic shift of the energy level with field is observed. In a magnetic field, the polarized luminescence spectra exhibit a splitting into doublets for the free-exciton emission. Fig. 212 shows the right- and left-circularly polarized spectra for a sample in a field of 6.4 T [24]. This splitting is as expected for the $J=1, 2$ exciton states in a magnetic field. Fig. 213 shows the field dependence of the peak energies of the various peaks in both polarizations, which clearly exhibits a quadratic dependence.

Henriques et al. [372] studied the magnetoluminescence of asymmetric, heavily modulation-doped ($8.2 \times 10^{12} \text{ cm}^{-2}$) GaAs/AlGaAs quantum wells in magnetic fields up to 15 T. Fig. 214 shows the PL spectra, in 1 T intervals, for fields up to 15 T. As the field increases the Landau levels shift to higher energy, and the higher Landau levels become increasingly weaker due to depopulation of these higher levels. At 15 T only the luminescence from the $n=0$ and $n=1$ Landau levels are evident. These peak energies versus magnetic field yield the familiar fan diagram shown in Fig. 215. There are several interesting features observable in this data. First, the E1-H1 transition splits above 12 T. This is believed to be due to the spin splitting in the valence band. Also, the fan diagram exhibits oscillations in the transition energy, most prominently in the 2s branch. Magnetoluminescence measurements of heavily modulation-doped quantum wells have also uncovered $n=2$ heavy- and light-hole transitions [373]. Fig. 216 shows the PL spectra of a heavily n-type modulation-doped GaAs/AlAs quantum

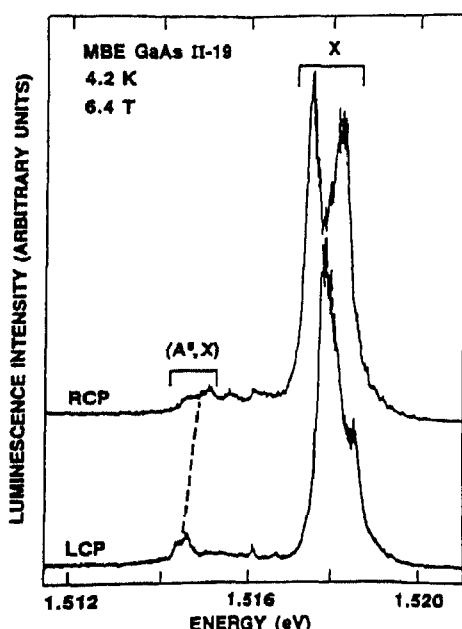


Fig. 212. Low-temperature PL spectra in a magnetic field of 6.4 T for both right- (RCP) and left-circularly-polarized (LCP) emission. (Reprinted from Koteles et al., *Solid State Commun.*, 62 (1987) 703, with permission from Elsevier Science Ltd., Pergamon Imprint, The Boulevard, Langford Lane, Kidlington OX5 1GB, UK.)

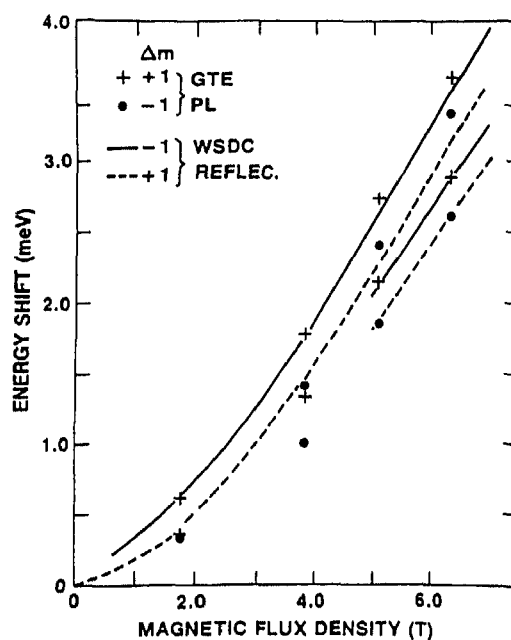


Fig. 213. Peak energy positions of the PL emissions versus magnetic field (Faraday geometry). (Reprinted from Koteles et al., *Solid State Commun.*, 62 (1987) 703, with permission from Elsevier Science Ltd., Pergamon Imprint, The Boulevard, Langford Lane, Kidlington OX5 1GB, UK.)

well at zero field and at 9 T [374]. The width of the PL at zero field (42 meV) yields the position of the Fermi level, and an electron density of 10^{12} cm^{-2} . In a magnetic field, the broad luminescence splits into three distinct peaks corresponding to the 0–0, 1–1, and 2–2 interband Landau transitions.

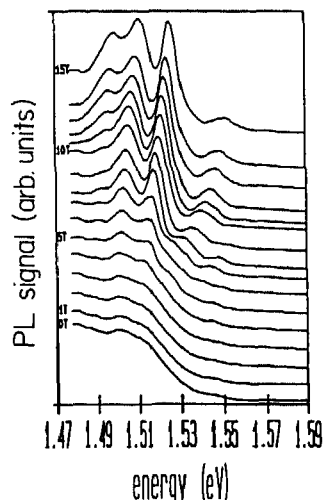


Fig. 214. PL spectra, in 1 T intervals, of a modulation-doped GaAs/AlGaAs quantum well (After Henriques et al. [372].)

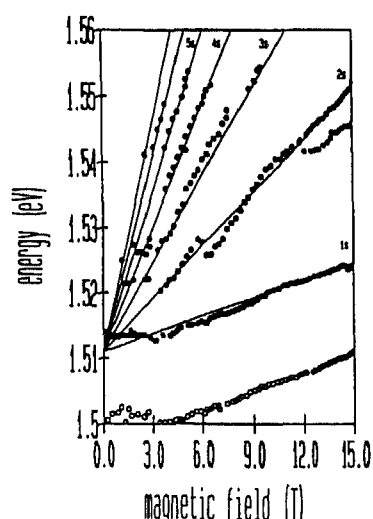


Fig. 215. Fan diagram of the PL peak energies versus magnetic field. —, theoretical model including non-parabolicity. (After Henriques et al. [372].)

Delalande et al. [375] have found that the Landau level spectra in n-type GaAs/AlGaAs modulation-doped quantum wells gives strong evidence for the complex structure of the valence band and the coupling between subbands in the valence bands.

Measurements of the net polarization of the luminescence of a sample in a magnetic field may be used to determine the spin relaxation time. If the net polarization of the luminescence is defined as

$$\rho = \frac{I^+ - I^-}{I^+ + I^-} \quad (33)$$

where I^+ and I^- are the luminescence intensities after excitation with right and left circularly polarized light, then the electron spin relaxation time may be determined from the relations

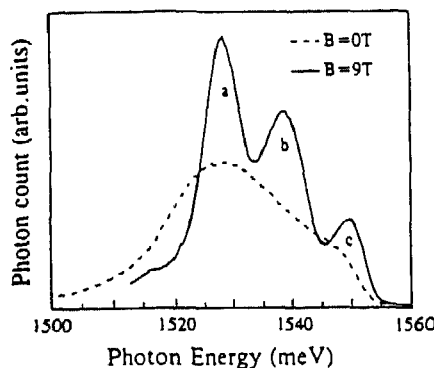


Fig. 216. 4.2 K PL spectra for magnetic fields of 0 and 9 T from a 150 Å/150 Å GaAs/AlAs modulation-doped (Si doped to $1.2 \times 10^{18} \text{ cm}^{-3}$ in the AlAs layers) superlattice.

$$\rho(0) = \frac{\rho_0(0)}{(1 + \tau/\tau_s)} \quad (34)$$

and

$$\rho(B)^{-1} = \rho(0)^{-1} [1 + (\gamma T_1 B)^2] \quad (35)$$

where the Hanle time, T_1 , is related to the electron spin relaxation time, τ_s , and the electron lifetime, τ , by

$$T_1^{-1} = \tau^{-1} + \tau_s^{-1} \quad (36)$$

and $\gamma = |g^*| \mu_B / \hbar = 3.87 \times 10^6 \text{ G}^{-1} \text{ s}^{-1}$. Miller et al. [61] measured the magnetic field dependence of the polarization of the excitonic luminescence from a GaAs quantum well. Fig. 217 shows their derived electron spin relaxation time and electron lifetime versus lattice temperature. They suggest that this data implies a scattering center with a small binding energy of $\sim 5 \text{ meV}$.

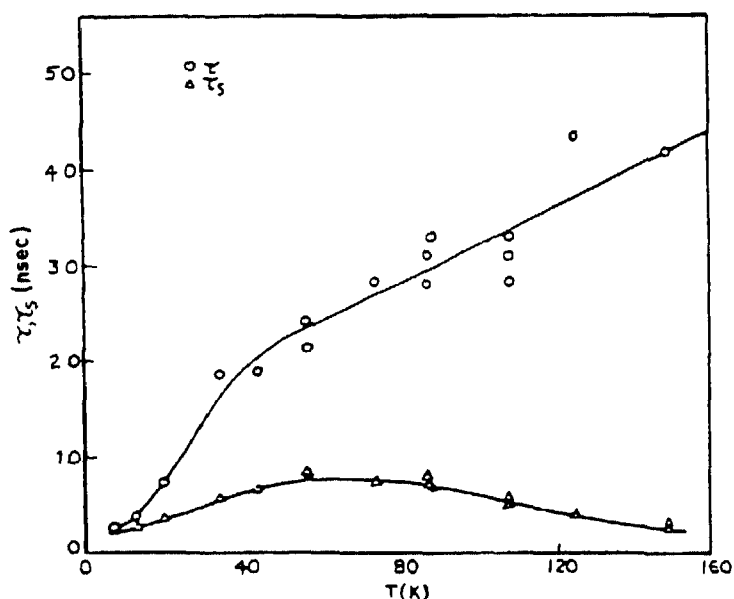


Fig. 217. Temperature dependence of the electron spin relaxation time and lifetime [61]

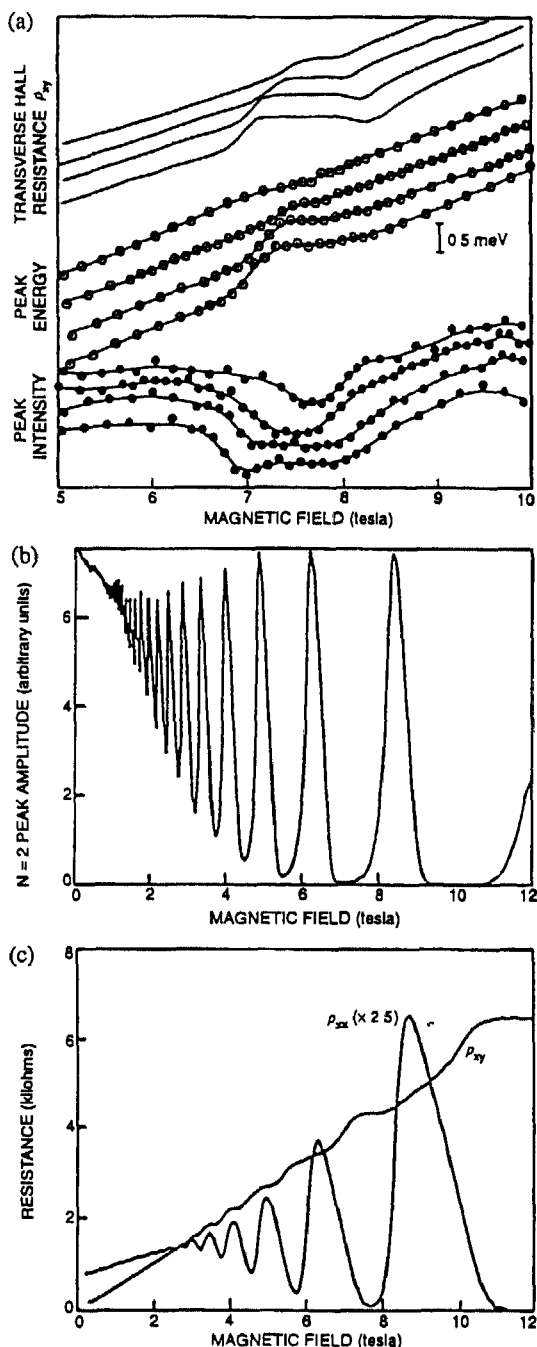


Fig. 218 (a) PL intensity (bottom set of curves), photon energy (middle curves), and Hall resistance ρ_{xy} (top curves) versus magnetic field, showing the near synchrony in field dependence of the features. The temperatures of each curve are 2.5, 1.3, 0.6, and 0.4 K from top to bottom. (b) PL intensity versus magnetic field in samples designed to enhance the Fermi edge singularity. (c) Hall resistance versus magnetic field showing the close synchrony of the quantum Hall effect with the PL intensity variations. (After Nurmiikko and Pinczuk [354].)

Magnetoluminescence has most recently been utilized as an optical probe of quasi-particle states in the integer and fractional quantum Hall regime [354,376]. Fig. 218 shows that the PL intensity undergoes large variations with magnetic field which are nearly synchronous with the quantum Hall

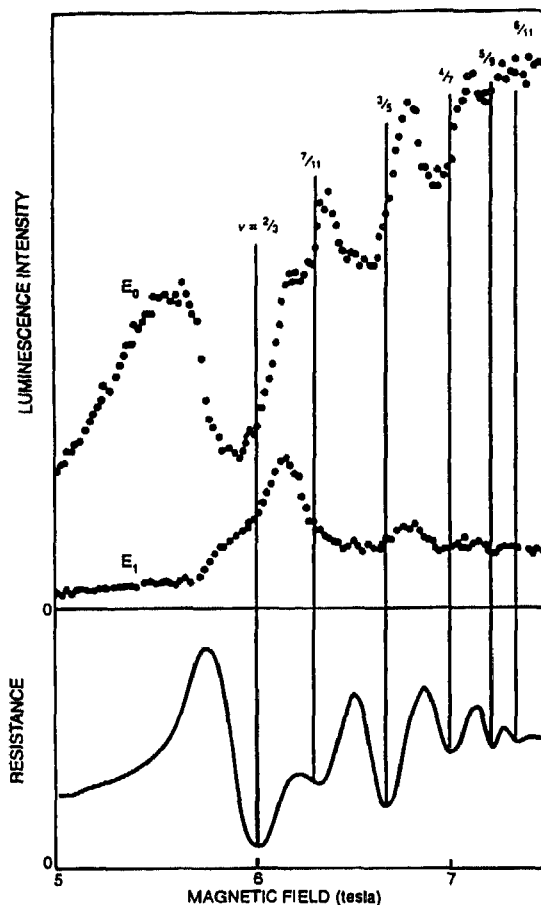


Fig. 219 PL intensity variation with magnetic field at 120 mK in a high-mobility GaAs structure together with the Hall resistance variation with field. This shows the simultaneous variations in resistance and PL intensity with field corresponding to fractional quantum Hall states. (After Nurmikko and Pinczuk [354].)

effect. Fig. 219 shows a similar behavior in the fractional quantum Hall regime, thus providing another possible tool for study of these quasi-particle states. Buhmann et al. [377] have examined the magneto-optical properties of GaAs/AlGaAs single heterojunctions in this extreme quantum limit. They observe a new luminescence line at low fractional filling factors and temperatures which they attribute to a pinned Wigner solid. This new line appears at high magnetic fields 1.4 meV lower in energy than the recombination line from 2D electrons.

Magnetic field perturbations are also useful in characterizing defects in semiconductors. The Zeeman splitting of impurity levels is capable of identifying the type of impurity. In a magnetic field the recombination of a donor-bound exciton, (D^0, X) , exhibits the splitting between the excited 2s and 2p terminal states. Additionally, the 2p states are split into three states $2p_+$, $2p_0$, and $2p_-$. The initial state of the complex is made up of two paired electrons and one unpaired hole. In a magnetic field these states exhibit a negative diamagnetic shift so that the lowest energy 2p state gives rise to the highest energy transition. For this system this is the $2p_-$ state. Fig. 220 shows the emission spectrum of a bulk GaAs sample in the vicinity of the $2p_-$ transition in a magnetic field of 4 T [94]. The inset shows the zero-field spectrum in the $n=2$ spectral region of the (D^0, X) . It is clear that the sample contains residual Si and S donors. The $2p_-$ transition shows the splitting of these two donors. These

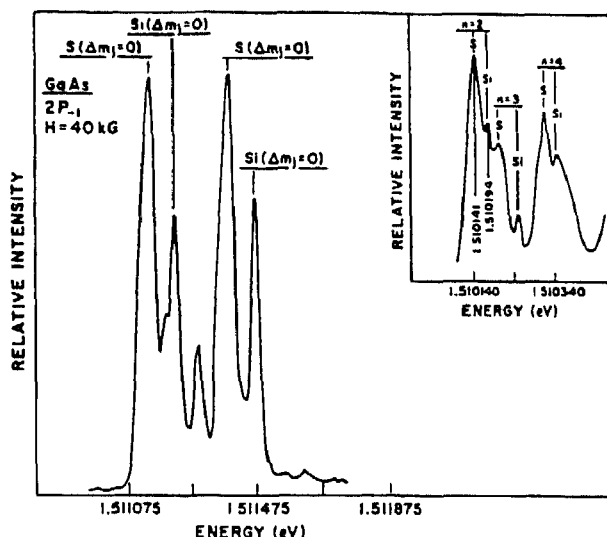


Fig. 220. Magneto-luminescence spectrum of high-purity GaAs at 40 kG. Spectrum shows peaks corresponding to the components of the $2P_{-1}$ state resulting from the collapse of an exciton bound to the first rotational state of the neutral donor for both sulfur and silicon. Inset shows the zero-field components of the same two donors resulting from higher rotational states. (After Reynolds et al. [94].)

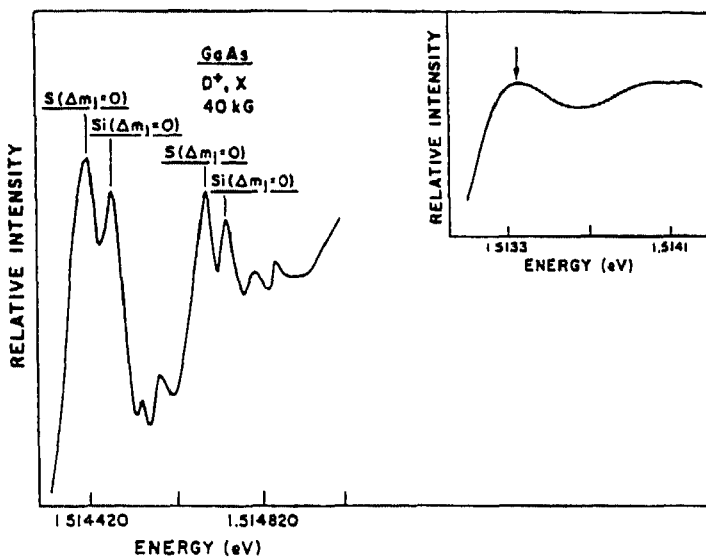


Fig. 221. PL spectrum of the Si and S donors in GaAs in a magnetic field of 40 kG. The inset shows the free hole-to-bound electron transition which covers the ionized donor-bound exciton transition. (After Reynolds et al. [94].)

donors were not resolvable in the zero-field spectrum due to broadened lines, however, the compression of the wavefunction in a magnetic field sharpens the optical transitions and allows an identification of the residual impurities. Also, the splitting between donor-bound exciton transitions associated with different donors increases with magnetic field. Similarly, an external magnetic field is useful in identifying ionized donor-bound exciton emission lines. Fig. 221 shows the PL spectrum of a bulk GaAs sample at 4 T and at 0 T (inset). The arrow in the inset marks the energy of the (D^0, h) transition which masks the (D^+, X) transition at zero field. At 4 T, however, the (D^+, X) transition is clearly evident for both Si and S donors.

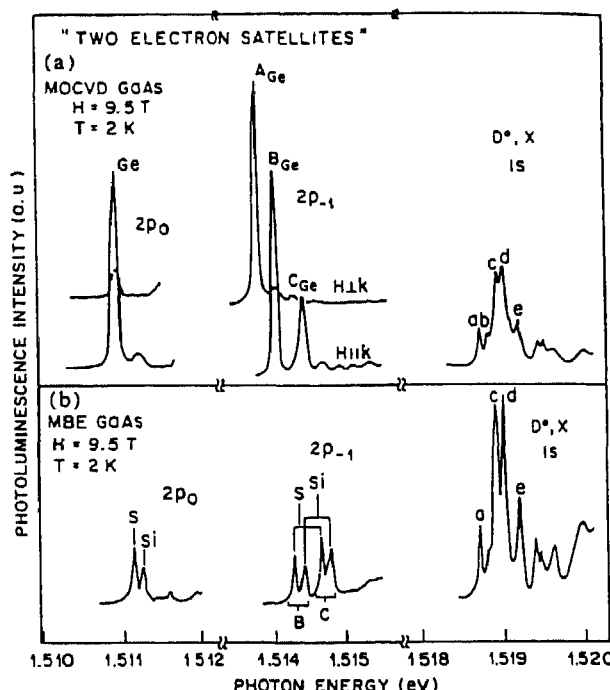


Fig. 222. High-resolution PL spectra of high-purity GaAs epilayers grown by (a) MOCVD and (b) MBE. (After Harris et al. [101].)

Harris et al. [101] examined the high magnetic field spectra of the donor-bound exciton and the two electron satellites. They find that the donor-bound exciton features may split into many components, with a single lowest energy feature. In the Faraday geometry the two electron satellite emissions exhibit two $2p_-$ components corresponding to each donor, with additional weaker lines at higher energies. The $2p_0$ emission exhibits only one strong peak for each donor. In contrast, in the Voigt geometry only one $2p_-$ emission line is observed. The energy shift between the lowest energy peaks in the (D^0, X) region to the $2p_-$ region allows identification of donor species through comparison with published far-infrared $1s \rightarrow 2p_-$ transition energies. These high-field features of the donor-bound exciton spectra are demonstrated in Fig. 222. Reynolds et al. [378] examined the magnetoluminescence of donor-bound excitons in their high-resolution spectroscopy. Fig. 223 shows the donor-bound exciton energy splittings in a magnetic field. Their phenomenological model involves Zeeman and diamagnetic terms at low fields, and Landau-level spectra at high fields. Fitting of their data yields the binding energy of the donor to be 5.77 ± 0.08 meV. Zemon and Lambert [379] also examined the high-resolution spectra in the vicinity of the donor-bound excitons of high-purity OMVPE GaAs samples in magnetic fields up to 6.4 T. Fig. 224 shows the PL spectra of one sample versus magnetic field. Peak E is identified as the recombination of (D^+, X_{Si}) , peak F is identified with the recombination of (D^+, X_{Ge}) , peak Γ is assigned to a (D^0, h) transition, and peak Γ' is attributed to a (D^+_{Ge}, X) transition. Fig. 225 shows a summary of the energy shift of these lines with magnetic field. The shift is approximately quadratic. Using a (D^+, X) model which consists of an electron ($J=1/2$) and a hole ($J=3/2$) bound to an ionized donor, yields the energy level diagram shown in Fig. 226. In the Faraday configuration left-circularly-polarized (LCP) and right-circularly-polarized (RCP) transitions have $DM_J = +1, -1$, respectively, which are represented by the solid lines in the figure. The dashed lines represent transitions which become allowed when mixing between $J=1$ and $J=2$ states at high fields is included. Their data also yield g-factors of $g_1 = 0.86$ and $g_2 = 0.5$. This is opposite in sign to the free exciton ($g_1 = g_2 = -1.9$).

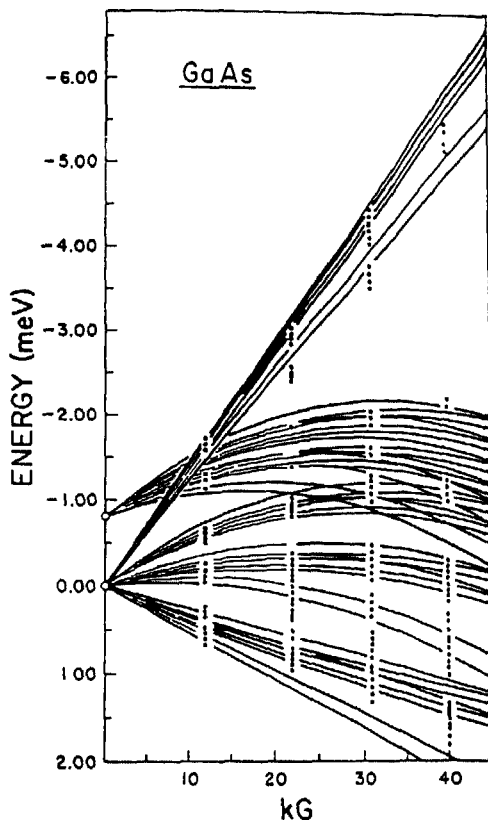


Fig. 223. Excited state energy difference for the donor-bound exciton versus magnetic field. Lines are theoretical fits to the experimental points (After Reynolds et al [378].)

The Walt's group at Simon Fraser has utilized high-resolution Fourier transform photoluminescence measurements in a magnetic field to identify and characterize impurities in GaAs [99,380]. The Fourier transform technique alleviates many of the problems of low throughput at high resolution (down to $3 \mu\text{eV}$) of conventional spectrometers. Fig. 227 shows the magneto-PL spectra of the $2p_-$ two-electron satellite region of an epilayer and bulk GaAs. The bulk sample is dominated by S donors, whereas the epilayer exhibits evidence for Si, Se, Sn, S, and Ge donors. Using resonant excitation in the magneto-PL measurements further elucidates the chemical nature of the donor species. Fig. 228 shows the non-resonant spectra (a), and (b-d) spectra resonant with the principal $1s$ energies of Ge, S, and Si, respectively. The absolute intensities yield donor concentration ratios of Ge:S:Si as 10:70:20. Fig. 229 shows the energy levels of the D^0 excited states relative to the $2p_-$ state versus magnetic field. The solid lines represent an effective mass theory which demonstrates the high accuracy of the effective mass approximation for the excited states of the neutral donor. They also observed transitions from the ground state of the (D^0, X) into the $2p_-$ state with spin projections $m_s = 1/2$ and $m_s = -1/2$. The magnetic field dependence of these transition energies yields the magnetic-field dependence of the g -factor in the $\langle 100 \rangle$ direction, as shown in Fig. 230. By rotating the sample with respect to the magnetic field, the anisotropy of the g -factor may be determined, as shown in Fig. 231. In total, their high-resolution magnetoluminescence measurements allowed the determination of the energy levels of the (D^0, X) including the paramagnetic splittings of the states, as shown in Fig. 232. Similarly, they arrived at an energy level model for the $2p$ two-electron satellite peaks of the donor-bound exciton.

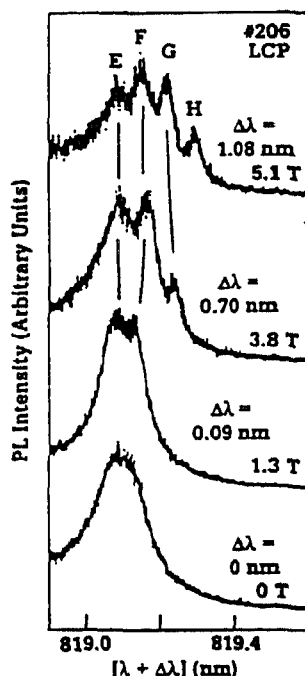


Fig. 224. Low-temperature (4.2 K) left-circularly-polarized PL spectra in the (D^+ , X) spectral region versus magnetic field. (From Zemon and Lambert, *Inst. Phys. Conf. Ser.* No. 106, IOP Publishing, Bristol, UK, 1989, p. 251.)

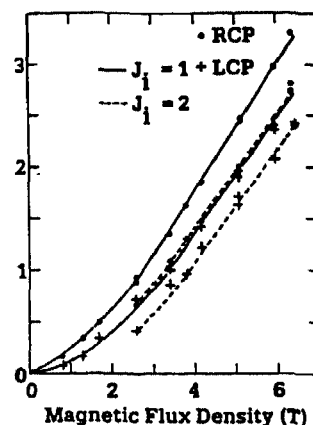


Fig. 225. Magnetic field dependence of the (D^+ , X) peak energies at 4.2 K. (From Zemon and Lambert, *Inst. Phys. Conf. Ser.* No. 106, IOP Publishing, Bristol, UK, 1989, p. 251.)

Magnetic fields are also useful in identifying impurity related transitions in quantum wells. Reynolds et al. [161] found that the heavy- and light-hole bound exciton transitions in quantum wells are split with increasing fields. The field splittings and diamagnetic shifts allowed identification of the transitions from light- and heavy-hole free excitons, (D^0 , X_l), (D^0 , X_h), (D^0 , h), and (A^0 , X_h). Magnetic fields also allow the determination of the donor 1s–2s transition energy through analysis of the two-electron satellite transition [162]. The donor-bound exciton line shifts to higher energies with magnetic field, and the two-electron satellite transition is red-shifted with magnetic field. Thus, the donor 1s–2s transition energy increases with field. The Zeeman splitting of acceptor-bound excitons is also observable in magnetoluminescence measurements [168]. Based upon these measurements, Holtz et al.

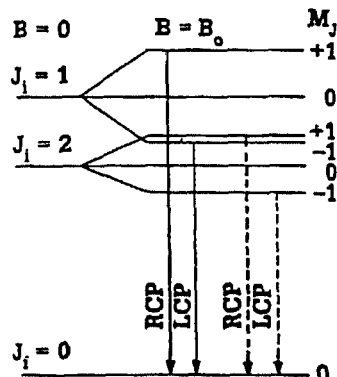


Fig. 226 Energy level diagram for the (D^+, X) . (From Zemon and Lambert, *Inst. Phys. Conf. Ser.* No. 106, IOP Publishing, Bristol, UK, 1989, p. 251.)

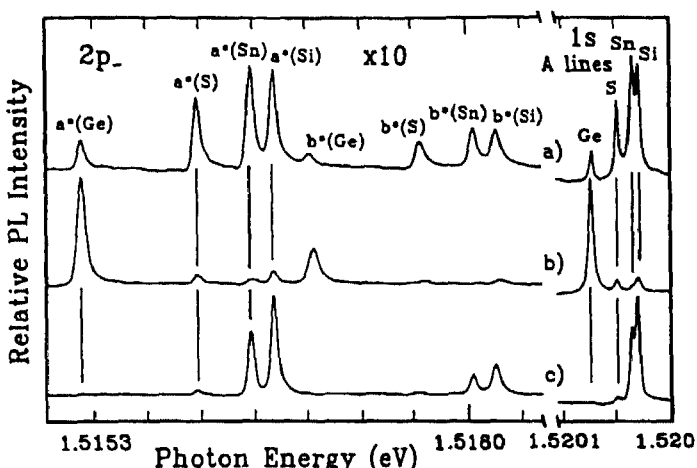


Fig. 227. Magneto-PL spectra of three samples after non-resonant excitation in a magnetic field of 12 T (Faraday geometry). (After Karasyuk et al. [99].)

[168] find that the hydrogenic radius of the acceptor-bound exciton is reduced by 13% from bulk to a 150 Å wide quantum well.

Reynolds et al. [381] have also observed the magnetic field induced splitting of DAP emission in bulk GaAs. Fig. 233 shows the field-induced splitting of the DAP emission at 1.51165 eV. Assuming that the initial state is a $J=3/2$ state and the final state is a $J=1/2$ state, they obtain an electron g value of $g_e = -0.35 \pm 0.15$, and a hole g value $K = 2.01 \pm 0.11$. They model this emission as due to a double-donor-acceptor complex or a double-acceptor-neutral donor complex. In addition Reynolds et al. [191] have observed a bound-to-bound transition in a 200 Å quantum well which exhibits a diamagnetic shift which is smaller than that expected for a free-to-bound transition, and consistent with that expected for a bound-to-bound transition.

Type-II GaAs/AlAs structures are less sensitive to magnetic fields than type-I GaAs/AlAs structures due to the heavier electron masses [382,383]. However, at high magnetic fields (~ 40 T) the diamagnetic shift of the excitons in these structures is observable, as shown in Fig. 234. The observed anisotropy in the diamagnetic shift suggests that the X_Z state is the ground electronic state. This data also yields the excitonic in-plane reduced mass of $0.15m_0$.

Magnetoluminescence of quantum well wires has also been observed [328,331,332,344,384]. Weman et al. [344] observed an anisotropic diamagnetic shift of the luminescence energy associated

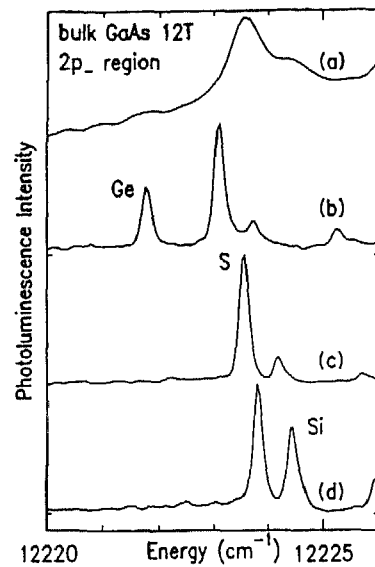


Fig. 228. PL spectra in the vicinity of the $2p_-$ transitions of bulk GaAs containing Ge, S, and Si dopants. (a) Spectrum for non-resonant excitation, (b)–(d) spectra for resonant excitation of the principal transitions for Ge, S, and Si, respectively. (After Beckett et al. [380])

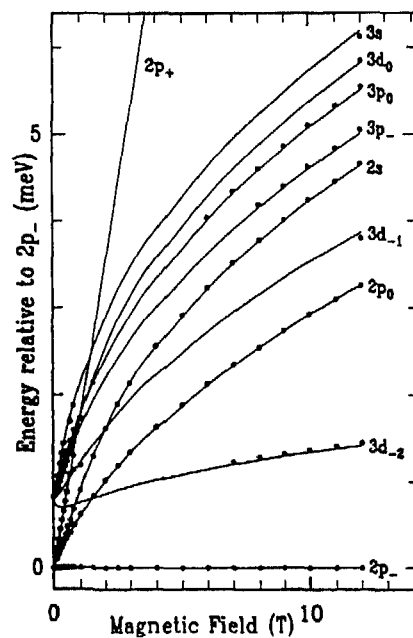


Fig. 229. Splittings of the various energy levels of the D^0 excited states relative to the $2p_-$ state in a magnetic field (After Karasyuk et al. [99])

with the serpentine-superlattice quantum well wires, as shown in Fig. 235. This anisotropy is direct confirmation of the one-dimensional nature of the excitonic wavefunctions. They find that the linewidth increases with field, and the increase is dependent upon the direction of the field with respect to the wires, which is a result of the reduced excitonic volume in a magnetic field. Lage et al. [332] quantified this diamagnetic shift of the $n = 1$ heavy-hole exciton state to be $\Delta E^{\text{dia}} = 0.039(2)B^2 \text{ meV T}^{-2}$. In contrast, they found the diamagnetic shift of the $n = 3$ heavy-hole exciton state to be $\Delta E^{\text{dia}} = 0.050(2)B^2$

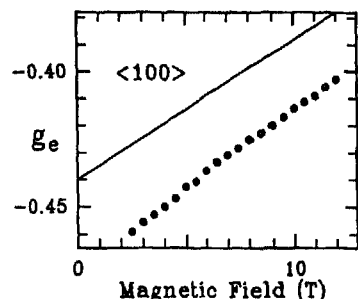


Fig. 230. Electron g -factor in a $2p^-$ state of a neutral Si donor versus magnetic field in the $<100>$ direction. See Ref. [155] for description of theoretical curve (—). (After Karasyuk et al. [99].)

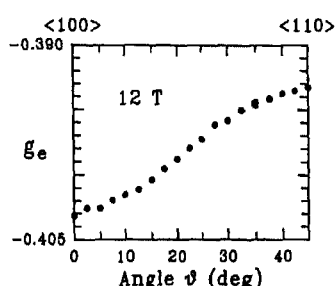


Fig. 231. Angular dependence of the g -factor at 12 T for Si D^0 in a $2p^-$ state. Here θ is the angle between B and the $<100>$ crystallographic axis. (After Karasyuk et al. [99].)

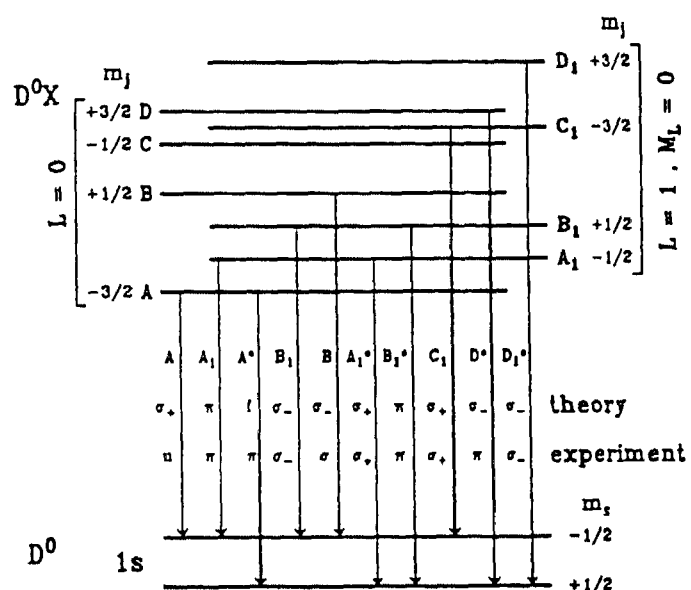


Fig. 232. Energy level diagram of the principal donor transitions in a magnetic field. f stands for forbidden dipole transitions, whereas u represents unpolarized transitions (After Karasyuk et al. [99].)

meV T⁻². Oestreich et al. [384] have observed a transition from one-dimensional quantization to Landau quantization in quantum well wires grown on grooved substrates. Fig. 236 shows the fan chart for the quantum well wire and quantum well samples. At approximately 6 T the typical fan behavior is observed in the quantum well wire sample, whereas at lower fields the 1D quantization is prevalent.

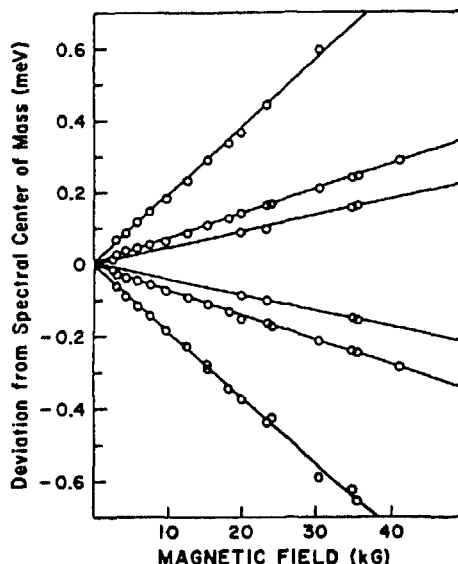


Fig. 233 Splitting of the donor-acceptor complex with magnetic field. (After Reynolds et al. [381].)

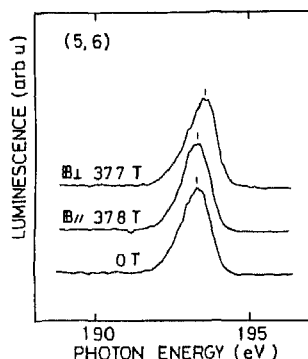


Fig. 234. High-field PL spectra of a $(\text{GaAs})_3/(\text{AlAs})_5$ short-period superlattice (After Sasaki et al [383])

They associate the appearance of Landau levels to the magnetic-field induced contraction of the 1D excitonic wavefunction below the size of the wire. For larger Bohr radii, cyclotron orbits are not possible, and the wavefunctions lose their Landau characteristics. Kohl et al. [328] found that the magnetic field behavior of the luminescence in their quantum wires indicates an enhancement of the reduced mass and of the exciton binding energy by about 15%. Magneto-optical measurements of quantum well wires fabricated in modulation-doped quantum wells were shown by Plaut et al. [331] to exhibit emission characteristic of the 1D density of states, and a energy dispersion (diamagnetic) which is 2–3 times steeper than that expected for excitonic behavior. They conclude that their results demonstrate the realization of 1D modulation-doped quantum wires.

Nagamune et al. [348] have used magnetoluminescence to estimate the exciton binding energy in quantum dot structures. Fig. 237 shows the measured PL spectra versus magnetic field from 0 to 12 T, together with the energy shifts of the various transitions versus magnetic field. The bulk GaAs emissions and the quantum well emissions all shift linearly with field at high fields (> 4 T). In contrast the PL peak due to the GaAs quantum dots shifts diamagnetically even in the high field regime. The magnetic field induced PL energy shift of the quantum dots is 0.5 meV at 12 T. From this energy shift, Nagamune et al. derive an exciton binding energy of ~ 10 meV, which is close to the difference

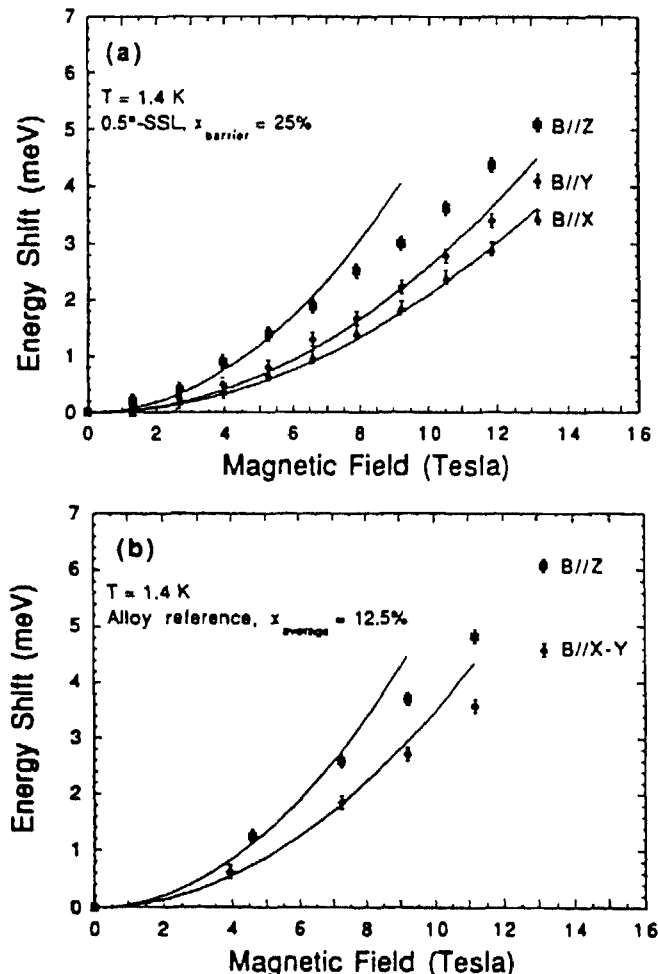


Fig. 235 Magnetic field dependence of the PL peak energy for B parallel to z and x,y axes of the serpentine superlattice (a), and the alloy well reference sample (b) (After Weman et al. [344])

between the calculated confinement energy and the observed blue-shift due to quantum confinement. Note that the quantum dot emission intensity does not change appreciably with magnetic field. This is a result of the insensitivity of the excitons in quantum dots to magnetic fields since they are localized in the small area of the dot structure and the magnetic-field induced contraction of the wavefunction therefore has little effect on their spatial extent (the cyclotron radius at 10 T is 81 Å and the dot size is 250 Å).

In Si, the free-exciton luminescence has been observed to decrease in intensity with field in a weak magnetic field [385]. Fig. 238 shows the change in PL intensity for the free exciton, Boron-bound exciton, and the Γ -line with increasing magnetic field at two excitation levels. The decrease in PL intensity with field is attributed to a strong enhancement of surface recombination resulting from magnetic-field induced localization of photoexcited free carriers near the surface.

2.4.3. Electric field

Electric fields may be used to shift or split the energy levels of a semiconductor or impurity in a semiconductor as well as for accelerating and/or polarizing charged and non-spherical neutral carriers (i.e. electrons or holes). An external bias tilts the conduction and valence bands of a semiconductor

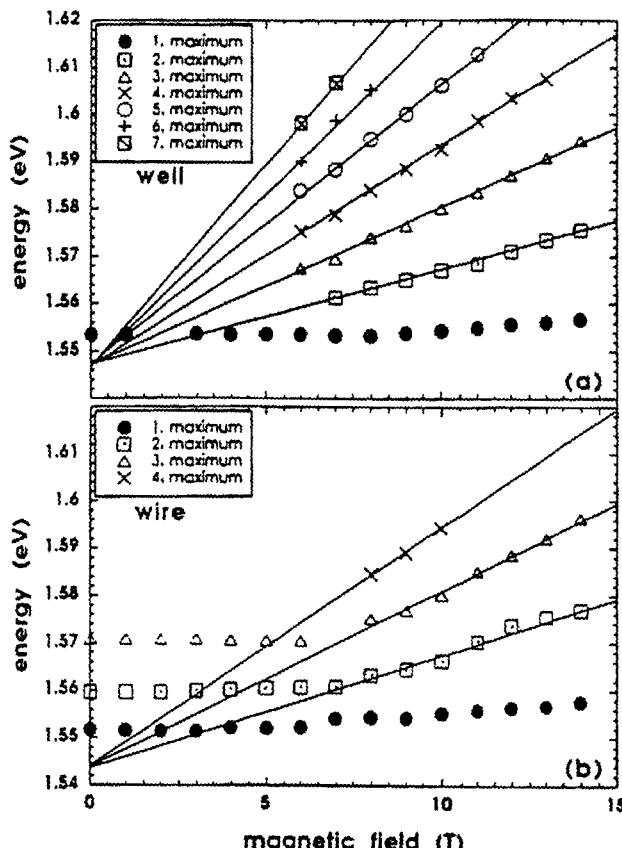


Fig. 236. Fan diagram versus magnetic field for (a) a quantum well, and (b) a quantum well wire sample. The peaks are determined from the time-integrated PL spectra from 40 to 120 ps after the excitation pulse. (After Oestreich et al. [384].)

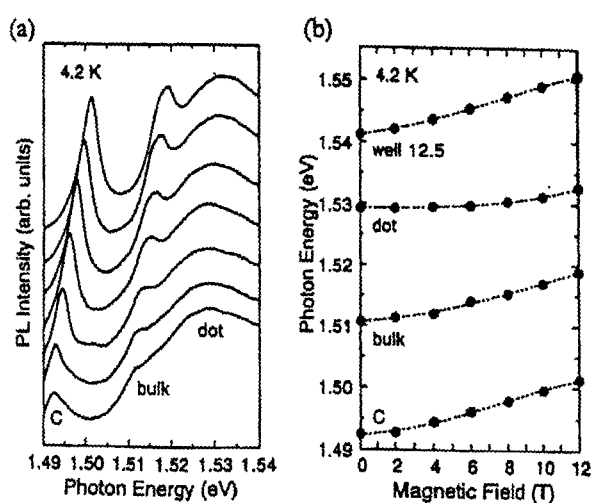


Fig. 237. (a) PL spectra at 4.2 K at several different magnetic fields from 0 to 12 T in 2 T increments. (b) Energies of the PL peaks evident in the spectra versus magnetic field applied perpendicular to the substrates. (After Nagamune et al. [348].)

such that the Fermi level is constant throughout the structure. This tilting causes the electrons and holes to be accelerated in opposite directions. For large electric fields the force due to the field may be stronger than forces binding the charged carrier to an impurity or to an excitonic state. This field

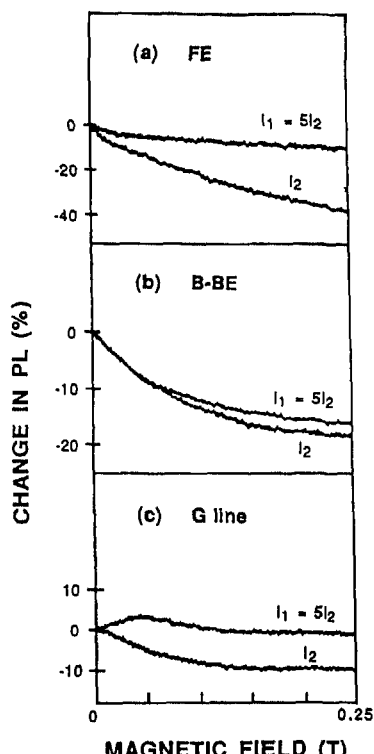


Fig. 238. Magnetic-field induced change in the PL spectra (%) from (a) free excitons, (b) B-related bound excitons, and (c) the G-line in Si. (After Chen et al [385].)

thereby ionizes the center, freeing the carrier to move. Very large fields ($\epsilon > 10^5 \text{ V cm}^{-1}$) may cause across the gap ionization of electron–hole pairs. Free carriers generated by these fields are subsequently accelerated and interact with valence electrons through a collision thereby causing an avalanche of electron–hole pair generation. Some of these pairs recombine radiatively with a typically very broad spectrum.

External biasing of semiconductors requires the fabrication of metallic contacts on the semiconductor. PL is typically collected from the biased region by forming semitransparent Schottky contacts on the semiconductor which allows excitation and collection of the luminescence from the biased region. Another approach involves growing the active region in the intrinsic region of a p–i–n structure, where in this case the field is built-in.

Bludau and Wagner [386] observed the impact ionization of excitons in bulk GaAs crystals. They formed ohmic contacts on the surface of their bulk GaAs sample, causing the electric field to be parallel to the sample surface. PL spectra versus applied field are shown in Fig. 239. The emission peaks near 8181 Å are the so-called UPB and LPB free-exciton emissions. Shallow donor and acceptor emissions are also clearly evident. With increasing field, all of these shallow luminescence lines are quenched. Their analysis of the integrated emission strengths of the various transitions versus applied field indicates that the critical field for impact ionization depends on whether the exciton is free, donor bound, or acceptor bound, as shown in Fig. 240. Further examination of their spectra reveals that as the shallow bound and free exciton emissions are quenched, the band-to acceptor emission increases with increasing field. This signifies an increase in the free-electron concentration in the conduction band.

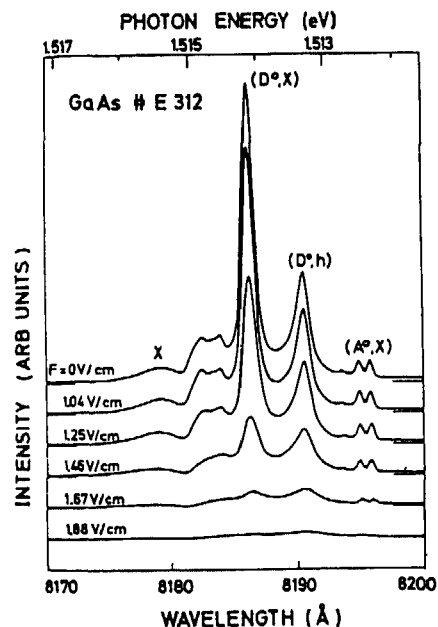


Fig. 239. Low-temperature PL spectra of bulk GaAs at several applied electric fields. (After Bludau and Wagner [386].)

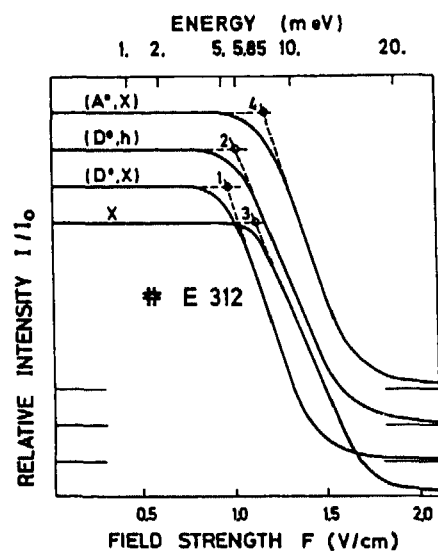


Fig. 240. Relative intensity of each near-edge emission line versus applied electric field (After Bludau and Wagner [386].)

Impact ionization of electrons and/or holes from bound exciton complexes in Si has been observed by Weman et al. [387,388]. For donor concentrations of $\sim 10^{14} \text{ cm}^{-3}$ of P, an external field of 50 V cm^{-1} is required to observe this effect. Fig. 241 shows the electric-field induced change in PL intensity from the shallow P donor-bound exciton luminescence (decreasing with field) as well as the change in PL intensities of deep level luminescence at 903 meV and 1119 meV (first increasing and then decreasing with increasing field). At low fields the decrease in shallow donor emission is due to impact ionization which deposits more carriers on the deep levels, thereby causing their luminescence intensity to increase. At still higher electric fields the impact ionization of the deep centers themselves causes a decrease in the luminescence intensity associated with these deep centers.

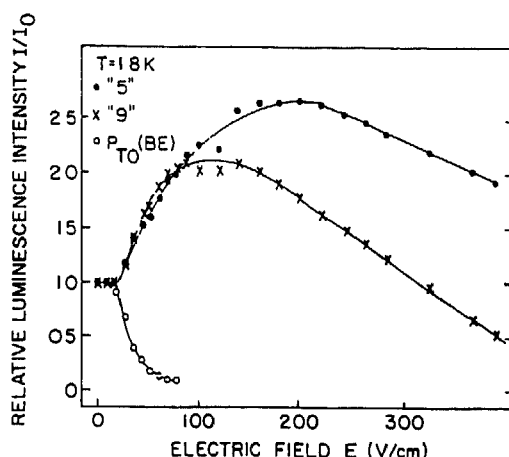


Fig. 241. Electric field dependence of the PL intensity of the luminescence associated with excitons bound to P in Si (emissions at 903 meV and 1119 meV) [141].

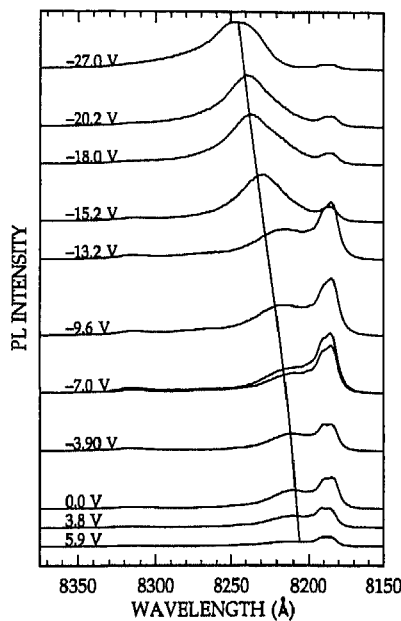


Fig. 242. Electric field dependence of the H-band emission in GaAs/AlGaAs double heterostructures at 2 K.

In section 2.3.2 a luminescence feature associated with the heterointerfaces of GaAs/AlGaAs structures was identified, and termed the H-band [281,389–392]. External electric fields tilt the bands of the heterostructure and therefore may significantly alter the potential notches at the heterointerface where the free carriers or excitons responsible for H-band emission reside. Fig. 242 shows the PL spectra in the vicinity of the H-band emission for various external biases applied to a wide GaAs/AlGaAs double heterostructure. The external bias was applied through evaporation of an ohmic ring and semitransparent Schottky barrier on the top surface of the structure. The shift in PL energy with electric field is a direct result of the tilting of the bands of the heterostructure. The blue-shift is a result of “driving” the bands to the flat-band condition, whereas the red-shift results from the field induced increasing of the potential notches at the heterointerfaces.

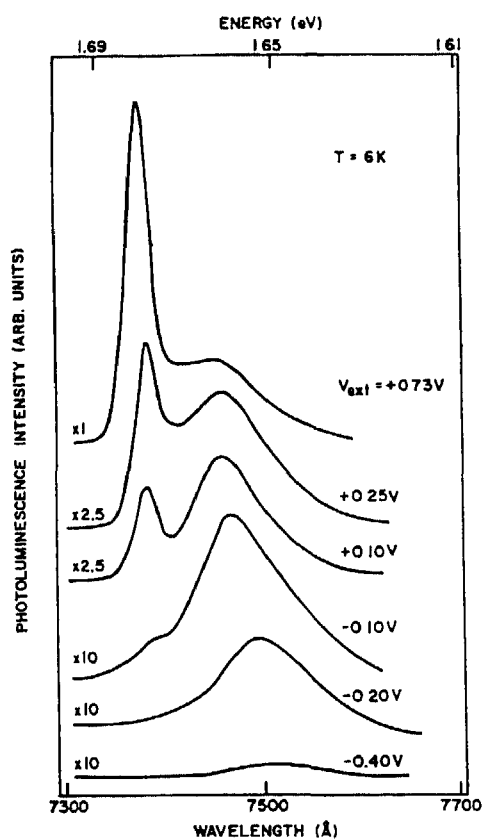


Fig. 243 PL spectra at several different applied voltages for a 35 Å GaAs quantum well. (After Mendez et al. [393].)

Exciton ionization has also been observed in GaAs/AlGaAs quantum wells [393,394]. Mendez et al. [393] observed the quenching of the free-exciton luminescence in a 35 Å quantum well, and simultaneously the more persistent, but still decreasing intensity of the band-to-acceptor emission, as shown in Fig. 243. These results are similar to the impact ionization observed in bulk GaAs. However, the (perpendicular) fields here are much larger (kV cm^{-1}). Instead, the quenching of the excitonic luminescence is due to the electric-field induced carrier separation. In contrast to this work, Weman et al. [394] observed a quenching of the luminescence of Si-doped quantum wells at fields of only a few V cm^{-1} parallel to the plane of the quantum well. Fig. 244 shows the relative PL peak intensity of the free exciton and bound exciton emissions in their quantum well sample of 145 Å width. The bound exciton emission quenches monotonically with increasing field, whereas the free exciton first decreases at 20 V cm^{-1} and then levels off with increasing field. This figure also shows that the threshold for the onset of the quenching is coincident with the threshold for the onset of the current through the sample. This is indicative of impact ionization, with donors being the major contributor at high fields. Weman et al. also measured the well-width dependence of the threshold field for quenching of the luminescence. They find that the threshold field increases with decreasing well thickness.

Externally biased quantum wells exhibit an effect called the quantum-confined Stark effect (QCSE). The QCSE causes a red-shift of both the absorption and luminescence spectra of the quantum well [395–398]. The field causes the quantum well exciton to become polarized, yet still confined within the well. Polland et al. [395] have examined the QCSE in GaAs/AlGaAs quantum wells and have observed a well-thickness-dependent red-shift of the luminescence originating from the wells.

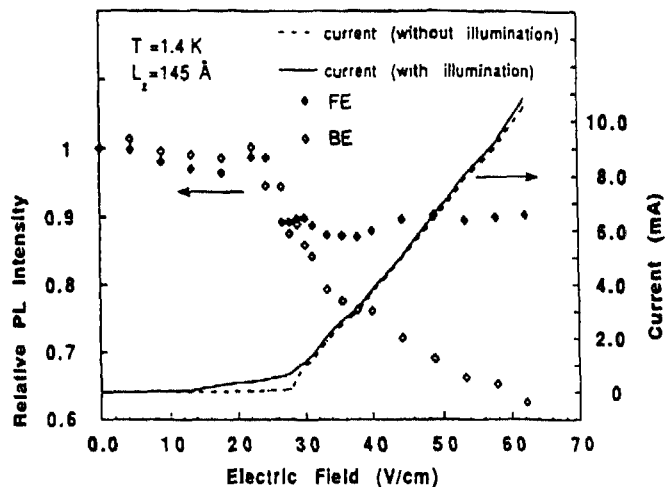


Fig. 244 Free exciton and bound exciton relative PL peak intensities versus electric field together with the current with and without illumination in a 145 Å Si-doped GaAs quantum well. (After Weman et al. [394].)

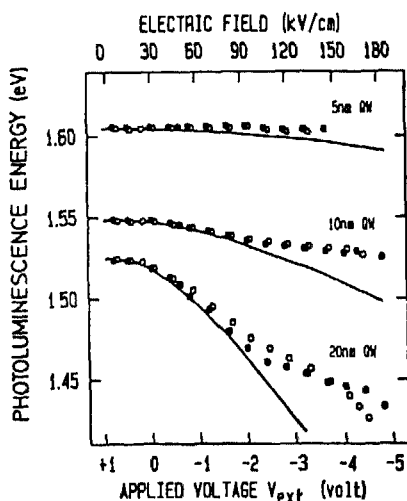


Fig. 245 Peak energy positions of the dominant PL line versus external voltage applied to the quantum wells of widths shown (After Polland et al. [395].)

Fig. 245 shows the PL peak energies of the emissions from a multiple quantum well sample versus sample bias. The red-shift is clearly larger for the wider wells. The intensities of these emission lines does not change appreciably with field, except for the widest quantum well. Red-shifts as large as 100 meV are observed at $V_{ext} = -4.4$ V. The solid lines in the figure are results of a variational calculation obtained by solution of Schrödinger's equation.

External biases may also be utilized to controllably transfer either photoexcited electrons or holes from thicker layers of a structure to quantum well regions of a structure. This then allows studies of carrier density effects. Andrews et al. [399] used this technique to examine the formation of the "Mahan exciton" which is a bound state with respect to the Fermi level. Fig. 246 shows the PL and PL-excitation spectra for the 5 nm quantum well of a multiple quantum well sample for several different external biases. There are several significant electric field induced changes in the spectra evident in this figure. The Stokes shift for both the e1-hh1 and e1-lh1 transitions is bias dependent. Second, the PL peak energy shifts with bias. Lastly, the PL is broadened with external bias. Fig. 247

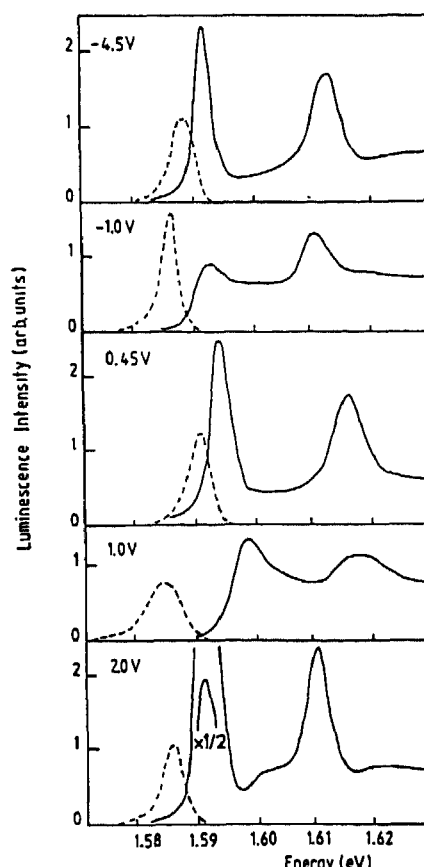


Fig. 246. PL and PLE spectra of a 5 nm quantum well at five different biases. (After Andrews et al. [399].)

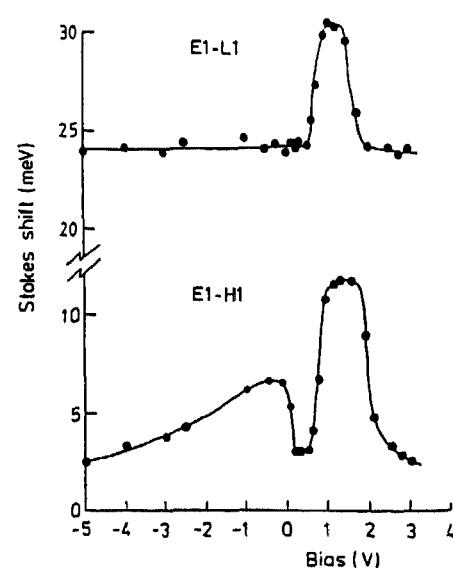


Fig. 247. External bias dependence of the Stokes shift between the PL and PLE peaks corresponding to the E1-H1 and E1-L1 transitions (After Andrews et al. [399].)

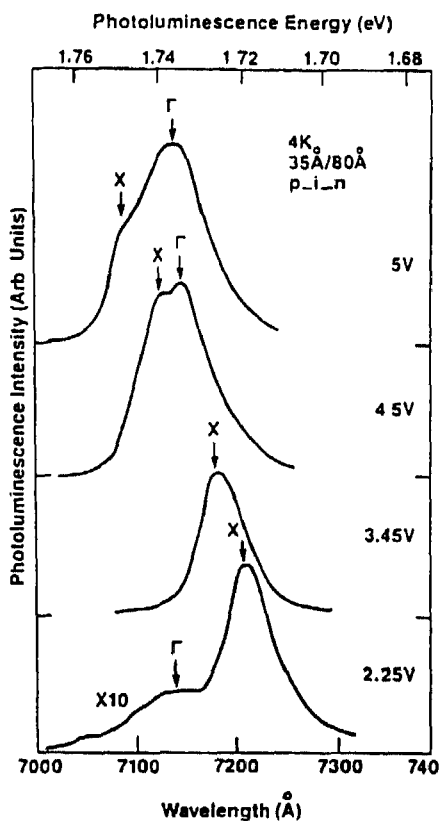


Fig. 248. PL spectra of a p-i-n structure with an embedded 35 Å GaAs/80 Å AlAs superlattice at several different applied voltages. X and Γ represent the indirect and direct transitions, respectively. (After Meynadier et al. [400].)

shows the Stokes shift for both heavy-hole and light-hole transitions versus external bias. The PL peak energy exhibits a significant change in the bias region of 0 to 1 V. The additional Stokes shifts for positive biases between 0.6 and 2.0 V is due to the presence of a Fermi sea of electrons since both hh1 and lh1 transitions exhibit similar Stokes shifts. For biases between 0 and -4 V the lh1 transition does not shift and is not broadened. This is evidence that there is a Fermi sea of heavy holes present, and the light-hole band is empty. The density of excess electrons or holes is directly proportional to the Stokes shift. From their temperature dependent studies for both forward and reverse biases they conclude that Mahan excitons exist up to nearly 100 K for a forward bias, whereas for a reverse bias, when the quantum well is dominated by a heavy-hole Fermi sea, the Mahan exciton is not formed.

Electric fields may also be used to change the electronic structure of nanostructures. Meynadier et al. [400] demonstrated that a GaAs/AlAs superlattice may be changed from type I to type II through the application of an axial electric field. Their short-period structures had a type-II band alignment under no external bias. The external bias causes a blue-shift of the transition energy. However, the QCSE causes a red-shift of the transition energy with increasing electric field. Fig. 248 shows the PL spectra of a 35 Å GaAs/80 Å AlAs superlattice taken with various applied biases. The peaks marked X and Γ are the type-II and type-I transitions respectively. Fig. 249 shows the peak energies of these transitions versus applied electric field. They find that the type-I and type-II transitions anticross at a field of 4.5×10^4 V cm⁻¹. The splitting at crossover is 2.5 meV. They attribute this anticrossing behavior to Γ -X mixing.

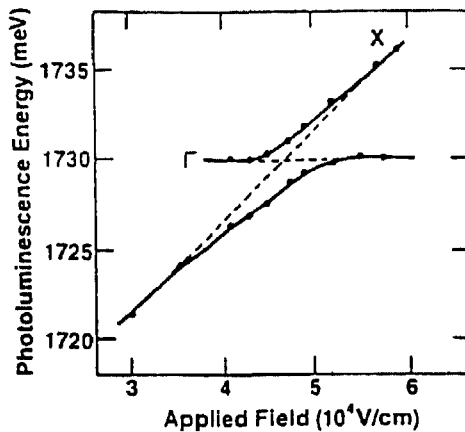


Fig. 249 Applied field dependence of the peak energies of the direct and indirect transitions. (After Meynadier et al. [400].)

2.4.4. Uniaxial strain

The density-of-states of a semiconductor may be altered through the application of strain, and the resulting distribution may be anisotropic. This redistribution of states also alters the occupation of those states, which may therefore alter the total energy of the semiconductor. In polar semiconductors local fields are present at each lattice site and these fields are altered through uniaxial strain. In III-V compounds, cubic symmetry allows one longitudinal (hydrostatic) deformation (discussed in section 2.4.1) and two transverse, shear deformations. The uniaxial strain also tends to lower the symmetry of the crystallographic sites. As a result, an impurity may exhibit splittings of its electronic structure which are evident in the spectrum, and this may be used for identification of the impurities.

The application of an axial strain breaks the symmetry of a cubic semiconductor, distorting the unit cell, and thereby modifying the band structure [401–405]. The total strain may be written in terms of a purely axial component

$$\epsilon_{ax} = \epsilon\parallel - \epsilon_{\perp} \quad (37)$$

and a hydrostatic component

$$\epsilon_{vol} = \epsilon\parallel + 2\epsilon_{\perp} \quad (38)$$

The orbital-strain Hamiltonian for a given band at the zone center may be expressed as [403]

$$H_{\epsilon}(i) = -a^{(i)}[\epsilon_{xx} + \epsilon_{yy} + \epsilon_{zz}] - 3b^{(i)}\left[\left(L_x^2 - \frac{1}{3}\vec{L}^2\right)\epsilon_{xx} + c.p.\right] - \left(\frac{6d(i)}{\sqrt{3}}\right)\left[\frac{1}{2}(L_x L_y + L_y L_x)\epsilon_{xy} + c.p.\right] \quad (39)$$

where the superscript i is the band index, $\epsilon_{\alpha\beta}$ represents the components of the strain tensor, L is the angular momentum operator, c.p. denotes cyclic permutation of the indices, $a^{(i)}$ is the hydrostatic pressure deformation potential for the i th band, and $b^{(i)}$ and $d^{(i)}$ are the uniaxial deformation potentials for strains of tetragonal and rhombohedral symmetry, respectively. At the zone center, the conduction band minimum for GaAs is an antibonding s-state. Strain produces a hydrostatic shift given by

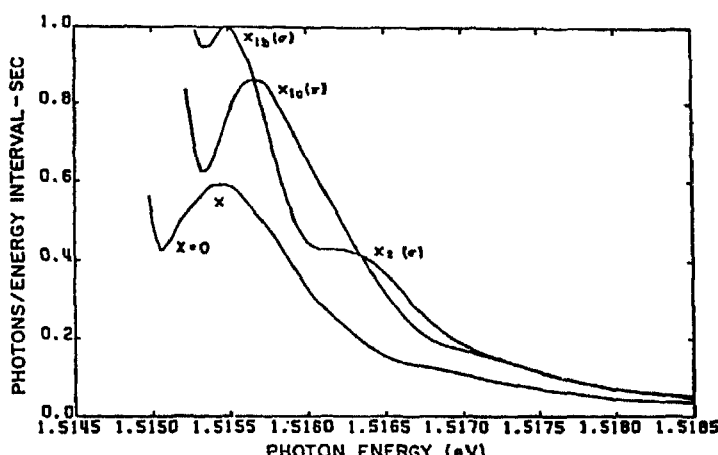


Fig. 250 PL spectra of n-type GaAs at 4.2 K in the spectral vicinity of the free exciton. Peak X is without strain; X_{1a} is with 136.6 kg cm^{-2} strain in the [100], π polarization; X_{1b} and X_2 are with 136.6 kg cm^{-2} strain in the [100], σ polarization. (After Gilleo et al. [406].)

$$H_\epsilon^c = a^c(\epsilon_{xx} + \epsilon_{yy} + \epsilon_{zz}) \quad (40)$$

In contrast, uniaxial strain has three important effects on the valence-band structure of semiconductors. First, it lifts the degeneracy of the light- and heavy-hole valence bands. The magnitude and ground state of this splitting depends upon the deformation potential of the material as well as the direction of the uniaxial or biaxial strain (i.e. tensile or compressive strain). Second, the valence bands become anisotropic. The valence band which is heavier along the strain direction is light perpendicular to that direction. Lastly, uniaxial strain splits the degeneracy of the spin-up and spin-down valence bands in the direction perpendicular to the strain. Band extrema at points away from the zone center are affected by the shear component of an applied uniaxial strain in the following ways: (1) states with different momentum which are degenerate may be split depending on the projections of their k vectors onto the stress direction, (2) degenerate orbital bands whose k vectors are not parallel to the stress may be split, and (3) neighboring bands may be coupled due to the stress [401]. These effects are especially important for indirect-gap semiconductors.

Gilleo et al. [406] examined the PL of free excitons in bulk GaAs for [100] stresses from 33 to 500 kg cm^{-2} . At zero strain, the $n = 1$ free exciton has three exchange-split lines: Γ_5 ($J = 1$) which is an allowed singlet, and Γ_3 and Γ_4 ($J = 2$) which are forbidden triplet lines, energetically below the singlet [25,406]. A [100] stress induces a splitting of the Γ_5 line into a high-energy line X_2 of s polarization, and a lower-energy line X_{1a} of π polarization. The Γ_4 line becomes allowed with strain, with a line X_{1b} of s polarization below X_{1a} due to the exchange interaction. Fig. 250 shows the strain-induced splitting of the free exciton for both σ and π polarizations. These spectra exhibit the splittings predicted above [406,407]. The stress dependence of these lines is shown in Fig. 251. Fitting of this data yields the deformation potentials for bulk GaAs as well as the exchange energy splitting of 0.37 meV. This exchange energy was later disputed by Sell et al. [25] who obtained a value of -0.12 meV. They also observed an anticrossing in the stress dependence of the p-polarized luminescence at low stresses. Jagannath and Koteles [408] used polarized PLE measurements combined with uniaxial stress to elucidate the structure of free exciton states, including the excited states of the free exciton. Fig. 252 shows the peak energies of the various transitions observed in their PLE spectra as a function of [100] stress. The more rapid variation of the energy of the light-hole states with stress causes an anticrossing behavior of EL1 and EH2 at approximately 0.5 kbar. This anticrossing yields an exchange energy of 0.3 meV.

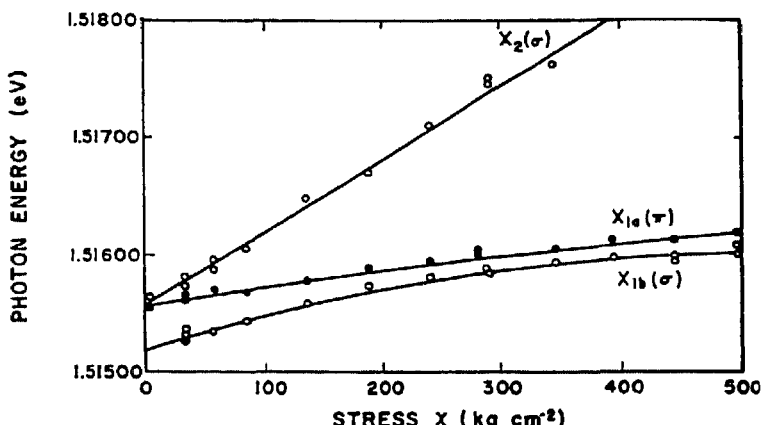


Fig. 251. Energy shift of the free-exciton components with [100] stress. (After Gillo et al. [406].)

Reynolds et al. [381] observed the strain-induced splitting of both neutral donor-bound exciton emission lines and neutral acceptor-bound exciton emission lines. Fig. 253 shows the strain-field behavior of the acceptor-bound exciton emission in bulk GaAs crystals. The splittings evident here result from the splitting of the bound exciton state due to the strain-induced splitting of the valence band of GaAs. Schmidt et al. [409] also examined the stress dependence of the (A^0, X) luminescence in bulk GaAs. They find that the three lines observed in their spectra (Fig. 254) may be labeled by angular momentum quantum numbers $J = 5/2, 3/2$, and $1/2$ in order of increasing energy. The uniaxial stress splits these three lines into seven or eight lines due to a weak crystal field interaction.

In Si uniaxial stress may split both the conduction and valence bands since the conduction band is multivalley in nature (six X valleys). A uniaxial compression along the $\langle 111 \rangle$ axes perturbs all six conduction band minima equally, leading to no lifting of their degeneracy. However, uniaxial compression along one of the cube axes or face axes will cause a splitting. For a [110] uniaxial stress the [001] valleys are at a higher energy than the [010] and [100] valleys. The splitting increases at $46.3 \text{ meV GPa}^{-1}$. The valence band may be split by uniaxial stress in any direction. Considering only the $J = 3/2$ states, the splittings are $45 \pm 2 \text{ meV GPa}^{-1}$, $35 \pm 2 \text{ meV GPa}^{-1}$, and $48 \pm 2 \text{ meV GPa}^{-1}$ for [001], [111], and [110] stresses, respectively. Since the valence band is split by any strain, the hole is always able to lower its energy in a strain-field that lowers the symmetry of the crystal. Thus, excitons are attracted towards lower-energy strained areas of a crystal. Fig. 255 shows an example of the stress dependence of the TO-phonon assisted indirect transition in Si with uniaxial stress in the [111] direction [410,411]. The splitting with stress is due to the splitting in the valence band. The splittings observed in the TO-phonon assisted transitions for uniaxial stress in the [110] and [001] directions are indicative of a combination of the stress-induced splittings of both the conduction and valence bands.

An example of a luminescent center in Si whose electronic structure is revealed under uniaxial stress is the 1045 meV four-Li atom complex which gives rise to the Q luminescent band. Uniaxial stress perturbations show that the Q lines have C_{3v} point group symmetry [141,412]. Fig. 256 shows the uniaxial stress dependence of the zero phonon lines in the region of the 1045 meV center for stress along the $\langle 001 \rangle$, $\langle 111 \rangle$, and $\langle 110 \rangle$ directions. This data shows forbidden crossings between electronic levels. The [001] stress splits the bound states by $60 \pm 12 \text{ meV GPa}^{-1}$, which is two-thirds that predicted for the conduction band minima, as expected.

For quantum wells the strain-induced energy shifts are very sensitive to the direction of the strain in relation to the growth axis (perpendicular to the quantum well interfaces) [402]. Strain applied

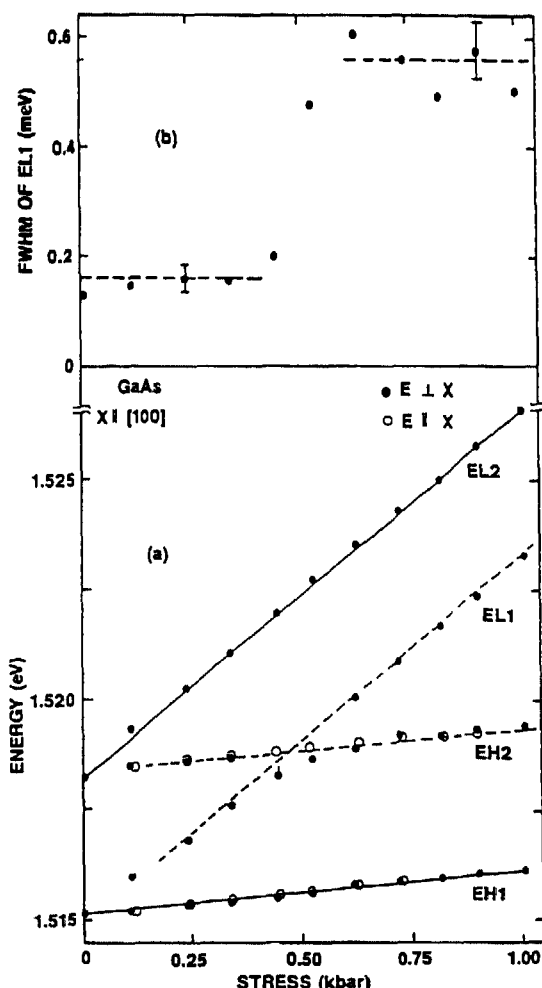


Fig. 252. (a) Uniaxial stress dependence [100] of the heavy- and light-hole excitons for two polarizations. (b) PL linewidth (FWHM) of the EL1 transition versus uniaxial stress. (Reprinted from Jagannath and Koteles, *Solid State Commun.*, 58 (1986) 417, with kind permission from Elsevier Science Ltd., Pergamon Imprint, The Boulevard, Langford Lane, Kidlington OX5 1GB, UK.)

perpendicular to the growth axis causes the heavy- and light-hole quantum well states to be admixed. As a result the transition energies associated with these states are non-linear functions of the applied strain and further depend upon the thickness of the well. Strain applied parallel to the growth axis only yields non-linear behavior for transitions associated with the light-hole states because there is no strain-induced admixing of heavy- and light-hole states. Uniaxial strain is advantageous, as is high-pressure perturbations, in being able to controllably perturb the semiconductor system. Lee et al. [413] and Jagannath et al. [414] have used uniaxial strain of GaAs/AlGaAs quantum wells to induce this admixing between light- and heavy-hole excitons. Their measurements were primarily PL-excitation measurements which will be discussed in section 2.5. Fig. 257 shows the low-temperature PL-excitation spectra of a multiple quantum well sample (220 Å wells) versus applied stress perpendicular to the growth direction. These data demonstrate the stress-induced changes in exciton energies and emission strengths. Further, they show that the light-hole excitons shift to higher energy much more rapidly than do the heavy-hole excitons. For example, the 22L transition moves to higher energy more rapidly than the peaks labeled 31H and 32H, as shown in Fig. 258. This data shows evidence for light-hole exciton and higher-lying heavy-hole exciton mixing. Jagannath et al. [414] have shown that the stress

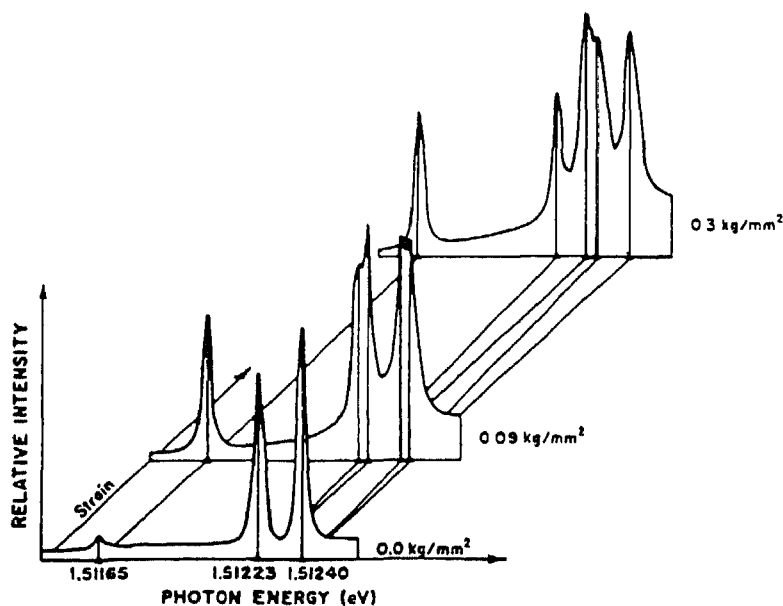


Fig. 253. PL spectra of acceptor bound exciton lines at three different strains. (After Reynolds et al. [381].)

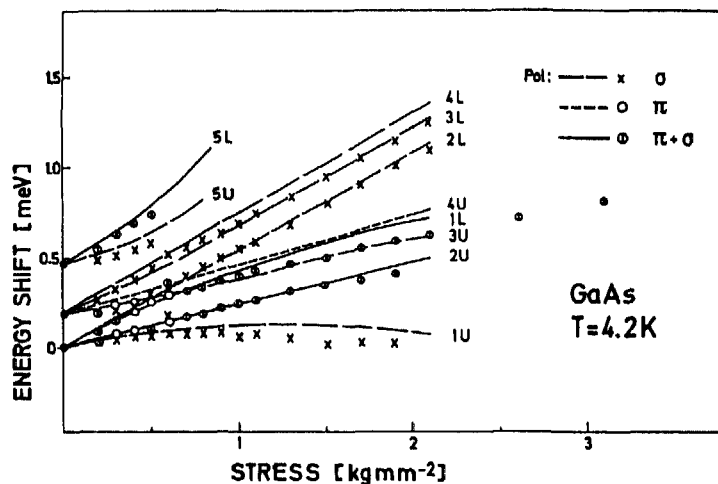


Fig. 254 [100] uniaxial stress dependence of the line shifts of shallow acceptors in bulk GaAs (After Schmidt et al. [409].)

dependence of the 2D exciton energies in a quantum well also depend upon the degree of quantum confinement (i.e. quantum well width). Their study involved PLE measurements of a multiple quantum well sample with well widths from 40 to 220 Å. Fig. 259 shows the uniaxial stress dependence of the heavy-hole and light-hole exciton energies for three quantum wells of widths 220, 110, and 40 Å. The dashed lines represent the energy shift of heavy-hole and light-hole excitons in bulk GaAs with applied stress. This data shows a systematic increase in slope of the heavy-hole exciton energy with decreasing well size, and a much smaller decrease in light-hole exciton energy with decreasing well size. The differences in the slopes of heavy- and light-hole exciton energies versus applied stress is a result of the effects of confinement on the exciton energies. As the well width decreases the wavefunction overlap between heavy and light holes, as well as their energy separation, changes, leading to these observed effects.

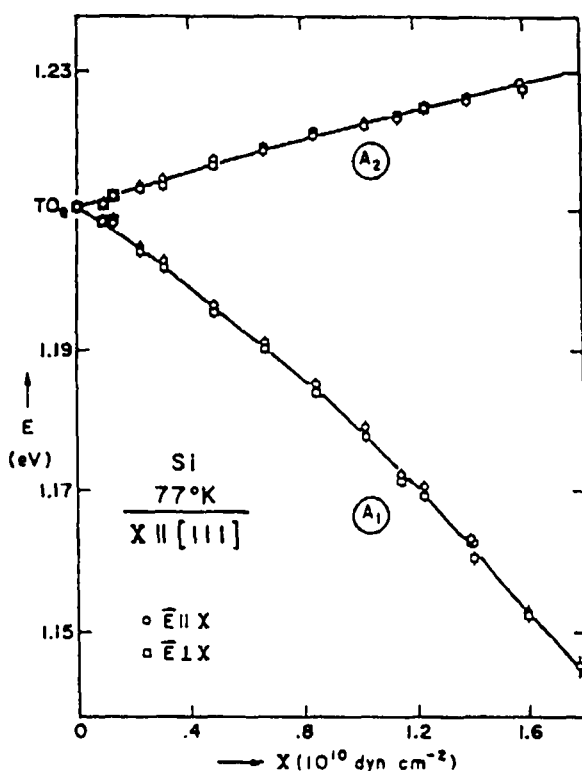


Fig. 255. Stress dependence (<111>) of the energy of the TO-phonon assisted indirect transition in Si at 77 K. (After Laude et al. [410].)

Uniaxial stress perturbations are especially suited to the study of type-II GaAs/AlAs superlattices. The indirect nature of the conduction band minimum (in the AlAs layer) and its multivalley nature (like Si) are sensitive to uniaxial perturbations. Information about the symmetry of the conduction band minimum may be obtained from both the shift and splitting of the type-II exciton with uniaxial stress. The [001] stress-induced splitting of the AlAs conduction band states (in meV) are predicted to be [415]:

$$\begin{aligned}
 & [0.42E_1(X) + 1.06E_2]\sigma \quad \text{for } X_z \\
 & [0.42E_1(X) - 0.53E_2]\sigma \quad \text{for } X_{x,y} \\
 & 0.14E_1(L)\sigma \quad \text{for } L
 \end{aligned} \tag{41}$$

where E_1 is the hydrostatic deformation potential, E_2 is the shear deformation potential, and σ is the uniaxial stress applied along the growth axis (z) in kbar. σ is negative for compressive stress, and $E_1 \ll E_2$ [415]. Therefore the energy of the X_z conduction band state should decrease with a slope of $-5.3 \text{ meV kbar}^{-1}$ with increasing stress, the energy of the $X_{x,y}$ states should increase with a slope of $+2.65 \text{ meV kbar}^{-1}$, and the energy of the L states should remain almost constant with increasing stress. The uniaxial stress induced shift in the transition energies will involve three mechanisms: the valence band splitting due to the shear strain, the hydrostatic strain induced change in the bandgap energy, and the splitting of the AlAs conduction band by the shear strain mentioned above. Ge et al. [316,416] measured this stress dependence of the emission energy in several $(\text{GaAs})_n/(\text{AlAs})_n$ short period superlattices. Fig. 260 shows the no-phonon line peak energy versus [001] stress. These data

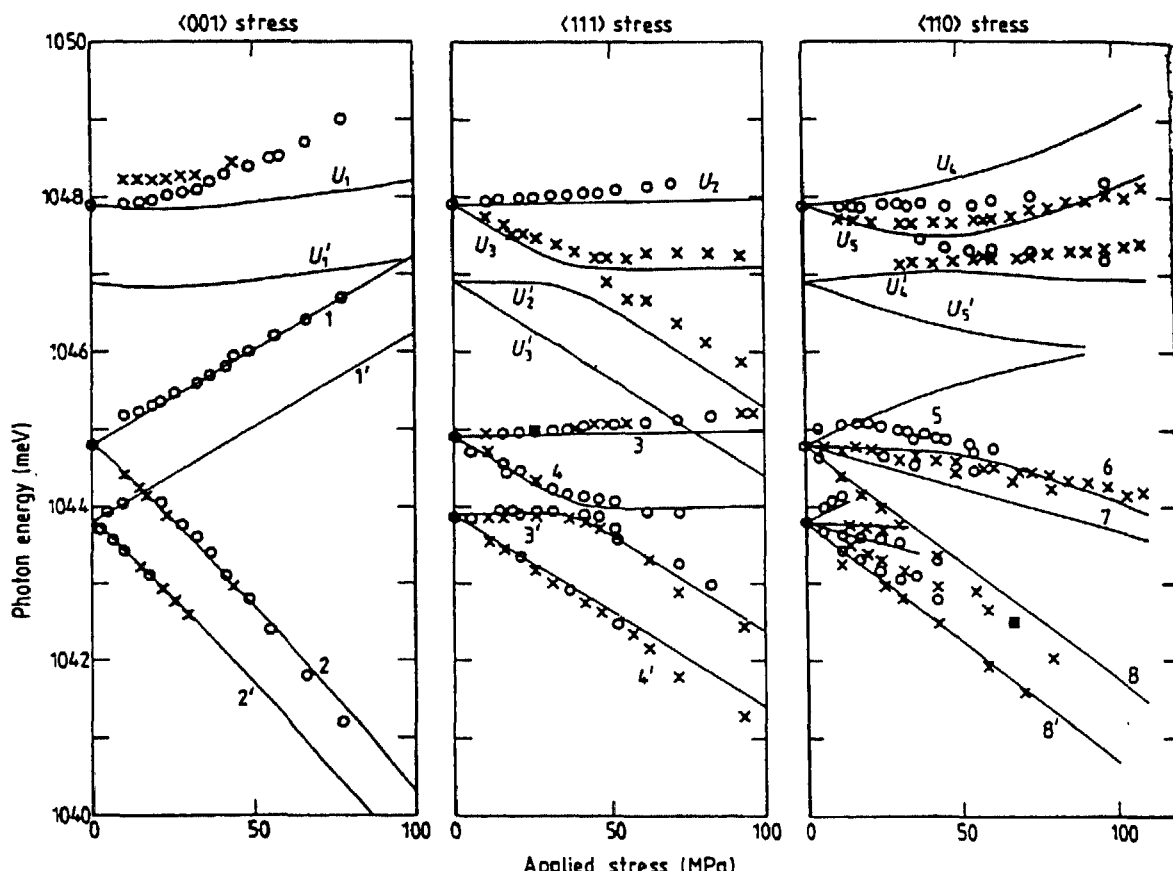


Fig. 256. Stress dependence of the energies of the 1044, 1045, and 1048 meV emission lines in Si under $<001>$, $<111>$, and $<110>$ stresses. (From Davies et al., *J. Phys. C: Solid State Phys.*, 17 (1984) L173.)

show that X_Z is the conduction band ground state for $n \geq 4$, $X_{X,Y}$ is the conduction band ground state at zero stress for $n \leq 3$, and X_Z is only 15 meV higher and may be shifted lower than $X_{X,Y}$ with increasing stress. An in-plane uniaxial stress may lead to different conduction band ground states than those for [001] stress [416]. Fig. 261 shows the PL spectra of a $(\text{GaAs})_4/(\text{AlAs})_4$ superlattice under various [110] stresses. There is a clear qualitative change in the shape of the PL spectra. As indicated in section 2.3.3.5, the relative amplitude of the no-phonon line to the phonon replicas is a good indication of the conduction band ground state of a type-II superlattice. In this data the spectra are indicative of an X_Z ground state at zero stress. However, as the stress is increased above 5 kbar, the spectra are indicative of an $X_{X,Y}$ ground state. Lastly, their uniaxial stress studies of $(\text{GaAs})_1/(\text{AlAs})_1$ superlattices do not support the prediction of an L conduction band ground state [317,416].

2.5. Photoluminescence excitation spectroscopy

As discussed in section 1, luminescence and absorption measurements are complementary techniques for characterizing the optical properties of semiconductors. There is an additional technique which is a combination of both luminescence and absorption called photoluminescence excitation (PLE). This technique measures the change in the intensity of a specific emission line (spectrally distinguished) as the excitation energy is scanned (usually to higher energies). The excitation process is fundamentally due to absorption. However, PLE differs from absorption measurements in that it is

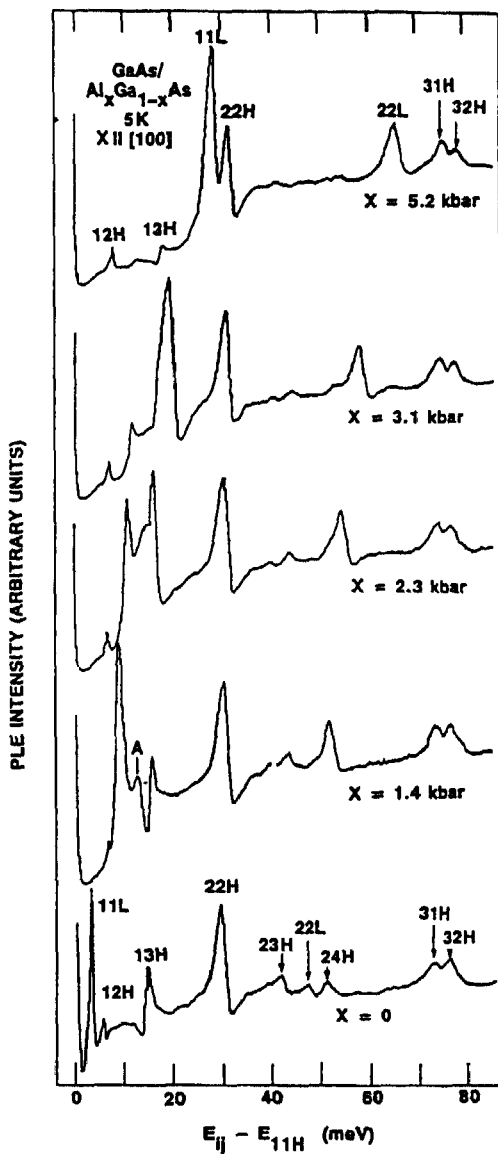


Fig. 257 5 K PLE spectra of a 22 nm GaAs/AlGaAs quantum well under several different compressive uniaxial stresses in the [100] direction. (After Lee et al. [413].)

selective. Namely, PLE is only sensitive to those absorption processes which eventually give rise to luminescence at the specific energy of detection. Thus, PLE measurements are capable of tracing the energy flow in a semiconductor system. PLE differs from PL spectroscopy since PLE measurements are sensitive to oscillator strengths independent of thermal populations of the various levels in a semiconductor. By far the most ubiquitous application of PLE spectroscopy to the characterization of semiconductors is for the quantification of the Stokes shift between absorption and emission of a specific emission line. This Stokes shift is an indication of energy relaxation of carriers to lower energy states following optical excitation and prior to the luminescence process examined. This is most often then interpreted as a measure of the inhomogeneous broadening of the sample due to defects, impurities, and/or structural imperfections.

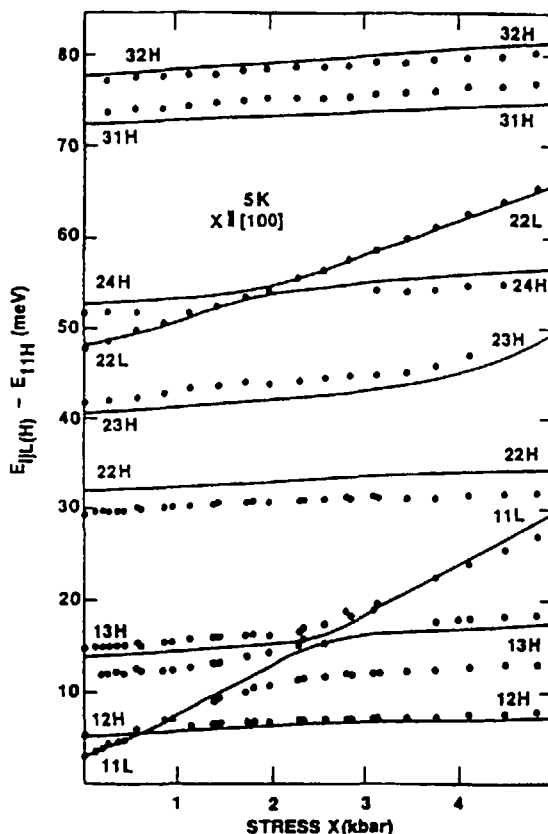


Fig. 258 Uniaxial stress dependence of the higher-energy exciton transitions with respect to the E_{11H} transition —, theoretical predictions. (After Lee et al [413])

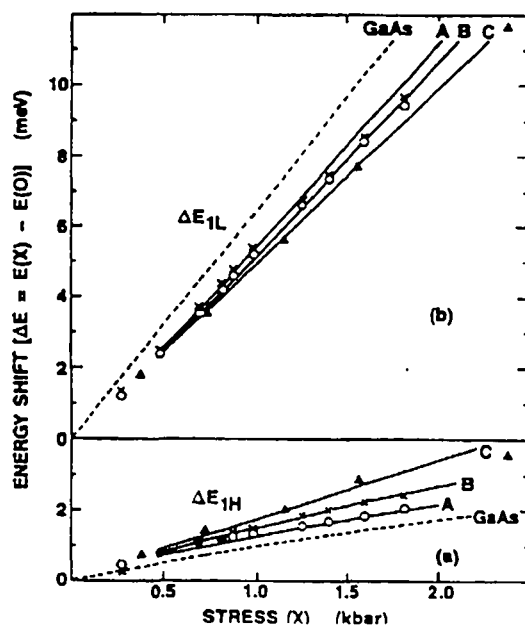


Fig. 259. Energy shifts of the (a) heavy-hole excitons and (b) light-hole excitons versus uniaxial stress. O, +, and Δ correspond to 220, 110, and 40 Å quantum wells, respectively (After Jagannath et al [414])

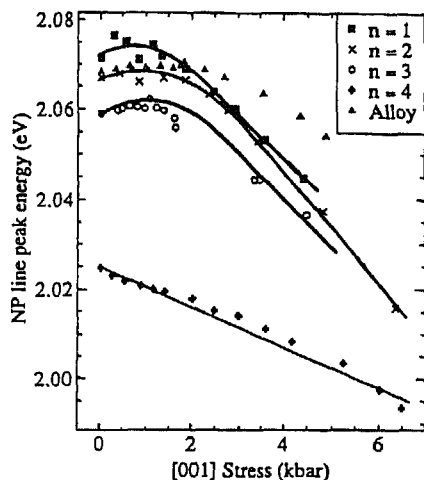


Fig. 260 [001] stress dependence of the peak energy of the PL emission in a series of $(\text{GaAs})_n/(\text{AlAs})_n$ short-period superlattices (After Ge et al. [316].)

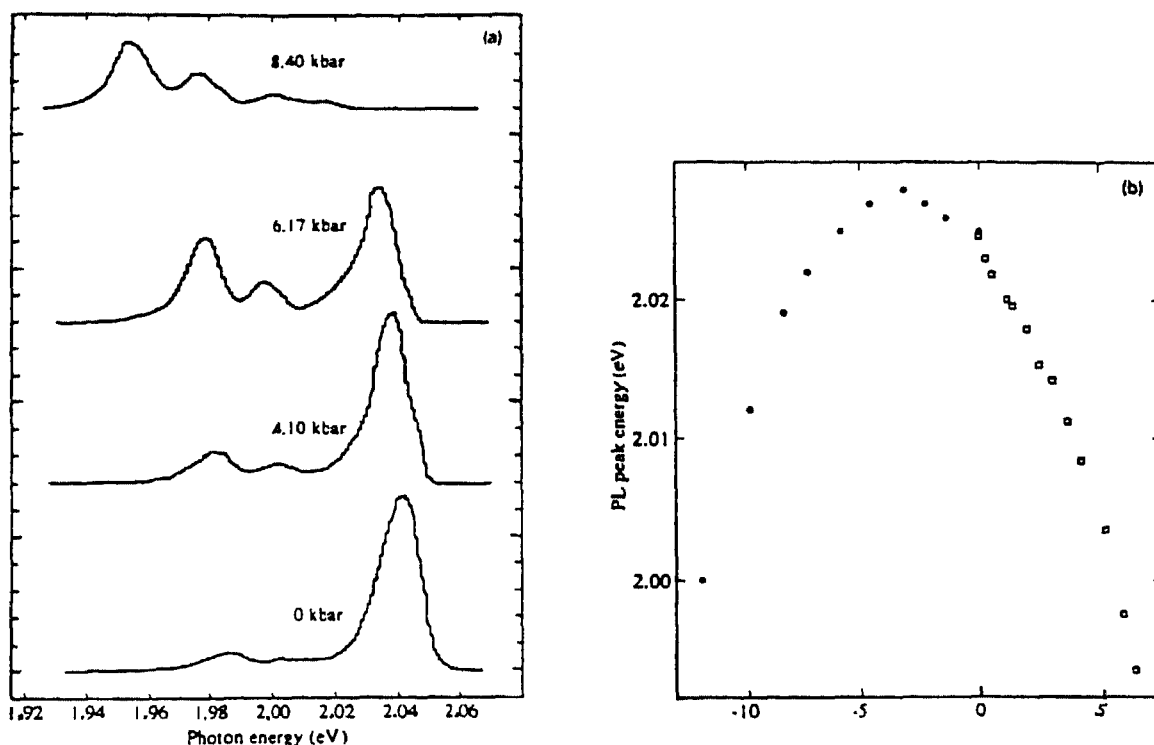


Fig. 261 (a) PL spectra of a $(\text{GaAs})_4/(\text{AlAs})_4$ short-period superlattice under several [110] stresses (b) Energy shift of the PL peak of the same superlattice under [001] and [110] stresses (After Ge et al. [416].)

PLE measurements are useful in identifying defects in semiconductors, as well as for the characterization of excited states of impurity complexes. For instance, PLE measurements may be used to characterize donors in semiconductors by monitoring a specific two-electron satellite transition and measuring the PLE spectrum in the vicinity of the shallow donor emission. The advantage of PLE is that it is not sensitive to the thermalization of carriers, and excited states may therefore be more pronounced. Karasyuk et al. [99] measured the PLE spectra of a bulk GaAs sample, monitoring the

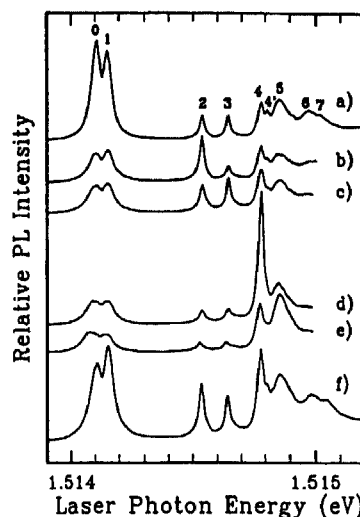


Fig. 262 PLE spectra at various detection energies within the TES emissions. Detection at (a) states 0 and 1, (b) state 2, (c) state 3, (d) state 4, (e) state 5, and (f) integrated TES spectral region. (After Karasyuk et al. [99].)

emission of different $n = 2$ two-electron satellite transitions. Fig. 262 shows the PLE spectra detecting at different peaks in the two-electron satellite transition region. These spectra clearly show the existence of eight excited states of the (D^0, X) . Further, some of the peaks present in the PL spectra are not present in the PLE spectra of the (D^0, X) two-electron satellite transitions. Thus, these peaks are not related to the donor-bound exciton. Beckett et al. [380] used PLE measurements in a magnetic field of 12 T to identify excited states of specific donor impurities. Fig. 263 shows the PLE spectra for bulk GaAs at 12 T, again monitoring the two-electron satellite transitions of Si and Ge donors. This data shows that the excited states of the Si-related transitions are shifted to higher energy relative to the excited state of the Ge-related transitions. This demonstrates the impurity-specific nature of the excited states. PLE measurements have also been used to understand the defect-induced bound exciton lines discussed in section 2.2.3.1.1(iv). Fig. 264 shows the polarization sensitive (of the excitation source) PLE spectra in the vicinity of the defect bound exciton emission (from 1.504 to 1.511 eV). The most important point of this data is that all of the sharp emission lines observed in the PL spectra in this spectral region are also observed in the PLE spectra. Skolnick et al. [119] conclude that all bound exciton emission lines are due to radiative recombination from the lowest state of the defect induced

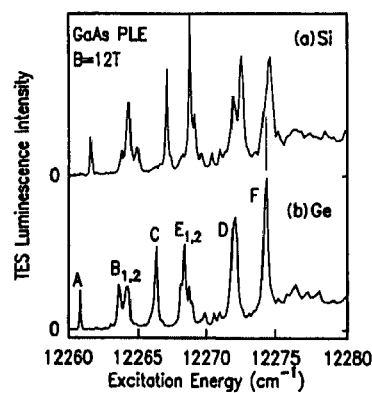


Fig. 263. PLE spectra of high-purity epitaxial GaAs. (a) and (b) correspond to Ge and Si donors, respectively. (After Beckett et al. [380].)

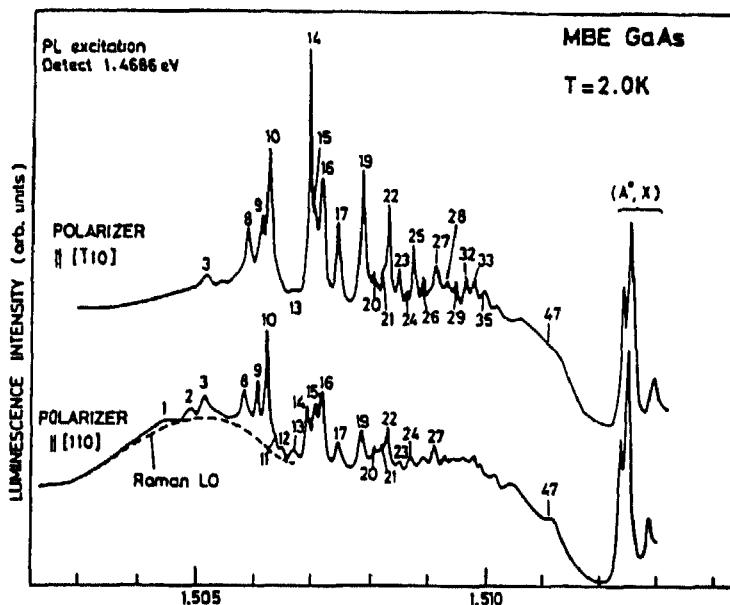


Fig. 264. 2 K PLE spectra in the region of the defect-bound exciton region. Emission was monitored at 1.4686 eV. Spectra are shown for [110] and [10] polarizations. (After Skolnick et al. [119].)

bound exciton to the ground state of the defect. Further, each line is due to a transition at independent centers.

PLE measurements are also effective in studying deep levels. Wolford et al. [196] measured the PLE spectrum of the isoelectronic N center in GaAs under hydrostatic pressure. Fig. 265 shows the PL, PLE, and resonant PL spectra of GaAs:N sample at 5 K and 62.3 kbar of hydrostatic pressure. The emission at 1.822 eV was monitored for the PLE measurements. Interestingly, the phonon replicas evident in the PL spectrum are mirrored in the PLE spectrum. The no-phonon lines ($N_X(A)$ and $N_X(B)$) are clearly distinguished due to the absence of a Stokes shift between emission and absorption. Note that the B line dominates the emission spectrum, whereas the A line dominates the excitation spectrum. This is consistent with the A line being dipole allowed and the B line being dipole forbidden.

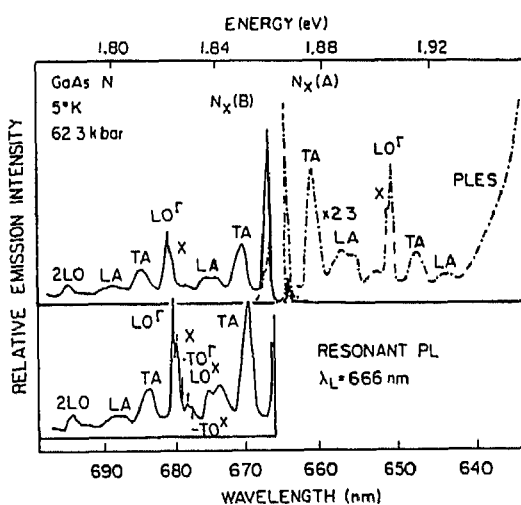


Fig. 265. PL, PLE, and resonant PL spectra of GaAs:N at a pressure of 62.3 kbar. (After Wolford et al. [196].)

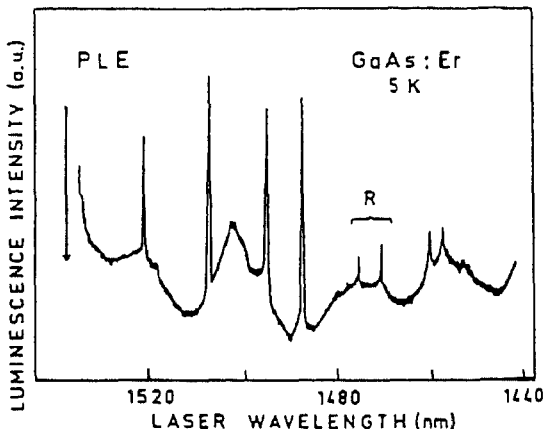


Fig. 266. PLE spectrum of erbium-doped GaAs grown by MBE. (After Ennen et al. [216].)

The relative strength of the B line in emission is simply due to a greater population in this lower energy state and the relatively large separation between A and B states of ~ 6 meV. The structure of rare-earth centers in semiconductors may also be elucidated through PLE measurements. PLE allows the determination of the crystal-field induced splitting of the excited spin-orbit J -manifold responsible for a particular intracenter 4f-4f transition. Furthermore, they give some insight into the site symmetry of the rare-earth center. Fig. 266 shows the PLE spectrum from a MBE-prepared GaAs:Er sample at 5 K in the vicinity of the principle near-infrared Er transition. This shows seven distinct no-phonon lines. For an Er^{3+} center substituted at a site of cubic symmetry, the PLE spectrum should consist of five no-phonon lines which result from transitions from the ground state to the crystal-field split excited level $^4\text{I}_{13/2}$. Thus, the site symmetry of the Er^{3+} ion must be lower than cubic symmetry. Dörnen et al. [219] used PLE measurements to understand the excitation mechanism for 4f-4f emission at 1.0 eV for Tm^{3+} -implanted GaAs. Fig. 267 shows the PLE spectra detecting at the peak of the Tm^{3+} emission (12 330 Å) and at the background (12 360 Å). The difference between these spectra is shown in spectrum 1. This shows that the 1.0 eV emission of Tm^{3+} may be excited by above-gap excitation as well as due to trapping of free excitons.

Lundström et al. [389] used PLE measurements to characterize the H-band emission in single heterojunction structures. Fig. 268 shows the PLE spectra with several different bias voltages, detecting

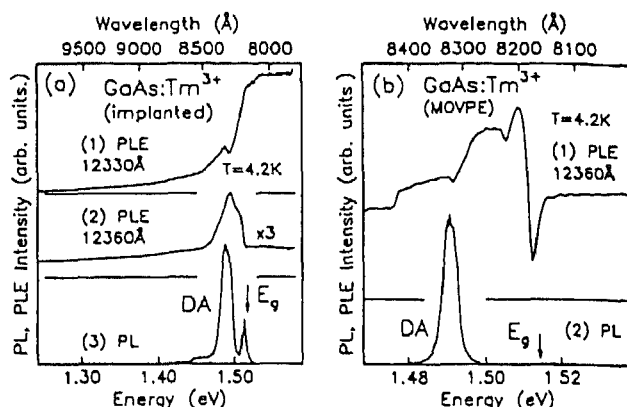


Fig. 267 (a) PL and PLE spectra of a Tm^{3+} -implanted GaAs sample; PLE monitored (1) line 1 at 1.233 μm , (2) background. (3) PL of near-edge region (b) MOVPE sample doped with Tm^{3+} ; (1) PLE of the background and (2) PL of near-edge region. (After Dörnen et al. [219].)

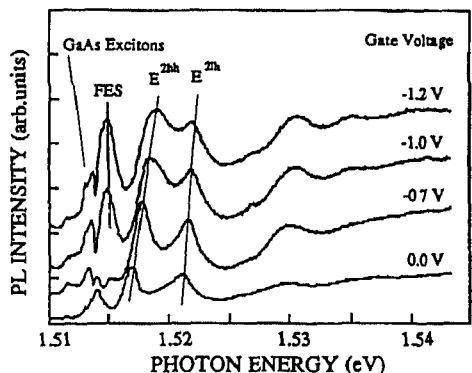


Fig. 268. PLE spectra versus applied bias in a GaAs heterostructure with a GaAs layer width of 500 Å. The Fermi edge singularity (FES) appears at a bias of -1.0 V. (Reprinted with permission from the *J. Electron. Mater.*, 22 (1993) 1353, a publication of The Minerals, Metals, and Materials Society, Warrendale, PA 15086, USA.)

at the H-band emission. This data demonstrates that the $n=2$ electron levels shift to higher energy with increasing negative gate voltage. These distinct peaks, E_{2hh} and E_{2lh} , are associated with excitons related to the $n=2$ excited electron level and the $n=1$ heavy-hole and light-hole levels, respectively. The fact that they are prominent in the excitation spectrum of the H-band emission (which is not of excitonic origin in these heavily-doped samples) signifies that the H-band, nevertheless, must originate in the trapping of excitons. The shifting of the peaks with applied field reflects the change in band-bending at the heterojunction.

The detailed structure of excited states of defect complexes in Si has also been elucidated through PLE measurements. In section 2.2.3.1.2 the 789 meV luminescent center associated with the C–O center was mentioned [141,417]. Fig. 269 shows the low-temperature PLE spectrum of the 789 meV center in Si. The many peaks evident in the spectrum are the excited states of the emission line, as indicated by the labels. This demonstrates the power of PLE measurements to uncover detailed electronic structure not accessible with PL or absorption measurements.

Weisbuch et al. [52,290] and Bastard et al. [53] demonstrated that PL and PLE measurements, when used together, are effective in the structural characterization of quantum wells. Fig. 28 demonstrates the Stokes shift between absorption and emission which characterizes the energy relaxation of

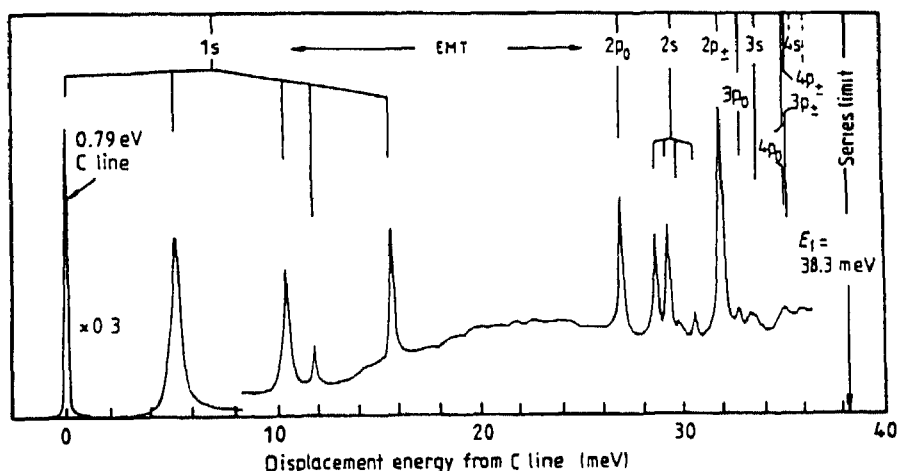


Fig. 269. PLE spectrum and an effective mass interpretation of the spectrum. (From Thonke et al., *J. Phys. C: Solid State Phys.*, 18 (1985) L795)

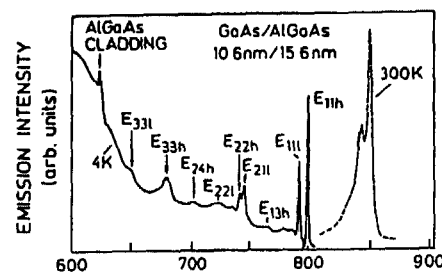


Fig. 270. PLE spectrum of a GaAs quantum well at 4 K. ---, the 300 K PL spectrum (After Cingolani and Ploog [2].)

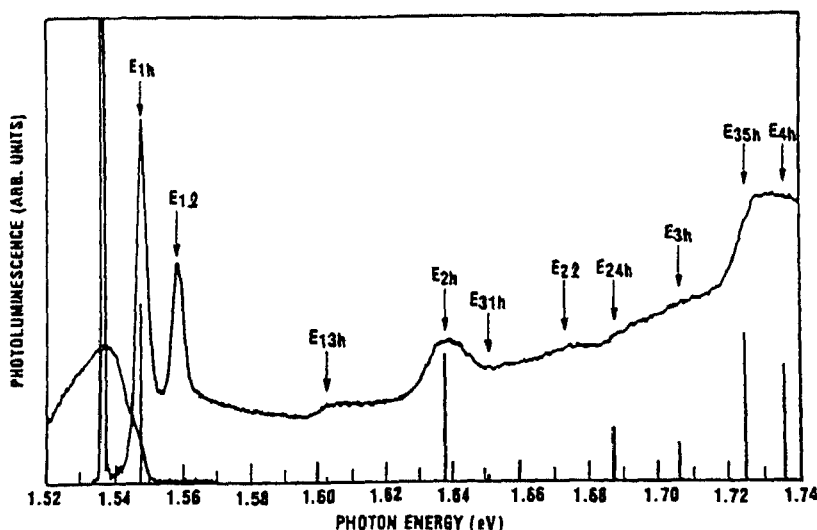


Fig. 271. 6 K PL and PLE spectra for a stepped quantum well sample. The PLE spectrum was detected at 1.537 eV. (After Miller et al. [418].)

excitons after absorption and prior to emission. The energy relaxation takes place within the inhomogeneously broadened absorption line, and the inhomogeneous broadening results from interfacial roughness. The PLE spectrum also demonstrates the splitting between the heavy hole and light hole. PLE may be further utilized to characterize excited state transitions in quantum wells. Fig. 270 shows the PLE spectrum of a quantum well together with the low- and room-temperature PL spectra [2]. The transitions to excited electron and hole states are clearly marked as, for example, E_{33l} for a transition from the $n = 3$ light-hole band to the $n = 3$ conduction band or E_{24h} for a transition from the $n = 4$ heavy-hole band to the $n = 2$ conduction band. The E_{11h} transition overlaps exactly the low-temperature emission spectrum. Miller et al. [418] used PLE measurements of a stepped quantum well (quantum well within a quantum well) to determine the band offsets for GaAs/AlGaAs structures. Fig. 271 shows the PL and PLE spectra of the stepped quantum well. The excitation spectrum was detected at 1.537 eV. They fit the subband structure, evident in the PLE spectrum, and deduced a valence band offset of 42%. PLE measurements may also show unique aspects of modulation-doped quantum wells. Fig. 272 shows the PL and PLE spectra of an n-type modulation-doped (10^{12} cm^{-2}) quantum well [374]. Even though this structure is degenerately doped, there is clear evidence for excitonic transitions in the PLE spectrum. The higher excitonic states may coexist with the 2DEG present in the sample due to the orthogonality of the excitonic wavefunctions and decreased screening for higher-lying levels.

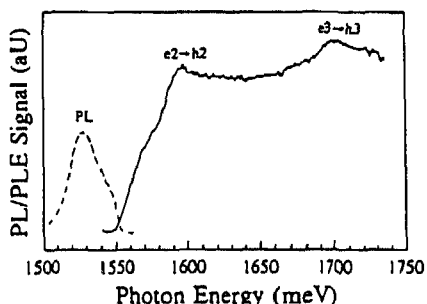


Fig. 272. PL (---) and PLE (—) at 10 K of a 150 Å/150 Å GaAs/AlAs modulation-doped (Si doped to $1.2 \times 10^{18} \text{ cm}^{-3}$ in the AlAs layers) superlattice.

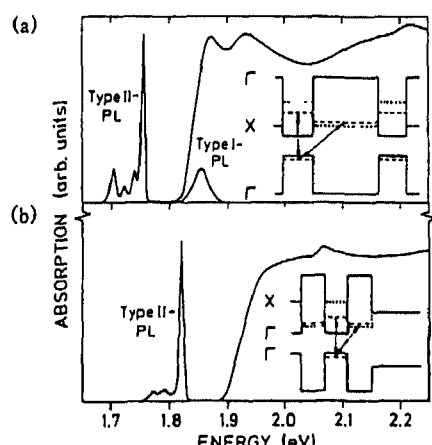


Fig. 273. PL and absorption spectra of (a) $(\text{GaAs})_{11}/(\text{AlAs})_{24}$ and (b) $(\text{GaAs})_9/(\text{AlAs})_9$ short-period superlattices. (After Feldmann et al. [419])

Type-II nanostructures exhibit distinctive characteristics in their PLE and PL spectra. Fig. 273 shows the PL and PLE spectra of two $(\text{GaAs})_n/(\text{AlAs})_m$ short-period superlattices with (a) $(n,m) = (11,24)$, and (b) $(n,m) = (9,9)$ [419]. The PLE was detected at the peak of the type-II no-phonon emission. Note that there is essentially no absorption into the type-II level or at energies directly above this level in energy. The absorption is, however, evident at the same energy as the type-I transition, as demonstrated in the PL spectra. This is proof of the interlayer electron scattering from the Γ point of the GaAs layer to the X point of the AlAs layer.

Phillips et al. [232] used PLE measurements to further authenticate biexciton emission in their quantum well structures. Fig. 274 shows the PLE spectrum of a GaAs/AlGaAs quantum well with the detection energy centered at the biexciton luminescence at 1.5495 eV. The upper inset shows PL spectra at excitation powers of 0.1 and 0.01 W cm⁻² and excitation resonant with the light-hole exciton absorption line. The lower inset shows PL spectra at excitation powers of 1 and 0.1 W cm⁻² and excitation at 1.57 eV (out of resonance). The higher excitation powers in the lower inset compensated for the lower absorption. They find that the biexciton emission is enhanced for resonant excitation of cold light-hole excitons. They obtained similar results for heavy-hole exciton excitation. These results demonstrate that injection of "hot carriers" is not conducive to biexciton formation due to the relative small binding energy of the biexciton.

Quantum well wire structures are especially amenable to PLE characterization. Polarized PLE is effective in qualifying the anisotropy of the absorption with respect to the orientation of the wire,

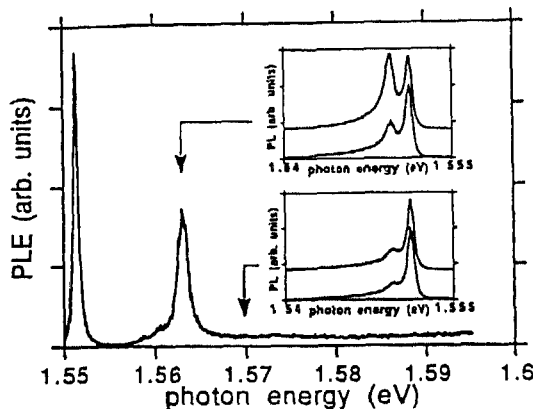


Fig. 274. PLE spectrum of the biexciton emission measured at 1.6 K. Detection was at the biexciton emission at 1.5495 eV. Insets show PL spectra for excitation resonant with the light-hole transition and for non-resonant excitation [232].

thereby confirming the lateral confinement. As mentioned in section 2.3.4, Fig. 185 demonstrates this optical anisotropy for a quantum well wire array [337]. Here the polarization-resolved PLE spectra of the quantum well (upper part) exhibits very little anisotropy, whereas the quantum well wire spectra (lower part) exhibits significant anisotropy. The broadening of the absorption peaks in the quantum well wire sample compared to the quantum well sample is evidence for inhomogeneous broadening. Miller et al. [343] have observed a similar anisotropy in the polarization-sensitive PLE measurements of serpentine superlattice quantum wire arrays. They find no indication of higher subband structure in their PLE measurements [342]. Further, they observed that the absorption is stronger parallel to the wires at energies a few meV below the PLE peak and is stronger perpendicular to the wires a few meV above the PLE peak. At still higher energies the absorption is observed to be isotropic. Kohl et al. [328] have used PLE measurements in a magnetic field to assess the quantization and excitonic properties of their etched quantum wires. Fig. 275 shows the energy positions of the maxima in the

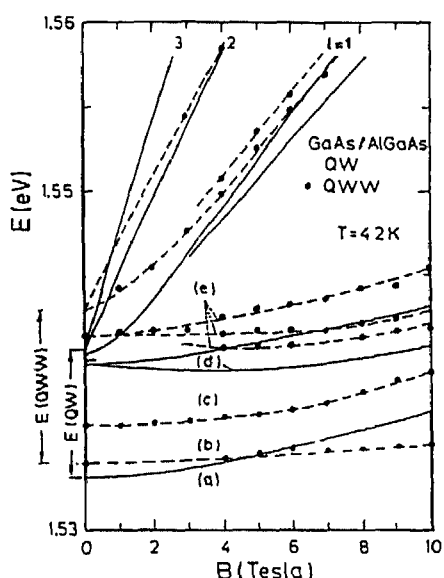


Fig. 275. Energies of the various peaks apparent in the PLE spectra of a 70 nm quantum well wire versus magnetic field. (a)–(e) denote the hh₁, hh₁₁, hh₁₂, lh₁, and lh₁₁ transitions, respectively (After Kohl et al. [318])

magnetic-field dependent PLE spectra of a 70 nm quantum well wire. The solid lines represent the dispersion for the transitions of a reference quantum well sample, clearly showing significant differences between the quantum well wire and quantum well samples. First, the hh_{11} ground state transition (lowest dashed line) exhibits a much smaller diamagnetic shift than the reference quantum well sample. This is an indication of a stronger excitonic interaction. Second, the hh_{12} transition (second lowest dashed line) is excitonic, but with a larger diamagnetic shift. Third, the inter-Landau-level separation (labeled $l = 1, 2, 3$) is smaller than in the reference sample. All of these results are consistent with 1D magnetoexciton properties. From this data, they deduced an enhancement of the reduced mass and of the exciton binding energy of the ground-state heavy-hole exciton (7.5 meV) of about 15%.

3. Time-resolved photoluminescence

3.1. Measurement techniques

There are many varieties of techniques for obtaining temporal as well as spectral information pertaining to the emission from semiconductors [420]. These techniques include phase-sensitive detection, time-resolved analog detection, time-correlated single-photon counting, Streak camera detection, pump-probe measurements (these types of measurements do not rely on luminescence emission, and, therefore, are beyond the scope of this article), and ultrafast luminescence upconversion detection. The most commonly used technique, by far, is time-correlated single-photon counting. All of these techniques require pulsed laser sources. The time resolution ultimately obtainable with any of these techniques is limited by the pulselwidth of the laser. (There are some studies of time-resolved phenomenon using incoherent light with, for example, nanosecond nitrogen laser pulses, but the fast time resolution obtainable (femtoseconds) is achieved using coherent transient effects. These techniques are beyond the scope of this article.)

In order to understand the analog detection and time-correlated single-photon counting techniques it is necessary to understand the operation of the equipment used to detect the luminescence, the photomultiplier tube (PMT). The luminescence from the sample is typically detected by a PMT after being spectrally dispersed by a spectrometer to discriminate the required spectral signature. The PMT then produces temporally short current pulses for each photon absorbed by the photocathode. This is accomplished in a multi-step process. The photocathode generates a primary electron which is accelerated by the high electric field between the photocathode and the anode. The primary electron is focused on a chain of dynodes between the photocathode and the anode which serve to generate an avalanche of secondary electrons which ultimately form the output current pulse. The gain of a PMT is typically 10^5 – 10^6 . The temporal characteristics of the current pulse are then characterized by the rise time of the pulse and the transit time dispersion of the electrons through the dynode chain, which are both typically a few nanoseconds. The spectral response is determined by the absorption of the photocathode. The most popular PMT in the visible region of the spectrum is the RCA C31034 (GaAs photocathode) which has a relatively flat spectral response from 200 to almost 900 nm. Another photon detector which has an even faster time response than the PMT is the microchannel plate (MCP). A MCP detector is a secondary electron multiplier consisting of an array of millions of glass capillaries (channels) with very small internal diameters (typically 10–20 μm). These capillaries are formed into the shape of a thin disk less than 1 mm thick. The inside wall of each capillary is coated with a secondary electron emissive material. Thus, each channel is an independent electron multiplier. MCP detectors are available with transit time spread (at FWHM) of only 22 ps.

3.1.1. Phase-sensitive detection

This technique involves the measurement of the phase shift between a sinusoidal excitation source and the resulting luminescence, and is potentially capable of time resolutions of 10 ps [421,422]. Fig. 276 shows a block diagram of the experimental arrangement for this type of time-resolved measurement. The laser beam excitation source is modulated at a frequency ω . Assuming that the luminescence decay constant, τ , is small compared to the period of modulation, the luminescence will be delayed by a time τ also, yielding a phase delay $\phi = \omega\tau$ of the luminescence relative to the excitation light. The time resolution of this technique varies inversely with the signal-to-noise ratio, and for a signal-to-noise ratio of 100, and a modulation frequency of 100 MHz may be as short as 16 ps. In the figure a mode-locked laser, operating at 100 MHz, is used as the excitation source. A reference signal is generated at this frequency by detecting a portion of the beam by a photodiode. The phase of the reference may be varied by sending it through a variable delay line. The luminescence signal is detected with a PMT, and that portion which is in phase with the excitation frequency of 100 MHz is detected with a balanced mixer. In addition to the pulsed laser, the laser is chopped at a low frequency (95 Hz in this example). The phase change in the PMT signal is then detected by measuring the zero point of the phase-detected signal corresponding to the $\pi/2$ out-of-phase condition between the reference and PMT signal. The phase delay, from which the lifetime of the luminescence is determined, is obtained by adjusting the variable phase delay of the reference signal until the phase-sensitive detected signal from the PMT goes to zero.

3.1.2. Time-resolved analog detection

Analog detection is perhaps the most straight-forward technique for detecting signals generated by photomultiplier tubes. The current pulses generated by the photons in the luminescence signal may be directly recorded, after amplification, by an oscilloscope. The signal may be analyzed in steady

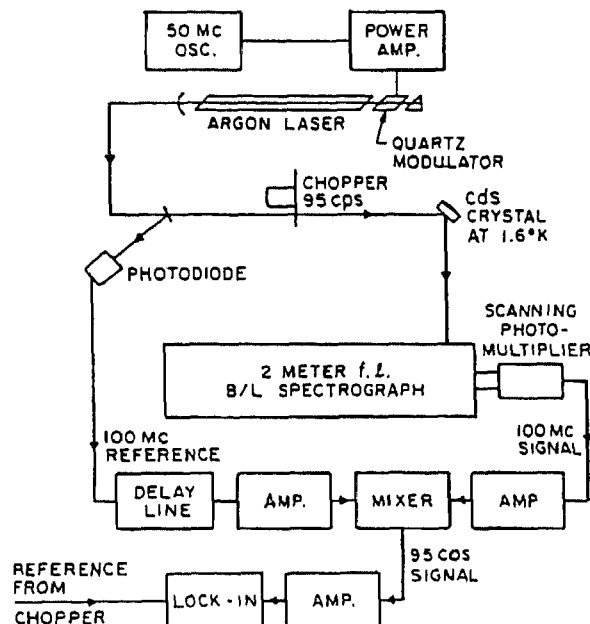


Fig. 276. Block diagram of the instrumentation used in the phase-shift technique for determining carrier lifetimes. (After Henry and Nassau [422].)

state for cw excitation or as a transient for pulsed excitation. For steady-state detection the voltage level of the pulses from the PMT (converting the current pulses to a voltage) are proportional to the number of photons detected by the PMT, assuming that there is no saturation. For transient detection care must be exercised so as not to distort the temporal characteristics of the current pulses either in the coaxial line or in the current-to-voltage converter. This requires care in selecting the RC (Resistance*Capacitance) time constants of the electronics used in the measurement. The temporal waveform of the detected signal may then also be displayed and recorded on an oscilloscope.

3.1.3. Time-correlated single-photon counting

Time-correlated single-photon counting utilizes a fast laser pulse to excite the semiconductor [423,424]. Fig. 277 shows a typical block diagram of the detection electronics used with this technique. The time difference between excitation and the detection of a single luminescence photon is measured with a time-to-amplitude converter (TAC). Thus, the time difference between the fixed (in time) excitation source and the delayed, and statistically varying luminescence pulses is converted to a voltage whose amplitude is proportional to this time delay. Successive excitation pulses thereby generate luminescence photons whose emission times relative to the excitation pulse vary in a statistical fashion. The time-correlated single-photon counting technique then converts this statistical distribution of delayed luminescence photons into a series of varying amplitude TAC output voltages. These TAC pulses (of varying amplitude) are then histogrammed (by a multichannel analyzer) to recreate the time distribution of the luminescence signal.

The reference signal (or start signal) used for the TAC conversion is generated by a split-off portion of the excitation laser pulse. This pulse is typically detected by a photodiode (PD) with a fast

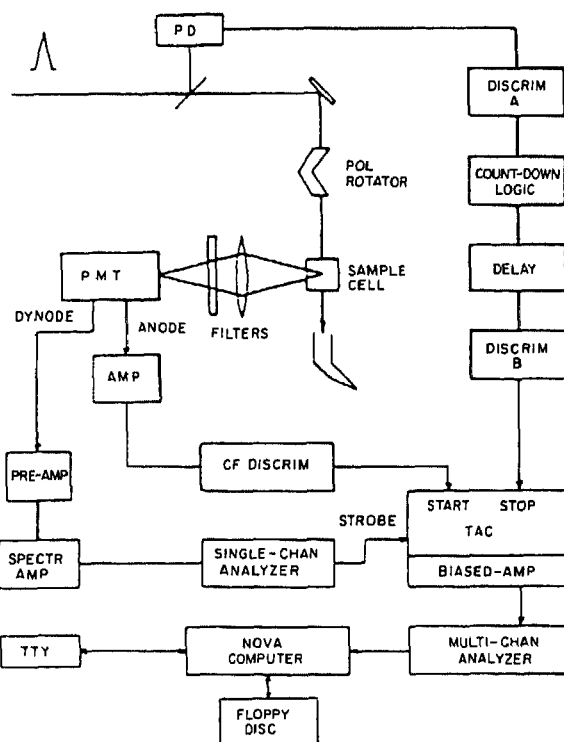


Fig. 277. Block diagram of the electronic elements necessary for single-photon counting. (After Spears et al. [423].)

time response. The stop signals are generated by the PMT or MCP detectors. These stop signals are then amplified by a fast preamplifier (typically 40 dBm and 500 MHz bandwidth). The start signal and the amplified stop signals are then discriminated by a constant fraction discriminator (CFD) which eliminates timing jitter due to pulse-height fluctuations. The discriminated start signal is then suitably delayed to vary the zero time. After being delayed the start signal is again discriminated by another CFD. The outputs from the start and stop CFDs are square voltage pulses which are the inputs to the TAC. With optimal choices of detectors, preamplifiers, PD, CFDs, and TAC, temporal resolutions of 500 ps and 30 ps may be obtained with PMT and MCP detectors, respectively.

3.1.4. Streak camera detection

Streak cameras are ultra-high speed photodetectors capable of detecting phenomena on the picosecond timescale. Incident light is focused onto an entrance slit which is then transferred via a transfer lens to the photocathode of the streak camera. This photocathode converts the incident photons into photoelectrons which are then accelerated by the electrostatic field between the photocathode and a mesh electrode. Subsequently, these electrons enter a deflection field (high-speed sweep of an electric field), and are swept onto the MCP at high speed in the direction perpendicular to the slit length (in the direction of the field sweep). This is done by applying the deflection field synchronously with the arrival of the electrons. This is illustrated in Fig. 278 [425]. The temporal information is determined by the spatial position of the electrons on the phosphor screen or other detector, and the intensity of the incident light is proportional to the density of the streak image. Additional information may be obtained from this type of detector by coupling the Streak camera to a monochromator. By projecting the spectrum on the slit of the Streak camera, after spectral dispersion by the monochromator, the horizontal axis of the streak image corresponds to wavelength. Thus, time-resolved spectra are easily measured with this configuration. Moreover, use of suitable optics allows the quantification of the time variation of the incident light with respect to spatial position. Streak cameras may operate in several different modes of operation, including single sweep mode, synchroscan mode, elliptical sweep mode, sampling mode, and framing mode. Temporal resolutions of less than 600 fs are obtainable with Streak cameras. However, the major disadvantage of Streak camera detection is that strong luminescence signals are typically required.

OPERATING PRINCIPLE, FUNCTIONS AND PERFORMANCE

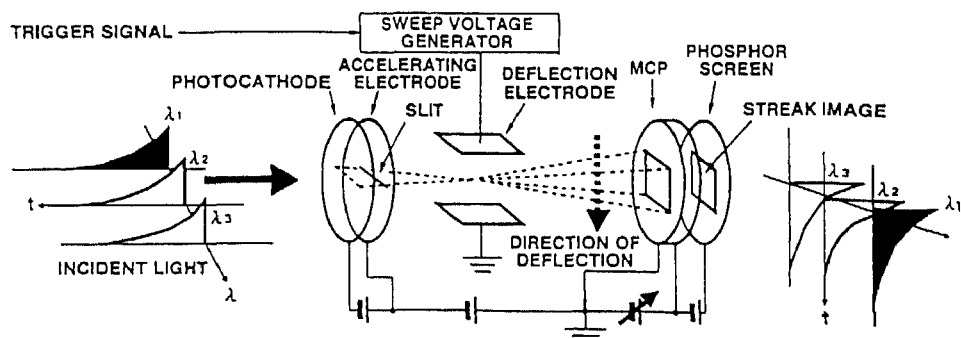


Fig. 278. Schematic diagram of the Streak camera operating principle. (Reproduced with permission).

3.1.5. Ultrafast luminescence upconversion measurements

This technique makes use of the non-linear optical properties of non-centrosymmetric crystals as a means of providing time resolution. In this technique, the luminescence excited by an ultrafast laser (pump pulse) is mixed with the laser (probe pulse) in a non-linear crystal to generate sum frequency radiation which is subsequently detected by a PMT [426]. Time resolution is then obtained by delaying the probe pulse with respect to the pump pulse, as illustrated in Fig. 279. The frequency mixing in the non-linear crystal serves as a gating mechanism, providing a time resolution comparable to the laser pulselength. Spectral information is obtained by "tuning" (i.e. rotating) the phasematching angle of the crystal. Ultimate time resolutions in this system require careful consideration of the group velocity dispersion of each and every optical element in the system, and is most often achieved through the exclusive use of reflective (as opposed to refractive) optics. Fig. 280 shows a schematic diagram of a luminescence upconversion system. In practice this system has been demonstrated to be capable of temporal resolutions of < 400 fs.

3.2. Intrinsic and extrinsic recombination

3.2.1. Free-carrier recombination (band-to-band recombination)

Free-carrier recombination in semiconductors is a bimolecular process (i.e. involving both electrons and holes). Eqs. (5) and (6) show that the probability for recombination is proportional to quadratic terms in the injected carrier density and linear terms in the injected carrier density. Thus, the

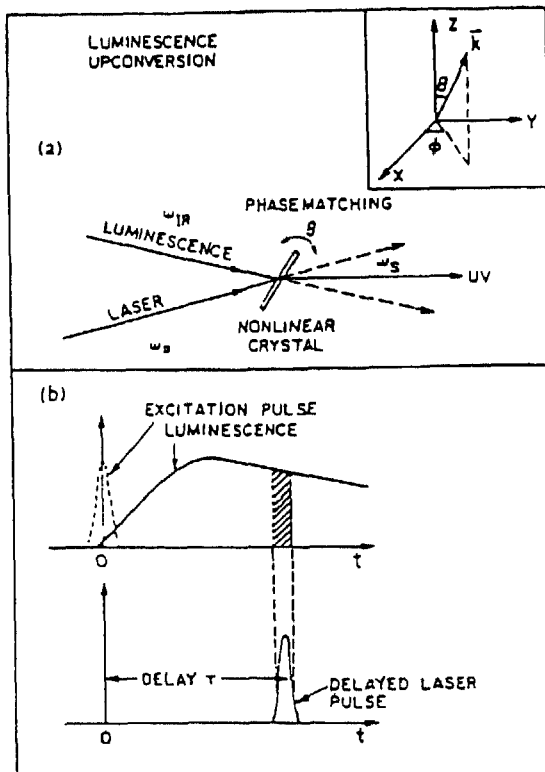


Fig. 279 Schematic of the PL upconversion technique. UV light generated from the sum-frequency mixing of the PL and laser light is only generated during the time that the laser pulse and PL are both present. (After Shah [426], © 1988 IEEE.)

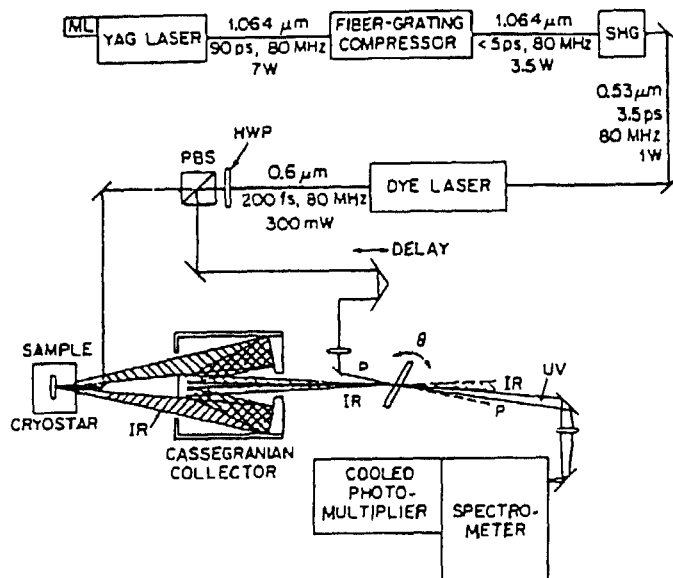


Fig. 280. Diagram of the PL upconversion system. Laser is split into two beams, and the PL is collected by non-dispersive optics. (After Shah [426], © 1988 IEEE.)

temporal shape of the PL time decay will be sensitive to the injected carrier density relative to the built-in carrier density (majority carrier, electrons or holes). The constant of proportionality in the bimolecular radiative recombination of free carriers is the radiative recombination coefficient. Nelson and Sobers [427] measured the PL time decays of free-carrier recombination at room temperature in bulk LPE GaAs samples doped with Ge acceptors to concentrations ranging from $1.9 \times 10^{15} \text{ cm}^{-3}$ to $1 \times 10^{19} \text{ cm}^{-3}$. Fig. 281 shows the PL time decay of a GaAs layer p-doped to $1.9 \times 10^{15} \text{ cm}^{-3}$. The lifetime, derived from the exponential tail of the decay (equal to the time at which the emission has decayed to e^{-1} of its $t=0$ value), is 1.3 ms. The exponential nature of the decay indicates that the recombination is dominated by the majority carrier species. If the decay were bimolecular then the decay would be due to the recombination of photoinjected carriers. These measurements are, therefore, in the low-injection regime. Fig. 282 shows the variation of the PL decay times with p-doping level.

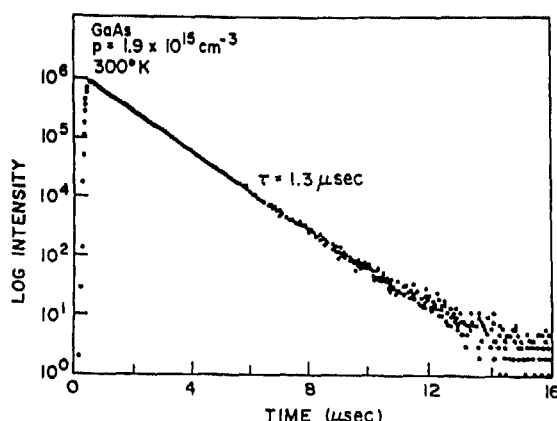


Fig. 281. PL time decay of LPE-grown GaAs double heterostructure with a background doping of $p = 1.9 \times 10^{15} \text{ cm}^{-3}$. (After Nelson and Sobers [427].)

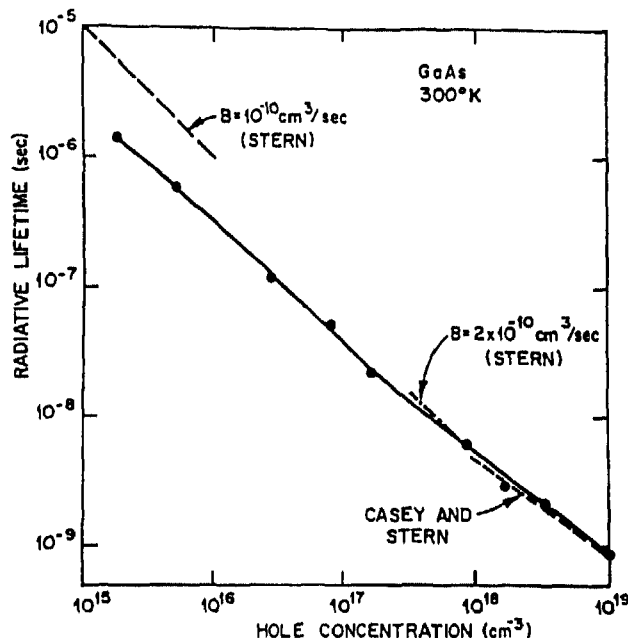


Fig. 282. Radiative lifetimes determined from PL kinetics measurements versus hole concentration. (After Nelson and Sobers [427].)

From these measurements a value of $2 \times 10^{-10} \text{ cm}^3 \text{ s}^{-1}$ is derived for the radiative B coefficient, which is consistent with other estimates [265,428].

Band-to-band recombination kinetics are sensitive to many factors including background doping, photoexcitation intensity, surface treatments (to be discussed in section 3.2.8), layer thickness, optical

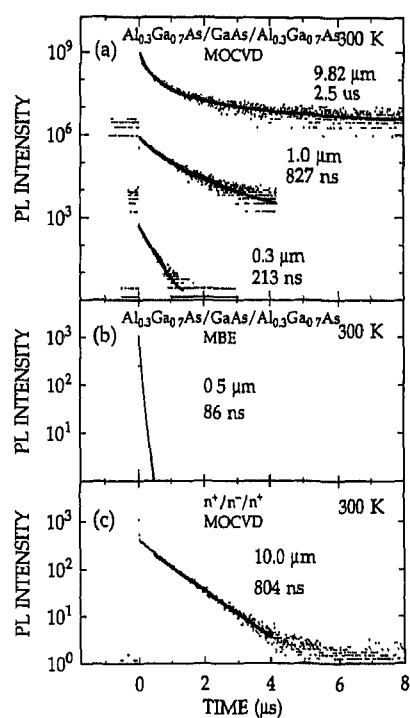


Fig. 283. Room-temperature free-carrier PL kinetics for three different structures. (After Wolford et al. [28].)

density, excitation energy, and temperature. Fig. 283 shows an example of the sensitivity of the decay kinetics to layer thickness and type of structure (heterostructures and homostructures) at room temperature and with the same excitation intensity [11,28]. At this temperature the thickest heterostructure exhibits bimolecular recombination with an exponential tail governed by non-radiative surface recombination. For thinner heterostructures, the decays become exponential and shorter with decreasing layer thickness. Wolford et al. [11,28] found that this systematic change in decay kinetics is evidence for "effective modulation doping" of the n-type GaAs layers by the p-type AlGaAs barriers (all of which were nominally undoped). The shorter lifetimes are indicative of an increase in the hole concentration in the layer. Essentially, as the GaAs layer becomes thinner, the n-type GaAs layer becomes fully depleted, and then begins to accumulate holes from the barrier layers (i.e. type conversion). In contrast the $n^+ / n / n^+$ homostructure exhibits only rigorously exponential decays consistent with the majority carrier density of electrons in the layer.

The temperature dependence of the decay kinetics, under constant excitation, also show evidence for the sensitivity of the recombination kinetics to the details of the structure. Fig. 284 shows the PL decay kinetics for three of these bulk GaAs structures versus temperature. The decay kinetics for the thick heterostructure are bimolecular at all temperatures down to under 10 K. Lifetimes derived from fits to the data decrease with decreasing temperature. The kinetics for thinner heterostructures are exponential at high temperatures (70–300 K), and become non-exponential at low temperatures. Wolford et al. also found that lifetimes first decrease and then increase with decreasing temperature. The results for the homostructures are similar to those of the thin heterostructures. Eq. (2) shows that the majority carrier density should vary with temperature as $T^{3/2}$. Therefore, the lifetime of recombination dominated by the majority-carrier density should also vary as $T^{3/2}$ [428]. Fig. 285 shows the minority-carrier lifetime for the homostructure versus temperature. Fits to the data are obtained by assuming a compensation ratio and calculating the steady-state Fermi-level followed by the majority-carrier density, all versus temperature. This comparison between experiment and theory shows that the lifetime data provides a useful way for determining compensation ratios. Fig. 284 also shows the complex temperature-dependent lifetimes for the thick and thin heterostructures. In region I, (thick

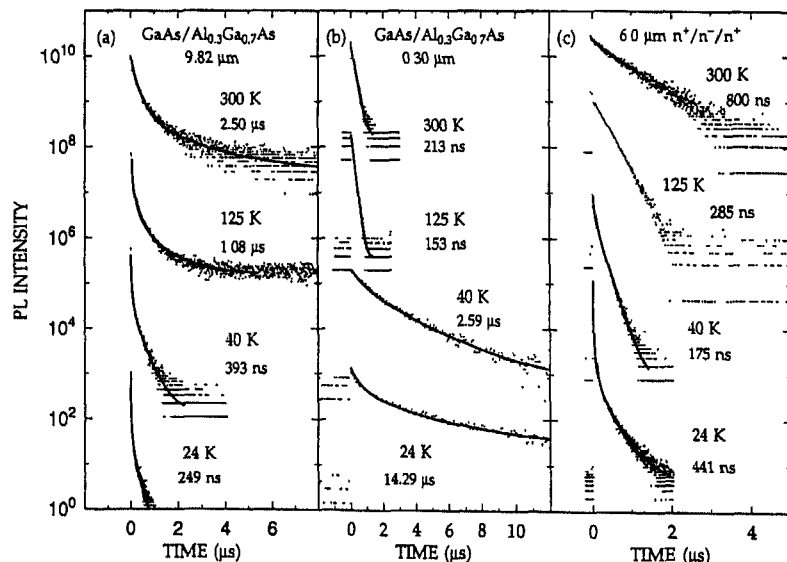


Fig. 284. PL decay kinetics at various temperatures for (a) $9.82 \mu\text{m}$ thick GaAs/AlGaAs double heterostructure, (b) $0.30 \mu\text{m}$ thick GaAs/AlGaAs double heterostructure, and (c) $6.0 \mu\text{m}$ thick $n^+ / n / n^+$ GaAs homostructure. (After Wolford et al. [11])

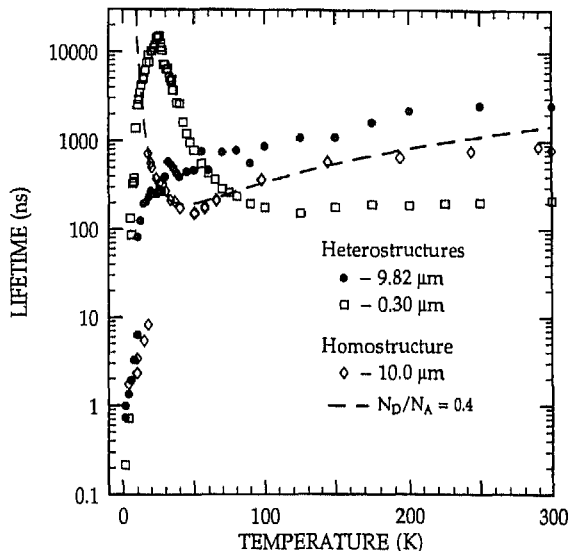


Fig. 285. Minority-carrier lifetimes versus temperature for two MOCVD-prepared GaAs/AlGaAs heterostructures, and a GaAs homostructure. (After Wolford et al. [28].)

structures for $70 < T < 300$ K) the decays are non-exponential, and bimolecular. The temperature dependence of the lifetimes varies as $T^{3/2}$. At room temperature we find a saturation in the lifetimes below the $T^{3/2}$ prediction, which may be attributed to bulk non-radiative decay or surface recombination. In region II, (thin structures and $70 < T < 300$ K) all decays are rigorously exponential. The monomolecular nature of the decays is a result of the dominating effects of the majority carrier density which increases with decreasing thickness due to the "effective modulation doping". In region III (for all structures between 25 and 70 K), the decays are non-exponential. Thin structures exhibit lifetimes which increase with decreasing thickness. This increase is due to the "freeze out" of the majority-carrier density. In the extreme case of the 0.30 μm structure, this leads to a 15 μs lifetime at 25 K. Wolford et al. attributed this to a temperature-dependent compensation effect resulting from the complex nature of the temperature-dependent freeze out and compensation. In region IV (for all structures at $T < 25$ K), the decays are non-exponential and become rigorously exponential at the lowest temperatures (1.8 K). This data shows the temperature-dependent coupling between free carriers and free excitons.

PL decay kinetics of emission in $\text{Al}_x\text{Ga}_{1-x}\text{As}$ are sensitive to the composition of the alloy [429]. Timmons et al. [429] examined the PL decay kinetics of OMVPE-grown AlGaAs layers grown as double heterostructures with active layer compositions ranging from $x=0.0$ to $x=0.36$. $\text{Al}_x\text{Ga}_{1-x}\text{As}$ barriers had a composition of $x=0.5$. They find a monotonic decrease in the lifetime (derived from the long-time portion of the PL time decays) with increasing Al composition, as shown in Fig. 286. They further find that the lifetimes are longer at higher growth temperatures. Their data suggests the presence of non-radiative centers which are introduced with the Al organometallic source.

3.2.2. Free-exciton recombination

The kinetics of free-exciton recombination have been the subject of much controversy for many years. Reported free-exciton lifetimes in bulk GaAs vary over four orders of magnitude, and reported free-exciton lifetimes in GaAs quantum wells vary over two orders of magnitude. The difficulties in predicting and determining the true radiative lifetime of free excitons arise from interactions of the

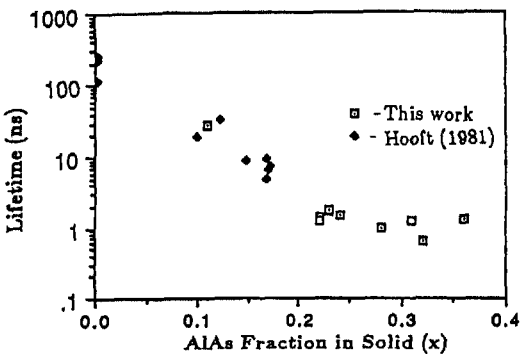


Fig. 286. Al-composition dependence of the free-carrier lifetime (After Timmons et al., *Inst. Phys. Conf. Ser.* No. 96, Chapter 5, IOP Publishing, Bristol, UK, 1988, p. 289.)

excitons with defects, surfaces, interfaces, and photons. In Si, the kinetics of free excitons are less uncertain due to the indirect nature of the transition.

3.2.2.1. GaAs

The earliest measurement of free-exciton decay kinetics in GaAs were those of Hwang [430]. They used the phase-shift technique to determine the free-exciton lifetime in GaAs crystals with varying impurity concentrations. He found free-exciton lifetimes which decreased from 2.9 ns for the purest crystals to 1.1 ns for samples with impurity concentrations of $\sim 10^{15} \text{ cm}^{-3}$. The free excitons may decay either by direct annihilation (and photon emission) or by impurity trapping. The transition probability for free excitons is given by

$$\tau_r = \frac{2\pi\epsilon_0 m_0 c^3}{\bar{n}e^2 \omega^2 f} \quad (42)$$

where \bar{n} is the index of refraction, and f is the oscillator strength. For GaAs, Eq. (42) predicts a free-exciton lifetime of 40 μs [229,430,431]. Hwang interpreted his observed much shorter lifetimes to be due to the trapping of the free excitons by impurities. Thus, in his view, the measured lifetime is an effective and not a radiative one, and will be very sensitive to the impurity concentration. 'tHooft et al. [229,431] examined the free-exciton decay kinetics in ultrapure, MBE-prepared GaAs double heterostructures. The impurity concentration in their sample was $< 2 \times 10^{14} \text{ cm}^{-3}$. Fig. 287 shows the

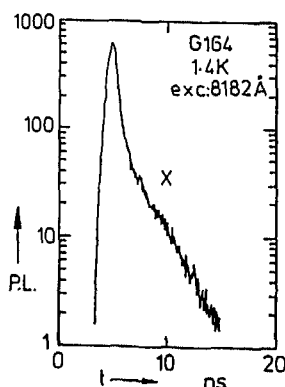


Fig. 287. PL time decay of the free-exciton line in bulk GaAs at 1.4 K. Excitation was resonant with the emission line with a density of 0.1 W cm^{-2} . (After 'tHooft et al. [431].)

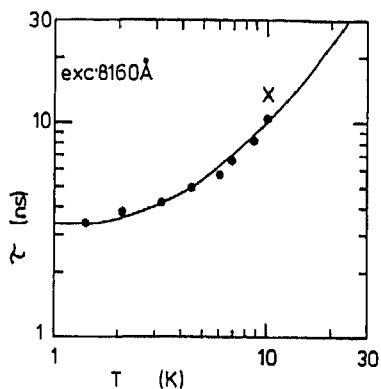


Fig. 288. Free exciton radiative lifetime versus temperature. Excitation is resonant with the bandgap of GaAs at low powers ($\sim 0.1 \text{ W cm}^{-2}$) [229].

PL decay kinetics of the free-exciton emission in their sample at 1.4 K under resonant excitation. The lifetime determined from the long-time tail of the decay is 3.3 ns. For excitation above 1.53 eV, they find the lifetime is longer by approximately 20%. Fig. 288 shows the free-exciton lifetime versus temperature. The solid line represents a model based upon the thermal occupation of a region near $k=0$, within the homogeneous linewidth. The oscillator strength of the free exciton must be on the order of unity, as opposed to the value of $\sim 10^{-5}$ derived from Eq. (42). The increase in oscillator strength is by a factor of $(a_{\text{ex}}/a)^3$, where a_{ex} is the free-exciton Bohr radius, and a is the GaAs unit cell length. This factor is just the number of unit cells per excitonic volume. Inclusion of this factor is consistent with the concept of the giant oscillator strength, which was introduced by Rashba [432]. Later, Rappel et al. [433] reinterpreted the results of 'tHooft et al. [229] in terms of the exciton polariton. Within the context of this model, they find that the free-exciton lifetime is two to three orders of magnitude smaller than earlier theoretical estimates (40 μs). They find a free-exciton lifetime of 8 ns at low temperatures. Steiner et al. [44] also examined the free-exciton luminescence in the

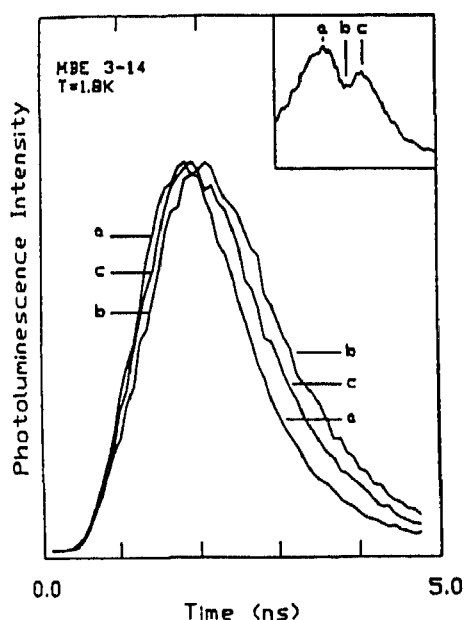


Fig. 289. PL kinetics of the free-exciton measured at three different spectral positions, as shown in the inset. (After Steiner et al. [44].)

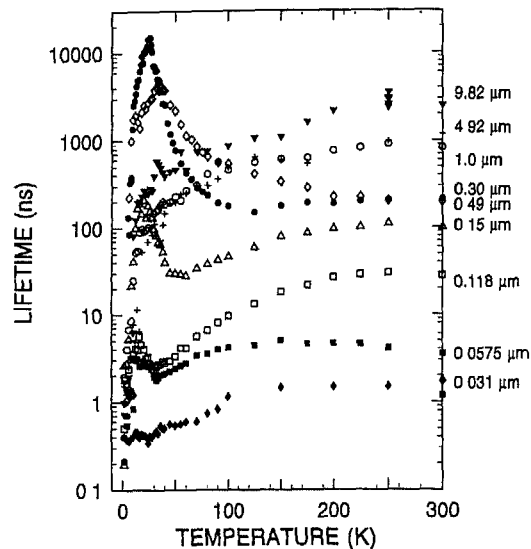


Fig. 290. PL lifetimes versus temperature of an entire series of GaAs/AlGaAs double heterostructures with the active GaAs layer thickness varied from 50 Å to 10 μm .

context of the exciton–polariton model. Fig. 289 shows the PL time decays taken at the spectral positions shown in the inset. The most noticeable feature is the increased delay time for the maximum emission intensity for the emission in the dip region (spectrum b). This is consistent with the increased neutral-donor scattering of polaritons in their model. Aaviksoo et al. [434] also observed this increased delay of the maximum intensity in the vicinity of the free-exciton resonance. Their samples were grown by VPE in a chloride system, and had impurity concentrations as low as $\sim 10^{12} \text{ cm}^{-3}$. In their purest sample they observe decay times of 4–5 ns, exceeding the value reported by 'tHooft et al. [229]. They further observed the time behavior of the LO-phonon replica of the free exciton, and observed identical kinetics to that of the free exciton. They therefore conclude that polariton diffusion is not an important factor in the kinetics of excitonic luminescence in GaAs. They find that the time delay for maximum luminescence intensity is caused by the energy relaxation of the photoexcited electrons and the slow thermalization of excitons in the vicinity of the exciton–polariton bottleneck. Samples with increased impurity concentrations exhibit faster energy relaxation rates due to increased inelastic impurity scattering. Further, they find that the electron–exciton interaction provides another channel for electron energy relaxation.

Wolford et al. [435] examined the free-exciton kinetics of undoped OMVPE-prepared bulk GaAs structures. Their results show that the free-exciton lifetime is determined almost entirely by thermalization with free carriers. They further find some discrepancies between their low-temperature free-exciton kinetics and exciton–polariton models. Fig. 290 shows the lifetimes of their structures versus temperature. The important aspect of this data is the lifetimes below 25 K. There is a variation five orders of magnitude in PL lifetime over this temperature range for some samples. However, some samples only exhibit a factor of 10–100 change in lifetime over this same temperature range. Wolford et al. find that this is consistent with the thermal coupling of the free excitons with varying densities of free carriers versus sample thickness. This is also consistent with the results of Hwang [430]. Wolford et al. [435] examined these low-temperature kinetics in detail. Fig. 291 shows the 1.8 K free-exciton lifetimes (all decays were rigorously exponential over more than 3 decades) versus thickness of the GaAs active layer. There is only a factor of 3–4 variation in lifetime for thickness variations over three orders of magnitude. This result is inconsistent with the exciton–polariton model, in which

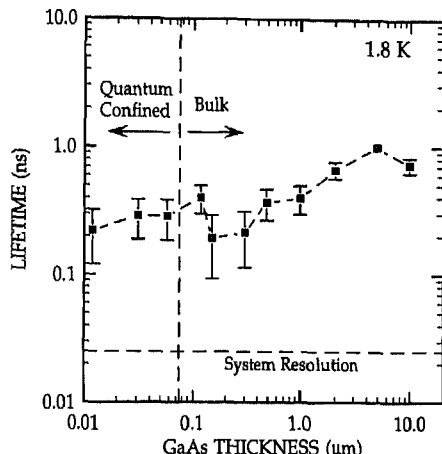


Fig. 291. Free-exciton lifetimes at 1.6 K versus GaAs layer thickness.

the free-exciton lifetime is essentially a transit time through the crystal. This transit time is governed by the exciton–polariton group velocity which is a strongly varying function of emission energy, with a minimum at the free-exciton resonance. This model therefore predicts lifetimes which vary directly with layer thickness and which are non-exponential and vary with emission energy. None of these phenomena were observed by Wolford et al.

3.2.2.2. Silicon

The kinetics of free-exciton recombination in Si are dominated by the forbidden nature of the transition. This forbidden transition results in long free-exciton lifetimes, with the maximum reported value of $60 \mu\text{s}$ [436]. Hammond and Silver [436] found that the exciton kinetics in Si are sensitive to the concentration and type of impurities as well as the sample temperature. Fig. 292 shows the measured excitonic lifetimes versus temperature for both an n-type and p-type sample. They have modeled their results using rate equations which include capture, evaporation, and recombination of excitons at neutral impurities. They find free-exciton lifetimes in n-type (p-type) Si to be $60 \mu\text{s}$ ($29 \mu\text{s}$) at 16 K. Further they find the capture cross-section of the exciton to be $0.75 \times 10^{12} \text{ cm}^2 \text{ K}^{-1}$. These results show the importance of shallow impurities even in samples with impurity concentrations as low as 10^{12} cm^{-3} . Gourley and Wolfe [238] found that the temperature dependence of the free-exciton lifetime increased with temperature at low temperatures as a result of thermalization of bound excitons. At higher temperatures ($> 12 \text{ K}$) the lifetime decreases due to thermalization of free excitons.

3.2.2.3. GaAs nanostructures

3.2.2.3.1. Quantum wells

Perhaps one of the seminal works dealing with exciton radiative recombination in quantum wells was the work of Feldmann et al. [437] reported in 1987. They demonstrated the fundamental relationship between the radiative exciton lifetime and the exciton linewidth. This dependence reflects the fact that the coherence volume of an exciton is determined by exciton scattering. Considering a two-dimensional system, they derived the following expression for the radiative lifetime of quantum well excitons

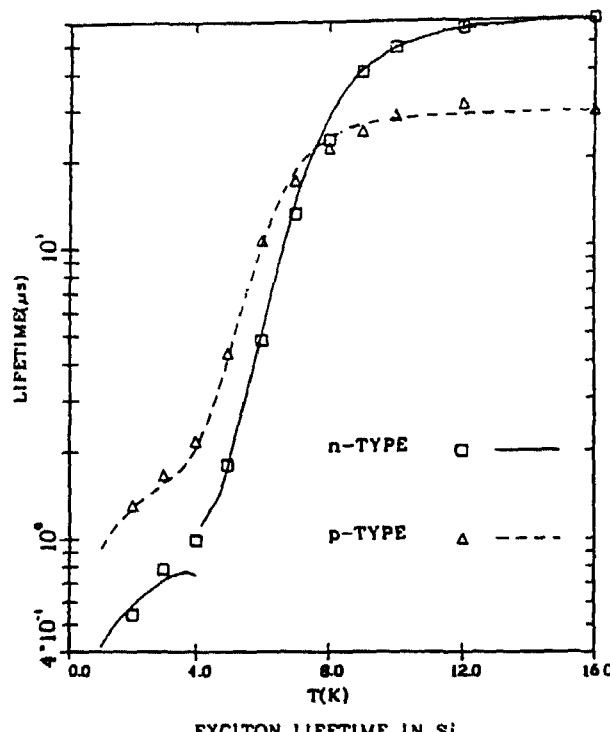


Fig. 292. Temperature dependence of the free-exciton lifetime in both n-type and p-type high-purity Si. (After Hammond and Silver [436].)

$$\rho_x^{2D} \alpha (E_B^{2D})^{-1} (M/\mu) [\Delta(T)/r(T)] \quad (43)$$

where $\Delta(T)$ is the homogeneous linewidth, $r(T)$ is the fraction of excitons within the spectral width $\Delta(T)$, μ is the reduced mass of the exciton, and E_B^{2D} is the exciton binding energy. This model is conceptually very similar to that of 'tHooft et al.'s [229] model for bulk free-exciton recombination. The radiative lifetime does not explicitly depend upon the thickness of the quantum well. Instead, the thickness dependence occurs implicitly through the dependence of the exciton binding energy on well thickness. The dependence of the radiative lifetime on the spectral linewidth evident in Eq. (43) is mediated by the coherence area of the quasi-2D exciton. Fig. 293 shows experimental verification of

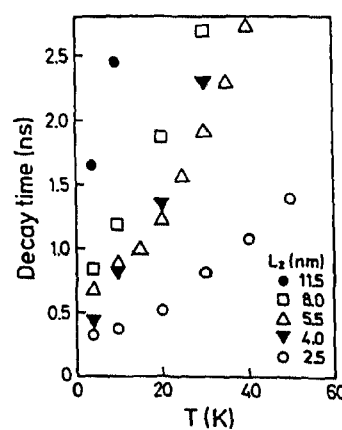


Fig. 293. Excitonic PL decay lifetimes versus temperature for various quantum wells with different well widths. (After Feldmann et al [437].)

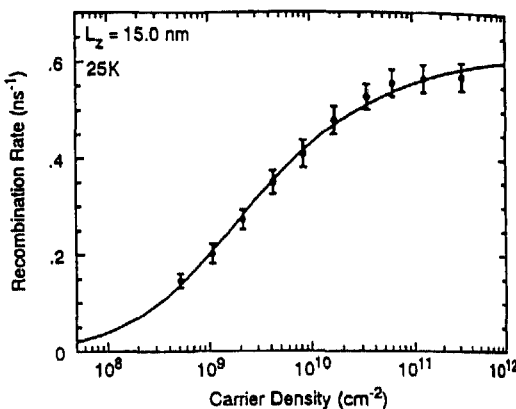


Fig. 294. Radiative recombination rate as a function of photojected carrier density in a 15 nm quantum well. (After Srinivas et al. [440].)

this model. Here the decay time versus temperature is shown for several quantum wells with thicknesses ranging from 25 to 115 Å. The decay times increase with increasing temperature while the PL intensity is constant over the same temperature range. This proves that the recombination is dominated by radiative recombination. Also, there appears a thickness dependence to the low-temperature decay times, consistent with the above model. Christen et al. [438] and Göbel et al. [439] also observed the well-width dependence of the excitonic recombination rate. Srinivas et al. [440] and Eccleston et al. [441] expanded on the Feldmann et al. model by examining the carrier-density dependence of the excitonic lifetime. In addition to agreeing with all of Feldmann's previous results, Srinivas et al. found that the thermodynamic equilibrium between free carriers and free excitons is important to the exciton dynamics. Fig. 294 shows the recombination rate versus injected carrier density for a 150 Å quantum well. The solid line represents a fit to the data with this thermal equilibrium model. Further strong evidence for the importance of free carriers may be obtained by examining the temperature dependence of the PL spectra of a quantum well. Fig. 295 shows a compilation of the measured PL spectra at

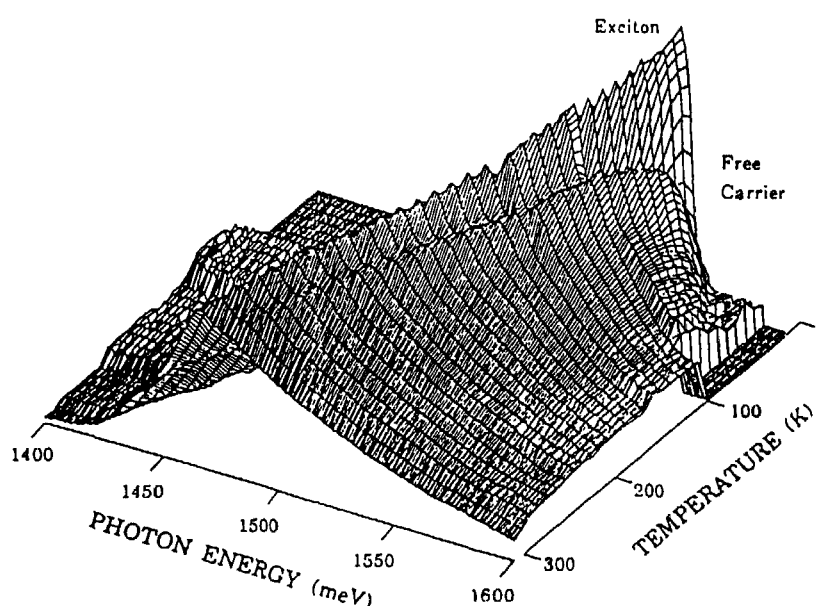


Fig. 295. Three-dimensional plot of the temperature dependence of the PL spectra from a 10 nm quantum well. The intensity is shown with a logarithmic scale. (From Bergman et al., *Inst. Phys. Conf. Ser.* No. 123, IOP Publishing, Bristol, UK, 1991, p. 73.)

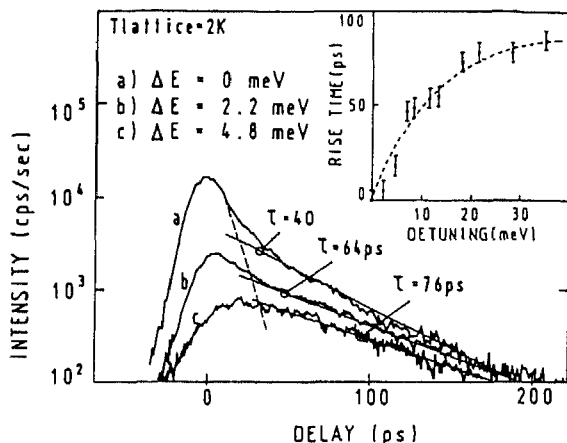


Fig. 296. Free exciton PL time decays versus excitation detuning. Inset shows the rise time of the excitonic luminescence versus detuning (After Deveaud et al [446].)

different temperatures for a 100 Å GaAs quantum well [442]. Clearly, the free-carrier emission increases in intensity with increasing temperature, and is 77% of the exciton recombination at room temperature. Fouquet and Siegman [443] also found that the room-temperature luminescence of GaAs quantum wells was governed by free carriers. They further conclude that non-radiative decay at room temperature causes the short (1 ns) exponential decays they observed. This is consistent with the theoretical predictions of Pickin and David [444].

Sernage et al. [445] and Deveaud et al. [71,446] examined, in detail, the free-exciton kinetics of high-quality GaAs quantum wells under resonant excitation. They deduce a radiative lifetime of 10 ± 4 ps at low temperatures. For resonant excitation at 1.7 K, they observe a radiative decay time as short as 24 ps. They further showed that temperatures above 2 K, high excitation densities (above $3 \times 10^9 \text{ cm}^{-2}$), and large excitation detuning (greater than 2 meV) yield an increase of the luminescence lifetime and homogeneous linewidth as a result of phase-breaking mechanisms. Fig. 296 shows the free-exciton PL time decays for three different excitation detunings from the exciton resonance, and the inset shows the measured rise time versus excitation detuning. The decays consist of two components, the first with a decay time of 17–40 ps, and the second with a decay time of 80–300 ps. They deduce the radiative lifetime from the fast component of the decay and include the effects of dephasing. Finally, they conclude that the fast (tens of picoseconds) lifetimes observed under resonant excitation are consistent with the exciton–polariton model of Andreani et al. [447,448]. However, these results are not universally accepted as indicative of the radiative lifetime. The short-component lifetime from which the radiative decay rate is deduced is not commonly quoted as the lifetime. Most authors deduce their lifetimes from the long-time component of the decay and attribute the short component to other effects, Rayleigh scattering, etc. [435]. Thus, care must be taken in interpreting and comparing PL time decays.

Vinattieri et al. [449] used the PL upconversion technique to study the exciton dynamics in GaAs quantum wells with high time resolution (5 ps). Fig. 297 shows their polarization resolved excitonic kinetics for resonant excitation. Here S and D represent the sum and difference of the time decays, respectively, for the different polarizations of exciting light. They modeled their results considering the enhanced radiative recombination of 2D excitons (exciton–polariton effects), the spin relaxation of excitons, holes, and electrons, and momentum scattering of excitons. They find that the initial fast decay of the I^+ curve is almost 50% due to fast radiative recombination. They derive a radiative

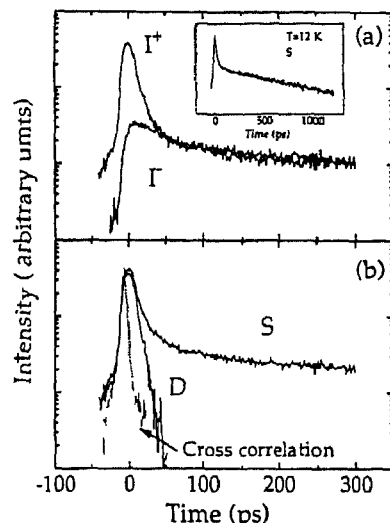


Fig. 297 PL time decays of the resonantly excited heavy-hole exciton in a 15 nm quantum well. (a) I^+ and I^- temporal evolutions; (b) S and D calculated from (a). Dotted spectrum is the cross correlation of the scattered laser light. (Reprinted from Vinattieri et al., *Solid State Commun.*, 88 (1993) 189, with kind permission from Elsevier Science Ltd, The Boulevard, Langford Lane, Kidlington OX5 1GB, UK.)

lifetime of 40 ps, which is in reasonably good agreement with theory and the results of Sermage et al. [445] and Deveaud et al. [446].

Damen et al. [72,450] made use of the PL upconversion technique to derive information regarding exciton formation times in GaAs quantum wells. They measured the rise time of the exciton emission as a function of temperature, excitation density, and excitation energy. They further measured the time-resolved PL spectrum. Fig. 33 shows the time evolution of the exciton luminescence at the peak of the emission versus temperature. The risetime below 10 K is nearly 300 ps, and only 20 ps at 60 K. Varying the excitation energy from 17 to 100 meV above the emission energy, they observed no discernible differences in risetime, even in the vicinity of the light-hole exciton energy. They did,

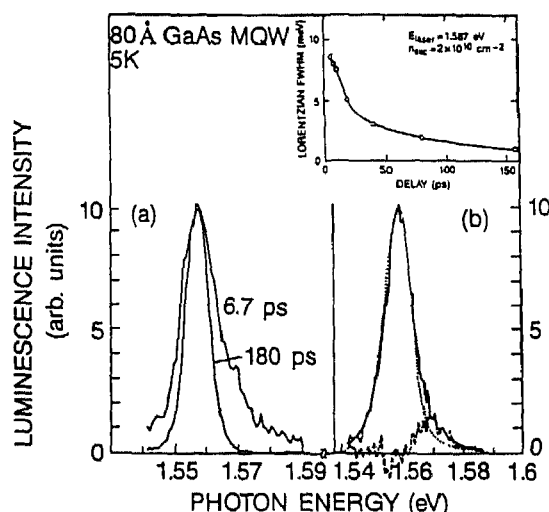


Fig. 298 (a) Time-resolved PL spectra of an 80 Å GaAs quantum well at 6.7 and 180 ps time delays. (b) Lineshape of the PL emission line —, experimental; ···, Gaussian-Lorentzian fit; ---twice the difference (corresponding to band-to-band recombination) Inset shows FWHM of the Lorentzian from these fits versus time. (After Damen et al. [72].)

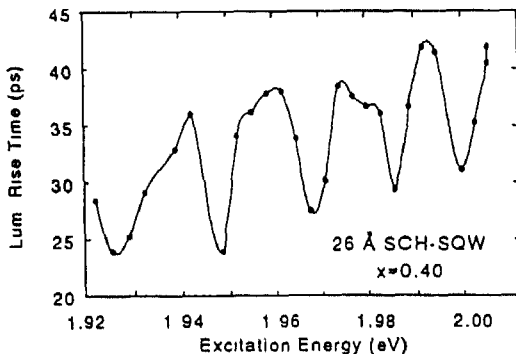


Fig. 299. Rise times of the exciton emission at 8 K versus excitation energy (excitation density, $5 \times 10^{10} \text{ cm}^{-2}$). Oscillations occur with a periodicity of $\sim 20 \text{ meV}$. (After Blom et al. [452].)

however, observe a shortening of the risetime with increasing excitation density. In order to understand these results, they measured the time-resolved PL spectra. Fig. 298 shows the excitonic emission spectra at two different time delays. The inset shows the spectral width of the luminescence as a function of time. The rapid decrease in the spectral width within the first 20 ps is an indication of the exciton formation time. Since exciton-electron collisions are more efficient in broadening the exciton distribution than are exciton-exciton collisions, they attribute this rapid decay in spectral width to a decrease in density of free electrons, which thus form excitons on this same time scale. Further, they find the distribution of excitons is non-thermal. Eccleston et al. [451] further investigated the density dependence of the excitonic luminescence from GaAs quantum wells. Consistent with Damen et al.'s results, they find that the exciton formation is a bimolecular process, and therefore is strongly density dependent. They derive the bimolecular exciton formation coefficient to be $6 \times 10^{-12} \text{ cm}^2 \text{ ps}^{-1}$. Blom et al. [452] examined the kinetics of exciton formation as a function of excess energy deposited by the laser excitation. They found (Fig. 299) that the risetime of the exciton luminescence (here defined as the exponential constant of the rise and not the time to reach the maximum intensity) exhibits oscillations versus excitation energy. The decreasing period of oscillations with increasing excitation energy rules out hot exciton effects (which would oscillate with a constant period of 36.8 meV, the LO-phonon energy). Instead, Blom et al. model these dynamics and find that the oscillations arise from LO-phonon assisted exciton formation from free electrons and holes. This process is dominant when the sum of the excess electron and hole energies is 25 meV with one of the particles at the center of the Brillouin zone.

Morris et al. [453] considered another aspect of exciton formation, namely the capture of electrons and holes from the barriers of the quantum well structure into the well itself. They also used the time-resolved PL upconversion technique, with a temporal resolution of 600 fs. Fig. 300 shows the temporal evolution of the barrier and well luminescence for three different well widths (84, 58, and 70 Å). The initial rise of both the barrier and well luminescence is due to carrier cooling. The rapid decay of the barrier luminescence is then due to carrier capture into the wells. The rise in the well luminescence corresponds to both carrier cooling and carrier capture from the barriers. From analysis of their data they find that holes are captured efficiently (in under 3 ps), whereas the electron capture time varies from 2 to 120 ps depending on the well width. Gurioli et al. [454] considered the reverse process, i.e. thermal escape of carriers from the wells. They find that the temperature dependence of the PL decay times yields an activation energy which corresponds to the thermal escape of the least-confined species from the quantum well. Fig. 301 shows their Arrhenius plots of the PL decay times versus inverse temperature. The activation energies derived from these data range from 20 to 100 meV, consistent with the hole confinement energy (assuming band offsets of $\sim 70:30$).

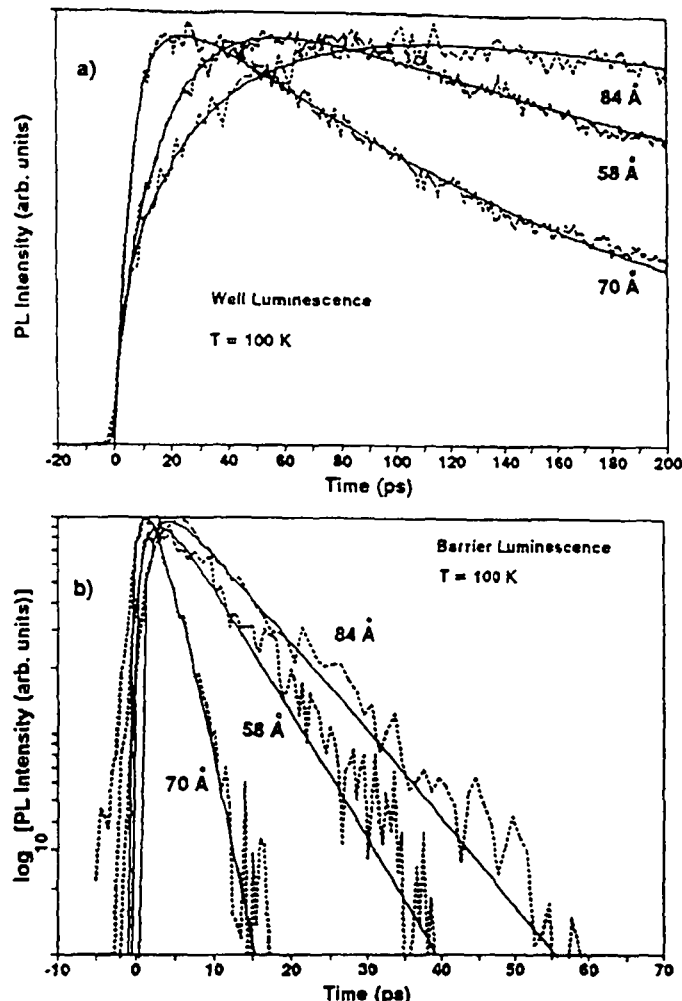


Fig. 300 PL decay kinetics for emission from (a) the $n=1$ well peak, and (b) the barrier peak for three GaAs quantum wells with well widths of 58, 70, and 84 Å (After Morris et al. [453])

3.2.2.3.2. Type-II superlattices

The rapid decrease in PL lifetime together with significant quenching of the type-II emission with increasing temperature are universally observed phenomena in type-II GaAs/AlAs superlattices [455]. Different theories were proposed to explain the observed exciton decay kinetics, and it is generally accepted that the decrease in lifetime results from thermal detrapping of localized excitons [307,309,311,312,456–458]. For instance, Angell and Sturge [459] recently proposed (see section 3.2.6) a theory of exciton decay in type-II structures based upon an exciton hopping process, with resulting excitonic optical transitions motionally averaged over a distribution of decay rates with increasing temperature as thermal delocalization sets in. However, this model does not include the effects of non-radiative decay and does not quantify the extent of spatial transport, and, therefore, does not adequately explain the observed quenching of the PL with increasing temperature. On the other hand, Gilliland et al. [460] have already directly measured such exciton spatial motion in these type-II structures, and have thereby proved the validity of the thermal detrapping model of the localized excitons. This work further shows the significance to the non-radiative decay in these structures. To

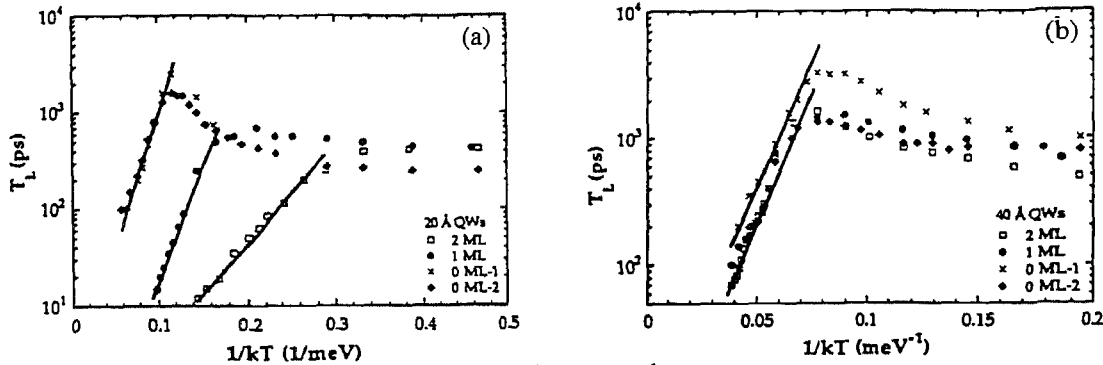


Fig. 301. PL decay time (T_L) versus inverse temperature for (a) 20 Å and (b) 40 Å quantum wells. Lines are best fits to the high-temperature lifetimes (After Gurioli et al. [454].)

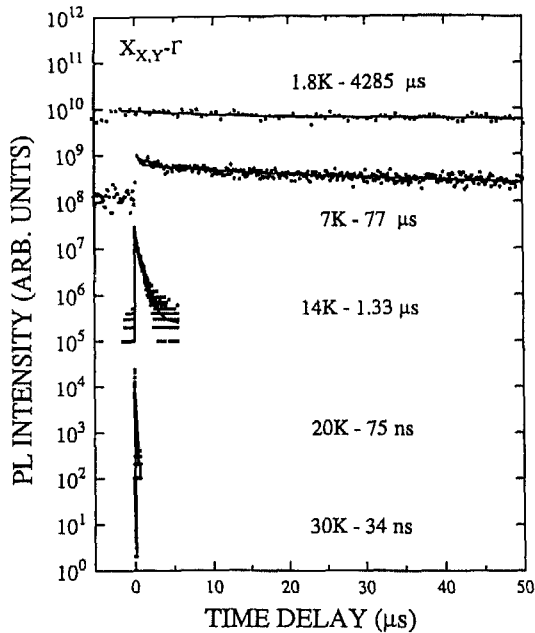


Fig. 302. PL decay kinetics versus temperature for a 25 Å/80 Å GaAs/AlAs superlattice. (After Fu et al. [461])

illustrate the drastic change in observed PL kinetics, Fig. 302 shows the PL decay kinetics of a 25 Å/80 Å GaAs/AlAs short-period superlattice versus temperature [461]. Lifetimes were obtained by fitting the decays with the Klein, Sturge and Cohen theory [462] for radiative decay of localized excitons in a disordered system (see section 3.2.6). There is a truly remarkable five orders of magnitude decrease in lifetime between 1.8 and 30 K. Moreover, the PL kinetics are strongly dependent on the sample structure. Fig. 303 shows the derived PL lifetimes versus temperature for three different samples with AlAs layer thicknesses ranging from 20 to 80 Å. Note that at all temperatures, the derived lifetimes systematically increase for increasing AlAs layer thickness, and, further, that the magnitude of the difference in lifetime decreases with increasing temperature, signifying the onset of a decay mechanism which is relatively less sensitive to sample structure. At the lowest temperature (1.8 K) there is a four orders of magnitude difference in lifetime for these three samples. Fu et al. [461] find that this large variation reflects the combined differences in electronic states (conduction band ground state of X_Z vs. $X_{X,Y}$), the micro-structural dependence of the wavefunction overlap between electrons and holes

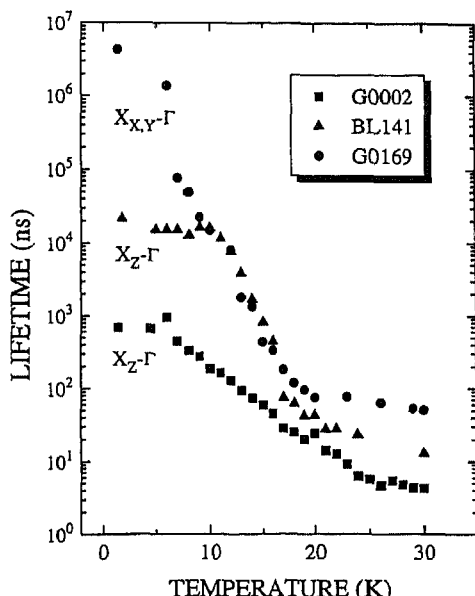


Fig. 303. Recombination lifetimes derived from the long-time tail of the PL decay kinetics versus temperature for samples with three different AlAs layer thicknesses: G0002, 20 Å, BL141, 50 Å, and GO169, 80 Å. (After Fu et al. [461].)

upon superlattice composition, and the variances in the magnitude of the Γ -X mixing potential which hybridizes the AlAs X-electron states, and gives rise to the observed no-phonon emission line. Using a simple perturbation theory, they find that the total Γ -X mixing potentials may be deduced, yielding 1.5 meV, 1.5 meV, and 0.2 meV for the samples with 20 Å, 50 Å, and 80 Å AlAs layer thicknesses, respectively. The difference in mixing potentials arises from symmetry considerations. The superlattice potential is not effective in mixing the Γ -X states for X conduction band minima of $X_{X,Y}$, whereas for X conduction band minima of X_Z this mechanism is effective. Lastly, they obtain, through comparison of the mixing potentials, the Γ -X superlattice mixing potential of 1.3 meV, and the Γ -X interfacial disorder mixing potential of 0.2 meV. At higher temperatures, the more rapid and exponential decays are consistent with the non-radiative decay found by Gilliland et al. [460]. More recently, Fu et al. [461] have shown that this non-radiative decay occurs within a monolayer of the heterointerface, and, therefore, occurs at heterointerfacially incorporated non-radiative defects.

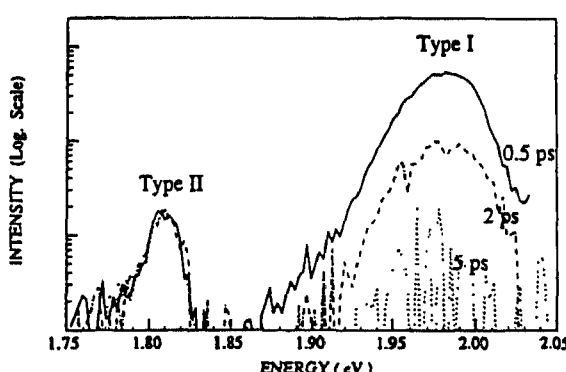


Fig. 304. Time-resolved PL spectra of a 25 Å/48 Å quantum well structure at 0.5, 2, and 5 ps time delays after the excitation pulse. The emission peak at 1.81 eV corresponds to the type-II transition, whereas the emission at 1.98 eV is the type-I transition. (From Deveaud et al., *Semicond. Sci. Technol.*, 9 (1994) 722.)

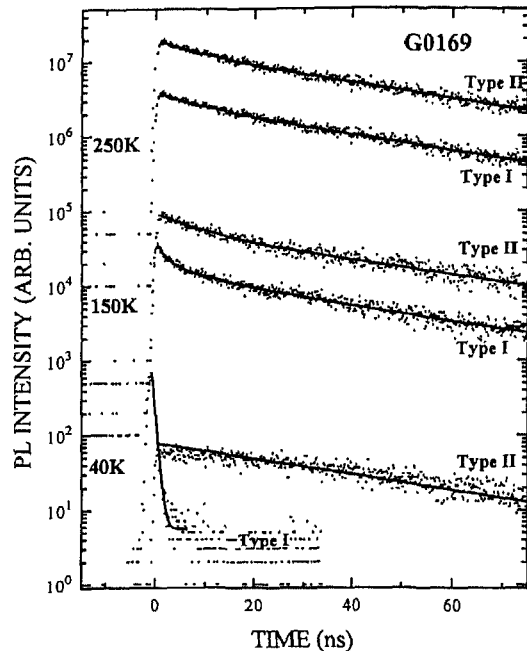


Fig. 305. PL decay kinetics for both type-I and type-II emissions at 40, 150, and 250 K. (After Fu et al. [464].)

It is also possible to observe the direct Γ - Γ transition in type-II structures. This emission occurs on a very fast time scale, and the lifetime of this emission is dominated by the ultrafast interlayer Γ -X electron scattering which eventually leads to the type-II emission. Fig. 304 shows the temporal evolution of both the type-I Γ - Γ transition (at 1.98 eV) and the type-II X- Γ transition (at 1.81 eV) at low temperature [463]. The lack of decay in the type-II emission on this time scale (5 ps) is due to the very long lifetime of the type-II emission. The type-I emission has an apparent lifetime (from 140 fs to 24 ps, depending upon sample parameters) much shorter than its radiative lifetime. In fact the observed lifetime increases monotonically with GaAs layer thickness. This decay constant therefore directly reflects the scattering of electrons from the Γ point in the GaAs layers to the X point in the AlAs layers. At higher temperatures, the kinetics become more complicated as the thermal coupling between Γ and X states is enhanced. Fu et al. [464] found that the back-transfer process, namely the transfer of electrons from the AlAs X states to the GaAs Γ states, becomes significant at temperatures above 150 K in their structure. Fig. 305 shows the PL time decays of both type-I and type-II emissions at three different temperatures. (At low temperatures, < 50 K, the type-I lifetime is resolution limited.) Note that with increasing temperature the type-I and type-II kinetics become identical, which is indicative of the increased thermalization between these two distinct states. Through detailed measurements of the PL kinetics and intensities, together with analysis using a three-level rate-equation model, they derive Γ -X and X- Γ scattering rates, which turn out to be consistent with other measurements [463].

3.2.2.3.3. Quantum wires

The coherence volume model for the radiative lifetime of excitons in bulk GaAs and GaAs quantum wells also applies to GaAs quantum wires. Kono et al. [324] examined the quantum wire lateral width dependence (from 70 to 350 Å) of the radiative exciton lifetime in GaAs/AlGaAs quantum well wires. Fig. 306 shows the quantum wire width dependence of the PL decay time. The

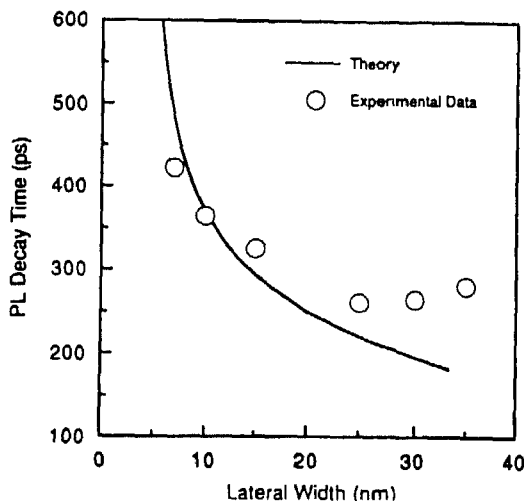


Fig. 306. Quantum wire lateral width dependence of the radiative lifetime. Solid line is a calculation based on the coherence length. (After Kono et al. [324].)

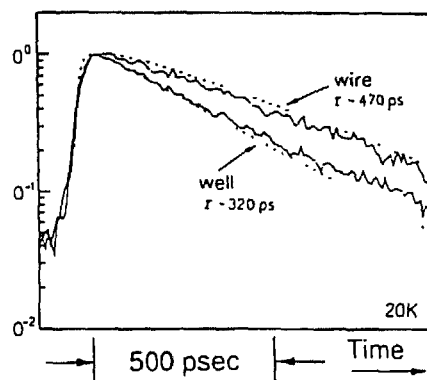


Fig. 307. PL kinetics at 10 K of a quantum wire and quantum well from which the wire was fabricated. (From Arakawa et al., *Semicond. Sci. Technol.*, 8 (1993) 1082.)

lifetime increases from 260 to 422 ps as the lateral width is reduced from 250 to 70 Å. Arakawa et al. [320] also examined the excitonic decay kinetics of quantum well wires. Fig. 307 shows the measured PL decays of the quantum wire and reference quantum well. Accounting for carrier diffusion, they derive excitonic lifetimes of 380 ps and 320 ps for the quantum wire and quantum well, respectively. The increase of the quantum wire exciton lifetime is due to the coherence effect. The exciton lifetime is proportional to V_c/a_B^2 where V_c is the coherence volume of the 1D excitons, and a_B is their Bohr radius. The enhanced binding energy of excitons in quantum wires compared to quantum wells causes a reduction of their Bohr radii. At the same time the coherence volume is reduced by ~ 2.5 . Taken together, this yields an exciton lifetime increase of 20–30%. Kohl et al. [329] examined the polarization dependence of the PL decay kinetics. They find that PL decays for the quantum wire transitions do not depend on the polarization of the excitation beam, but are different for hh_{11} and hh_{12} transitions. Rate equation analysis yields an effective relaxation time of ~ 70 ps. Additionally, they observe a population transfer from the hh_{12} to the hh_{11} state within 100 ps. Temperature-dependent measurements imply that the PL decays are not dominated by non-radiative decay since the lifetimes increase with temperature. This increase in lifetime with temperature was also observed by Grundmann et al. [465], and is shown in Fig. 308. The radiative lifetime clearly increases linearly with lattice temperature. Zhang

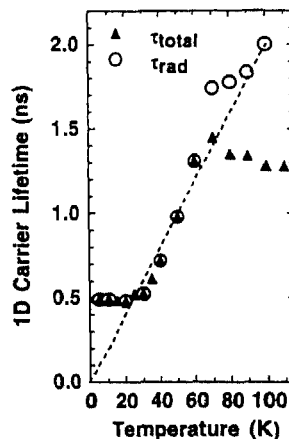


Fig. 308. Quantum wire radiative lifetime and total lifetime versus lattice temperature. (From Grundmann et al., *Semicond. Sci. Technol.*, 9 (1994) 1939.)

et al. [466] found that the excitonic lifetime in their strain-confined quantum well wires varied as $T^{1.71}$ which is in disagreement with the results of Grundmann et al. [465] as well as theoretical predictions of a $T^{0.5}$ dependence [467]. They attribute this more rapid temperature dependence as being due to the larger exciton localization energy in the wire resulting from the width fluctuations. In total these kinetics results are clearly not fully understood.

3.2.2.3.4. Quantum dots

At this time there are very few reported studies of the kinetics of excitons or free carriers in GaAs quantum dots. This is primarily due to the relative immaturity of the technology for preparing quantum dots. Most of these studies have interpreted their observed kinetics as the intrinsic radiative decay of free excitons. Zhang et al. [468] examined the PL kinetics of strain-confined quantum dots as a function of temperature. Their results demonstrate that the PL decay times at low temperatures are indicative of the radiative decay of localized excitons, increasing with the size of the dot. The temperature dependence of the PL lifetime is found to increase with temperature and is influenced by localization due to disorder in confinement size. Measured low temperature lifetimes are more than a factor of two larger than the theoretically predicted lifetime of 107 ps for a $20 \times 20 \times 10 \text{ nm}^3$ quantum dot. Wang et al. [469] have examined the PL kinetics of self-assembled InGaAs/GaAs quantum dots, and their results will be summarized here as they are also instructive in the kinetics of recombination of excitons in 0D structures. They grew InGaAs/GaAs quantum dots *in situ* utilizing the coherent islanding effect, or the self-assembled quantum dot formation. The mean diameters of their dots ranged from 125 to 275 Å, with a standard deviation of only 10%. The luminescence intensity of the quantum dot sample was comparable to that of the reference quantum well sample even though the quantum dot coverage was much less than that of the quantum well. This indicates the absence of deleterious non-radiative recombination effects so commonly observed in quantum dots. The PL kinetics from these samples was detected with a Streak camera with 100 ps time resolution. Fig. 309 shows the PL decay kinetics of the quantum dots and quantum well reference samples at 1.4 K. The quantum dot lifetime is longer than that of the reference quantum well at all temperatures, by at least a factor of two at low temperatures. The enhanced binding energy of the quantum dots should cause a reduction in exciton lifetime, and therefore cannot be responsible for these observations. Another possible explanation is the phonon bottleneck effect. However, this may be ruled out as well since the luminescence

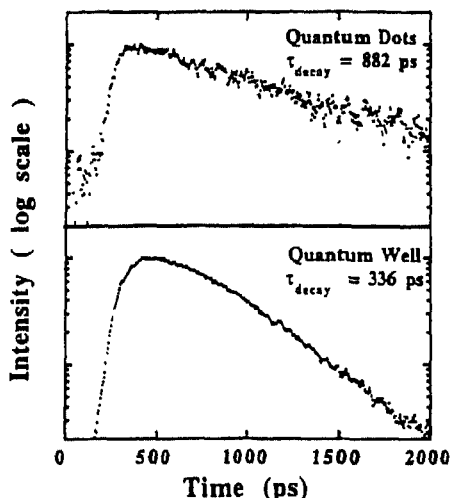


Fig. 309. PL time decays of GaAs quantum dots and quantum wells at 1.4 K. (After Wang et al. [469])

efficiency is high, in contrast with that expected from the bottleneck effect. At temperatures below 30 K, the exciton lifetime in the quantum dots is constant in contrast to the linear temperature dependence of the quantum well lifetime. This is attributed to the localized nature of the excitons in the quantum dots. At higher temperatures the exciton lifetime in the quantum dots increases with temperature, and is attributed to the thermionic emission of carriers from the quantum well to the quantum dots.

3.2.3. Defect photoluminescence

The recombination kinetics of carriers bound to defects may yield information, with appropriate modeling, regarding the nature of the carrier wavefunction in both real and momentum space, the localization energy of the carrier, capture times and cross-sections, and coherence volumes.

3.2.3.1. Bound excitons

Impurities in semiconductors, like all defects, destroy the translational symmetry of the underlying crystal structure. The consequence of this is that carriers may become localized at these defects—point defects for simple substitutional chemical impurities such as donors and acceptors—and their wavefunctions will then reflect this localization. As was discussed in section 1, the kinetics of recombination are sensitive to the wavefunctions of the carriers involved in recombination. Thus, the localization of carriers at donors and acceptors should yield discernible differences in the kinetics. This may also be interpreted in terms of the coherence volume of the bound exciton.

3.2.3.1.1. GaAs

Hwang [430] performed the first measurements of bound exciton recombination kinetics in GaAs. He examined bulk GaAs grown by liquid phase epitaxy, with impurity concentrations ranging from 3×10^{14} to $7 \times 10^{14} \text{ cm}^{-3}$. PL spectra in these samples clearly exhibited both donor and acceptor-bound exciton emission. He determined the bound exciton lifetimes using the phase-shift technique, described in section 3.1.1. His results show that the (D^0, X) lifetime is $1.07 \pm 0.1 \text{ ns}$, the (D^+, X) lifetime is $0.8 \pm 0.08 \text{ ns}$, and the (A^0, X) lifetime is $1.6 \pm 0.6 \text{ ns}$. These lifetimes were found to decrease

Table 4
Neutral donor and acceptor bound exciton lifetimes at low temperatures in Si [141]

Impurity	B	Al	Ga	In	Tl	P	As	Bi	Li
Lifetime (ns)	1055	76	77	2.7	0.27	272	183	8.6	1150

with increasing impurity concentration. In general, Hwang finds that bound excitons decay at a faster rate than do free excitons. The absolute lifetime values obtained by Hwang are not widely quoted primarily due to the indirect nature of the measurement technique used. Determination of these lifetimes required detailed analysis and knowledge of several other parameters. Further, his results were obtained with non-resonant excitation. Finkman et al. [470] examined the bound exciton lifetime in OMVPE GaAs epilayers using resonant excitation, measuring the decay of the two-electron satellite transition after resonantly exciting the donor-bound exciton. They also examined the effects of layer thickness on the kinetics in order to elucidate any possible photon recycling, and did not observe any appreciable effect. They also conclude that non-radiative surface recombination is unimportant in their samples. In the end they find a donor-bound exciton lifetime of 0.75 ± 0.15 ns, and an acceptor-bound exciton lifetime of 1.0 ± 0.1 ns. These results are in partial agreement with theoretical predictions. Sanders and Chang [471] predicted a donor-bound exciton lifetime of 0.031 ns and an acceptor-bound exciton lifetime of 0.96 ns. Thus, the results of Finkman et al. are in agreement with theory for acceptor-bound excitons, but are 20 times longer than theory for donor-bound excitons. This discrepancy may occur because measured decays may not reflect the true radiative lifetime of the bound exciton, but instead may in actuality reflect the formation time of the bound exciton.

3.2.3.1.2. Silicon

Neutral donor- and acceptor-bound excitons exhibit PL kinetics which are governed not by the intrinsic radiative recombination of these bound excitons, but by radiationless Auger decay. This non-radiative decay mechanism, which will be discussed further in section 3.2.4, involves the recombination of the bound exciton and the subsequent radiationless energy transfer of this energy to excite the electron/hole remaining on the neutral donor/acceptor [141]. The measured radiative decay lifetimes, at low temperatures, decrease with increasing binding energy. This is a manifestation of the increased localization of the exciton with increasing binding energy. Typical values for the low-temperature lifetimes for various donor and acceptor-bound excitons are shown in Table 4. Fig. 310 shows PL time decays for three In-doped Si samples with doping levels of (a) $4 \times 10^{16} \text{ cm}^{-3}$, (b) $2 \times 10^{17} \text{ cm}^{-3}$, and (c) $5 \times 10^{17} \text{ cm}^{-3}$ [472]. The theoretical radiative lifetime is very long ($\sim 750 \mu\text{s}$) and the oscillator strength is low ($\sim 10^{-5}$ to 10^{-4}) and, thus, these measured lifetimes are indicative of very low quantum efficiencies.

3.2.3.1.3. GaAs nanostructures

In section 2.2.3.1.3 the properties of intentionally-doped quantum wells were examined, and it was shown that the binding energy of a shallow acceptor depends on both the position of the impurity in the well (i.e. center or edge) and the quantum well width. However, very little is known about the decay kinetics of bound exciton emission in quantum wells. Bergman et al. [473,474] examined just this aspect of impurity-related emission in quantum wells. They found that the free-exciton lifetime was reduced by the presence of impurities intentionally introduced within the quantum well. Fig. 311 shows the temperature dependence of the free-exciton PL lifetimes for both (acceptor) doped and undoped samples. (This data was obtained with a microchannel plate detector (S1 response) with a temporal resolution of 200 ps. All kinetics were exponential and were deconvolved with the instrument

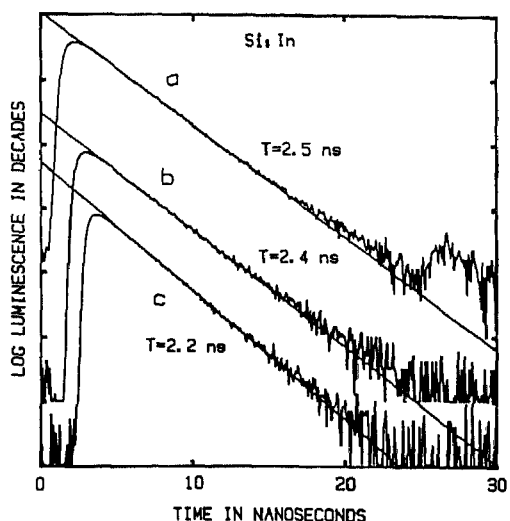


Fig. 310. PL decay kinetics of the In-bound exciton in various Si samples, (a) $4 \times 10^{16} \text{ cm}^{-3}$, (b) $2 \times 10^{17} \text{ cm}^{-3}$, and (c) $5 \times 10^{17} \text{ cm}^{-3}$ In concentration. (Reprinted from Steiner and Thewalt, *Solid State Commun.*, 49 (1984) 1121, with permission from Elsevier Science Ltd., Pergamon Imprint, The Boulevard, Langford Lane, Kidlington OX5 1GB, UK.)

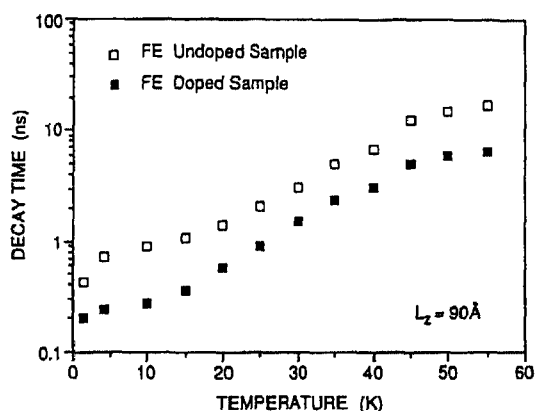


Fig. 311 Free exciton decay time versus temperature for a 90 Å quantum well which was undoped and doped in the central 20% of the well to $2 \times 10^{10} \text{ cm}^{-2}$. (After Bergman et al [473].)

response function to yield lifetimes on the order of the temporal response function.) The doped samples were Be-doped to 10^{17} cm^{-3} in the central 20% of the well. The temperature dependence of the free-exciton lifetimes in quantum wells was discussed in section 3.2.2.3, and it was shown that the free-exciton lifetime in undoped samples increases linearly with temperature, and this same increase is observed here. However, importantly, the free-exciton lifetime in doped samples is uniformly shorter by a factor of 2–3 over the entire temperature range. Bergman et al. [473,474] also found that the measured bound exciton lifetime was longer than that of the free exciton, as shown in Fig. 312, and was insensitive to excitation power and excitation wavelength (resonant versus non-resonant). Yet the temperature dependence of the bound exciton demonstrated the connection between free-exciton and bound exciton kinetics. They found that at low temperatures the free-exciton lifetime was shorter than that of the bound excitons, but that as temperature is raised the free-exciton lifetime approaches that of the bound exciton, as shown in Fig. 313. Here, it is not possible to explain the temperature dependence of the bound exciton emission based solely upon a thermal distribution model, as was

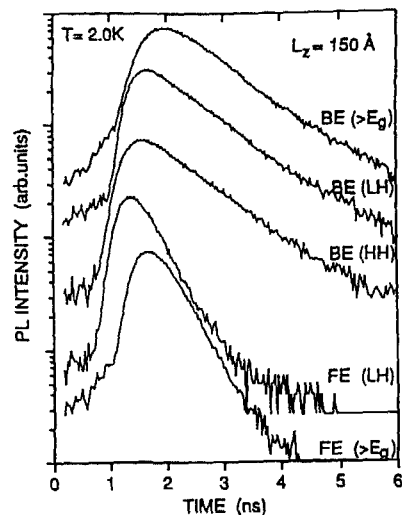


Fig. 312. Bound and free exciton PL kinetics for a quantum well of 150 Å width. Data were taken after excitation resonant with the light hole, heavy hole, and above gap. (After Bergman et al. [473].)

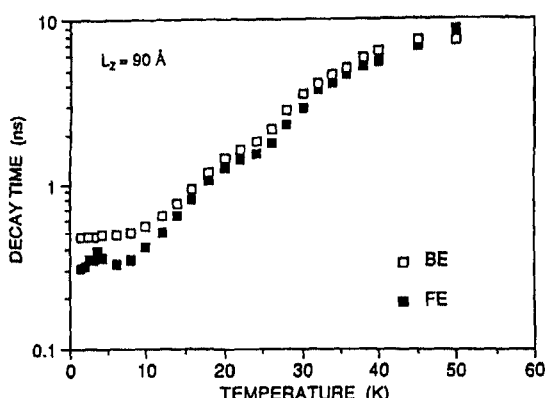


Fig. 313. Free and bound exciton lifetimes versus temperature in a 90 Å quantum well. (After Bergman et al. [473].)

done for the free excitons, since a localized state should exhibit no distribution in momentum, and, therefore, should have a temperature-independent recombination rate. Thus, they conclude that there is a strong thermal interaction between bound and free excitons, and that an adequate, but not perfect, understanding of the data may be had with coupled rate equations for the free- and bound-exciton densities. Comparison with data yields a free- to bound-exciton capture rate of $0.12 \text{ cm}^2 \text{ s}^{-1}$ for an 80 Å quantum well.

Zhao et al. [475,476] more recently examined the kinetics of bound exciton emission in structures designed to bridge the region from 2D to 3D behavior. Their structures were essentially simple double quantum wells with 100 Å GaAs wells doped to $5 \times 10^{16} \text{ cm}^{-3}$ in the central 25 Å of each well, and Al_{0.3}Ga_{0.7}As barriers ranging in thickness from 10 to 150 Å. Decreasing barrier thickness causes increased interaction between the wells, and such structures represent the quasi-3D limit, whereas, in contrast, for increasing barrier widths, the wells are isolated and are truly two dimensional. Fig. 314 shows the measured lifetimes of bound exciton emission versus barrier width; the inset shows several of the actual bound exciton PL time decays. The lifetime of the acceptor-bound exciton increases by

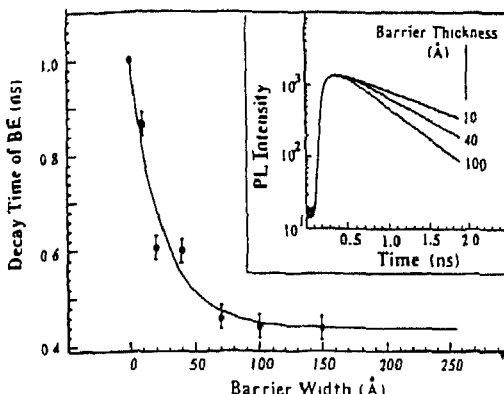


Fig. 314. PL lifetimes of the bound exciton emission versus AlGaAs barrier thickness at 2 K. Inset shows PL time decays of the bound exciton for three different structures after resonant excitation with the heavy-hole exciton [476].

more than a factor of two with decreasing $\text{Al}_{0.3}\text{Ga}_{0.7}\text{As}$ barrier width. The solid line is a fit to the data with the expression

$$\tau = \tau_\infty + (\tau_0 - \tau_\infty) \exp(-L_b/R_a) \quad (44)$$

where R_a represents the extension of the wavefunction into the barrier layer, and L_b is the barrier width (this expression just signifies the exponential decay of the wavefunction into the $\text{Al}_{0.3}\text{Ga}_{0.7}\text{As}$ barrier). The best fit is obtained with $R_a = 25 \text{ \AA}$. The increase in bound exciton lifetime may be attributed to the decreased localization of the electron with decreasing barrier thickness, i.e. as the system becomes quasi-3D. Zhao et al. conclude that it is this spatial extent of the electron wavefunction, relative to that of the hole, that determines the oscillator strength of the bound exciton rather than a correlation with the bound exciton binding energy. Lastly, their measurements show that the capture rate of the heavy-hole free exciton to the neutral acceptor-bound exciton state increases by a factor of seven in going from the 2D to the quasi-3D system.

3.2.3.2. Free-to-bound transitions

The kinetics of recombination of band-to-acceptor and donor-to-valence band transitions have not received much attention other than that which has been studied in regard to hot electron cooling. At least part of the difficulty in examining these transitions is that they spectrally overlap other transitions. The donor-to-valence band transition overlaps the donor-bound exciton transitions, whereas the band-to-acceptor transition partially overlaps the donor-acceptor pair transition. This spectral overlap tends to obscure the kinetics inherent to the free-to-bound recombination. The only reported lifetime, which I have found in the literature of a 10 ns lifetime for the free-electron-to-acceptor transition reported by Fasol et al. [273]. Their study focused on the mechanisms involved in hot electron cooling, and did not deal directly with the recombination of the band-to-acceptor transition.

3.2.3.3. Donor-acceptor pair transitions

Time-resolved measurements provide an important criteria by which to identify donor-acceptor pair emission in semiconductors. The kinetics of DAP emission provides a means for certifying the DAP nature of the emission as well as the acceptor binding energy. Thomas et al. [477] developed the theory for the radiative recombination of deep centers. They find that the recombination rate depends exponentially on the donor and acceptor separation. The kinetics may be solved exactly for

excess donors or acceptors, but for the case of near compensation, the kinetics are more complicated. For the simple case the recombination rate is given by

$$W(r) = W_{\max} \exp[-2r/R_d] \quad (45)$$

where R_d is the Bohr radius of the donor, and r is the separation between the donor and acceptor. This leads to a PL time decay of the form

$$I(t) = 4\pi N_d \left[\int_0^{\infty} W(r) \exp(-W(r)t) r^2 dr \right] \left\{ \exp \left[4\pi N_d \int_0^{\infty} (\exp(-W(r)t) - 1) r^2 dr \right] \right\} \quad (46)$$

where N_d is the majority dopant density. Zeiger [478] derived a complementary theory for DAP recombination for the case of shallow donor-acceptor pairs (assuming hydrogen-like states for both donors and acceptors).

A more accurate theoretical treatment of DAP emission kinetics was given by Adams and Landsberg [479]. They find a DAP radiative recombination rate of

$$W_{DA}(r) = \frac{4e^2 E_{ph} n}{m^2 \hbar^2 c^3} |M_{cv}|^2 I^2 \quad (47)$$

where E_{ph} is the photon energy, n is the refractive index, e is the charge of the electron, m is the mass of the electron, M_{cv} is the matrix element between the conduction and valence bands, and I is the overlap integral between the envelope functions of donor and acceptor states. Lawaetz [480] showed that the matrix element is related to the band parameter, E_p , by

$$|M_{cv}|^2 = \frac{1}{6} m E_p \quad (48)$$

where $E_p = 25.7$ eV for GaAs. The overlap integral may be calculated analytically, yielding

$$\begin{aligned} I &= \frac{1}{\pi(a_A a_D)^{3/2}} \int \exp \left[-\frac{R}{a_A} - \frac{|\tilde{R} - \tilde{r}|}{a_D} \right] dR \\ &= \frac{8\alpha^{3/2}}{(\alpha^2 - 1)^3 \rho} \{ \exp(-\alpha\rho)[\rho(\alpha^2 - 1) + 4\alpha] + \exp(-\rho)[\rho(\alpha^2 - 1) - 4\alpha] \} \end{aligned} \quad (49)$$

where a_A and a_D are the effective Bohr radii of acceptor and donor envelope functions, respectively, $\alpha = a_A/a_D$, and $\rho = r/a_A$.

Dingle [481] demonstrated that the recombination rate of DAP emission in uncompensated samples is extremely sensitive to the acceptor binding energy, thus providing a means for determination of the acceptor binding energy or acceptor chemical species. He found that the lifetime, in accordance with Eq. (46), is shorter with higher concentrations. In the case of near compensation, the situation is more complex, but increased dopant levels will shorten the lifetime. Physically, this results from the reduction in donor-acceptor pair separation with increased impurity concentrations, yielding an increased probability for recombination. This is clearly evident in Fig. 315 for the 1.488 eV emission. The complex nature of the DAP emission is evidenced by the time-resolved spectra shown in Fig. 316. This data clearly exhibits the red-shift of the peak energy of the emission with time, shifting by 4.5 meV in 3.4 μ s. Dingle showed, by assuming a donor binding energy of 6.5 meV and an acceptor binding energy of 28.5 meV, that the $t=0$ DAP spectrum corresponds to pairs separated by ~ 150 Å, whereas at later times, the average separation was 450 Å.

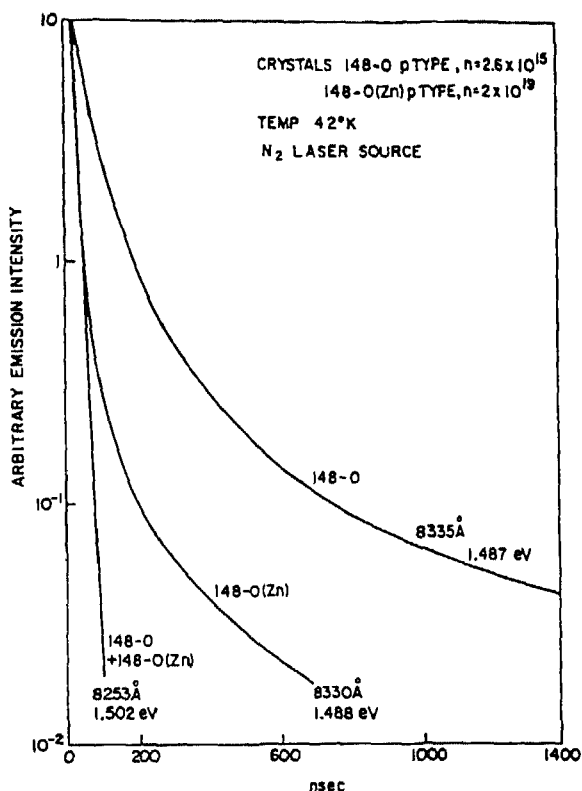


Fig. 315. PL decay kinetics for a GaAs sample with and without Zn impurities. The added Zn impurities drastically shorten the PL lifetimes. (After Dingle [481])

Kamiya and Wagner [482] demonstrated the validity of the theory of Adams and Landsberg (Eqs. (47)–(49)), through detailed measurements at low temperatures in a high-mobility n-type LPE GaAs sample. Fig. 317 shows their measured PL decays at various emission energies within the DAP emission band. The decays are non-exponential and have shorter lifetimes at higher energies. The emission energies may be correlated with pair separations using Eq. (15), and for the energies shown in the figure, the pair separations are 256, 296, 350, and 430 Å. The lifetimes determined from this data may be shown to be in excellent agreement with the theory of Adams and Landsberg. Fig. 318 shows the calculated and experimental DAP lifetimes versus emission wavelength. The theoretical curves here correspond to non-radiative decay lifetimes ranging from 10^6 to 2×10^{-7} s. Kamiya and Wagner find that the lifetime is very sensitive to the acceptor binding energy. For example, at an emission wavelength of 8309 Å, a change of 0.2 meV in the acceptor binding energy results in a 25% change in the lifetime. They thus arrive at values of 26.2 meV for carbon acceptors and 34.3 meV for silicon acceptors.

3.2.4. Auger recombination

Auger recombination involves the transfer of energy released by the recombination of an electron-hole pair to a second electron or to a second hole, which is subsequently excited high up into the band or into another band. These hot Auger carriers then dissipate this excess energy through the emission of phonons. In the midst of this non-radiative “cooling” or relaxation, the radiative recombination of this hot electron (hole) with a “cold” hole (electron) is possible, giving rise to a weak luminescence

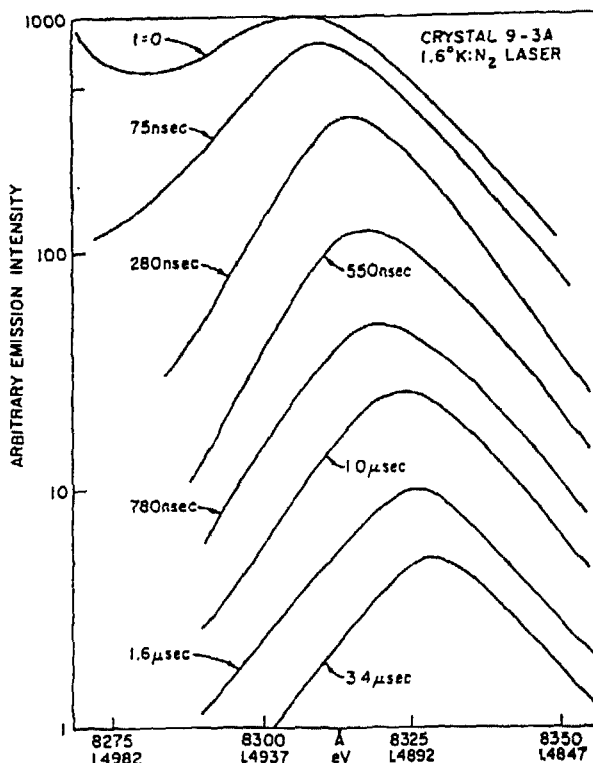


Fig. 316. Time-resolved PL spectra at 1.6 K. With increasing time the emission band shifts to lower energy. (After Dingle [481].)

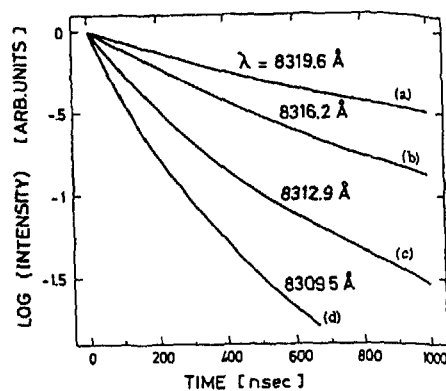


Fig. 317. PL decay kinetics of the DAP emission at various emission energies within the band. (After Kamiya and Wagner [482].)

above the bandgap. Auger recombination is just the inverse process to impact ionization. There are many different varieties of Auger recombination which depend on the nature of the possible transitions and the carrier concentration. The simplest forms of Auger recombination involve free electrons and free holes. Auger recombination may also occur from electrons at donor levels or holes at acceptor levels or through a combination of bound electrons and holes (i.e. the DAP transition). Auger recombination is a third-order reaction (involving three particles), and is therefore most significant at high densities. It is this high-density criterion of Auger recombination which yields its importance. Auger recombination effectively limits the charge-carrier lifetime at high carrier densities, and this is important for heavily-doped semiconductor devices or high-current devices. Experimental proof for

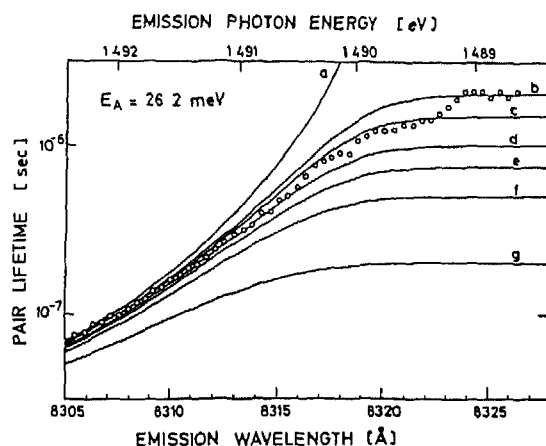


Fig. 318 Experimental and theoretical DAP lifetimes versus emission wavelength. Solid curves are theoretical calculations using the acceptor binding energy of 26.2 meV. Nonradiative lifetimes are (a) 10^6 s, (b) 2×10^{-6} s, (c) 1.5×10^{-6} s, (d) 1.0×10^{-6} s, (e) 7.5×10^{-7} s, (f) 5×10^{-7} s, and (g) 2×10^{-7} s. (After Kamiya and Wagner [482].)

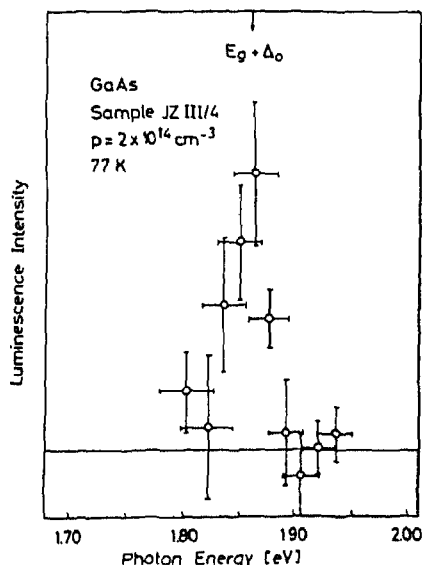


Fig. 319. PL intensity at various energies in bulk GaAs at 77 K showing the weak emission band at $E_g + \Delta_0$. (After Benz and Conradt [483].)

Auger recombination may be had through observation of the above bandgap luminescence mentioned above, or, more commonly through measurements of the free-carrier lifetime versus carrier density.

The emission of hot carriers associated with Auger recombination has been observed in GaAs [483]. Fig. 319 shows the PL of a sample of p-type GaAs at energies well above the bandgap. The PL peak at 1.86 eV is attributed to the recombination of free or shallow-bound conduction band electrons with holes in the split-off valence band which are generated by Auger recombination. The energy of this peak corresponds closely with that of the bandgap energy plus the split-off band energy (1.519 eV + 0.341 eV). Both PL and electroluminescence measurements show this peak to be many orders-of-magnitude weaker than the emission from the band edge. The Auger coefficient may be estimated from the ratio of the intensities of the integrated intensity of the bandgap to Auger emissions, which is approximately 10^9 , yielding an Auger coefficient of $10^{-31} \pm 1 \text{ cm}^6 \text{ s}^{-1}$ at 77 K. Reported

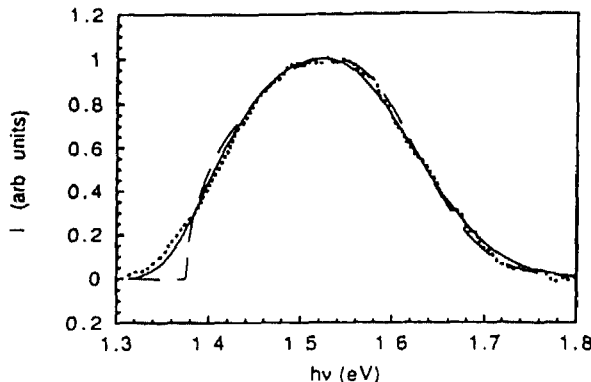


Fig. 320. PL spectrum of GaAs at a time delay of 105 ps after the excitation pulse. ···, experimental results; ---, a theoretical fit without energy broadening; —, a fit with Lorentzian broadening (After Strauss et al. [484].)

Auger coefficients in GaAs range from 10^{-31} to $10^{-26} \text{ cm}^6 \text{ s}^{-1}$ [484]. In order to more accurately quantify the Auger coefficient, Strauss et al. [484] measured the carrier recombination kinetics in structures designed to suppress both diffusion and stimulated emission. Fig. 320 shows the transient energy spectrum of GaAs at 105 ps after the excitation pulse, which had an excitation fluence of $80 \mu\text{J cm}^{-2}$. The rate equation for electrons, including Auger recombination is

$$\frac{dn}{dt} = -An - Bn_{\Gamma}p - C_p n_{\Gamma}p^2 - C_{n\Gamma\Gamma}n_{\Gamma}^2p - C_{n\Gamma L}n_{\Gamma}n_Lp - C_{nLL}n_L^2p \quad (50)$$

where n_{Γ} and n_L are the electron densities in the Γ and L conduction band valleys, respectively. The coefficients C_p and C_n represent the valence-band and conduction-band Auger processes, respectively. It is necessary to include the population of the L valley at high electron densities, however k conservation will cause the Auger recombination involving L electrons to be negligible. Fig. 321 shows the rate of change of the electron population versus $n_{\Gamma}p$. The data here were obtained from the transient spectra integrated over a 35 ps window. The linear increase in dn/dt with $n_{\Gamma}p$ (for $n_{\Gamma} = 1.5 \times 10^{19} \text{ cm}^{-3}$) is due to bimolecular recombination. At higher densities, the increase is superlinear, indicative of Auger recombination. The least-squares fit to the data with Eq. (50) yields $C_p = (6 \pm 2) \times 10^{-30} \text{ cm}^6 \text{ s}^{-1}$. In addition a conduction-band Auger process is also possible with an Auger coefficient of $C_{n\Gamma\Gamma} = (9 \pm 2) \times 10^{-30} \text{ cm}^6 \text{ s}^{-1}$.

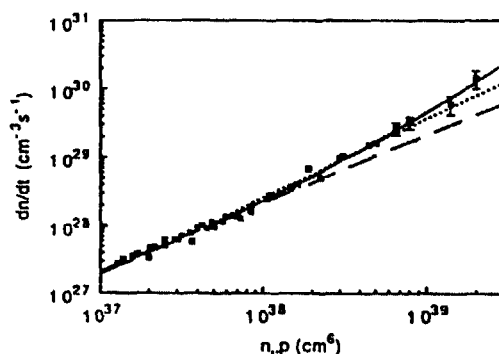


Fig. 321. Change in the carrier density with time versus the product of G-electron and hole densities. ■, measured data; —, fits with a valence-band Auger process; ···, a fit with a G-conduction band Auger process; ---, a calculation without Auger processes. (After Strauss et al. [484].)

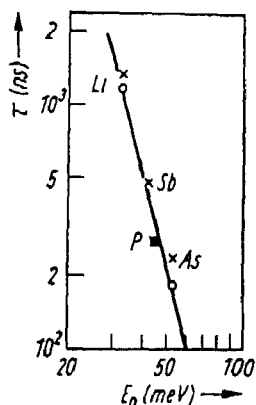


Fig. 322. Lifetimes of excitons bound to donors Li, P, and As in Si versus donor ionization energy. (After Schmid [486].)

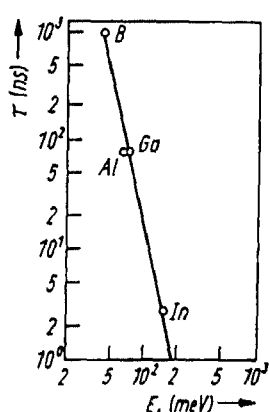


Fig. 323. Lifetimes of excitons bound to acceptors B, Al, Ga, and In in Si versus acceptor ionization energy (After Schmid [486].)

Some of the earliest work on Auger recombination in silicon dealt with the Auger recombination of bound excitons decaying at neutral donors [485]. Schmid [486] examined the PL lifetimes of excitons bound at Li, P, and As shallow, neutral donors, as well as B, Al, Ga, and In shallow, neutral acceptors. He found that the low-temperature lifetimes, which were all rigorously exponential, varied monotonically with the binding energy of the impurity. In fact, the variation appeared to follow a power-law dependence, as shown in Figs. 322 and 323, with exponents of -3.9 and -4.6 for donor-bound excitons and acceptor-bound excitons, respectively ($\tau_D \propto E_E^{-3.9}$ and $\tau_A \propto E_A^{-4.6}$). Schmid presented a theory for the localized, phononless Auger recombination involving two holes and an electron for the acceptor-bound excitons which yielded a power law dependence of the lifetime with an exponent of -4.67 . The theory for donor-bound excitons are not as good as for acceptors. His results demonstrate that the binding energy and Auger decay rate arises from the more delocalized nature of the excitonic wavefunction in k space for more deeply bound excitons. Further, the data do not support a phonon-assisted Auger transition since the delocalized wavefunctions in k space do not require an activation energy to fulfill momentum conservation. A phonon-assisted Auger recombination would therefore result in only a weak dependence of the recombination rate on binding energy. Steiner and Thewalt [472] extended the work of Schmid to that of simple deep impurities in Si. They examined the PL decays of excitons bound at Tl and Bi impurities, the deepest simple acceptor and donor in silicon, respectively. They found that for the Tl acceptor the measured lifetime is 270 ± 50 ps, in good agreement with the theoretically predicted Auger decay rate of 75–300 ps [472]. Thus, the effective

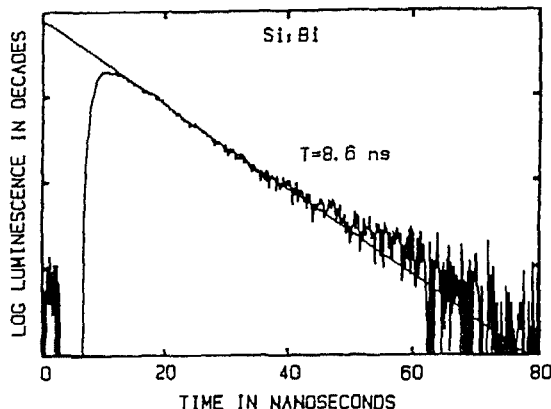


Fig. 324. PL decay kinetics of the Bi-bound exciton in Si. (Reprinted from Steiner and Thewalt, *Solid State Commun.*, 49 (1984) 1121, with permission from Elsevier Science Ltd, Pergamon Imprint, The Boulevard, Langford Lane, Kidlington OX5 1GB, UK.)

mass approximation which underlies the calculation of bound exciton lifetimes is valid for the deep Tl acceptor. On the other hand, results for the Bi deep donor do not agree with this simple theory. Using the power law obtained by Schmid for donors together with a binding energy of 69 meV yields a donor-bound exciton lifetime of ~ 60 ns, whereas the measured lifetime was only 8.6 ns, as shown in Fig. 324. The reason for this factor of seven discrepancy is unknown.

Cuthbert [487,488] examined the recombination of free excitons and the EHL in Si, and found that Auger recombination is the dominant process governing the recombination of the EHL in Si. He concluded that the non-radiative Auger recombination is a four-particle process whereby the recombination energy resulting from the decay of one of the constituent electron-hole pairs of the EHL is given to another electron-hole pair of the EHL, analogous to that of the bound exciton Auger recombination. Later, Haug [489] showed that the normal phononless Auger recombination, the dominant non-radiative process for bound excitons, is impossible for the case of a degenerate EHL (i.e. low temperatures and high densities). He concluded that a phonon-assisted Auger recombination process must be involved in the non-radiative decay of the EHL. This process involves an electron-phonon scattering to an intermediate state, and an Auger transition from this intermediate state to the final state. He derives a total phonon-assisted Auger recombination coefficient of $C = 7.19 \times 10^{-31} \text{ cm}^6 \text{ s}^{-1}$.

3.2.5. Hot-carrier recombination and intervalley scattering

Carrier cooling in semiconductors occurs on a subpicosecond to picosecond time scale, and, therefore, it is difficult to temporally resolve the emission and cooling of these hot carriers directly. This difficulty has caused researchers to utilize almost every conceivable technique for time resolving the emission of hot carriers, including Streak camera detection, PL upconversion, band-to-acceptor emission (discussed in section 2.2.8), and time-resolved measurements with fast micro-channel plate detectors. The mechanisms for carrier cooling which have been elucidated through spectroscopic studies include electron-phonon interaction, intervalley scattering, carrier-carrier scattering, and electron-hole scattering. Shah [490] has given a thorough review of these processes in semiconductors and semiconductor nanostructures as they relate to carrier relaxation. In this section, results of these studies in bulk and semiconductor nanostructures will be given to demonstrate the efficacy of each of these techniques, as well as the physics gleaned from the results.

3.2.5.1. Bulk

Elsaesser et al. [491], Shah et al. [492], and Rota et al. [493] utilized femtosecond PL upconversion measurements as a means of time-resolving the electron distribution after non-resonant, "hot" excitation. The emission intensity is proportional to the product of the distribution function of electrons with that of the holes (primarily heavy holes since the electron \rightarrow heavy hole emission is dominant), $f_e f_h$, which is in contrast to absorption measurements which measure the sum of the electron and hole distribution functions, $f_e + f_h$. Further, PL emission requires the electrons and heavy holes to both exist at the same k vector. Both of these studies measured the temporal and spectral evolution of the PL in bulk GaAs after femtosecond excitation near 2.0 eV with plasma densities of 5.0×10^{16} to 1×10^{18} cm^{-3} , all detected with 100 fs resolution (via PL upconversion). Fig. 325 shows the PL spectra of the sample at various times after the excitation pulse. The solid lines are the results at the highest excitation density whereas the dashed lines are the results at the lowest excitation density. The PL covers the entire range from the bandgap (1.42 eV at room temperature) up to 1.7 eV. Fig. 326 shows the time evolution of the PL emission at a fixed emission energy on both femtosecond (left-hand side) and picosecond (right-hand side) timescales. The slower picosecond response evident in some of these spectra is indicative of the backscattering of electrons from the L and X valleys to the Γ valley as well as to carrier cooling (note that excitation sufficiently high above the bandgap may result in the fast scattering of the absorbed electrons into other valleys in the conduction band). The back-scattering of

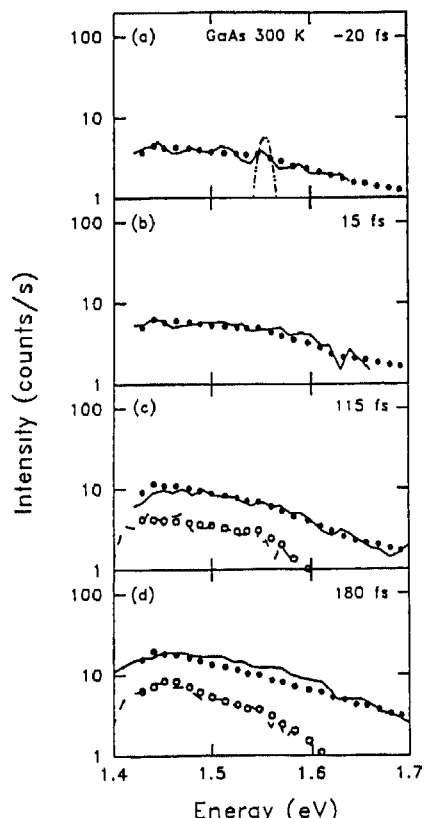


Fig. 325 Time-resolved (a) -20 fs, (b) 15 fs, (c) 115 fs, and (d) 180 fs PL spectra of GaAs after femtosecond excitation at 1.93 eV with a density of $7 \times 10^{17} \text{ cm}^{-3}$ (—) and $1.7 \times 10^{17} \text{ cm}^{-3}$ (---). Symbols represent spectra calculated from Monte Carlo simulations. (After Rota et al [493].)

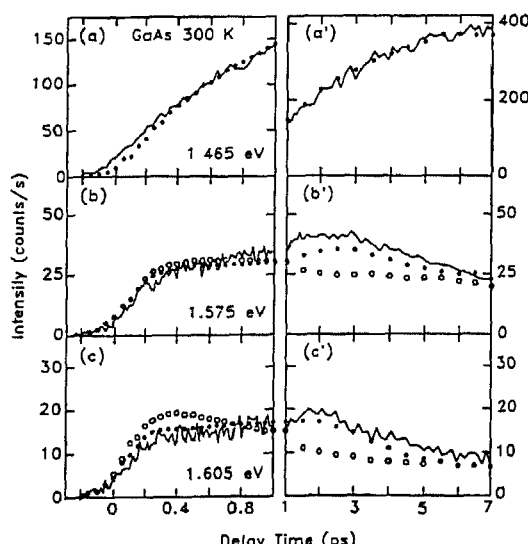


Fig. 326. Femtosecond (left side) and picosecond (right side) evolution of the PL in GaAs at photon energies of: (a), (a') 1.465 eV; (b), (b') 1.575 eV; and (c), (c') 1.605 eV (After Rota et al. [493].)

electrons from the L valleys to the Γ valley is also a source of “persistent” heating on the time scale of the scattering time (2.5 ps) [492]. Further, the spectra indicate that the carriers are thermalized as early as 0.5 ps after the excitation pulse. The PL emission at low energies, 1.465 eV, reaches a maximum after ~ 10 ps, and then decays with the lifetime of the electron–hole plasma. The large spectral width of the emission on the femtosecond time scale is evidence for the equilibration of electrons and holes in the Γ valley in < 100 fs. The excitation creates electrons in the Γ valley through the absorption from the split-off band as well as from the heavy- and light-hole bands. Some of these electrons may then be scattered to the X and L valleys, but the important point is that the remaining electrons in the Γ valley are created with a very narrow energy distribution, unlike that evident in the PL spectra at these early times. The absence of structure, as shown in the band-to-acceptor PL of section 2.2.8, is characteristic of carrier–carrier scattering as the mechanism of thermalization as opposed to LO-phonon emission. The integrated intensity over the entire spectrum at 180 fs is approximately 15% of that at the PL maximum at 10 ps, which signifies that at these early times most of the carriers have been scattered to the subsidiary valleys.

Snoke et al. [494] capitalized on the idea of using band-to-acceptor emission, discussed in section 2.2.8 with regard to cw PL measurements of the electron distribution and cooling, as a means of observing the thermalization of conduction electrons in GaAs. Their experiment consisted of time-resolved measurements, using a Streak camera, of the electron–acceptor luminescence in bulk, LPE GaAs, doped p-type to $(4\text{--}10) \times 10^{16} \text{ cm}^{-3}$. Their samples were doped with Ge acceptors since it has the largest known acceptor binding energy (40.5 meV), thereby allowing better spectral resolution of the band-to-acceptor emission. Ge is amphoteric, but the preferential occupation of acceptor sites over donor sites is 3:1, thus, DAP emission is present, but weaker, and has a long lifetime as shown in section 3.2.3.3. Fig. 327 shows the time-resolved energy distribution of conduction band electrons at 10 K after excitation with a 5 ps laser pulse at 1.536 eV. In all spectra here, the cw component (longer lived) of the emission due to DAP emission has been subtracted out. In the figure, part a, the dotted line corresponds to a pulse excitation energy of 30 pJ ($4 \times 10^{14} \text{ cm}^{-3}$ pair density), the dashed line is a best fit by a Maxwell–Boltzmann energy distribution with a carrier temperature of 60 K, and the solid line is the energy distribution after pulsed excitation with an energy of 3 pJ ($4 \times 10^{13} \text{ cm}^{-3}$ pair density).

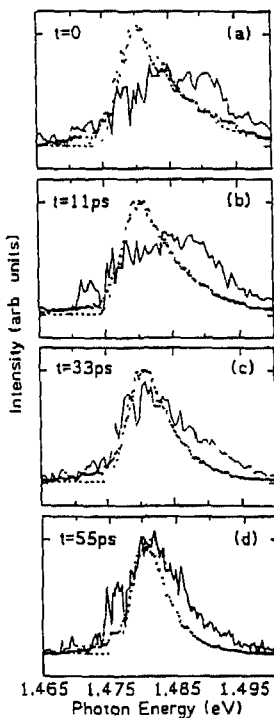


Fig. 327. Energy distribution of electrons in p-type Ge-doped GaAs at 10 K at various times after the excitation pulse. (a) $t=0$, pair density of $4 \times 10^{14} \text{ cm}^{-3}$ (●) and $4 \times 10^{13} \text{ cm}^{-3}$ (—), Maxwell-Boltzmann distribution with $T=60 \text{ K}$ (---). (b) $t=11 \text{ ps}$, energy distribution for pair density of $4 \times 10^{14} \text{ cm}^{-3}$ (●), energy distribution for pair density of $4 \times 10^{13} \text{ cm}^{-3}$ (—), and Maxwell-Boltzmann distribution with $T=53 \text{ K}$ (---). (c) $t=33 \text{ ps}$, energy distribution for pair density of $4 \times 10^{14} \text{ cm}^{-3}$ (●) and $4 \times 10^{13} \text{ cm}^{-3}$ (—), and Maxwell-Boltzmann distribution with $T=42 \text{ K}$ (---). (d) $t=55 \text{ ps}$, energy distribution for pair density of $4 \times 10^{14} \text{ cm}^{-3}$ (●) and $4 \times 10^{13} \text{ cm}^{-3}$ (—), and Maxwell-Boltzmann distribution with $T=50 \text{ K}$. (After Snoke et al. [494].)

density). In parts b and c the carrier temperature derived from the Maxwell-Boltzmann fits are 53 and 42 K. In part d the Maxwell-Boltzmann fit was performed on the low-density spectrum, yielding a carrier temperature of 50 K. The most important aspect of the data is that the energy distribution at low excitation powers is much broader than that at higher excitation powers. At high powers the Maxwell-Boltzmann distribution adequately fits the energy distribution even at 11 ps, whereas at lower powers this is not the case, the energy distribution is non-Maxwellian. By 55 ps, both the high and low power spectra are fit well by the Maxwell-Boltzmann distribution. This data, therefore, shows the evolution of the low-power spectra from a non-Maxwellian energy distribution into a Maxwellian distribution. Despite the fact that the low-power spectra exhibit a non-Maxwellian distribution, the spectra are much broader than that of the excitation source, and accordingly significant electron scattering must occur. One possible mechanism for this fast, non-Maxwellian broadening at low powers is electron-hole scattering of the geminate pair. At higher powers the uncorrelated electron-electron scattering will dominate. The redistribution of electrons due to electron-electron scattering will result in electrons above the optical phonon energy in the high-energy tail of the Boltzmann distribution. These high-energy electrons may then cool through the emission of optical phonons, with the results of an effective increase in the overall cooling rate of the gas. To put these results in context with those of Elsaesser et al. [491] and Rota et al. [493], the excitation density used by Snoke et al. was ~ 500 times lower; thus the thermalization time of 100 fs observed by Elsaesser et al. and Rota et al. is consistent with the extrapolated results of Snoke et al. at these high densities.

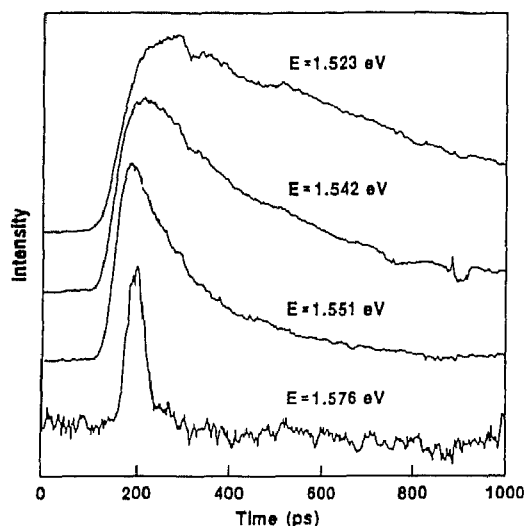


Fig. 328. Hot luminescence of a GaAs/AlGaAs quantum well versus time. Excitation was at 2.03 eV with a carrier density of $5 \times 10^{18} \text{ cm}^{-3}$ and lattice temperature of 4 K. (After Ryan et al [495])

In summary, electron-phonon scattering times are typically ~ 150 fs, intervalley scattering times for Γ -L scattering are ~ 30 fs, electron-electron scattering times (which causes thermalization among the ensemble of electrons) are < 500 fs at high excitation densities (pump-probe measurements have shown, with 6 fs resolution, the thermalization time due to electron-electron scattering to be ~ 10 fs [490]), and ~ 50 ps at low excitation densities, and the backscattering or re-entrant scattering of electrons from L to Γ occurs with a time constant of 2.5 ps.

3.2.5.2. Quantum wells

The cooling rate of the ensemble of photoexcited carriers in quantum well structures, just as in bulk semiconductors, has been found to be reduced from that expected theoretically [490]. There was some controversy regarding the nature of the carrier cooling mechanism, however it is now widely accepted that the effect of hot phonons, rather than screening of the carrier-phonon interaction, is the dominant mechanism.

In 1984 Ryan et al. [495] used a Streak camera system to measure the time-resolved PL from a modulation-doped quantum well. They determined the carrier temperature from Maxwell-Boltzmann fits to the high-energy tail of the emission spectrum, as has been commonly done. Fig. 328 shows the PL time decays versus detection energy after excitation at 2.03 eV with a carrier density of $5 \times 10^{18} \text{ cm}^{-3}$ at a lattice temperature of 4 K. This data shows that the observed lifetime decreases with increasing energies, and that the risetime of the luminescence increases for decreasing emission energies. Their results are consistent with the LO-phonon emission governed energy loss rate of an electron gas

$$P(t) = \frac{E_{\text{LO}}}{\tau_0} \exp[-E_{\text{LO}}/kT_e(t)] \quad (51)$$

where P is the mean power lost per carrier, and τ_0 is the relaxation time constant. The data is best fit with $\tau_0 = 7$ ps, considerably larger than the theoretical value of 0.11 ps for the unscreened electron-phonon interaction. Reduction of the excited electron density from 10^{18} to 10^{14} cm^{-3} results in a reduction of a factor of at least seven in this time constant, from 750 ps to 100 ps, respectively. In total

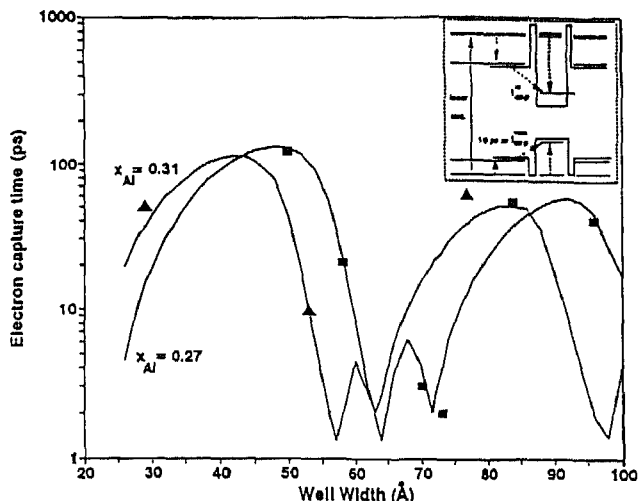


Fig. 329. Well-width dependence of the electron capture time in "spike-modified" quantum well samples. The theoretical curves correspond to different Al concentrations in the two different samples (From Deveaud et al., *Semicond. Sci. Technol.*, 9 (1994) 722.)

they find that the cooling of the hot carriers is 60 times slower than predicted for a 3D non-degenerate electron gas.

Another important aspect of carrier dynamics in quantum wells is that of carrier capture into the wells. Deveaud et al. [463] examined the temporal behavior of the luminescence signals originating both from the barrier (AlGaAs layer) and the well (GaAs layer) of a quantum well structure. In the former case, they examined the decay time, whereas in the latter they examined the rise time. These rise and decay times correspond to the electron and hole capture times. Fig. 329 shows the electron capture time versus the well width. The data exhibit clear resonances in the capture time due to resonant tunneling, and the solid lines are theoretical curves corresponding to slightly different Al concentrations in the barriers. The kinetics also show that hole capture times are approximately constant with well width. This is a result of the much smaller hole mean free path compared to the period of the sample, corresponding to the incoherent tunneling through a 22 Å barrier.

An additional mechanism of energy loss is through the electron–hole Coulomb scattering or energy transfer. Höpfel et al. [496] simultaneously measured the electron velocity, PL spectra, and hole current as a function of applied electric field. They find that there exists a non-equilibrium plasma state with different electron and hole distribution functions, wherein the electron distribution is "hot" and the hole distribution remains at room temperature. Importantly, they find that the energy-loss rate per electron is much larger in the presence of a hole plasma than in the absence of the hole plasma. They applied a pulsed electric field along the planes of the quantum well samples which were p-type doped. The measured photocurrent pulse then yielded the drift velocity of the electrons. In steady state the energy-loss rate is equal to the input power per electron, $e\mu_e E^2$. Time-resolved PL spectra allow determination of the carrier temperature. Their data exhibit clear exponential high-energy tails indicative of the carrier temperature. Taking this data in total, Fig. 330 shows the inverse temperature versus energy loss rate per electron for minority electrons in a hole plasma. The theoretical curves represent electron–phonon and electron–hole scattering mechanisms. These results demonstrate that the hot, minority electron energy-loss rate in a cool hole plasma is a factor of two higher than that of majority electrons in the absence of holes. The solid line represents a theoretical energy-loss rate for the sum of the electron–hole and electron–phonon scattering mechanisms.

The cooling of excitons in semiconductor nanostructures has also been examined by Masumoto et al. [497] and Marie et al. [498]. Masumoto et al. used a Streak camera to measure the temporal

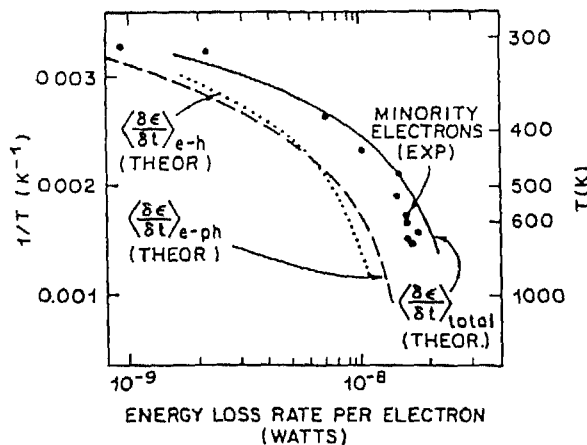


Fig. 330 Inverse electronic temperatures derived from high-energy side of PL spectrum versus energy loss rate. Lines represent different scattering mechanisms (electron-phonon scattering, electron-hole scattering, and total energy loss). (After Höpfel et al. [496].)

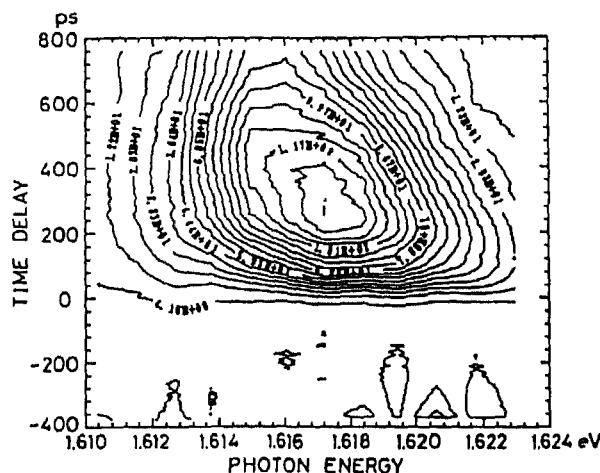


Fig. 331. Contour map of the time-resolved PL of excitons in a GaAs/AlAs quantum well at a lattice temperature of 4.2 K. (After Masumoto et al. [497]).

behavior of the spectral distribution of excitons in MBE-grown quantum wells. Fig. 331 shows a contour map of the spectral distribution of the emission as a function of time. At low energies (1.616 eV) it takes almost 400 ps for the intensity to reach a maximum. This directly reflects the energy distribution of the excitons. From this data they calculate the average energy of the excitons as a function of time, and find that the excitons lose energy at a rate of $1.0 \times 10^6 \text{ eV s}^{-1}$. The decrease in kinetic energy of the excitons occurs through the deformation-potential interaction with LA phonons, which has the following time dependence

$$\left\langle \frac{dE(t)}{dt} \right\rangle = \left(\frac{2M^2 D^2}{\hbar^3 \rho} \right) [kT_e(t) - kT_L] \quad (52)$$

where D is the exciton deformation potential, ρ is the areal mass density, $T_e(t)$ is the effective temperature of the 2D excitons, and T_L is the lattice temperature. Integrating this expression and using $D = 9.6 \text{ eV}$, $M = 0.7m_0$, $\rho = 4.0 \times 10^{-6} \text{ g cm}^{-2}$, and $T_L = 4.2 \text{ K}$ yields a time constant of 24 ps for energy loss, a result much faster than the observed rate. Thus, the exciton-phonon interaction is not

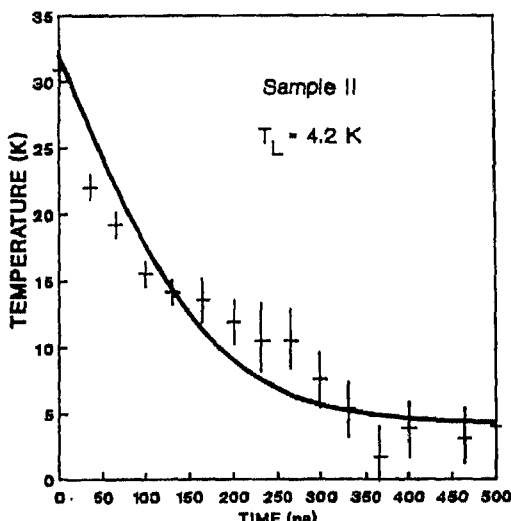


Fig. 332 Excitonic cooling curves, determined experimentally (+) and theoretically (—). (After Marie et al. [498].)

responsible for the observed slow energy relaxation of 2D excitons. Masumoto et al. conclude that localization effects and spectral migration (to be discussed in section 3.2.14) are instead responsible. Marie et al. examined the spectral lineshape of the excitonic emission as a function of time after the 5 ps pulse in a series of short-period superlattices. Temporal resolution was obtained with the PL-upconversion technique. In order to eliminate possible electron-hole plasma effects, all experiments were carried out at low temperatures (4.2 K) and low excitation powers (typically 4 mW average power at a 7.6 MHz repetition rate), with a non-resonant excitation 115 meV above the ground state. Fits to the exponential tail on the high-energy side of the emission spectra yield the excitonic temperature. Fig. 332 shows the experimental and theoretical results for the excitonic temperature as a function of time after the laser pulse. The initial excitonic temperature is ~ 35 K, and the temperature decreases rapidly with time due to the exciton-phonon interaction until the lattice temperature is reached in several hundred picoseconds. The predominant LO-phonon emission occurs within the time resolution of these experiments (5 ps). Thus, the data here shows the cooling due to the emission of acoustic phonons. The model is based upon both the deformation potential and piezoelectric exciton-acoustic phonon interaction. The measured cooling rate is also found to vary with sample structure due to the dimensionality dependence of the exciton-acoustic phonon interaction. So, in contrast to the work of Masumoto et al., Marie et al. found that the exciton-acoustic phonon interaction alone, without resorting to localization and spectral migration effects, may explain the cooling of the 2D exciton gas.

3.2.5.3. Type-II structures

There are many different types of intervalley scattering in type-II GaAs/AlAs structures. Most prominent and important among these is the electron scattering from the Γ point in the GaAs layers to the X point in the AlAs layers, actually an interlayer scattering process. In addition electron scattering among the different inequivalent X valleys in the AlAs layers may be present. Deveaud et al. [463] have examined the kinetics of electron interlayer/intervalley scattering in type-II GaAs/AlAs structures. They measured the luminescence (both type I and type II from the same samples) at 20 K with excitation densities ranging from 10^{15} to 10^{19} cm^{-3} . Fig. 333 shows the PL from the type-I emission at 20 K in three different samples with different periods (here 21/24 represents a structure with 21 monolayers of GaAs and 24 monolayers of AlAs, repeated many times). The observed type-I lifetime

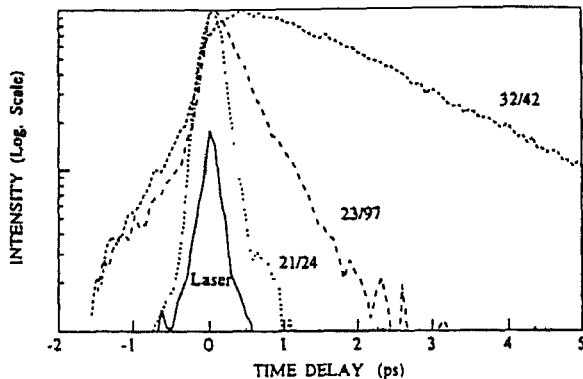


Fig. 333. PL decay kinetics of the direct type-I emission in three different samples with GaAs/AlAs layer widths shown (in Å). Also shown, solid curve, is the autocorrelation trace of the scattered laser light. (From Deveaud et al., *Semicond. Sci. Technol.*, 9 (1994) 722.)

(240 fs to 24 ps) is much shorter than the known radiative lifetime of a type-I quantum well. The lifetime also increases with GaAs layer thickness and is independent of the AlAs layer thickness. Since the absorption occurs within the GaAs layer, and the holes are not scattered (intervalley), the PL kinetics evident here directly reflect the interlayer/intervalley scattering of electrons. Further, the observed kinetics are roughly invariant with excitation density. Fig. 334 shows the measured type-I lifetime versus GaAs layer thickness together with a theoretical model based upon a perturbative analysis.

Intervalley electron scattering between inequivalent X conduction band valleys in type-II $\text{Al}_x\text{Ga}_{1-x}\text{As}/\text{AlAs}$ multiple quantum wells has been recently examined by Charbonneau et al. [499]. They applied uniaxial stress to alter the energy separation between the X_Z and $X_{X,Y}$ conduction band states of the AlAs layers, and measured the PL emission lifetimes of the higher-lying X_Z state as a function of this energy separation, which was accurately determined directly from the PL spectra. Their samples were chosen judiciously to have an energy level structure near that at which the X_Z and $X_{X,Y}$ states cross in energy. Uniaxial stress was applied along the [110] direction and resulted in an increase in ΔE , the energy difference between X_Z and $X_{X,Y}$ states. Fig. 335 shows the measured lifetimes for two samples as a function of the energy difference, ΔE . The solid line corresponds to the TA phonon-assisted recombination in these samples. For small ΔE , the observed PL decay time is constant. At the onset of the appearance of the TA phonon-assisted transition, the observed lifetime

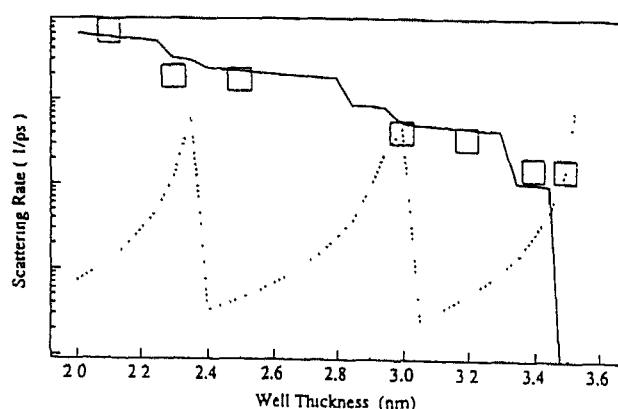


Fig. 334. Electron scattering rate (\square) and theoretical scattering rate in a GaAs/AlAs type-II superlattice. Theories include (—) intervalley scattering, and (···) state mixing and intervalley scattering. (From Deveaud et al., *Semicond. Sci. Technol.*, 9, (1994) 722.)

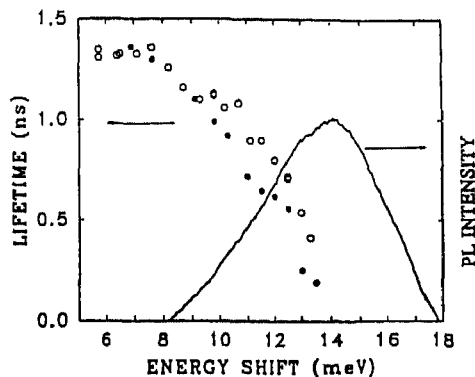


Fig 335. PL lifetime of the hot X_Z state versus energy shift between X_Z and $X_{X,Y}$ states for two different type-II AlGaAs/AlAs quantum well samples. Also shown is the TA phonon-assisted recombination centered 14 meV below the no-phonon line. (After Charbonneau et al. [499].)

begins to decrease rapidly, and is resolution limited at the peak of the TA phonon-assisted peak at 14 meV. They ascribe the decay time to intervalley $X_Z \rightarrow X_{X,Y}$ electron scattering. The invariance of the lifetime for ΔE smaller than the AlAs phonon energies (TA, LA, TO, or LO) indicates that the scattering occurs via interfacial roughness induced intervalley scattering. The reduction in lifetime at the onset of the appearance of the relatively broad TA phonon-assisted PL peak (~ 8 meV) is a result of processes which broaden these levels from the peak energy of 14 meV. This decrease is strong evidence for the TA phonon-assisted $X_Z \rightarrow X_{X,Y}$ intervalley scattering.

3.2.5.4. Quantum well wires

The dynamics of carrier cooling in 1D quantum well wires have only recently been examined. The difficulty in all such types of measurements in quantum wires or quantum dots is that the technology for fabrication is immature, and the resulting structures are far from perfect, leading to dynamics which may be entirely dominated by extrinsic processes. Nevertheless, Maciel et al. [500] reported time-resolved PL measurements (done with a Streak camera) of the quantum well wire associated emission in structures which were patterned using holographic lithography. The wires were formed in V-grooves of width 9.3 nm at the bottom to 2.2 nm at the top. Excitation was provided by a subpicosecond laser with an emission wavelength of 760 nm, well below the bandgaps of the superlattice and capping layer. As a result, the photoexcited carriers are excited entirely within the V-groove quantum well wire region of the structure. Fig. 336 shows the PL time decays of the emissions from the first two laterally-confined subbands of the quantum well wire versus excitation intensity. As the excitation intensity is decreased the $n_y=1$ lifetime becomes systematically and monotonically longer, whereas, the $n_y=2$ emission exhibits a rapid decay in the first 300 ps of the emission. These data are evidence for the time-dependent carrier relaxation and band filling within the 1D confined states. Further details regarding the cooling mechanism(s) and energy loss rates requires detailed measurements of the time-dependent carrier temperatures.

3.2.6. Radiative decay in a disordered system

Klein, Sturge, and Cohen [462] (KSC) examined the effect a distribution of radiative rates would have on the observed PL kinetics in a semiconductor. The stochastic nature of the intervalley alloy scattering is an example of a mechanism which gives rise to a distribution of no-phonon radiative decay rates. The radiative decay rate is proportional to the matrix element of the transition squared

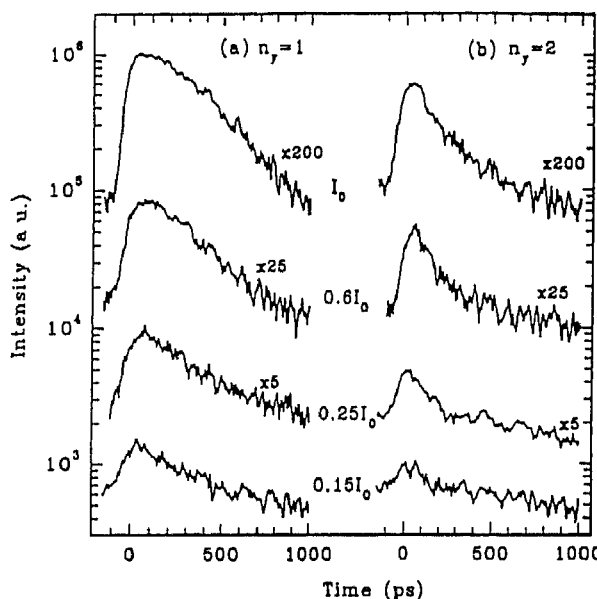


Fig. 336. Time-resolved PL from (a) $n_y = 1$ and (b) $n_y = 2$ versus excitation density (After Maciel et al. [500].)

(by Fermi's golden rule), and if the matrix element, V , is taken as a stochastic variable, then the radiative decay rate is also a stochastic variable. KSC assumed that the distribution of V is Gaussian

$$p(V^2) = (2\pi V^2 \langle V^2 \rangle_{\text{avg}})^{-1/2} \exp\left(\frac{-V^2}{\langle V^2 \rangle_{\text{avg}}}\right) \quad (53)$$

so that the distribution of V^2 is exponential. After including a phenomenological non-radiative decay w_{nr} , they find the temporal dependence of the PL decay to be

$$I_{\text{np}}(t) = e^{-w_{\text{nr}}t} [1 + \langle w \rangle_{\text{avg}} t]^{-2} \quad \text{for } k \neq k_X \quad (54)$$

and

$$I_{\text{np}}(t) = e^{-w_{\text{nr}}t} [1 + 2\langle w \rangle_{\text{avg}} t]^{3/2} \quad \text{for } k = k_X \quad (55)$$

For phonon-assisted transitions, the PL time dependence is similar to that of Eq. (54) Eq. (55), except that the exponents are -1 and $-1/2$, respectively. Fig. 337 shows PL decay curves of the no-phonon exciton line at 2 K for $\text{Al}_x\text{Ga}_{1-x}\text{As}$ with (a) $x = 0.48$, and (b) $x = 0.445$. These fits agree well with the data. It must be noted that this theory is only applicable to the case of immobile (localized) excitons. Angell and Sturge [459] have extended this theory to include the effects of excitons motionally averaging the distribution of decay rates as thermal delocalization occurs. They targeted their theory towards the explanation of the decay kinetics of type-II GaAs/AlAs superlattices. Their model has one fitting parameter, γ , which is the ratio of the exciton lifetime to the time it takes an exciton to jump from one localized site to another. Importantly, the model does not take into account the effects of spectral diffusion in which excitons at higher energy sites jump to lower energy sites as they migrate spatially. Fig. 338 shows several PL decays for a type-II GaAs/AlAs superlattice versus temperature. The agreement between experiment and theory is reasonable. They conclude from these fits that two delocalization processes govern the PL decay kinetics, namely thermal activation from the localized states and the exciton binding energy. In section 3.2.2.3.2, we have shown that the PL emission of excitons in type-II GaAs/AlAs superlattices is strongly influenced by non-radiative decay, and this

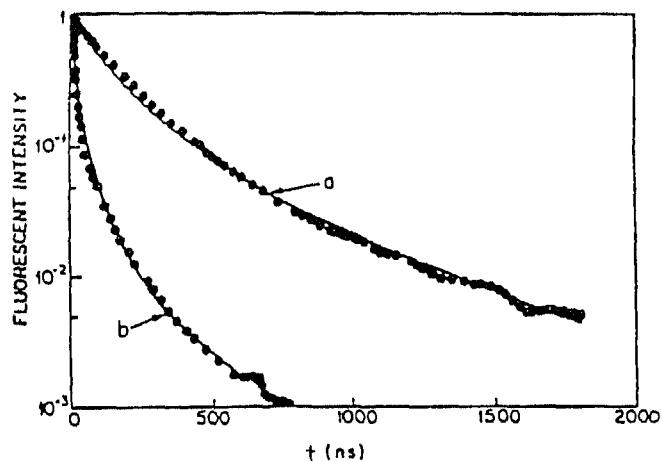


Fig. 337. PL decay kinetics of the no-phonon emission at 2 K for two different $\text{Al}_x\text{Ga}_{1-x}\text{As}$ alloys, (a) $x = 0.48$ and (b) $x = 0.445$. (After Klein et al. [462].)

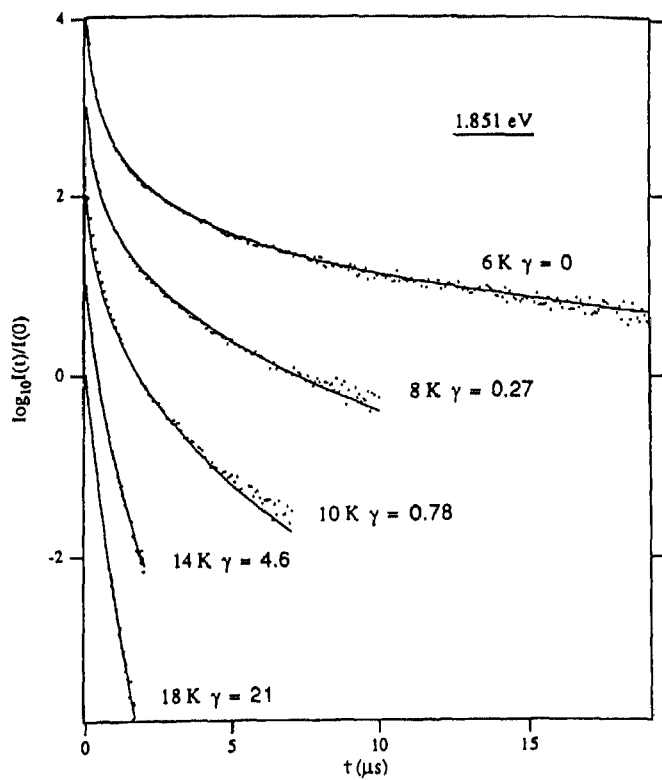


Fig. 338. PL decay kinetics of the no-phonon line in a type-II GaAs/AlAs superlattice at various temperatures. Solid lines were calculated using the theory of Angell and Sturge, yielding the values of γ shown. (After Angell and Sturge [459].)

non-radiative decay quenches the PL emission with increasing temperature. The theory of Angell and Sturge does not include non-radiative decay, and therefore cannot provide a complete description to the PL decay of excitons in type-II structures. Nevertheless, it may still be a valid extension of the early work of Klein, Sturge, and Cohen for other structures.

3.2.7. Shockley–Read–Hall recombination

PL kinetics are influenced by the sum of all possible recombination rates of the various recombination pathways. One possible recombination pathway, a non-radiative mechanism, is through non-luminescing states within the gap of the semiconductor. The so-called Shockley–Read–Hall (SRH) center has such a state. These recombination centers may be located throughout a layer or in thin slabs at the surfaces or interfaces of a layer. This later distribution allows for an analysis of non-radiative surface recombination in terms of SRH recombination.

A recombination center is different from an electron or hole trap, in that after capturing an electron (hole) it captures a hole (electron) [501]. Semiconductor statistics may be used to analyze the generation and recombination of carriers, including the capture of electrons and holes by these traps. For a spatially uniform minority-carrier density, the SRH expression for recombination at a single defect level leads to a rate equation for the excess minority-carrier density (here holes), and, ignoring drift and diffusion, leads to the continuity equation

$$\frac{d\Delta p}{dt} = - \frac{\sigma_n \sigma_p v_{th} N (\Delta p N_D - \Delta p^2)}{\sigma_n (N_D + \Delta p + n_i e^{(E_i - E_d)/kT}) + \sigma_p (\Delta p + n_i e^{(E_i - E_d)/kT})} \quad (56)$$

where N_D is the majority-carrier density, v_{th} is the hole thermal velocity, N is the defect density, and σ_n (σ_p) are the capture cross-sections for electrons (holes), respectively. This expression assumes that the trap density is smaller than the majority-carrier density, as assumed in the bulk of the Shockley and Read paper. Assuming a midgap defect energy level, and using $\tau_n^{-1} = (v_{th} N \sigma_n)^{-1}$ and $\tau_p^{-1} = (v_{th} N \sigma_p)^{-1}$ (the electron and hole lifetimes) yields the rate equation for the instantaneous injection level

$$\frac{dI}{dt} = \frac{I + I^2}{\tau_p (1 + I) + \tau_n I} \quad (57)$$

For low-injection levels, the observed lifetime is that of the minority holes (exponential decay), whereas for high-injection levels, the observed exponential decay should be the sum of majority- and minority-carrier lifetimes. Since there is a finite number of recombination centers, saturation of these centers will decrease the recombination rate, thereby increasing the effective lifetime. If instead of considering a uniform distribution of recombination centers throughout the epilayer, their distribution is limited to thin layers at the interfaces, the rate equation governing the intensity is identical to Eq. (57) but with τ_p and τ_n replaced by $1/S_n$ and $1/S_p$ and a multiplicative prefactor of $2/d$ (where d is the thickness of the epilayer). Thus, the surface recombination velocity at low injection is S_p , whereas at high injection it is $[S_p S_n / (S_p + S_n)]$.

Ahrenkiel et al. [502] examined these effects in a series of $\text{Al}_{0.3}\text{Ga}_{0.7}\text{As}/\text{GaAs}$ double heterostructures. Fig. 339 shows the PL time decays for a sample doped n-type to $1.5 \times 10^{17} \text{ cm}^{-3}$ for three different excitation intensities, 0.1, 1.0, and 10.0 mW mm^{-2} for curves A, B, and C, respectively. The solid lines in the figure are fits to the data using a numerical solution of Eq. (57) and a minority-carrier lifetime of 32.3 ns and a majority-carrier lifetime of 31.2 ns. At low-injection levels, a second recombination center was included in Eq. (57) to provide an adequate fit to the data. The non-exponential behavior observed here is indicative of a transition from a high-carrier to low-carrier density regime, yielding the “S”-shaped kinetics. The long lifetime observed initially corresponds to the sum of majority- and minority-carrier lifetimes, whereas the long-time lifetime corresponds to the minority-carrier lifetime (taking into account possible photon-recycling effects).

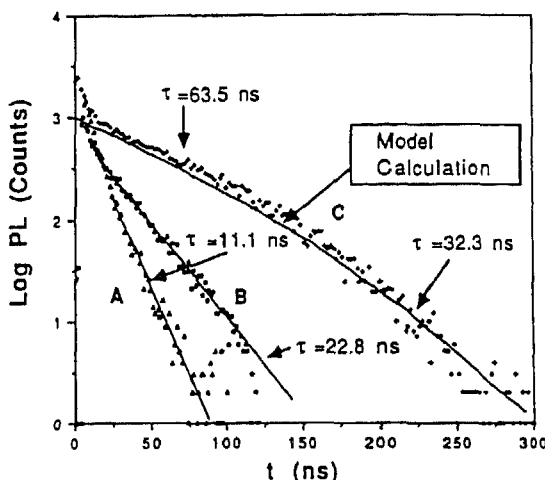


Fig. 339. PL time decays of a GaAs/AlGaAs double heterostructure grown at 700 °C. Curves A, B, and C correspond to excitation powers of 0.1, 1.0, and 10.0 mW, respectively. (After Ahrenkiel et al. [502].)

3.2.8. Bulk non-radiative decay and surface recombination

Non-radiative decay of carriers in semiconductors is generally deleterious to the performance of most devices fabricated from such materials. This non-radiative decay is generally classified according to the position at which it occurs in the material or structure, within the bulk or at surfaces and interfaces. This non-radiative decay may drastically reduce PL efficiencies and lifetimes in GaAs structures, and may dominate minority-carrier kinetics, thereby limiting the performance of minority-carrier GaAs optoelectronic devices such as injection lasers, light-emitting diodes, photodetectors, etc. [503]. In order to include the effects of these non-radiative decay processes to the rate equations describing free-carrier recombination, it is necessary to add two additional terms to the original rate equation (Eq. (6))

$$\frac{dp}{dt} = -B(np + n_0p + p_0n) - \frac{P}{\tau_{nr}} = \frac{(S_1 + S_2)p}{d} \quad (58)$$

where it has been assumed the material is n-type (minority carriers are holes, p), τ_{nr} is the phenomenological bulk non-radiative decay rate, d is the thickness of the active layer, and S_1 and S_2 are the surface recombination velocities of the two interfaces of the active layer [11,28,32,503–506]. The term $[(S_1 + S_2)/d]$ represents the non-radiative decay of carriers at each heterointerface. This simple phenomenological term arises from the boundary conditions to the solution of the classical diffusion equation, yielding a term

$$\left(\frac{d^2}{\pi_2 D} + \frac{d}{S_1 + S_2} \right) \quad (59)$$

where D is the diffusion constant [507]. By assuming that the distance between heterointerfaces is small compared to the minority-carrier diffusion coefficient, this term may be approximated as the surface recombination term in Eq. (42). Measured lifetimes (τ) may be used to calculate interface recombination velocities, S_1 and S_2 , using the expression

$$\frac{1}{\tau} = \frac{1}{\tau_{nr}} + \frac{(S_1 + S_2)}{d} + B(n_0 + p_0) \quad (60)$$

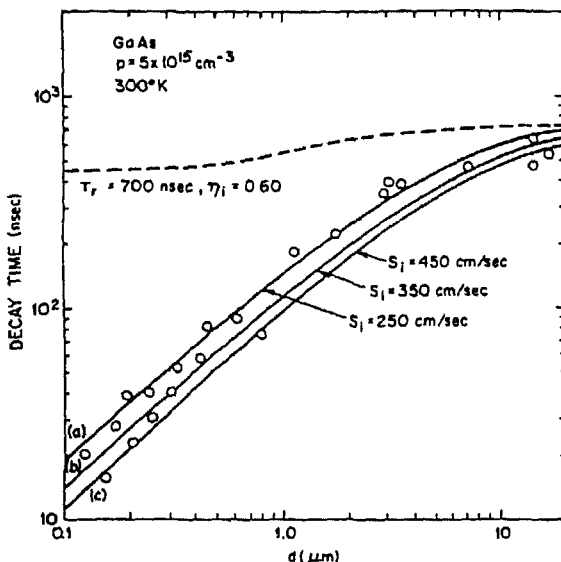


Fig. 340. PL decay lifetimes of several GaAs/AlGaAs double heterostructure samples versus layer thickness. The background doping in the samples was $p = 5 \times 10^{15} \text{ cm}^{-3}$ ---, calculation including self-absorption; ——, different values of interface recombination velocities. (After Nelson [504])

Ettenberg and Kressel [508], Nelson [504] and Nelson and Sobers [505] conducted some of the most thorough early studies of surface recombination in GaAs. They all found that the lifetime increased with the thickness of the active layer. Fig. 340 shows Nelson's measured PL lifetimes versus active-layer thickness of their LPE-grown double heterostructures. The solid lines are derived using Eq. (53). Their data is consistent with a surface recombination velocity of $\sim 300 \text{ cm s}^{-1}$, and an internal quantum efficiency of 60%. More recently, Wolford et al. [11,28,503] and Gilliland et al. [32] have examined the room temperature decay kinetics of both MBE- and OMVPE-prepared GaAs/AlGaAs double heterostructures in an effort to quantify the surface recombination of layers grown with these more modern growth techniques. Fig. 341 shows their measured lifetimes versus thickness for their MBE heterostructures, OMVPE heterostructures, OMVPE heterostructures with the top AlGaAs layer chemically-etch removed and repassivated with a topical chemical surface treatment (Na_2S), and the same OMVPE heterostructures with the top AlGaAs layer chemically-etch removed and left "bare". These results suggest interface recombination velocities as low as 40 cm s^{-1} for the OMVPE double heterostructures, 250 cm s^{-1} for the MBE double heterostructures, 5500 cm s^{-1} for the Na_2S repassivated heterostructures, and 34000 cm s^{-1} for the heterostructure with a bare surface. (They also found that bulk non-radiative decay must occur with a lifetime no smaller than $3 \mu\text{s}$).

In the limit of thin structures, i.e. the quantum limit, this phenomenological picture of interface recombination is clearly not sufficient. Here, the carriers are affected by any interfacial decay at both interfaces simultaneously. Thus, d is a meaningless quantity, and the dynamics of carrier transport in the direction perpendicular to the quantum well plane clearly cannot be modeled classically. Thus, discussions of surface recombination velocities in quantum wells are without foundation, and should instead be formulated in terms of bulk non-radiative decay since it is impossible to distinguish between these two forms of non-radiative decay in nanostructures. Lastly, surface recombination in Si is not nearly as severe as in GaAs. This is due to the propensity of GaAs to have surface dangling bonds or to incorporate defects at interfaces, whereas in Si this is much less of a problem.

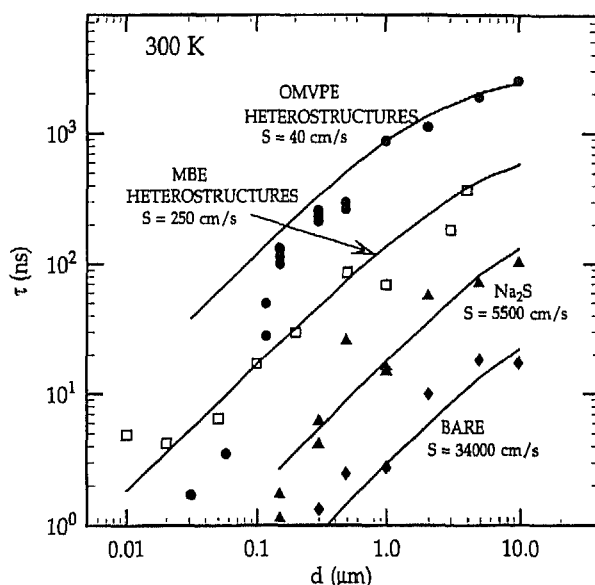


Fig. 341. Room-temperature free-carrier lifetimes for OMVPE-prepared GaAs/AlGaAs double heterostructures, MBE-prepared double heterostructures, $\text{Na}_2\text{S}/\text{GaAs}/\text{AlGaAs}$ heterostructures, and "bare" GaAs/AlGaAs heterostructures as a function of GaAs layer thickness. (After Wolford et al. [503].)

3.2.9. Photon recycling

It has been suggested that band-to-band recombination kinetics in direct-gap semiconductors, and in particular GaAs, may be significantly affected by photon recycling [32, 506, 509, 510]. The large value of the absorption coefficient in direct-gap semiconductors, typically 10^4 cm^{-1} , may lead to the reabsorption of radiatively emitted photons. This resonant radiative reabsorption and subsequent re-emission of photons may cause a lengthening of the measured lifetime, and increases in importance with the thickness of the active layer of the semiconductor. It is generally accepted that photon recycling is only important for layers thicker than the absorption depth of the semiconductor. The effects of photon recycling are quite complicated and the possibly drastic change in decay kinetics are critically dependent on experimental and sample geometry [511]. Asbeck's simple theory for photon recycling consisted of writing the bulk lifetime in terms of a photon recycling factor φ , as [509]

$$\frac{1}{\tau_B} = \frac{1}{\tau_{nr}} + \frac{1}{\varphi\tau_r} + \frac{2S}{d} \quad (61)$$

where τ_r is the radiative lifetime (Bn_0 , where n_0 is the majority carrier density). Asbeck reanalyzed the data of Ettenberg and Kressel [508] in terms of this photon recycling mechanism. Their lifetime of ~ 20 ns for $d > 10 \mu\text{m}$ and a majority-carrier density of $1.2 \times 10^{18} \text{ cm}^{-3}$ is five times greater than the calculated radiative lifetime of 4.1 ns. For a layer thickness of $4 \mu\text{m}$, Asbeck predicted φ to be approximately 6. Thus, the measured lifetime may be greater than the radiative lifetime. Fig. 342 shows the measured PL time decays of $4 \mu\text{m}$ and $8 \mu\text{m}$ GaAs structures with majority-carrier densities of $1.0 \times 10^{17} \text{ cm}^{-3}$ and $1.3 \times 10^{17} \text{ cm}^{-3}$, respectively. The measured lifetimes are 190.2 and 152.6 ns, whereas the calculated radiative lifetimes are 38.5 and 50.0 ns, respectively. Thus, the measured lifetimes are greater than the radiative lifetimes by approximately a factor of 3–5, corresponding to photon recycling factors, φ , of 8.4 and 13.6, respectively.

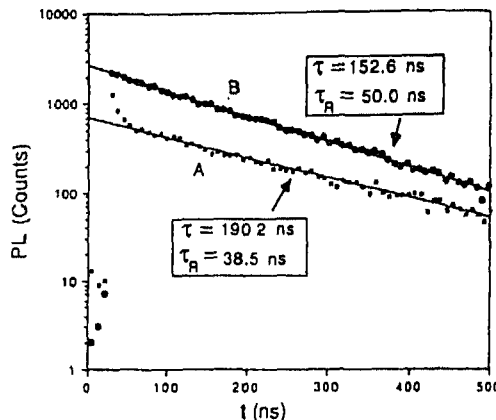


Fig. 342 PL decay kinetics for two GaAs double heterostructures (A) $d = 4 \mu\text{m}$ and (B) $d = 8 \mu\text{m}$ grown at 800°C (After Ahrenkiel et al. [506].)

Since photon recycling is a complex mechanism which may involve the “cooling” of carriers intermediate to the re-emission and absorption processes, the PL spectra of a sample in which photon recycling is important should exhibit a red-shift in the PL peak emission energy for increasing GaAs layer thicknesses [512]. Gilliland et al. [32] examined their double heterostructures, in which they observed long room-temperature lifetimes, and correspondingly low surface recombination velocities, for the effects of photon recycling. They found no evidence for photon recycling based upon several observations. First, they did not observe any red-shift in the PL spectra for samples with active layer thicknesses from 0.1 to $10.0 \mu\text{m}$. Second, they did not observe any anomalous transport results. Thirdly, low temperature measurements in thin structures ($0.3 \mu\text{m}$ active layer thickness) yielded, in some cases, lifetimes up to $15 \mu\text{s}$. Thus, thin samples in which photon recycling is known to be negligible may exhibit very long lifetimes, even greater than that observed at room temperature. This suggests a low doping level in the sample. Lastly, the method of observation may have excluded the observation of photon recycling effects. Gilliland et al. performed their kinetics measurements with a defocused laser beam ($\sim 3 \text{ mm}$ spot size), and the backscattered PL was detected only over a narrow range of this spot ($200 \mu\text{m}$ spectrometer slits and approximately $4 \times$ magnification of the PL image), thus excluding possible detection and measurement of photon recycling effects in the direction parallel to the heterointerfaces.

3.2.10. Biexcitons

Biexcitons are only rarely observed in bulk GaAs due to their small binding energy, as was noted in section 2.2.4, and as a result there have been no studies of biexciton kinetics in bulk GaAs. There have, however, been several studies of biexciton kinetics in Si and GaAs nanostructures. Gourley and Wolfe [238] found that the kinetics of the biexcitons and free excitons in their high-purity Si were well described by a chemical equilibrium between two ideal gases at the lattice temperature. Fig. 343 shows the decay kinetics for both biexcitons and free excitons at 5.2 K . Both decays are exponential and several microseconds long, and the ratio of lifetimes is 1.8, close to the predicted value of 2. The 10% discrepancy in this ratio may be indicative of the extent to which chemical equilibrium between biexcitons and free excitons is achieved within their radiative lifetime. Within the context of chemical equilibrium at low biexciton densities, the biexciton population will quadratically track (bimolecular formation from free excitons) the free-exciton population. Thus the observed free-exciton decay lifetime will be τ_x , and the corresponding biexciton decay lifetime will be $\tau_x/2$. In the opposite extreme

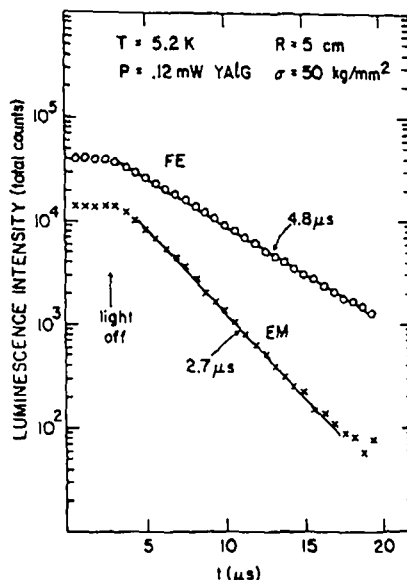


Fig. 343. PL time decays of the excitonic molecule and free exciton at 5.2 K. Ratio of the lifetimes corresponds to the expected value of 2 for quasi-equilibrium [238].

of high densities, the observed biexciton decay time is $2\tau_b$, while the observed free-exciton decay time is $4\tau_b$. This is since one exciton is left after each biexciton decay. (Here τ_b is the radiative lifetime of biexcitons, and τ_x is the radiative lifetimes of free excitons [239].) Gourley and Wolfe's studies showed that the biexciton-free exciton thermalization time is much less than the recombination times of either biexcitons or free excitons. Both Charbonneau et al. [230] and Kim et al. [234] have examined the kinetics of biexcitons in GaAs quantum wells. Kim et al. find that the biexciton decay occurs at twice the rate of the free-exciton decay, just as in Si. Fig. 344 shows the PL decay kinetics after excitation with a 5 ps laser pulse. The lower half of this figure demonstrates the quadratic relationship between the biexciton and free-exciton intensities as a function of time. In this figure the solid and open symbols correspond to excitation densities of 10^{12} and 10^{11} cm^{-2} . Note that the decays do not overlap. This is due to the fact that the intensity is plotted rather than the particle density. (It is the particle densities of the biexcitons and free excitons which have a quadratic relationship, not strictly the intensities.) This shows that the PL intensity does not consistently give an accurate measure of the areal density of the excitons or biexcitons. This is also borne out by time- and spatially-resolved PL measurements.

3.2.11. Electron-hole liquid

The PL kinetics of the EHL in Si reveal the interesting dynamics of this condensed electronic phase in semiconductors. They expose the complexities of EHL droplet formation, radiative and non-radiative decay, as well as the motion of the EHL (to be discussed in section 4). Cuthbert [487,488] measured the EHL kinetics using an 86 ns e-beam source. Fig. 345 shows the PL kinetics of the electron-hole liquid at 1.8 K, together with several theoretical curves obtained through solution of coupled rate equations for free excitons and the EHL. These fits yield a capture coefficient of the EHL from the free excitons of $(1-3) \times 10^{-9} \text{ cm}^3 \text{ s}^{-1}$, and a decay time of 59 ns. This much more rapid decay time of the EHL compared to the free exciton (on the order of 200 μ s) is attributed to a non-radiative Auger recombination process involving two pairs of electrons and holes whereby the recom-

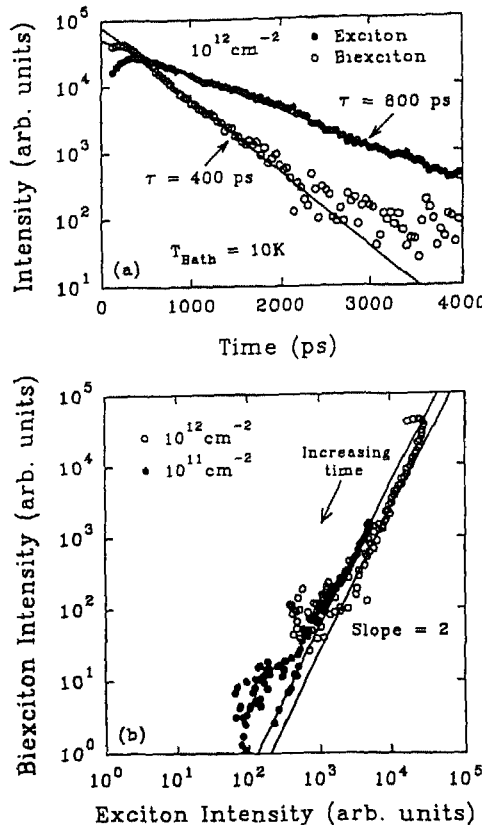


Fig. 344. (a) Exciton and biexciton integrated intensities versus time. (b) Biexciton intensity versus exciton intensity, with time as the parametric variable. Open (closed) symbols correspond to excitation to 10^{12} cm^{-2} (10^{11} cm^{-2}). Results for two different excitation densities do not overlap, implying that the gas areas for the two sets of data are not the same [234].

bination of one of the constituent electron–hole pairs of the EHL is given to the electron and hole of another exciton within the EHL. Gourley and Wolfe [513] and Cuthbert [487,488] examined the PL decay kinetics of the EHL in Si. Gourley and Wolfe demonstrated that the PL kinetics depend strongly upon the equilibrium properties of the EHL, such as the equilibrium density, which they were able to controllably change through the application of stress. Fig. 346 shows the EHL PL time decays at zero, intermediate, and high stress, with all decays being rigorously exponential over three decades, and the lifetimes increasing with stress. The zero-stress lifetime is $0.14 \mu\text{s}$. The exponential nature of these decays, in contrast to non-exponential decays observed by others [514], is attributed to the impeded free-exciton evaporation from the EHL by the strain gradient of the potential well (Hertzian stress geometry) in contrast to the normal enhanced evaporation in a uniform stress geometry. The increase in lifetime is directly related to the decrease in density. As discussed previously in section 3.2.4 Auger recombination is the dominant decay mechanism for electrons and holes, and this decay is non-radiative in nature. Fig. 347 shows the measured EHL lifetimes versus equilibrium density together with the enhancement factor, $g_{eh}(0)$, which is the probability for finding an electron at the spatial location of a hole. The lifetime of an electron–hole pair in the EHL is given by

$$\frac{1}{\tau} = C g_{eh}^2(0) n^2 \quad (62)$$

where C is a constant independent of density. This Auger mechanism involves two holes and an

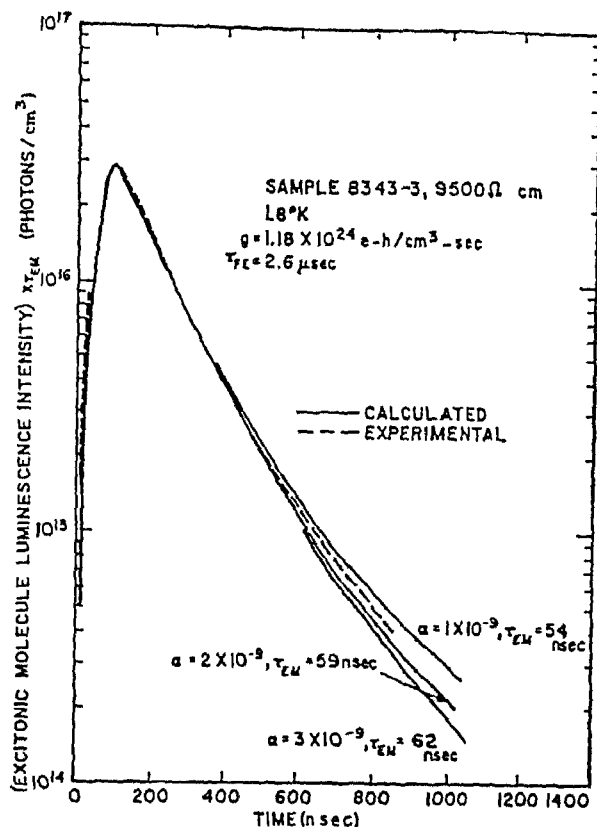


Fig. 345. Experimental and theoretical biexciton PL decay curves at 18 K. (After Cuthbert [488].)

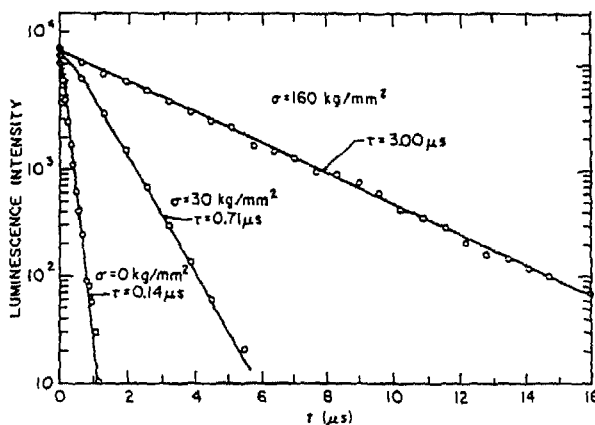


Fig. 346. EHL PL kinetics at three different stresses. All decays are exponential over many decades with lifetimes increasing with stress (After Gourley and Wolfe [513].)

electron. At low densities Gourley and Wolfe find the Auger coefficient, C , to be $C = 2.7 \times 10^{-31} \text{ cm}^6 \text{ s}^{-1}$, two times lower than the zero-stress value. Also, the enhancement factor is observed to decrease with increasing density. These results show the exact quadratic dependence, at low densities, of the recombination rate on density, as predicted by theory; whereas at higher densities the changes in the electron-hole correlation modify this relationship. Lastly, Gourley and Wolfe convincingly demonstrated that a uniform strain, which reduces the stability of the EHL, enhances the decay mechanism

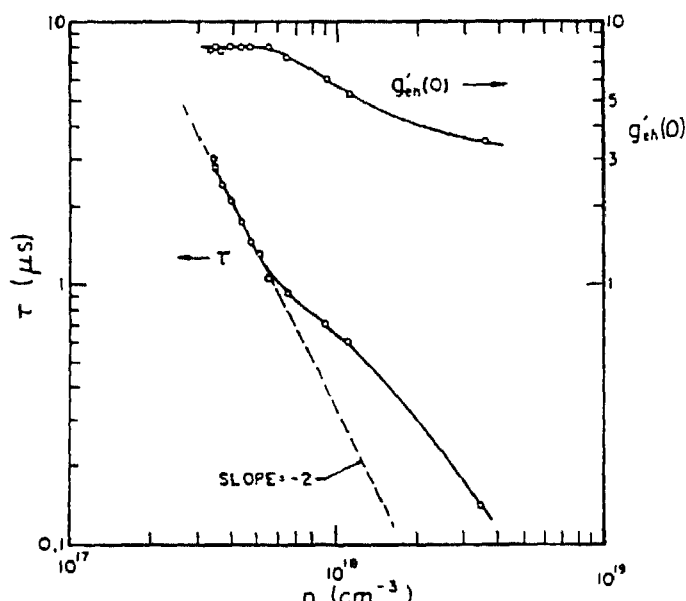


Fig. 347. Density dependence of the EHL lifetime showing the quadratic dependence at low densities. At higher densities the deviation from quadratic is due to the density dependence of the enhancement factor $g_{eh}'(0)$ (After Gourley and Wolfe [513].)

involving the "boil off" of excitons from the EHL, and that this mechanism may be eliminated in a strain-confined EHL.

Shah and Dayem [515] were the first to measure the kinetics of formation of the EHL in Si with excitation pulses and detectors fast enough to truly resolve the build-up of the emission. Interestingly, they showed that at high laser excitation intensities the EHL is formed directly from a dense, hot electron-hole plasma instead of from the nucleation of a gas of excitons. They monitored the TO-, LO-, and TA-phonon-assisted transitions in the PL spectrum of a Si sample after excitation by a cavity-dumped Ar^+ laser (15 ns pulselength). Fig. 348 shows the PL kinetics detected at the strong TO-LO-assisted EHL band and the TO-LO-assisted exciton band at 1.080 and 1.097 eV, respectively. The maximum PL intensity of the excitonic luminescence occurs at 35 ns, whereas for the EHL band the maximum PL intensity occurs at 55 ns after the beginning of the laser excitation pulse. The PL kinetics of the excitonic emission are suggestive of a two-phase process, wherein the early phase is a hot, dense electron-hole plasma, with a relatively short decay time, and the later phase is that of an excitonic gas in equilibrium with the electron-hole liquid, with a correspondingly longer lifetime. Their time-resolved spectra clearly show the existence of the electron-hole plasma with a carrier temperature, derived from the slope of the high-energy tail of the PL, considerably hotter than that of the lattice, which was in a liquid-helium bath. At later times, the spectra are indicative, in shape and energy, of that expected for a "cold" EHL, and simultaneously a free-exciton associated peak appears in the spectra. This excitonic peak remains much weaker than that of the EHL, which shows that a smaller number of excitons than the total number of electron-hole pairs in the liquid, as well as of a partial phase separation between the EHL and free excitons. This is unmistakable evidence for the formation of a cold EHL nucleating directly from a hot electron-hole plasma.

3.2.12. DEG and 2DHG

In section 2.2.7 the FES was shown to manifest itself as an enhancement in the PL intensity at the Fermi energy. Richards et al. [268] showed that this enhancement was more pronounced for excitation at higher energies. Their examination of the time evolution of the 2DHG associated emission

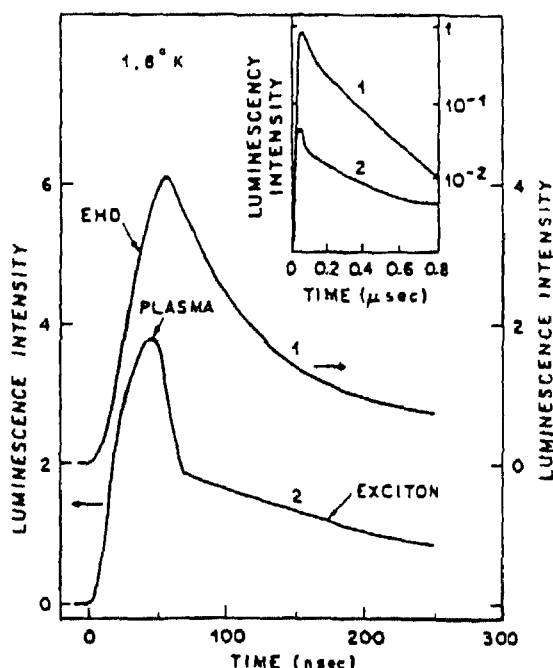


Fig. 348 PL decay kinetics of Si EHL emission (at 1.080 eV and 1.097 eV for curves 1 and 2, respectively) after excitation by a 15 ns laser pulse

in their modulation-doped heterostructures also exhibited this dependence. They find that the spectral evolution of the 2DHG emission is associated with the temporal change in the density of photogenerated carriers due to recombination. Fig. 349 shows the temporal evolution of the emission after excitation at 3.07 eV. At early times the lineshape attests to the hot distribution of carriers. After thermalization ($t > 200$ ps) a FES becomes evident on the high-energy side of the emission, just as was observed in the cw luminescence spectrum. The decay lifetime of the FES is approximately 300 ps. At still later times the spectral shape of the emission is invariant with time. In the next section the kinetics of the EHP and dynamical bandgap renormalization are discussed and the reader is referred there for additional details regarding the kinetics of the 2DEG or 2DHG.

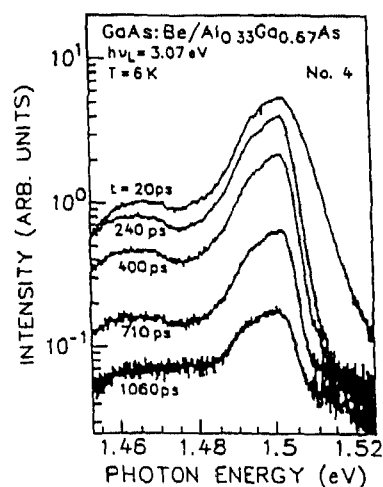


Fig. 349. Time-resolved PL spectra for sample doped p-type to $3.1 \times 10^{13} \text{ cm}^{-2}$ after excitation at 3.07 eV [268].

3.2.13. Electron-hole plasma

Göbel et al. [248] measured the kinetics of the electron-hole plasma (EHP) in bulk GaAs. Fig. 350 shows the PL kinetics of the EHP at various emission energies, and the circles represent fits to the PL decays with a bimolecular recombination coefficient of $5 \times 10^{-8} \text{ cm}^3 \text{ s}^{-1}$. Within the spectral bandwidth of the EHP emission (lower two traces), the kinetics are virtually identical, supporting the interpretation of the low energy portion of the EHP emission as a plasmon sideband. Near the band edge (upper traces), the onset of excitonic emission is evident. At early times excitons are screened out by the free carriers. As the density of free carriers decreases due to recombination and transport (see section 4), this screening of the Coulomb interaction is reduced and excitons begin to form in about 200–300 ps. Thus, the build-up in the emission intensity at late times is a result of exciton formation and radiative decay, and is indicative of the dynamic Mott transition. Tanaka et al. [249] investigated the possible formation of an electron-hole liquid from the EHP. Fig. 351 shows the time-dependent changes in the high-energy edge (HEE) and the low-energy edge (LEE) of the EHP time-resolved spectra all versus excitation power density. (The spectra are almost independent of excitation density.) In the first 150 ps, the HEE shifts to lower energy, indicating that the carrier temperature is cooling rapidly. The LEE shifts to slightly higher energy with increasing time, and this is attributed to the density dependence of the bandgap renormalization which should decrease (increase in energy) as the density decreases due to radiative recombination. Derived carrier temperatures and densities after a time delay of 200 ps are 50 K and $2 \times 10^{17} \text{ cm}^{-3}$, which implies that EHL formation is highly improbable.

The time dependence of the bandgap renormalization mentioned above has been quantified by Cingolani et al. [516]. They find that the initial peak position of the EHP is excitation density dependent, and that this emission blue-shifts with increasing time until it eventually merges and is masked by the excitonic luminescence. Fig. 352 shows the time dependence of the peak energy of the EHP emission for various excitation densities. The dashed curves represent a $e^{-t/\tau}$ dependence, consistent with the expected $[n(t)]^{1/3}$ dependence of the bandgap renormalization $[n(t) \sim e^{-t/\tau}]$ and therefore $\Delta E \sim$

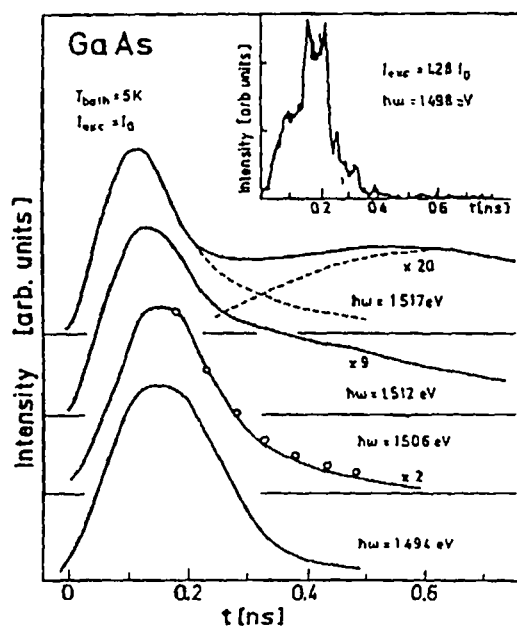


Fig. 350. PL kinetics of the electron-hole plasma in bulk GaAs at different emission energies (After Göbel et al. [248])

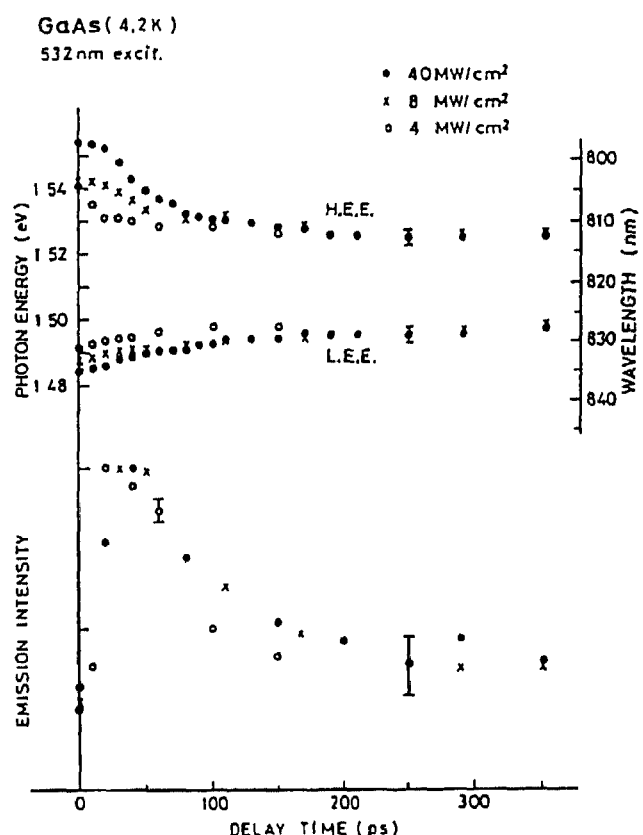


Fig. 351. Time dependence of the high-energy edge (HEE) and low-energy edge (LEE), and emission intensity of the electron-hole plasma in bulk GaAs (Reprinted from Tanaka et al., *Solid State Commun.*, 33 (1980) 167, with kind permission from Elsevier Science Ltd., The Boulevard, Langford Lane, Kidlington OX5 1GB, UK.)

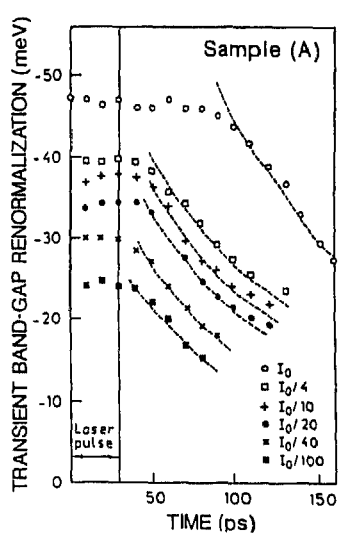


Fig. 352. Intensity dependence of the bandgap renormalization versus time in GaAs quantum wells. The dashed curves are functions of the form $e^{-t/\tau}$. (After Cingolani et al. [516].)

$(e^{-t/\tau})^{-1/3}$. At the highest excitation densities, the expected temporal behavior of the bandgap renormalization is delayed by several tens of picoseconds, and this delay increases with increasing excitation density. This may arise from difficulties in determining the peak energy of the EHP emission since the bulk GaAs buffer layer is in this spectral region.

3.2.14. Localization and spectral migration

There are many examples of carrier localization in semiconductors, but perhaps none is as important as that of localized carriers in quantum wells. Christen et al. [438] and Göbel et al. [439] found that this carrier localization at well-width fluctuations is manifested by an enhancement in the recombination rate of these carriers. This enhancement causes the otherwise impurity-dominated recombination to be relatively fast and strong. Göbel et al. [439] find that the quantum well lifetime decreases from 1 ns for a 140 Å well to 350 ps for a 50 Å well. These numbers were derived from coupled rate equation fits to the barrier and well luminescence for these samples, as shown in Fig. 353. The decrease in lifetime corresponds to a shrinkage of the Bohr radius by a factor of 1.7, which then increases the recombination probability due to the increased overlap of electron and hole wavefunctions. Christen et al. observed similar phenomena in their quantum well structures. In addition, they observed that the enhanced radiative recombination rate in the narrower quantum wells suppressed the capture of free carriers by traps. Lastly, they found that the enhancement factor is unchanged at room temperature, i.e. the ratio of the observed lifetimes in two quantum well samples of different thicknesses (here 52 Å and 113 Å) is unchanged between room temperature and 5 K.

In section 2.3.3.3 it was shown that the presence of a Stoke's shift between the luminescence and absorption spectra in a quantum well sample was indicative of inhomogeneous broadening and localization. This localization and the spectral migration of carriers within the inhomogeneously broadened lineshape to lower energy states has been examined by several researchers. Brener et al. [36] examined the LO-phonon sidebands of the free exciton as a means of quantifying the in-plane localization in $\text{GaAs}/\text{Al}_x\text{Ga}_{1-x}\text{As}$ quantum wells. Localization destroys the translational symmetry in a crystal, thereby relaxing k conservation. Hopfield [517] has shown that optical transitions with well-defined momentum have negligible phonon-sideband emissions. On the other hand, localized states are spread out in k space and therefore k conservation is relaxed, allowing phonon-sideband emission. The spectral

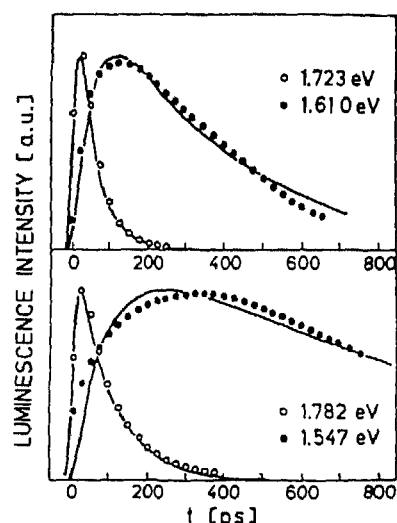


Fig. 353. PL decay kinetics of the AlGaAs (○) and quantum well PL (●) for two different quantum well samples, a double quantum well sample with 14 nm wells and 8 nm barrier and a 5 nm single quantum well sample. (After Göbel et al. [439].)

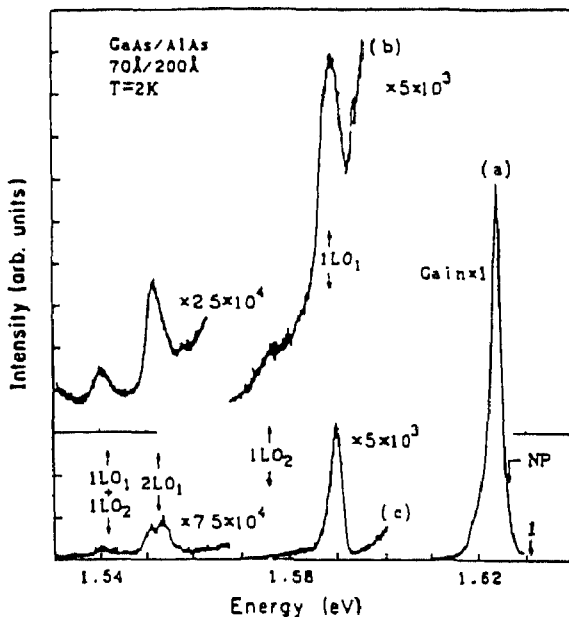


Fig. 354. PL spectra of GaAs quantum well (70 Å well width) after laser excitation at 1.632 eV. (a) Spectrum of no-phonon band, (b) and (c) time-resolved spectra at 300 ps and 3.8 ns after the laser pulse, respectively. (After Brener et al. [36].)

width of these phonon sidebands will be large since the Fröhlich interaction varies inversely with k , and is only strong for $k < 10^6 \text{ cm}^{-1}$ which is a narrow region of the LO-phonon dispersion curve. Eq. (16) shows the relative intensity of the phonon sidebands may be quantified by the Huang-Rhys factor, S . S is a measure of the coupling strength of the radiative transition to the LO-phonon field, and is given by

$$S = \frac{1}{2\hbar\omega_{\text{LO}}^3} \sum_p |D_q|^2 \quad (63)$$

where D_q is proportional to the q th Fourier transform coefficient of the electron distribution, and is therefore related to the localization. The presence of large q components will yield a large phonon-coupling strength, S , and concomitantly stronger phonon sideband emissions. Localized wavefunctions will contain large q components, and thus relatively strong phonon sidebands. Brener et al. [36] found the existence of three different types of localized electron-hole pairs: (1) weakly localized excitons which do not exhibit any phonon sidebands, (2) tightly localized excitons which show strong phonon sidebands, and (3) electrons and holes which are localized at different spatial sites which also show strong phonon sidebands. Fig. 354 shows the PL spectra of their 70 Å GaAs/AlAs quantum well sample at various times after the laser excitation pulse. The LO-phonon sidebands correspond to AlAs LO-phonons. The kinetics of the phonon sidebands are not identical to that of the no-phonon line. Part c shows that the phonon-sideband emission at times longer than the radiative decay of the no-phonon excitonic emission, and the peak energies are blue-shifted by ~ 2 meV from their early time energies. Thus, at late times the phonon sidebands evident in the spectra are not associated with the no-phonon exciton emission. Brener et al. compared the relative intensities of two phonon sidebands at various times after the laser pulse, and obtained Huang-Rhys factors of $S_f = 0.4$ and $S_s = 0.1$ for the fast and slow components of the phonon-sideband decays, respectively. Extending this to the phonon sideband to no-phonon emission ratio yields a ratio of 2.5, whereas the observed ratio is 10^4 , implying that most excitons do not contribute to the early-time phonon-sideband emission. At times longer than the

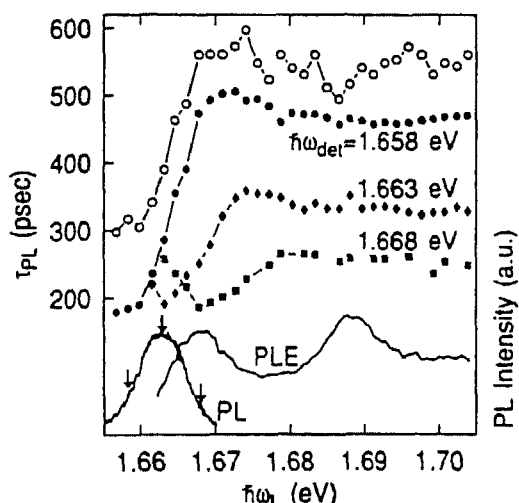


Fig. 355. PL rise time (\circ) and decay time (\bullet) versus excitation energy. The sample is a GaAs quantum well with no growth interrupts. Also shown are the PL and PLE spectra of the sample taken at 18 K (After Zachau et al [518].)

exciton lifetime, the observed phonon sidebands cannot be related to excitons, and must be related to electron–hole pairs. These electrons and holes may become localized at different sites in the crystal, and the distribution of separations would yield non-exponential kinetics, as observed. This is similar to DAP recombination. At these late times the Huang–Rhys factor of 0.1 corresponds to a localization size of $\sim 20 \text{ \AA}$ for either electrons or holes. The nature of these localizing centers is not known, but is certainly not associated with donors or acceptors, and may be associated with a shallow bound state related to a deep isoelectronic trap.

The mechanisms of localization subsequent to non-resonant excitation were examined by Zachau et al. [518]. They measured the PL decay and rise times as a function of excitation energy with 25 \AA wells, and their results are shown in Fig. 355. They find that the PL lifetime is shortest for near-resonant excitation, and the PL lifetime increases with increasing excitation energy until a saturation in lifetime is reached. The longest PL lifetimes at high excitation energies are observed for detection on the low-energy edge of the emission spectrum. The variation in the PL lifetimes observed here are due to the drift-diffusion times rather than variations in the radiative decay time. The increase in PL lifetime with decreasing emission energy results from the increasing distance and time the excitons must drift to a site which yields the same recombination energy as that detected. Further, the shorter lifetimes on the high-energy side of the PL compared to the low-energy side are due to the spectral diffusion of these excitons within the inhomogeneously broadened line to lower energy sites. The increase in rise time of the PL with excitation energy is not due to kinetic energy relaxation since the rise time also increases with increasing temperature. The exciton may lose all of its kinetic energy and still have excess potential energy due to inhomogeneities in the quantum well. The drift diffusion of the excitons will then eventually find the excitons in the low-energy localized sites. This is the essence of spectral diffusion.

3.2.15. Spin relaxation

Optical selection rules compel the consideration of spin as an important quantity in luminescence measurements. In GaAs the conduction band edge has a symmetry of $S = 1/2$, whereas the valence band has a symmetry of $S = 3/2$. Emitted light then couples these spin states with angular momentum

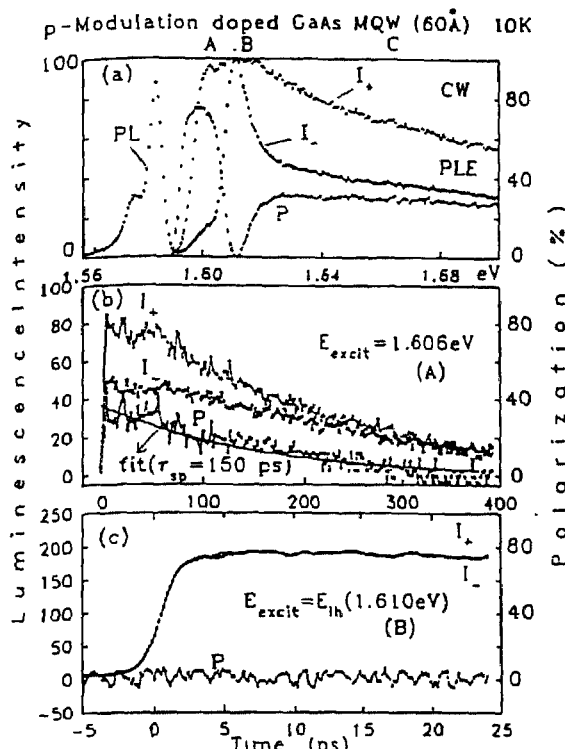


Fig. 356. (a) cw PL, PLE, and polarized (P) spectra, (b) I^+ , I^- , and P versus time for excitation at A, and (c) I^+ , I^- , and P versus time for excitation at B, all for a p-type modulation-doped sample (After Damen et al. [522].)

of +1 ($\sigma+$) or -1 ($\sigma-$). The luminescence intensities of the emitted light in each of these polarizations is then dependent upon the initial spin populations and the spin relaxation processes. Time-resolved polarization measurements are therefore useful in quantifying spin relaxation times and mechanisms. For a general review of spin relaxation in semiconductor quantum wells see the article by Sham [519].

Seymour and Alfano [520] measured the polarization-resolved kinetics of the luminescence from a bulk GaAs sample at 77 K using a Streak camera. They used both right and left circularly polarized excitation and detected both right and left circularly polarized luminescence. From their data they deduce a spin relaxation time of 44 ± 17 ps. They attribute this relaxation time to electron-hole exchange interaction. Zerrouati et al. [521] utilized the Hanle effect (section 2.4.2) to determine the spin relaxation time of photoexcited electrons in p-type GaAs as a function of p-type doping. They find the spin relaxation time are consistent with the Bir, Aronov, and Pikus theory of electron scattering with holes, with an exchange splitting of 0.12 meV, and relaxation times of several hundred picoseconds. Moreover, the strong band mixing between heavy- and light-hole bands in bulk GaAs together with the spin-orbit interaction causes, what is assumed to be, an instantaneous depolarization of the hole [519].

Damen et al. [522] measured the excitation polarization dependence of the luminescence from GaAs quantum wells versus time using their luminescence upconversion technique. Fig. 356 shows the PL, PLE, and luminescence polarization, P , together with the time-evolutions of the I^+ , I^- , and net polarization after excitation at 1.606 and 1.610 eV of their p-type modulation-doped sample. Note that there is no net polarization at any time for excitation at 1.610 eV since there is an almost equal population of spin $+1/2$ and $-1/2$ electrons due to absorption by both heavy and light holes. However,

for excitation at 1.606 eV, the peak of the heavy-hole absorption, the polarization decays with a lifetime of 150 ps, indicative of electron-spin relaxation. This is three times faster than for bulk GaAs. Damen et al. [522] repeated these measurements for an n-type modulation-doped sample. For photoexcitation at 1.645 eV, photoexcited electrons are close to the Fermi energy, and the observed polarization decay lifetime is ~ 4 ps, whereas for excitation at 1.7 eV, excitation from both heavy- and light-hole bands, there is an additional ~ 200 ps slow component. They attribute this fast relaxation component to the spin relaxation of holes (4 ps) which is not instantaneous in contrast to the bulk case. Their results show that the electron spin relaxation time decreases from 150 to 50 ps as the excitation intensity is decreased. In total, they find that the spin relaxation of holes is slower in 2D than in bulk, and is faster in 2D than in bulk for electrons.

3.3. Characterization of structures

Time-resolved photoluminescence measurements are also useful for characterizing and quantifying some of the basic optical, electronic, and structural properties of semiconductors. Information regarding defects at interfaces, surfaces, and in the bulk of a structure may be readily obtained from such measurements. Details regarding the distribution of excitons within the inhomogeneous structure of a nanostructure is also obtainable. Also, in section 3.2.8 it was shown how the bulk and surface recombination may be quantified through PL time-decay measurements.

3.3.1. Heterostructures

The kinetics of carriers in GaAs/AlGaAs heterostructures may be significantly influenced by the geometry and perfection of the heterostructure itself. In section 3.2.8 the issue of non-radiative decay at surfaces and interfaces was discussed, and it was shown that high-quality AlGaAs cladding layers may be beneficial to the carrier kinetics by reducing, if not eliminating, this deleterious non-radiative decay. In section 2.3.2 the steady-state properties of photoexcited carriers which have drifted and/or diffused next to the heterointerfaces was shown to be strongly influenced by those interfaces. Here, the transient properties of photoexcited carriers which reside next to heterointerfaces will be presented. Gilliland et al. [390–392] examined the kinetics of H-band emission in symmetric, undoped $\text{Al}_{0.3}\text{Ga}_{0.7}\text{As}$ (p)/GaAs (n)/ $\text{Al}_{0.3}\text{Ga}_{0.7}\text{As}$ (p) heterostructures versus GaAs layer thickness. The heterointerfacial related emission in these structures has been thoroughly studied in terms of its cw properties, and has been termed the H-band. Gilliland et al. showed that in their undoped structures, in contrast to the doped structures of Yuan et al. [281], that the mechanism responsible for the H-band emission is the recombination of quasi-two-dimensional excitons, and is not due to either the recombination of carriers bound at impurities and/or defects, or the recombination of 2D carriers with 3D free carriers, as was the case for the structures studied by Yuan et al. The study of Gilliland et al. consisted of time-resolved measurements of the H-band emission versus GaAs layer thickness. They find that the H-band emission is not spectrally stationary, but instead shifts to lower energy (red-shift) with increasing time after the excitation pulse. Fig. 357 shows the PL decay lifetimes derived from the exponential tails of the non-exponential decays versus detection energy for samples with GaAs layer thicknesses ranging from 300 Å to 2.0 μm . Generally, they find that lifetimes increase exponentially with decreasing emission energy, and range from several ns to 50 μs . H-band kinetics are identical for all structures with GaAs layer thicknesses greater than 0.5 μm , whereas for thinner structures the lifetime tends to saturate at shorter lifetimes with decreasing thickness for decreasing emission energies. Thus, the H-band kinetics are intimately connected with the geometry of the structure. Furthermore, they found that structures which have a larger interfacial recombination velocity, and are otherwise

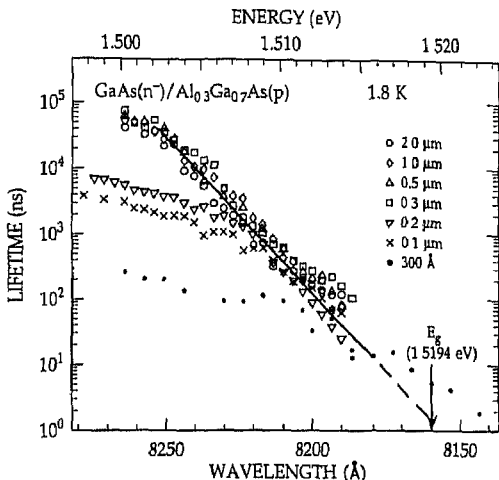


Fig. 357 Measured long-time PL lifetimes versus emission energy across the H-band for a variety of GaAs/AlGaAs double heterostructures with different GaAs layer thicknesses (After Gilliland et al [390].)

identical, yield drastically shorter non-exponential H-band kinetics and corresponding lifetimes. At the same time the PL emission of the H-band in both structures is virtually identical. Hence, H-band kinetics in optically- and electronically-inferior samples (as determined here by the interfacial recombination velocity) are not indicative of an intrinsic decay process, but instead are indicative of extrinsic non-radiative decay processes. This demonstrates the sensitivity of these quasi-2D excitons to the heterointerfacial quality. Gilliland et al. modeled their results in terms of excitons quantum-mechanically bound at the potential notch at the heterointerfaces formed by the bandbending. Their model parameterized the dynamical bandbending of the structure which is caused by the time-dependent screening of the built-in heterointerfacial electric field (the time dependence arises from the time-dependent carrier density which is a result of recombination). They find that this simple model accurately reproduces the kinetics observed in Fig. 357, specifically, the saturation in lifetime at low energies for thin structures. This model therefore demonstrates that this saturation is caused by the "sharing" of these quasi-2D interfacial excitons by both interfaces. The kinetics and time-dependent red-shift observed for H-band emission are then completely analogous to the QCSE, except that the field is built-in and is screened by the carriers themselves.

3.3.2. Quantum wells and superlattices

Defects incorporated at the interfaces in quantum wells may be characterized by their effects on the carrier recombination properties. Köhrbrück et al. [170] examined the effects of growth interrupts at both the normal and inverted interfaces in GaAs/AlGaAs quantum wells. Fig. 358 shows the PL time decays for samples grown with interrupts of 10, 100, and 300 s at either the normal (GRI-G) or inverted interfaces (GRI-A). Increasing growth interrupt time clearly causes an increase in the decay rate for growth interrupts at the inverted interfaces, whereas results for the normal interfaces do not yield any significant increase in non-radiative trap incorporation at the interfaces. Gérard et al. [523] have further clarified the non-radiative decay at the normal versus inverted interfaces through time-resolved studies of special quantum wells. Their quantum wells were grown with a single InAs monolayer quantum well inserted at various positions within the GaAs/AlGaAs quantum well. The InAs quantum well was placed at positions ranging from near the inverted interface to positions near the normal interface. Fig. 359 shows the non-radiative decay rate determined from their PL time decay

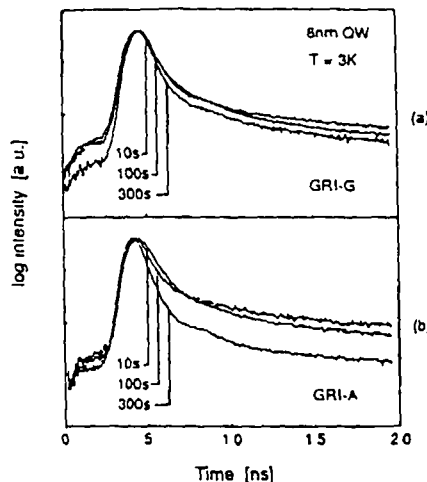


Fig. 358 Time-resolved PL spectra of an 80 Å quantum well for samples with (a) growth interrupts at the GaAs surface, and (b) growth interrupts at the AlGaAs surface with interrupt times as shown (After Köhrbrück et al [170].)

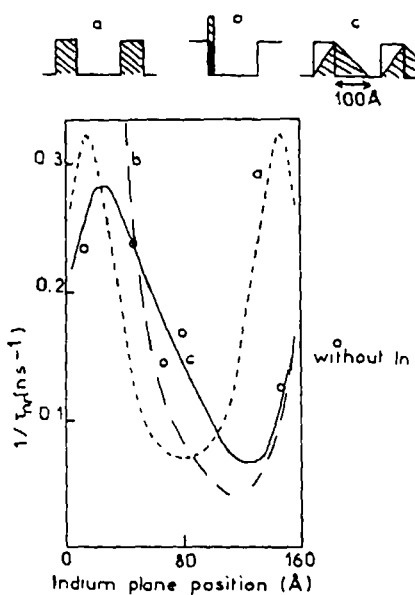


Fig. 359. Non-radiative decay rate versus In plane position. Theoretical curves correspond to three different distributions of non-radiative centers, as shown. (After Gérard et al. [523])

measurements versus position of the InAs quantum well within the 160 Å GaAs/AlGaAs quantum well. The non-radiative decay rate near the inverted interface (4 ns^{-1}) is clearly larger than that for the InAs quantum well near the normal interface (8 ns^{-1}). The lines represent fits to the data assuming distributions of non-radiative centers sketched in the upper part of the figure. The asymmetric results indicate that the non-radiative defect profile must be similar to that in sketch c.

Deveaud and coworkers [524,525], Fujiwara et al. [526], and Kohl et al. [292] used time-resolved PL measurements to quantify the structural aspects of their quantum wells. Fig. 360 shows the PL spectra of a 25 Å wide GaAs/AlGaAs quantum well at three different delay times after the excitation pulse [524,525]. The two peaks in the spectra at 1.695 and 1.682 eV correspond to excitonic recombination in ten- and eleven-monolayer wide islands of the quantum well, respectively. With

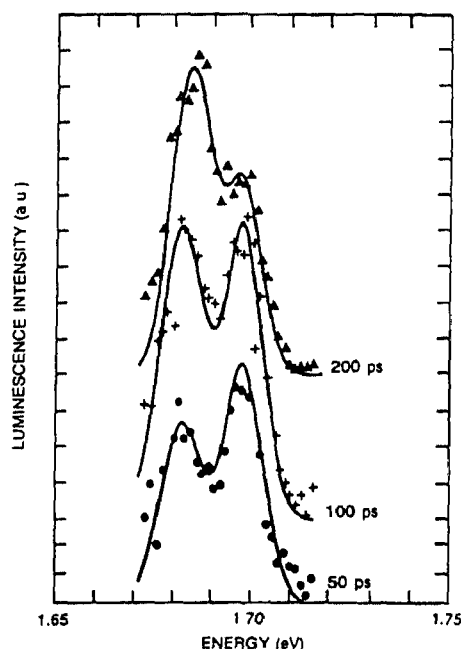


Fig. 360. Time-resolved PL spectra at time delays of 50, 100, and 200 ps. Sample is a 25 Å quantum well (After Deveaud et al. [524])

increasing time, the higher-energy emission decreases in intensity relative to the lower-energy emission. This physically corresponds to exciton transfer from the narrow islands to the wide islands. Assuming an exciton mobility of $1500 \text{ cm}^2 \text{ V}^{-1} \text{ s}^{-1}$, the excitons will then diffuse over a distance of approximately 2000 Å. Comparison of the time for transfer to the wider islands (250 ps) yields a typical island size of 0.6 to 1.5 μm. Fujiwara et al. [526] found that the decay kinetics in their quantum well sample exhibited two-exponential decays. They also modeled their kinetics in terms of inter- and intra-growth-island exciton transfer. Kohl et al. [292] further examined the inter-island exciton transfer in GaAs quantum wells, and found that the time-dependent measurements accurately yielded the area ratios of the islands only when all island regions were populated with the same exciton density. This is due to the different relaxation processes which occur at different excitation energies.

3.3.3. Quantum well wires

The effect of non-radiative recombination at the surfaces of quantum well wires laterally structured by high-resolution electron beam lithography and reactive ion etching is readily discernible through time-resolved PL measurements [527]. Fig. 361 shows the PL time decays for quantum well wires with lateral widths from 0.5 to 5.0 μm. The PL lifetime is 670 ps for the 5.0 μm wires and decreases to a resolution-limited 100 ps for the 0.5 μm wires. This, together with the observed quenching of the PL emission with decreasing wire width, is a strong indication of non-radiative surface recombination. As discussed in section 3.2.8 the phenomenological concept of a surface recombination velocity in quantum structures is not meaningful, and instead, this non-radiative decay should be treated in terms of non-radiative decay at deep-level surface/interface states. Nevertheless, Mayer et al. [527] derived the surface recombination velocity for their quantum well wire structures from the lateral width dependence of the PL kinetics. They find a surface recombination velocity of $2.6 \times 10^5 \text{ cm s}^{-1}$, which is consistent with room-temperature surface recombination velocities of free GaAs surfaces.

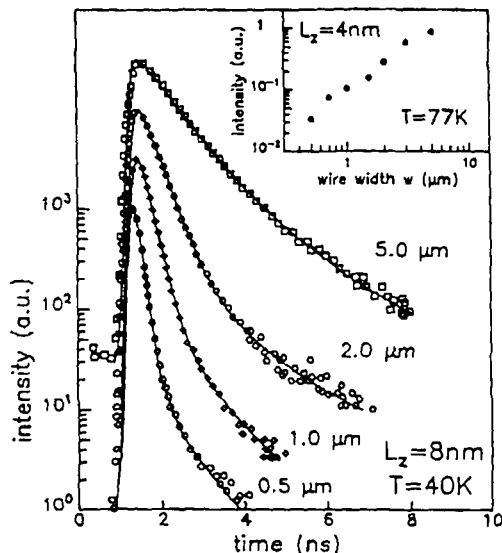


Fig. 361 PL time decays at 40 K of GaAs quantum wires of different lateral width ——, biexponential fits to the data. Inset shows the wire-width dependence of the luminescence intensity. (After Mayer et al [527])

3.4. Additional perturbations

The perturbations considered in section 2.4 are also useful in elucidating electronic structure, kinetics, and dynamics when coupled with time-resolved PL measurements. These perturbations may alter, in a controllable fashion, for example, the electronic structure, the wavefunction, the crystal symmetry, the Fermi level, and the Bohr radii of carriers. In this section the effects of these four perturbations on the kinetics of PL recombination in semiconductors will be examined.

3.4.1. High pressure

Very little work has been done which combines the techniques of high-pressure and time-resolved spectroscopy. Nonetheless, these two techniques, when combined, provide a powerful means for examining the electronic structure of semiconductors. PL kinetics are especially sensitive to inter-level mixing between different conduction band states, even more so than is the PL spectrum which is indicative of the eigenvalue of the system. Mariette et al. [528] and Wolford [361] have examined the PL kinetics of donor-bound excitons in GaAs under pressure. As shown in section 2.4.1 these researchers have measured the pressure-dependent PL spectra of high-purity GaAs in the vicinity of the edge-bound excitons, specifically the donor-bound excitons. They have also measured the PL kinetics of the emissions associated with these same bound excitons for both direct and indirect shallow-bound excitons, i.e. for pressures both above and below the direct-indirect Γ -X crossover (41.3 kbar). They find that the direct donor-bound excitons exhibit lifetimes that are uniformly fast (1 ns) over the entire direct-gap pressure range, and indirect donor-bound excitons show lifetimes which increase monotonically to ~ 100 ns for pressures beyond the Γ -X crossover. Fig. 362 shows PL decay kinetics, at 8 K, of excitons bound to donors in high-purity ($2 \times 10^{14} \text{ cm}^{-3}$) GaAs at pressures of 21 kbar (below the Γ -X crossover), 41.4 kbar (at the Γ -X crossover), and pressures from 53 to 73 kbar (above the Γ -X crossover). All PL decays were recorded at the peak of the emission line, and all kinetics were exponential. Fig. 363 summarizes the lifetimes deduced from the kinetics for both (D_{Γ}^+, X) and (D_X^0, X) bound excitons. For pressures below the Γ -X crossover all lifetimes are short

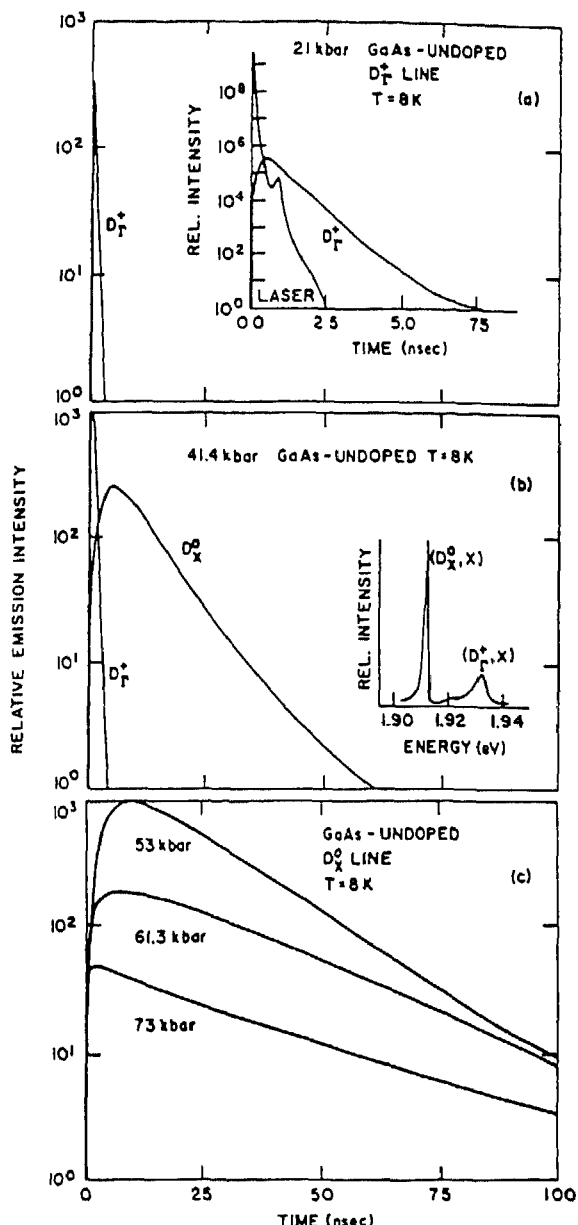


Fig. 362. PL decay kinetics of excitons bound to residual donors versus hydrostatic pressure at 8 K. (a) Kinetics for direct-gap bandstructure, (b) near the G-X crossover where both fast (D_T^+, X) and slower (D_X^0, X) exciton emissions are observable, and indirect gaps where only the slower (D_X^0, X) transitions are present. (After Mariette et al [528].)

(< 1 ns), and at pressures corresponding to the indirect-gap bandstructure, the lifetimes become much longer. At crossover, emission from both direct and indirect donor-bound excitons is observed simultaneously, and the PL kinetics (Fig. 363(b)) are indicative of the direct versus indirect nature of the transition (short versus long lifetimes, respectively). In our discussion of bound exciton lifetimes in Si (section 3.2.3.1.2 section 3.2.4) it was shown that a non-radiative Auger decay process is believed to govern the observed PL kinetics. This may also be true for bound excitons in GaAs for pressures at which the GaAs bandstructure is indirect. Hence, the observed decay rate should actually represent the sum of the radiative and Auger decay rates. However, Mariette et al. conclude that the increase in

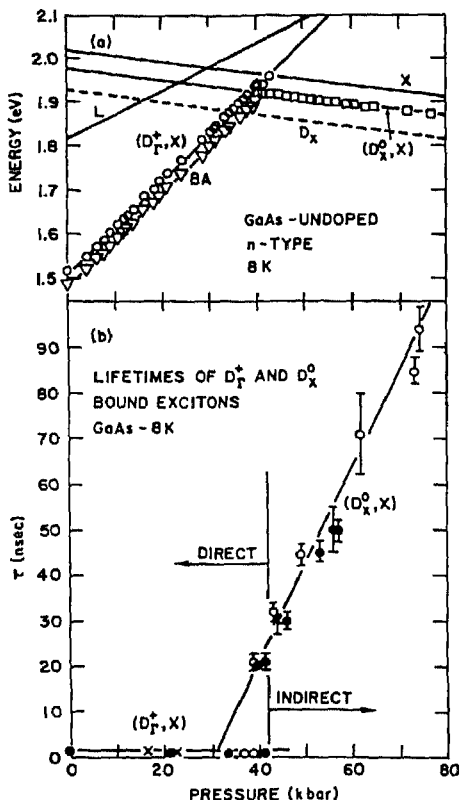


Fig. 363. 8 K PL transition energies and lifetimes versus pressure for donor bound excitons in GaAs. (After Mariette et al. [528].)

lifetime of 2.2 ns kbar^{-1} above the Γ -X crossover is not a result of pressure-dependent Auger recombination—generally, Auger lifetimes for shallow states are expected to decrease as bandgap decreases, as is the case for the X conduction band edge in GaAs with increasing pressure. As an explanation, they therefore resort to a pressure dependence of the oscillator strength which must be due to a pressure-dependent mixing between the Γ and X conduction band states. The increase in lifetime and corresponding decrease in oscillator strength is indicative of the diminished mixing of the zone-center ($k=0$) amplitude admixed into the electron portion of the wavefunction for the indirect donor-bound exciton. Thus, the pressure dependence of the PL kinetics for these bound excitons is a result of the band-structure enhancement of the oscillator strength.

Wolford et al. [305] and Spain et al. [365] have also measured the PL kinetics of GaAs/Al_xGa_{1-x}As quantum wells and superlattices under pressure. Wolford et al. examined both the direct and indirect transitions in their MOCVD-grown multiple quantum wells, whereas Spain et al. measured the PL kinetics of the indirect transitions in short-period GaAs/AlAs superlattices which are near the type I to type II transition at zero pressure. Wolford et al. find that the direct $\Gamma_{\text{te}}-\Gamma_{\text{lhh}}$ transition kinetics at 1.8 K are exponential with a lifetime of $\sim 300 \text{ ps}$, consistent with a dipole-allowed transition. In contrast, the $\text{X}_e-\Gamma_{\text{lhh}}$ transition is doubly forbidden, and is found to exhibit long PL lifetimes. Fig. 364 shows the monotonic increase in lifetime for this indirect transition versus pressure, increasing from a sub- μs decay just above crossover (29.5 kbar) to over 20 μs near 43 kbar. Spain et al. [365] observed a similar increase in lifetime with pressure for several different samples. (The data in this figure for the (11,8) superlattices was shifted horizontally by 1.5 kbar to overlap that of the (12,8) superlattice.) Spain et al., like Wolford et al., attribute the rapid change in lifetime with pressure as

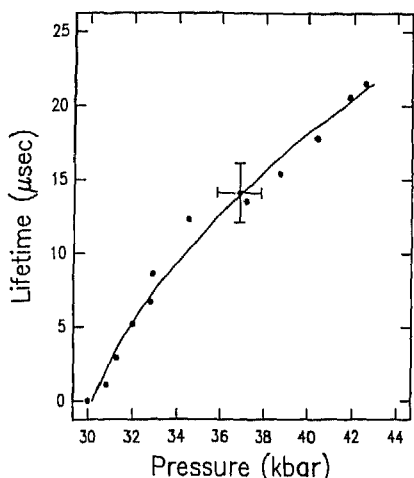


Fig. 364 2 K pressure dependence of the PL lifetimes of the X-G_{1m} transition in a GaAs/Al_{0.24}Ga_{0.76}As superlattice with 70 Å wells and barriers. Type I to type II crossover occurs at 29.5 kbar. (After Wolford et al. [305].)

due to Γ -X mixing. They model their kinetics with first-order perturbation theory which predicts a quadratic pressure dependence of the lifetime. The saturation in lifetime at high pressures for the samples grown at low temperatures is indicative of non-radiative decay. Inclusion of this decay mechanism, phenomenologically, yields non-radiative decay rates of 22 and 40 μs for the structures grown at 620 °C and 650 °C, respectively. This is consistent with their findings of weaker defect-related emissions in the sample grown at 650 °C. These results demonstrate the importance of non-radiative decay channels in GaAs/AlAs superlattices.

3.4.2. Magnetic field

In addition to the standard applications of time-resolved spectroscopy, time-resolved measurements of recombination processes in the presence of a magnetic field are useful for examining many phenomena, including the properties of semiconductors in the quantum Hall regime and even the Wigner solid regime, and for elucidating quantum beats of electron Larmor precession, etc.

Quantum beats are the temporal modulation of the signal observed in an experiment which arises from the interference between quantum states. Measurements of the temporal period of these beats allows high-resolution determination of energy splittings between quantum states in a system which may be induced by a magnetic field. The damping of these quantum beats in time most commonly occurs through the dephasing of the coherently prepared ensemble of carriers (it is this coherence which allows the interference between quantum states). Similarly, Heberle et al. [529] have observed quantum beats from free excitons in GaAs quantum wells which persist for times much longer than the dephasing time. Their sample was a multiple quantum well with 25 nm GaAs wells. The emission from this sample exhibits, at low excitation densities, a linewidth of 0.3 meV which is comparable to the homogeneous linewidth of 0.18 meV. Their time-resolved magneto-optical measurements were performed in the Voigt configuration, and detected with 10 ps resolution by a Streak camera. Fig. 365 shows the polarized luminescence decays at 0 and 2 Tesla; here I_+ corresponds to the same polarization for the luminescence and reflected laser beam, whereas I_- corresponds to opposite polarization. The magnetic field causes pronounced oscillations to appear in the emission kinetics. Furthermore, there is a phase shift between the I_+ and I_- emissions. Note that the oscillations persist for very long times compared to the dephasing time of 7 ps. The origin of these oscillations, or quantum beats, is the

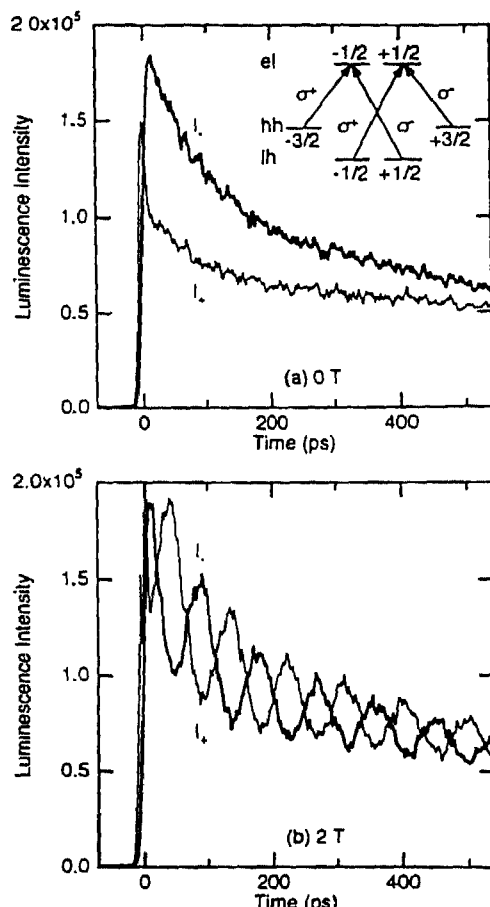


Fig. 365. PL time decays at (a) 0 T and (b) 2 T. Excitation was circularly polarized at the light-hole exciton. I^+ (I^-) correspond to the luminescence with the same (opposite) circular polarization as the excitation laser (After Heberle et al [529].)

Larmor precession of the electron spins around the axis of the magnetic field, which thereby modulates the polarization of the luminescence. These results allow for an accurate determination of the Landé g factor since the Larmor frequency is given by

$$\omega_L = \frac{g\mu_B B}{\hbar} \quad (64)$$

Thus, the oscillations are quantum beats between spin-split levels which are separated by an energy difference $\hbar\omega_L$. Interestingly, they find that these oscillations are still present for non-resonant excitation, even up to 25 meV into the heavy-hole continuum, and for high excitation densities (10^{12} cm^{-2}). Thus, carrier cooling does not appear to alter the spin phase memory. As expected the oscillation period is a strong function of the applied magnetic field, decreasing linearly with increasing field. The electron g -factor deduced from these measurements is -0.39 for fields below 3 T. The difference between this value and that for bulk GaAs (-0.44) is due to non-parabolicity in the conduction band. The independence of this g -factor on excitation density implies that this is not an excitonic g -value, but is instead a free-electron g -value. Thus, the electron spin to magnetic-field coupling is stronger than that between the electron and hole spin. The longitudinal spin relaxation time determined from these measurements is 500 ps. Note that the oscillations observed here are not, strictly speaking, due to a polarization interference, but are quantum mechanical in nature.

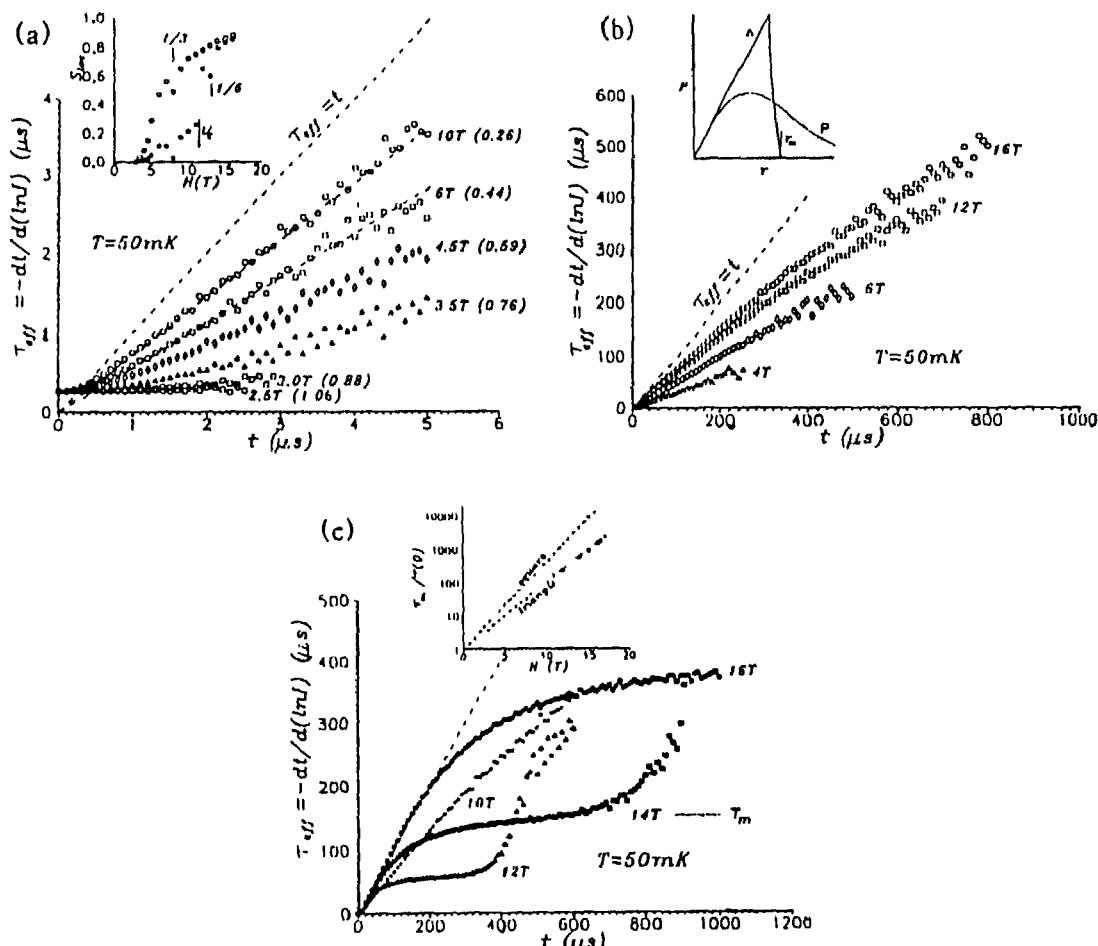


Fig. 366. Time dependence of the instantaneous recombination time t_{eff} at different magnetic fields for (a), (b) low-mobility samples, and (c) a high-mobility sample. Inset (a) portion of localized electrons (S_{loc}) measured for low-mobility samples (open symbols) and high-mobility samples (closed symbols); (b) distribution function, $P(r)$, of distances between electrons and holes for various electronic configurations (P , Poisson distribution; Δ , triangular distribution), (c) measured and calculated field dependence of τ_m for (1) triangular and (2) square lattices (After Kukushkin et al. [530].)

Kukushkin et al. [530] used time-resolved PL spectroscopy to probe the local spatial structure of the electronic system of a high-mobility modulation-doped sample. At low lattice temperatures (mK) and high magnetic fields they access the Wigner solid regime, and established that the local spatial configuration of electrons is consistent with a triangular lattice. They used the kinetics of recombination of the 2D electrons with an acceptor-bound photoexcited hole to probe the local spatial structure. Since the recombination probability, and hence, rate, depends on the spatial overlap integral of the 2D electron wavefunction with that of the localized, bound hole, the observed recombination rate will be sensitive to the short-range configuration of electrons. They measured the recombination time versus magnetic field, thereby varying the filling factor, $\nu \leq 1$. Fig. 366 shows the effective recombination time ($\tau_{\text{eff}} = -[d\ln I(t)/dt]^{-1}$) versus time for (a), (b) a low-mobility sample, and (c) a high-mobility sample. They use this effective recombination time to arrive at power-law exponents. For a Poisson distribution of localization centers for electrons the recombination takes a power-law form $I(t) = I_0(\nu t_0/t)^{1+\nu}$ where ν is the filling factor. At $\nu = 1$, the electron distribution is homogeneous, and all hole positions are equivalent, thereby yielding an exponential decay. At other

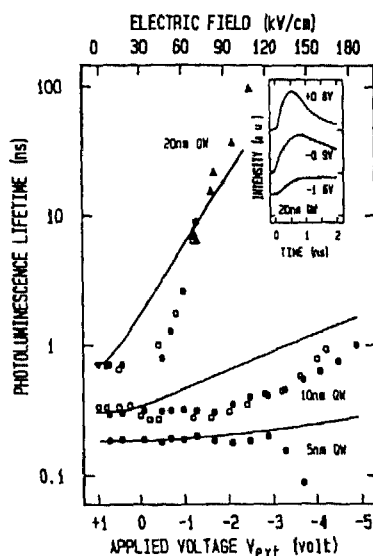


Fig. 367 Electric field dependence of the PL lifetime for three quantum wells with well widths shown. (After Polland et al. [395].)

filling factors, the distribution is not homogeneous, and therefore the decays are non-exponential. This figure shows that $\tau_{\text{eff}}(t)$ approaches a linear t dependence for filling factors $\nu \ll 1$ (number in parenthesis). In the high-mobility sample, (c), the fraction of localized electrons increases abruptly at a critical filling factor ν_c . Kukushkin et al. find that these results are consistent with a triangular lattice only (inset in part c). Thus, they have shown a novel technique for deriving local spatial configuration information about a many-body electronic state.

3.4.3. Electric field

External electric fields applied perpendicular to the plane of quantum wells may significantly alter the emission kinetics of the carriers. In section 2.4.3 the effects of an electric field were shown to cause a red-shift of the emission energy, and this is known as the quantum-confined Stark effect. Polland et al. [395] also found that the QCSE causes an increase in the recombination lifetime, and the physical explanation for this is simply due to the decreased electron-hole wavefunction overlap. Fig. 367 shows their measured PL lifetimes versus applied voltage for three different quantum well samples of widths 5, 10, and 20 nm. Plainly, the field dependence is much stronger for the wide quantum well than the narrow quantum well. Spectacularly, the lifetime of the 20 nm quantum well increases from 660 ps at zero field to ~ 100 ns at $V_{\text{ext}} = -2.4$ V. The solid lines in the figure represent theoretical calculations based upon envelope wavefunction overlap between electrons and holes, and are in reasonably good agreement with experiment. Thus, the observed lifetime enhancement caused by the external bias is governed by the charge separation within the quantum well. This QCSE was extended further by Alexandrou et al. [531] to the case of coupled double quantum wells separated by an $\text{Al}_{0.3}\text{Ga}_{0.7}\text{As}$ barrier of thickness varying from 25 to 60 Å. They find that the ratio of the intensity of the direct transition (between electrons and holes within the same well) to that of the indirect transition (between electrons and holes in the different wells) in the presence of an external bias is strongly dependent upon the barrier thickness, indicative of the tunneling dependence on barrier thickness. Fig. 368 shows the measured lifetime of the indirect transition versus applied field for the three structures examined in this study. Again, there is an increase in lifetime with increasing field,

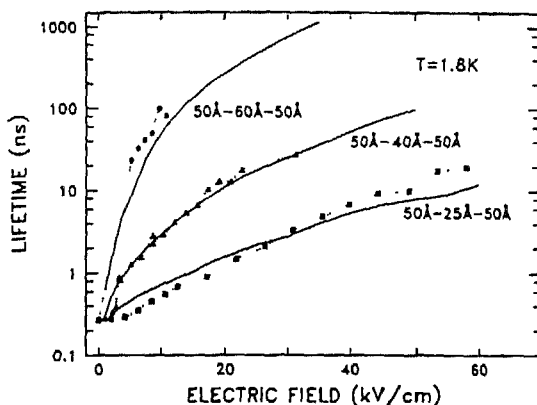


Fig. 368. Electric field dependence of the spatially-indirect exciton lifetime in symmetric coupled double quantum wells for barrier thicknesses of 25, 40, and 60 Å. (After Alexandrou et al. [531].)

which is attributable to charge separation. Wider barriers yield less wavefunction overlap, and concomitantly longer lifetimes.

These longer exciton lifetimes in biased quantum wells may also be taken advantage of to study the energy distribution of excitons. Kash et al. [532] did just this in a p-i-n diode sample consisting of two 50 Å GaAs quantum wells separated by 40 Å $\text{Al}_{0.3}\text{Ga}_{0.7}\text{As}$ barriers repeated several times within the intrinsic region of the structure. They measured the time-resolved spectra of the excitonic emission in an applied field of 30 kV cm^{-1} at various temperatures. At these fields the excitons are “indirect”, with electrons and holes spatially confined in different quantum wells. Fig. 369 shows these spectra at 6, 12, and 18 K. Note the long lifetimes here which are a result of the QCSE discussed above. The solid lines in the figure represent fits to the data with a Fermi-Dirac distribution function with the chemical potential determined self-consistently. Maxwell-Boltzmann fits do not accurately reproduce

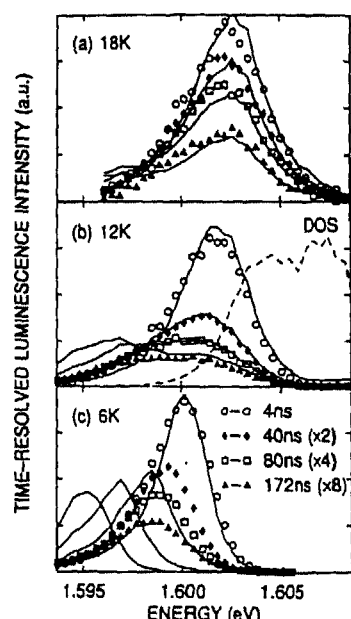


Fig. 369. Time-resolved PL spectra of coupled quantum well indirect excitons at three different lattice temperatures. —, calculated spectra. (b) ---, the density-of-states (DOS) used in the calculations. (After Kash et al. [532].)

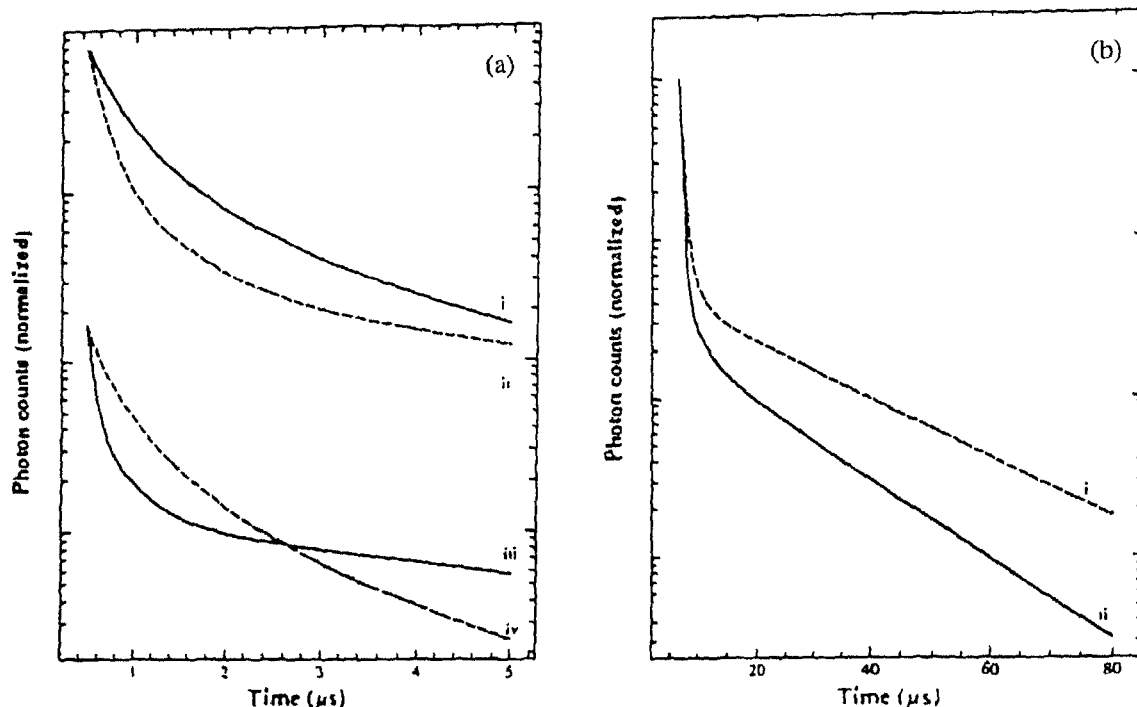


Fig. 370. PL time decays for (a) $m+n=\text{even}$ superlattices, (i) $(\text{GaAs})_4/(\text{AlAs})_4$ at zero stress, (ii) $(\text{GaAs})_4/(\text{AlAs})_4$ under [110] stress of 5.96 kbar, (iii) $(\text{GaAs})_1/(\text{AlAs})_1$ at zero stress, and (iv) $(\text{GaAs})_1/(\text{AlAs})_1$ under [001] stress of 1.43 kbar; and (b) $m+n=\text{odd}$ superlattices; (i) $(\text{GaAs})_2/(\text{AlAs})_3$ at zero stress, (ii) $(\text{GaAs})_2/(\text{AlAs})_3$ under [001] stress of 4.03 kbar. (After Ge et al. [416].)

the spectra at these temperatures. This Fermi-Dirac distribution results from a strong, but short-ranged repulsion between these excitons (which are boson like). This repulsion may arise from the electrostatic repulsion between the excitons which have become polarized by the applied field. This Fermi-Dirac distribution adequately fits the data for $T > 10$ K and at energies above the line center. The inadequacy of the fit at lower temperatures and energies may be due to a metastable distribution of the excitonic energies which is still consistent with the Fermi-Dirac distribution model. Specifically, at low temperatures, excitons may become localized in local potential minima with an energy barrier to the absolute minimum which is insurmountable via thermal activation.

3.4.4. Uniaxial strain

Not many studies have combined the power of time-resolved measurements with the electronic structure altering perturbation of uniaxial strain. Nonetheless, one good example of a study taking advantage of these techniques is that of Ge et al. [316,416], which dealt with the non-degenerate X_Z and $X_{X,Y}$ conduction band minima in type-II GaAs/AlAs superlattices. In this type of structure, the transition rate is directly related to the symmetry of the conduction band minimum (X_Z versus $X_{X,Y}$), thereby allowing determination of the identity of the state involved in the transition. In section 3.2.6 the issue of radiative recombination in a disordered system was considered, and explored in the context of a type-II superlattice. This same model was used by Ge et al. [316,416] to examine the kinetics of their type-II superlattices under the influence of uniaxial strain. Fig. 370 shows typical decay curves for short period superlattices, $(\text{GaAs})_m/(\text{AlAs})_n$, under different stresses, for $m+n=\text{even}$ and $m+n=\text{odd}$. The slow non-exponential decays are characteristic of forbidden transitions in a disordered system. They attribute the initial rapid decay to tunneling to non-radiative centers. The solid line is at

zero stress, whereas the dashed lines correspond to data taken under sufficient stress to reverse the energy order of the X_Z and $X_{X,Y}$ states. Note that for the $m+n=\text{even}$ samples the application of uniaxial stress causes an increase in the decay rate, whereas for the $m+n=\text{odd}$ sample the decay rate decreases. (They find that $X_{X,Y}$ is the conduction band minimum for $m,n < 4$, whereas X_Z is the conduction band minimum for $m=n \leq 4$.) This data indicates that the superlattice potential contributes significantly to the decay of excitons associated with X_Z , only. These results are consistent with parity considerations in these structures.

4. Spatially-resolved photoluminescence

The last aspect of PL spectroscopy which remains to be explored is that combining spatial resolution with the spectral and temporal resolution techniques described above. The motivating factors for extracting spatial information from the emission in semiconductors are many; foremost among them are the desire to obtain topographic or structural information, and the need to quantify carrier transport. Spatial mapping of the luminescent properties of a semiconductor structure may directly demonstrate the structural properties of semiconductor nanostructures, the impurity content across a wafer, or the homogeneous or inhomogeneous nature of the luminescence from a sample. Quantification of carrier transport through time-resolved luminescence mapping is desirable, and sometimes advantageous over other more conventional techniques, for the demonstration of anisotropic transport, for correlation of the spectral and transport properties as a means of identifying the migrating carrier, and for quantifying excitonic transport.

4.1. Measurement techniques

There are many different varieties of techniques for spatial PL measurements. Nonetheless, a useful criterion for categorizing these techniques is based upon a fundamental physical limitation of their spatial resolution, namely the measurements may be performed in the near- or far-field; and the spatial resolution is correspondingly limited by diffraction or is not limited by diffraction, respectively. This categorization has only become possible in the last few years through the revolutionary development of near-field scanning optical microscopy (NSOM). The far-field techniques are varied in their approaches to achieving high-spatial resolution. One variety of this technique directly images the PL from the sample, possibly in a time-resolved fashion. Another collects the PL from the sample which has been processed with an opaque mask containing a microscopic hole from which the luminescence photons can escape and be detected, again, possibly in a time-resolved fashion. A third variation on this technique, which may be essentially the same as the direct PL imaging technique, is that of confocal PL imaging. This technique is advantageous in its enhanced depth resolution. Each of these techniques will be briefly discussed below.

Prior to a detailed discussion of each of these techniques, it is useful to review the issues relevant to spatially resolving an image optically. The resolution of an image generated optically is defined as the smallest distinguishable distance between two closely spaced features on the object [533]. Diffraction is the ultimate factor limiting the achievable resolution in a system. In the far-field the minimum feature size is given by

$$d = \frac{1.21987\lambda f}{D} \quad (65)$$

where λ is the wavelength of light forming the image, D is the aperture of the light, and f is the focal

length of the lens forming the image. Note that the resolution is a direct function of the wavelength of the light. In contrast, near-field microscopy does not focus the light, and diffraction effects do not limit the ultimate spatial resolution. Instead, the light (either collected or excitation) is collected or delivered from a light pipe (fiber optic) with an aperture smaller than the wavelength of light. The light pipe is placed within a few angströms of the object, and the light is delivered or collected. The size of the probe that either illuminates the sample or collects luminescence from the sample is a geometrical projection of the aperture of the light pipe (in contrast to far-field techniques where it is its Fourier transform). Fourier analysis shows that a propagating electromagnetic wave cannot convey information with a spatial frequency greater than $1/\lambda$ since the higher spatial frequencies (smaller dimensions) decay exponentially with distance from the source. In contrast to far-field measurements near-field microscopy is sensitive to these higher frequency modes. As a result the limits of diffraction theory do not apply, and the spatial resolution is instead given by

$$d = \frac{0.61}{R} \quad (66)$$

where R is the radius of the aperture. Spatial resolutions of < 10 nm are predicted theoretically for near-field microscopy [533]. Note that the resolution does not depend on the wavelength of light.

4.1.1. Direct PL spatial imaging

The classic 1951 Haynes–Shockley experiment [534], which allows measurement of injected carrier mobilities, has motivated the development of optical analogs to this entirely electrical technique. In this important experiment carriers are electrically injected at one point on a sample and detected, again electrically, at a spatially separated point. This obviously requires contacting to the sample and concomitantly all of the technological difficulties associated with metallization. In order to avoid these technological difficulties as well as to utilize the power of PL spectroscopy, a number of researchers have developed direct optical imaging techniques suitable for quantifying carrier transport as well as emission properties (uniformity, defect incorporation, etc.) across a semiconductor wafer or nanostucture [535–544]. In general the technique used for quantifying carrier transport involves the localized injection of carriers, through photoexcitation, followed by spatially-resolved detection of the resultant luminescence, all in a time-resolved fashion. This spatial resolution may be in one, two, or three dimensions depending on the sophistication of the experimental apparatus. Fig. 371 shows the implementation of this technique used by Gilliland et al. [538]. Whole wafer imaging may be accomplished through a simple raster scan of the excitation and coincident detection points. This technique has several advantages over conventional electrical techniques for characterizing samples, including: (1) it is totally contactless thereby eliminating the technological difficulties often present in metallizing samples; (2) it is sensitive to neutral particle, i.e. exciton, transport unlike electrical techniques which use the field to accelerate charged carriers; (3) it retains spectral information thus allowing possible discrimination of the species involved in the transport as well as the location within the structure; and (4) has potential for high time resolution.

4.1.2. PL imaging through an opaque mask

One form of time-of-flight (TOF) technique which may be used for quantifying carrier transport is that employed by Hillmer and coworkers [545–547] and later by Takahashi et al. [548]. This technique is conceptually very simple, but more difficult to implement and analyze. Fig. 372 shows a cartoon of this technique. The sample is illuminated with laser light, and subsequent luminescence

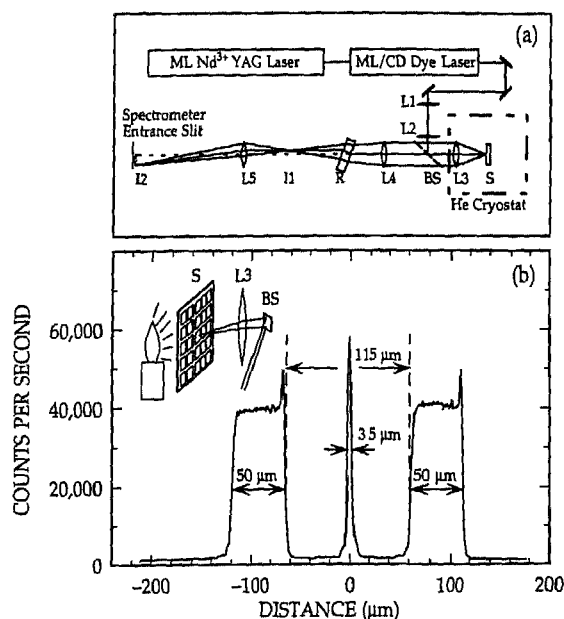


Fig. 371. (a) Apparatus for spatially-resolved PL measurements; L1–L5, lenses; BS, beam splitter, S, sample, I1–I2, PL images; and R, refractory block (b) Calibration of distance was achieved with a photolithographically defined target which was backlit and simultaneously illuminated with laser light. Laser spot size, 3.5 μm [538].

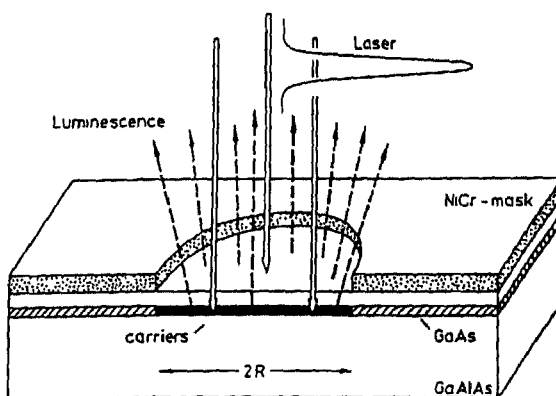


Fig. 372. Illustration of the opaque mask implemented by Hillmer et al. [545] for their lateral transport studies.

photons are collected through a tiny aperture in an opaque mask. These microstructured masks, as developed by Hillmer and coworkers, are NiCr layers (200 nm thick) evaporated on thin glass substrates. The circular holes are defined by optical lithography and dry etching. Resulting circular apertures have radii ranging from 0.5 to 100 μm . These masks are placed directly on the surface of the sample. Transport information is obtained by measuring the time-resolved luminescence emanating from that part of the sample under the aperture in the opaque mask. Since the PL intensity is proportional to the density of carriers, this measurement thereby directly measures the density of only those carriers directly within the lateral area defined by this aperture in the mask. Drift or diffusion of photoexcited carriers into a region under the opaque portion of the mask will result in a decrease of this detectable carrier density (as will radiative or non-radiative decay). Thus, comparison of PL time decays for various sized apertures, or for samples with and without apertures, allows determination of transport properties. Hillmer and coworkers used a microscope objective to focus their laser excitation through

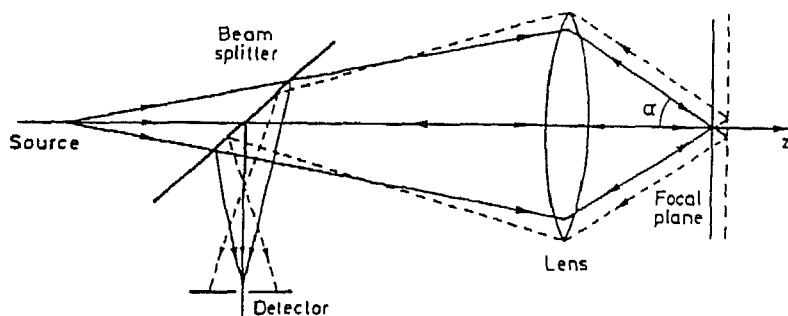


Fig. 373. Schematic ray-tracing diagram showing the origin of the depth discrimination or optical sectioning property of confocal imaging systems. (After Wilson [551].)

the mask, and the luminescence was collected through the same objective, dispersed by a monochromator, and detected by a MCP photomultiplier. Temporal resolutions of 50 ps, and spatial resolutions in the lateral direction of $\sim 0.1 \mu\text{m}$ were claimed by Hillmer and coworkers.

Assuming diffusive transport, Hillmer and coworkers and Takahashi et al. were able to analyze their data and obtain diffusion constants of the photoexcited carriers. The photoexcited carrier density obeys the 2D diffusion equation

$$\frac{\partial n}{\partial t} = D \left[\frac{\partial^2}{\partial x^2} + \frac{\partial^2}{\partial y^2} \right] n - \frac{n}{\tau} \quad (67)$$

which may be integrated for the case of a uniformly excited circular hole (initial condition) to give

$$n(\bar{r}, t) = \left(\frac{n_0}{2Dt} \right) e^{(-r^2/4Dt)} e^{(-t/\tau)} \int_0^R r' e^{(-r'^2/4Dt)} I_0 \left(\frac{rr'}{2Dt} \right) dr' \quad (68)$$

where n_0 is the initial density of photoexcited carriers and I_0 is the modified Bessel function [548]. The PL intensity detected through the mask aperture is then proportional to the density of carriers integrated over the area of the aperture. Eq. (68) may thus be integrated and compared to the data in order to obtain the diffusivities of photoexcited carriers.

4.1.3. Confocal PL imaging

Confocal imaging is a technique which has superior imaging properties compared to conventional optical microscopic techniques. It is a far-field technique that adds the ability for depth discrimination not present in conventional microscopy. Confocal imaging has several other advantages over conventional imaging techniques, including enhanced spatial resolution and relative insensitivity to scattered light. A major difference between confocal microscopy and conventional microscopy is that confocal imaging utilizes a point detector rather than a large-area detector, otherwise the techniques are similar [549]. Naturally, as the area of the detector increases the image intensity broadens to that of conventional microscopy. For example for a 0.6 numerical aperture lens and He-Ne laser light (6328 Å) a 6.7 μm diameter pinhole or less is required for confocal imaging. Further, the depth sectioning is less sensitive than the lateral resolution to the detector size (pinhole diameter). The essential features of a confocal imaging system are matched excitation and collection optics and back focal-plane apertures to detect either the reflection or transmission of only a single focal spot in the sample [550]. Fig. 373 illustrates the essential concept of confocal imaging. Here an object out of focus in the focal plane of the lens (dashed line) is defocused on the point detector (pinhole), and, therefore, the intensity of the

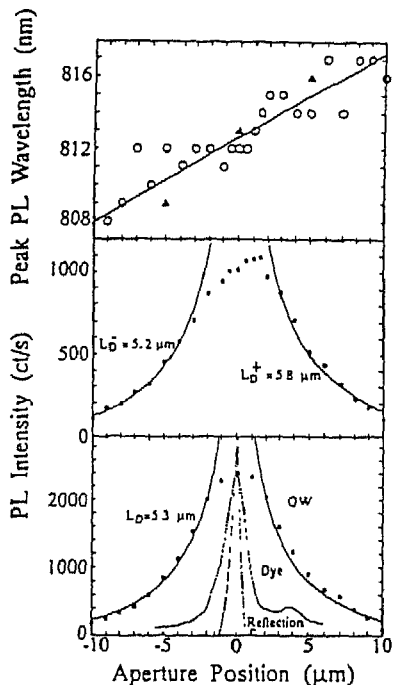


Fig. 374 Bottom panel: bright-field reflectivity of the excitation laser (width $\sim 0.75 \mu\text{m}$) (narrowest scan) and the PL from a thin film of LDS-821 laser dye. This demonstrates the resolution at the detection wavelength ($\sim 800 \text{ nm}$) of $\sim 1.8 \mu\text{m}$. Also shown is a PL spatial scan in the center of the sample. Middle panel: PL spatial distribution at the edge of the sample (15 μm from edge). Top panel: Peak PL wavelength versus spatial position [550].

light detected from this out-of-focus object point is attenuated compared to those object points which are in the focal plane (solid lines). This depth resolution combined with the lateral resolution yields the capability to image in three dimensions. The conventional microscope is a parallel instrument, imaging the entire object field simultaneously, whereas in contrast the confocal microscope images only one point in the object field at a time, and the entire image is constructed from a raster scan of the object field [551]. Essentially, the resolution is increased at the expense of the field of view, which may then be regained through scanning. Wilson [551] points out that the maximum spatial frequency (smallest spatial feature) present in a confocal microscope image is twice (half) that of a conventional microscope image.

This technique may also be utilized with PL spectroscopy. Confocal photoluminescence imaging is an incoherent process in which the depth resolution (optical sectioning) is degraded with increasing emission wavelength [551]. Further, because the depth resolution is sensitive to the luminescence wavelength, the best depth resolution is obtained for monochromatic detection. Thus, detection of a range of wavelengths will contain information from a range of depths within the sample. Further, the optimal lateral resolution is realized for the detection wavelength as close as possible to the excitation wavelength.

Confocal PL imaging is essentially the same technique as the direct PL imaging technique as implemented by Gilliland et al. [538] and described in section 4.1.1. Fong and Brueck [550] have also demonstrated the confocal resolution obtainable with confocal PL imaging, and obtained a spatial resolution of $< 1 \mu\text{m}$. They used a $60\times$ (NA = 0.85) microscope objective to generate a $\sim 0.75 \mu\text{m}$ spot with 514.5 nm laser light. The pinhole aperture before the detector was 50 μm in diameter, and was placed immediately before the spectrometer. The semiconductor sample they examined was a

GaAs quantum well laser structure (a so-called GRINSCH structure) grown by MOCVD. Fig. 374 demonstrates the resolution achievable with confocal PL imaging. The narrowest peak in the bottom panel of the figure is the bright-field confocal reflectivity of the laser source (spatial width $\sim 0.75 \mu\text{m}$). The middle peak in the same panel is from a reference dye film that shows the experimental resolution ($\sim 1.8 \mu\text{m}$) at the luminescence wavelength. The widest scan in the bottom panel is that from the PL originating in the central portion of the sample. The other two panels correspond to spatial scans at different points on the wafer and the peak PL emission wavelength for this data. The asymmetry in the middle panel is due to the gradient in quantum well width across the scan area, as shown in the top panel.

4.1.4. Near-field scanning optical microscopy

As early as 1928 Synge proposed a near-field scanning optical system that is not encumbered by the diffraction limit [552]. In 1972 Ash and Nichols [553] demonstrated the sub-wavelength resolution capability of near-field microscopy with 3 cm microwaves, achieving a resolution of $\lambda/60$. In general, near-field detection is the generalization of the Rayleigh criterion for non-radiating waves. The spatial resolution depends not only on the contrast (through the modulation transfer function) but also on the detected signal strength [554].

NSOM has many advantages over other optical techniques for achieving spatial resolution including: it has high spatial resolution (down to $\sim 12 \text{ nm}$), many types of contrast mechanisms exist, it is non-destructive, and it is useful over a wide spectral range [555]. Image contrast may be obtained through absorption, polarization, refractive index, photoluminescence, and reflectivity [555,556].

A major difficulty in performing near-field measurements is in collecting or sourcing photons into or from a sub-wavelength aperture [552]. Optical fibers which have been laser heated and pulled to a tip as small as 20 nm and then coated with a cladding of aluminum have currently proven to be the best probe tip. Mertz et al. [557] have also demonstrated near-field imaging with a semiconductor probe tip which detects the non-radiating field through the surface photovoltaic effect. NSOM suffers from low signal-to-noise due to the small number of photons collected or used for excitation [558]. These losses take two forms: (1) the loss intrinsic to a fiber probe with a small aperture, $\lambda/10$, is $\sim 10^5$; and (2) the luminescence scales with the size of the region sampled, which for $\lambda/10$ resolution causes a reduction in signal by 10^2 . In practice, Grober et al. [558] found that the ultimate spatial resolution of 12 nm was not achievable with semiconductor samples, instead, they were forced to use fibers with tip diameters of 150–250 nm for near-field spectroscopy at a wavelength of 800 nm.

The electromagnetic field in the near-field has evanescent components which depend strongly on the distance from the sample. A Fourier analysis shows that diffracted light contains both propagating and non-propagating (or evanescent) waves, with the relative proportion dependent on the size and structure of the object. Smaller objects (with higher spatial frequencies) exhibit a stronger confinement of the non-propagating field over the surface of the object [559]. This exacerbates the importance of keeping the sample–probe tip distance constant so as not to generate artificial features. However, this is difficult to achieve in practice due to the scanning nature of the measurement, and where not practical, it is important that the sample topography be small compared to the claimed resolution [555]. Clearly the achievable spatial resolution strongly depends on the sample–probe tip separation. This is an important limitation to the imaging of sub-surface objects, such as buried quantum wells.

The essential features of the low-temperature AT&T NSOM built by Grober et al. [558] are: (1) in-situ translation stages for coarse positioning; (2) piezoelectric elements for fine positioning of the fiber tip; (3) in-situ optics for far-field excitation or imaging of the sample; (4) a mechanism for height regulation of the NSOM tip over the sample; and (5) cryogenic cooling of the sample. Fig. 375

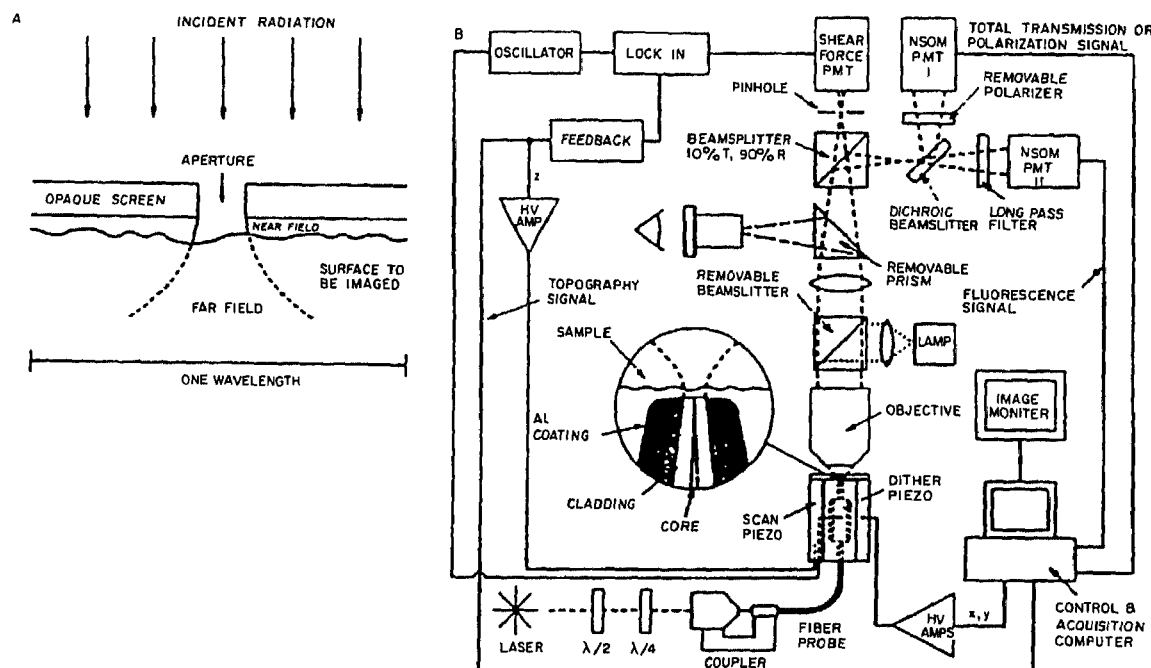


Fig. 375. Major elements of a near-field scanning optical microscope. (Reprinted with permission from *Science*, 257 (1994) 189. Copyright 1994 American Association for the Advancement of Science) [555].

shows a block diagram of the major elements in Betzig and Trautman's near-field microscope [555]. Here laser light is coupled into the near-field optical probe (a fiber tip as described above). Luminescence generated from the near-field excitation is collected by an objective lens of a conventional microscope. Spatial resolution is achieved by scanning the tip over the sample with piezoelectrically driven and computer-controlled elements. The probe-sample separation is maintained with a shear-force probe. This technique is based upon the observation that the amplitude of motion of the fiber tip dithered at the natural vibrational resonance in a plane parallel to the sample decreases as the probe tip approaches the surface. Grober et al. [558] implemented this feedback by scattering diode laser light off the laser tip and measuring the amplitude of the scattered light with a photodiode, and analyzing it with a lock-in amplifier. Most probe tips are coated with a metal coating which is mostly opaque (finite conductivity) which confines, but not perfectly, the light wave to the aperture size. There is an optimal size for the probe tip such that smaller apertures do not yield smaller effective probes. This is a consequence of the fact that in the visible portion of the spectrum no material is perfectly opaque and therefore the effective probe aperture is larger than the actual size [554]. The minimum diameter of the fiber probe aperture is limited by the finite skin depth of the metal used for the opaque coating [560]. Aluminum is a commonly used coating, and typical thicknesses are 100 nm due to its skin depth of 6.5 nm at a 500 nm wavelength. Probes may be used as a source or detector in the near-field in either transmission or reflection. Van Hulst et al. [560] have reported some of the recent trends in near-field microscopy.

4.1.5. Spatially-resolved pump-probe

Another important technique for obtaining spatial resolution which deserves mentioning, but will not be dealt with here beyond it fundamentally not being based on luminescence emission from the semiconductor, is a spatially- and temporally-resolved pump-probe measurement, demonstrated by

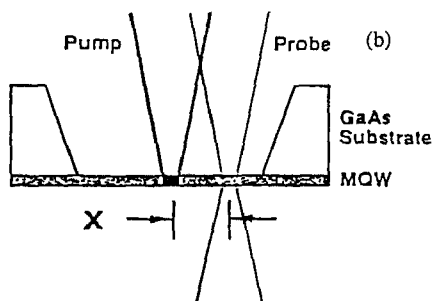


Fig. 376. Schematic diagram of the spatially-resolved pump–probe technique. Here the substrate has been removed from the epilayer to allow transmission through the epilayer. The probe beam is scanned relative to the spatially-fixed pump beam. (After Smith et al. [561])

Smith et al. [561,562], Wake et al. [563], Yoon et al. [564], and Olsson et al. [565]. Fig. 376 shows how the conventional pump–probe technique may be augmented to obtain spatial resolution as well. The limit of the spatial resolution is determined by the spot size of the laser beams. The probe beam is scanned spatially by a slight deflection of a mirror, whereas temporal resolution is obtained with an optical delay line. Changes in the intensity of the transmitted or reflected probe beam as a function of time and spatial position then yield the photoexcited carrier transport properties. As such, this technique is not based upon luminescence, rather it is based upon absorption or reflection changes induced by the migrating and time-dependent photoexcited carriers. However, in the work of Olsson et al. [565] the pump–probe technique is based upon a non-linearity in the luminescence resulting from a bimolecular recombination of the free carriers. In their scheme that portion of the detected luminescence which originates from the carrier recombination generated by the probe pulse with those generated by the pump pulse is isolated with an appropriate signal processing arrangement.

4.2. Carrier transport

Carrier transport is most commonly quantified through electrical measurements such as Hall measurements or Haynes–Shockley measurements. However, these are not the only techniques capable of quantifying carrier transport, and these techniques are limited in sensitivity to only charged-carrier transport. In contrast, the optical techniques described above are capable of characterizing both free-carrier and neutral-particle (exciton) transport, and are, therefore, both complementary and supplementary to electrical techniques.

4.2.1. Vertical transport

Most of the techniques presented above for achieving spatial resolution are designed to yield information about carrier transport in the lateral plane (perpendicular to the direction of observation). However, another TOF technique has been demonstrated with spatial resolution in the “vertical” direction (usually the growth direction). This is accomplished by inserting at growth, thin probe layers (quantum wells) with distinct spectral signatures within the sample structure at different spatial positions along the growth axis. Fig. 377 shows an example of such a structure. In order to simplify the analysis of data it is convenient to obtain a 1D transport geometry, in the growth direction. This is done by defocusing the excitation laser to a spot size larger than the vertical transport distance. The rise and fall kinetics of the PL from the probe quantum well layers are then analyzed to yield the desired transport information.

Due to the nature of this experiment, particularly the design of the samples, the processes which may affect or govern the transport include alloy scattering, surface and interface non-radiative recom-

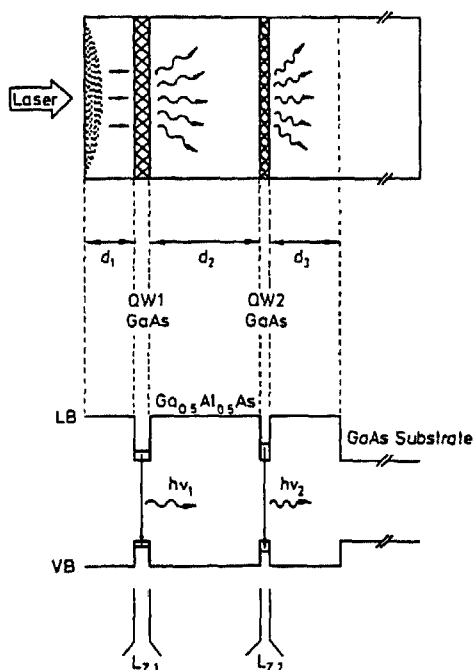


Fig. 377. Schematic diagram of probe quantum-well layers inserted into a sample during growth for vertical transport studies. The probe layers (quantum wells) have different widths in order to allow spectral distinguishment of their emission to be correlated with their spatial position. (After Hillmer et al. [566].)

bination, acoustic-deformation potential scattering, polar-optical phonon scattering, carrier capture into quantum wells, tunneling, and thermionic emission [566–569]. Hillmer et al. [566] have examined the vertical ambipolar transport of photoexcited carriers in a series of double-well GaAs/Al_{0.5}Ga_{0.5}As heterostructures. Fig. 378 depicts the time-resolved PL from the front quantum well (10 nm, denoted by triangles) and from the back quantum well (4.2 nm, denoted by circles) for various

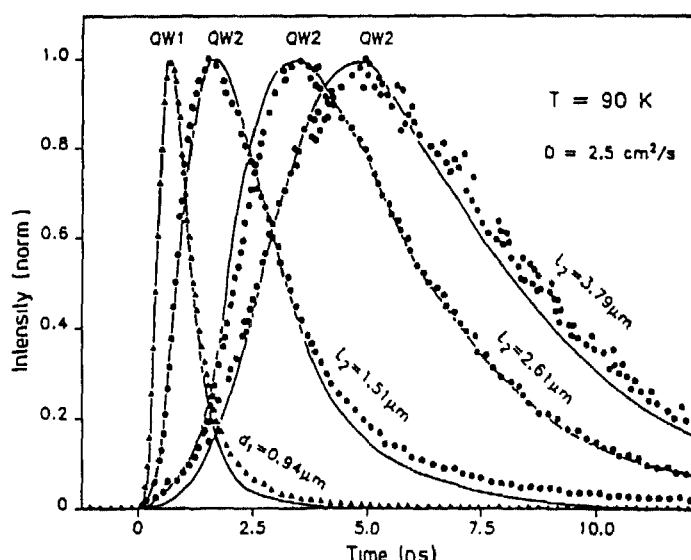


Fig. 378. PL kinetics of the emission from the two quantum well layers QW1 (\blacktriangle) and QW2 (\bullet) for various distances from the sample surface (d_1, L_2). (After Hillmer et al. [566].)

samples with different distances between the probe quantum wells. These measurements were performed with above-gap excitation and thus are affected by all of the effects of transport, capture, and recombination. The effect each of these processes has on the observed dynamics may be distinguished by examining the PL kinetics of each quantum well for resonant and non-resonant excitation and for structures with different distances between the probe quantum well layers. The solid lines in the figure represent best fits to the kinetics using a model including diffusion, carrier capture into the quantum wells, and surface/interface non-radiative recombination. This procedure yields a diffusion constant, at this temperature (90 K), of $2.5 \text{ cm}^2 \text{ s}^{-1}$ and interface recombination velocities of the order of 10^7 cm s^{-1} . The capture probabilities (by the probe quantum wells) may be obtained through the difference in interface recombination velocity of the two interfaces of each well, and is found to increase to near unity with increasing temperature ($T > 100 \text{ K}$). Analysis of the temperature dependence of the diffusion constant, converted to a mobility in these non-degenerate conditions using the Einstein relation, shows the dominance of alloy-disorder scattering for $40 < T < 120 \text{ K}$, and of acoustic and optical phonon scattering at higher temperatures.

Amand et al. [567] also examined the vertical transport of excitons within GaAs/AlGaAs superlattices using this vertical transport technique. They find that the exciton diffusion constant depends strongly upon the barrier thickness of the superlattice, decreasing with increasing barrier thickness. Nakamura et al. [568,569] also examined the tunneling-assisted radiative recombination of electrons and holes in different wells of a GaAs/AlAs superlattice sample. They find that the introduction of a large quantum well into a short-period superlattice sample causes a reduction in the PL lifetime. Their rate equation analysis shows that this reduction in lifetime is associated with the dynamics of photoexcited carriers which are trapped into the wider (lower-energy) quantum well via vertical transport. This capture time was determined to be $\sim 1 \text{ ns}$.

4.2.2. Free-carrier transport

Gilliland et al. [538] and Wolford et al. [570] demonstrated the utility and accuracy of all-optical techniques in quantifying free-carrier transport using the direct time-resolved PL imaging technique. They examined the time-resolved spatial PL profiles of a series of MOCVD-prepared GaAs double heterostructures versus temperature. At room temperature they observed an effective modulation doping for thin GaAs layers (GaAs layers were inherently n-type, whereas AlGaAs cladding layers were inherently p-type). Fig. 379 shows the room-temperature PL spatial profiles as a function of time for a double heterostructure with $9.82 \mu\text{m}$ and $0.30 \mu\text{m}$ GaAs layer thicknesses. For diffusive transport, the radially-symmetric diffusion equation yields a time- and space-dependent minority-carrier density given by

$$p(\tilde{r},t) = \left[\frac{p_0 \Delta_0^2}{4Dt + \Delta_0^2} \right] e^{[-r^2/(4Dt + \Delta_0^2)]} e^{[-t/\tau]} \quad (69)$$

where Δ_0 is the initial ($t = 0$) minority-carrier distribution FWHM, D is the diffusion constant, and τ is the minority-carrier lifetime (assuming the exponential decay of minority carriers, thereby neglecting the bimolecular recombination expected for intrinsic material). This Gaussian distribution of carriers is clearly reflected in the PL spatial distributions, and thus a plot of the FWHM as a function of time yields the diffusion constant, as

$$\Delta^2(t) = [16\ln(2)]Dt + 4\ln(2)\Delta_0^2 \quad (70)$$

Fig. 380 shows the derived FWHM squared as a function of time for these bulk MOCVD GaAs samples. The results are clearly not linear for all samples. Gilliland et al. [538] understood these data

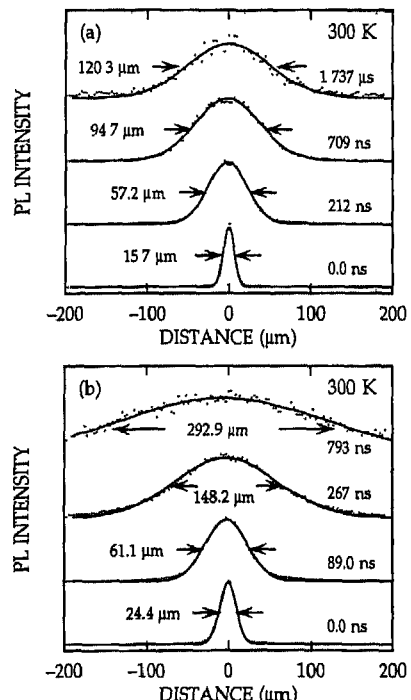


Fig. 379. 300 K PL distributions versus time. —, Gaussian fits to the data. (a) Results for 9.82 μm sample, (b) results for 0.30 μm sample [570].

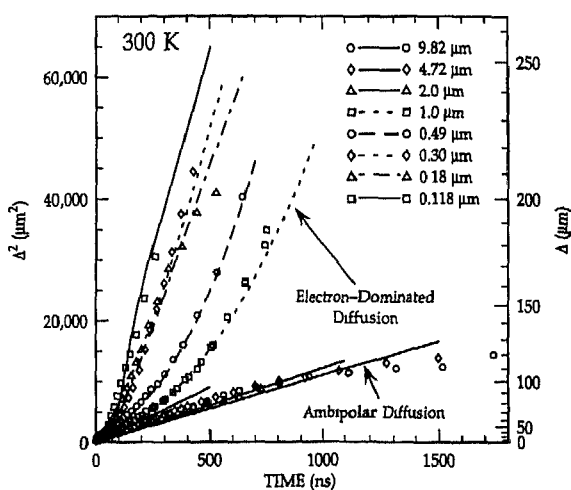


Fig. 380. Squared FWHM of the PL versus time at 300 K for a series of bulk samples [538].

in terms of the time-dependent free-carrier densities together with the inherent background doping present in these samples. They find that these dynamics are well described by ambipolar transport with a diffusion constant

$$D = \frac{[(n+n_0)+(p+p_0)]D_e D_h}{(n+n_0)D_e + (p+p_0)D_h} \quad (71)$$

where $n(p)$ is the time-dependent photojected carrier density, n_0 (p_0) is the built-in background

majority-carrier density, and D_e (D_h) is the electron (hole) diffusion constant. Using Eqs. (70) and (71) together with the measured PL kinetics (for defocused excitation where transport may be neglected) substituted for the time-dependent minority-carrier density yields the theoretical lines shown in the figure. They find that a constant n-type background density, for all samples, of $\sim 10^{15} \text{ cm}^{-3}$, together with a p-type background doping density, which increases from $5 \times 10^{14} \text{ cm}^{-3}$ for thick samples to 10^{18} cm^{-3} for thin samples, adequately fits the data in the figure. This GaAs layer thickness dependence of the p-type background concentration is simply due to the complete depletion of the GaAs layer at a layer thickness of $\sim 1 \mu\text{m}$, and beyond that (for thinner GaAs layers) the accumulation of holes from the p-type AlGaAs layers. This yields a type conversion (from n- to p-type) and therefore a change in the minority carrier species from electrons to holes. This type conversion is strongly dependent on the time-dependent carrier density as well as the thickness of the structure, as is evident in the data. The relatively flat slope evident in the figure for all samples at early times, and for thicker samples at all times, is indicative of the hole-dominated ambipolar diffusion, whereas the steeper slope evident in the data for the thin samples at later times is indicative of electron-dominated diffusion. For comparison with electrically-determined transport results in comparable structures, both n- and p-type, it is convenient to convert these measured diffusivities into mobilities through the Einstein relation

$$\mu = \frac{D_e}{kT} \quad (72)$$

This gives minority-electron (minority-hole) mobilities at room temperature of $5000 \text{ cm}^2 \text{ V}^{-1} \text{ s}^{-1}$ ($350 \text{ cm}^2 \text{ V}^{-1} \text{ s}^{-1}$), which is in good agreement with electrically-determined majority-electron (majority-hole) mobilities. These kinetic and transport results also allow determination of the minority-carrier diffusion length. Gilliland et al. find room-temperature diffusion lengths, in their surface-free double heterostructures, of $> 100 \mu\text{m}$, decreasing with decreasing GaAs layer thickness. This is indicative of the truly high-quality of the heterointerfaces of these samples since carriers are “reflected” many times during transport from the interfaces without suffering deleterious non-radiative decay.

Olsson et al. [565] also used their non-linear luminescence pump-probe technique to measure the transport of free carriers in a GaAs double heterostructure. They also observed a linear increase in the FWHM squared versus time, however, they examined the implications of bimolecular recombination on the transport. The addition of a bimolecular recombination term to the diffusion equation requires numerical solutions. Olsson et al. did just this, and discovered that the spatial profiles and the slope of the FWHM squared versus time is also only slightly affected by this additional term. They deduced a 300 K electron (hole) mobility of $7000 \text{ cm}^2 \text{ V}^{-1} \text{ s}^{-1}$ ($340 \text{ cm}^2 \text{ V}^{-1} \text{ s}^{-1}$) in good agreement with electrical measurements and the results of Gilliland et al. [538].

This technique also accurately quantifies carrier transport at different lattice temperatures. Wolford et al. [570] demonstrated this in the same undoped GaAs double heterostructures used above, and Smith et al. [571] did the same thing in a series of GaAs homostructures. They find similar results in both sets of samples. Fig. 381 shows the FWHM of the measured PL spatial distributions squared versus time for several different lattice temperatures (from 30 to 300 K). There is a clear increase in slope with decreasing temperature, which is indicative of an increase in diffusivity, and therefore mobility. Note that at these temperatures and excitation densities, the degeneracy effects of the Einstein relation may be ignored, and Eq. (72) may be used directly to convert measured diffusivities to mobilities. Fig. 382 shows that the thus obtained mobilities versus lattice temperature together with electrically-determined mobilities in a bulk p-type GaAs sample. The solid line is a theoretical fit to the data with acoustic and non-polar optical deformation potentials as adjustable parameters. The best fit to the data yields the deformation potentials shown, which are in good quantitative agreement with

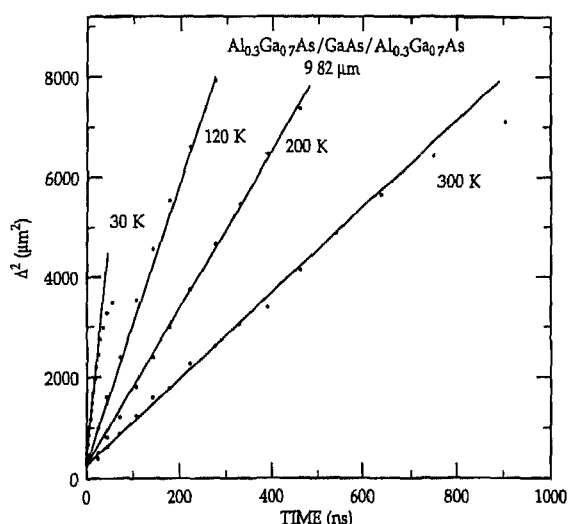


Fig. 381 Temperature dependence of the squared FWHM versus time obtained for the 9.82 μm thick double heterostructure [570]

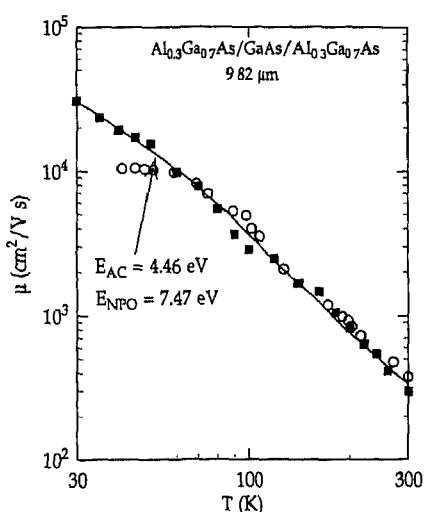


Fig. 382. Temperature dependence of the minority-hole mobility in the 9.82 μm double heterostructure (■). ○, mobilities for majority holes in p-type GaAs obtained electrically [570].

other estimates. Lastly, they observe that at these temperatures there is no excitation power (carrier density) dependence to the measured diffusivities.

4.2.3. Electron-hole plasma transport

Romanek et al. [572] measured the dynamical behavior of the EHP in bulk GaAs with the direct PL imaging technique. Fig. 383 portrays the 2 K PL spectrum after intense optical excitation of the GaAs epilayer at different distances from the center of the laser spot which was focused to 75 μm . The peak energy of the luminescence near the spatial center of the excitation spot (from 0 to 250 μm) is at 1.505 eV, exhibiting the red-shift expected for the EHP in GaAs, as discussed in section 2.2.6. Analysis of these cw PL images reveals that the EHP is spatially expanding. At 140 μm from the spot center, the excitation intensity is $\sim 10\%$ of that at the center, and is therefore insufficient to create a

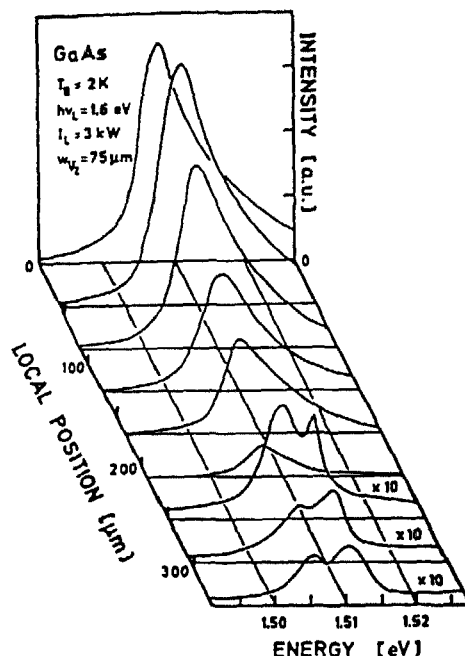


Fig. 383. Spatially-resolved PL spectra at 2 K after intense optical excitation. (After Romanek et al [572].)

free-carrier density above the Mott density. Thus, under consideration of the excitation density profile alone, the presence of the EHP in the emission spectra at spatial locations where the EHP was not originally created strongly points to the transport of the EHP. At still greater distances ($> 250 \mu\text{m}$) free- and bound-exciton emission is plainly evident. The expansion of the EHP is very rapid. Gilliland et al. [573] measured the time-resolved spatial profiles of the EHP in bulk GaAs double heterostructures, and discovered a strong density dependence to the initial EHP spatial distribution. Their measurements were limited in temporal resolution to $\sim 50 \text{ ps}$, and they found that on this time scale the EHP distribution expands by as much as a factor of five for excitation densities increasing by a factor of 1000. This strong density dependence of the EHP spatial expansion must be due to the Fermi pressure present in a non-equilibrium plasma which is strongly density dependent. A consequence of this increased expansion with increasing excitation intensity is that the achievable density of the EHP is limited, and this was indeed observed by Romanek et al. Both Romanek et al. and Gilliland et al. estimate the EHP expansion velocity to be $> 10^7 \text{ cm s}^{-1}$. Romanek et al. also determined the local EHP carrier temperature from lineshape fits to their spectra, and find that the carriers cool, almost linearly, as they expand away from the excitation spot.

In contrast to GaAs, EHP lifetimes in Si (indirect bandgap) are long, thereby allowing thermal equilibrium to be reached with the lattice. Forchel et al. [574] made use of two different techniques to quantify the transport of the EHP in Si. Their first technique is conceptually similar to the vertical transport technique described above (section 4.2.1) only instead of using quantum well layers as probes of the transport, they used surface doping with shallow impurities as a spatial marker of the EHP transport in the thin Si wafers investigated. They used both In and Tl as shallow dopants since their radiative lifetimes were fast (2.7 ns and 270 ps, respectively), their emission signatures are spectrally distinct from the intrinsic Si emissions, and they are relatively stable thermally, thus allowing higher-temperature investigations. Fig. 384 shows the PL kinetics of In bound exciton emission from an In surface-doped Si sample which was excited on both sides of the $95 \mu\text{m}$ thick wafer (the dotted curve corresponds to direct excitation of In bound excitons, whereas the solid curve represents exci-

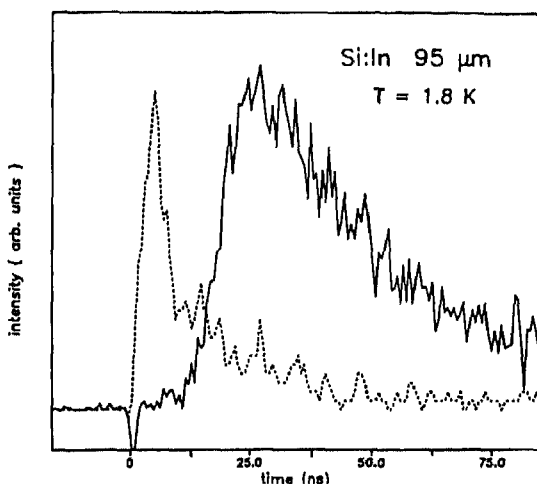


Fig. 384. PL kinetics of In-bound exciton emission at 1.8 K after (i) direct excitation of In-implanted surface, and (ii) excitation of the undoped surface. (After Forchel et al. [574].)

tation on the back side of the wafer). The indirect excitation data has a maximum intensity after a delay of 20 ns, and the onset of the PL occurs at 10 ns. From these data, Forchel et al. deduce expansion velocities of $5 \times 10^5 \text{ cm s}^{-1}$ and $1 \times 10^6 \text{ cm s}^{-1}$, respectively. Thus, a significant portion of the carriers traverse the sample with a supersonic velocity, and this velocity is damped with increasing temperature. Their second technique is based upon detailed knowledge of the Mott density in Si. They measured the PL kinetics of the EHP and free-exciton emissions in their undoped Si sample. They observe the EHP emission rises very quickly, whereas the free-exciton emission rises slowly, and peaks at time delays of 10–40 ns. The excitation pulse creates a dense EHP, 100 times greater than the Mott density in Si, and thus no free excitons are present. The Fermi pressure and density gradients cause an expansion of the EHP, and a concomitant reduction in the EHP density. As the density drops eventually free excitons will begin to form in those regions where the density is locally below the Mott density. This will continue until the entire EHP density is below the Mott density, and then free excitons will exist everywhere spatially. Since they have measured the time delay for the maximum free-exciton emission, and the Mott density is well known in Si, they are able to easily determine the expansion velocity of the EHP, and arrive at velocities of 8×10^6 to $1 \times 10^5 \text{ cm s}^{-1}$. Wolfe [535] also examined the transport of the EHP, only he used the direct, time-resolved PL imaging technique. He finds that the EHP has an initial average velocity of $1.7 \times 10^5 \text{ cm s}^{-1}$ at 25 K, increasing with decreasing temperature from 2×10^5 to $\sim 5 \times 10^5 \text{ cm s}^{-1}$ as the temperature is lowered from 50 to 3 K; however, he never observes a supersonic expansion velocity. His measured expansion velocities are considerably lower than those measured by Forchel et al. [536,574]. Wolfe argued that the expansion is intimately connected with the interaction between these charged carriers and high-frequency phonons, and is thus limited to the sound velocity, as was observed in the transport of the EHL in both Si and Ge. These results, which are at odds with one another, remain to be fully resolved.

Höpfel et al. [537] measured the simultaneous drift and diffusion of minority electrons in a p-type modulation-doped GaAs quantum well using the direct PL imaging, without time resolution. They found that the strong electron–hole Coulomb interaction causes the ambipolar transport of minority electrons such that there is a negative absolute mobility of electrons (i.e. the electrons drift with the holes to the negative pole of the contact). These cw measurements allowed determination of the drift length, and separate picosecond time-resolved measurements yielded the carrier lifetimes. The combination of these two results allows determination of the drift velocities ($v_d \tau_r = l_d$). Fig. 385 shows the

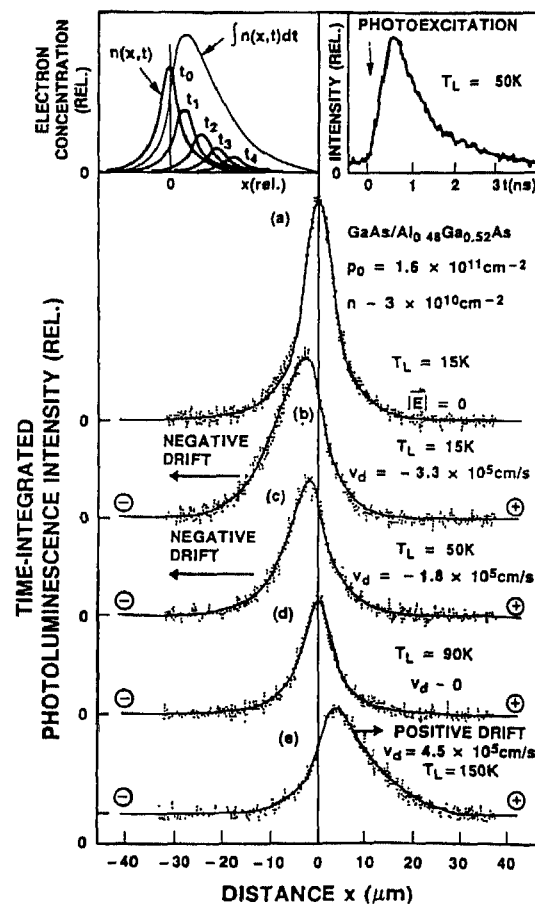


Fig. 385. Time-integrated PL images versus lattice temperature and electric field: (a) $T_L = 15 \text{ K}$, $E = 0$, (b) $T_L = 15 \text{ K}$, $E = 20 \text{ V cm}^{-1}$, (c) $T_L = 50 \text{ K}$, $E = 120 \text{ V cm}^{-1}$, (d) $T_L = 90 \text{ K}$, $E = 280 \text{ V cm}^{-1}$, and (e) $T_L = 150 \text{ K}$, $E = 600 \text{ V cm}^{-1}$. Solid black lines are calculated images. (After Höpfel et al. [537].)

time-integrated luminescence images for different lattice temperatures and electric fields. Image (a) shows, at low temperatures (15 K) and no applied electric field, that the spatial image is symmetric, indicative only of diffusion. The addition of an electric field (curve (b)) causes a shift of the image in the direction of the negative contact. This shift becomes smaller with increasing field (curve (c)) vanishing at 90 K, while at still higher temperatures (150 K) the shift is in the direction of the positive contact (curve (e)). PL images (b) and (c) demonstrate unambiguously that, under these conditions of low temperatures and small fields, electrons drift from the positive electrode toward the negative electrode, i.e. they have a negative absolute mobility. The physical mechanism responsible for these observed effects involves the strong momentum scattering of electrons by the high-density hole plasma, and the observed temperature dependence just reflects the competition between this momentum scattering and the relative electron and hole mobilities, including limiting scattering processes (i.e. ionized impurity scattering, etc.) which are all temperature dependent.

4.2.4. Exciton transport

In the time-resolved PL imaging experiments carried out by Gilliland et al. [538] and Wolford et al. [570] (described in section 4.2.2) they found that as they lowered the lattice temperature below 50 K the diffusion constants derived from their time-dependent spatial expansion (measured at the

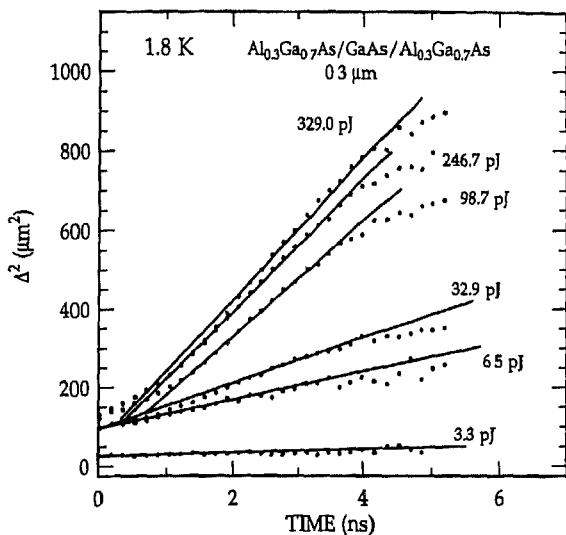


Fig. 386 Squared FWHM of the PL spatial distributions as a function of time versus laser excitation power [575].

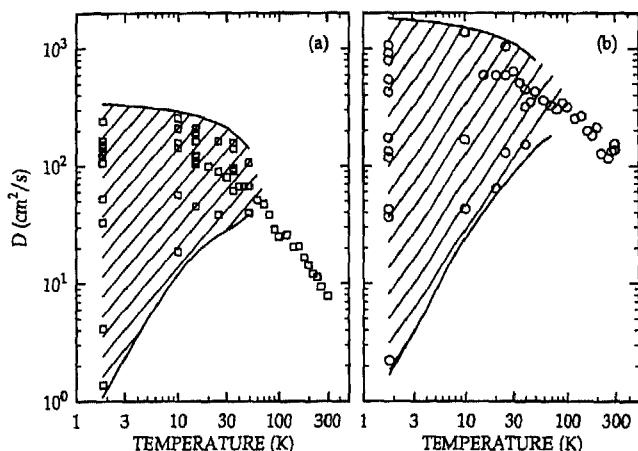


Fig. 387 Diffusivities versus temperature and laser excitation power for two bulk, OMVPE-prepared GaAs/AlGaAs double heterostructures [576].

peak of the free-exciton emission which becomes evident and eventually dominate at these temperatures) exhibited a laser excitation power dependence, which was absent above 50 K [575,576]. Fig. 386 shows the power dependence of the squared PL spatial distribution FWHM versus time. The slopes, which are proportional to the diffusion constant, clearly increase with increasing excitation power and are shown in Fig. 387. The extremely high diffusivities observed at 1.8 K of $\sim 1000 \text{ cm}^2 \text{ s}^{-1}$ are not inconsistent with those observed in other semiconductors, such as that by Trauernicht and Wolfe [577] in Cu₂O. Further, Gilliland et al. conclude that their observed diffusivities actually represent the joint transport of free excitons and free holes, since the excitation was above-gap and non-resonant, and the power dependence is indicative of the change in relative populations of free excitons and free carriers.

Temporally- and spatially-resolved PL measurements of the quasi-2D excitons responsible for H-band emission in nominally undoped GaAs heterostructures were employed by Gilliland et al. [578] to quantify the effects of the heterointerfacial roughness and bandbending on the transport of these

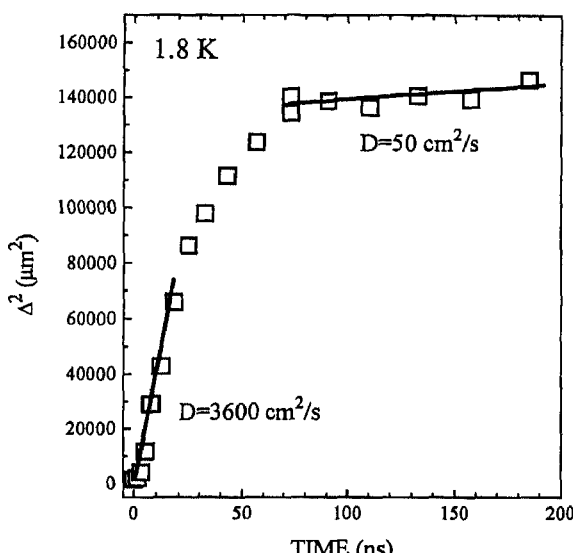


Fig. 388. Squared FWHM of the PL spatial distributions corresponding to the H-band emission versus time [578].

heterointerfacially-confined excitons. In their study they encountered a difficulty in accurately measuring the transport of these excitons, namely, as discussed in section 3.3.1, the H-band emission is not spectrally stationary but red-shifts with increasing time by as much as 30 meV. The difficulty was in choosing the correct spectral position to detect the H-band emission in their transport measurements. Their solution was to “spectrally window” almost the entire H-band emission (from 8200 to 8300 Å). In so doing they excluded the transport of free excitons as well as that of the carriers directly responsible for the band-to-acceptor emissions, both of which energetically bracket the H-band emission. Their results clearly show the macroscopic expansion of the quasi-2D excitons from a FWHM of 39 μm to almost 400 μm within their lifetime. The large spatial width of the H-band emission is attributed to the free excitons which rapidly diffuse (within the first few nanoseconds) and then evolve into the quasi-2D excitons. Fig. 388 shows the FWHM squared versus time derived from this spatial expansion data. The data are clearly not linear (as expected for diffusive transport). Nevertheless, an instantaneous diffusion constant may be deduced from the data—yielding $3600 \text{ cm}^2 \text{ s}^{-1}$ initially and $50 \text{ cm}^2 \text{ s}^{-1}$ at later times. The initial transport is much too rapid to be purely diffusive, and instead Gilliland et al. attribute it to the spatially non-uniform bandbending at the heterointerface which therefore gives rise to a lateral expansion force. In order to further understand these anomalous results, they measured the time- and space-resolved H-band emission, and from the temporally- and spatially-varying peak energy of the H-band emission—which was, in the context of their quasi-2D exciton model, directly related to the heterointerfacial bandbending—they deduce the lateral bandbending force. They find that this force becomes negligible after ~20 ns, which is consistent with the “saturation” in the expansion evident in Fig. 388. This is a very lucid demonstration of the power of these time- and space-resolved techniques for ascertaining the physical mechanisms behind the observed transport.

Hillmer et al. [545,546] made use of their opaque mask technique as a means of examining excitonic transport in GaAs/AlGaAs quantum wells. They demonstrated very effectively one of the most powerful aspects of the optical techniques for characterizing carrier transport; specifically, the ability to ascertain where the transport is occurring within the sample. Their samples consisted of several single quantum wells of varying width (i.e. a multiple quantum well sample). Thus, the unique spectral signature of each well allows distinctions to be drawn concerning the spatial location of the

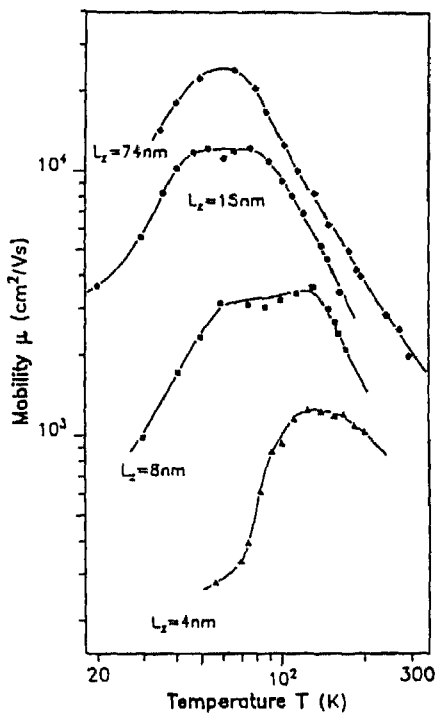


Fig. 389 Exciton mobilities in 2D GaAs/AlGaAs quantum wells versus temperature and quantum well width. Mobilities were obtained using measured diffusivities and the Einstein relation [546].

transport within the structure. After their detailed analysis of the PL kinetics of the emission from each quantum well, they deduce the diffusivities of the excitons as a function of temperature (importantly, they find that the obtained diffusivities do not depend on the size of the aperture in the mask). For the low excitation densities used, they are able to directly use the simple Einstein relation to convert measured diffusivities to mobilities, as shown in Fig. 389. Note the peak mobilities of $\sim 12\ 200\ \text{cm}^2\ \text{V}^{-1}\ \text{s}^{-1}$ at 70 K for the 15 nm quantum well. This data exhibits a clear dependence on both temperature and well width. The temperature dependence at high temperatures ($T > 70\ \text{K}$) is explained in terms of a combination of polar-optical scattering, barrier-alloy-disorder scattering, and acoustic-deformation-potential scattering. At low temperatures the strong thickness dependence is a result of interface roughness scattering, which may drastically reduce the excitonic mobility. In order to further elucidate the effects of heterointerfacial roughness on the 2D exciton transport, Hillmer et al. [547] examined the exciton transport in GaAs quantum wells grown continuously and GaAs quantum wells with growth interruption (which is known to smoothen the heterointerfaces). They found that heterointerfacial roughness-induced exciton scattering may be significantly reduced in quantum well samples grown with appropriate growth interruptions. They find that the excitonic lifetime, at all temperatures, is shorter in the growth-interrupted sample than the continuously-grown sample—possibly due to the unintentional incorporation of defects during the growth interruption which may cause non-radiative decay. In contrast, they find the exact opposite behavior for the deduced mobilities, i.e. mobilities at all temperatures are higher in the growth-interrupted sample. Specifically, with decreasing temperature mobilities rise in both samples, until at $\sim 70\ \text{K}$, the sample grown continuously begins to show a decrease in mobility, and the growth-interrupted sample saturates at a mobility of $4000\ \text{cm}^2\ \text{V}^{-1}\ \text{s}^{-1}$. In general they find that the mobility increases rapidly with increasing well width for both growth-interrupted and continuously grown quantum wells, however, growth interruption yields significantly

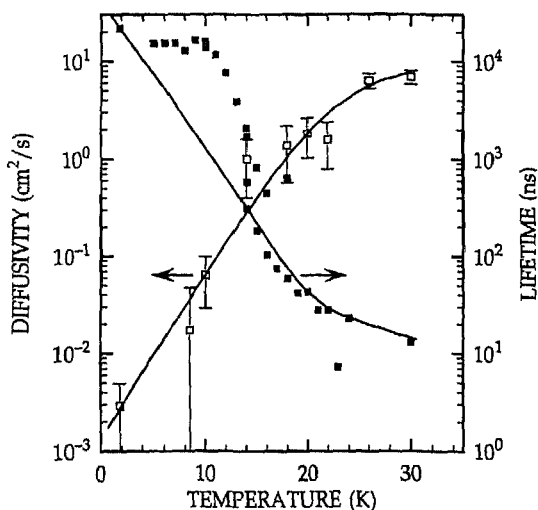


Fig. 390. Temperature dependence of measured diffusivities and PL lifetimes measured at the peak of the no-phonon emission line [460].

higher mobilities for well widths up to 75 nm. Takahashi et al. [548] also used the opaque mask technique to measure the lateral transport of excitons in a 5 nm MBE-prepared quantum well. In contrast to the work of Hillmer et al., they find that at temperatures below 20 K the exciton diffusion is enhanced, whereas at higher temperature their results agree qualitatively with those of Hillmer et al. They find, through Monte Carlo simulation of the classical transport model, that the observed transport is well explained with the excitons being thermally activated from localized to extended states which move with a velocity of $1.4 \times 10^6 \text{ cm s}^{-1}$. This yields an instantaneous mean-free-path of $1.4 \mu\text{m}$ which increases with decreasing excitation density, implicating exciton-exciton scattering as a possible contributing scattering mechanism. In total the results of exciton transport in GaAs quantum wells are not fully understood, and will require further work to elucidate many of the details of the transport. However, one thing is clear, namely, that exciton mobilities may be very high.

Recently, Gilliland et al. [460,579] took advantage of the sensitivity of the all-optical PL imaging technique to excitonic transport to quantify the transport of the “cross-interface” excitons in type-II GaAs/AlAs short-period superlattices. A novel feature of these experiments was the sensitivity of these excitons to the microscopic atomic structure of the heterointerfaces (i.e. interface roughness-induced potential disorder). This disorder can affect not only the electronic structure of these type-II nanostructures but also the transport of carriers along the heterointerfaces. Further, it has been postulated, based upon PL kinetics measurements versus temperature alone, that these excitons are localized at these potential fluctuations at low temperatures. In their experiments Gilliland et al. proved this hypothesis, and through detailed temperature studies showed the excitons are thermally activated to mobile states. Fig. 390 shows the lifetimes of the no-phonon emission line of a 30 Å/50 Å GaAs/AlAs superlattice at the emission peak energy as derived from the fits to the PL kinetics. Lifetimes were taken from the exponential long-time tail of the decays. This figure also shows their measured diffusivities of these type-II excitons versus temperature. At 1.8 K the diffusion constant is just $2 \times 10^{-3} \text{ cm}^2 \text{ s}^{-1}$, and increases monotonically to $\sim 10 \text{ cm}^2 \text{ s}^{-1}$ at 30 K. This is conclusive proof of the heretofore only postulated localization of the type-II excitons. In an effort to glean even more information from these data, they arrived at a microscopic model for the exciton transport in two dimensions along the heterointerfaces. The model was based upon essentially a two-dimensional random walk in a sea of randomly spaced “perfectly-absorbing” defects. Thus, as the diffusivity of the excitons increases they are more likely to encounter a non-radiative defect which will then quench the PL

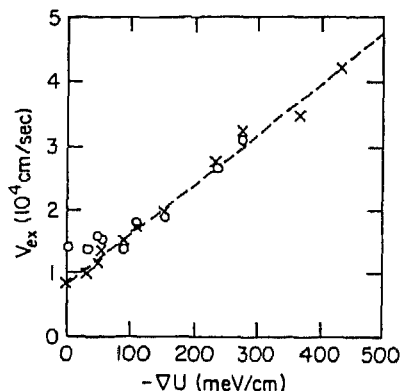


Fig. 391 Low-temperature (11 K) dependence of the exciton velocity on the strain-induced force. ○, average velocities for $50 \mu\text{m} < x < 150 \mu\text{m}$; ×, represent average velocities measured for $50 \mu\text{m} < x < 400 \mu\text{m}$ into the sample. The velocity at zero strain is due to diffusion [544].

intensity and shorten the observed lifetime. From a comparison of this model with the data they deduce the average density of non-radiative defects at the heterointerfaces, and obtain a value of $\sim 10^7 \text{ cm}^{-2}$. This corresponds to an average spacing between non-radiative point defects of $\sim 3 \mu\text{m}$. The diffusion length of the excitons, $L_d = \sqrt{D\tau}$, as derived from their kinetics and transport data is also $\sim 3 \mu\text{m}$, independent of temperature. This seems to indicate that these defects are indeed point defects, and perfectly absorbing, namely, the capture cross-section is the geometrical cross-section of the exciton itself.

Tamor and Wolfe [544] and Gourley and Wolfe [239] made some of the first measurements of free-exciton transport in semiconductors. Their spatial PL imaging experiments of free-exciton transport in ultrapure Si subjected to uniaxial stress, in order to create a strain gradient, reveal that the mobility of these excitons are very high, and that the temperature dependence and magnitude of the mobility is characteristic of acoustic-phonon scattering as the limiting factor governing the transport. The applied strain in the indirect bandgap semiconductor Si causes a reduction in the bandgap, and therefore a strain gradient will produce a force acting on the excitons. They were able to measure this strain gradient from the spectral shift of the free-exciton luminescence peak energy with distance into the crystal. They found that they were able to vary this strain-induced force up to 0.5 eV cm^{-1} . Time-resolved measurements of this same sort allowed determination of the exciton velocity as a function of applied stress, as shown in Fig. 391. The velocity obtained at zero stress was attributed to diffusion, with an exciton diffusion constant of $D = 100 \text{ cm}^2 \text{ s}^{-1}$. The momentum relaxation time was obtained from the slope of the data in this figure, and then repeated as a function of temperature. They find that the relaxation time decreases with increasing temperature as $T^{-3/2}$. At 1.3 K the free-exciton mobility is $4 \times 10^6 \text{ cm}^2 \text{ V}^{-1} \text{ s}^{-1}$. This conclusively shows that even "heavy" particles such as free-excitons in Si ($m = 0.45m_0$) may have extremely high mobilities.

4.2.5. Biexciton transport

Gourley and Wolfe [238] carefully examined the thermodynamics of excitonic molecules in Si. In thermal equilibrium there is a definite temperature-dependent relationship between the densities of free-excitons and excitonic molecules. Thus, while the intensity of the luminescence is proportional to the density of excitons or excitonic molecules, the spatial distribution of such luminescence provides an even more careful check of the thermodynamic relationship between the respective densities of free-exciton and biexciton species. Fig. 392 shows the cw spatial distribution of the luminescence originating from the free excitons and biexcitons in ultrapure Si at 4.5 K. Here the carriers are confined

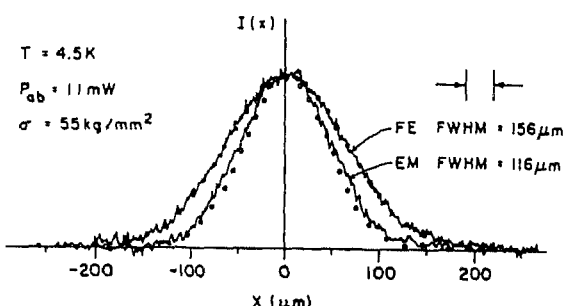


Fig. 392. Spatial profiles of the excitonic molecule and free exciton distributions at 4.5 K [238].

in a parabolic strain potential well with the application of uniaxial stress in a Hertzian stress geometry. Clearly the biexciton distribution is narrower than that of the free excitons. They find that a Gaussian lineshape fits the free-exciton spatial distribution, whereas a squared Gaussian lineshape closely mimics the biexciton spatial profile. This is excellent proof of the thermodynamic equilibrium between these two excitonic species.

In this same vein, Kim et al. [234] used the direct, time-resolved PL imaging technique to examine the thermodynamics of biexcitons in a GaAs quantum well. Just as in Si, they find strong evidence for the thermal and chemical equilibrium of excitonic and biexcitonic species. However, they have taken advantage of space- and time-resolved measurements to show the interdependence between these two parameters of phase space which define the relevant densities in the system. The "law of mass action" in two dimensions implies that

$$\frac{n_x^2}{n_{xx}} = g \left[\frac{1}{2\pi\hbar^2} \frac{m_x^2}{m_{xx}} \right] (kT_E) e^{(-\phi_{xx}/kT_B)} \quad (73)$$

where g is the effective degeneracy factor, ϕ_{xx} is the binding energy of the biexciton with respect to two unbound excitons, and T_E is the exciton temperature. This shows explicitly the temperature-dependent relationship between the exciton and biexciton densities. Kim et al. measured the time-dependent excitonic and biexcitonic luminescence profiles, and find, just as with Si discussed above, that the biexcitonic spatial distribution is always narrower than that of the free excitons. For chemical equilibrium, there is a $\sqrt{2}$ relationship between the spatial FWHMs of the respective excitonic and biexcitonic distributions. Kim et al. found, after appropriate deconvolution, that this is indeed observed. Thus, fast interconversion between excitons and biexcitons allows the two species to reach thermal and chemical equilibrium very quickly. From the time dependence of the luminescence spatial profiles they deduce diffusion constants for the excitons and biexcitons, and conclude that the exciton diffusion constant is $14 \text{ cm}^2 \text{ s}^{-1}$. Further, and more importantly, they find that the spatial distribution relationship dictated by the law of mass action holds at all times. This indicates that chemical equilibrium is maintained throughout the diffusive expansion of the excitonic and biexcitonic gas.

4.2.6. Electron-hole liquid transport

Perhaps the best and most famous example of the use of optical techniques to characterize the transport of carriers in semiconductors is that of the EHL in Si and Ge. Wolfe's group at the University of Illinois performed the seminal experiments in this field using their PL imaging technique. They demonstrated the motion of the EHL, its coupling to the "phonon wind", and the anisotropy of the droplet motion. Greenstein and Wolfe [580] measured the infrared luminescence from the cloud of electron-hole droplets and connected the formation of the electron-hole cloud with phonons. The

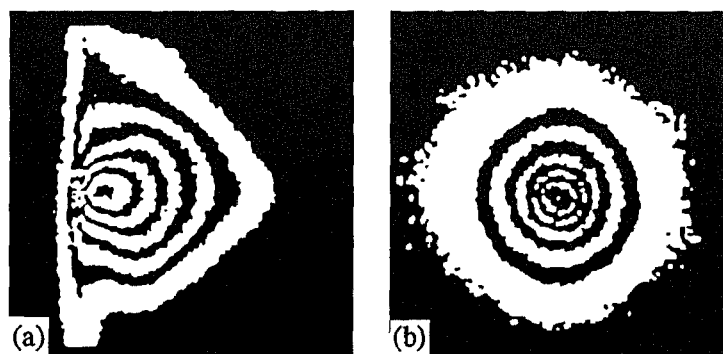


Fig. 393 PL images of the EHL emission in Si. Image of the (a) side view (b) face view is presented as a contour map. Both images are 600 μm edge-to-edge. (After Tamor and Wolfe [581].)

high-density of the EHL in Si ($3.3 \times 10^{18} \text{ cm}^{-3}$) causes the lifetime of the EHL to be short, 140 ns, yielding an electron–hole droplet cloud that is small and weakly luminescent. Fig. 393 shows a contour map of the luminescence from the side of a Si crystal after laser excitation from the left side of the crystal [581]. This data clearly shows that the maximum EHL luminescence intensity occurs $\sim 50 \mu\text{m}$ from the surface of the sample and that the shape of the droplet cloud is anisotropic. Slit scans of these PL images yield the average pair density in the electron–hole droplet cloud as $n_{\text{avg}} = N/\Delta$, where Δ is the FWHM of the PL image and N is the total number of pairs in the droplet. Laser excitation power dependence measurements show a linear increase in average pair density at low powers and a saturation in the pair density at higher powers due to the expansion of the cloud of droplets. They deduce an average droplet velocity of $(1.2\text{--}7.5) \times 10^4 \text{ cm s}^{-1}$, increasing with increasing excitation power. The anisotropy evident in the image shown above suggests the existence of phonon focusing, namely the channeling of slow TA phonons along the $<100>$ axis. Tamor and Wolfe [543] performed the same measurements as described above for free excitons in Si under a strain gradient for the EHL in Si, and determined the drift velocity of the electron–hole droplets over a range of applied strains. They observe a saturation in the drift velocity at velocities just below the sound velocity which is indicative of a strong increase in damping. They interpret their results as consistent with a Cherenkov-type emission of phonons leading to a “sound barrier” for the droplet velocity.

4.3. Characterization of structures

Spatial imaging of the luminescence from semiconductors and semiconductor nanostructures naturally lends itself to the characterization of the geometrical aspects of size, uniformity, defect distribution, and carrier transport. Each of the spatial imaging techniques described above has been used to characterize various aspects of the spatial properties of semiconductors and semiconductor structures, but perhaps none has had, or is expected to have, as much impact as that of the near-field technique. This technique is especially well suited to the measurement of the luminescence from semiconductor nanostructures. The advent of new low-dimensional semiconductor structures (quantum wires and dots) and the technological need for a non-invasive and non-destructive probe of semiconductor wafers has and will continue to drive the application of spatially-resolved PL spectroscopy. Here, a brief review of some of this work will be given.

4.3.1. Wafer topography

The technological need for thorough characterization of semiconductor wafers utilized in the production of integrated circuits has driven the application of optical imaging of semiconductor wafers. Non-uniformities in dislocation defects, intrinsic defects, and electrically active impurities are all

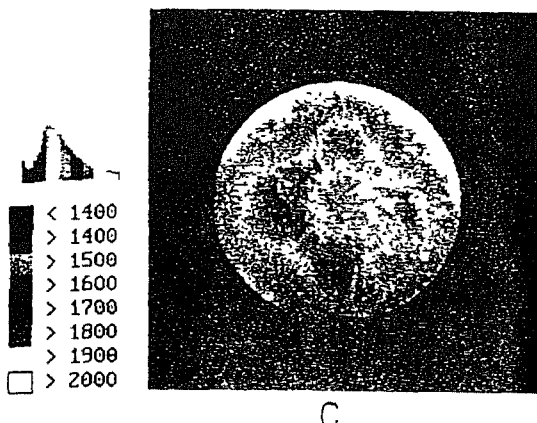


Fig. 394. PL topographic image of GaAs wafer. Here the intensity corresponds to a detected wavelength of 832 nm. (After Steiner et al. [539].)

critical to the fabrication of semiconductor devices on semiconductor wafers. Throughout this article it has been shown that PL spectroscopy is especially well suited to the identification of impurities in semiconductors. With this in mind, Steiner et al. [539] Wang et al. [541,582] and Rühle and Leo [540] have developed PL topography systems with a variety of capabilities. Steiner et al. attempted to correlate the PL images of their wafers with the EL2 absorption spectra across the wafers. Fig. 394 shows the PL image of a wafer of GaAs of 75 mm diameter. The PL imaged here was centered at 832 nm in the vicinity of the DAP emission. The spatial variation in DAP emission intensity is attributed to the variation in spatial distribution of deep recombination centers. Through comparisons of this PL image with the absorption image corresponding to the EL2 center they conclude that this deep center is not EL2 due to the lack of correlation in spatial intensity maps. Wang et al. [582] measured the topography of the near-edge emissions—(F,X), (D⁰,X), (D⁰,h⁰), (A⁰,X), (e,A⁰), and DAP—in an epilayer of bulk GaAs in order to ascertain the spatial distributions across the wafer of the impurities responsible for each of these emissions. Fig. 395 shows the topograms for most of these transitions. The free-exciton emission in the GaAs epilayer is very homogeneous, which is in strong contrast to that observed in the GaAs substrate. The donor-related near-edge emissions show several bright spots, indicative of a locally-high donor concentration. In contrast the acceptor-related emissions are more strongly spatially varying (as seen in the line scan), and this is reflected in the DAP emission as well. Although not fully understood, these results show that the non-uniformity of impurities and defects in the substrate seem to affect that of epilayers grown on the substrate, at least for acceptors. Wang et al. [541] extended this work to include PL kinetic topography since the cw PL topograms are not sufficient to extract impurity concentrations across the wafer. This is due to the complications introduced by competing non-radiative transitions which may also vary across the wafer. Their technique involved the spatial mapping of the cw PL from the sample and the subsequent correlation between the carrier temperature (derived from the slope of the high-energy tail of the PL emission) and the carrier lifetime. They find that the spatial variation in the measured PL intensity is controlled by the spatial variation of deleterious non-radiative decay processes and not a spatial variation in radiative efficiency. In this vein, Rühle and Leo measured the PL kinetics across an undoped semi-insulating GaAs wafer using a two-dimensional Streak camera with picosecond resolution. They find that in their sample there is a strong, almost periodic, variation in lifetime (by a factor of two) over distances of 300 μm . They also monitored the PL intensities of several near-edge emissions together with several deep, near-infrared emissions. They find that the emission intensity of one of the near-infrared emissions (at 0.8 eV) is strongest when the lifetime of free carriers is shortest, and thus the center responsible for this emission

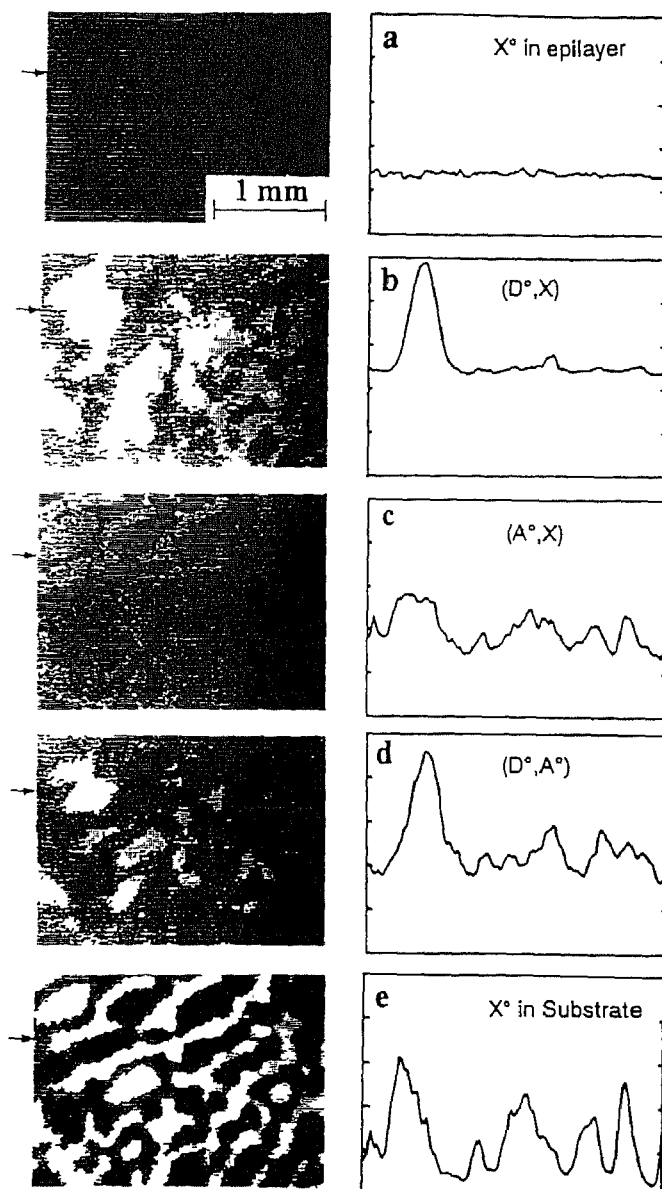


Fig. 395. PL topographic images and line scans of various near-edge transitions at a lattice temperature of 2 K. (a)–(d) are epitaxial layer images of X , (D°, X) , deconvoluted (A°, X) , and (D°, A°) , (e) is a PL image of the free-exciton transition in the Si GaAs substrate. (After Wang et al [582].)

may be an effective non-radiative trap for free carriers. This level may be the Shockley–Read–Hall deep level which “shunts” the radiative decay of free carriers.

4.3.2. Nanostructures

This past year one of the most dramatic examples of PL spatial imaging from semiconductors was published. Hess et al. [583] used the near-field optical technique to measure the excitonic emission from a GaAs/AlGaAs multiple quantum well sample at liquid helium temperatures and in magnetic fields up to 8 Tesla. Fig. 396 shows a comparison of the PL spectrum from their sample (in the spectral

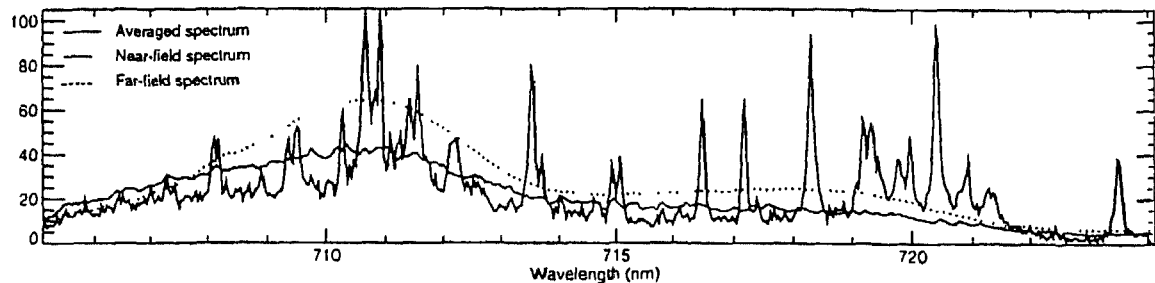


Fig. 396. 2 K PL spectra from a 23 Å GaAs/AlGaAs quantum well after excitation at 696 nm in the near-field, far-field, and spatially averaged near-field (Reprinted with permission from *Science*, 264 (1994) 1740 Copyright 1994 American Association for the Advancement of Science) [583].

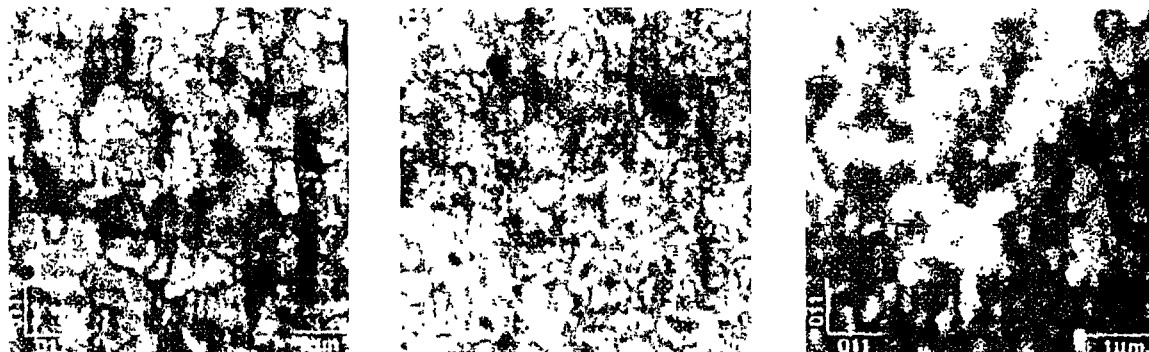


Fig. 397 Near-field PL images from (a) a 23 Å quantum well grown at 610 °C, (b) a 31 Å quantum well in the same sample and same region as (a), and (c) a 27 Å quantum well grown on a different substrate at 650 °C. (Reprinted with permission from *Science*, 264 (1994) 1740. Copyright 1994 American Association for the Advancement of Science) [583].

vicinity of the 23 Å quantum well) in the far-field and near-field regimes. The near-field spectrum exhibits a forest of very sharp emission lines (<0.07 meV in width) whose average overlaps nicely with that obtained in the far-field spectrum. Each of these narrow emission lines is identified as due to the emission from an individual, three dimensionally-confined, quantum state, strongly suggesting the localized nature of the excitons involved in the recombination process. This is more spectacularly shown in the x - y spatial map of the luminescence from several quantum wells, as shown in Fig. 397. Part (a) of this figure corresponds to the near-field PL image of a 23 Å quantum well grown at 610 °C, part (b) to a 31 Å quantum well in the same sample, and part (c) to a 27 Å quantum well grown at 650 °C. The intensity variations evident in part (b) are similar to those observed in the same sample, part (a). This shows that the well-thickness variations which cause the localization of the excitons is well correlated between the two quantum wells in this multiple quantum well sample. The sample grown at higher temperatures, and without growth interrupts (in contrast to the sample in parts (a) and (b)), shown in part (c), displays smaller and more gradual spatial variations, thus indicating that higher growth temperatures suppress the large-length scale fluctuations but maintain the small-scale atomic structure responsible for the localization of these 2D excitons.

Brunner et al. [584] recently conducted a study of the microscopic variations in spatially- and spectrally-resolved PL and PLE intensities of a GaAs/AlGaAs quantum well sample grown with growth interruptions. Their sample was mounted in a cold-finger He-flow cryostat on an xyz translation stage with positioning accuracy of $\sim 50 \mu\text{m}$. The excitation laser was focused onto the sample with a microscope objective with numerical aperture N.A. = 0.55. The resulting luminescence had an effective probe size of approximately $1.5 \mu\text{m}$. Fig. 398 shows the PL spectra of their sample with growth

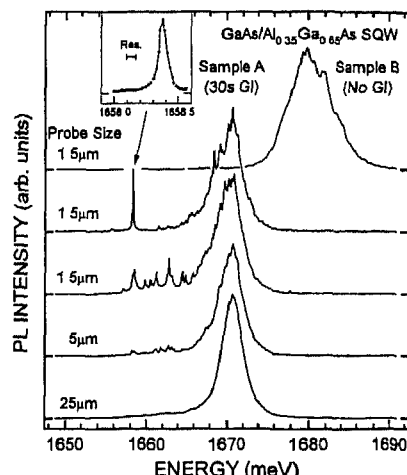


Fig. 398 PL spectra of a GaAs/Al_{0.35}Ga_{0.55}As quantum well for various probe sizes ranging from 1.5 to 25 μm . Inset shows one of the sharp emission lines with a spectral width of 0.07 meV (After Brunner et al. [584].)

interrupts (sample A) with various probe sizes varying from 25 μm down to 1.5 μm together with their control sample which was grown without growth interrupts (sample B). Just as was the case for the near-field spectroscopy of excitons in a quantum well, presented above, the smallest probe sizes used here also yield extremely fine structure in the spectra which is not evident with larger probe sizes. These sharp lines are also absent in the sample grown without interrupts, and thus the growth interrupts appear to increase the bandgap fluctuations (well-width fluctuations) which cause the localization of the excitons. Brunner et al. were also able to map out the spatial non-uniformity of the exciton emission in their quantum wells over a distance scale of several microns. They find, just as with the near-field measurements, that there exists a strong spatial inhomogeneity across the sample.

Grober et al. [585] used the NSOM technique to show spectacular PL images from quantum wires grown via cleaved-edge overgrowth of a quantum well sample. Fig. 399 shows the far-field spectrum of their sample (part a), and the spatial variation of the Wire (b), SQW (c), and MQW (d) peaks. Each of the images corresponds well with the known structure of the sample, shown as solid lines in the figures. The quantum wire emission is clearly strongest at the intersection of the MQW region and the SQW region, whereas the MQW and SQW regions exhibit strong luminescence in the appropriate spatial position. These images were taken over a range of $2 \times 2 \mu\text{m}^2$ with a lateral resolution of 0.1 μm . Note that the MQW and SQW luminescence is quenched at their intersection, i.e. the location of the quantum wires. Also the quantum wire luminescence is 6 \times greater than the MQW emission. This is clear evidence for the spatial and spectral diffusion of carriers from the quantum wells into the quantum wires.

Zrenner et al. [542] approached the issue of quantum well width fluctuations from a conceptually different perspective than others. Based upon the recent evidence for a distribution of length scales for the heterointerfacial roughness and the localization of the excitons at this interfacial disorder, they treat their narrow quantum well samples as a disordered array of quantum dots with arbitrary dimensions. They examined an electric-field tunable coupled quantum well system in which both the direct and indirect transitions are observable. Using a technique similar to that reported above by Brunner et al. [584] they observe very sharp emission lines in the emission spectrum when a small excitation spot (2 μm) is used, and a broad, relatively featureless, emission for larger spot sizes. Interestingly, they only observe these sharp features in the emission of the indirect line. Further, they find that the amount of structure evident in this line is strongly dependent on external bias, as shown in Fig. 400.

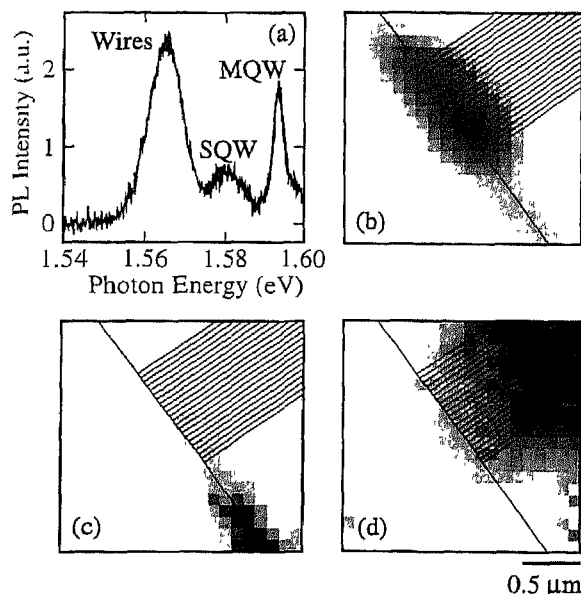


Fig. 399. (a) Far-field PL spectrum showing emission from the multiple quantum well, single quantum well, and quantum well wire regions. (b)–(d) PL images obtained by monitoring the emissions corresponding to the wire, single quantum well, and multiple quantum well spectral regions, respectively. Superimposed is a schematic showing the orientation of the epilayers. (After Grober et al. [585].)

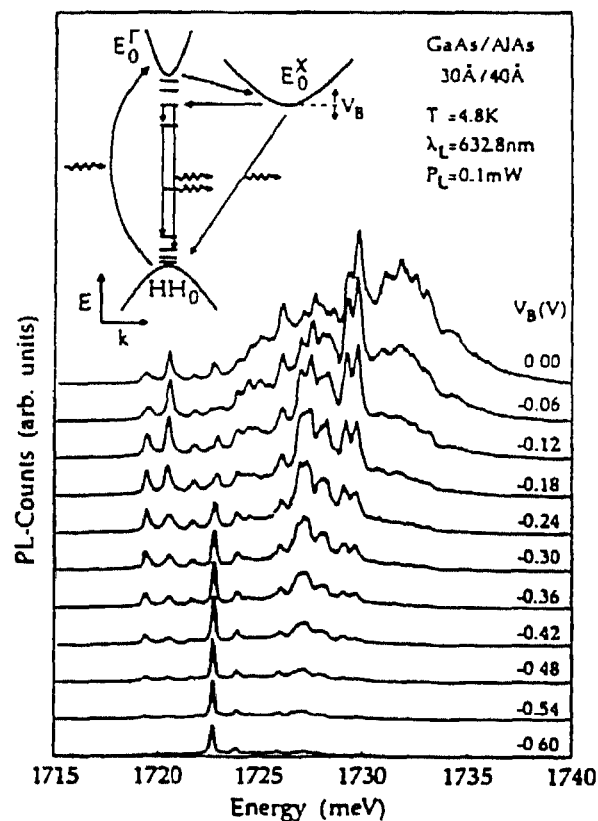


Fig. 400. PL spectra versus externally applied bias in the indirect regime. The diameter of the optically probed area is 2 μm. Inset shows a schematic diagram of the relevant emission and relaxation processes. (After Zrenner et al. [542].)

Note that there is no Stark shift evident for these sharp lines. This indicates that the origin of these sharp lines cannot be associated with a real- and momentum-space indirect recombination process, but instead must originate from zero-dimensional states in the local potential minima of the GaAs quantum well. Essentially, the X states of the AlAs layers act as reservoirs which may populate the interfacial quantum dots, and the coupling between these levels is voltage tunable. For large energetic separations between these levels only the deepest quantum dot potentials may be populated and the spectra correspondingly simplify. Zrenner et al. further used their high-resolution spectroscopy of the interfacial disorder to map out this in-plane disorder over a $45 \mu\text{m} \times 36 \mu\text{m}$ area of the structure. They find that the direct emission line is invariant to the position on the sample, but that the structure and intensity of these sharp emission lines are sensitive to both the lateral position and external bias. Their data show that the well width fluctuations, which form the quantum dots, occur on a broad distribution of length scales, however, a detailed analysis of their results remains to be done.

5. Conclusions

In the preceding chapters the basis, utility, and accuracy of PL spectroscopies has been demonstrated, primarily through examples. It has been shown that cw PL spectroscopy is useful in characterizing semiconductors with regard to impurity type and concentration, uniformity, quantum-confinement dimensions and disorder, electronic phase transitions, and the affects various external perturbations may have on the electronic structure of semiconductors and semiconductor nanostructures. In section 3 time-resolved PL spectroscopy was discussed in relation to how this powerful technique augments the capabilities of conventional cw PL spectroscopy. In particular, this technique quantitatively determines oscillator strengths, bulk non-radiative decay, non-radiative surface recombination, and disorder. Analysis of these results may be used to yield information regarding the spatial location of carriers which recombine, their spatial extent, and the cooling of "hot" carriers, among a wide variety of other phenomena. In section 4 the relatively new addition to the class of PL spectroscopic techniques of spatially-resolved PL was discussed. These techniques are continually evolving in complexity and resolution, and are on the forefront of all physics research today. In this section, the ability of spatially- and temporally-resolved PL spectroscopy to accurately quantify carrier, and, importantly, exciton transport was demonstrated in a variety of semiconductor systems. Further, the spatial discrimination was shown to provide a powerful tool for the characterization of semiconductor nanostructures and quantification of their lateral dimensions. Lastly, topographical information was shown to be readily obtainable from such spectroscopic techniques.

All of these spectroscopic techniques are extremely powerful in their ability and flexibility to measure various physical phenomena or constants in semiconductors, and all are still evolving and being used ubiquitously throughout not only the semiconductor community, but throughout biology, chemistry, physics, and engineering disciplines. Nonetheless, this class of spectroscopy (PL), as I have defined and used here, will always need to supplement or be supplemented by other spectroscopic techniques in order to gain a full understanding of the dynamics and structure of semiconductor structures. In the following a brief description of a few other techniques which are important and useful in characterizing semiconductors is given (note this is not intended to be an exhaustive list or to provide an exhaustive description—the reader is urged to consult the appropriate references for further information, as this is beyond the scope of this article).

5.1. Cathodoluminescence

Cathodoluminescence is the process of generating luminescence through the injection of electrons, most commonly from an e-beam source. The high resolution of the electron-beam source together with the ability to scan the source allows for the direct spatial mapping of the luminescence properties topographically with up to 300 nm resolution (for a 5 kV source) [586]. This is useful, and has been demonstrated [586,587] to yield information regarding the atomic-scale fluctuations at heterointerfaces in quantum well structures. An important limitation to the resolution of this technique is imposed by the possible migration of the injected charge, and care must be exercised in analysis of data obtained using this technique due to this effect.

5.2. Cross-sectional STM excited luminescence

The advent of scanning tunneling microscopy (STM) has revolutionized many aspects of microscopy, and even spectroscopy, as discussed in section 4. Recently, this technique has been demonstrated as effective in its ability to spatially map out the energy bandstructure of semiconductor heterostructures. Renaud and Alvarado [588] used this concept to map out the heterostructure bandbending profile and band offsets of a $\text{Al}_x\text{Ga}_{1-x}\text{As}$ heterostructure with nanometer resolution. Their technique involves the excitation of luminescence through the injection of electrons from the tip of a STM. This process occurs in three steps: (i) vacuum tunneling from the STM tip to the semiconductor surface, (ii) transport of the injected electrons into the bulk of the semiconductor, and (iii) radiative recombination of the injected electrons with residual holes. This local probe of the luminescence properties of semiconductors and semiconductor nanostructures is useful in determining conduction-band discontinuities, band bending, the width of the depletion region, and the energy of the quantized levels within a single quantum well. This powerful microscopic technique will undoubtedly become more prevalent in the near future.

5.3. Pump-probe coherent spectroscopy

There are many different varieties of time-resolved pump-probe spectroscopy. Among them are differential transmission measurements, differential reflection measurements, degenerate and non-degenerate four-wave mixing measurements, hole burning, free-induction decay measurements, and photon echo measurements. Each of these measurements is sensitive to the changes in the properties of a semiconductor induced by photoexcitation (of real or virtual carriers). Much work has been done using these techniques to characterize the properties of semiconductors. Some of the most important of these measurements are: (1) Schultheis et al.'s [589] and Leo et al.'s [590] measurements of the phase coherence and orientational relaxation of excitons in GaAs using the degenerate four-wave mixing technique; (2) Hegarty and Sturge's [591] studies of exciton localization in quantum well structures using hole burning and four-wave mixing techniques; and (3) Mycek et al.'s [592] measurements of the free-induction decay of excitons in GaAs quantum wells, to name just a few. These techniques yield a wealth of information about many complex phenomena, including many-body effects, and often the analysis of the data is very involved.

Acknowledgements

I would like to thank the many people who assisted me in writing this article. First, I would like to thank Dr T.F. Kuech for inviting me to write this review article. Second, I would like to thank Dr L.P. Fu, Dr K.K. Bajaj, Dr L.M. Smith, Dr G.A. Northrop, Dr H.P. Hjalmarson, and Dr D.J. Wolford for sharing their deep knowledge of the field, reviewing the manuscript, and assistance in finding

references. I would also like to thank Ms Connie Copeland for her immense efforts assisting in the writing of letters for figure reproduction permission. Lastly, I want to thank my wife, Marcy, and children for their patience with me during the time in which I have been working on this review article.

References

- [1] C. Weisbuch and B. Vinter, *Quantum Semiconductor Structures*, Academic Press, New York, 1991.
- [2] R. Cingolani and K. Ploog, *Adv. Phys.*, **40** (1991) 535.
- [3] L. Esaki and L.L. Chang, *Phys. Rev. Lett.*, **33** (1974) 495.
- [4] R. Dingle, W. Wiegmann and C.H. Henry, *Phys. Rev. Lett.*, **33** (1974) 827.
- [5] M. Asada, Y. Miyamoto and Y. Suematsu, *IEEE J. Quantum Electron.*, **QE-22** (1986) 1915.
- [6] H. Barry Bebb and E.W. Williams, in R.K. Willardson and A.C. Beer (eds.), *Semiconductors and Semimetals*, Vol. 3, Academic Press, New York, 1967, p. 181.
- [7] J.I. Pankove, *Optical Processes in Semiconductors*, Dover Publications, New York, 1971.
- [8] S. Perkowitz, *Optical Characterization of Semiconductors*, Academic Press, London, 1993.
- [9] K.K. Smith, *Thin Solid Films*, **84** (1981) 171.
- [10] E.S. Koteles and J.Y. Chi, *Phys. Rev.*, **B37** (1988) 6332.
- [11] D.J. Wolford, G.D. Gilliland, T.F. Kuech, L.M. Smith, J. Martinsen, J.A. Bradley, C.F. Tsang, R. Venkatasubramanian, S.K. Ghandhi and H.P. Hjalmarson, *J. Vac. Sci. Technol.*, **B9** (1991) 2369.
- [12] P. Lautenschlager, M. Garriga, S. Logothetidis and M. Cardona, *Phys. Rev.*, **B35** (1987) 9174.
- [13] A. Manoogian and A. Leclerc, *Phys. Status Solidi B*, **93** (1979) K23.
- [14] D.L. Dexter and R.S. Knox, *Excitons*, Wiley-Interscience, New York 1965.
- [15] R.J. Elliot, Theory of Excitons I, in C.G. Kuper and G.D. Whitfield (eds.), *Polarons and Excitons*, Plenum, New York, 1963, p. 269.
- [16] J.O. Dimmock, in R.K. Willardson and A.C. Beer (eds.), *Semiconductors and Semimetals*, Vol. 3, Academic Press, New York, 1967, p. 270.
- [17] D.C. Reynolds and T.C. Collins, *Excitons: Their Properties and Uses*, Academic Press, New York, 1981.
- [18] M.D. Sturge, *Phys. Rev.*, **127** (1962) 768.
- [19] D.D. Sell, *Phys. Rev.*, **B6** (1972) 3750.
- [20] M.A. Gillego, D.E. Hill and F.V. Williams, *Bull. Am. Phys. Soc.*, **12** (1967) 656.
- [21] M. Heiblum, E.E. Mendez and L. Osterling, *J. Appl. Phys.*, **54** (1983) 6982.
- [22] M.T. Ramsbey, I. Szafranek, G. Stillman and J.P. Wolfe, *Phys. Rev.*, **B49** (1994) 16427.
- [23] G.S. Elman, E.S. Koteles, S.A. Zemon and J.Y. Chi, *J. Vac. Sci. Technol.*, **B7** (1987) 57.
- [24] E.S. Koteles, B.S. Elman and S.A. Zemon, *Solid State Commun.*, **62** (1987) 703.
- [25] D.D. Sell, S.E. Stokowski, R. Dingle and J.V. DiLorenzo, *Phys. Rev.*, **B7** (1972) 4568.
- [26] E.S. Koteles, J. Lee, J.P. Salerno and M.O. Vassell, *Phys. Rev. Lett.*, **55** (1985) 867.
- [27] J. Lee, E.S. Koteles, M.O. Vassell and J.P. Salerno, *J. Luminesc.*, **34** (1985) 63.
- [28] D.J. Wolford, G.D. Gilliland, T.F. Kuech, J. Martinsen, J.A. Bradley, C.F. Tsang, R. Venkatasubramanian, S.K. Ghandhi, H.P. Hjalmarson and J. Klem, *Inst. Phys. Conf. Ser.*, **120** (1992) 401.
- [29] G.D. Gilliland, L.M. Smith, T.F. Kuech, J. Martinsen, J.A. Bradley, D.J. Wolford, R. Venkatasubramanian, S.K. Ghandhi, H.P. Hjalmarson and J. Klem, unpublished work.
- [30] W.L. Bloss, E.S. Koteles, E.M. Brody, B.J. Sowell, J.P. Salerno and J.V. Gormley, *Solid State Commun.*, **54** (1985) 103.
- [31] R. Dingle, C. Weisbuch, H.L. Stormer, H. Morkoc and A.Y. Cho, *Appl. Phys. Lett.*, **40** (1982) 507.
- [32] G.D. Gilliland, D.J. Wolford, T.F. Kuech, J.A. Bradley and H.P. Hjalmarson, *J. Appl. Phys.*, **73** (1993) 8386.
- [33] J.M. Calleja, A.R. Goni, J.S. Weiner, B.S. Dennis, A. Pinczuk, L.N. Pfeiffer and K.W. West, in D.J. Lockwood and Aron Pinczuk (eds.), *Optical Phenomena in Semiconductor Structures of Reduced Dimensions*, Kluwer, London, 1992, p. 267.
- [34] D. Gershoni, J.S. Weiner, E.A. Fitzgerald, L.N. Pfeiffer and N. Chand, in D.J. Lockwood and Aron Pinczuk, *Optical Phenomena in Semiconductor Structures of Reduced Dimensions*, Kluwer, London, 1992, p. 337.
- [35] E.S. Koteles and J.Y. Chi, *Superlatt. Microstruct.*, **2** (1986) 421.
- [36] I. Brener, M. Olszakier, E. Cohen, E. Ehrenfreund, A. Ron and L. Pfeiffer, *Phys. Rev.*, **B46** (1992) 7927.
- [37] B.J. Skromme, C.J. Sandroff, E. Yablonovitch and T. Gmitter, *Appl. Phys. Lett.*, **51** (1987) 2022.
- [38] B. Fischer and H.J. Stoltz, *Appl. Phys. Lett.*, **40** (1982) 56.
- [39] D.C. Reynolds, D.C. Look, D.N. Talwar, G.L. McCoy and K.R. Evans, *Phys. Rev.*, **B51** (1995) 2572.
- [40] B. Sermage and M. Voos, *Phys. Rev.*, **B15** (1977) 3935.
- [41] K. Aoki, T. Kinugasa and K. Yamamoto, *Phys. Lett.*, **72A** (1979) 63.
- [42] S.I. Pekar, *Sov. Phys. JETP*, **6** (1958) 785.
- [43] J.J. Hopfield, *Phys. Rev.*, **112** (1958) 1555.
- [44] T. Steiner, M.L.W. Thewalt, E.S. Koteles and J.P. Salerno, *Phys. Rev.*, **B34** (1986) 1006.
- [45] C. Weisbuch and R.G. Ulbrich, *Phys. Rev. Lett.*, **39** (1977) 654.

- [46] P.J. Dean, J.R. Haynes and W.F. Flood, *Phys. Rev.*, **161** (1967) 711.
- [47] P. Mc Colley and E.C. Lightowers, *Semicond. Sci. Technol.*, **2** (1987) 157.
- [48] M.L.W. Thewalt and W.G. McMullan, *Phys. Rev.*, **B30** (1984) 6232.
- [49] M.A. Vouk and E.C. Lightowers, *J. Phys.*, **C10** (1977) 3689.
- [50] G.S. Mitchard and T.C. McGill, *Phys. Rev.*, **B25** (1982) 5351.
- [51] I. Pelant, J. Dian, J. matouskova, J. Valenta, J. Hala, M. Ambroz, M. Vacha, V. Kohlova, K. Vojtechovsky and K. Kaslik, *J. Appl. Phys.*, **73** (1993) 3477.
- [52] C. Weisbuch, R.C. Miller, R. Dingle, A.C. Gossard and W. Wiegnann, *Solid State Commun.*, **37** (1981) 219.
- [53] G. Bastard, C. Delalande, M.H. Meynadier, P.M. Frijlink and M. Voos, *Phys. Rev.*, **B29** (1984) 7042.
- [54] D. Bimberg, D.E. Mars, J.N. Miller, R.K. Bauer and D. Oertel, *J. Vac. Sci. Technol.*, **B4** (1986) 1014.
- [55] D. Bimberg, D.E. Mars, J.N. Miller, R. Bauer, D. Oertel and J. Christen, *Superlatt. Microstruct.*, **3** (1987) 79.
- [56] R. Köhrbrück, S. Munnix, D. Bimberg, E.C. Larkins and J.S. Harris, Jr., *Appl. Phys. Lett.*, **54** (1989) 623.
- [57] Ch. Maierhofer, S. Munnix, D. Bimberg, R.K. Bauer, D.E. Mars and J.N. Miller, *Appl. Phys. Lett.*, **55** (1989) 50.
- [58] Ch. Maierhofer, S. Munnix, D. Bimberg, R.K. Bauer, D.E. Mars and J.N. Miller, *Appl. Phys. Lett.*, **55** (1989) 50.
- [59] R. Köhrbrück, S. Munnix, D. Bimberg, E.C. Larkins and J.S. Harris, Jr., *Appl. Phys. Lett.*, **54** (1989) 623.
- [60] S. Munnix, R.K. Bauer, D. Bimberg, J.S. Harris, Jr., R. Khrbrück, E.C. Larkins, Ch. Maierhofer, D.E. Mars and J.N. Miller, *J. Vac. Sci. Technol.*, **B7** (1989) 704.
- [61] R.C. Miller, D.A. Kleinman, W.A. Nordland, Jr. and A.C. Gossard, *Phys. Rev.*, **B22** (1980) 863.
- [62] R.C. Miller, W.T. Tsang and O. Munteanu, *Appl. Phys. Lett.*, **41** (1982) 374.
- [63] M.H. Meynadier, J.A. Brum, C. Delalande, M. Voos, F. Alexandre and J.L. Lievin, *J. Appl. Phys.*, **58** (1985) 4307.
- [64] P. Dawson, G. Duggan, H.I. Raiph and K. Woodbridge, *Phys. Rev.*, **B28** (1983) 7381.
- [65] D. Bimberg, J. Christen, A. Werner, M. Kunst, G. Weinmann and W. Schlapp, *Appl. Phys. Lett.*, **49** (1986) 76.
- [66] K. Fujiwara, N. Tsukada and T. Nakayama, *Appl. Phys. Lett.*, **53** (1988) 675.
- [67] J.E. Fouquet and A.E. Siegman, *Appl. Phys. Lett.*, **46** (1985) 280.
- [68] P. Dawson, G. Duggan, H.I. Raiph and K. Woodbridge, *Phys. Rev.*, **B28** (1983) 7381.
- [69] D. Bimberg, J. Christen, A. Werner, M. Kunst, G. Weinmann and W. Schlapp, *Appl. Phys. Lett.*, **49** (1986) 76.
- [70] K. Fujiwara, N. Tsukada and T. Nakayama, *Appl. Phys. Lett.*, **53** (1988) 675.
- [71] B. Deveaud, F. Clerot, B. Sermage, C. Dumas and D.S. Katzer, in D.J. Lockwood and Aron Pinczuk (eds.), *Optical Phenomena in Semiconductor Structures of Reduced Dimensions*, Kluwer, London, 1992, p. 129.
- [72] T.C. Damen, J. Shah, D.Y. Oberli, D.S. Chemla, J.E. Cunningham and J.M. Kuo, *Phys. Rev.*, **B42** (1990) 7434.
- [73] J. Kusano, G.E.W. Bauer and Y. Aoyagi, *J. Appl. Phys.*, **75** (1994) 289.
- [74] J. Kusano, Y. Segawa, M. Miura, Y. Aoyagi and S. Namba, *Solid State Commun.*, **72** (1989) 215.
- [75] M. Kohl, D. Heitmann, P. Grambow and K. Ploog, *Phys. Rev.*, **B37** (1988) 10927.
- [76] C. Weisbuch, *J. Luminesc.*, **24/25** (1981) 373.
- [77] L.C. Andreani and F. Bassani, *Phys. Rev.*, **B41** (1990) 7536.
- [78] L. Schultheis and K. Ploog, *Phys. Rev.*, **B29** (1984) 7058.
- [79] M.A. Lampert, *Phys. Rev. Lett.*, **1** (1958) 450.
- [80] D.J. Ashen, P.J. Dean, D.T.J. Hurle, J.B. Mullin, A.M. White and P.D. Greene, *J. Phys. Chem. Solids*, **36** (1975) 1041.
- [81] U. Heim and P. Hiesinger, *Phys. Status Solidi B*, **66** (1974) 461.
- [82] A.M. White, P.J. Dean and B. Day, *J. Phys. C: Solid State Phys.*, **7** (1974) 1400.
- [83] A.M. White, P.J. Dean, L.L. Taylor, R.C. Clarke, D.J. Ashen and J.B. Mullin, *J. Phys. C: Solid State Phys.*, **5** (1972) 1727.
- [84] C.J. Hwang, *Phys. Rev.*, **B8** (1973) 646.
- [85] A.M. White, P.J. Dean, L.L. Taylor, R.C. Clarke, D.J. Ashen and J.B. Mullin, *J. Phys.*, **C5** (1972) 1727.
- [86] A.M. White, P.J. Dean and B. Day, *J. Phys.*, **C7** (1974) 1400.
- [87] U. Heim and P. Hiesinger, *Phys. Status Solidi B*, **66** (1974) 461.
- [88] E.W. Williams and H.B. Bebb, in R.K. Willardson and A.C. Beer (eds.), *Semiconductors and Semimetals*, Vol. 8, Academic Press, New York, 1970, p. 321.
- [89] E. Finkman, M.D. Sturge and R. Bhat, *J. Luminesc.*, **35** (1986) 235.
- [90] D.J. Wolford and J.A. Bradley, *Solid State Commun.*, **53** (1985) 1069.
- [91] J. Shah, R.C.C. Leite and R.E. Nahory, *Phys. Rev.*, **184** (1969) 811; D. Bimberg, M. Sondergeld and E. Grobe, *Phys. Rev.*, **B4** (1971) 3451; J.A. Rossi, C.M. Wolfe and J.O. Dimmock, *Phys. Rev. Lett.*, **25** (1970) 1614.
- [92] B.J. Skromme, S.S. Bose, B. Lee, T.S. Low, T.R. Lepkowski, R.Y. DeJule, G.E. Stillman and J.C.M. Hwang, *J. Appl. Phys.*, **58** (1985) 4685.
- [93] C. Benoit à la Guillaume and P. Lavallard, *Phys. Status Solidi B*, **70** (1975) K143.
- [94] D.C. Reynolds, K.K. Bajaj, C.W. Litton and E.B. Smith, *Phys. Rev.*, **B28** (1983) 3300.
- [95] C. Benoit à la Guillaume and P. Lavallard, *Phys. Status Solidi B*, **70** (1975) K143.
- [96] W. Rühle and W. Klingenstein, *Phys. Rev.*, **B18** (1977) 7011.
- [97] R.R. Sharma and S. Rodriguez, *Phys. Rev.*, **159** (1967) 649.
- [98] D.C. Herbert, *J. Phys.*, **C10** (1977) 3327.
- [99] V.A. Karasyuk, D.G.S. Beckett, M.K. Nissen, A. Villemaire, T.W. Steiner and M.L.W. Thewalt, *Phys. Rev.*, **B49** (1994) 16381.
- [100] J.C. Garcia, A.C. Beye, J.P. Contour, G. Neu, J. Massies and A. Barski, *Appl. Phys. Lett.*, **52** (1988) 1596.

- [101] T.D. Harris, M.S. Skolnick, J.M. Parsey, Jr. and R. Baht, *Appl. Phys. Lett.*, **52** (1988) 389.
- [102] G.E. Stillman, D.M. Larsen, C.M. Wolfe and R.C. Brandt, *Solid State Commun.*, **9** (1971) 2245.
- [103] B.J. Skromme, S.S. Bose, B. Lee, T.S. Low, T.R. Lepkowski, R.Y. DeJulie and G.E. Stillman, *J. Appl. Phys.*, **58** (1985) 4685.
- [104] N.O. Lipari and A. Baldereschi, *Phys. Rev. Lett.*, **25** (1970) 1660.
- [105] D.W. Kisker, H. Tews and W. Rehm, *J. Appl. Phys.*, **54** (1983) 1332.
- [106] H. Künzel and K. Ploog, *Appl. Phys. Lett.*, **37** (1980) 416.
- [107] M.A. Gilleo, P.T. Bailey and D.E. Hill, *Phys. Rev.*, **174** (1968) 898.
- [108] S.K. Brierley, H.T. Hendriks, W.E. Hoke, P.J. Lemonias and D.G. Weir, *Appl. Phys. Lett.*, **63** (1993) 812.
- [109] N. Pan, B. Lee, S.S. Bose, M.H. Kim, J.S. Hughes, G.E. Stillman, K. Arai and Y. Nashimoto, *Appl. Phys. Lett.*, **50** (1987) 1832.
- [110] J. Chevallier, W.C. Dautremont-Smith, C.W. Tu and S.J. Pearton, *Appl. Phys. Lett.*, **47** (1985) 108.
- [111] S.J. Pearton, W.C. Dautremont-Smith, J. Chevallier, C.W. Tu and K.D. Cummings, *J. Appl. Phys.*, **59** (1986) 2821.
- [112] A. Jaiti, J. Chevallier, R. Azoulay and A. Mircea, *J. Appl. Phys.*, **59** (1986) 3774.
- [113] W.C. Dautremont-Smith, J.C. Nabity, V. Swaminathan, Michael Stavola, J. Chevallier, C.W. Tu and S.J. Pearton, *Appl. Phys. Lett.*, **49** (1986) 1098.
- [114] Jorg Weber, S.J. Pearton and W.C. Dautremont-Smith, *Appl. Phys. Lett.*, **49** (1986) 1181.
- [115] Y. Chung, D.W. Langer, R. Becker and D. Look, *IEEE J. Electron Devices*, **ED-32** (1985) 40.
- [116] B.J. Skromme, S.S. Bose, B. Lee, T.S. Low, T.R. Lepkowski, R.Y. DeJulie, G.E. Stillman and J.C.M. Hwang, *J. Appl. Phys.*, **58** (1985) 4688.
- [117] P.K. Bhattacharya, H.J. Buhlmann, M. Illegems and J.L. Staehli, *J. Appl. Phys.*, **53** (1982) 6391.
- [118] A.C. Beye and G. Neu, *J. Appl. Phys.*, **58** (1985) 3549.
- [119] M.S. Skolnick, C.W. Tu and T.D. Harris, *Phys. Rev. B*, **33** (1986) 8468.
- [120] F. Briones and D.M. Collins, *J. Electron. Mater.*, **11** (1982) 847.
- [121] M.S. Skolnick, T.D. Harris, C.W. Tu, T.M. Brennan and M.D. Sturge, *Appl. Phys. Lett.*, **46** (1985) 427.
- [122] P.W. Yu, D.N. Talwar, C.E. Stutz, *Appl. Phys. Lett.*, **62** (1993) 2608.
- [123] N. Ohnishi, Y. Makita, H. Asakura, T. Lida, A. Yamada, H. Shibata, S. Uekusa and T. Matsumori, *Appl. Phys. Lett.*, **62** (1993) 1527.
- [124] F. Briones and D.M. Collins, *J. Electron. Mater.*, **11** (1982) 847.
- [125] J.P. Contour, G. Neu, M. Leroux, C. Chaix, B. Levesque and B. Etienne, *J. Vac. Sci. Technol. B*, **1** (1983) 811.
- [126] E.V.K. Rao, F. Alexandre, J.M. Masson, M. Allovon and L. Goldstein, *J. Appl. Phys.*, **57** (1985) 503.
- [127] B.J. Skromme, S.S. Bose, B. Lee, T.S. Low, T.R. Lepkowski, R.Y. DeJulie, G.E. Stillman and J.C.M. Hwang, *J. Appl. Phys.*, **58** (1985) 4685.
- [128] D.C. Reynolds, K.K. Bajaj, C.W. Litton, E.B. Smith, P.W. Yu, W.T. Masselink, F. Fisher and H. Morkoc, *Solid State Commun.*, **52** (1984) 685.
- [129] M.S. Skolnick, T.D. Harris, C.W. Tu, T.M. Brennan and M.D. Sturge, *Appl. Phys. Lett.*, **46** (1985) 427.
- [130] A.P. Roth, R.G. Goodchild, S. Charbonneau and D.F. Williams, *J. Appl. Phys.*, **54** (1983) 3427.
- [131] J.P. Contour, G. Neu, M. Leroux, C. Chaix, B. Levesque and P. Etienne, *J. Vac. Sci. Technol. B*, **1** (1983) 811.
- [132] N. Ohnishi, Y. Makita, A. Yamada, H. Asakura and T. Matsumori, *Appl. Surf. Sci.*, **50** (1991) 233.
- [133] M.S. Skolnick, C.W. Tu and T.D. Harris, *Phys. Rev. B*, **33** (1986) 8468.
- [134] D.C. Reynolds, K.K. Bajaj, C.W. Litton, E.B. Smith, P.W. Yu, W.T. Masselink, F. Fisher and H. Morkoc, *Solid State Commun.*, **52** (1984) 685.
- [135] L. Eaves and D.P. Halliday, *J. Phys. C: Solid State Phys.*, **17** (1984) L705.
- [136] C.W. Litton, D.C. Reynolds, K.K. Bajaj and E. Smith, *Bull. Am. Phys. Soc.*, **29** (1984) 346.
- [137] K. Akimoto, M. Dohsen, M. Arai and N. Watanabe, *Appl. Phys. Lett.*, **45** (1984) 922.
- [138] Y. Makita, *Materials Science and Engineering Reports* R16 (6-8), 1996.
- [139] Y. Makita, T. Nomura, M. Yokota, T. Matsumori, T. Izumi, Y. Takeuchi and K. Kudo, *Appl. Phys. Lett.*, **47** (1985) 623.
- [140] Y. Takeuchi, Y. Makita, K. Kudo, T. Nomura, H. Tanaka, K. Irie and N. Ohnishi, *Appl. Phys. Lett.*, **48** (1986) 59.
- [141] G. Davies, *Phys. Rep.*, **176** (3/4) (1989) 83-188.
- [142] J.R. Haynes, *Phys. Rev. Lett.*, **4** (1960) 361.
- [143] E.C. Lightowers, M.O. Henry and M.A. Vouk, *J. Phys. C*, **10** (1977) L713.
- [144] E.C. Lightowers, *Semicond. Sci. Technol.*, **5** (1990) 1161.
- [145] E.C. Lightowers, V. Higgs, M.J. Gregson, G. Davies, S.T. Davey, C.J. Gibbons, C.G. Tuppen, F. Schaffler and E. Kasper, *Thin Solid Films*, **183** (1989) 235.
- [146] E.C. Lightowers, M.O. Henry and M.A. Vouk, *J. Phys. C: Solid State Phys.*, **10** (1977) L713.
- [147] P.J. Dean, J.R. Haynes and W.F. Flood, *Phys. Rev.*, **161** (1967) 711.
- [148] M.O. Henry and E.C. Lightowers, *J. Phys. C*, **11** (1978) 1555.
- [149] M.O. Henry and E.C. Lightowers, *J. Phys. C: Solid State Phys.*, **11** (1978) L555.
- [150] M.L.W. Thewalt, in E.I. Rashba and M.D. Sturge (eds.), *Excitons*, North-Holland, Amsterdam, 1982, p. 393.
- [151] J. Wagner, *Phys. Rev.*, **B29** (1984) 2002.
- [152] E.C. Lightowers, L.T. Canham, G. Davies, M.L.W. Thewalt and S.P. Watkins, *Phys. Rev. B*, **29** (1984) 4517.
- [153] A.P.G. Hare, G. Davies and A.T. Collins, *J. Phys. C*, **5** (1972) 1265.
- [154] M.L.W. Thewalt, E.C. Lightowers and J.I. Pankove, *Appl. Phys. Lett.*, **46** (1985) 689.
- [155] B.V. Shanabrook and J. Comas, *Surf. Sci.*, **142** (1984) 504.

- [156] D.C. Reynolds, K.K. Bajaj, C.W. Litton, P.W. Yu, W.T. Masselink, R. Fischer and H. Morkoc, *Phys. Rev.*, **B29** (1984) 7038.
- [157] Y. Nomura, K. Shinozaki and M. Ishii, *J. Appl. Phys.*, **58** (1985) 1864.
- [158] X. Liu, A. Petrou, B.D. McCombe, J. Ralston and G. Wicks, *Phys. Rev.*, **B38**, (1988) 8522.
- [159] D.C. Reynolds, C.E. Leak, K.K. Bajaj, C.E. Stutz, R.L. Jones, K.R. Evans, P.W. Yu and W.M. Theis, *Phys. Rev.*, **B40** (1989) 6210.
- [160] W.T. Masselink, Y.C. Chang and H. Morkoc, *Phys. Rev.*, **B28** (1983) 7373.
- [161] D.C. Reynolds, K.K. Bajaj, C.W. Litton, P.W. Yu, W.T. Masselink, R. Fischer and H. Morkoc, *Phys. Rev.*, **B29** (1984) 7038.
- [162] P.O. Holtz, B. Monemar, M. Sundaram, J.L. Merz and A.C. Gossard, *J. Electron. Mater.*, **23** (1994) 513.
- [163] D.M. Larsen, *Phys. Rev. Lett.*, **42** (1979) 742.
- [164] S. Holmes, J.P. Cheng, B.D. McCombe and W. Schaff, *Phys. Rev. Lett.*, **69** (1992) 2571.
- [165] L.P. Fu, W.Y. Yu, G.D. Gilliland, A. Petrou, B.D. McCombe, J.P. Cheng and W.S. Schaff, *Proc. 22nd Int. Conf. on the Physics of Semiconductors, Vancouver, Canada, 1994*, World Scientific, Singapore, 1994, p. 2271.
- [166] W.T. Masselink, Y.C. Chang and H. Morkoc, *Phys. Rev.*, **B32** (1985) 5190.
- [167] D.C. Reynolds, K.G. Merkel, C.E. Stutz, K.R. Evans, K.K. Bajaj and P.W. Yu, *Phys. Rev.*, **B43** (1991) 1604.
- [168] P.O. Holtz, Q.X. Zhao, B. Monemar, M. Sundaram, J.L. Merz and A.C. Gossard, *Phys. Rev.*, **B47** (1993) 15675.
- [169] P.O. Holtz, M. Sundaram, K. Doughty, J.L. Merz and A.C. Gossard, *Phys. Rev.*, **B40** (1989) 12338.
- [170] R. Köhrbrück, S. Munnix, D. Bimberg, D.E. Mars and J.N. Miller, *Appl. Phys. Lett.*, **57** (1990) 1025.
- [171] H. Scheffler, A. Ostmann, D. Bimberg, D. Mars and J.N. Miller, unpublished work.
- [172] C.M. Wolfe, G.E. Stillman and W.T. Lindley, *J. Appl. Phys.*, **41** (1970) 3088.
- [173] M. Tajima, *Jpn. J. Appl. Phys.*, **21** (Suppl. 21-1) (1982) 113.
- [174] A.S. Kaminskii, L.I. Kolesnik, B.M. Leiferov and Ya.E. Pokrovski, *J. Appl. Spectrosc.*, **36** (1982) 516.
- [175] T.F. Kuech and E. Veuhoff, *J. Cryst. Growth*, **68** (1984) 148.
- [176] V. Swaminathan, D.L. VanHaren, J.L. Zilkko, P.Y. Lu and N.E. Schumaker, *J. Appl. Phys.*, **57** (1985) 5349.
- [177] J.K. Hsu, S.H. Jones and K.M. Lau, *J. Appl. Phys.*, **60** (1986) 3781.
- [178] J.C. Garcia, A.C. Beye, J.P. Contour, G. Neu, J. Massies and A. Barski, *Appl. Phys. Lett.*, **52** (1988) 1596.
- [179] T. Kamiya and E. Wagner, *J. Appl. Phys.*, **48** (1977) 1928.
- [180] Z.H. Lu, M.C. Hanna, D.M. Szymyd, E.G. Oh and A. Majerfeld, *Appl. Phys. Lett.*, **56** (1990) 177.
- [181] T. Kamiya and E. Wagner, *J. Appl. Phys.*, **48** (1977) 1928.
- [182] B.J. Skromme and G.E. Stillman, *Phys. Rev.*, **B29** (1984) 1982.
- [183] Y.E. Pokrovsky, *Proc. 7th Int. Conf. on the Physics of Semiconductors*, Paris, 1964, Published by Springer-Verlag, NY, p. 129.
- [184] B.V. Shanabrook and J. Comas, *Surf. Sci.*, **142** (1984) 504.
- [185] J.J. Hopfield, D.G. Thomas, M. Gershenson, *Phys. Rev. Lett.*, **10** (1963) 162.
- [186] P.J. Dean, in J.O. McCaldin and G. Somorjai (eds.), *Progress in Solid State Chemistry*, Vol. 8, Pergamon Press, Oxford, 1973, p. 1.
- [187] G. Lucovsky, A.J. Varga and R.F. Schwartz, *Solid State Commun.*, **3** (1965) 9.
- [188] E.H. Bogardus and H.B. Bebb, *Phys. Rev.*, **176** (1968) 993.
- [189] B.J. Skromme, S.S. Bose and G.E. Stillman, *J. Electron. Mater.*, **15** (1986) 345.
- [190] R.C. Enck and A. Honig, *Phys. Rev.*, **177** (1969) 1182.
- [191] D.C. Reynolds, K.R. Evans, K.G. Merkel, C.E. Stutz and P.W. Yu, *Phys. Rev.*, **B43** (1991) 9087.
- [192] D.C. Reynolds, D.N. Talwar, M.O. Manasreh and C.E. Stutz, *Phys. Rev.*, **B47** (1993) 13304.
- [193] M. Jaros, *Adv. Phys.*, **29** (1980) 409.
- [194] D.G. Thomas and J.J. Hopfield, *Phys. Rev.*, **150** (1966) 680.
- [195] D.J. Wolford, J.A. Bradley, K. Fry, J. Thompson and H.E. King, *Inst. Phys. Conf. Ser.*, **65**, *Int. Symp. GaAs and Related Compounds, Albuquerque, 1982*, IOP, Bristol, UK, 1982, p. 477.
- [196] D.J. Wolford, J.A. Bradley, K. Fry and J. Thompson, in J.D. Chadi and W.A. Harrison (eds.), *Proc. of the 17th Int. Conf. on the Physics of Semiconductors*, Springer-Verlag, New York, 1985, p. 627.
- [197] D.J. Wolford, J.A. Bradley, H.E. King and J. Thompson, *Bull. Am. Phys. Soc.*, **27** (1982) 316.
- [198] K. Huang and A. Rhys, *Proc. R. Soc. London Ser. A*, **204** (1950) 406.
- [199] X. Liu, M.E. Pistol, L. Samuelson, S. Schwielicke and W. Seifert, *Appl. Phys. Lett.*, **56** (1990) 1451.
- [200] X. Liu, M.E. Pistol and L. Samuelson, *Phys. Rev.*, **B42** (1990) 7504.
- [201] M. Singh, W.M. Chen, N.T. Son, B. Monemar and E. Janzen, *Solid State Commun.*, **93** (1995) 415.
- [202] J.T. Hsu, T. Nishino and Y. Hamakawa, *Jpn. J. Appl. Phys.*, **26** (1987) 685.
- [203] Ch. Uihlein and L. Eaves, *Phys. Rev.*, **B26** (1982) 4473.
- [204] M.S. Skolnick, M.R. Brozel and B. Tuck, *Solid State Commun.*, **43** (1982) 379.
- [205] H. Shen, Y. Makita, S. Niki, A. Yamada, T. Iida, H. Shibata, A. Obara and S. Uekusa, *Appl. Phys. Lett.*, **63** (1993) 1780.
- [206] W. Schairer and M. Schmidt, *Phys. Rev.*, **B10** (1974) 2501.
- [207] L. Samuelson and S. Nilsson, *J. Luminesc.*, **40/41** (1988) 127.
- [208] C.E. Third, F. Weinberg, M. Thewalt and L. Young, *Appl. Phys. Lett.*, **58** (1991) 714.
- [209] H.J. Queisser and C.S. Fuller, *J. Appl. Phys.*, **37** (1966) 4895.
- [210] J. van de Ven, W.J.A.M. Hartmann and L.J. Gilling, *J. Appl. Phys.*, **60** (1986) 3735.
- [211] I. Fabre, *Phys. Status Solidi A*, **9** (1972) 259.
- [212] R.L. Bell, *J. Appl. Phys.*, **34** (1963) 1563.
- [213] G.S. Pomrenke, H. Ennen and W. Haydle, *J. Appl. Phys.*, **59** (1986) 601.

- [214] H Ennen, G Pommrenke, A. Axmann, K Eisele, W Haydl and J Schneider, *Appl Phys Lett.*, **46** (1985) 381.
- [215] Y.H Xie, E.A Fitzgerald and Y.J. Mui, *J Appl Phys.*, **70** (1991) 3223.
- [216] H. Ennen, J. Wagner, H.D. Müller and R.S. Smith, *J. Appl Phys.*, **61** (1987) 4877.
- [217] F. Priolo, S. Coffa, G. Franzo, C. Spinella, A. Carnera and V. Bellani, *J. Appl. Phys.*, **74** (1993) 4936.
- [218] G.S. Pommrenke, P.B. Klein and D.W. Langer (eds.), *Rare Earth Doped Semiconductors*, Materials Research Society Symposium Proceedings, Vol. 301, MRS, Pittsburgh, PA, 1993; A. Cornen, K. Pressel, C. Hiller, D. Haase, J. Weber and F. Scholz, *Mater. Res. Soc. Symp. Proc.*, **301** (1993) 195.
- [219] A. Dornen, D. Haase, C. Hiller, K. Pressel, J. Weber and F. Scholz, *J. Appl. Phys.*, **74** (1993) 6457.
- [220] M.K. Nissen, A. Villemaire and M.L.W. Thewalt, *Phys. Rev. Lett.*, **67** (1991) 112.
- [221] T.W. Steiner, M.K. Nissen, S.M. Wilson, Y. Lacroix and M.L.W. Thewalt, *Phys. Rev.*, **B47** (1993) 1265.
- [222] P.W. Yu and D.C. Walters, *Appl. Phys. Lett.*, **41** (1982) 863.
- [223] P.W. Yu and D.C. Walters, *Appl. Phys. Lett.*, **41** (1982) 863.
- [224] P.W. Yu, *Solid State Commun.*, **43** (1982) 953.
- [225] P.W. Yu, *Appl. Phys. Lett.*, **44** (1984) 330.
- [226] P.W. Yu, *Phys. Rev.*, **B42** (1990) 11889.
- [227] J.F. Wagner and J.A. Van Vechten, *J. Appl. Phys.*, **62** (1987) 4192.
- [228] D.A. Kleinman, *Phys. Rev.*, **B33** (1986) 2540.
- [229] G.W. 'tHooft, W.A.J.A. van der Poel, L.W. Molenkamp and C.T. Foxon, *Phys. Rev.*, **B35** (1987) 8281.
- [230] S. Charbonneau, T. Steiner, M.L.W. Thewalt, E.S. Koteles, J.Y. Chi and B. Elman, *Phys. Rev.*, **B38** (1988) 3583.
- [231] D.C. Reynolds, K.K. Bajaj, C.E. Stutz, R.L. Jones, W.M. Theis, P.W. Yu and K.R. Evans, *Phys. Rev.*, **B40** (1989) 3340.
- [232] R.T. Phillips, D.J. Lovering, G.J. Denton and G.W. Smith, *Phys. Rev.*, **B45** (1992) 4308.
- [233] K.-H. Pantke, D. Oberhauser, V.G. Lyssenko, J.M. Hvam and G. Weimann, *Phys. Rev.*, **B47** (1993) 2413.
- [234] J.C. Kim, D.R. Wake and J.P. Wolfe, *Phys. Rev.*, **B50** (1994) 15099.
- [235] R.C. Miller, D.A. Kleinman, A.C. Gossard and O. Montenau, *Phys. Rev.*, **B25** (1982) 6545.
- [236] D.A. Kleinman, *Phys. Rev.*, **B28** (1982) 871.
- [237] A.G. Steele, W.G. McMullan and M.L.W. Thewalt, *Phys. Rev. Lett.*, **59** (1987) 2899.
- [238] P.L. Gourley and J.P. Wolfe, *Phys. Rev.*, **B20** (1979) 3319.
- [239] P.L. Gourley and J.P. Wolfe, *Phys. Rev.*, **B25** (1982) 6338.
- [240] W. Schmid, *Phys. Rev. Lett.*, **45** (1980) 1726.
- [241] J.S. Wang and C. Kittel, *Phys. Lett.*, **42A** (1972) 189.
- [242] T.N. Morgan, *Nuovo Cimento Soc. Ital. Fis. B*, **39** (1977) 602.
- [243] R.B. Hammond, T.C. McGill and J.W. Mayer, *Phys. Rev.*, **B13** (1976) 3566.
- [244] L.V. Keldysh, The electron-hole liquid in semiconductors, in F. Bassani, F. Fumi and M.P. Tosi (eds.), *Proc. of the Int. School of Physics Enrico Fermi Course LXXXIX, Highlights of Condensed Matter Theory*, Elsevier, New York, 1985, p. 644.
- [245] H. Kalt, W.W. Rühle, K. Reimann, M. Rinker and E. Bauser, *Phys. Rev.*, **B43** (1991) 12364.
- [246] N.F. Mott, *Metal-Insulator Transitions*, Barnes and Noble, New York, 1974.
- [247] T. Moriya and T. Kushida, *J. Phys. Soc. Jpn.*, **43** (1977) 1646.
- [248] E.O. Göbel, W. Graudszus and P.H. Liang, *J. Luminesc.*, **24/25** (1981) 573.
- [249] S. Tanaka, H. Kobayashi, H. Saito and S. Shionoya, *Solid State Commun.*, **33** (1980) 167.
- [250] H. Nather and L.G. Quagliano, *Solid State Commun.*, **50** (1984) 75.
- [251] O. Hildebrand, E.O. Göbel, K.M. Romanek, H. Weber and G. Mahler, *Phys. Rev.*, **B17** (1978) 4775.
- [252] M. Capizzi, S. Modesti, A. Frova, J.L. Staehli, M. Guzzi and R.A. Logan, *Phys. Rev.*, **B29** (1984) 2028.
- [253] J. Shah, M. Combescot and A.H. Dayem, *Phys. Rev. Lett.*, **38** (1977) 1497.
- [254] L.M. Smith and J.P. Wolfe, *Proc. 18th Int. Conf. on the Physics of Semiconductors, Stockholm, 1986*, World Scientific, Singapore, 1987, p. 1409; *Phys. Rev.*, **B51** (1995) 7521.
- [255] D. Pekete, S. Borenstein, A. Ron, E. Cohen and R.D. Burnham, *Superlatt. Microstruct.*, **1** (1985) 245.
- [256] P. Vashishta and R.K. Kalia, *Phys. Rev.*, **B25** (1982) 6492.
- [257] E. Göbel, H. Herzog, M.H. Pilkhu and K.H. Zschauer, *Solid State Commun.*, **13** (1973) 719.
- [258] G. Tränkle, E. Lach, A. Forchel, F. Scholz, C. Ell, H. Haug, G. Weimann, G. Griffiths, H. Kroemer and S. Subbanna, *Phys. Rev.*, **B36** (1987) 6712.
- [259] K. Bohnert, H. Kalt, A.L. Smirl, D.P. Norwood, T.F. Boggess and I.J. DHænens, *Phys. Rev. Lett.*, **60** (1988) 37.
- [260] G. Tränkle, H. Leier, A. Forchel, H. Haug, C. Ell and G. Weimann, *Phys. Rev. Lett.*, **58** (1987) 419.
- [261] P.T. Lansberg, *Phys. Status Solidi*, **15** (1966) 623.
- [262] S. Schmitt-Rink, D.S. Chemla and D.A.B. Miller, *Adv. Phys.*, **38** (1989) 89.
- [263] S. Kim, M. Kim, S. Min and C. Lee, *J. Appl. Phys.*, **74** (1993) 6128.
- [264] S. Kim, Y. Kim, M.S. Lee, M. Kim and S. Min, *Solid State Commun.*, **88** (1993) 743.
- [265] H.C. Casey, Jr. and F. Stern, *J. Appl. Phys.*, **47** (1976) 631.
- [266] H. Peric, B. Jusserand, D. Richards and B. Etienne, *Phys. Rev.*, **B47** (1993) 12722.
- [267] W. Chen, M. Fritze, A.V. Nurmi, C. Colvard, D. Ackley and H. Lee, *Phys. Rev. Lett.*, **64** (1990) 2434.
- [268] D. Richards, J. Wagner, H. Schneider, G. Hendorf, M. Maier, A. Fischer and K. Ploog, *Phys. Rev.*, **B47** (1993) 9629.
- [269] K. Oe and K. Tsubaki, *J. Appl. Phys.*, **59** (1986) 3527.

- [270] C.H. Yang, J.M. Carlson-Swindle, S.A. Lyon and J.M. Worlock, *Phys. Rev. Lett.*, **55** (1985) 2359.
- [271] D.N. Mirlin, I.Ja. Karlik, L.P. Nikitin, I.I. Reshina and V.F. Sapega, *Solid State Commun.*, **37** (1981) 757.
- [272] G. Fasol, K. Ploog and E. Bauser, *Solid State Commun.*, **54** (1985) 383.
- [273] G. Fasol, W. Hackenberg, H.P. Hughes, K. Ploog, E. Bauser and H. Kano, *Phys. Rev.*, **B41** (1990) 1461.
- [274] J.A. Kash, *Phys. Rev.*, **B40** (1989) 3455.
- [275] R.G. Ulbrich, J.A. Kash and J.C. Tsang, *Phys. Rev. Lett.*, **62** (1989) 949.
- [276] M. Zachau, J.A. Kash and W.T. Masselink, *Phys. Rev.*, **B44** (1991) 4048.
- [277] J.A. Kash, *Phys. Rev.*, **B47** (1993) 1221.
- [278] J. Shah, A. Pinczuk, A.C. Gossard and W. Wiegmann, *Phys. Rev. Lett.*, **54** (1985) 2045.
- [279] A. Leitenstorfer, A. Lohner, T. Elsaesser, S. Haas, F. Rossi, T. Kuhn, W. Klein, G. Boehm, G. Traenkle and G. Weimann, *Phys. Rev. Lett.*, **73** (1994) 1687.
- [280] T.F. Kuech, D.J. Wolford, E. Veuhoff, V. Deline, P.M. Mooney, R. Potemski and J. Bradley, *J. Appl. Phys.*, **62** (1987) 632.
- [281] Y.R. Yuan, K. Mohammed, M.A.A. Pudensi and J.L. Merz, *Appl. Phys. Lett.*, **45** (1984) 739.
- [282] H. Kawai, K. Kaneko and N. Watanabe, *J. Appl. Phys.*, **56** (1984) 463.
- [283] D. Gammon, B.V. Shanabrook and D.S. Katzer, *Phys. Rev. Lett.*, **67** (1991) 1547.
- [284] P.L. Gourley, C.P. Tigges, R.P. Schneider, Jr., T.M. Brennan, B.E. Hammons and A.E. McDonald, *Appl. Phys. Lett.*, **62** (1993) 1736.
- [285] H. Morkoc, L.C. Witkowski, T.J. Drummond, C.M. Stanchak, A. Cho and B.G. Streetman, *Electron. Lett.*, **16** (1980) 753.
- [286] W.T. Masselink, Y.L. Sun, R. Fischer, T.J. Drummond, Y.C. Chang, M.V. Klein and H. Morkoc, *J. Vac. Sci. Technol.*, **B2** (1984) 117.
- [287] K. Fujiwara and K. Ploog, *Appl. Phys. Lett.*, **45** (1984) 1222.
- [288] M. Tanaka and H. Sakaki, *J. Cryst. Growth*, **81** (1987) 153.
- [289] R.K. Kopf, E.F. Schubert, T.D. Harris and R.S. Becker, *Appl. Phys. Lett.*, **58** (1991) 631.
- [290] C. Weisbuch, R. Dingle, A.C. Gossard and W. Wiegmann, *Solid State Commun.*, **38** (1981) 709.
- [291] J. Singh, K.K. Bajaj, D.C. Reynolds, C.W. Litton, P.W. Yu, W.T. Masselink, R. Fischer and H. Morkoc, *J. Vac. Sci. Technol.*, **B3** (1985) 1061.
- [292] M. Kohl, D. Heitmann, S. Tarucha, K. Leo and K. Ploog, *Phys. Rev.*, **B39** (1989) 7736.
- [293] R.C. Miller, A.C. Gossard, W.T. Tsang and O. Munteanu, *Phys. Rev.*, **B25** (1982) 3871.
- [294] P.M. Petroff, R.C. Miller, A.C. Gossard and W. Wiegmann, *Appl. Phys. Lett.*, **44** (1984) 217.
- [295] K. Fujiwara, K. Kanamoto, N. Tsukada, H. Miyatake and H. Koyama, *J. Appl. Phys.*, **66** (1989) 1488.
- [296] R.F. Kopf, E.F. Schubert, T.D. Harris, R.S. Becker and G.H. Gilmer, *J. Appl. Phys.*, **74** (1993) 6139.
- [297] J. Massies, C. Deparis, C. Neri, G. Neu, Y. Chen, B. Gil, P. Auvray and A. Regreny, *Appl. Phys. Lett.*, **55** (1989) 2605.
- [298] W. Seidel, E. Lugagne-Delpont, P. Voisin, E.V.K. Rao, Ph. Krauz and F. Alexandre, *J. Appl. Phys.*, **74** (1993) 2968.
- [299] R. Dingle, A.C. Gossard and W. Wiegmann, *Phys. Rev. Lett.*, **34** (1975) 1327.
- [300] D.J. Wolford, T.F. Kuech, J.A. Bradley, M.A. Gell, D. Ninno and M. Jaros, *J. Vac. Sci. Technol.*, **B4** (1986) 1043.
- [301] B.A. Wilson, *IEEE J. Quantum Electron.*, **25** (1989) 1012.
- [302] B.A. Wilson, *IEEE J. Quantum Electron.*, **QE-24** (1988) 1763.
- [303] P. Dawson, B.A. Wilson, C.W. Tu and R.C. Miller, *Appl. Phys. Lett.*, **48** (1986) 541.
- [304] T.W. Steiner, D.J. Wolford, T.F. Kuech and M. Jaros, *Superlatt. Microstruct.*, **4** (1988) 227.
- [305] D.J. Wolford, T.F. Kuech, T.W. Steiner, J.A. Bradley, M.A. Gell, D. Ninno and M. Jaros, *Superlatt. Microstruct.*, **4** (1988) 525.
- [306] R. Cingolani, L. Baldassarre, M. Ferrara, M. Lugara and K. Ploog, *Phys. Rev.*, **B40** (1989) 6101.
- [307] E. Finkman, M.D. Sturge, M.H. Meynadier, R.E. Nahory, M.C. Tamargo, D.M. Hwang and C.C. Chang, *J. Luminesc.*, **39** (1987) 57.
- [308] T.J. Drummond and I.J. Fritz, *Appl. Phys. Lett.*, **47** (1985) 284.
- [309] P. Dawson, C.T. Foxon and H.W. van Kesteren, *Semicond. Sci. Technol.*, **5** (1990) 54.
- [310] G. Danan, B. Etienne, F. Mollot, R. Planel, A.M. Jean-Louis, F. Alexandre, B. Jusserand, G. Le Roux, J.Y. Marzin, H. Savary and B. Sermage, *Phys. Rev.*, **B35** (1987) 6207.
- [311] P. Dawson, C.T. Foxon and H.W. Van Kesteren, *Inst. Phys. Conf. Ser.*, **106**, 387 (1989); K.J. Moore, G. Duggan, P. Dawson and C.T. Foxon, *Phys. Rev.*, **B38** (1988) 5535.
- [312] D. Scalbert, J. Cernogora, C. Benoit a la Guillaume, M. Maaref, F.F. Charfi and R. Planel, *Surf. Sci.*, **229** (1990) 464.
- [313] H.W. van Kesteren, E.C. Cosman, P. Dawson, K.J. Moore and C.T. Foxon, *Phys. Rev.*, **B41** (1990) 13426.
- [314] A.M. de Paula and G. Weber, *Appl. Phys. Lett.*, **65** (1994) 1281.
- [315] H.W. van Kesteren, E.C. Cosman, W.A.J.A. van der Poel and C.T. Foxon, *Phys. Rev.*, **B41** (1990) 5283.
- [316] W. Ge, W.D. Schmidt, M.D. Sturge, L.N. Pfeiffer and K.W. West, *J. Luminesc.*, **48/49** (1991) 759.
- [317] D.B. Laks and A. Zunger, *Phys. Rev.*, **B45** (1992) 11411.
- [318] K. Kash, *J. Luminesc.*, **46** (1990) 69.
- [319] H. Benisty, C.M. Sotomayor-Torres and C. Weisbuch, *Phys. Rev.*, **B44** (1991) 10945.
- [320] Y. Arakawa, Y. Nagamune, M. Nishioka and S. Tsukamoto, *Semicond. Sci. Technol.*, **8** (1993) 1082.
- [321] S. Tsukamoto, Y. Nagamune, M. Nishioka and Y. Arakawa, *Appl. Phys. Lett.*, **63** (1993) 355.
- [322] S. Tsukamoto, Y. Nagamune, M. Nishioka, Y. Arakawa, *J. Appl. Phys.*, **71** (1992) 533.
- [323] M.S. Lee, Y. Kim, M.S. Kim, S. Kim, S.K. Min, Y.D. Kim and S. Nahm, *Appl. Phys. Lett.*, **63** (1993) 3052.

- [324] T Kono, S Tsukamoto, Y. Nagamune, F Sogawa, M. Nishioka and Y Arakawa, *Appl. Phys. Lett.*, 64 (1994) 1564.
- [325] R Rinaldi, R Cingolani, M Lepore, M Ferrara, I.M Catalano, U Marti, D. Martin, U Morier-Gemoud, P. Ruterana and F K. Reinhart, *Superlatt. Microstruct.*, 16 (1994) 217.
- [326] R Rinaldi, R. Cingolani, M Ferrara, H Lage, D Heitmann and K Ploog, *Phys. Rev.*, B47 (1993) 7275.
- [327] R Cingolani, H Lage, L. Tapfer, H Kalt, D Heitmann and K Ploog, *Phys. Rev. Lett.*, 67 (1991) 891.
- [328] M Kohl, D Heitmann, P. Grambow and K. Ploog, *Phys. Rev. Lett.*, 63 (1989) 2124
- [329] M Kohl, D Heitmann, W.W Rühle, P. Grambow and K Ploog, *Phys. Rev.*, B41 (1990) 12338.
- [330] J.S. Weiner, G. Danan, A. Pinczuk, J. Valladares, L.N. Pfeiffer and K. West, *Phys. Rev. Lett.*, 63 (1989) 1641.
- [331] A.S. Plaut, H Lage, P Grambow, D. Heitmann, K von Klitzing and K. Ploog, *Phys. Rev. Lett.*, 67 (1991) 1642
- [332] H Lage, D Heitmann, R. Cingolani, P. Grambow and K. Ploog, *Phys. Rev.*, B44 (1991) 6550.
- [333] M.A. Reed, R.T. Bate, K. Bradshaw, W.M. Duncan, W.R. Frensel, J.W. Lee and H.D. Shih, *J. Vac. Sci. Technol.*, B4 (1986) 358.
- [334] J A Lebens, C.S. Tsai, K.J. Vahala and T.F. Kuech, *Appl. Phys. Lett.*, 56 (1990) 2642
- [335] R Notzel, N.N Ledentsov and K Ploog, *Phys. Rev.*, B47 (1993) 1299.
- [336] K. Kash, B P. Van der Gaag, D.D. Mahoney, A S. Gozdz, L.T. Florez, J P Harbison and M D. Sturge, *Phys. Rev. Lett.*, 67 (1991) 1326
- [337] M. Tsuchiya, J.M. Gaines, R.H. Yan, R J. Simes, P O. Holtz, L A. Coldren and P.M Petroff, *Phys. Rev. Lett.*, 62 (1989) 466.
- [338] H Kanbe, A Chavez-Pirson, H. Ando, H. Saito and T Fukui, *Appl. Phys. Lett.*, 58 (1991) 2969
- [339] E Colas, E Kapon, S Simphony, H M Cox, R. Bhat, K Kash and P.S.D. Lin, *Appl. Phys. Lett.*, 55 (1989) 867
- [340] H Leier, A Forchel, B E. Maile, G. Mayer, J. Hommel, G. Weimann and W. Schlapp, *Appl. Phys. Lett.*, 56 (1990) 48
- [341] W Wegscheider, L. Pfeiffer, M. Dignam, A Pinczuk, K. West and R Hull, *Semicond. Sci. Technol.*, 9 (1994) 1933.
- [342] H. Weman, M S Miller, C E Pryor, Y J. Li, P. Bergman, P.M. Petroff and J.L. Merz, *Phys. Rev.*, B48 (1993) 8047
- [343] M S Miller, H Weman, C E Pryor, M Krishnamurthy, P M. Petroff, H. Kroemer and J.L. Merz, *Phys. Rev. Lett.*, 68 (1992) 3464.
- [344] H Weman, E.D. Jones, C.R McIntyre, M S Miller, P M. Petroff and J L. Merz, *Superlatt. Microstruct.*, 13 (1993) 5.
- [345] L. Davis, K.K. Ko, W Q. Li, H.C Sun, Y. Lam, T. Brock S W. Pang and P.K. Bhattacharya, *Appl. Phys. Lett.*, 62 (1993) 2766
- [346] Y. Nagamune, M. Nishioka, S. Tsukamoto and Y. Arakawa, unpublished work
- [347] T Takahashi, Y. Arakawa, M. Nishioka and T Ikoma, *J. Cryst. Growth*, to be published.
- [348] Y Nagamune, M. Nishioka, S. Tsukamoto and Y Arakawa, *Appl. Phys. Lett.*, 64 (1994) 2495.
- [349] I.H Tan, R. Mirin, V. Jayaraman, S Shi, E. Hu and J. Bowers, *Appl. Phys. Lett.*, 61 (1992) 300
- [350] K. Brunner, U. Bockelmann, G. Abstreiter, M. Walther, G. Bohm, G. Trankle and G. Weimann, *Phys. Rev. Lett.*, 69 (1992) 3216.
- [351] H. Temkin, G. Dolan, M. Panish and S Chu, *Appl. Phys. Lett.*, 50 (1987) 413
- [352] T Aizawa, K Shimomura, S. Arai and Y Seumatsu, *Photon. Technol. Lett.*, 3 (1991) 907.
- [353] J Patillon, C. Delalande, C. Jay, J. Andre, R Gamonal, M. Iost, B. Soucail, M Voos and G Martin, *22nd Conference on Solid State Devices and Materials*, Sendai, Business Center for Academic Societies, Tokyo, 1990, p. 107.
- [354] A Nurmiikkko and A. Pinczuk, *Physics Today*, American Institute of Physics, Woodbury, NY, 1993, p 24.
- [355] G Abstreiter, G. Bohm, K. Brunner, F. Hirler, R Strenz and G Weimann, in D.J. Lockwood and Aron Pinczuk (eds.), *Optical Phenomena in Semiconductor Structures of Reduced Dimensions*, Kluwer, London, 1992, p. 327.
- [356] M Asada, Y Miyamoto and Y. Suematsu, *IEEE J. Quantum Electron.*, QE-22 (1986) 1915.
- [357] M A Reed, *Sci. Amer.*, 268 (1993) 118
- [358] P D Wang, C M. Sotomayor-Torres, H Benisty, C. Weisbuch and S.P. Beaumont, *Appl. Phys. Lett.*, 61 (1992) 946.
- [359] E M. Clausen, Jr , H.G Craighead, J.M. Worlock, J P Harbison, L.M. Schiavone, L. Florez and B. Van der Gaag, *Appl. Phys. Lett.*, 55 (1989) 1427
- [360] P.M. Petroff, A.C. Gossard, R.A. Logan and W. Weigmann, *Appl. Phys. Lett.*, 41 (1982) 626.
- [361] D J Wolford, in O. Engstrom (ed.), *18th Int. Conf. on the Physics of Semiconductors*, World Publishing, Singapore, 1987, p. 1115.
- [362] P Yu and B. Welber, *Solid State Commun.*, 25 (1978) 209.
- [363] W P Roach, M. Chandrasekhar, H R Chandrasekhar and F.A. Chambers, *Phys. Rev.*, B44 (1991) 13404.
- [364] G A Northrop and D J Wolford, in E M. Anastassakis and J D. Joannopoulos (eds.), *Proc. Int. Conf. on the Physics of Semiconductors*, Aug 6–10, Thessaloniki, Greece, World Scientific, Singapore, 1990, p. 577.
- [365] I.L. Spain, M S. Skolnick, G W. Smith, M K Saker and C.R. Whitehouse, *Phys. Rev.*, B43 (1991) 14091.
- [366] W Zhou, C H. Perry and J.M. Worlock, *Phys. Rev.*, B42 (1990) 9657.
- [367] A R Adams, Properties of Gallium Arsenide, *Electronic Materials Information Service Data Review Series No. 2*, Information Services Division of the Institution of Electrical Engineers, London, 1986, Chapter 6.5.
- [368] D C Reynolds, D C. Look, B. Jogai, C E Stutz, R. Jones and K K. Bajaj, *Phys. Rev.*, B50 (1994) 11710.
- [369] S K Lyo, E.D. Jones and J F. Klem, *Phys. Rev. Lett.*, 61 (1988) 2265.
- [370] S I. Zubarev, T Ruf, M. Cardona and K Ploog, *Phys. Rev.*, B48 (1993) 1647.
- [371] S B. Nam, D.C. Reynolds, C W Litton, R.J. Almasy, T.C. Collins and C.M. Wolfe, *Phys. Rev.*, 13 (1976) 761.
- [372] A B Henrique, E T.R. Chidley, R.J. Nicholas, P. Dawson and C.T. Foxon, *Phys. Rev.*, B46 (1992) 4047.
- [373] F A J.M. Driessens, S.M. Olsthoorn, T T J.M. Berendschot, L J. Giling, D.M. Frigo, G.A.C. Jones, D.A. Ritchie and J.E.F. Frost, *Phys. Rev.*, B47 (1993) 1282.
- [374] T Schmiedel, L.P. Fu, S.T. Lee, W Y. Yu, A. Petrou, M. Dutta, J. Pamulapati, P.G. Newman and J. Bovatzis, *J. Appl. Phys.*, 74 (1993) 2100.

- [375] C. Delalande, J.A. Brum, J. Orgonasi, M.H. Meynadier, G. Bastard, J.C. Maan, G. Weimann and W. Schlapp, *Superlatt. Microstruct.*, 3 (1987) 29.
- [376] A.S. Plaut, I.V. Kukushkin, K. v. Klitzing and K. Ploog, *Phys. Rev., B42* (1990) 5744.
- [377] H. Buhmann, W. Joss, K. v. Klitzing, I.V. Kukushkin, A.S. Plaut, G. Martinez, K. Ploog and V.B. Timofeev, *Phys. Rev. Lett.*, 66 (1991) 926.
- [378] D.C. Reynolds, C.W. Litton, T.C. Collins, S.B. Nam and C.M. Wolfe, *Phys. Rev., B12* (1975) 5723.
- [379] S. Zemon and G. Lambert, *Proc. of Int. Symp. on GaAs and Related Compounds, Karuizawa, Japan*, Inst. Phys. Conf. Ser. No. 106, Chapter 5, IOP Publishers, Bristol, UK, 1989, p. 251.
- [380] D.J.S. Beckett, M.K. Nissen and M.L. W. Thewalt, *Can. J. Phys.*, 69 (1991) 427.
- [381] D.C. Reynolds, R.J. Almassy, C.W. Litton, S.B. Nam and G.L. McCoy, *J. Appl. Phys.*, 49 (1978) 5336.
- [382] N. Miura and S. Sasaki, *Superlatt. Microstruct.*, 10 (1991) 253.
- [383] S. Sasaki, N. Miura and Y. Horikoshi, *Appl. Phys. Lett.*, 59 (1991) 96.
- [384] M. Oestreich, A.P. Heberle, W.W. Rühle, H. Lage, D. Heitmann and K. Ploog, *J. Luminesc.*, 60/61 (1994) 390.
- [385] W.M. Chen, O.O. Awadelkarim, H. Weman and B. Monemar, *Phys. Rev., B42* (1990) 5120.
- [386] W. Bludau and E. Wagner, *Phys. Rev., B13* (1976) 5410.
- [387] H. Weman, Q.X. Zhao and B. Monemar, *Phys. Rev., B36* (1987) 5054.
- [388] H. Weman, B. Monemar and Q.X. Zhao, *Phys. Rev., B38* (1988) 61.
- [389] T. Lundström, P.O. Holtz, Q.X. Zhao, J.P. Bergman, B. Monemar, M. Sundaram, J.L. Merz and A.C. Gossard, *J. Electron. Mater.*, 22 (1993) 1353.
- [390] G.D. Gilliland, D.J. Wolford, T.F. Kuech and J.A. Bradley, *Phys. Rev., B49* (1994) 8113.
- [391] G.D. Gilliland, D.J. Wolford, T.F. Kuech and J.A. Bradley, *J. Vac. Sci. Technol.*, B9 (1991) 2377.
- [392] G.D. Gilliland, D.J. Wolford, T.F. Kuech and J.A. Bradley, *Phys. Rev., B43* (1991) 14251.
- [393] E.E. Mendez, G. Bastard, L.L. Chang, L. Esaki, H. Morkoc and R. Fischer, *Phys. Rev., B26* (1982) 7101.
- [394] H. Weman, G.M. Treacy, H.P. Hjalmarson, K.K. Law, J.L. Merz and A.C. Gossard, *Phys. Rev., B45* (1992) 6263.
- [395] H.J. Polland, L. Schultheis, J. Kuhl, E.O. Göbel and C.W. Tu, *Phys. Rev. Lett.*, 55 (1985) 2610.
- [396] L. Vina, R.T. Collins, E.E. Mendez, W.I. Wang, L.L. Chang and L. Esaki, *Superlatt. Microstruct.*, 3 (1987) 9.
- [397] S. Fukuta, H. Goto, N. Sawaki, T. Suzuki, H. Ito and K. Hara, *Semicond. Sci. Technol.*, 8 (1993) 1881.
- [398] E.E. Mendez and F. Agullo-Rueda, *J. Luminesc.*, 44 (1989) 223.
- [399] S.R. Andrews, A.S. Plaut, R.T. Harley and T.M. Kerr, *Phys. Rev., B41* (1990) 5040.
- [400] M.H. Meynadier, R.E. Nahory, J.M. Worlock, M.C. Tamargo, J.L. de Miguel and M.D. Sturge, *Phys. Rev. Lett.*, 60 (1988) 1338.
- [401] F.H. Pollak, in P. Pearsall (ed.), *Semiconductors and Semimetals*, Academic Press (New York, 1990), vol. 32, p. 17.
- [402] D.L. Smith and C. Mailhiot, *Rev. Mod. Phys.*, 62 (1990) 173.
- [403] F.H. Pollak and M. Cardona, *Phys. Rev.*, 172 (1968) 816.
- [404] M. Silver, W. Batty, A. Ghiti and E.P. O'Reilly, *Phys. Rev., B46* (1992) 6781.
- [405] A. Gavini and M. Cardona, *Phys. Rev., B1* (1970) 672.
- [406] M.A. Gilleo, P.T. Bailey and D.E. Hill, *J. Luminesc.*, 1/2 (1970) 562.
- [407] P.T. Bailey, *Phys. Rev., B1* (1970) 588.
- [408] C. Jagannath and E.S. Koteles, *Solid State Commun.*, 58 (1986) 417.
- [409] M. Schmidt, T.N. Morgan and W. Schairer, *Phys. Rev., B11* (1975) 5002.
- [410] L.D. Laude, F.H. Pollak and M. Cardona, *Phys. Rev., B3* (1971) 2623.
- [411] J.C. Merle, M. Capizzi, P. Fiorini and A. Frova, *Phys. Rev., B17* (1978) 4821.
- [412] G. Davies, L. Canham and E.C. Lightowers, *J. Phys. C: Solid State Phys.*, 17 (1984) L173.
- [413] J. Lee, C. Jagannath, M.O. Vassell and E.S. Koteles, *Phys. Rev., B37* (1988) 4164.
- [414] C. Jagannath, E.S. Koteles, J. Lee, Y.J. Chen, B.S. Elman and J.Y. Chi, *Phys. Rev., B34* (1986) 7027.
- [415] P. Lefebvre, B. Gil, H. Mathieu and R. Planet, *Phys. Rev., B40* (1989) 7802.
- [416] W. Ge, W.D. Schmidt, M.D. Sturge, L.N. Pfeiffer and K.W. West, *J. Luminesc.*, 59 (1994) 163.
- [417] K. Thonke, A. Hangleiter, J. Wagner and R. Sauer, *J. Phys. C: Solid State Phys.*, 18 (1985) L795.
- [418] R.C. Miller, A.C. Gossard and D.A. Kleinman, *Phys. Rev., B32* (1985) 5443.
- [419] J. Feldmann, R. Sattmann, E.O. Göbel, J. Kuhl, J. Hebling, K. Ploog, R. Muralidharan, P. Dawson and C.T. Foxon, *Phys. Rev. Lett.*, 62 (1989) 1892.
- [420] G.R. Fleming, *Chemical Applications of Ultrafast Spectroscopy*, Oxford University Press, New York, 1986.
- [421] C.H. Henry and K. Nassau, *J. Luminesc.*, 1/2 (1970) 299.
- [422] C.H. Henry and K. Nassau, *Phys. Rev., B1* (1970) 1628.
- [423] K.G. Spears, L.E. Cramer and L.D. Hoffland, *Rev. Sci. Instrum.*, 49 (1978) 255.
- [424] D.V. O'Conner and D. Phillips (eds.), *Time-Correlated Single Photon Counting*, Academic Press, London, 1984.
- [425] *Guide to Streak Cameras*, Hamamatsu Photonics K.K., 1994.
- [426] J. Shah, *IEEE J. Quantum Electron.*, QE-24 (1988) 276.
- [427] R.J. Nelson and R.G. Sobers, *J. Appl. Phys.*, 49 (1978) 6103.
- [428] G. Lasher and F. Stern, *Phys. Rev.*, 133 (1964) 553.
- [429] M.L. Timmons, J.A. Hutchby, R.K. Ahrenkiel and D.J. Dunlavy, *Proc. Int. Symp. GaAs and Related Compounds, Atlanta, GA, 1988*, IOP Publishing, Bristol, Inst. Phys. Conf. Ser. No. 96, 1989, p. 289

- [430] C.J. Hwang, *Phys. Rev.*, **B8** (1973) 646.
- [431] G.W. t'Hooft, W.A.J.A. van der Poel, L.W. Molenkamp and C.T. Foxon, in R. Del Sole, A. D'Andrea and A. Lapicciarella (eds.), *Excitons in Confined Systems*, Springer-Verlag, New York, 1988, p. 59.
- [432] E.I. Rashba, *Sov. Phys. Semicond.*, **8** (1975) 807.
- [433] W.J. Rappel, L.F. Feiner and M.F.H. Schuurmans, in R. Del Sole, A. D'Andrea and A. Lapicciarella (eds.), *Excitons in Confined Systems*, Springer-Verlag, New York, 1988, p. 63.
- [434] J. Aaviksoo, I. Reimand, V.V. Rossin and V.V. Travnikov, *Phys. Rev.*, **B45** (1992) 14773.
- [435] D.J. Wolford, G.D. Gilliland, T.F. Kuech, J.A. Bradley and H.P. Hjalmarson, in P. Jiang and H. Zheng (eds.), *Proc. of the 21st International Conference on the Physics of Semiconductors*, World Scientific, Singapore, 1992, p. 241.
- [436] R.B. Hammond and R.N. Silver, *Appl. Phys. Lett.*, **36** (1980) 68.
- [437] J. Feldmann, G. Peter, E.O. Göbel, P. Dawson, K. Moore, C. Foxon and R.J. Elliott, *Phys. Rev. Lett.*, **59** (1987) 2337.
- [438] J. Christen, D. Bimberg, A. Steckenborn and G. Weimann, *Appl. Phys. Lett.*, **44** (1984) 84.
- [439] E.O. Göbel, H. Jung, J. Kuhl and K. Ploog, *Phys. Rev. Lett.*, **51** (1983) 1588.
- [440] V. Srinivas, J. Hrynewicz, Y.J. Chen and C.E.C. Wood, *Phys. Rev.*, **B46** (1992) 10193.
- [441] R. Eccleston, B.F. Feuerbacher, J. Kuhl, W.W. Rühle and K. Ploog, *Phys. Rev.*, **B45** (1992) 11403.
- [442] J.P. Bergman, P.O. Holtz, B. Monemar, M. Sundaram, J.L. Merz and A.C. Gossard, *Optics of Excitons in Confined Systems*, Inst. Phys. Conf. Ser. No. 123, IOP Publishing, Bristol, UK, 1992, p. 73.
- [443] J.E. Fouquet and A.E. Siegman, *Appl. Phys. Lett.*, **46** (1985) 280.
- [444] W. Pickin and J.P.R. David, *Appl. Phys. Lett.*, **56** (1990) 268.
- [445] B. Sermage, B. Deveaud, K. Satzke, F. Clerot, C. Dumas, N. Roy, D.S. Katzer, F. Mollot, R. Planell, M. Berz and J.L. Oudar, *Superlatt. Microstruct.*, **13** (1993) 271.
- [446] B. Deveaud, F. Clerot, N. Roy, K. Satzke, B. Sermage and D.S. Katzer, *Phys. Rev. Lett.*, **67** (1991) 2355.
- [447] L.C. Andreani, A. d'Andrea and R. del Sole, *Phys. Lett.*, **A168** (1992) 451.
- [448] L.C. Andreani, *Solid State Commun.*, **77** (1991) 641.
- [449] A. Vinattieri, J. Shah, T.C. Damen, D.S. Kim, L.N. Pfeiffer and L.J. Sham, *Solid State Commun.*, **88** (1993) 189.
- [450] T.C. Damen, J. Shah, D.Y. Oberli, D.S. Chemla, J.E. Cunningham and J.M. Kuo, *J. Luminesc.*, **45** (1990) 181.
- [451] R. Eccleston, R. Strobel, J. Kuhl and K. Kohler, *Optics of Excitons in Confined Systems*, Inst. Phys. Conf. Ser. No. 123, IOP Publishing, Bristol, UK, 1992, p. 57.
- [452] P.W.M. Blom, P.J. van Hall, C. Smit, J.P. Cuypers and J.H. Wolter, *Phys. Rev. Lett.*, **71** (1993) 3878.
- [453] D. Morris, B. Deveaud, A. Regreny and P. Auvray, *Phys. Rev.*, **B47** (1993) 6819.
- [454] M. Gurioli, J. Martinez-Pastor, M. Coloccia, C. Deparis, B. Chastaingt and J. Massies, *Phys. Rev.*, **B46** (1992) 6922.
- [455] F. Minami, K. Hirata, K. Era, T. Yao and Y. Masumoto, *Phys. Rev.*, **B36** (1987) 2875.
- [456] J. Ihm, *Appl. Phys. Lett.*, **50** (1987) 1068.
- [457] P. Dawson, K.J. Moore, C.T. Foxon, G.W. t'Hooft and R.P.M. van Hal, *J. Appl. Phys.*, **65** (1989) 3606.
- [458] M.D. Sturge, J.L. Mackay, C. Maloney and J.K. Pribram, *J. Appl. Phys.*, **66** (1989) 5639.
- [459] J.F. Angell and M.D. Sturge, *Phys. Rev.*, **B48** (1993) 4650.
- [460] G.D. Gilliland, A. Antonelli, D.J. Wolford, K.K. Bajaj, J. Klem and J.A. Bradley, *Phys. Rev. Lett.*, **71** (1993) 3717.
- [461] L.P. Fu, F.T. Bacalzo, G.D. Gilliland, R. Chen, K.K. Bajaj, J. Klem and D.J. Wolford, *Phys. Rev.*, **B52** (1995) 2682.
- [462] M.V. Klein, M.D. Sturge and E. Cohen, *Phys. Rev.*, **B25** (1982) 4331.
- [463] B. Deveaud, D. Morris, A. Regreny, R. Planell, J.M. Gerard, M.R.X. Barros and P. Becker, *Semicond. Sci. Technol.*, **9** (1994) 722.
- [464] L.P. Fu, F.T. Bacalzo, G.D. Gilliland, R. Chen, K.K. Bajaj and J. Klem, *Phys. Rev.*, **B51** (1995) 17630.
- [465] M. Grundmann, J. Christen, M. Joschko, O. Stier, D. Bimberg and E. Kapon, *Semicond. Sci. Technol.*, **9** (1994) 1939.
- [466] Y. Zhang, M.D. Sturge, K. Kash, B.P. Van der Gaag, A.S. Gozd, L.T. Florez and J.P. Harbison, *J. Luminesc.*, **60/61** (1994) 400.
- [467] D.S. Citrin, *Phys. Rev. Lett.*, **69** (1992) 3393.
- [468] Y. Zhang, M.D. Sturge, K. Kash, B.P. Van der Gaag, A.S. Gozd, L.T. Florez and J.P. Harbison, *Superlatt. Microstruct.*, **17** (1995) 201.
- [469] G. Wang, S. Fafard, D. Leonard, J.E. Bowers, J.L. Merz and P.M. Petroff, *Appl. Phys. Lett.*, **64** (1994) 2815.
- [470] E. Finkman, M.D. Sturge and R. Bhat, *J. Luminesc.*, **35** (1986) 235.
- [471] G.D. Sanders and Y.C. Chang, *Phys. Rev.*, **B28** (1983) 5887.
- [472] T. Steiner and M.L.W. Thewalt, *Solid State Commun.*, **49** (1984) 1121.
- [473] J.P. Bergman, P.O. Holtz, B. Monemar, M. Sundaram, J.L. Merz and A.C. Gossard, *Phys. Rev.*, **B43** (1991) 4765.
- [474] J.P. Bergman, P.O. Holtz, B. Monemar, M. Sundaram, J.L. Merz and A.C. Gossard, in D.J. Wolford, J. Bernholc and E.E. Haller (eds.), *Impurities, Defects and Diffusion in Semiconductors: Bulk and Layered Structures*, Mater. Res. Soc. Symp. Proc., Vol. 163, Materials Research Society, Philadelphia, PA, 1990.
- [475] Q.X. Zhao, P.O. Holtz, C.I. Harris, B. Monemar and E. Veje, *Appl. Phys. Lett.*, **64** (1994) 2721.
- [476] Q.X. Zhao, P.O. Holtz, C.I. Harris, B. Monemar and E. Veje, *Phys. Rev.*, **B50** (1994) 2023.
- [477] D.G. Thomas, J.J. Hopfield and W.M. Augustyniak, *Phys. Rev.*, **B140** (1965) 202.
- [478] H.J. Zeiger, *J. Appl. Phys.*, **35** (1964) 1657.
- [479] M.J. Adams and P.T. Landsberg, in C.H. Goch (ed.), *Gallium Arsenide Lasers*, Wiley-Interscience, London, 1969, p. 5.
- [480] P. Lawaetz, *Phys. Rev.*, **B1** (1971) 3460.
- [481] R. Dingle, *Phys. Rev.*, **184** (1969) 788.

- [482] T. Kamiya and E. Wagner, *J. Appl. Phys.*, **32** (1976) 1928.
- [483] G. Benz and R. Conradt, *Phys. Rev.*, **B16** (1977) 843.
- [484] U. Strauss, W.W. Ruhle and K. Kohler, *Appl. Phys. Lett.*, **62** (1993) 55.
- [485] D.F. Nelson, J.D. Cuthbert, P.J. Dean and D.G. Thomas, *Phys. Rev. Lett.*, **17** (1966) 552.
- [486] W. Schmid, *Phys. Status Solidi B*, **84** (1977) 529.
- [487] J.D. Cuthbert, *J. Luminesc.*, **1/2** (1970) 307.
- [488] J.D. Cuthbert, *Phys. Rev.*, **B1** (1970) 1552.
- [489] A. Haug, *Solid State Commun.*, **25** (1978) 477.
- [490] J. Shah, *Superlatt. Microstruct.*, **6** (1989) 293.
- [491] T. Elsaesser, J. Shah, L. Rota and P. Lugli, *Phys. Rev. Lett.*, **66** (1991) 1757.
- [492] J. Shah, B. Deveaud, T.D. Damen, W.T. Tsang, A.C. Gossard and P. Lugli, *Phys. Rev. Lett.*, **59** (1987) 2222.
- [493] L. Rota, P. Lugli, T. Elsaesser and J. Shah, *Phys. Rev.*, **B47** (1993) 4226.
- [494] D.W. Snoke, W.W. Ruhle, Y.C. Lu and E. Bauser, *Phys. Rev. Lett.*, **68** (1992) 990.
- [495] J.F. Ryan, R.A. Taylor, A.J. Turberfield, A. Maciel, J.M. Worlock, A.C. Gossard and W. Wiegmann, *Phys. Rev. Lett.*, **53** (1984) 1841.
- [496] R.A. Höpfel, J. Shah and A.C. Gossard, *Phys. Rev. Lett.*, **56** (1986) 765.
- [497] Y. Masumoto, S. Shionoya and H. Kawaguchi, *Phys. Rev.*, **B29** (1984) 2324.
- [498] X. Marie, T. Amand, B. Dareys, I. Razdobreev, Y. Shekun, J. Barrau and J.C. Brabant, *Superlatt. Microstruct.*, **12** (1992) 7.
- [499] S. Charbonneau, J.F. Young and P.T. Coleridge, *Phys. Rev.*, **B47** (1993) 1932.
- [500] A.C. Maciel, J.F. Ryan, R. Rinaldi, R. Cingolani, M. Ferrara, U. Marti, D. Martin, F. Morier-Gemoud and F.K. Reinhart, *Semicond. Sci. Technol.*, **9** (1994) 893.
- [501] R.N. Hall, *Phys. Rev.*, **87** (1952) 387; W. Shockley and W.T. Read, Jr., *Phys. Rev.*, **87** (1952) 835.
- [502] R.K. Ahrenkiel, B.M. Keyes and D.J. Dunlavy, *J. Appl. Phys.*, **70** (1991) 225.
- [503] D.J. Wolford, G.D. Gilliland, T.F. Kuech, J.F. Klem, H.P. Hjalmarson, J.A. Bradley, C.F. Tsang and J. Martinsen, *Appl. Phys. Lett.*, **64** (1994) 1416.
- [504] R.J. Nelson, *J. Vac. Sci. Technol.*, **15** (1978) 1475.
- [505] R.J. Nelson and R.G. Sobers, *Appl. Phys. Lett.*, **32** (1978) 761.
- [506] R.K. Ahrenkiel, D.J. Dunlavy, B. Keyes, S.M. Vernon, T.M. Dixon, S.P. Tobin, K.L. Miller and R.E. Hayes, *Appl. Phys. Lett.*, **55** (1989) 1088.
- [507] G.W. tHooft and C. van Opdorp, *J. Appl. Phys.*, **60** (1986) 1065.
- [508] M. Ettenberg and H. Kressel, *J. Appl. Phys.*, **47** (1976) 1538.
- [509] P. Asbeck, *J. Appl. Phys.*, **48** (1977) 820.
- [510] B. Bensaïd, F. Raymond, M. Leroux, C. Verie and B. Fofana, *J. Appl. Phys.*, **66** (1989) 5542.
- [511] A.B. Suchocki, G.D. Gilliland, R.C. Powell, J.M. Bowen and J.C. Walling, *J. Luminesc.*, **37** (1987) 29.
- [512] S.D. Lester, T.S. King and B.G. Streetman, *J. Appl. Phys.*, **63** (1988) 853.
- [513] P.L. Gourley and J.P. Wolfe, *Phys. Rev.*, **B24** (1981) 5970.
- [514] V.D. Kulakovskii, V.B. Timofeev and V.M. Edelshtein, *Zh. Eksp. Teor. Fiz.*, **74** (1978) 372 (*Sov. Phys. JETP*, **47** (1978) 193).
- [515] J. Shah and A.H. Dayem, *Phys. Rev. Lett.*, **37** (1976) 861.
- [516] R. Cingolani, H. Kalt and K. Ploog, *Phys. Rev.*, **B42** (1990) 7655.
- [517] J.J. Hopfield, *J. Phys. Chem. Solids*, **10** (1959) 110.
- [518] M. Zachau, J.A. Kash and W.T. Masselink, *Phys. Rev.*, **B44** (1991) 8403.
- [519] L.J. Sham, *J. Phys. Condens. Matter*, **5** (1993) A51.
- [520] R.J. Seymour and R.R. Alfano, *Appl. Phys. Lett.*, **37** (1980) 231.
- [521] K. Zerrouati, F. Fabre, G. Bacquet, J. Bandet, J. Frandon, G. Lampel and D. Paget, *Phys. Rev.*, **B37** (1988) 1334.
- [522] T.C. Damen, L. Vina, J.E. Cunningham, J. Shah and L.P.J. Sham, *Phys. Rev. Lett.*, **67** (1991) 3432.
- [523] J.M. Gerard, B. Serrage, L. Bergomi and J.Y. Marzin, *Superlatt. Microstruct.*, **8** (1990) 417.
- [524] B. Deveaud, T.C. Damen, J. Shah and C.W. Tu, *Appl. Phys. Lett.*, **51** (1987) 828.
- [525] B. Deveaud, A. Chomette, F. Clerot, P. Auvray, A. Regreny, R. Ferreira and G. Bastard, *Phys. Rev.*, **B42** (1990) 7021.
- [526] K. Fujiwara, H. Katahama, K. Kanamoto, R. Cingolani and K. Ploog, *Phys. Rev.*, **B43** (1991) 13978.
- [527] G. Mayer, B.E. Maile, R. Germann, A. Forchel, *Superlatt. Microstruct.*, **5** (1989) 579.
- [528] H. Mariette, D.J. Wolford and J.A. Bradley, *Phys. Rev.*, **B33** (1986) 8373.
- [529] A.P. Heberle, W.W. Ruhle and K. Ploog, *Phys. Rev. Lett.*, **72** (1994) 3887.
- [530] I.V. Kukushkin, V.I. Falko, R.J. Haug, K. von Klitzing, K. Eberl and K. Totemayer, *Phys. Rev. Lett.*, **72** (1994) 3594.
- [531] A. Alexandrou, J.A. Kash, E.E. Mendez, M. Zachau, J.M. Hong, T. Fukuzawa and Y. Hase, *Phys. Rev.*, **B42** (1990) 9225.
- [532] J.A. Kash, M. Zachau, E.E. Mendez, J.M. Hong and T. Fukuzawa, *Phys. Rev. Lett.*, **66** (1991) 2247.
- [533] Mehmet Sarikaya, *Ultramicroscopy*, **47** (1992) 1.
- [534] J.R. Haynes and W. Shockley, *Phys. Rev.*, **81** (1951) 835.
- [535] J.P. Wolfe, *J. Luminesc.*, **30** (1985) 82.
- [536] A. Forchel, H. Schweizer and G. Mahler, *Phys. Rev. Lett.*, **51** (1983) 501.
- [537] R.A. Höpfel, J. Shah, P.A. Wolff and A.C. Gossard, *Phys. Rev. Lett.*, **56** (1986) 2736.
- [538] G.D. Gilliland, D.J. Wolford, T.F. Kuech and J.A. Bradley, *Appl. Phys. Lett.*, **59** (1991) 216.

- [539] T W Steiner, M L.W. Thewalt, M Maciaszek and R P Bult, *Can J Phys.*, **69** (1991) 333
- [540] W W Ruhle, K Leo and N.M Haegel, *Proc Int Symp GaAs and Related Compounds, Heraklion, Greece, 1987*, Inst. Phys Conf Ser 91, IOP Publishing, Bristol, UK, 1987, p 105.
- [541] Z M Wang, J Windscheif, D J As and W Jantz, *J. Appl Phys.*, **73** (1993) 1430.
- [542] A. Zrenner, L.V. Butov, M Hagn, G. Abstreiter, G. Bohm and G. Weimann, *Phys. Rev. Lett.*, **72** (1994) 3382
- [543] M.A. Tamor and J.P. Wolfe, *Phys. Rev. B26* (1982) 5743
- [544] M.A. Tamor and J.P. Wolfe, *Phys. Rev. Lett.*, **44** (1980) 1703
- [545] H. Hillmer, S. Hansmann, A. Forchel, M. Morohashi, E. Lopez, H.P. Meier and K. Ploog, *Appl. Phys. Lett.*, **53** (1988) 1937.
- [546] H. Hillmer, A. Forchel, S. Hansmann, M. Morohashi, E. Lopez, H.P. Meier and K. Ploog, *Phys. Rev. B39* (1989) 10901.
- [547] H. Hillmer, A. Forchel, R. Sauer and C.W. Tu, *Phys. Rev. B42* (1990) 3220.
- [548] Y. Takahashi, K. Muraki, S. Fukatsu, S.S. Kano, Y. Shiraki and R. Ito, *Jpn. J. Appl. Phys.*, **32** (1993) 5586
- [549] T. Wilson, in T. Wilson (ed.), *Confocal Microscopy*, Academic Press, San Diego, CA, 1990, pp. 93–142.
- [550] Y Fong and S.R.J Brueck, *Appl. Phys. Lett.*, **61** (1992) 1332.
- [551] T. Wilson, in T. Wilson (ed.), *Confocal Microscopy*, Academic Press, San Diego, CA, 1990, pp. 1–64
- [552] G.P. Collins, *Physics Today*, American Institute of Physics, Woodbury, NY, May 1994, p. 17.
- [553] E.A. Ash and G. Nichols, *Nature*, **237** (1972) 510.
- [554] M. Isaacson, J. Cline and H. Barshatzky, *Ultramicroscopy*, **47** (1992) 15
- [555] E. Betzig and J.K. Trautman, *Science*, **257** (1992) 189
- [556] U Ch. Fischer, U.T. Durig and D.W. Pohl, *Scanning Microsc.*, **3** (1989) 1
- [557] J. Mertz, M. Hipp, J. Mlynek and O. Marti, *Appl. Phys. Lett.*, **64** (1994) 2338
- [558] R.D. Grober, T.D. Harris, J.K. Trautman and E. Betzig, *Rev. Sci. Instrum.*, **65** (1994) 626.
- [559] D. Courjon, C. Bannier, C. Girard and J.M. Vigoureux, *Ann. Phys.*, **2** (1993) 149.
- [560] N.F. Van Hulst, M.H.P. Moers and B. Bolger, *J. Microsc.*, **171** (1993) 95.
- [561] L.M. Smith, J.S. Preston, J.P. Wolfe, D.R. Wake, J. Klem, T. Henderson and H. Morkoc, *Phys. Rev. B39* (1989) 1862.
- [562] L.M. Smith, D.R. Wake, J.P. Wolfe, D. Levi, M.V. Klein, J. Klem, T. Henderson and H. Morkoc, *Phys. Rev. B38* (1988) 5788.
- [563] D.R. Wake, H.W. Yoon, J.S. Preston, H. Morkoc and J.P. Wolfe, in C.B. Harris, E.P. Ippen, G.A. Mourou and A.H. Zewail (eds.), *Ultrafast Phenomena VII*, Springer Series in Chemical Physics, Vol 53, Springer–Verlag, Berlin, 1992, p. 262.
- [564] H.W. Yoon, D.R. Wake, J.P. Wolfe and H. Morkoc, *Phys. Rev. B46* (1992) 13461.
- [565] A. Olsson, D.J. Erskine, Z.Y. Xu, A. Schremer and C.L. Tang, *Appl. Phys. Lett.*, **41** (1982) 659.
- [566] H. Hillmer, A. Forchel, T. Kuhn, G. Mahler and H.P. Meier, *Phys. Rev. B43* (1991) 13992.
- [567] T. Amand, J. Barrau, X. Marie, N. Lauret, B. Dareys, M. Brousseau and F. Laruelle, *Phys. Rev. B47* (1993) 7155.
- [568] A. Nakamura, K. Fujiwara, Y. Tokuda, T. Nakayama and M. Hirai, *Phys. Rev. B34* (1986) 9019
- [569] A. Nakamura, K. Fujiwara, Y. Tokuda, T. Nakayama and M. Hirai, *J. Luminesc.*, **40/41** (1988) 719.
- [570] D.J. Wolford, G.D. Gilliland, T.F. Kuech, J.A. Bradley and H.P. Hjalmarson, *Phys. Rev. B47* (1993) 15601.
- [571] L.M. Smith, D.J. Wolford, J. Martinsen, R. Venkatasubramanian and S.K. Ghandhi, *J. Vac. Sci. Technol.*, **B8** (1990) 787.
- [572] K.M. Romanek, H. Nather, J. Fischer and E.O. Göbel, *J. Luminesc.*, **24/25** (1981) 585.
- [573] G.D. Gilliland, D.J. Wolford, J.A. Bradley and T.F. Kuech, unpublished work.
- [574] A. Forchel, B. Laurich, H. Hillmer, G. Tränkle and M. Pilkuhn, *J. Luminesc.*, **30** (1985) 67.
- [575] D.J. Wolford, G.D. Gilliland, T.F. Kuech, J.A. Bradley and H.P. Hjalmarson, *Inst. Phys. Conf. Ser.*, **120** (1992) 271.
- [576] G.D. Gilliland, D.J. Wolford, H.P. Hjalmarson, M.S. Petrovic, J. Klem, T.F. Kuech, G.A. Northrop and J.A. Bradley, *Acta Phys. Polonica A*, **84** (1993) 409, Published by Polish Academy of Sciences, Institute of Physics, Warsaw, Poland. *Proc. of the XXII Int. School of Semiconducting Compounds, Jaszowiec, 1993*
- [577] D.P. Trauernicht and J.P. Wolfe, *Phys. Rev. B33* (1986) 8506
- [578] G.D. Gilliland, D.J. Wolford, G.A. Northrop, M.S. Petrovic, T.F. Kuech and J.A. Bradley, *J. Vac. Sci. Technol.*, **B10** (1992) 1959.
- [579] G.D. Gilliland, D.J. Wolford, J.A. Bradley, J. Klem and M. Jaros, *J. Vac. Sci. Technol.*, **B11** (1993) 1647.
- [580] M. Greenstein and J.P. Wolfe, *Phys. Rev. Lett.*, **41** (1978) 715
- [581] M.A. Tamor and J.P. Wolfe, *Phys. Rev. B21* (1980) 739
- [582] Z.M. Wang, D.J. As, J. Windscheif, K.H. Bachem and W. Jantz, *Appl. Phys. Lett.*, **60** (1992) 1609.
- [583] H.F. Hess, E. Betzig, T.D. Harris, L.N. Pfeiffer and K.W. West, *Science*, **264** (1994) 1740.
- [584] K. Brunner, G. Abstreiter, G. Bohm, G. Tränkle and G. Weimann, *Appl. Phys. Lett.*, **64** (1994) 3320
- [585] R.D. Grober, T.D. Harris, J.K. Trautman, E. Betzig, W. Wegscheider, L. Pfeiffer and K. West, *Appl. Phys. Lett.*, **64** (1994) 1421.
- [586] J. Christen, M. Grundmann and D. Birnberg, *J. Vac. Sci. Technol.*, **B9** (1991) 2358
- [587] D. Birnberg, J. Christen, T. Fukunaga, H. Nakashima, D.E. Mars and J.N. Miller, *J. Vac. Sci. Technol.*, **B5** (1987) 1191.
- [588] P. Renaud and S.F. Alvarado, *Phys. Rev. B44* (1991) 6340
- [589] L. Schultheis, J. Kuhl, A. Honold and C.W. Tu, *Phys. Rev. Lett.*, **57** (1986) 1797.
- [590] K. Leo, E.O. Göbel, T.C. Damen, J. Shah, S. Schmitt-Rink, W. Schafer, J.F. Müller, K. Kohler and P. Ganser, *Phys. Rev. B44* (1991) 5726
- [591] J. Hegarty and M.D. Sturge, *J. Opt. Soc. Am. B2* (1985) 1143.
- [592] M.A. Mycek, S. Weiss, J.Y. Bigot, S. Schmitt-Rink, D.S. Chemla and W. Schaefer, *Appl. Phys. Lett.*, **60** (1992) 2666
- [593] C.J. Summers, R. Dingle and D.E. Hill, *Phys. Rev. B1* (1970) 1603